C 55.2 : C 61/2/980

PENNSYLVANIA STATE UNIVERSITY
APR 29 1981
DOCUMENTS COLLECTION

Proceedings of the Fifth Annual Climate Diagnostics Workshop

Joint Institute for the Study of the
Atmosphere and Ocean
University of Washington
Seattle, Washington

October 22-24, 1980

U.S. DEPARTMENT OF COMMERCE
National Oceanic and Atmospheric Administration

Proceedings of the Fifth Annual Climate Diagnostics Workshop

Held at the

Joint Institute for the Study of the
Atmosphere and Ocean
University of Washington
Seattle, Washington

October 22-24, 1980

March 1981

U. S. DEPARTMENT OF COMMERCE
Malcolm Baldrige, Secretary

National Oceanic and Atmospheric Administration
James P. Walsh, Acting Administrator

U. S. Depository Copy

Preface

On behalf of NOAA's Climate Analysis Center, I wish to thank Prof. Mike Wallace, Director of the Joint Institute for the Study of the Atmosphere and Ocean, for hosting this Fifth Annual Climate Diagnostics Workshop at the University of Washington. The efforts expended by him and Ingrid Quertermous in making the excellent local arrangements for the Workshop are much appreciated. Thanks are also due John Horel, Harry Edmon, Carl Youngblut, and Keith Ronnholm for providing valuable support at Seattle; Eugene Rasmusson, Donald Gilman, and Mike Wallace for aiding me in organizing the program; Luke Mannello for preparation of these Proceedings for publication; and Norma Jaxel for her extensive help throughout the various stages of organizing the Workshop and assistance with these Proceedings. I am also indebted to Mike Wallace, Richard Reed, Dennis Hartmann, William Sprigg, and Donald Gilman for effective chairing of Workshop sessions. Finally, I thank all of the participants for their contributions to a very full three days of informative presentations and discussions.

As in the four preceding years, these Proceedings are designed to provide synopses of the presentations at the Workshop. For the most part, papers are arranged in the order of scheduled presentation. One paper not given at the Workshop is included -- a study of droughts in northeast Brazil by Moura and Shukla.

The Workshop began with a review of the past year's climate fluctuations (Session 1). This was followed by more general studies of variations in the large scale circulation (Session 2). Session 3 dealt with data and methods for monitoring snow and ice, water vapor, and volcanic aerosols. Sessions 4 and 5 concentrated on the second major topic of the Workshop this year -- large scale sea-air interactions with principal emphasis in Session 4 on the equatorial Pacific, Southern Oscillation, El Niño, and related phenomena. Session 6 dealt with modeling results, one of which (Miyakoda et al.) involved promising GCM predictions for January 1977. Finally, statistical prediction and verification results were presented in Session 7.

Jay S. Winston
January 1981

List of Participants
Climate Diagnostics Workshop
October 22-24, 1980

Julian Adem	Lamont-Doherty Geological Observatory, Columbia Univ.
Bruce R. Barkstrom	NASA/Langley
Timothy P. Barnett	Scripps Institution of Oceanography, U. of Calif.
Mary Batteen	Oregon State University
Craig Berg	NOAA/NESS/ESG
Kenneth H. Bergman	National Science Foundation
A. Berroir	Univ. of Paris, Laboratoire de Meteorologie Dynamique
Maurice L. Blackmon	NCAR
Jerome B. Blechman	University of Wisconsin
George J. Boer	Canadian Climate Centre, Atmospheric Environment Serv.
Tom Boettge	NCAR
V. G. Boldyrev	USSR State Committee for Hydrometeorology and Control of the Natural Environment, Moscow
Ye. P. Borisenkov	Main Geophysical Observatory, Leningrad
Reid A. Bryson	University of Wisconsin
R. Caverly	NOAA/ERL/GFDL
Chih-Pei Chang	U. S. Naval Postgraduate School
P. S. Chu	University of Wisconsin
Philip F. Clapp	NOAA/NWS/CAC
Nathan E. Clark	Scripps Institution of Oceanography, U. of Calif.
Robert R. Dickson	NOAA/NWS/CAC
Gerald J. Dittberner	USAF/ETAC/DNC
William L. Donn	Lamont-Doherty Geological Observatory, Columbia Univ.
Arthur V. Douglas	Scripps Institution of Oceanography, U. of Calif.
Yves Durocher	Canadian Climate Centre, Atmospheric Environment Serv.
Harold J. Edmon, Jr.	University of Washington
Edward S. Epstein	NOAA/NCPO
Carl O. Erickson	NOAA/NWS/CAC
Steven K. Esbensen	Oregon State University
Inez Fung	Goddard Institute for Space Studies
Joyce Gavin	Lamont-Doherty Geological Observatory, Columbia Univ.
Donald L. Gilman	NOAA/NWS/CAC
Brian M. Goodman	University of Wisconsin
William Grady	Oregon State University
Arnold Gruber	NOAA/NESS/MSL
David Halpern	NOAA/ERL/PMEL
Young-June Han	Oregon State University
Kirby J. Hanson	NOAA/ERL/GMCC
Robert P. Harnack	Rutgers University
Edwin F. Harrison	NASA/Langley
Dennis L. Hartmann	University of Washington
Stanley Hayes	NOAA/ERL/PMEL
Richard R. Heim, Jr.	University of Nebraska
John D. Horel	University of Washington
V. A. Ivanov	Main Geophysical Observatory, Leningrad
R. Kandel	Service d'Aeronomie, CNRS
Y. Ye. Kazakov	USSR State Committee for Hydrometeorology and Control of the Natural Environment, Moscow

Richard A. Keen	CIRES/University of Colorado
Siri Jodha Singh Khalsa	CIRES/University of Colorado
Jeong-Woo Kim	Oregon State University
Arthur F. Krueger	NOAA/NWS/CAC
Ernest C. Kung	University of Missouri
G. P. Kurbatkin	USSR National Academy of Sciences, Novosibirsk
Yochanan Kushnir	Oregon State University
Peter J. Lamb	Illinois State Water Survey
K. M. Lau	U. S. Naval Postgraduate School
Sheng-Wei Lee	Oregon State University
Cho-Teng Liu	University of Washington
Paul Y.T. Louie	Canadian Climate Centre, Atmospheric Environment Serv.
James P. McGuirk	Texas A&M
Jerry Meehl	NCAR
L. S. Meeres	Atmospheric Environment Service/Canada
Alvin J. Miller	NOAA/NWS/CAC
John A. Mirabito	NOAA/RD
Takio Murakami	University of Hawaii
Jerome Namias	Scripps Institution of Oceanography, U. of Calif.
Alfredo R. Navato	Massachusetts Inst. of Technology
Bette L. Otto-Bliesner	University of Wisconsin
Stephen Pazan	Scripps Institution of Oceanography, U. of Calif.
Rudolph W. Preisendorfer	NOAA/ERL/PMEL
Patricia Pullen	NOAA/ERL/PMEL
William H. Quinn	Oregon State University
Roderick S. Quiroz	NOAA/NWS/CAC
Ehrhard Raschke	University of Cologne
Richard Reed	University of Washington
Keith Ronnholm	University of Washington
Richard D. Rosen	Environmental Research & Technology, Inc.
Garry Schaefer	Atmospheric Environment Service/Canada
Gunter R. Seckel	NOAA/NMFS/PEG
William A. Sprigg	NOAA/NCPO
Leonard Steinberg	Canadian Climate Centre, Atmospheric Environment Serv.
Ellen J. Steiner	CIRES/University of Colorado
V. G. Susloparov	USSR State Committee for Science & Technology, Leningrad
Harry van Loon	NCAR
A. James Wagner	NOAA/NWS/CAC
John M. Wallace	University of Washington
Bryan C. Weare	University of California
R. B. Wearn	University of Washington
Peter Webster	CSIRO, Australia
Klaus Weickmann	University of Wisconsin
Jay S. Winston	NOAA/NWS/CAC
Klaus Wyrtki	University of Hawaii
Carl Youngblut	JISAO, University of Washington

TABLE OF CONTENTS

Page

Preface iii

List of Participants iv

Session 1: Review of Climate Fluctuations of the Year, September 1979 - August 1980.

The circulation and weather of Fall 1979 and Winter 1979-80 . . . . A. James Wagner 1

The circulation and weather of Spring and Summer 1980 . . . . Robert R. Dickson 8

Canadian climate extremes and impacts for the period September 1979 to August 1980 . . . . Yves Durocher 21

Special aspects of the long-wave and zonal mean structure from Winter to Summer 1980 . . . . R. S. Quiroz 29

The heavy California winter rains of 1979-80 as a manifestation of macroscale air/sea coupling . . . . Jerome Namias 35

Snow and ice in 1979 - 1980: A global overview . . . . G. Kukla and J. Gavin 51

The tropical circulation during 1980 and its relation to that of recent years . . . . Arthur F. Krueger 59

Atlantic and eastern Pacific tropical cyclones in 1980 and some relations with the large-scale circulation . . . . Carl O. Erickson 70

Session 2: Variations in the Large Scale Circulation.

A rotated principal component analysis of the interannual variability of the 500 mb height field . . . . John D. Horel 80

Time evolution of teleconnection patterns . . . . Harold J. Edmon, Jr. 85

Low frequency circulation modes as revealed by eigenvector analysis of the 250 mb and 850 mb wind fields . . . . Klaus M. Weickmann and John E. Kutzbach 93

Orographic influence of the Rocky Mountains on the winter circulation over the contiguous United States. Part I: Large-Scale Aspects . . . . Steven W. Lyons and Takio Murakami 105

Interannual variability of vacillating planetary-scale waves . . . . James P. McGuirk 112

Interannual climatic anomalies: Do they propagate? . . . . W. H. Quinn, S. K. Esbensen, and D. B. Enfield 123

Session 3: Monitoring of Snow and Ice, Water Vapor, and Volcanic Aerosols.

Page

Digitization of the NOAA/NESS continental snow cover data base . . . . Michael Matson and Marylin S. Varnadore 138

Normals of monthly surface Northern Hemisphere albedo . . . . William L. Donn and Julian Adem 144

The Air Force operational global snow-ice data set as a possible source for studies of short-term climate fluctuations . . . . Philip F. Clapp and Thomas H. Carpenter 153

Application of near real-time water budgets in monitoring climate related events . . . . P. Y. T. Louie and W. I. Pugsley 158

Modeling mean annual stratospheric aerosol loading in the Northern Hemisphere due to large volcanic activity . . . . . Brian M. Goodman 167

Session 4: The Southern Oscillation, El Niño, and Related Phenomena

The Southern Oscillation and global anomalies in December, January, February . . . . Harry van Loon 176

Fluctuations in mid and upper tropospheric flow associated with the Southern Oscillation . . . . P. A. Arkin, W.-Y. Chen, and E. M. Rasmusson 180

El Niño and variations in the atmosphere over the tropical Pacific Ocean . . . . Bryan C. Weare 190

Correlation between the easterly wind stress and the zonal sea surface temperature variance in the eastern tropical Pacific . . . . Cho-Teng Liu 196

Pacific trade wind fluctuations and the Southern Oscillation index . . . . Stephen Pazan and Gary Meyers 200

Comparison of four equatorial wind indices over the Pacific and El Niño outlook for 1981 . . . . Klaus Wyrtki 211

Synoptic processes over the South Pacific Ocean during years of contrasting equatorial circulation and SST anomalies . . . . Richard A. Keen 219

An analysis of seasonal trade wind divergence in the Pacific and its relationship to circulation in higher latitudes . . . Robert Harnack 226

On the influence of warm equatorial conditions in the Central Pacific on climatic patterns in the United States: 1977-80 . . . . Arthur V. Douglas 239

The response of the atmospheric boundary layer to sea surface temperature anomalies . . . . Siri Jodha Singh Khalsa 251

Session 5: Large Scale Sea Air Interaction

Page

Droughts in northeast Brazil . . . . A. D. Moura and J. Shukla 257

Relation of ocean currents to wind in the Southern Hemisphere . . . . Richard B. Wearn, Jr. and D. James Baker, Jr. 264

A first estimate of the annual variation of Atlantic Ocean heat transport . . . . Peter J. Lamb 268

A comparison of winds and SST's from four Pacific marine data sets . . . . Ellen Steiner 272

Computation of the seasonal cycle of the surface heat flux over the global ocean . . . . Y.-J. Han, S.-W. Lee, S. Esbensen and Y. Kushnir 279

Large scale heat exchange across the air-sea interface in the North Pacific Ocean during recent fall and winter seasons . . . . Nathan E. Clark 285

On the influence of Pacific Ocean temperatures on atmospheric CO_2 concentrations at Ocean Station P . . . . Kirby J. Hanson, James T. Peterson, Jerome Namias, Robert Born, and C. S. Wong 292

Session 6: Modeling and Prediction

Diagnostic equations in pressure coordinates including the effects of variable surface pressure . . . . G. J. Boer 301

Seasonal simulation experiments with a low-order general circulation model . . . . Bette L. Otto-Bliesner and David D. Houghton 307

Preliminary analysis of the angular momentum balance in the O.S.U. two-level atmospheric general and circulation model . . . . J.-W. Kim and W. Grady 314

Comparison of the earth-atmosphere radiation budget and albedo determined by a climate model and by satellite observations . . . . Julian Adem and William L. Donn 319

Studies of the radiation budget and cloudiness in a circulation model and by satellite data . . . . E. Raschke, A. Hense, H.-J. Preuss, E. Ruprecht, and F. Geleyn 328

Simulation of a blocking event in January 1977 . . . . K. Miyakoda, T. Gordon, R. Caverly, W. Stern, J. Sirutis, and W. Bourke 331

Some preliminary thoughts on comparing General Circulation Models with observed data fields . . . R. W. Preisendorfer and T. P. Barnett 341

Atmospheric Response to Sea Surface Temperature Anomalies . . . . Peter J. Webster 345

Session 7: Prediction Methods

Page

Measuring skill in climate model forecasts . . . . Gerald J. Dittberner 348

On the inherent superiority of the persister in forecasting Markovian weather patterns . . . . Rudolph W. Preisendorfer 354

An experimental short-term climate forecasting procedure for U.S. winter temperatures and its verification . . . . . Alfredo R. Navato 360

Multi-regression approach in the seasonal range forecasting with antecedent patterns of the large-scale circulation . . . . Ernest C. Kung 364

Application of seasonally nonstationary linear prediction models . . . . T. P. Barnett 368

Some diagnostic results and experimental forecasts using the ARIMA Procedure . . . . Leonard Steinberg 376

USAFETAC sea level pressure model seasonal outlook for the past year . . . . James G. Schofield 380

Long range precipitation forecasting with a new UW model . . . . Jerome B. Blechman and Reid A. Bryson 384

The circulation and weather of Fall 1979 and Winter 1979-80

A. James Wagner
Climate Analysis Center
NMC/NWS/NOAA
Washington, D. C. 20233

1. FALL 1979

The 700 mb circulation was characterized by faster than normal westerlies at middle latitudes, especially over the oceans where stronger than normal northward-displaced subtropical highs coexisted with deep lows extending from northeastern Siberia to the Aleutians and also over the North Atlantic. The positive anomalies associated with the subtropical highs were about two and one-half standard deviations from the 1948-1970 normal height. At high latitudes, there was some blocking in evidence with an area of positive height anomaly over the Polar Basin associated with the northern portions of ridges over northwestern Canada and central Asia. The generally zonal circulation was most amplified over North America, where downstream from the northwestern Canadian ridge a deeper than normal trough extended southwestward from the eastern shore of Hudson Bay to the southern Great Plains (Fig. 1A).

Even though the moderately amplified pattern over North America might have indicated a substantial area of below normal temperatures in the middle of the country, there were no extensive areas of unusually cold weather for the fall as a whole (Fig. 1B). Most of the United States had near or slightly above normal temperatures, with the warmest weather relative to normal in the West. There were sharp contrasts in the precipitation pattern. Substantially heavier than normal totals fell over most of the East and South as far inland as the lower Mississippi and Ohio Valleys (Fig. 1C), due mainly to the passage of two hurricanes and an unnamed tropical disturbance during September. Heavy precipitation over the north-central states was due mainly to late fall storms, while other areas of the Southwest and the northern and southern Great Plains received less than half their normal totals.

September had patterns of circulation, temperature and precipitation similar to those for the whole fall. In sharp contrast to the intense tropical downpours over the southeastern third of the country, one of the driest Septembers on record was observed at many cities in the upper Midwest and Great Lakes area.

Unusually fast westerlies during October led to changeable and at times unusual weather. A record late-season heat wave with temperatures going over 100°F at some localities in Texas lasted much of the first half of the month, while a record early season snowstorm struck an area from the central Appalachians to southern New England on October 10th, doing much damage to deciduous trees still in full leaf.

During November an amplified ridge over western Canada drove colder than normal air into the West, following several months of above normal temperatures. The strong high prevailing over the western Atlantic brought increased southerly flow to the Atlantic Coast States, giving New York City's Central Park Observatory its warmest November in over 100 years of records.

2. WINTER 1979-1980

The 700 mb circulation became more amplified, and the westerlies moved considerably farther south during winter, especially over the Pacific, where a large negative anomaly centered at 40°N, 160°W covered most of the Pacific Ocean Basin north of 20°N. The central value of 95 m below normal was more than two standard deviations from the 1948-70 mean. Anomalies associated with the ridge over Canada and the North Atlantic low were not exceptional, being only a little over one standard deviation (Fig. 2A).

The lack of either a strong anomalous component of cold advection from the Arctic or depressed westerlies over the United States resulted in a generally moderate winter over most of the country. The temperature averaged within 4°F of normal at most locations and there were none of the cold extremes of the past three winters (Fig. 2B). This is perhaps somewhat surprising, as the severely cold winters of 1976-77 and 1977-78 had large, intense negative height anomalies over the central North Pacific, similar to this winter. Different circulation patterns over North America and the lack of a strong transarctic ridge extending from Canada toward Siberia to advect polar air southward into the United States were probably the main factors for the generally mild winter in 1979-80. The anomalously strong ridge over Canada was associated mainly with relatively mild air of Pacific origin.

Precipitation was less than normal over most areas east of the Great Plains, but much of the West and Southwest had substantially more than the normal amount (Fig. 2C). The heaviest precipitation in these areas fell in connection with several storms mainly in January and February, that crossed the Pacific at relatively low latitudes, bringing copious amounts of tropical moisture with them into the southwestern United States.

The mild and dry characteristic of the winter was most in evidence during December when fast zonal flow and above normal 700 mb heights prevailed over the entire United States and southern Canada, effectively shutting out Arctic air masses. Temperatures averaged as much as 10°F above normal in the Northern Great Plains and more than 6°F above normal over portions of the Great Lakes States and Northeast. A paucity of storms kept precipitation well under normal across much of the country. Due to the combination of unusually mild and dry weather, a number of cities from the northern Mississippi Valley eastward to New England had record or near-record light December snowfall totals.

During January, the westerlies began to move southward, especially over the Pacific, and strong height rises occurred at high latitudes. Precipitation increased dramatically over the United States, especially over the southern and central Plateau where a number of locations reported as much as three times the normal amount or had a near record wet January. Temperatures remained above normal over most of the country, but colder than normal conditions prevailed over the Northwest and portions of the Rocky Mountains and high plains. Continued mild and dry weather over the Northeast again led to several more record and near-record light monthly snowfall totals.

Not until the end of January, when a strong full-latitude ridge amplified over the eastern Pacific, did extensive Arctic air penetrate the United States. It was also at this time that the first major Pacific storm struck southern California with heavy rains. Although there was a break during early February, several storms struck in rapid succession later in the month causing extensive flooding, mudslides and damage to crops. Precipitation continued to be much less than normal during February over much of the interior of the South and the Northeast.

The coldest weather of the winter in the East occurred during February, which averaged as much as 8°F below normal over the Ohio Valley and 6°F below normal over portions of the South Atlantic Coast. This latter area was paralyzed by two record heavy snowstorms, the first in February and the second in early March at the conclusion of the amplified circulation regime. Norfolk, VA and Elizabeth City, NC had seasonal snowfall totals greater than most eastern locations as far north as Maine during 1979-80.

FIGURES

Fig. 1(A) Mean 700 mb contours (solid) in dekameters and departures from normal (dashed) in meters, (B) departure from normal of average surface temperature (°F), and (C) percentage of normal precipitation for fall (September, October and November 1979).

Fig. 2. As in Fig. 1, except for winter (December 1979) and January and February 1980.

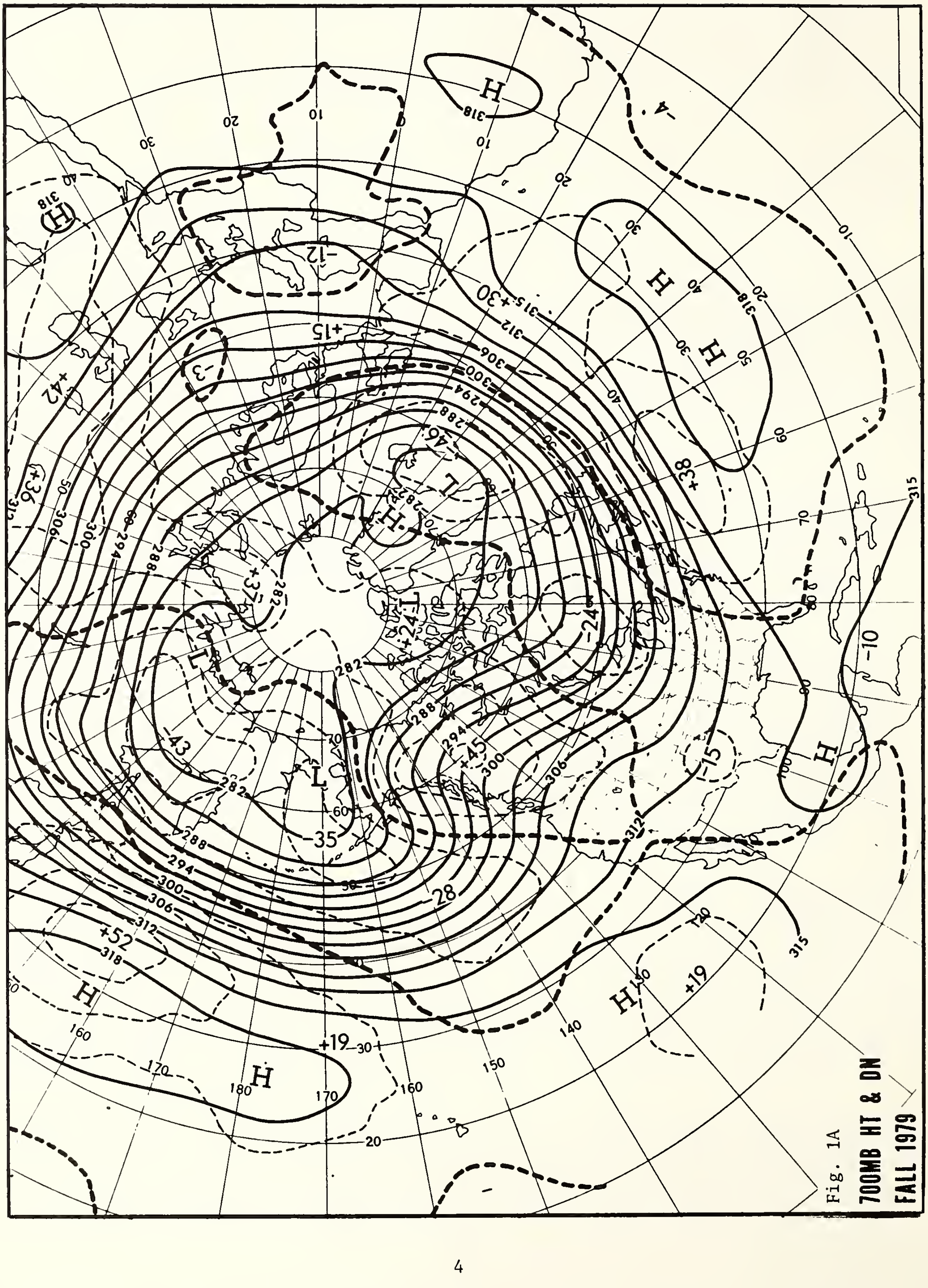

Fig. 1A
700MB HT & DN
FALL 1979

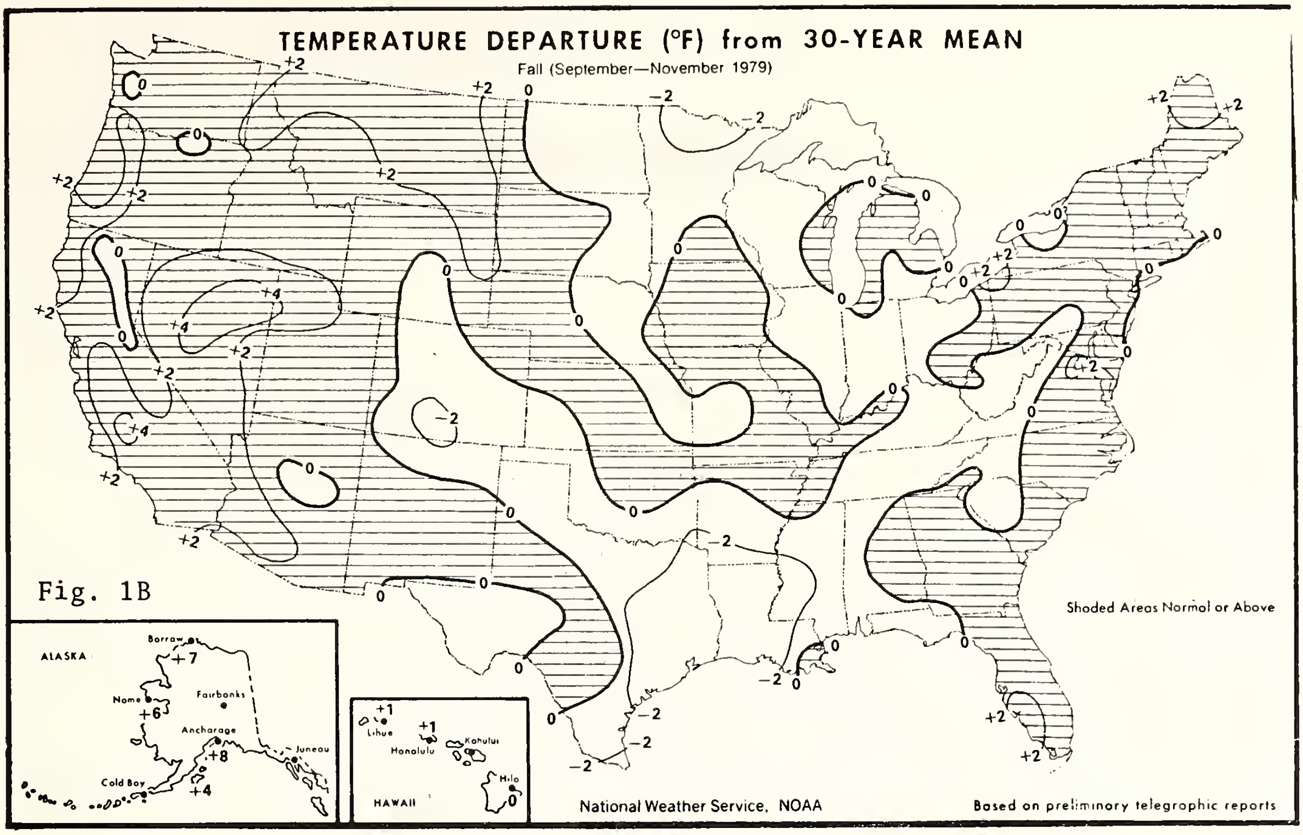
TEMPERATURE DEPARTURE (°F) from 30-YEAR MEAN
Fall (September—November 1979)
Shaded Areas Normal or Above
ALASKA
Barrow +7
Nome +6
Fairbanks
Anchorage +8
Juneau
Cold Bay +4
HAWAII
Lihue +1
Honolulu +1
Kahului
Hilo 0
National Weather Service, NOAA
Based on preliminary telegraphic reports

Fig. 1B

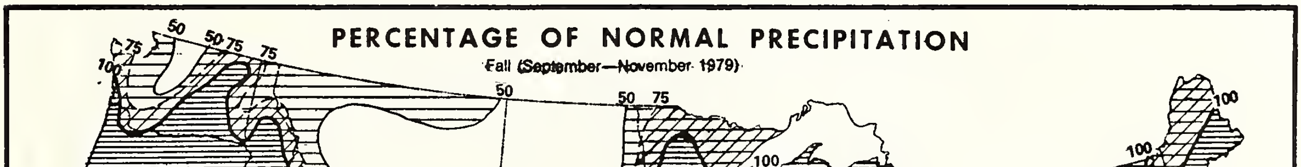
PERCENTAGE OF NORMAL PRECIPITATION
Fall (September—November 1979)
SCALE OF SHADES
Under 50 Percent
50 to 75
75 to 100
100 to 150
Over 150
ALASKA
Barrow 60
Nome 178
Fairbanks
Anchorage 167
Juneau
Kodiak 148
Cold Bay
HAWAII
Lihue 71
Honolulu 29
Kahului
Hilo 94
National Weather Service, NOAA
Based on preliminary telegraphic reports

Fig. 1C

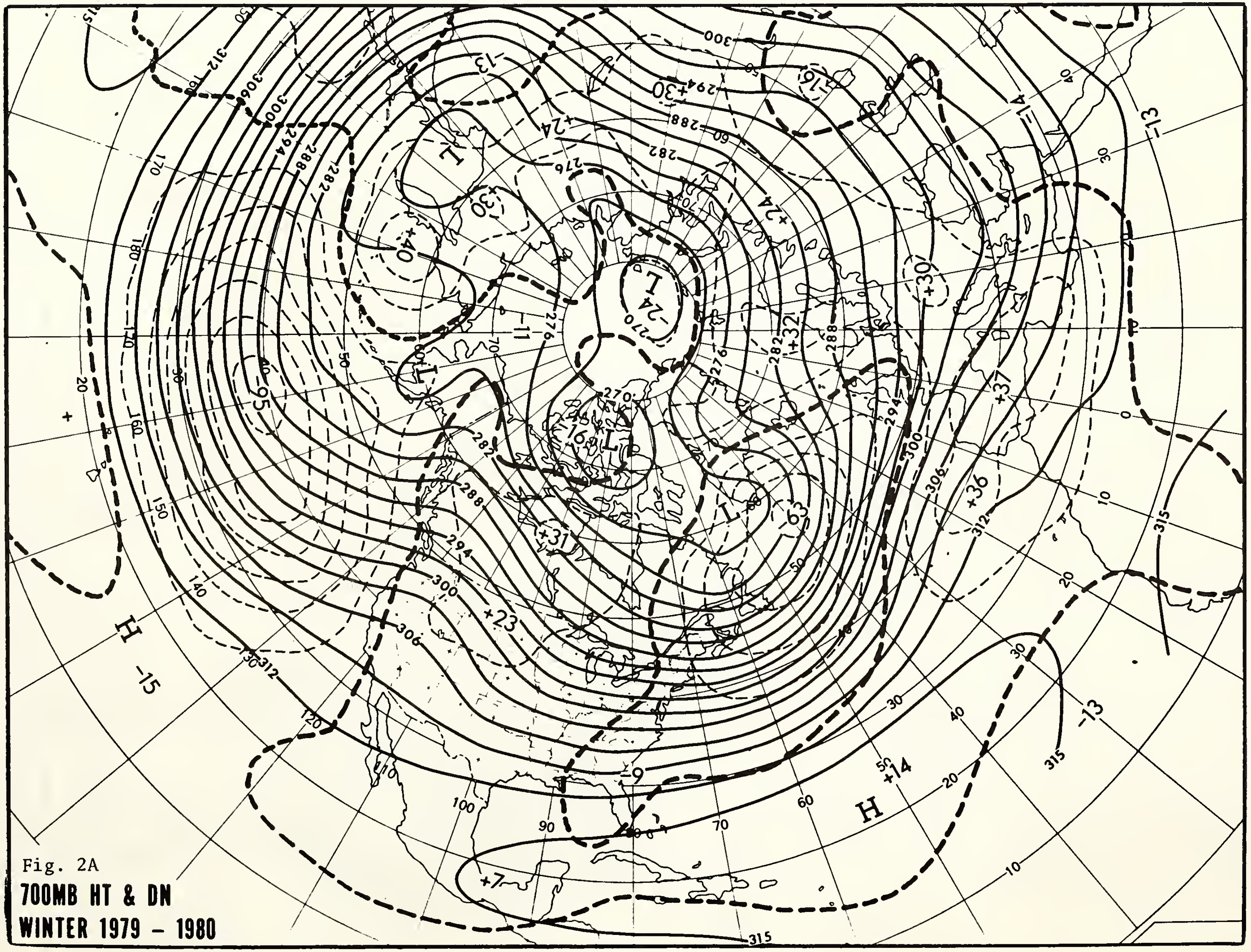

Fig. 2A
700MB HT & DN
WINTER 1979 - 1980

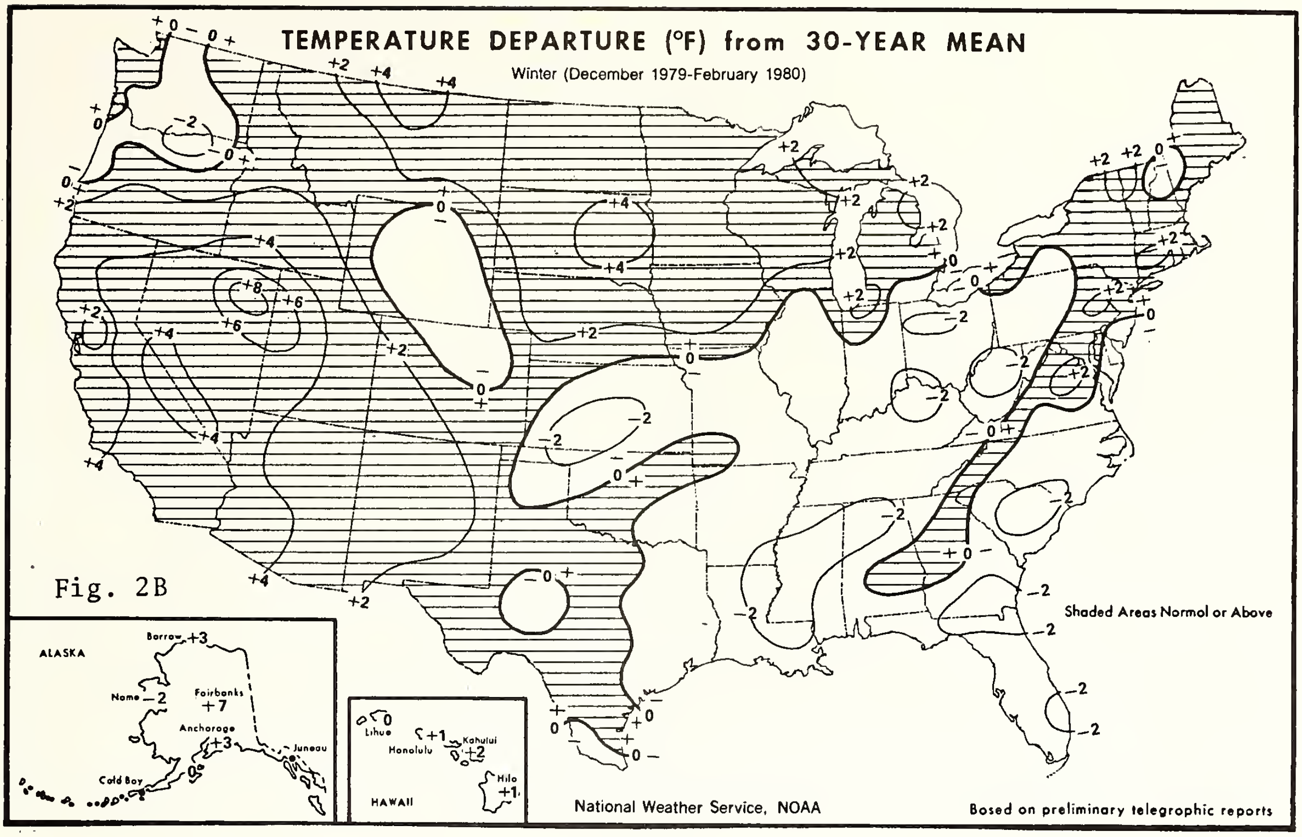
TEMPERATURE DEPARTURE (°F) from 30-YEAR MEAN
Winter (December 1979-February 1980)
Shaded Areas Normal or Above
National Weather Service, NOAA
Based on preliminary telegraphic reports
ALASKA
Barrow +3
Nome -2
Fairbanks +7
Anchorage +3
Juneau
Cold Bay 0
HAWAII
Lihue 0
Honolulu +1
Kahului +2
Hilo +1

Fig. 2B

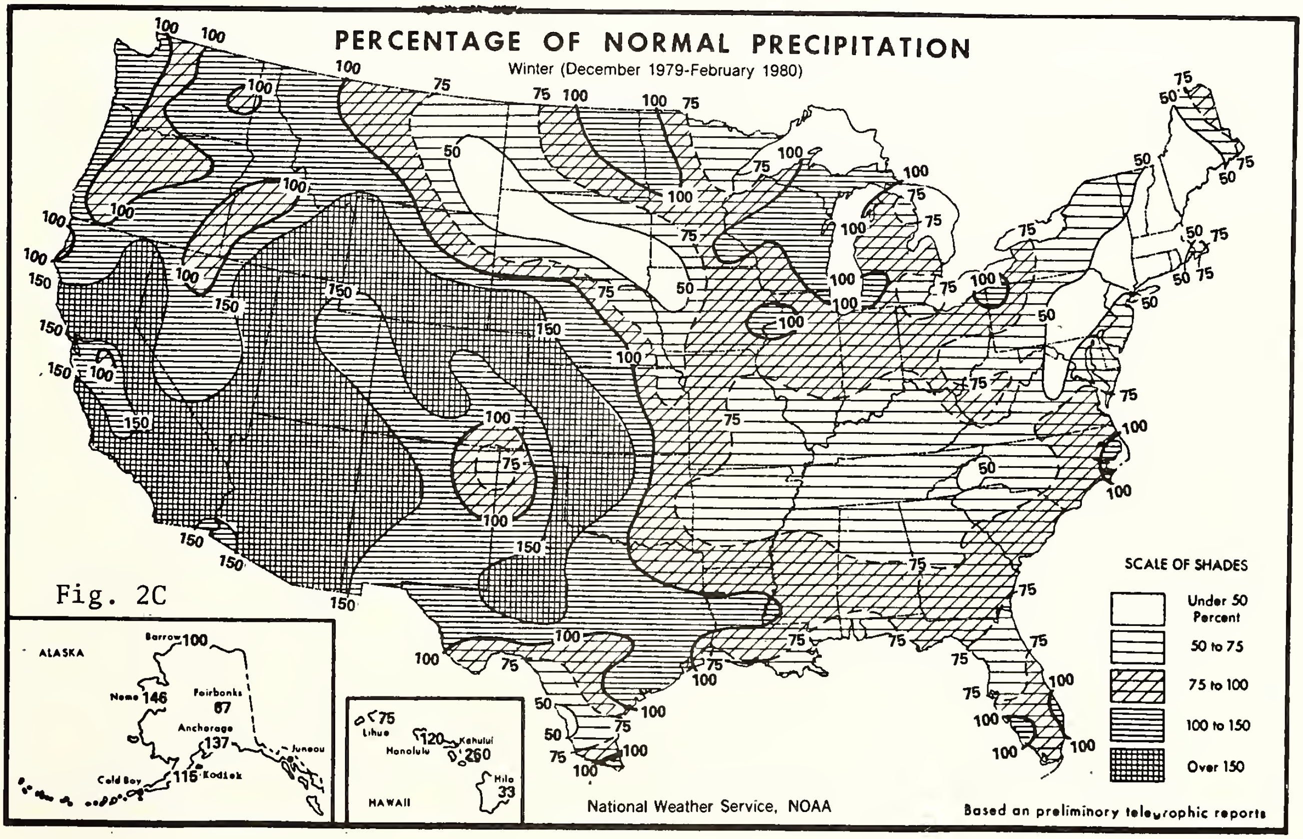
PERCENTAGE OF NORMAL PRECIPITATION
Winter (December 1979-February 1980)
SCALE OF SHADES
Under 50 Percent
50 to 75
75 to 100
100 to 150
Over 150
National Weather Service, NOAA
Based on preliminary telegraphic reports
ALASKA
Barrow 100
Nome 146
Fairbanks 67
Anchorage 137
Juneau
Kodiak 115
Cold Bay
HAWAII
Lihue 75
Honolulu 120
Kahului 260
Hilo 33

Fig. 2C

The Circulation and Weather of Spring and Summer 1980

Robert R. Dickson
Climate Analysis Center
NMC/NWS/NOAA
Washington, D.C. 20233

Spring 1980. As was the case in winter, strong Pacific westerlies were observed at 700 mb during spring, but at a higher latitude (Fig. 1). This extremely fast westerly current split about a strong blocking ridge over the northern Great Plains with one segment moving along the northern reaches of this ridge and another passing through a broad trough across the southern United States. The latter was stronger than normal and south of normal along most of its course. The mid-latitude wave pattern from the Atlantic to east Asia was highly amplified. Heights were well above normal in the Arctic where the normal low was absent. Storm systems approaching the North American blocking ridge were generally deflected to the north or south giving bountiful precipitation to most of the conterminous United States (Fig. 2A). Monthly precipitation totals were near record levels in parts of the Southeast in March, the lower Mississippi Valley in April, and Northern Rockies in May. In the vicinity of the blocking ridge, over portions of the northern Great Plains and northern Mississippi Valley, the dearth of storm systems produced dry weather and severe drought (Figs. 2A and 2B). Both April and May were among the driest months of record in parts of this region. Spring temperatures averaged well above normal near and just west of the blocking ridge while cool weather prevailed over most of the southern half of the country (Fig. 3).

Summer 1980. As the speed of the mid-latitude Pacific westerlies declined from the extreme values of spring, wave features in the vicinity of North America generally retrograded, and amplified ridges appeared over the eastern Pacific, mid-United States, and mid-Atlantic (Fig. 4). The transition from the rather stable spring regime to that of summer took place from the last week of May to about mid-June. The summer wave pattern which evolved was quite similar to that which accompanied the hot and droughtly summers of 1952-54 (as discussed by Namias in 1955). This similarity embraced not only the trio of amplified ridges in the vicinity of North America, but also the deep Arctic low. Adequate precipitation during summer was largely limited to areas affected by transient waves in the westerlies -- to the north of the strong continental anticyclone (Fig. 5A). Under the anticyclone summer precipitation was 25-50% of normal over a large area and summer temperatures averaged 4-8°F above normal (Figs. 5A and 5B). The heat wave and drought of this summer contributed to over 1200 deaths and crop and livestock losses estimated at nearly 20 billion dollars. The persistence of the east Pacific and continental anticyclones during summer is shown in Figure 6. By August the east Pacific ridge had built far enough eastward and northward that vorticity was driven over the West and the northern Great Plains and the heat wave ridge migrated eastward. The growth of the heat wave to a July maximum with a subsequent decline and extension eastward in August is shown in Figure 7. By the end of June, temperatures of 100°F or more were common over the central and southern Great Plains and several June and all-time records were set. The most notable of these was an all-time record high of

117°F at Wichita Falls, TX on 28 June. By July, monthly mean temperatures reached remarkable extremes of 8-10°F above normal under the upper level anticyclone; the most extreme departures were about three times the standard deviation of July mean temperatures for the 1941-70 period. July was either the hottest month of record or the hottest July at several locations from Kansas to southern Illinois and southward to the Gulf as well as in parts of the Southwest. By the end of July temperatures of 100°F or more had been observed in 41 states from the Gulf Coast to the northern border and from coast to coast. Temperatures at Dallas, TX equalled or exceeded 100°F on 42 consecutive days through 3 August. During June and July at least a dozen all-time high temperature records were either equalled or set, mostly in the South. Monthly precipitation maps during summer (Fig. 8) illustrate the drying out of the central United States during the July maximum of the heat wave and the subsequent eastward spread of the area of scant precipitation as the associated upper level ridge moved eastward. A notable break in the drought over southern Texas occurred on 9 and 10 August as Hurricane Allen crossed the area. It was one of the driest Augusts of record in much of the South and in parts of the mid-Atlantic Coast States. The Crop Moisture Index map at the end of July (Fig. 9) illustrates the desiccation of soils during the heat wave and the great changes which occurred from the end of spring (Fig. 2B). A review of summer mean temperature anomaly maps since 1881 helps put the present summer in proper prospective. Other hot summers occurred in 1881, 1901, 1921, 1934, 1936, and 1954. Despite the problem of varying normals used during this period, it seems clear that extreme summer mean temperatures were most extensive during the Dust Bowl summer of 1936. The mean temperature distribution during summer 1980 is compared with the three most recent hot summers in Figure 10. It appears that summer 1980 would be a candidate for the third hottest summer of the last 100 years (based on the extent of extreme summer mean temperatures).

FIGURE LEGEND

Fig. 1	Mean 700 mb height contours (dam) and departures from normal (m) for Spring 1980.
Fig. 2	(A) Percentage of normal precipitation for Spring 1980 and (B) Crop Moisture Index for 31 May 1980 (from Weekly Weather and Crop Bulletin). For explanation of Crop Mositure Index, see legend to Figure 9.
Fig. 3	Departure from normal of average surface air temperature (°F) for Spring 1980 (from Weekly Weather & Crop Bulletin.)
Fig. 4	Mean 700 mb height contours (dam) and departure from normal (m) for Summer 1980.
Fig. 5	(A) Percentage of normal precipitation for Summer 1980, and (B) Departure from normal of average surface air temperature (°F) for Summer 1980 (from Weekly Weather & Crop Bulletin).
Fig. 6	Monthly mean 700 mb height anomaly centers (m) in the vicinity of North America during Summer 1980. Month designator is in parentheses.
Fig. 7	Departure from normal of monthly average surface air temperature (°F) during June, July and August 1980 (from Weekly Weather and Crop Bulletin).
Fig. 8	Percentage of monthly normal precipitation during June, July and August 1980 (from Weekly Weather & Crop Bulletin.
Fig. 9	Crop Moisture Index for 2 August 1980 (from Weekly Weather and Crop Bulletin).
Fig. 10	Departure from normal of surface air temperature (°F) for Summers of 1934, 36, 1954 and 1980.

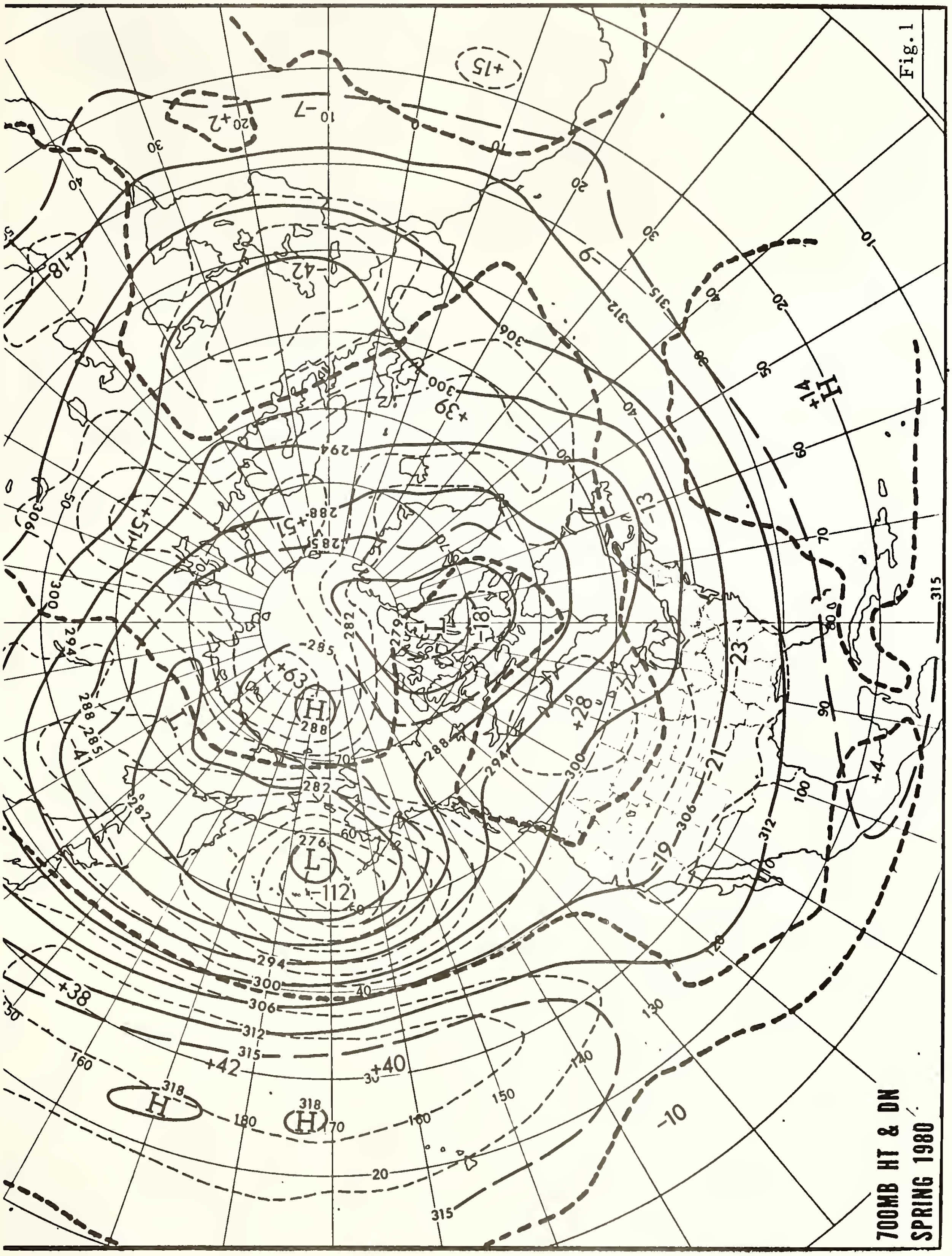

Fig. 1

700MB HT & DN
SPRING 1980

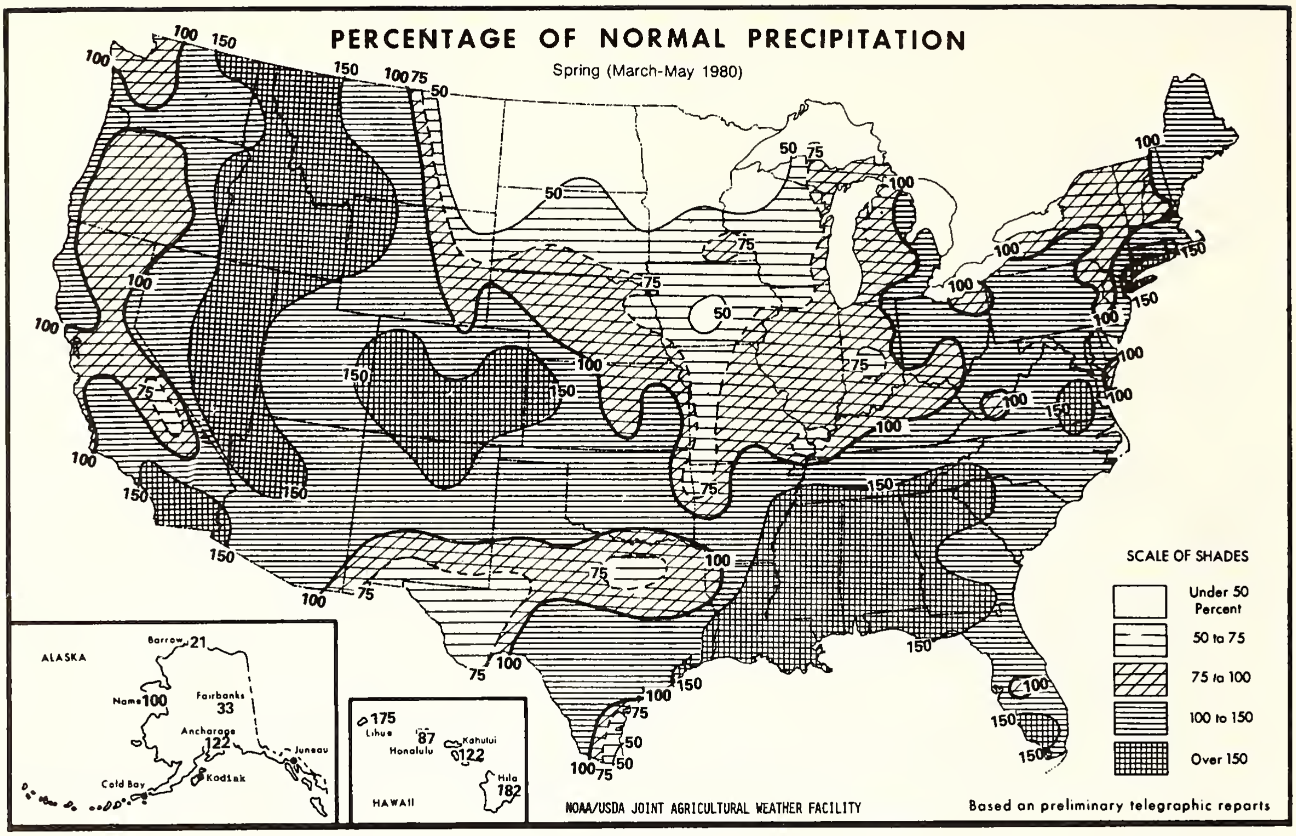
PERCENTAGE OF NORMAL PRECIPITATION
Spring (March-May 1980)
SCALE OF SHADES
Under 50 Percent
50 to 75
75 to 100
100 to 150
Over 150
ALASKA
Barrow 21
Nome 100
Fairbanks 33
Anchorage 122
Juneau
Cold Bay
Kodiak
HAWAII
Lihue 175
Honolulu 87
Kahului 122
Hilo 182
NOAA/USDA JOINT AGRICULTURAL WEATHER FACILITY
Based on preliminary telegraphic reports

Fig. 2A

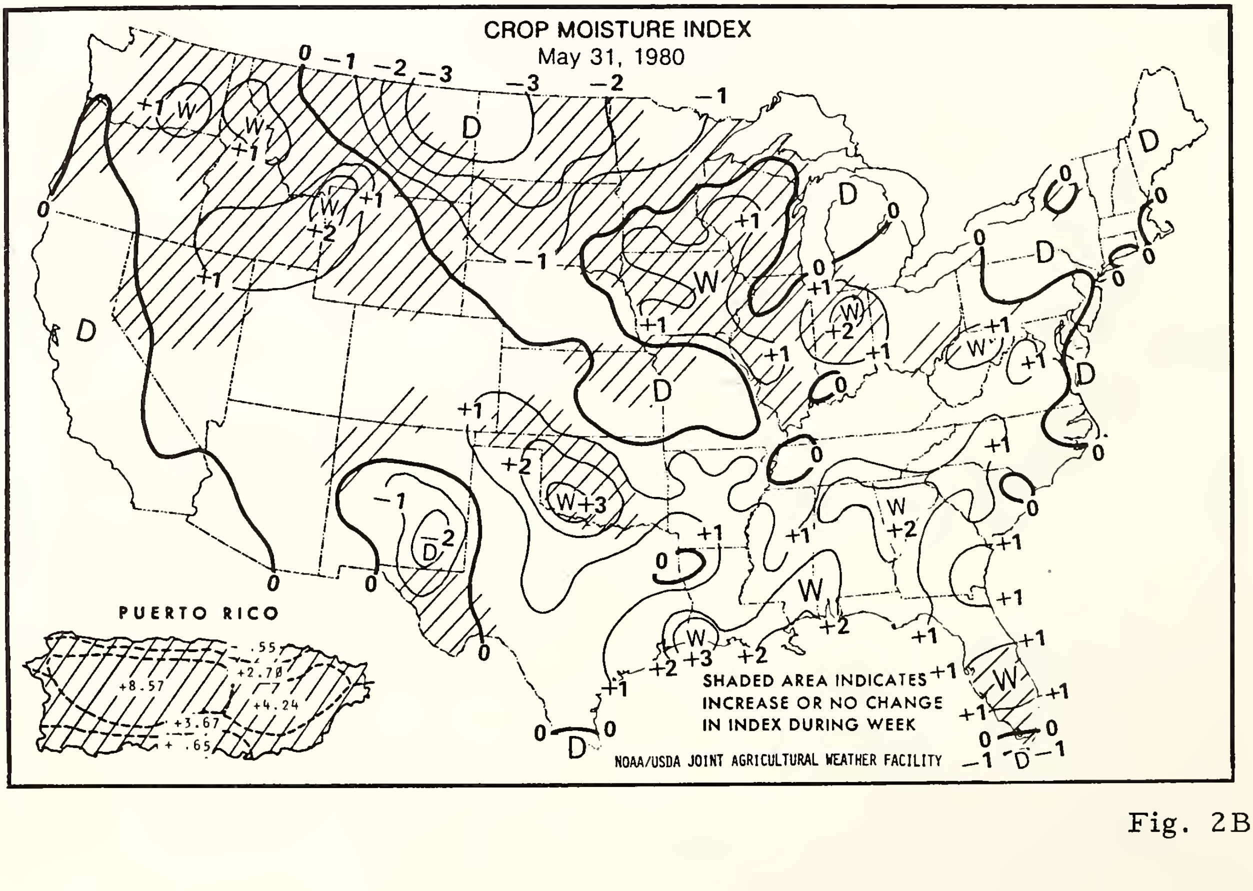
CROP MOISTURE INDEX
May 31, 1980
PUERTO RICO
.55
+2.70
-.7
+8.57
+4.24
+3.67
+ .65
SHADED AREA INDICATES INCREASE OR NO CHANGE IN INDEX DURING WEEK
NOAA/USDA JOINT AGRICULTURAL WEATHER FACILITY

Fig. 2B

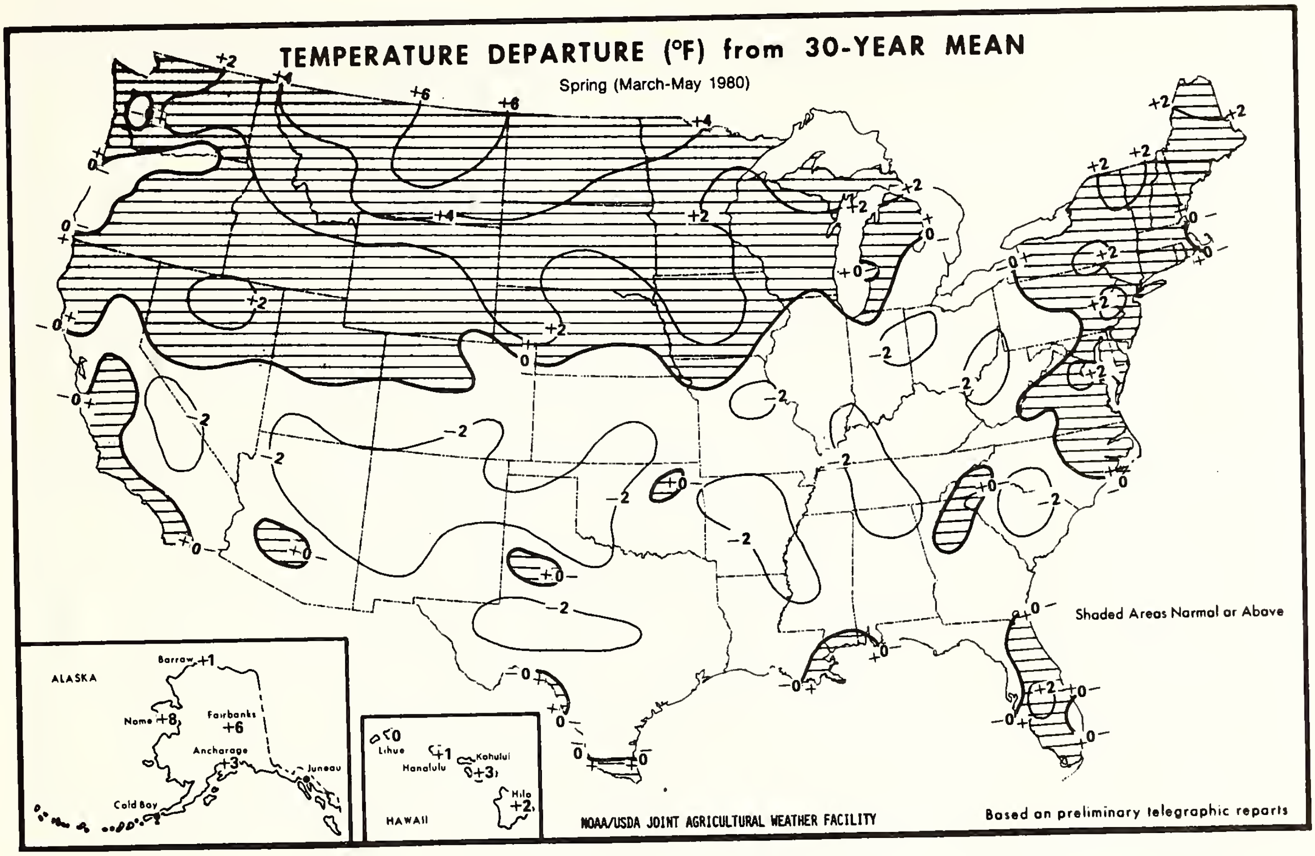
TEMPERATURE DEPARTURE (°F) from 30-YEAR MEAN
Spring (March-May 1980)
Shaded Areas Normal or Above
NOAA/USDA JOINT AGRICULTURAL WEATHER FACILITY
Based on preliminary telegraphic reports
ALASKA
Barrow +1
Nome +8
Fairbanks +6
Anchorage +3
Juneau
Cold Bay
HAWAII
Lihue 0
Honolulu +1
Kahului +3
Hilo +2

Fig. 3

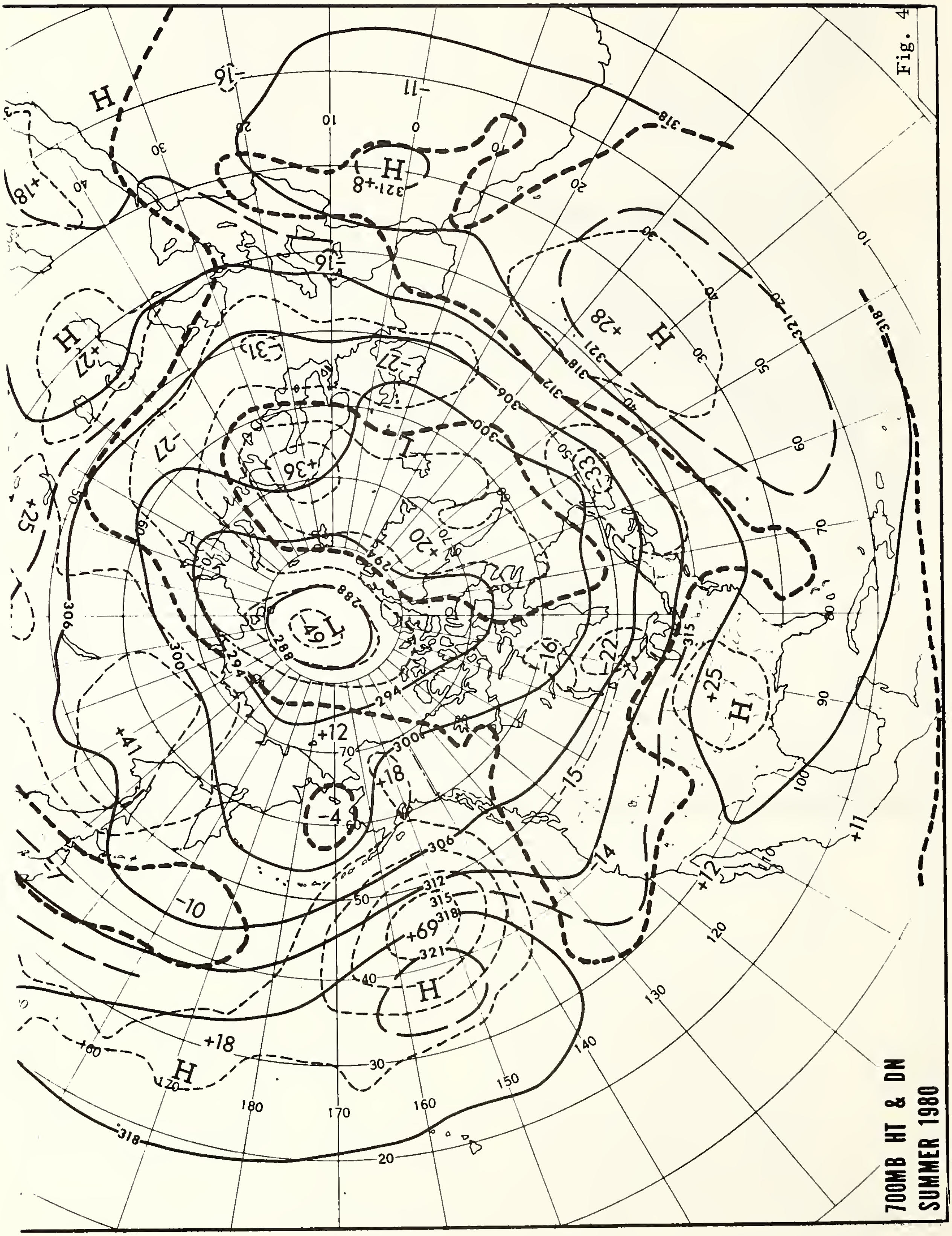

Fig. 4

700MB HT & DN
SUMMER 1980

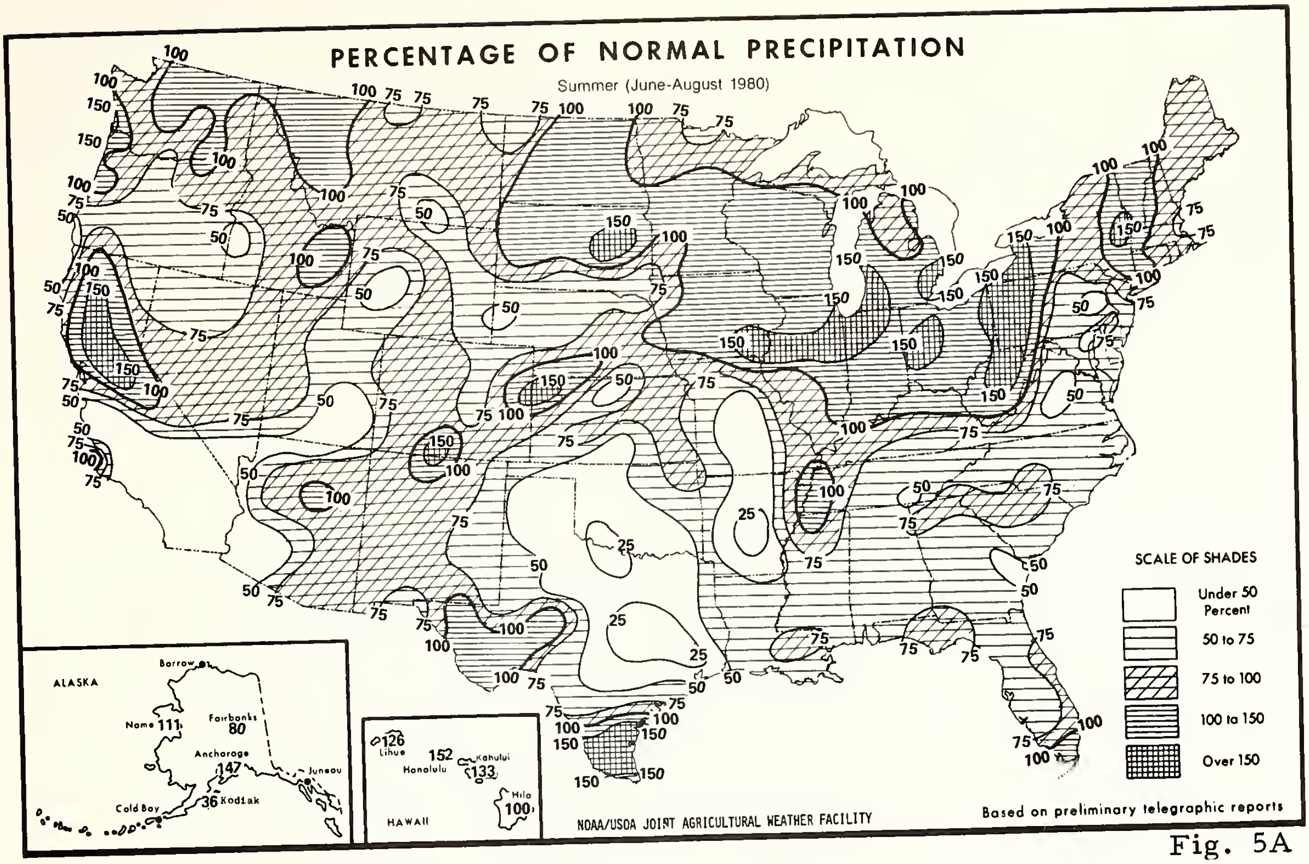
PERCENTAGE OF NORMAL PRECIPITATION
Summer (June-August 1980)
SCALE OF SHADES
Under 50 Percent
50 to 75
75 to 100
100 to 150
Over 150
ALASKA
Barrow
Nome 111
Fairbanks 80
Anchorage 147
Juneau
Cold Bay
36 Kodiak
HAWAII
Lihue 126
Honolulu 152
Kahului 133
Hilo 100
NOAA/USDA JOINT AGRICULTURAL WEATHER FACILITY
Based on preliminary telegraphic reports

Fig. 5A

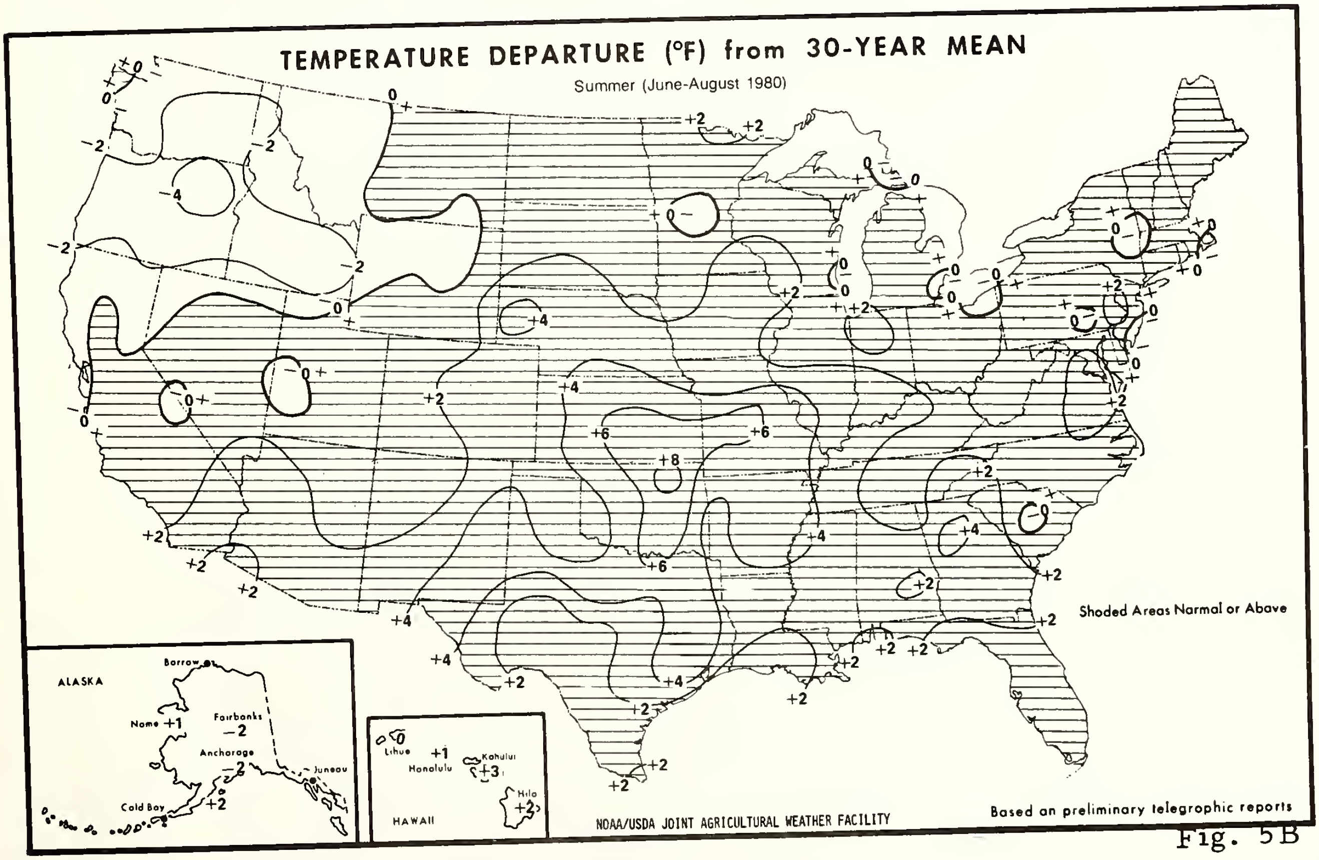
TEMPERATURE DEPARTURE (°F) from 30-YEAR MEAN
Summer (June-August 1980)
Shaded Areas Normal or Above
ALASKA
Barrow
Nome +1
Fairbanks −2
Anchorage −2
Juneau
Cold Bay +2
HAWAII
Lihue 0
Honolulu +1
Kahului +3
Hilo +2
NOAA/USDA JOINT AGRICULTURAL WEATHER FACILITY
Based on preliminary telegraphic reports

Fig. 5B

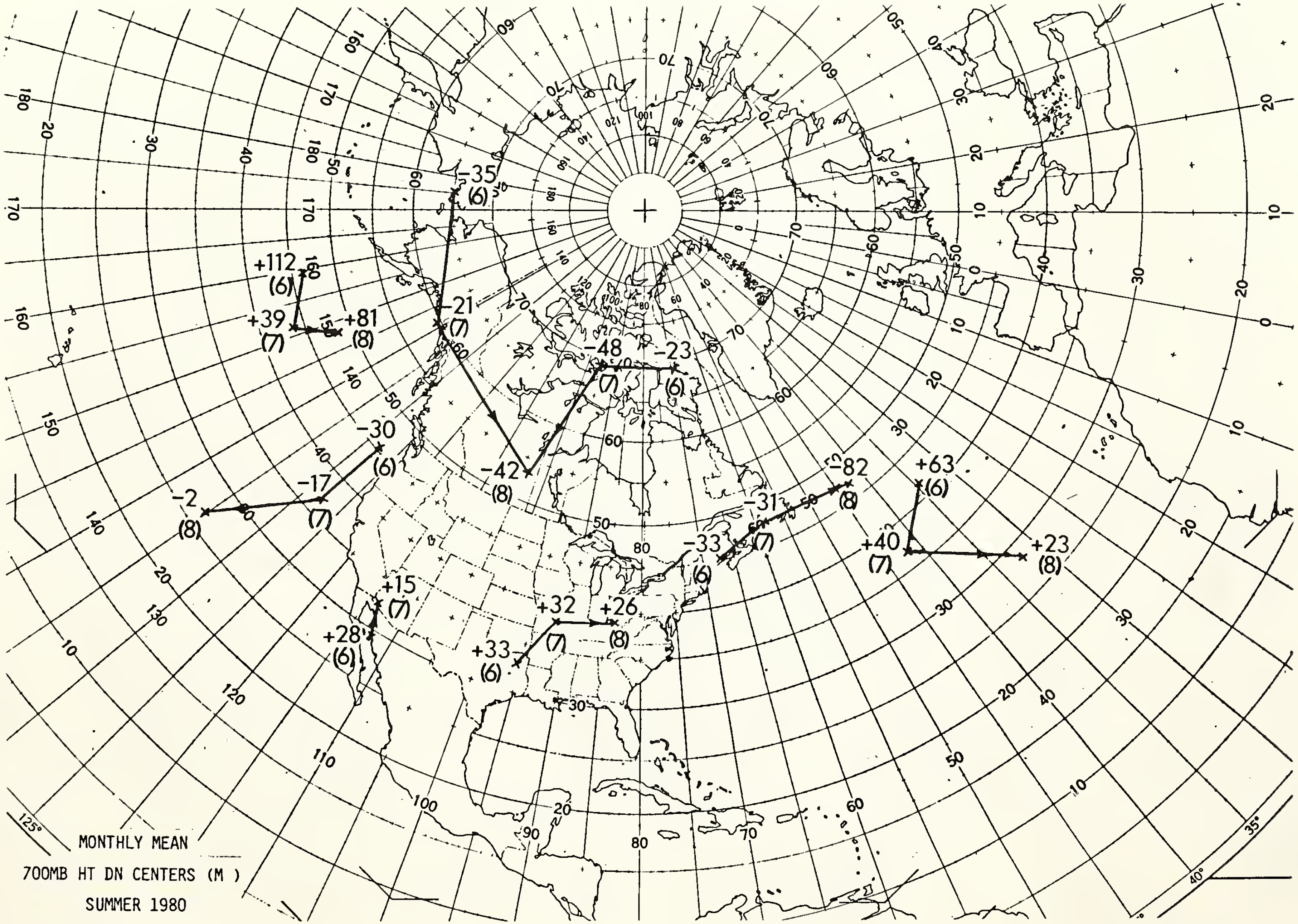
MONTHLY MEAN
700MB HT DN CENTERS (M)
SUMMER 1980
-35 (6)
-21 (7)
-42 (8)
-48 (7)
-23 (6)
+112 (6)
+39 (7)
+81 (8)
-30 (6)
-17 (7)
-2 (8)
+15 (7)
+28 (6)
+33 (6)
+32 (7)
+26 (8)
-33 (6)
-31 (7)
-82 (8)
+63 (6)
+40 (7)
+23 (8)

Fig. 6

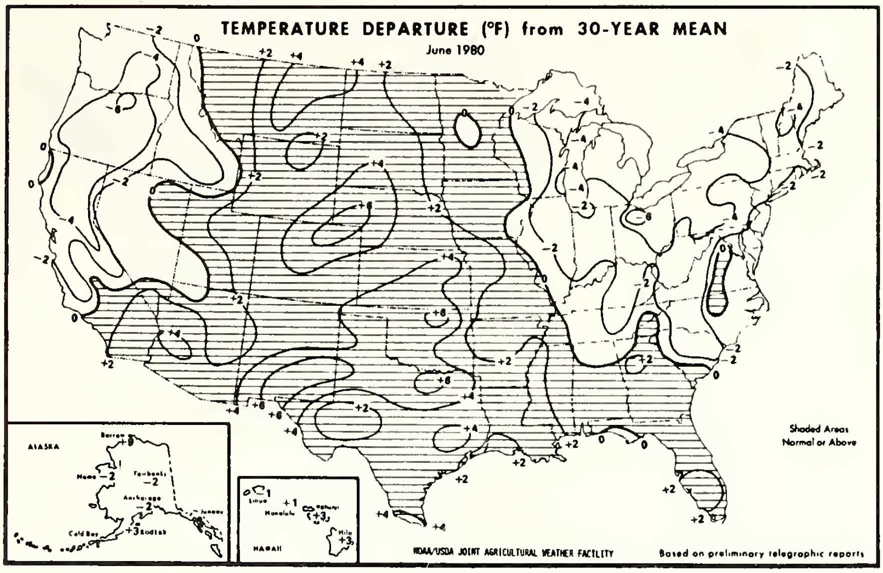
TEMPERATURE DEPARTURE (°F) from 30-YEAR MEAN
June 1980
Shaded Areas Normal or Above
ALASKA
Barrow
Nome
Fairbanks
Anchorage
Juneau
Cold Bay
Kodiak
HAWAII
Lihue
Honolulu
Kahului
Hilo
NOAA/USDA JOINT AGRICULTURAL WEATHER FACILITY
Based on preliminary telegraphic reports

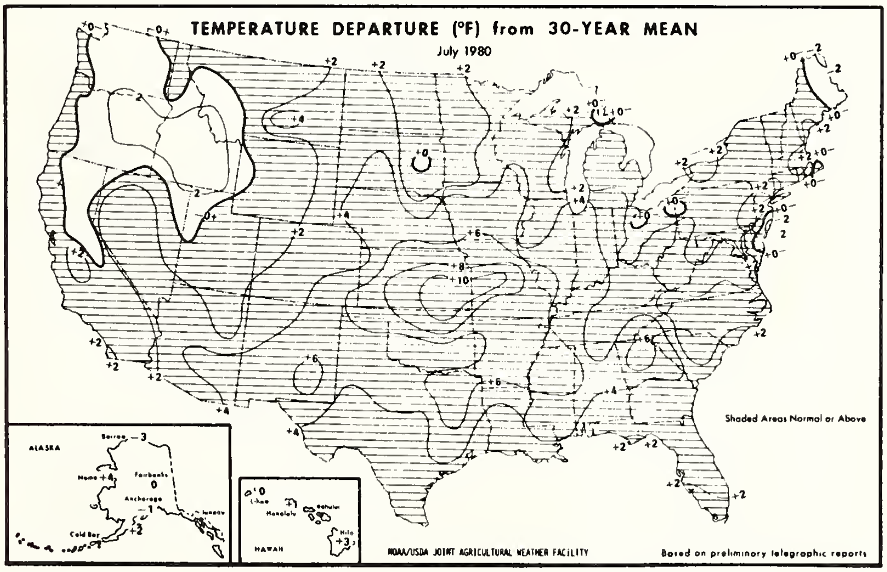
TEMPERATURE DEPARTURE (°F) from 30-YEAR MEAN
July 1980
Shaded Areas Normal or Above
ALASKA
Barrow
Nome
Fairbanks
Anchorage
Juneau
Cold Bay
HAWAII
Lihue
Honolulu
Kahului
Hilo
NOAA/USDA JOINT AGRICULTURAL WEATHER FACILITY
Based on preliminary telegraphic reports

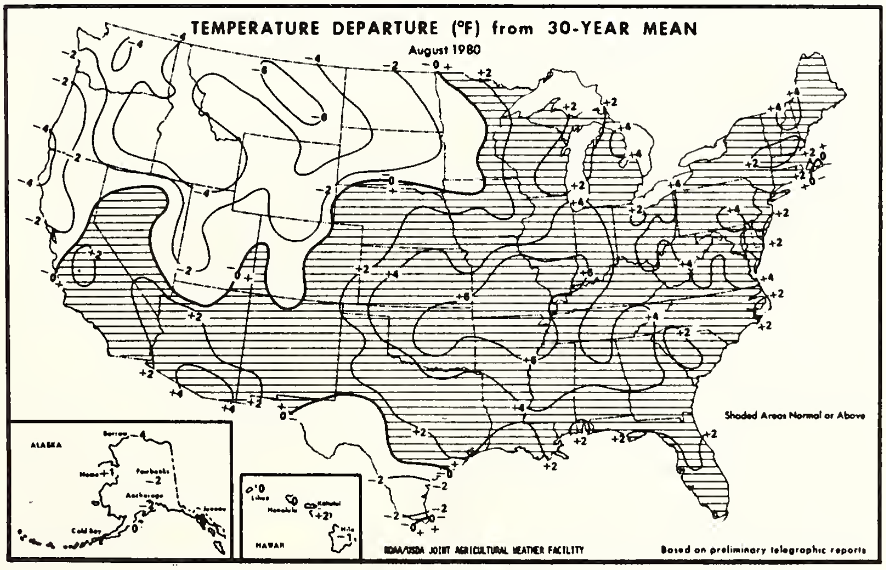
TEMPERATURE DEPARTURE (°F) from 30-YEAR MEAN
August 1980
Shaded Areas Normal or Above
ALASKA
Barrow
Nome
Fairbanks
Anchorage
Juneau
Cold Bay
HAWAII
Lihue
Honolulu
Kahului
Hilo
NOAA/USDA JOINT AGRICULTURAL WEATHER FACILITY
Based on preliminary telegraphic reports

Fig. 7

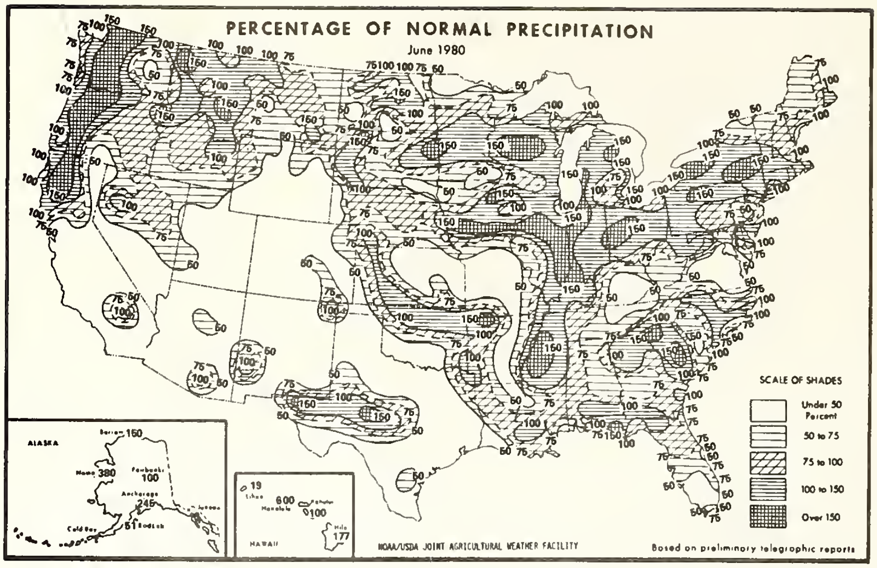

PERCENTAGE OF NORMAL PRECIPITATION
June 1980

NOAA/USDA JOINT AGRICULTURAL WEATHER FACILITY

Based on preliminary telegraphic reports

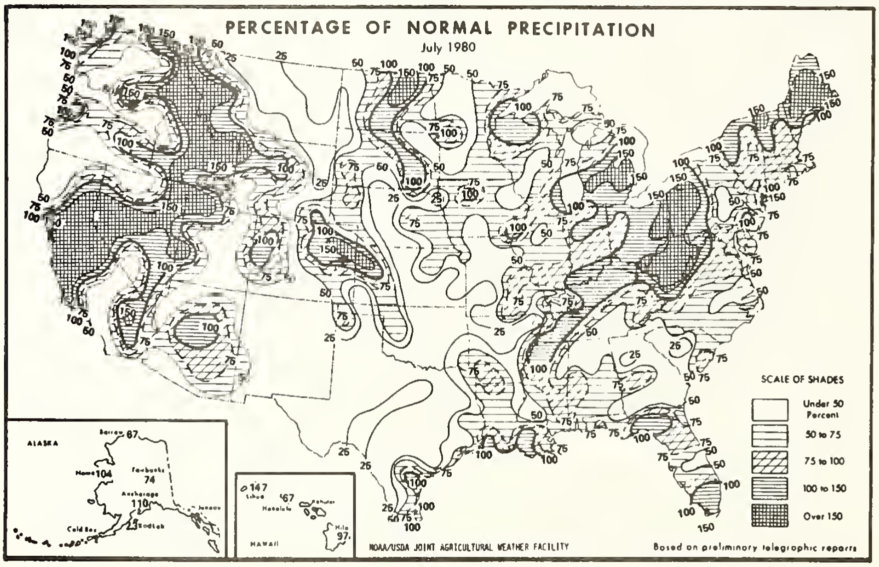

PERCENTAGE OF NORMAL PRECIPITATION
July 1980

NOAA/USDA JOINT AGRICULTURAL WEATHER FACILITY

Based on preliminary telegraphic reports

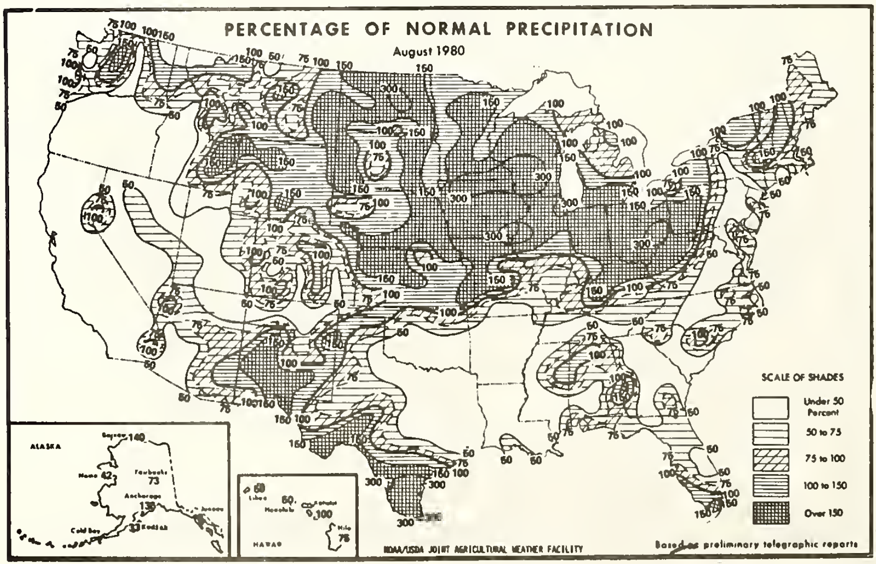

PERCENTAGE OF NORMAL PRECIPITATION
August 1980

NOAA/USDA JOINT AGRICULTURAL WEATHER FACILITY

Based on preliminary telegraphic reports

Fig. 8

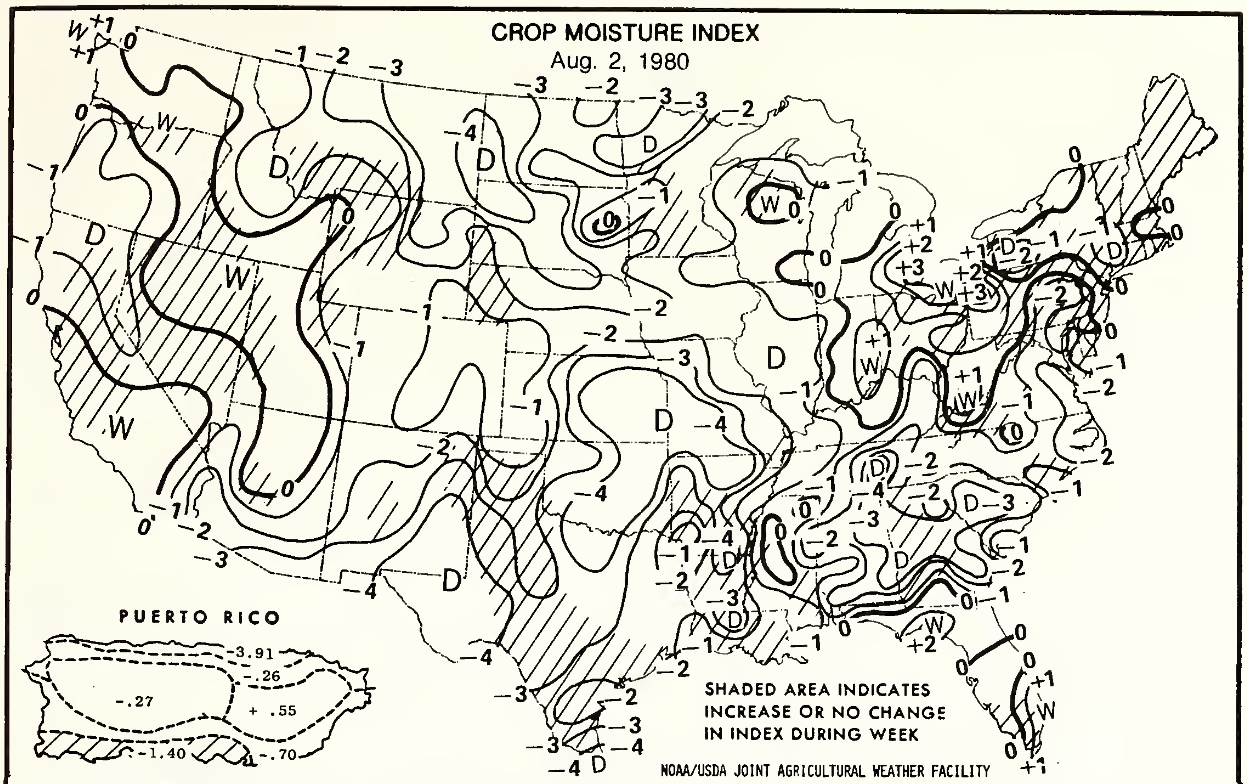
CROP MOISTURE INDEX
Aug. 2, 1980
PUERTO RICO
-3.91
-.26
-.27
+ .55
-1.40
-.70
SHADED AREA INDICATES INCREASE OR NO CHANGE IN INDEX DURING WEEK
NOAA/USDA JOINT AGRICULTURAL WEATHER FACILITY

The Crop Moisture Index measures the degree to which moisture requirements of growing crops were met during the previous week. The index is computed from average weekly values of temperature and precipitation. These values are used to calculate the potential moisture demand. Taking into account the previous soil moisture condition and current rainfall, the actual moisture loss is determined.

If the potential moisture demand, or potential evapotranspiration, exceeds available moisture supplies, actual evapotranspiration is reduced and the CMI gives a negative value. However, if moisture meets or exceeds demand the index is positive.

Shaded areas indicate the index was unchanged or increased from the previous week's value; soils dried in the unshaded areas. Centers of positive and negative areas are identified by W for wet and D for dry.

Local moisture conditions may vary because of differences in rainfall distribution or soil types. The type of agriculture and stage of crop development must be considered when assessing the impact of moisture conditions based on the Crop Moisture Index. Some general guidelines follow.

UNSHADED AREAS:			INDEX DECREASED
ABOVE		3.0	SOME DRYING BUT STILL EXCESSIVELY WET
2.0	to	3.0	MORE DRY WEATHER NEED, WORK DELAYED
1.0	to	2.0	FAVORABLE, EXCEPT STILL TOO WET IN SPOTS
0	to	1.0	FAVORABLE FOR NORMAL GROWTH AND FIELDWORK
0	to	-1.0	TOPSOIL MOISTURE SHORT, GERMINATION SLOW
-1.0	to	-2.0	ABNORMALLY DRY, PROSPECTS DETERIORATING
-2.0	to	-3.0	TOO DRY, YIELD PROSPECTS REDUCED
-3.0	to	-4.0	POTENTIAL YIELDS SEVERELY CUT BY DROUGHT
BELOW		-4.0	EXTREMELY DRY, MOST CROPS RUINED

SHADED AREAS:			INDEX INCREASED OR DID NOT CHANGE
ABOVE		3.0	EXCESSIVELY WET, SOME FIELDS FLOODED
2.0	to	3.0	TOO WET, SOME STANDING WATER
1.0	to	2.0	PROSPECTS ABOVE NORMAL, SOME FIELDS TOO WET
0	to	1.0	MOISTURE ADEQUATE FOR PRESENT NEEDS
0	to	-1.0	PROSPECTS IMPROVED BUT RAIN STILL NEEDED
-1.0	to	-2.0	SOME IMPROVEMENT BUT STILL TOO DRY
-2.0	to	-3.0	DROUGHT EASED BUT STILL SERIOUS
-3.0	to	-4.0	DROUGHT CONTINUES, RAIN URGENTLY NEEDED
BELOW		-4.0	NOT ENOUGH RAIN, STILL EXTREMELY DRY

THE EXTREMELY DRY AREA IN OKLAHOMA, KANSAS, AND MISSOURI HAS EXPANDED AND BECOME EVEN DRIER AS CROP DEMAND FOR MOISTURE HAS EXCEEDED THE SUPPLY. THE SCANTY SOIL MOISTURE RESERVE IS BEING DEPLETED RAPIDLY. THE WESTERN CORN BELT--IOWA AND ILLINOIS--IS DRYING RAPIDLY, BUT SOME SOIL MOISTURE RESERVE REMAINS. RAIN IS BADLY NEEDED IN THESE AREAS. LARGE AREAS IN THE SOUTHEASTERN UNITED STATES ARE SERIOUSLY DRY.

Fig. 9

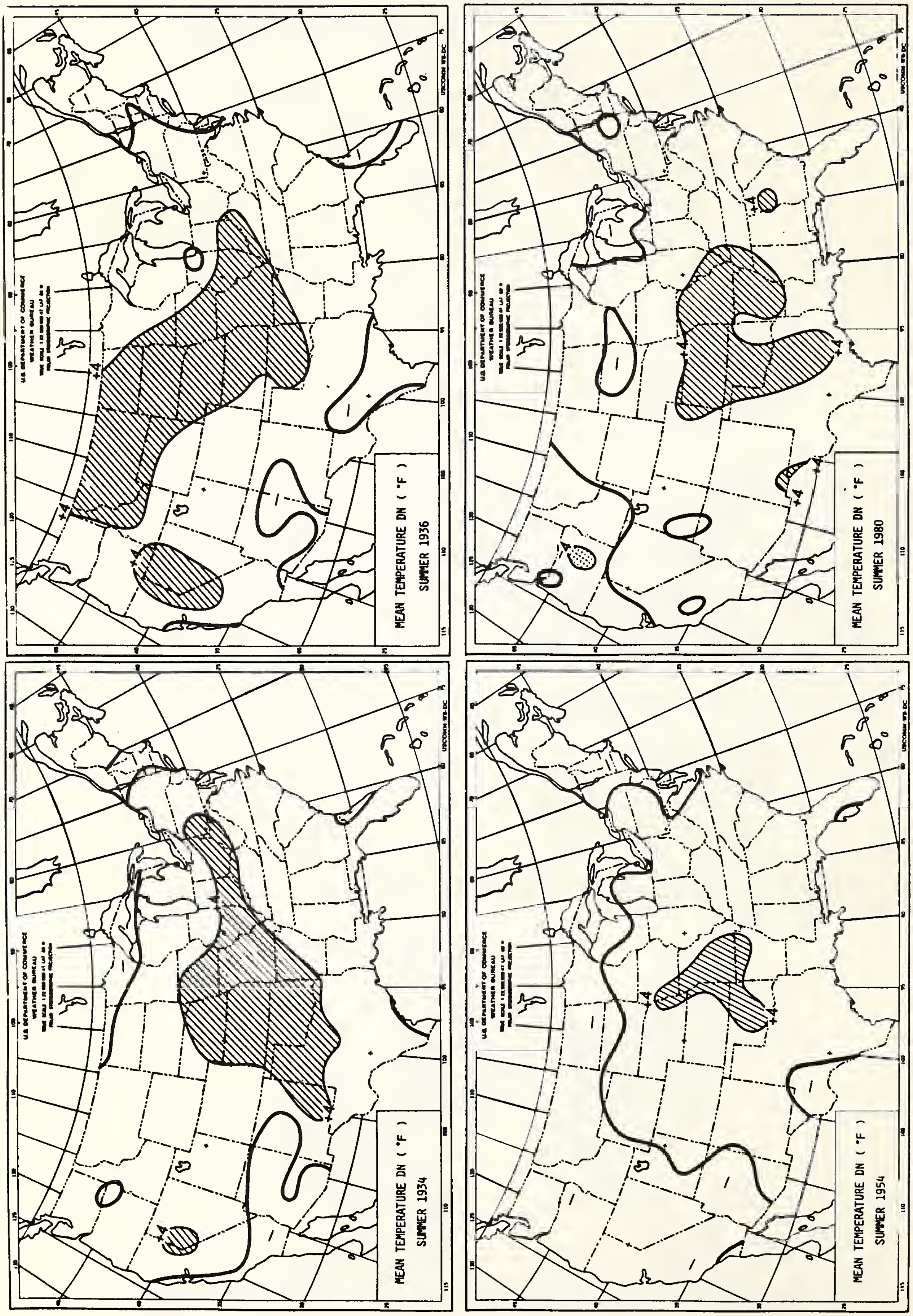
MEAN TEMPERATURE DN (°F)
SUMMER 1934
MEAN TEMPERATURE DN (°F)
SUMMER 1936
MEAN TEMPERATURE DN (°F)
SUMMER 1954
MEAN TEMPERATURE DN (°F)
SUMMER 1980
U.S. DEPARTMENT OF COMMERCE
WEATHER BUREAU
USCOMM WB-DC
+4
-
+

Fig. 10

Canadian Climate extremes and impacts for the period

September 1979 to August 1980

Yves Durocher
Atmospheric Environment Service
Downsview, Ontario

Annual

The 12 month period from September 1979 to August 1980 was characterized by above normal mean temperature for all regions of Canada with the exceptions of southern Ontario, the upper St.-Laurence Valley and most of the Atlantic provinces. The precipitation totals for the year show a significant deficit over the Prairies and a large surplus over Newfoundland. These two anomalies were disastrous to agriculture in Canada since they occurred during critical agricultural periods.

Fall 1979

The temperature regime was very stable during this period. For three consecutive monthly maps, the temperature pattern underwent very little change; the only variations were in amplitude. The warm anomaly in the west contrasted with the cold anomaly in the east. Following a pattern almost identical to September and October where the main anomaly centres were of the order of 2°C, the monthly temperature anomaly for November increased to more than 11°C above normal in the Mackenzie Delta. At Inuvik, five consecutive weekly mean temperatures covering the entire month remained more than 10°C above normal. These mild temperatures in the arctic allowed an extension of the drilling operations in the Beaufort Sea up to the end of November; on an experimental basis, some drilling operations were further extended to mid-December.

Although not as well defined, the precipitation regime was also characterized by an east-west contrast. The precipitation deficit turned out to be an important factor contributing to the severe rash of forest fires and poor germination in the following spring. At this time of year, precipitation is needed to replenish soil moisture content for the following growing season. This year, the precipitation before soil freeze-up totalled less than normal over most agricultural areas with large anomalies over the richest farm land. There was also a severe lack of precipitation in northwestern Ontario and northern Alberta, where forest fire activity would be at its highest in the following spring. There was also a severe water deficit in central British Columbia, and the year 1979 was the driest on record. Ranchers were worrying about poor irrigation during following seasons.

Winter

The winter of 1979-80 (December to February) turned out to be warmer than normal in all of Canada with few exceptions. The mean temperature exceeded 5° in the northern Prairies and southern Mackenzie District.

In the east, winter gave the impression of being much warmer than it actually was for three reasons. First, the last three winters have been very cold. This winter, on the contrary, has only exceeded normal by a small amount. Second, snow cover was scant, not because the snowfalls were slight, but mainly because the snow melted rapidly afterwards. Finally, the Christmas holiday period was much warmer than normal and rain prevailed instead of snow; this short period became the subjective feeling for the entire winter.

The total absence of snow during the Christmas holidays and the negligible snow cover to the end of February in certain areas caused serious financial problems for ski resort operators and sporting goods retailers; some were driven into bankruptcy. Some municipalities made savings on their snow removal budgets; however, some contractors, not protected by minimum price guarantees, suffered heavy losses. The number of automobile accidents also decreased because of the lack of snow; drivers were pleased but auto repair shops lost business.

Finally, milder weather and the prevalence of rain rather than snowfall resulted in thinner ice layers and lower albedo which allowed greater heating by radiation. Thus, the seaway opened on a record early date this year; ice breakup in eastern Canada was several weeks ahead of normal.

Precipitation continued to be scarce in the interior of British Columbia. Moreover, much of it fell as rain instead of snow; on the frozen ground rain ran off while the snowcover would have remained until spring. Compounding the problem, the light snowcover allowed the ground to freeze to a greater depth. Water reserves in the area were at their lowest levels. This situation continued to worry fruit growers in the Okanagan Valley and ranchers in the Thompson Valley. Hydro-electric companies were also affected. The water levels were so low that any continuing trend would have forced them to reduce their electrical generation. Although forestry and oil and gas exploration activities benefitted from the dry weather at first, the lack of snowcover resulted in early muddy road conditions, thus shortening these seasonal operations.

Spring

The spring of 1980 (March, April, May) was catastrophic for the Prairies. A severe drought affected southern Saskatchewan and Manitoba. A record of 52 consecutive days with only a trace or less of precipitation was established at Dauphin. It was the driest May on record at several stations in the southern Prairies. The precipitation accumulation for the three month period represented only 17% of normal at Winnipeg. Most fields had to be reseeded in these regions and many farmers had to turn to other crops in view of the shortened growing season. As is often the case in these situations, insects infested the area, thus further reducing the crop yields. The lack of rain severely affected the hay crop; hay had to be shipped from the eastern provinces.

Spring started with a drought in Alberta, but rain appeared at the end of May and remained quite abundant afterwards. In fact, the excess precipitation caused some problems in low lying areas.

In northern regions of the Prairie provinces and in northwestern Ontario, the dry spring followed a dry fall and a very dry winter. The moisture reserves in the ground were at their lowest and the forest fires started.

to rage very early in the season. Before the spring was over, the province of Alberta had already spent their fire fighting budget for the entire season and were heading towards an all time record. The worst areas were in the vicinity of Lake Athabasca and north of Lake Superior.

During this period, precipitation reappeared in the interior of British Columbia and brought all water levels to normal. In fact, the twelve month total from September 1979 to August 1980 was above normal in southern British Columbia, mostly due to spring precipitation.

The temperature was above normal for the whole of Canada, with only a few exceptions despite a rather cold March. Unfortunately, all this heat and sunshine was wasted as far as agriculture was concerned.

Summer

The Prairie drought continued into June and up to mid-July in southern Saskatchewan and Manitoba. Hay crops were only 10% to 50% of normal in Manitoba. The dry spell also resulted in the death of 10,000 ducks at Oak Lake refuge in Manitoba. The damage estimate of the drought reached $10 billion at one point. There were more than 10,000 crop insurance claims, the highest in 20 years. The amount of subsidies and insurance payments has been evaluated at more than $500 million.

Precipitation returned in mid-July, thus bringing some relief to the hard hit agricultural areas. The summer total finally exceeded the seasonal normal in southwestern Manitoba. The second seeding was much more successful. Precipitation was sufficient in most of Alberta; it was even too abundant in central Alberta. The crop yields in Alberta were very good this year. Overall, the three Prairie provinces produced a much better crop than anticipated earlier, although it was still below normal.

Conclusion

The 12 month period from September 1979 to August 1980 was characterized by a sequence of dry spells from fall to beginning of summer that resulted in an extreme forest fire situation and heavy losses in agriculture. On a smaller scale, the poor snowcover resulted in bankruptcy for some ski resort operators and winter equipment retail stores.

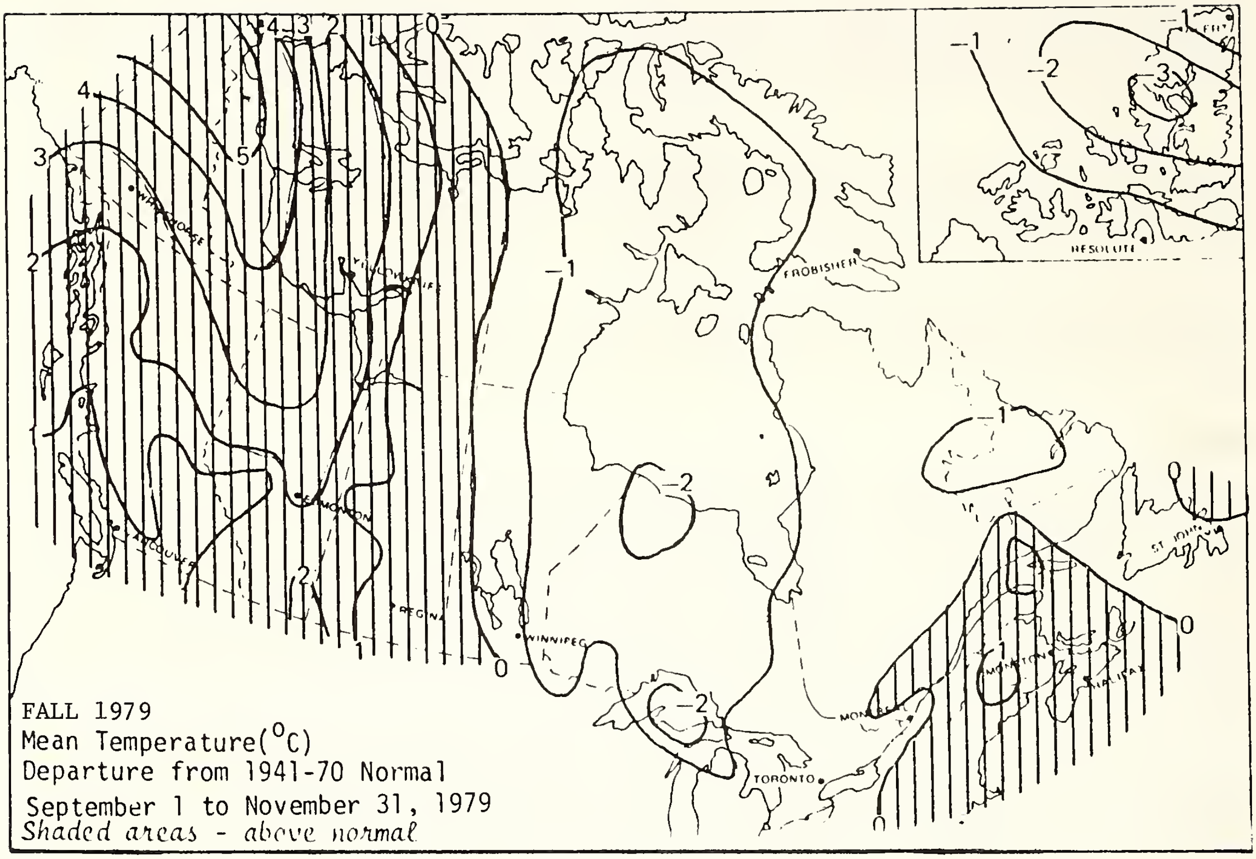

FALL 1979
Mean Temperature(^{o}C)
Departure from 1941-70 Normal
September 1 to November 31, 1979
Shaded areas - above normal

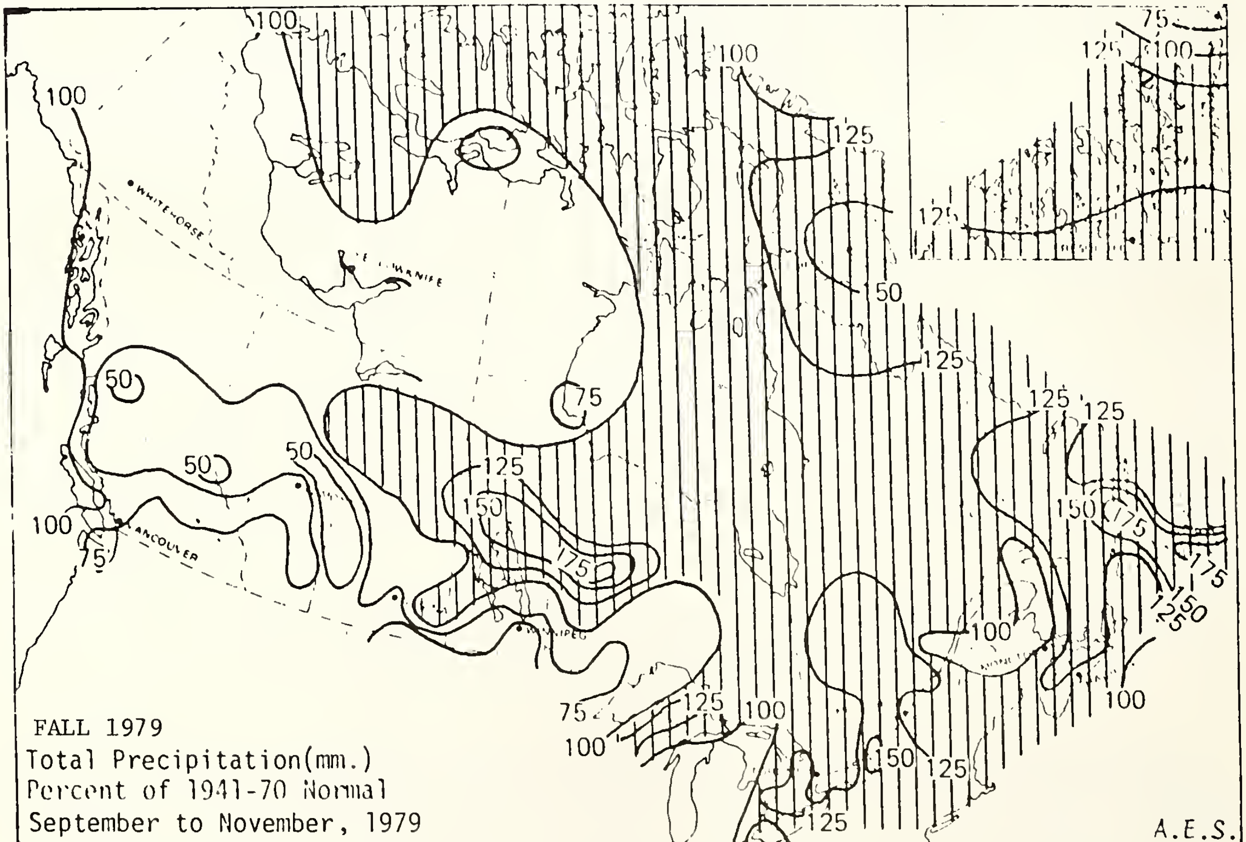

FALL 1979
Total Precipitation(mm.)
Percent of 1941-70 Normal
September to November, 1979

Note: Values are non-representative in non-uniform topographical regions such as the Rocky Mts.

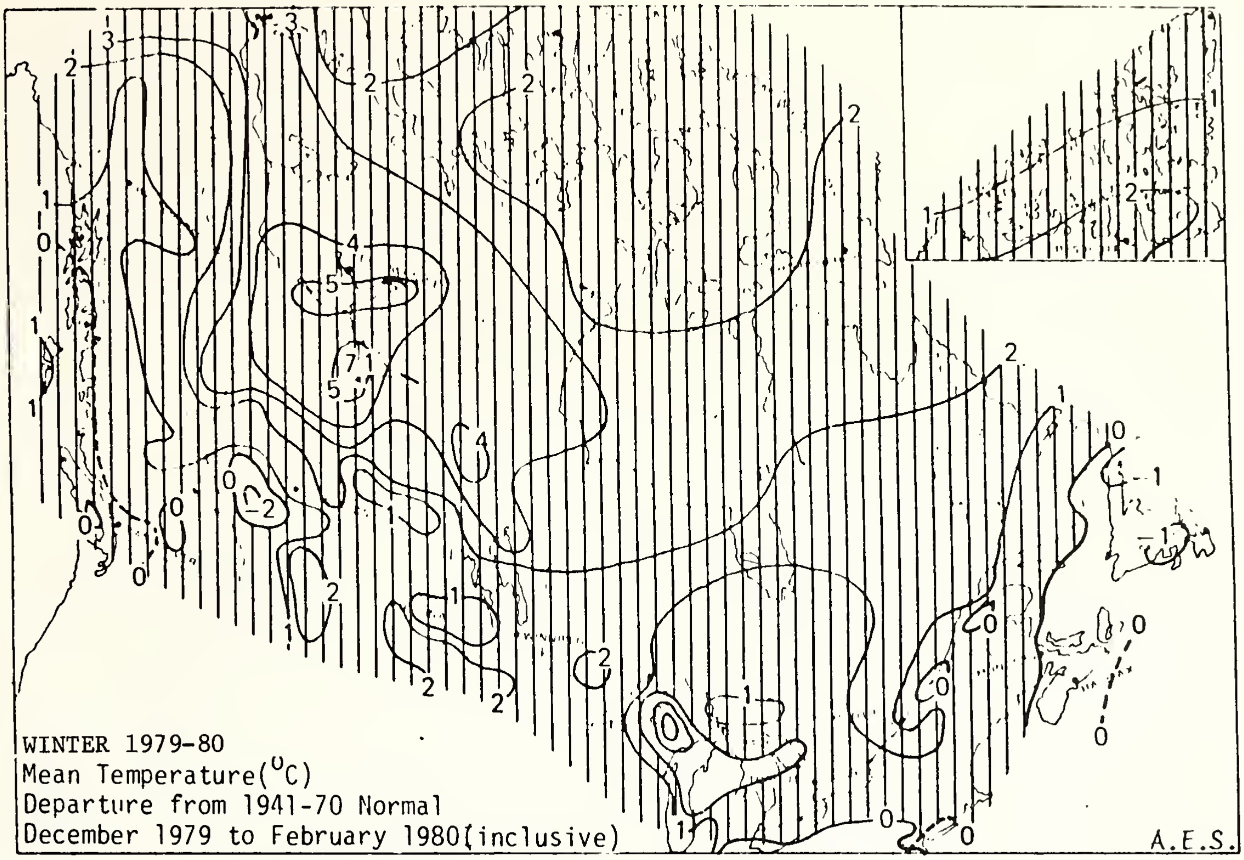

WINTER 1979-80
Mean Temperature(°C)
Departure from 1941-70 Normal
December 1979 to February 1980(inclusive)

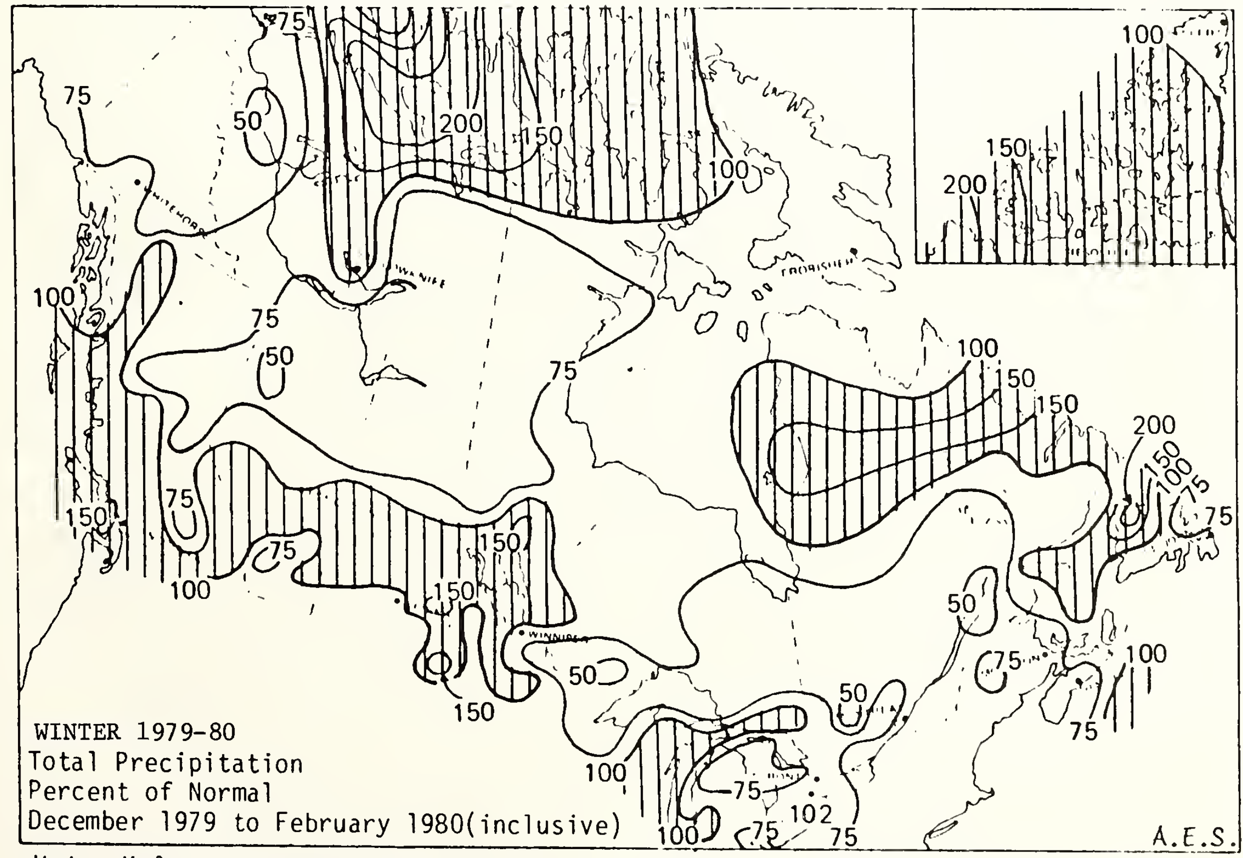

WINTER 1979-80
Total Precipitation
Percent of Normal
December 1979 to February 1980(inclusive)

Note: Values are non-representative in non-uniform topographical regions such as the Rocky Mountains.

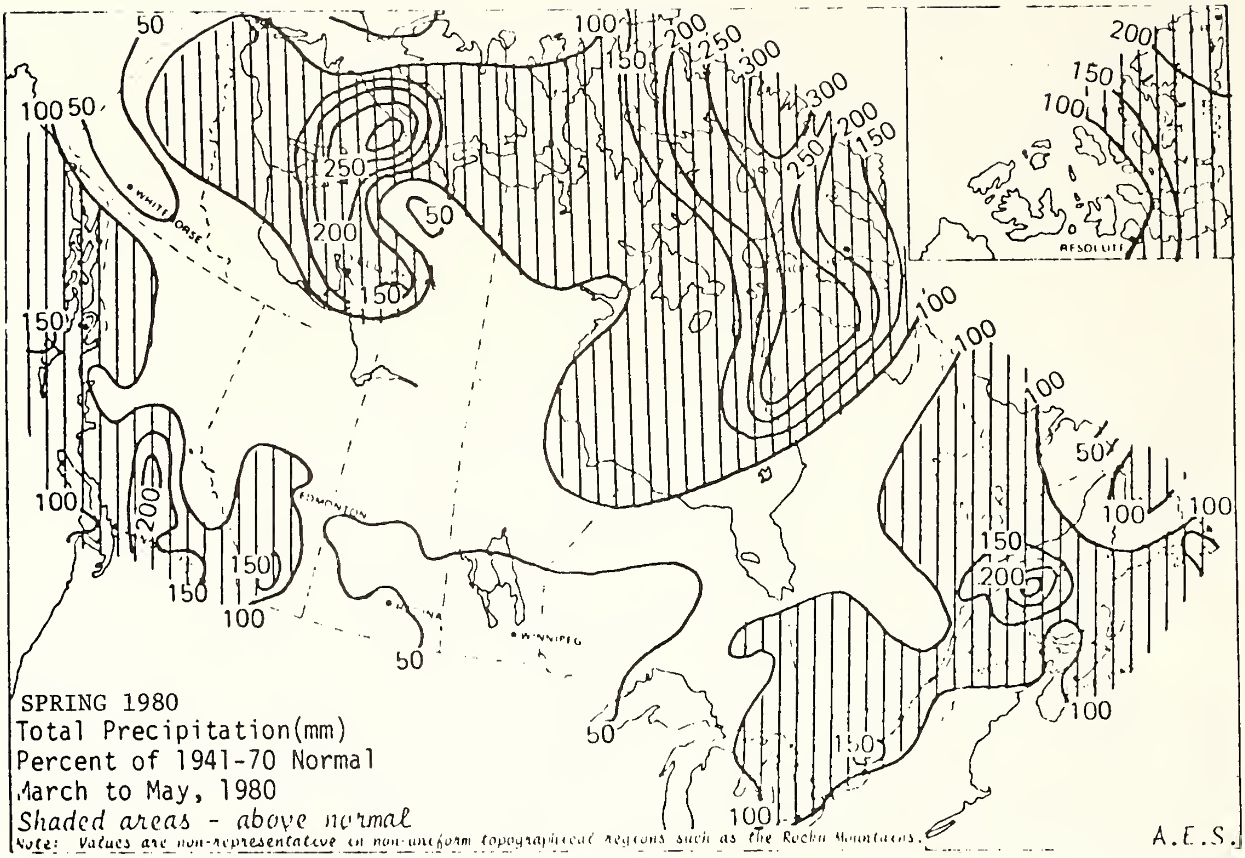

SPRING 1980
Total Precipitation(mm)
Percent of 1941-70 Normal
March to May, 1980
Shaded areas - above normal
Note: Values are non-representative in non-uniform topographical regions such as the Rocky Mountains.

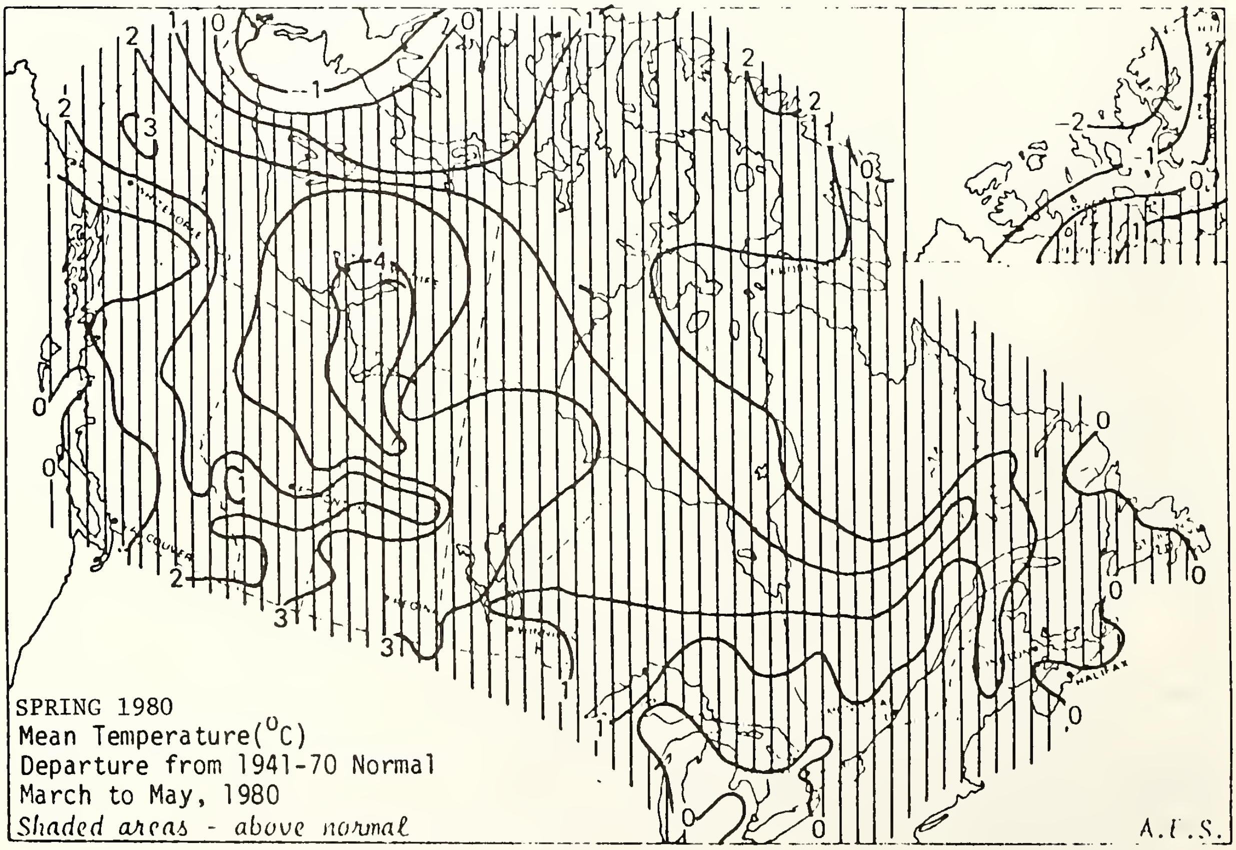

SPRING 1980
Mean Temperature(^{0}C)
Departure from 1941-70 Normal
March to May, 1980
Shaded areas - above normal

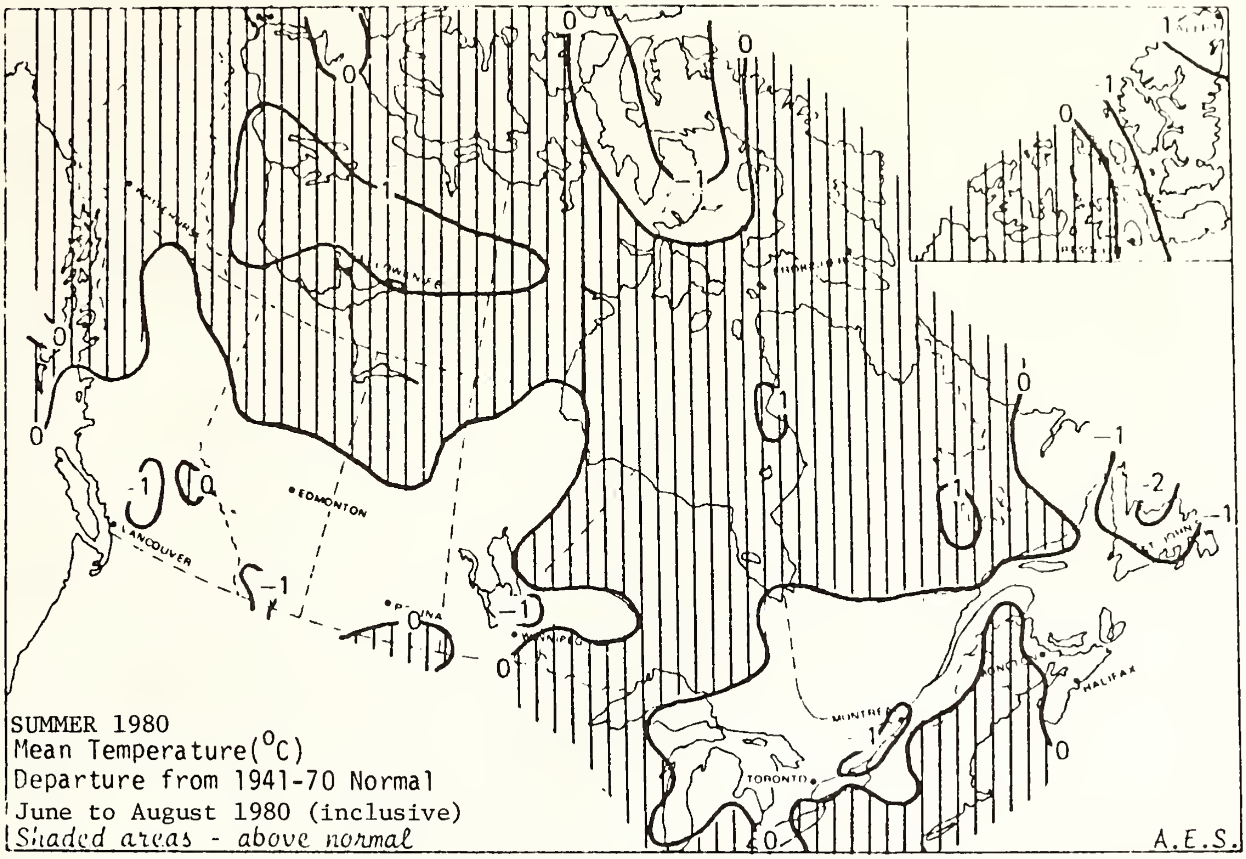

SUMMER 1980
Mean Temperature(^{o}C)
Departure from 1941-70 Normal
June to August 1980 (inclusive)
Shaded areas - above normal

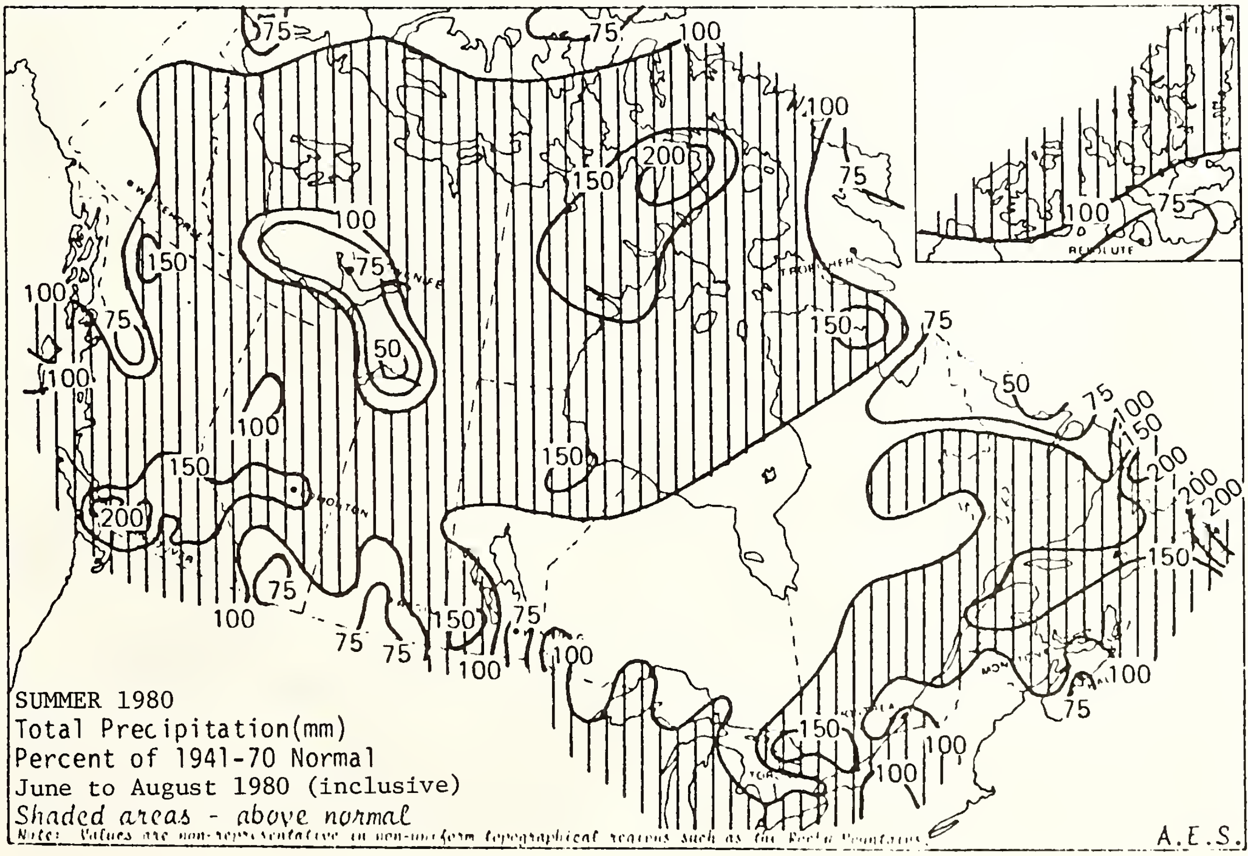

SUMMER 1980
Total Precipitation(mm)
Percent of 1941-70 Normal
June to August 1980 (inclusive)
Shaded areas - above normal
Note: Values are non-representative in non-uniform topographical regions such as the Rocky Mountains.

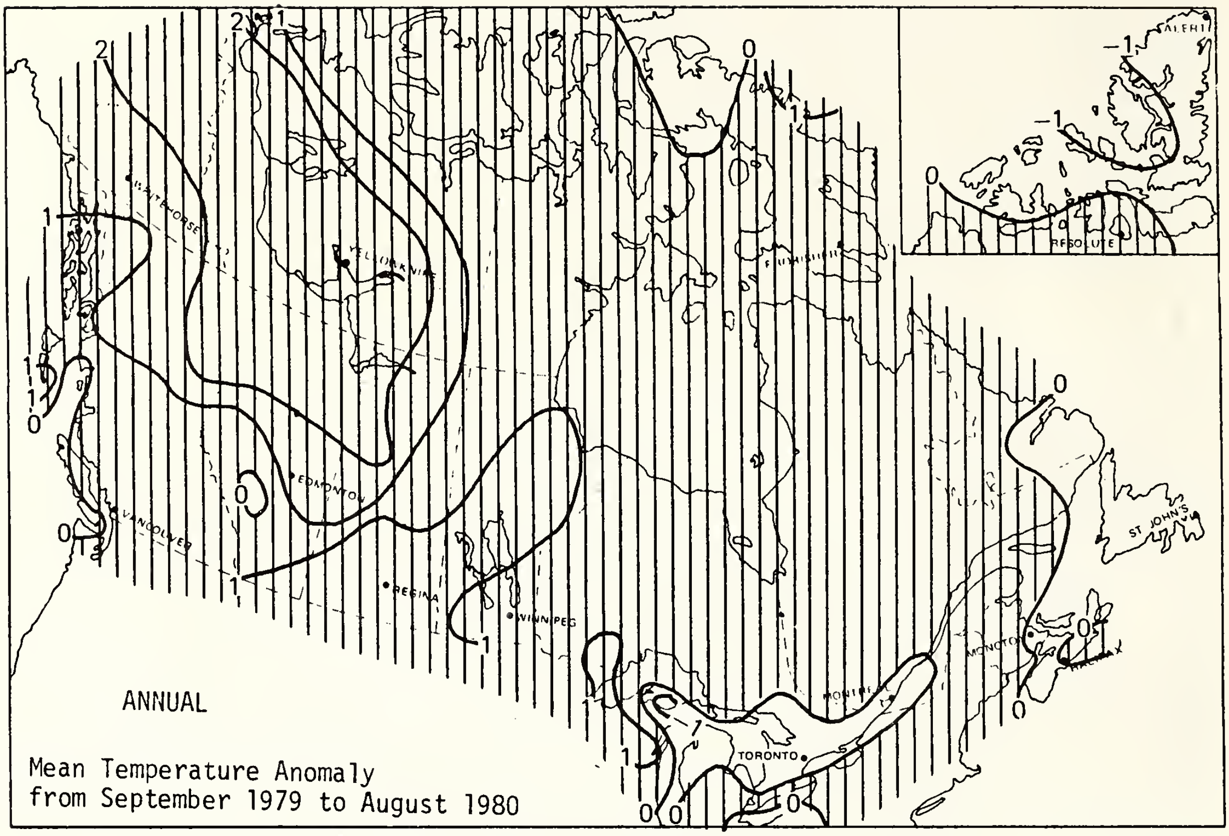

Mean Temperature Anomaly
from September 1979 to August 1980

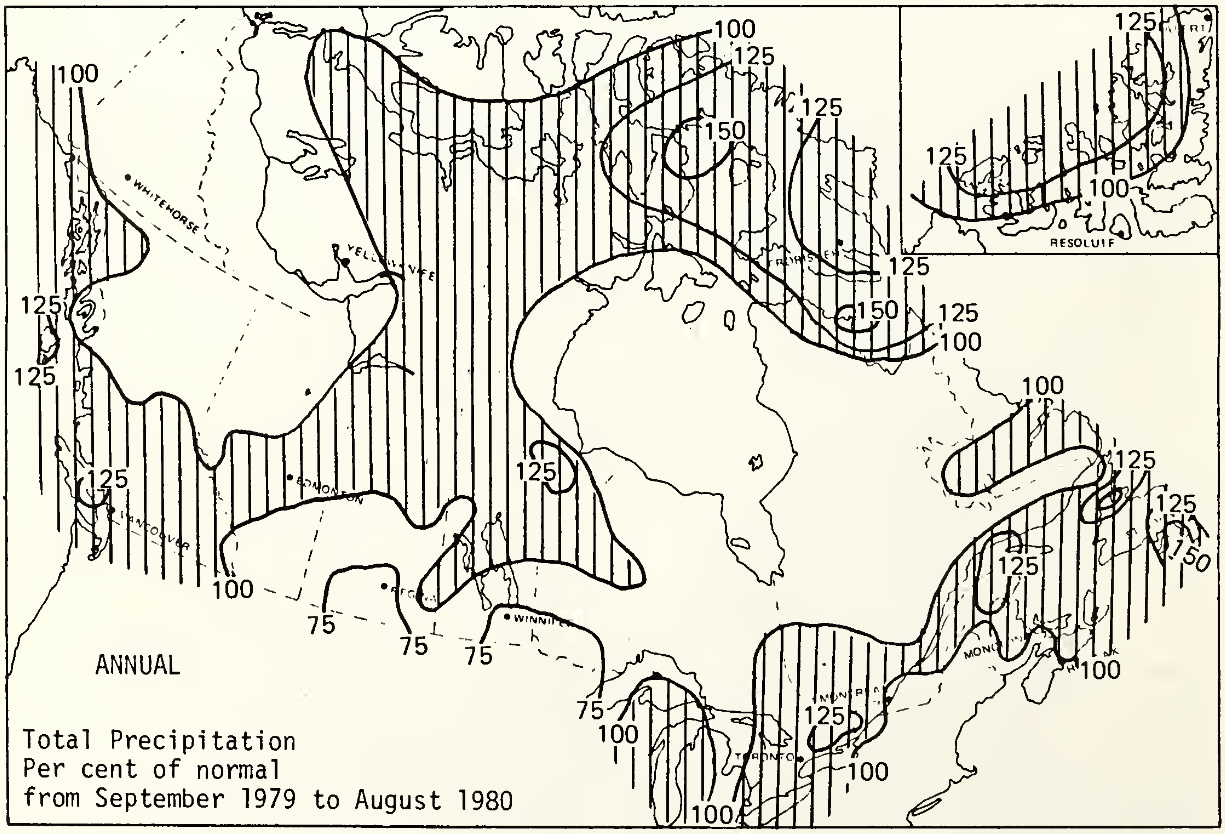

Total Precipitation
Per cent of normal
from September 1979 to August 1980

Special Aspects of the Long-Wave and Zonal Mean Structure from Winter to Summer 1980

R. S. Quiroz
Climate Analysis Center
NMC/NWS/NOAA
Washington, D. C. 20233

In the fields of zonal mean temperature and flow, three hemispheric events stand out from mid-1979 to mid-1980, (1) a radical change in the tropospheric temperature and flow patterns from early to late winter, which will be shown to be related to the peculiar development of planetary zonal height wave 2: (2) a major stratospheric warming event peaking at the end of February 1980; and (3) anomalous tropospheric warmth in summer 1980. Data used for this diagnosis consist mainly of zonal mean data and long-wave amplitudes and phases based on NMC maps at 700-10 mb.

The tropospheric winter changeover. Fig. 1 shows anomalies of zonal mean temperature at 500 mb (amplitudes at 700 mb are larger, but pattern is similar) and of zonal mean wind at 200 mb, near the level of maximum tropospheric winds. Note the switchover from warm (cold) in middle (high) latitudes around November-December to cold (warm) in middle (high) latitudes, beginning in January. Note the (hydrostatically) corresponding regions of positive and negative 200-mb wind anomaly, whose axes are aligned along the channels of maximum and minimum thermal gradient, respectively. Note also the time-scale of the anomalies, about 2-4 months, and the appearance of low-to-high latitude propagation.

What accounts for this remarkable transition from early to late winter? Saltzman and Teweles (1964) showed from 500-mb data that among zonal waves 1-15, wave 2 in winter leads in the transfer of KE to the mean zonal current. Recent work by van Loon and by the author shows further the importance of quasi-stationary wave 2 in wintertime patterns of meridional heat transport (with maximum cooling just south of its latitude of maximum amplitude). Fig. 2 shows the monthly amplitude of height wave 2 versus latitude at 500 mb (top), its departure from "normal" (middle), and axes of maximum (minimum) wave amplitude and corresponding axes of maximum (minimum) wind anomaly at 200 mb, the latter from Fig. 1. Note that at fixed latitude, wind features tend to follow wave features by one or more months (suggesting the possibility of developing a predictive capability). Note that at fixed time, there is a typical latitudinal displacement between wave and wind features of 5-20°. Using data for 60 months (October 1975-September 1980), we have correlated 200-mb wind at 35°N with 500-mb wave amplitude at 50°N, and find correlations greater than +0.8 for total wind and total wave amplitude and near +0.6 for their anomalies. This result indicates promise in the utility of wave-2 monitoring for diagnostic, and possibly predictive, uses.

Stratospheric warming. Reviews of observational and theoretical knowledge of the sudden warming phenomenon have been given by the author (in NASA RP 1049, Dec. 1979) and by Holton (Ann. Rev. Earth Plan. Sci., 1980). During the 1979-80 winter, the stratospheric event of greatest interest was the explosive warming at the end of February, which resulted in a reversal of the Equator-to-pole 10-mb temperature gradient around Feb. 27 (Fig. 3) followed by a reversal of the polar vortex flow at 65°N from westerly to easterly (Fig. 4). An earlier sudden increase in the arctic temperature occurred after Feb. 9 (Fig. 3), contributing to a total rise at 80°N by more than 50°C in 20 days. In both warmings the amplitude of thermal wave 1 at 10 mb (up to 21°C) exceeded that of wave 2; but the two warmings were associated with superpositioning of wave 1 and 2 at about 55-65°N near 170°N around Feb. 11, and near 120°E around Feb. 27, respectively. Note in Fig. 4 the successive reductions of mean zonal wind at 10 mb. The minimum on Mar. 20 was associated with warming concentrated in the lower stratosphere. Coupling of the tropospheric and stratospheric flow is discussed elsewhere by the author.

The general transition from westerly to easterly flow in the stratosphere, at 10 mb, is shown in Fig. 5. What is of particular interest from a quasi-climatic point of view is the long time scale, perhaps 2-4 months, of the wind anomalies, and as in the troposphere, the appearance of low-to-high latitude propagation of wind anomaly.

Anomalous tropospheric warmth in summer 1980. Detailed discussion is omitted here except for calling attention to the extraordinarily large positive height anomaly at 100 mb and 30°N (Fig. 6), which is the culmination of a rising trend since 1976. Another point of interest is the relationship between ridging over western longitudes at 700 mb (including the enhanced wave pattern over the U.S. related to the well-observed "heat wave") to ridging over southern Eurasia in the upper troposphere (the "Tibetan" anticyclone). A somewhat coherent behavior of these features is suggested by a similarity of amplitude and phase changes during the summer. These and other factors suggest that the U.S. heat wave was but one aspect of a broad hemispheric behavior.

In summary, the change in tropospheric temperature and wind regime from early to late winter was associated with a systematic development of planetary wave 2, marked by low to high latitude propagation of wave amplitude anomaly. The relationships indicated among wave and wind anomalies suggest there may be diagnostic, and possibly predictive, value in monitoring wave 2 developments. In the stratosphere, the major warming of early 1980 has provided further evidence of the importance of wave-wave interaction for warming events. In this respect, observation may be a little ahead of theory, because model simulations invoking certain theoretical concepts, to date, have assumed single-wave forcing for this phenomenon. With regard to the U.S. heat wave in summer 1980, we have strong indications that this was but one aspect of anomalous hemispheric behavior, and full understanding of what happened in the U.S. will probably require careful study of hemispheric variables.

FIGURE LEGENDS

Fig. 1 Anomaly in 500-mb mean zonal temperature (departure from "climatology"), deg C (top); and anomaly in 200-mb mean zonal wind m s^{-1} (bottom). In February, positive anomaly reached 8 m s^{-1} near 30°N.

Fig. 2 Amplitude (gpm) of 500-mb height wave 2, based on monthly mean charts (top) and anomaly in same (middle); and axes of maximum and minimum anomaly in wave amplitude and zonal wind, the latter at 200 mb (bottom). Axes are drawn exactly according to the numerical data.

Fig. 3 Traces of daily 10-mb zonal mean temperature near the Equator and North Pole, showing gradient reversal in late February.

Fig. 4 Time-section of zonal mean geostrophic wind at 65°N (m s^{-1}), showing reversal to easterlies by early March.

Fig. 5 Time-latitude sections, based on monthly data, of 10-mb zonal mean wind (top) and its anomaly (bottom). Note long time-scale of anomalies and lead from low latitudes.

Fig. 6 Anomaly in 100-mb zonal mean height at 30°N, for summer months 1976-80.

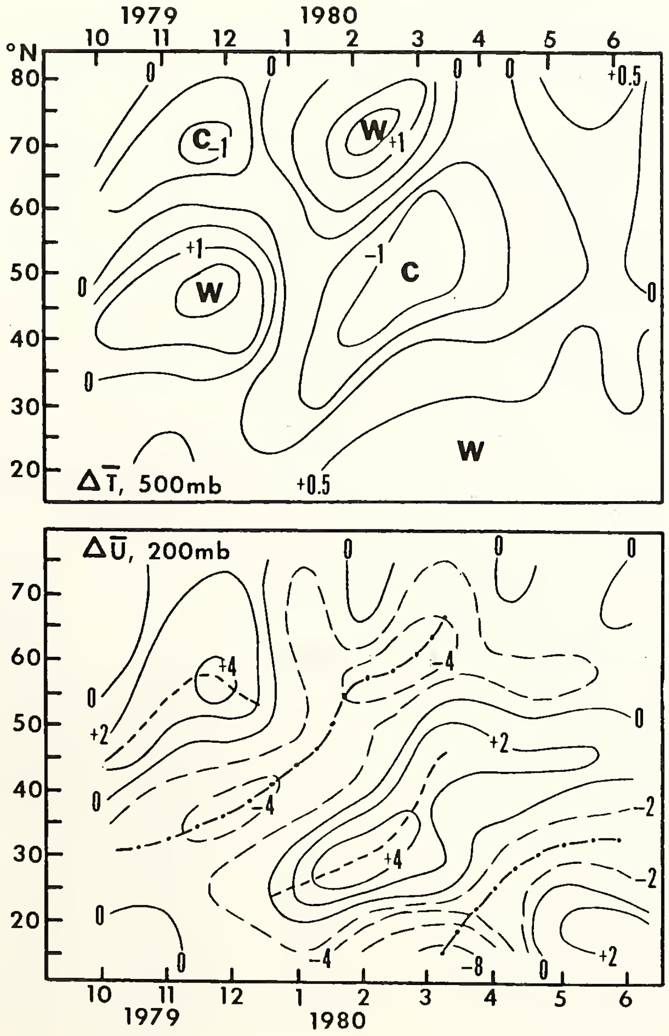

Figure 1

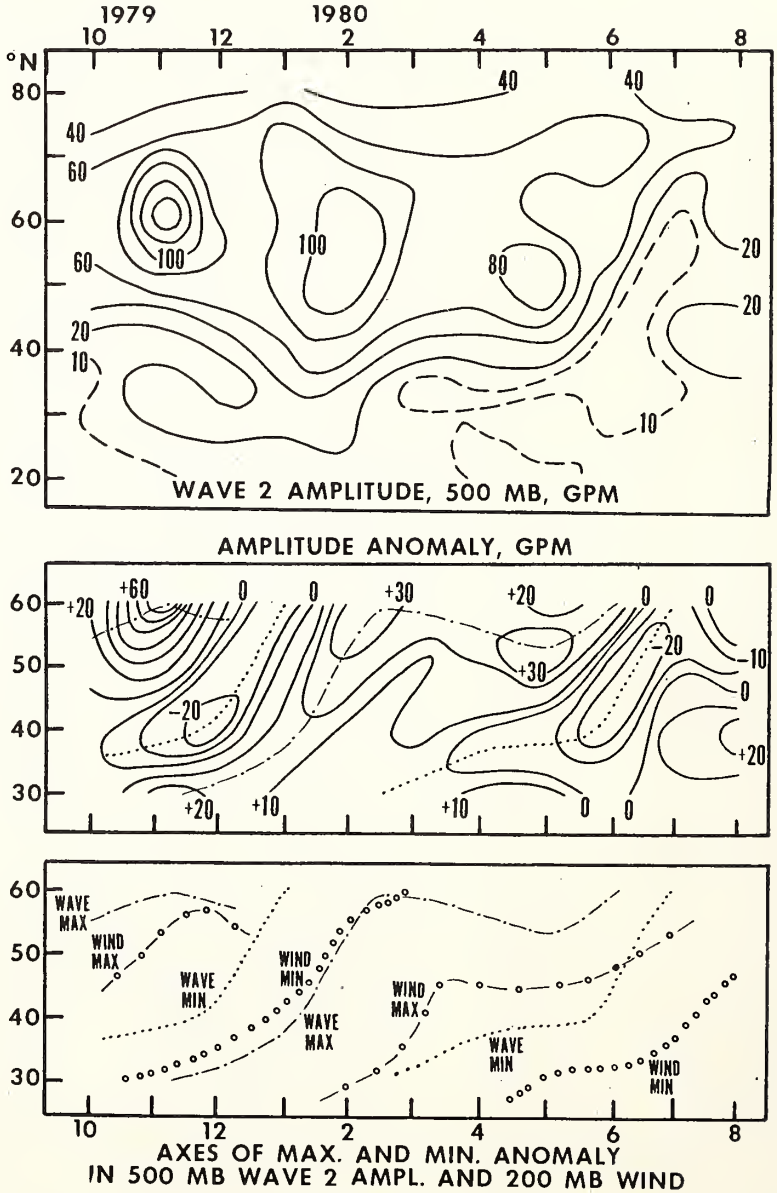

Figure 2

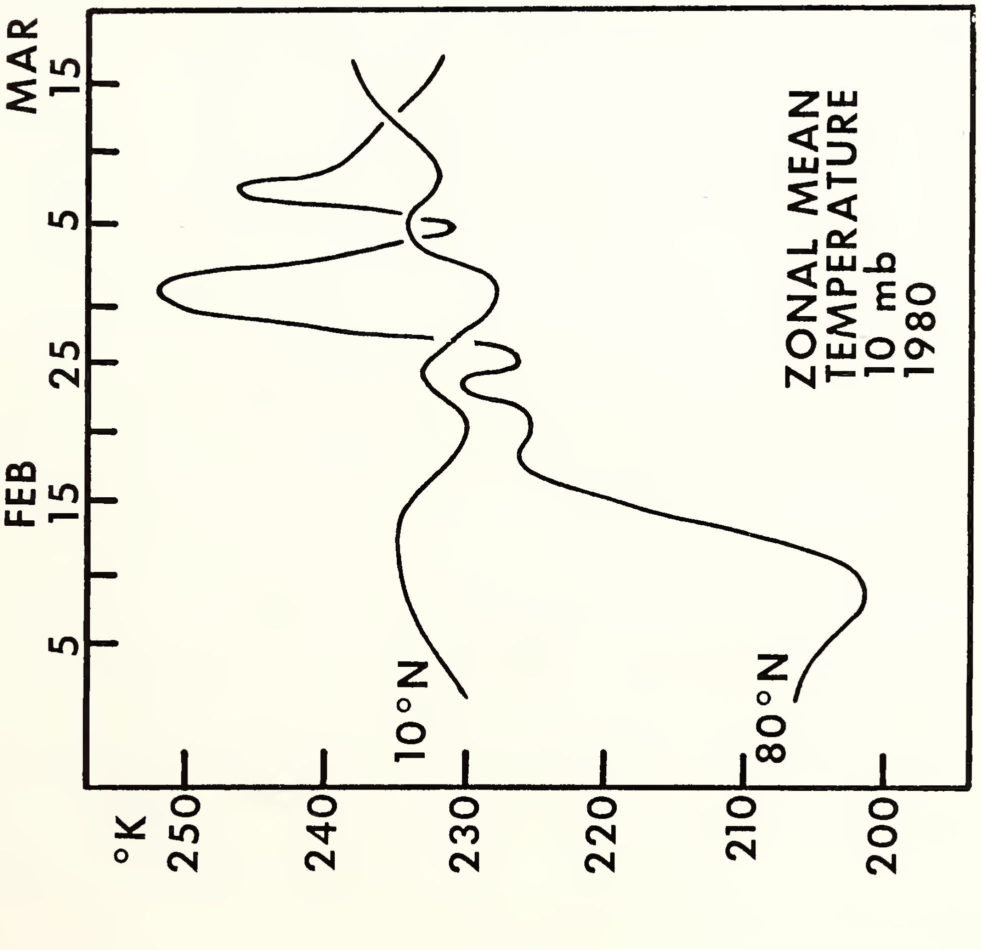

Figure 3

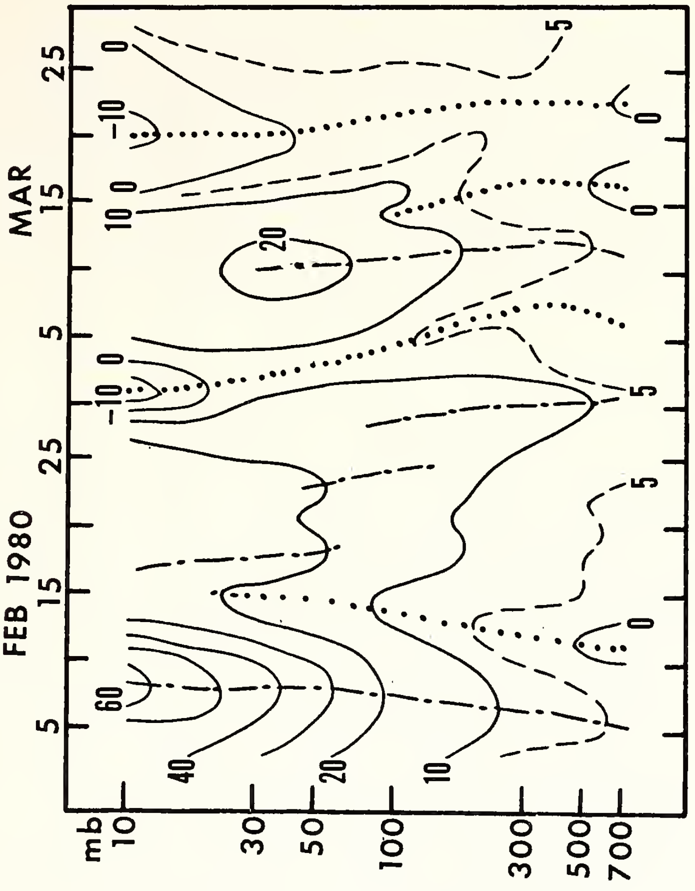

Figure 4

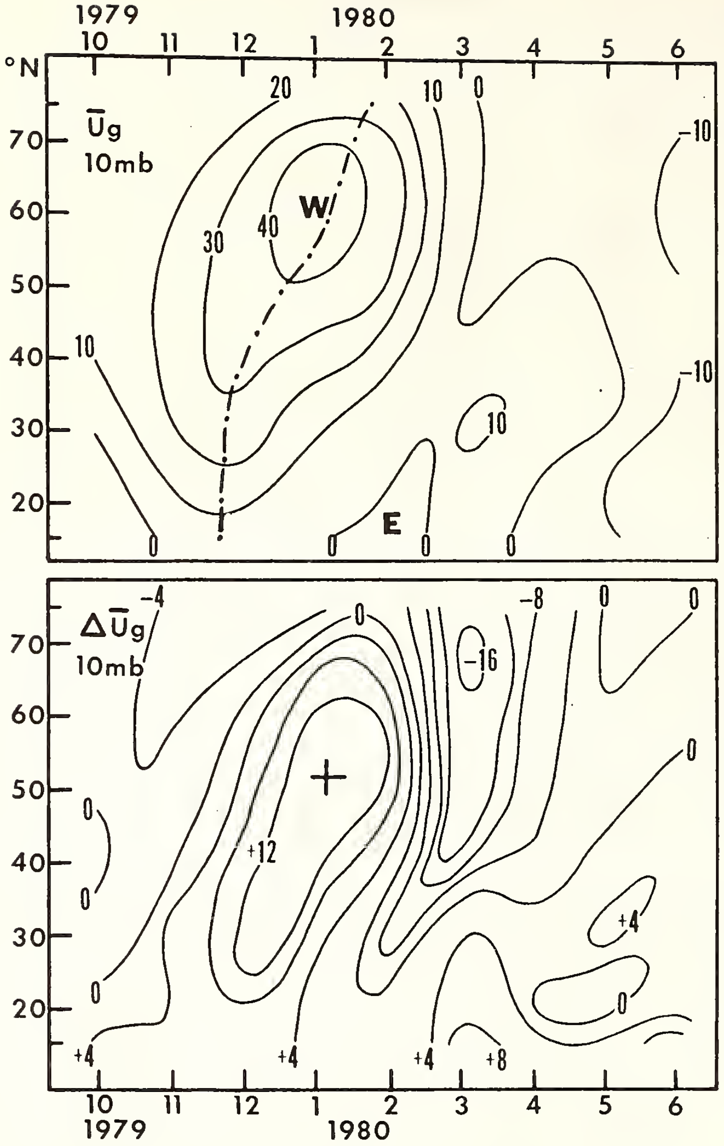

Figure 5

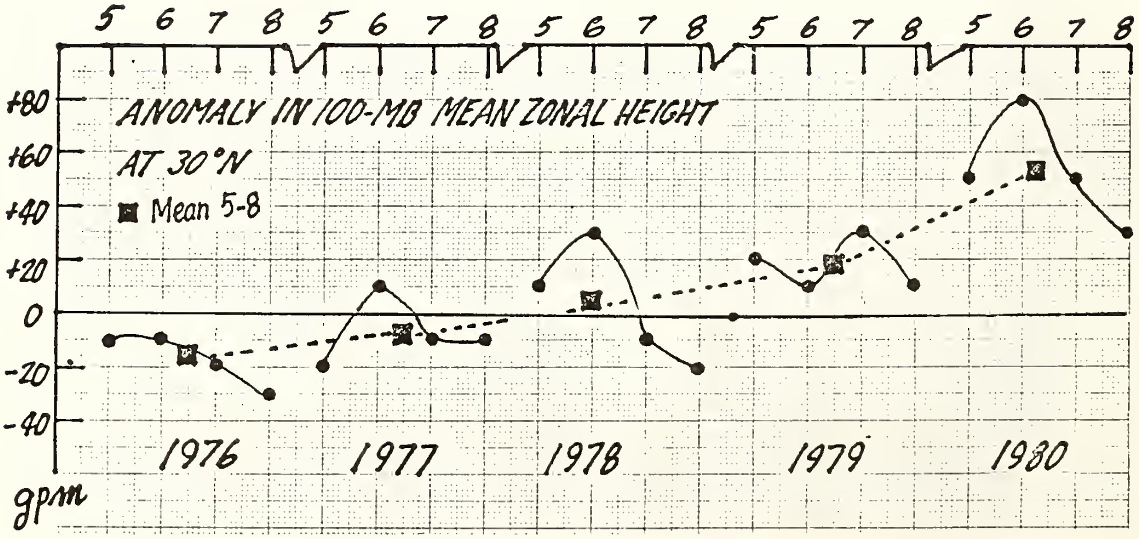

Figure 6

The heavy California winter rains of 1979-80 as a manifestation of macroscale air/sea coupling

Jerome Namias
University of California, San Diego
Scripps Institution of Oceanography
La Jolla, California 92093

This paper represents an attempt to show that heavy California rains such as occurred in the winter of 1979-80 are frequently associated and probably caused by large-scale interactions between the eastern Pacific atmospheric circulations and the coupled sea surface temperatures. The immediate causes of the heavy rainfalls are discussed and indicate the sensitivity of southern California coastal rainfall to the prevailing mid-tropospheric flow impinging on the coast. The individual processes involve orographic lifting, atmospheric vertical motions associated with fronts and storms, humidity and temperature distribution with elevation and inducement of tropical air into the systems, and air-sea temperature contrasts.

Some of the above physical factors are shown to be implied by correlation fields between southern California rainfall in winter months and the contemporary anomalous wind patterns in mid-troposphere. This correlation pattern also implies the conditions leading to extremely dry situations often associated with the well known Santa Anas.

Although the winter 1979-80 was an extreme period in terms of precipitation, it is shown that the winters of 1977-78 and 1968-69 had similar characteristics—particularly in terms of sea surface temperature patterns. These patterns involve very cold water in the Central Pacific but abnormally warm water extending southwestward from California. The anomalous gradient between these two extensive water masses was sharp and existed perhaps 25-30° westward of California.

It is shown that this gradient of sea surface temperature existed for several months before the onset of the winter rains, a fact which holds out the hope for longer than one season prediction of atmospheric climatic anomalies.

It must be stressed, however, that, in order for the resident sea surface temperature pattern to influence the overlying atmosphere, proper reinforcement from the atmospheric pattern must occur. In this case the excitation of the storms may have been provided by the sea surface temperature gradient. This coupling could occur mainly during late winter when westerlies and storm tracks are normally at their farthest south position.

Obviously, the sea surface temperature distribution described will not produce excitation of storms in other seasons, when the normal seasonal forcing provides for a northerly storm track. This coupling is so sensitive as to make small scale one season predictions very difficult, but, in spite of this, modest success has been achieved for the California and, indeed, western U. S. area over the past five years.

LEGENDS TO FIGURES

Fig. 1 Isopleths of correlation (drawn for every 0.10) between winter precipitation in southern California coastal area (heavy black) and sea level pressure elsewhere. Note that heavy southern California precipitation is associated with low pressure, southwest anomalous flow immediately off coast, and higher pressure than normal in the central Pacific. Dry conditions (Santa Anas) are associated with opposite type circulation.

Fig. 2 Observed percentages of normal precipitation over western third of U. S. (top) for winters of 1975-76 through 1970-80, and predicted Heavy, Moderate or Light classes (below). Note severe drought of 1976-77 winter and heavy rains in 1977-78 and 1979-80 winters.

Fig. 3 (Lower) Observed sea surface temperature anomalies and anomalies of 700 mb height for winter 1979-80. Temperatures warmer than 1°F are shaded to the right of the strong gradient while below normal temperatures are to the left. (Top) Specified SST patterns from lower 700 mb anomalies and also specified 700 mb anomalies from observed SST anomalies. Note reasonable agreement between specified and observed field.

Fig. 4 Principal cyclone tracks in February 1980. Note southward displacement of tracks associated with southward displacement of westerlies.

Fig. 5 Vertical temperature and dewpoint distribution for wet month of February 1980 and dry February 1977. Note the higher surface temperatures and dewpoints in boundary layer for wet month relative to dry.

Fig. 6 700 mb contours (solid) and sea surface temperature anomalies (shaded) for December 1979 and January and Feburary 1980. Note strong SST gradient near area of maximum cyclonic curvature.

Fig. 7 700 mb contours and SST anomalies for September, October, November and December 1979. Note persistence over long period which held roughly throughout the subsequent winter.

Fig. 8 (Lower) Observed winter 700 mb height anomalies (solid lines) and SST anomalies (shaded). Note strong SST gradient and relationship to anomalous trough off West Coast. (Top) Specified SST anomalies and 700 mb anomalies based on conditions observed in lower portion of figure.

Fig. 9 SST anomalies preceding and during the 1968-69 winter. Note strong gradient with southwest-northwest orientation.

Fig. 10 SST anomalies for the antecedent months to 1969 winter. Note persistence of strong gradient between cold and warm water.

Fig. 11 Antecedent months SST anomalies for March, April, May and June 1968. Note tenacity of strong northwest-southeast gradient off West Coast.

Fig. 12 Winter SST anomalies during wet winter 1977-78. Note strong gradient off coast.

Fig. 13 Isopleths of 700 mb anomalies (solid) and SST anomalies (shaded) for the dry winter 1976-77. While strong gradient between cold and warm water is indicated note that it is oriented north-south in contrast with wet winters. Note also the domination of the West Coast by positive height anomalies.

Fig. 14 (Upper) Pattern correlation between SST field in 1980 with patterns of other winters—also 700 mb height pattern correlations. Bottom of figure shows total precipitation observed in south coast of California drainage area. Note that the wet winters of 1978 and 1969 had similar large scale SST patterns to 1980. However, other years like 1958 and 1959 do not show comparable precipitation because of great sensitivity of small southern California areal precipitation to SST and 700 mb patterns. In other words, tuning between atmosphere and ocean must be fine to use in prediction studies.

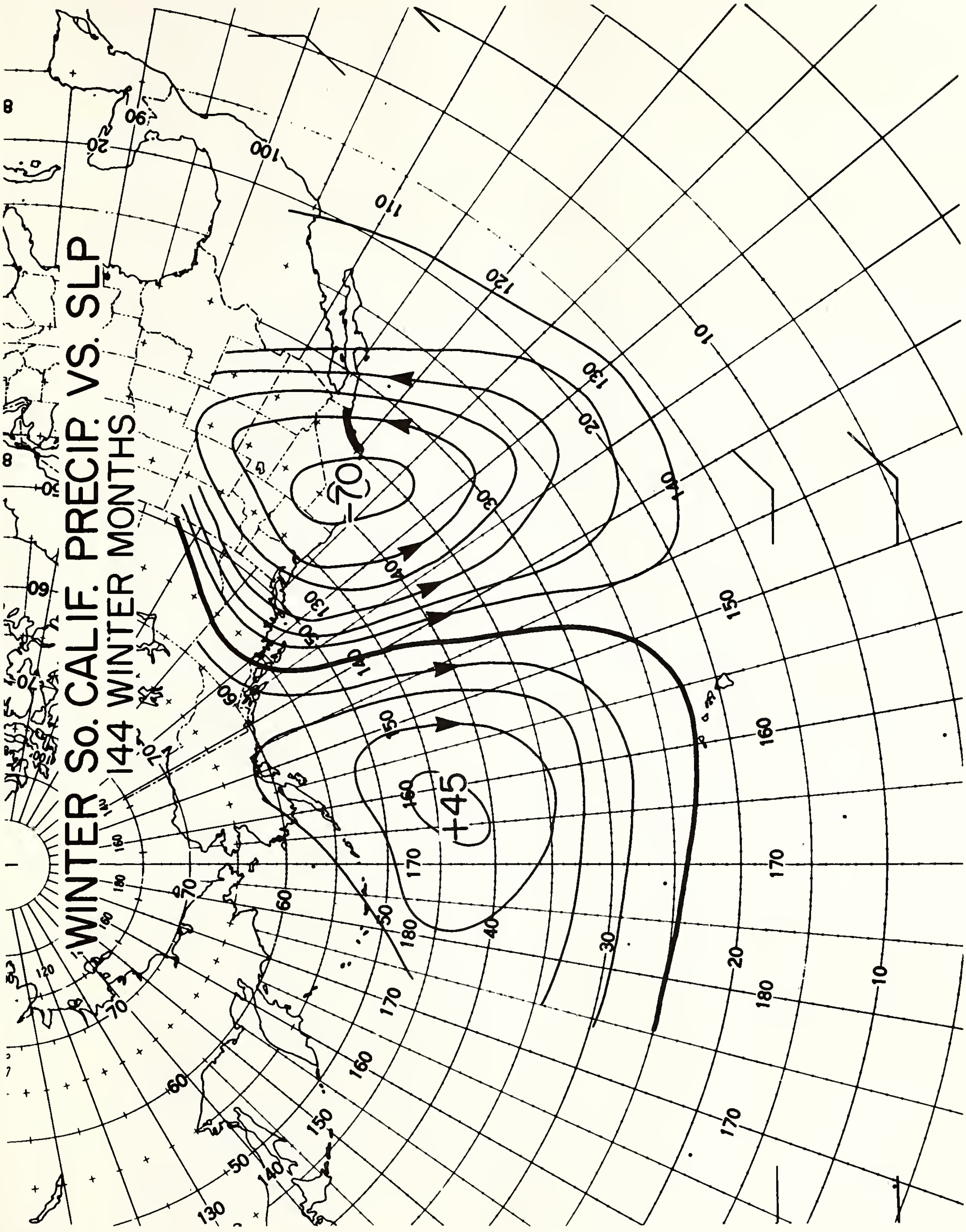
WINTER So. CALIF. PRECIP. VS. SLP
144 WINTER MONTHS
-70
+45
10
20
30
40
50
60
140
150
160
170
180
130
120
110
100
90
70

Figure 1

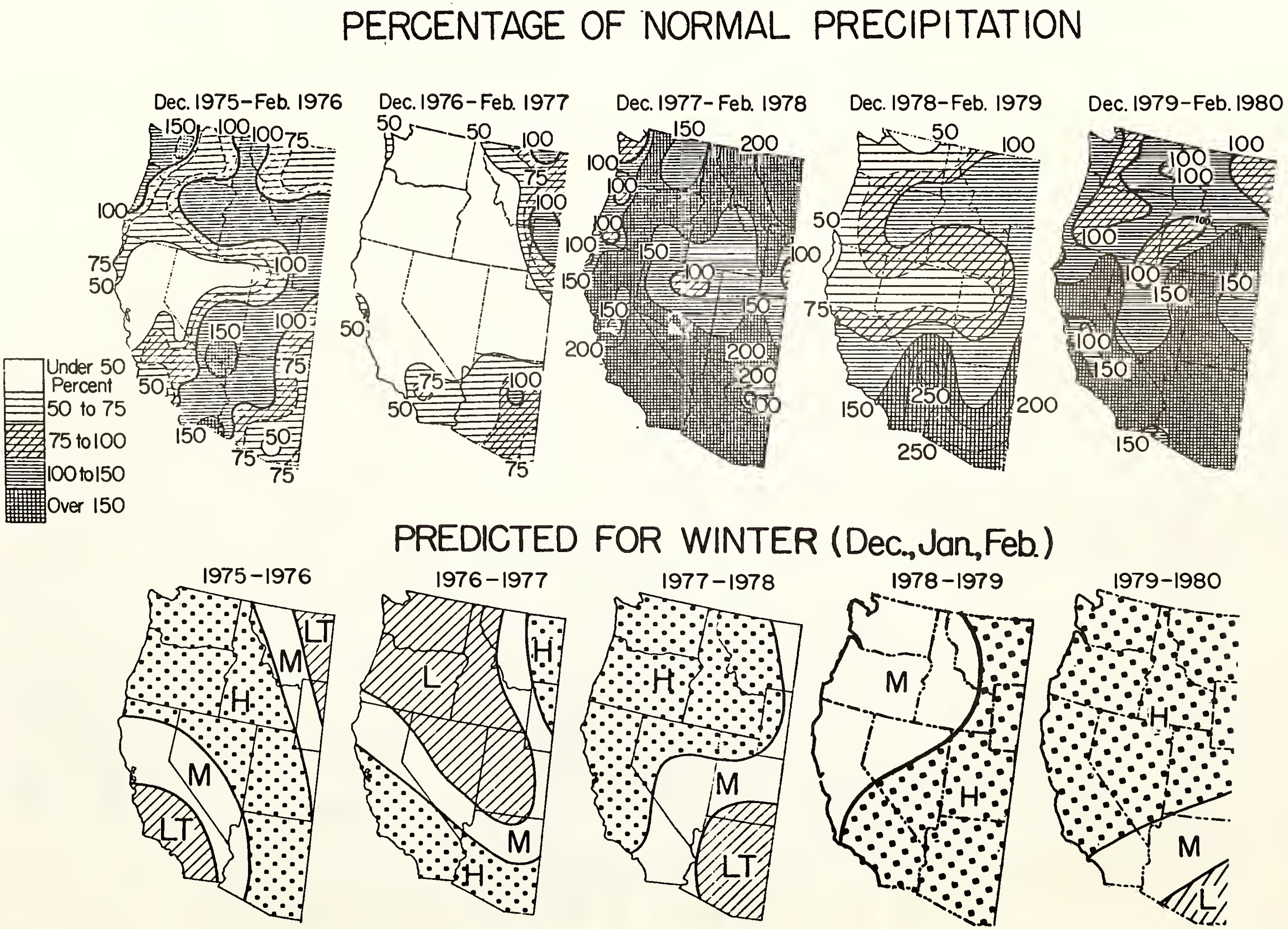
PERCENTAGE OF NORMAL PRECIPITATION
Dec. 1975-Feb. 1976
150
100
100
75
100
75
50
100
150
100
75
50
150
50
75
75
Dec. 1976-Feb. 1977
50
50
100
75
100
50
75
50
100
75
Dec. 1977-Feb. 1978
150
200
100
100
100
100
150
150
100
100
150
150
200
200
200
Dec. 1978-Feb. 1979
50
100
50
75
150
250
250
200
Dec. 1979-Feb. 1980
100
100
100
100
100
100
150
150
100
150
150
Under 50 Percent
50 to 75
75 to 100
100 to 150
Over 150
PREDICTED FOR WINTER (Dec., Jan, Feb.)
1975-1976
LT
M
H
M
LT
1976-1977
L
H
M
H
1977-1978
H
M
LT
1978-1979
M
H
1979-1980
H
M
L

Figure 2

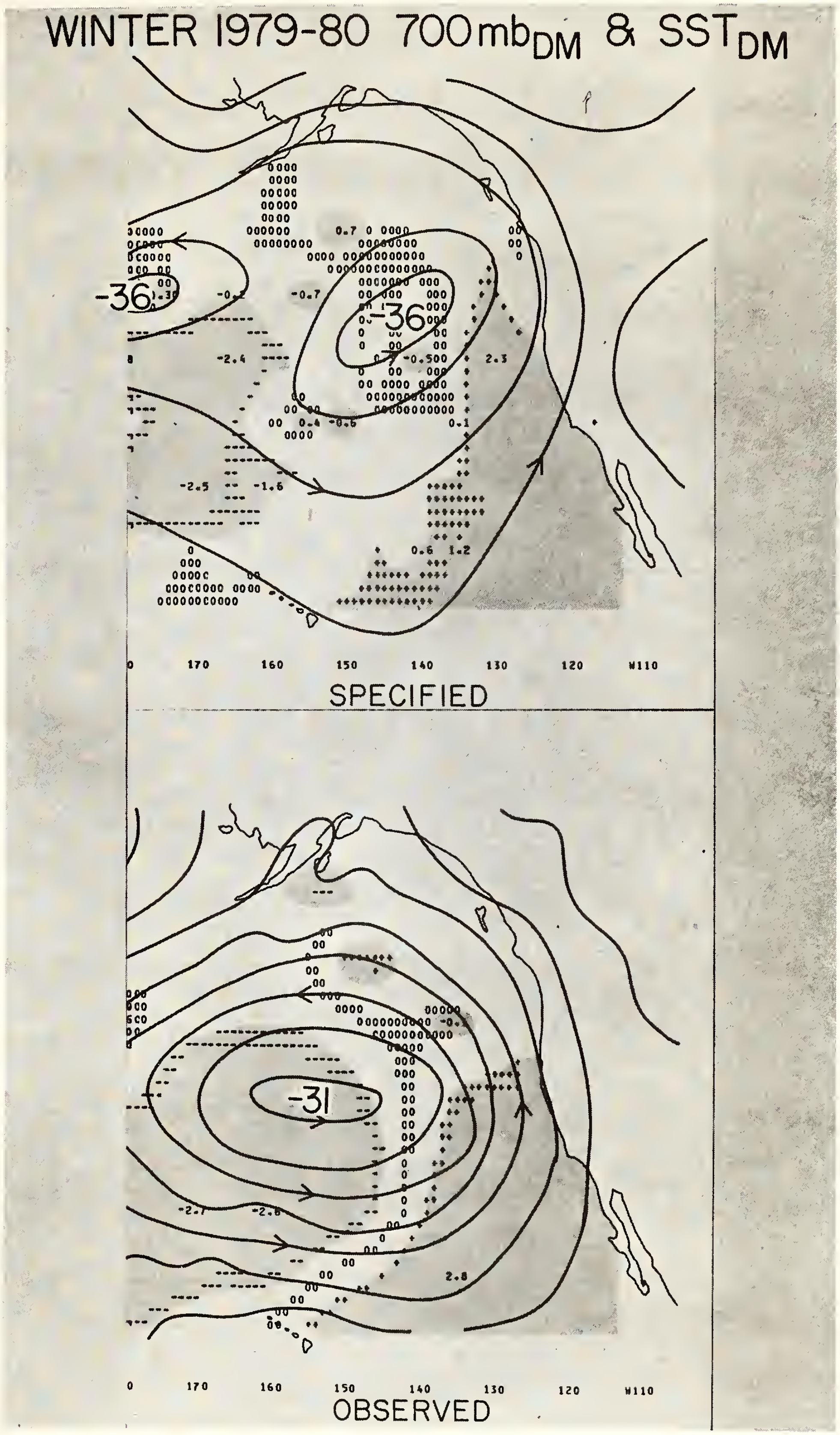
WINTER 1979-80 700mb$_{DM}$ & SST$_{DM}$
-36
-36
0.7
-0.7
-2.4
-0.500
2.3
0.4
-0.6
0.1
-2.5
-1.6
0.6
1.2
170
160
150
140
130
120
W110
SPECIFIED
-31
-2.7
-2.8
2.8
170
160
150
140
130
120
W110
OBSERVED

Figure 3

Principal Tracks of Centers of Cyclones at Sea Level, North Pacific

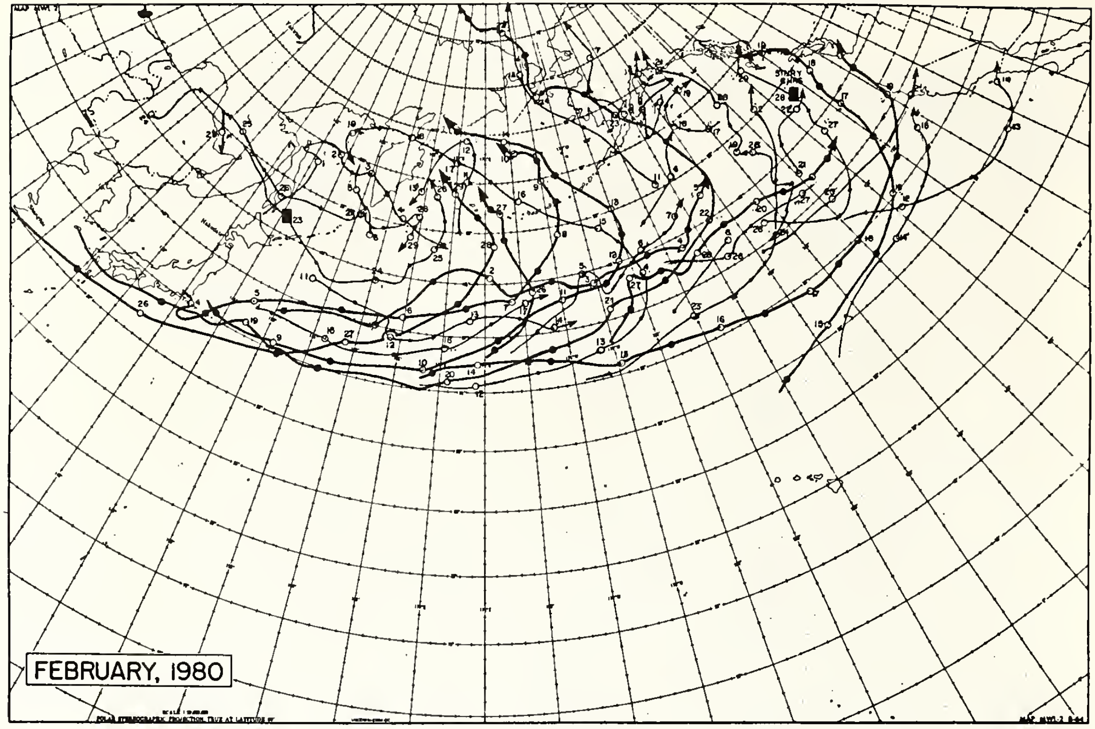

Figure 4

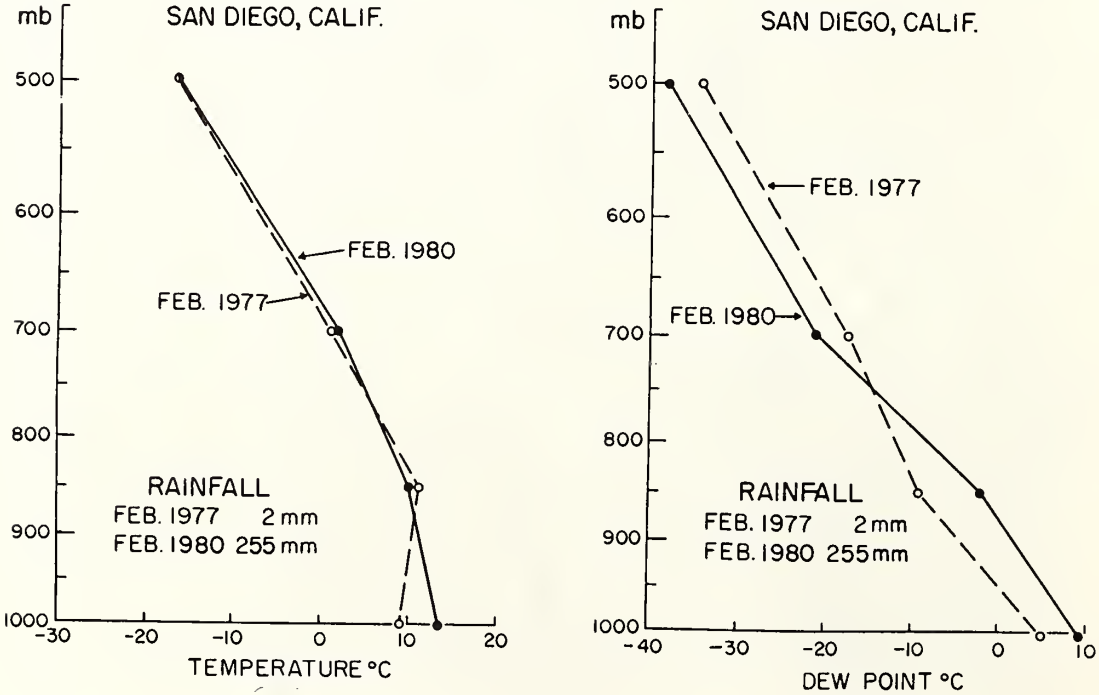

A

B

Figure 5

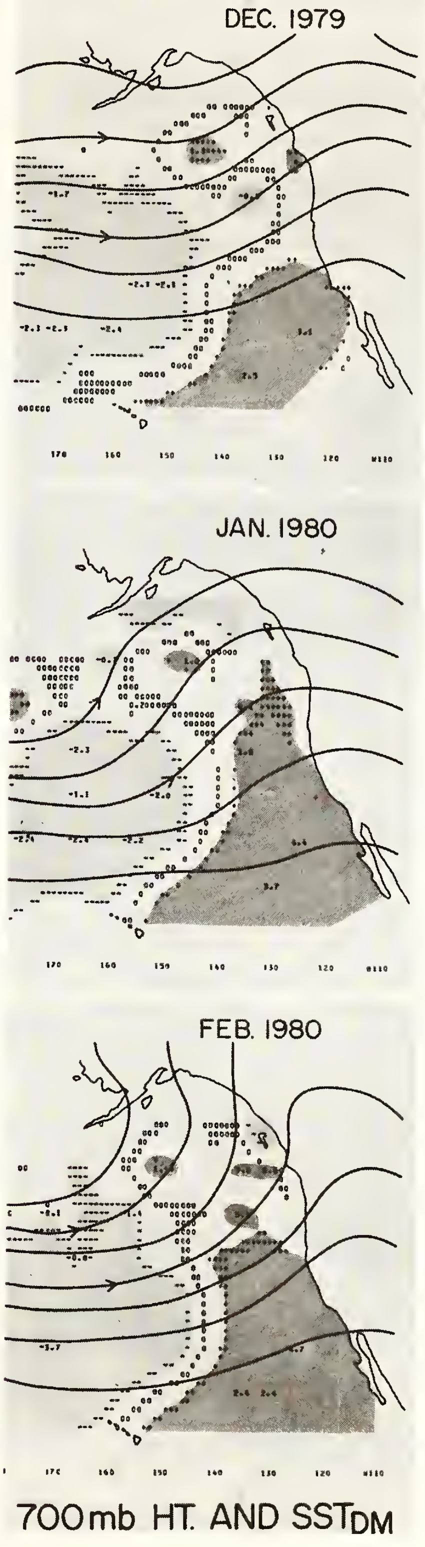

DEC. 1979

JAN. 1980

FEB. 1980

700mb HT. AND SST$_{DM}$

Figure 6

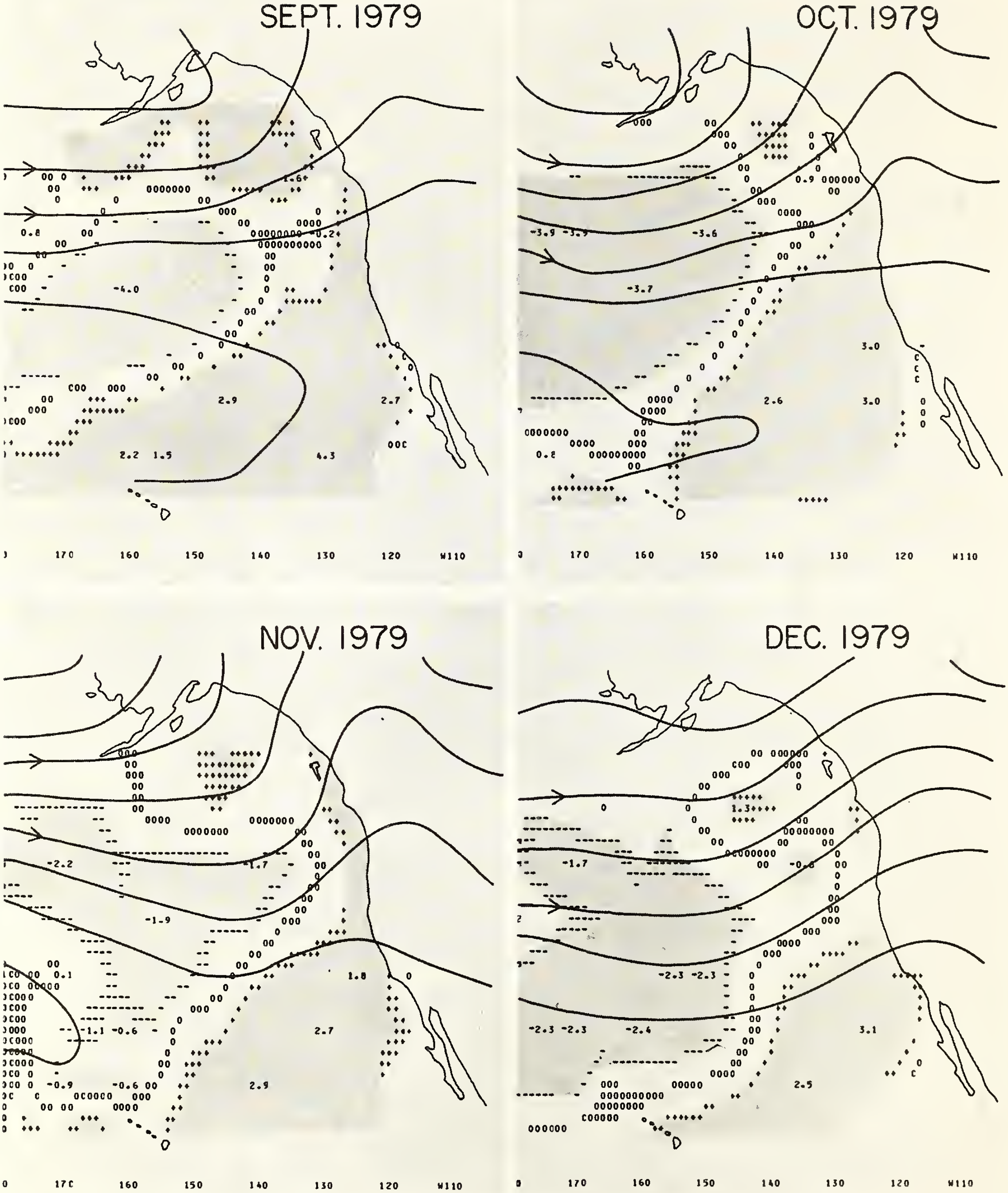

OBSERVED 700mb HT. AND SST_{DM}

Figure 7

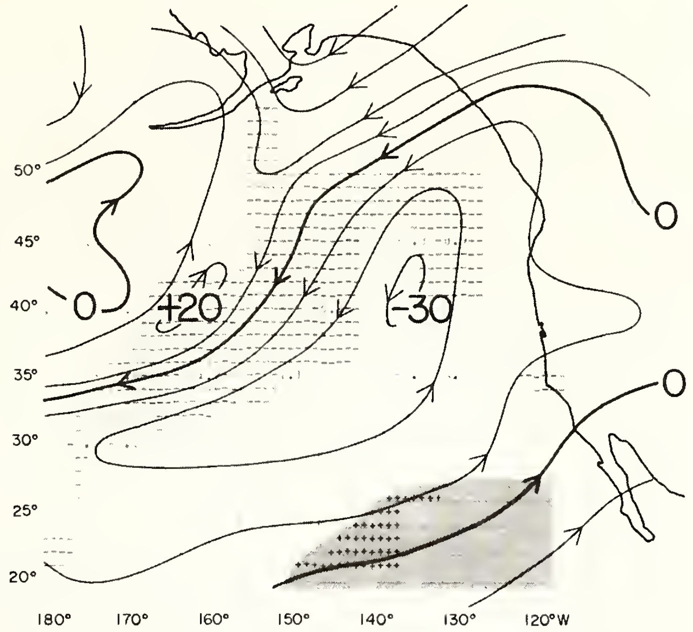

SPECIFIED WINTER 1968-69

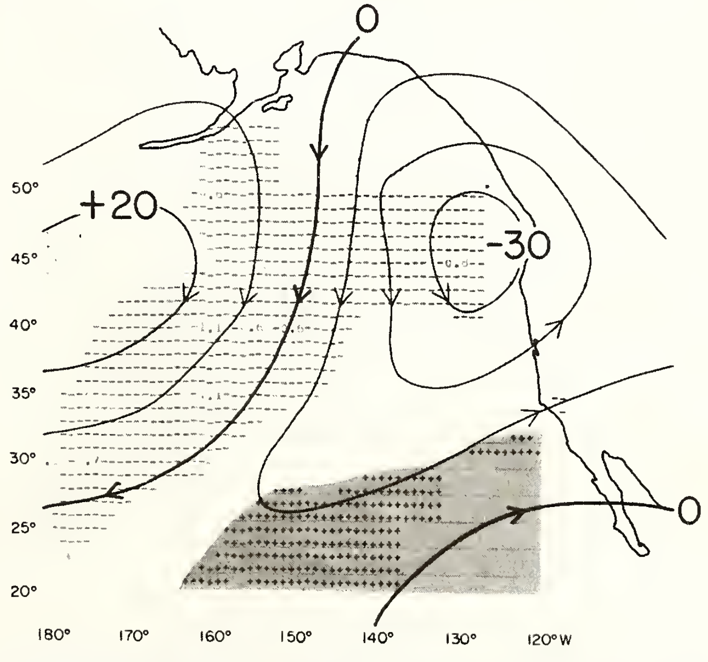

OBSERVED WINTER 1968-69

Figure 8

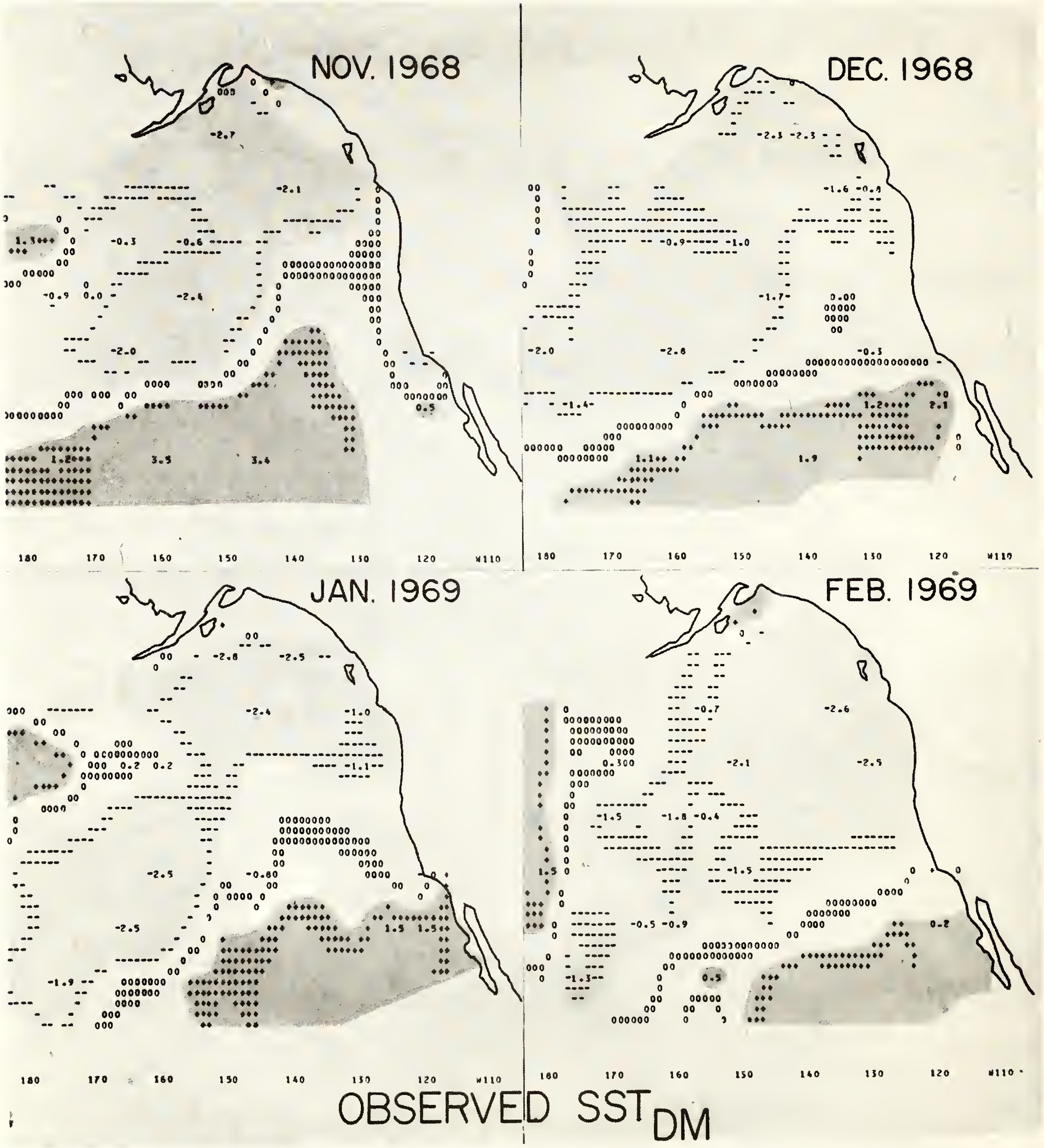
NOV. 1968
DEC. 1968
JAN. 1969
FEB. 1969
180
170
160
150
140
130
120
W110
OBSERVED SST_{DM}

Figure 9

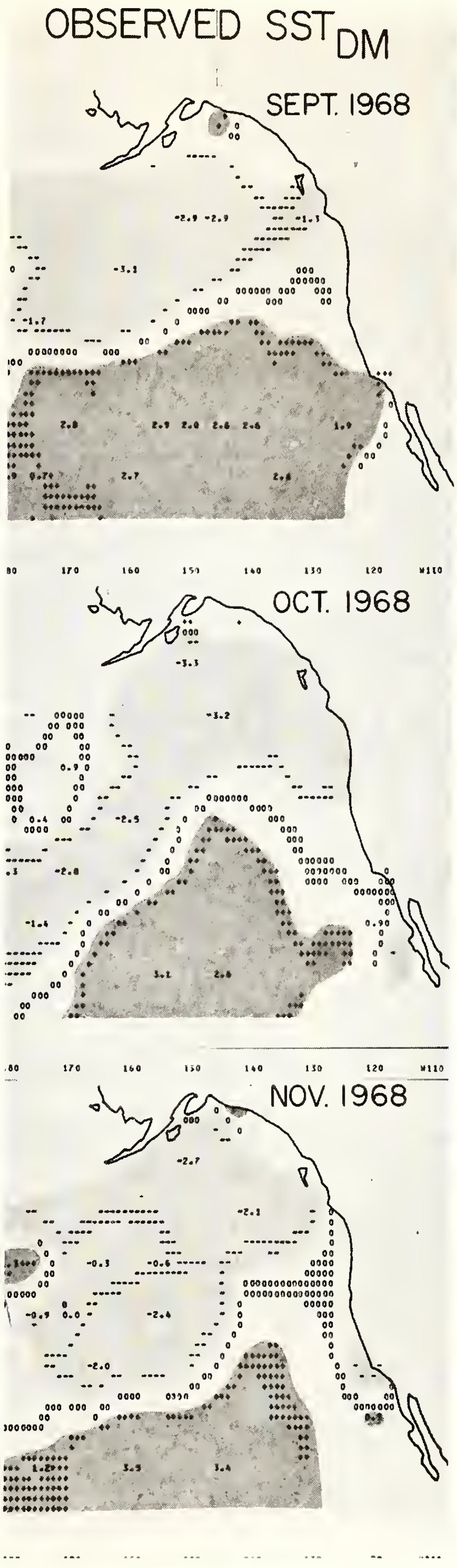
OBSERVED SST$_{DM}$
SEPT. 1968
OCT. 1968
NOV. 1968
80
170
160
150
140
130
120
W110

Figure 10

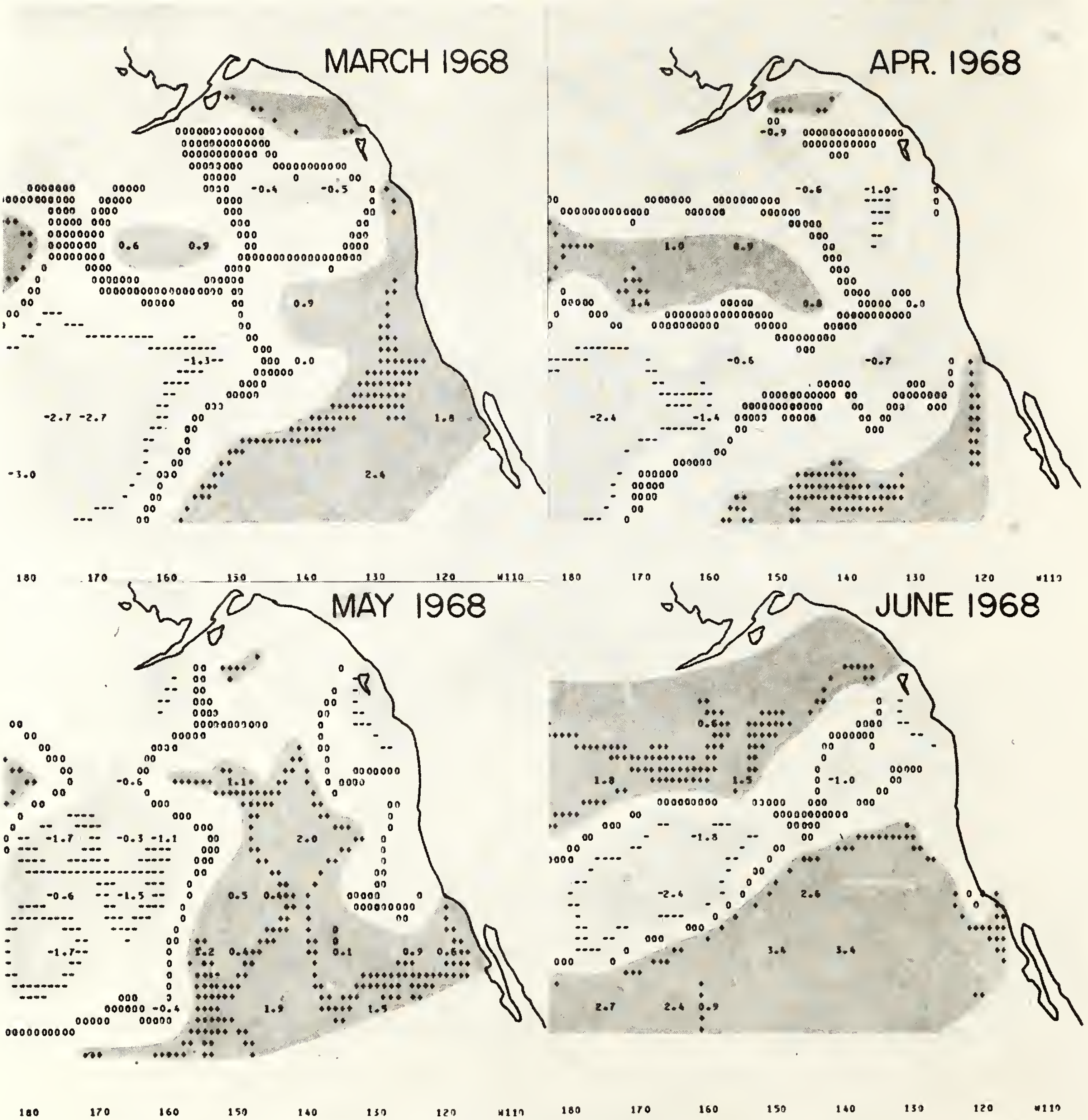

OBSERVED SST_{DM}

Figure 11

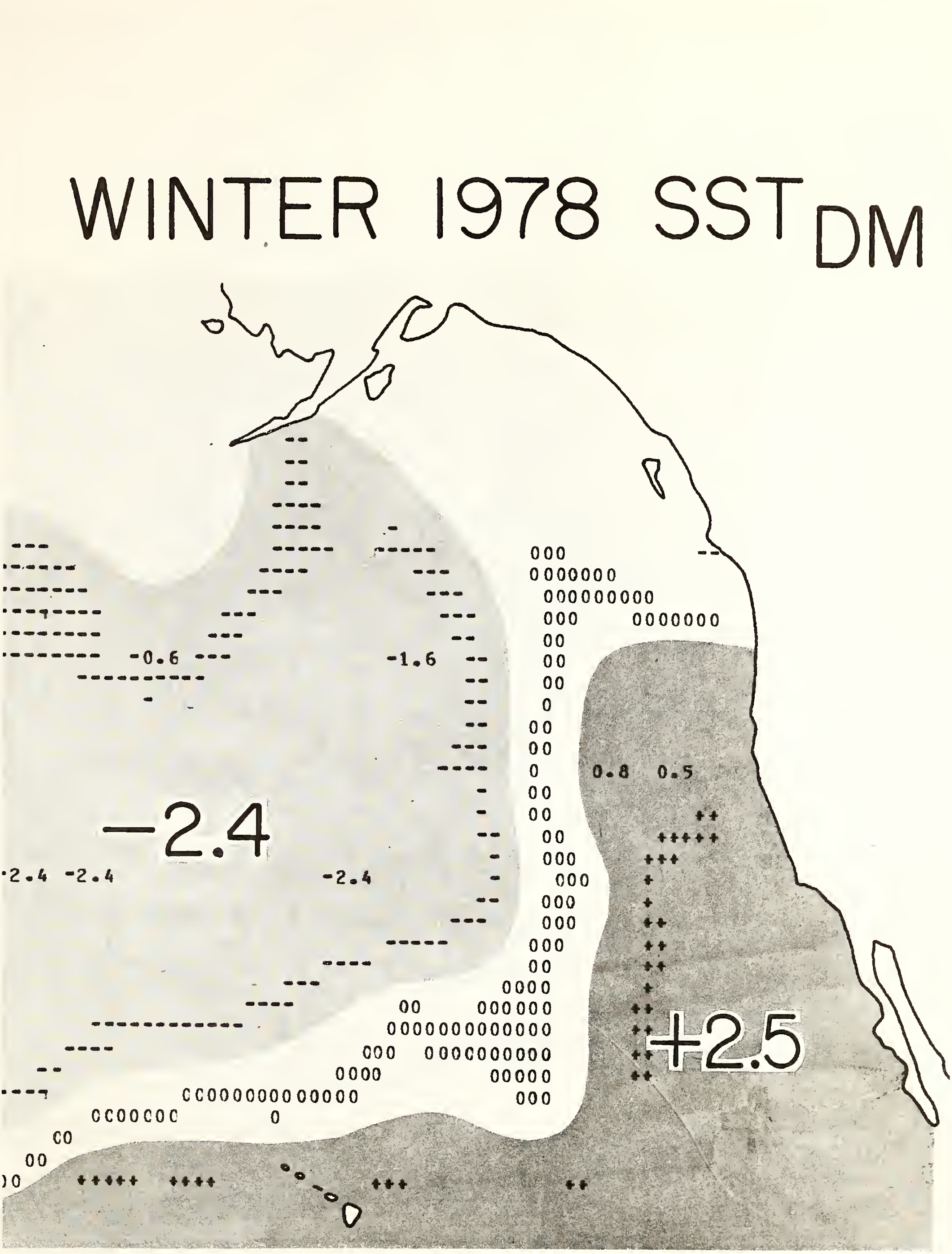
WINTER 1978 SST$_{DM}$
-0.6
-1.6
0.8
0.5
−2.4
-2.4
-2.4
-2.4
+2.5
180
170
160
150
140
130
120
W110

Figure 12

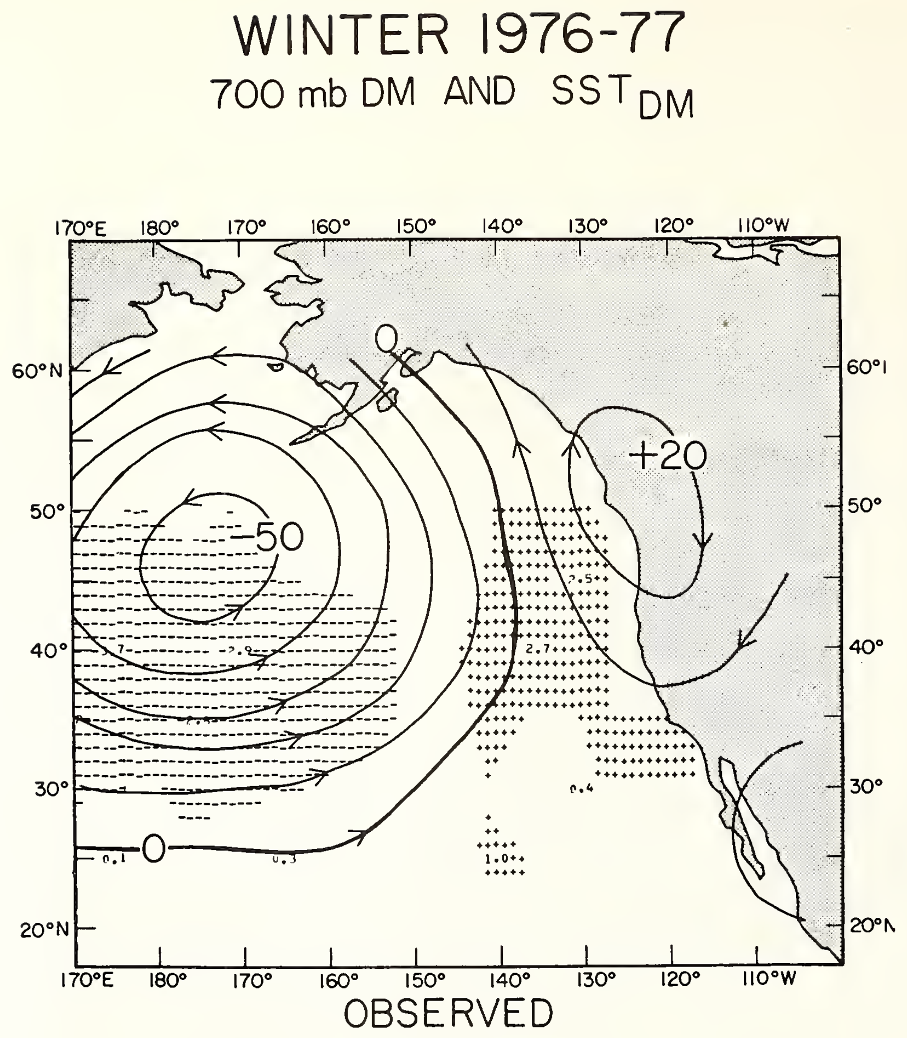

Figure 13

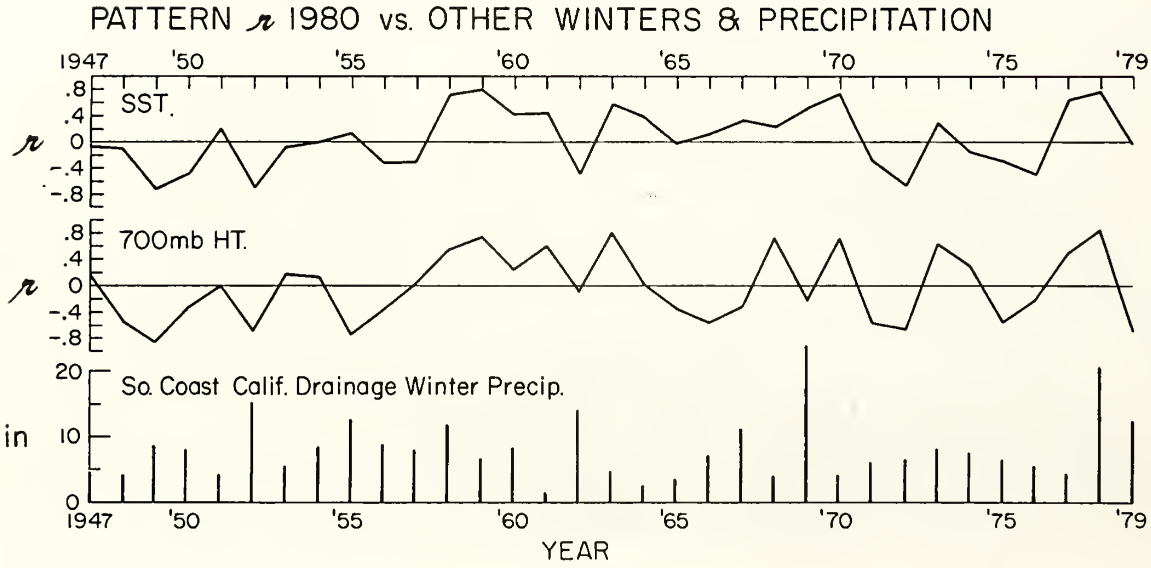

Figure 14

SNOW AND ICE IN 1979-80: A GLOBAL OVERVIEW

G. Kukla and J. Gavin

Lamont-Doherty Geological Observatory
Palisades, NY 10965 USA

Snow and sea ice indices were updated through July 1980 from information contained in the NOAA and Navy charts. Both the area and the parametrized surface reflectivity are reported on a global and regional basis. The following general observations can be made:

1) Snow in the Northern Hemisphere was less extensive than the previous year in all months with the most marked decrease occurring from October 1979 through January 1980 (Fig. 1). Expectably, the 12 month running means of total snow cover area and surface reflectivity for land north of 30°N showed a decrease (Fig. 2). (Figures for October and November are preliminary and will require future revisions since there were insufficient data available at the time of the original analysis.)

2) The parameterized surface reflectivity for land between 30-90°N increased from February through April 1980 with both March and April at record high levels (Fig. 1). Regionally this increase can be attributed to eastern Asia, eastern Europe and, to a lesser extent, central Asia (Fig. 3).

3) Arctic ice was less extensive in all months except May, June, and August. The largest decrease of ice area, compared to the previous year, occurred in October. As a result, the 12 month running means of ice cover extent and of the sea surface reflectivity decreased (Fig. 5). The reflectivity index showed an increase from April through July but decrease in other seasons (Fig. 4).

4) Regionally, the departures of ice cover in the North Atlantic segment (Barents and the East Greenland Sea) and in the Sea of Okhotsk were generally out of phase with that in the Bering, Chuckchee, and Beaufort Seas (Fig. 6).

5) The Antarctic pack ice extent decreased compared to the previous year in all months except September

through November of 1979 (Fig. 7). The monthly averages for December 1979 through July 1980 are the lowest of the analysed interval. This is also true for the 12 month running means of the total ice extent and of the surface reflectivity index (Fig. 8). An especially large negative departure of the sea ice area was observed in the Ross Sea segment (Fig. 9).

……

Kukla, G. and Gavin, J. 1978. Proceedings of the Third Annual Climate Diagnostics Workshop, October 31-November 2, 1978, Miami, Florida. 9-1/9-15.

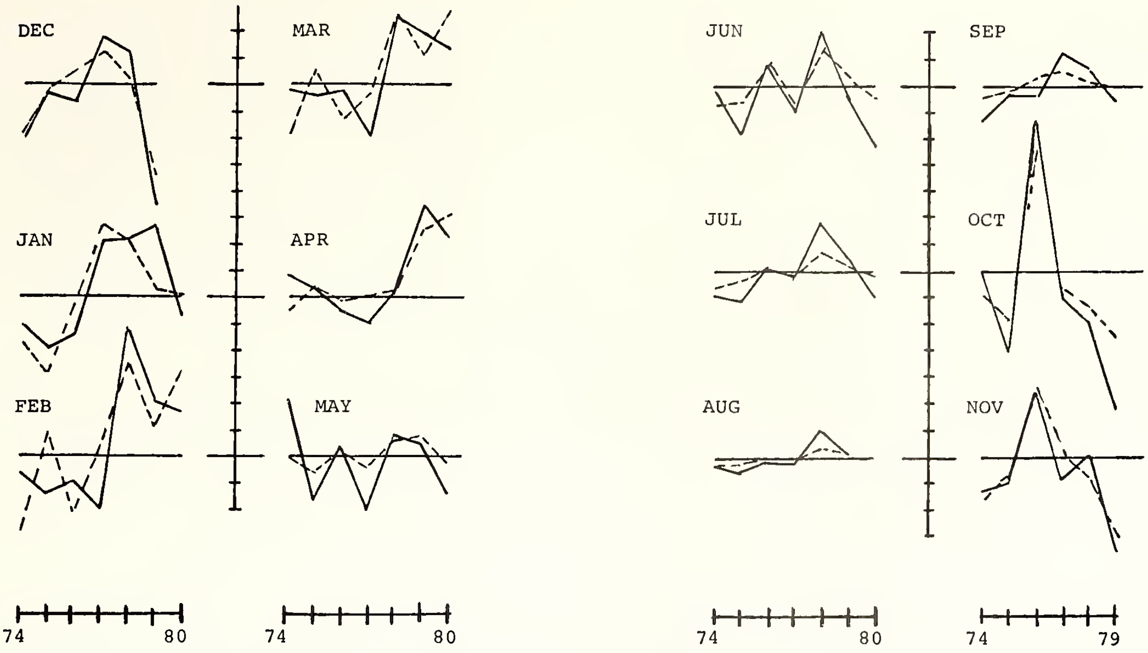

Fig. 1. Average monthly departures from the 1974-78 means of total snow extent in the Northern Hemisphere (solid line) and of the surface reflectivity index (dashed line) for land between 30-90°N. Vertical scale in increments of $10^6 km^2$ of snow cover area and 1% of surface reflectivity. More extensive snow area and higher reflectivity plotted upwards. Data through July 1980. Observe the decrease of snow cover compared to the previous year but an increase of relative reflectivity in February, March and April.

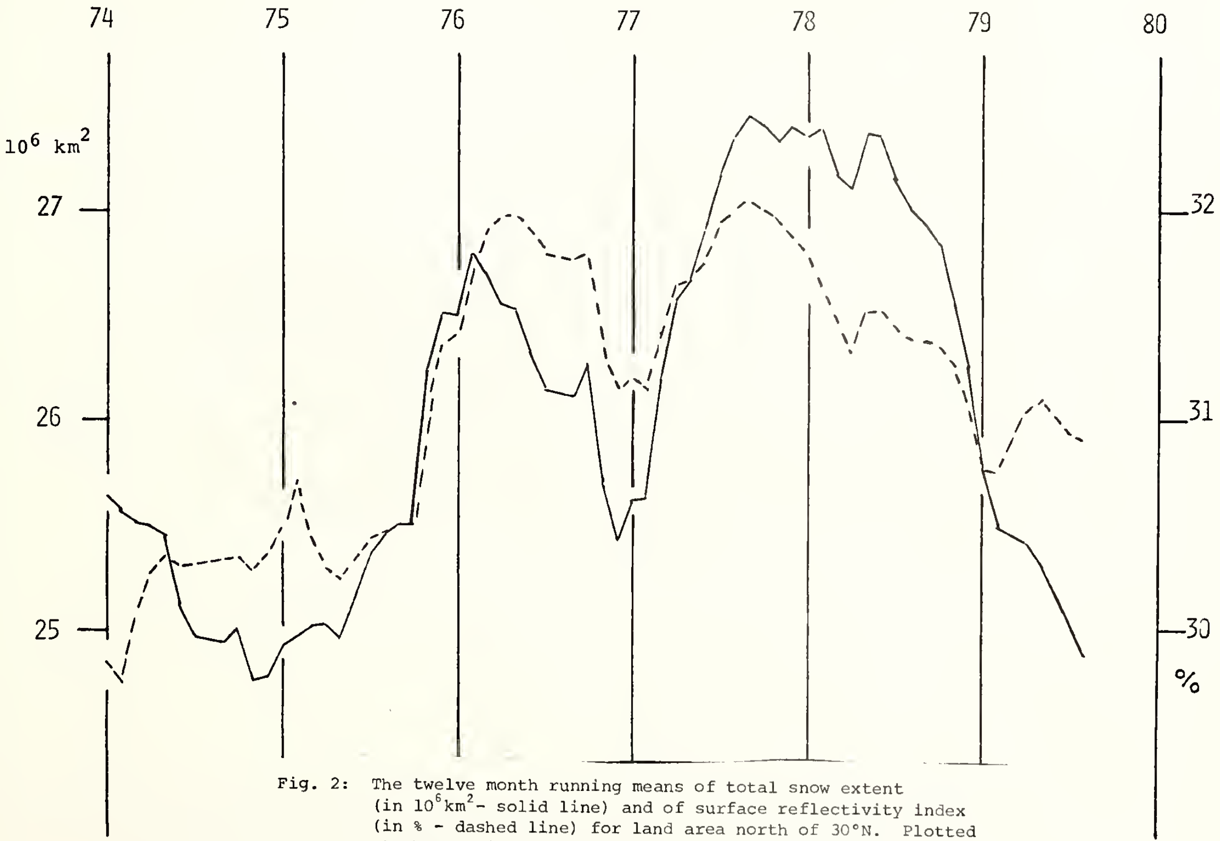

Fig. 2: The twelve month running means of total snow extent (in $10^6 km^2$- solid line) and of surface reflectivity index (in % - dashed line) for land area north of 30°N. Plotted at the terminal date with the end of each year marked. Note the continued drop from 1978 in both variables.

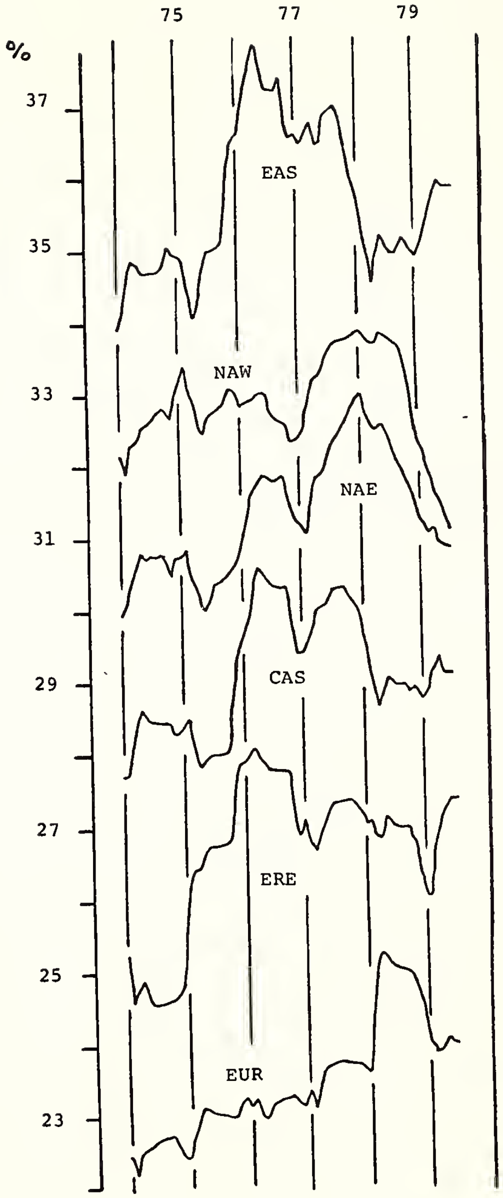

Fig. 3. Twelve month running means of land surface reflectivity index north of 30°N. Meridional segments EAS from 120°E-170°W; NAW: 170°W-100°W; NAE: North America and Greenland east of 100°W; CAS: 60-120°E; ERE: 30-60°E; EUR: Europe to 30°E. Plotted at the terminal date. Scale in % of surface reflectivity. Observe the last year's drop of surface reflectivity in North America and Europe and increase in Asia.

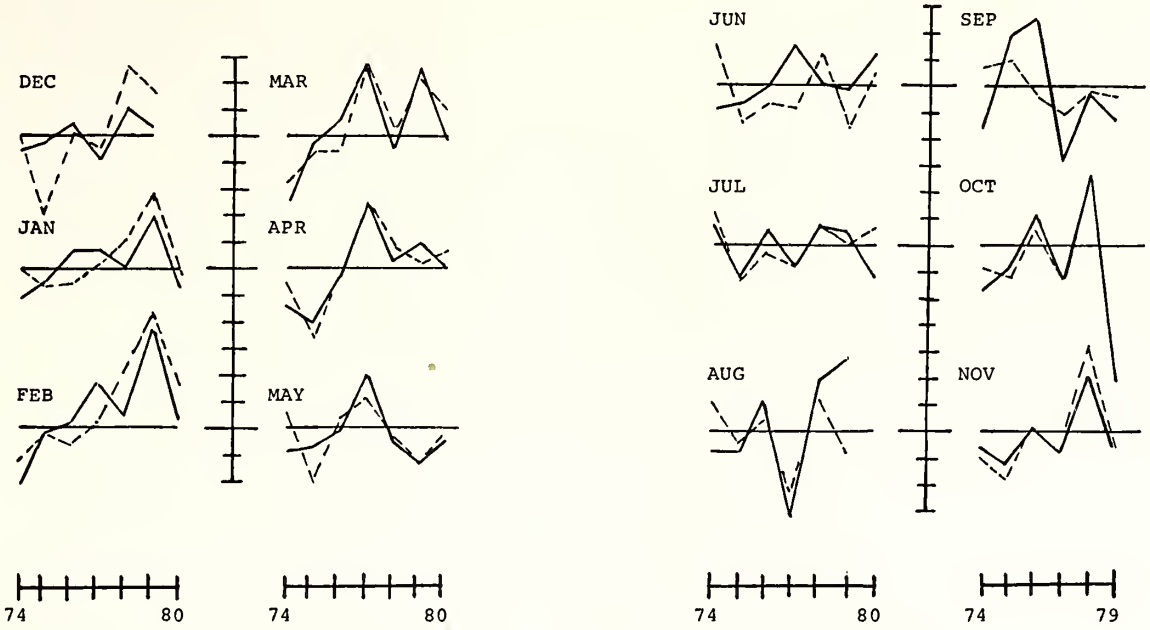

Fig. 4. Average monthly departures from the 1974-78 means of total ice extent (solid line) and of surface reflectivity (dashed line) for the ocean north of 30°N. Scale in units of .2 million km^2 and .2% of surface reflectivity. Ice extent represents concentrations greater than 1/10 or 1/8 and includes polynyas. The surface reflectivity index increased from April through July 1980 but decreased in other seasons.

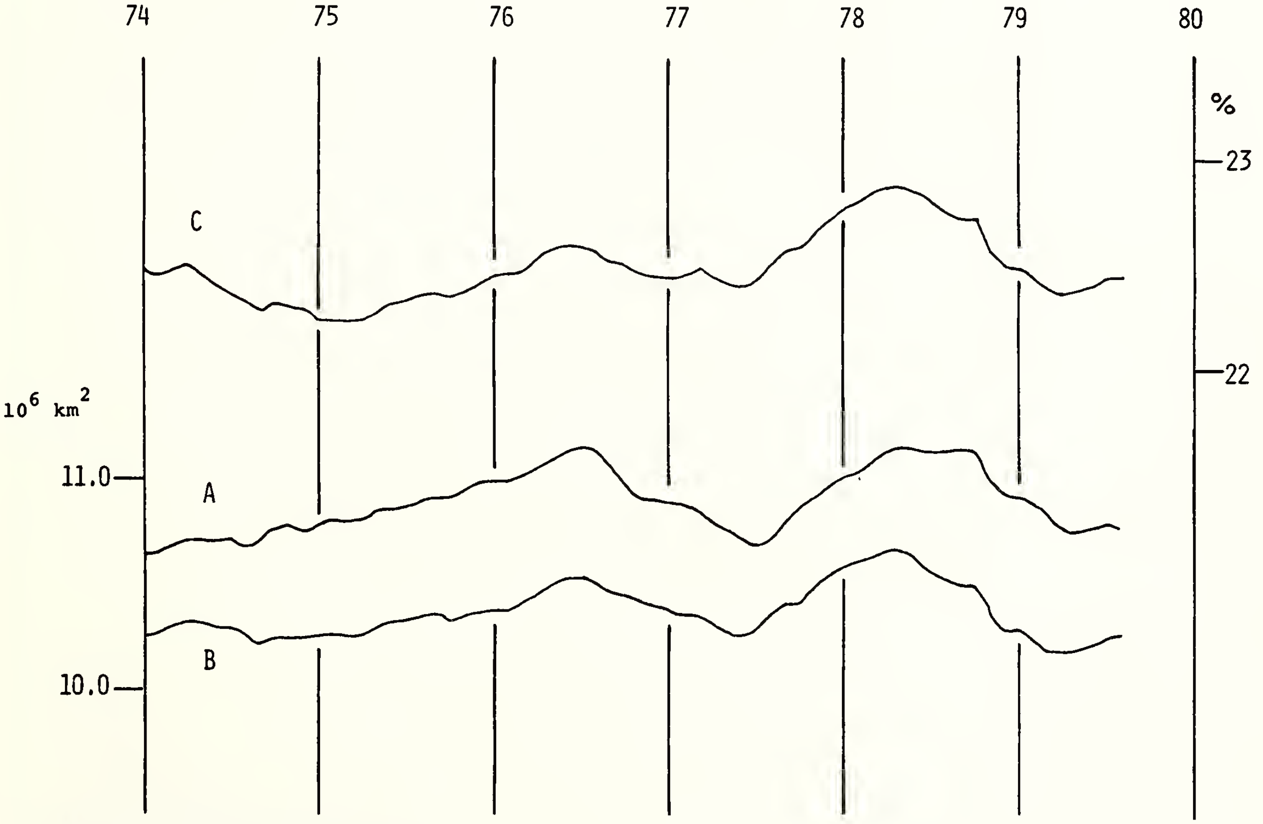

Fig. 5. Twelve month running means of: ocean reflectivity north of 30°N (C); total ice extent in concentrations greater than 1/10 or 1/8 including polynyas (A) and ice extent in concentrations $\geq$ 50% excluding polynyas (B). Plotted at terminal date with end of each year marked. Observe the moderate decrease of all three variables during the last year.

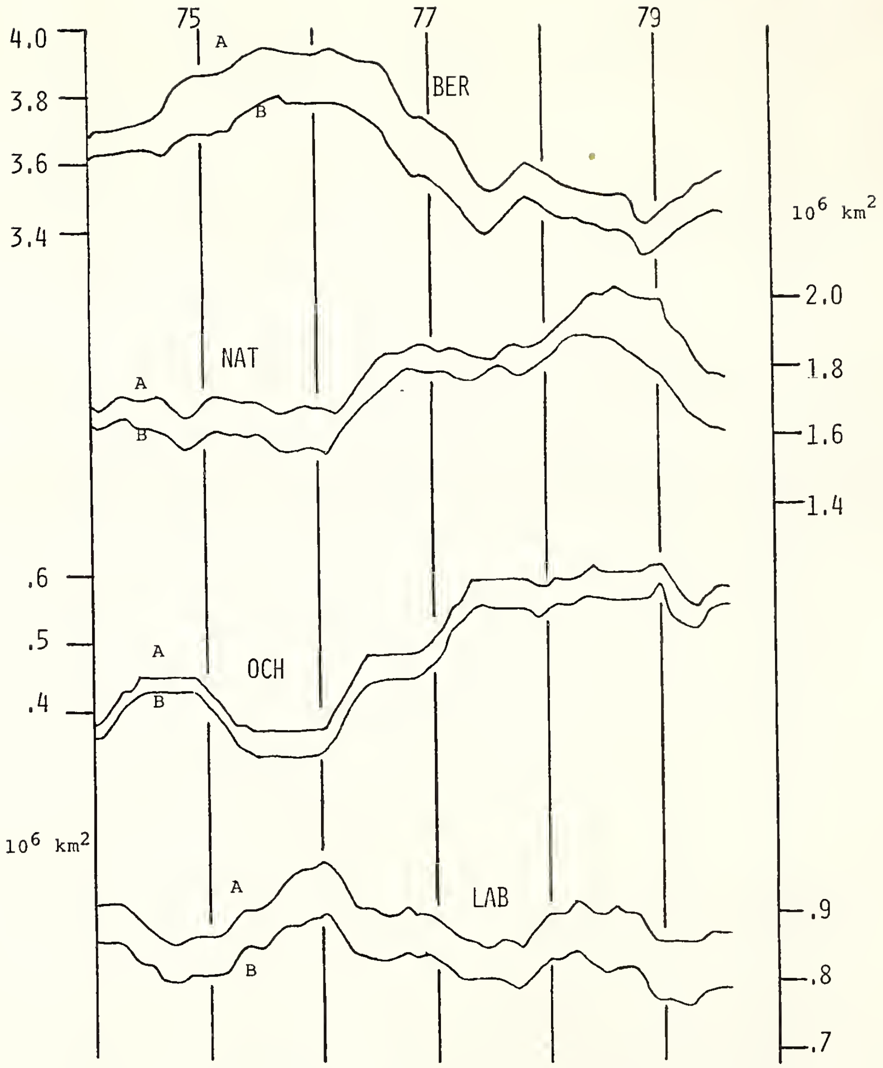

Fig. 6. Twelve month running means of ice extent for selected geographic regions (curves A and B) (description as in Figure 5). Selected segments are BER: Bering, Chuckchee, and Beaufort Seas; NAT: Barents and East Greenland Seas; OCH: Ochotsk Sea; LAB: Labrador Sea. Segment boundaries in Kukla and Gavin (1978). Scale in millions km^2.

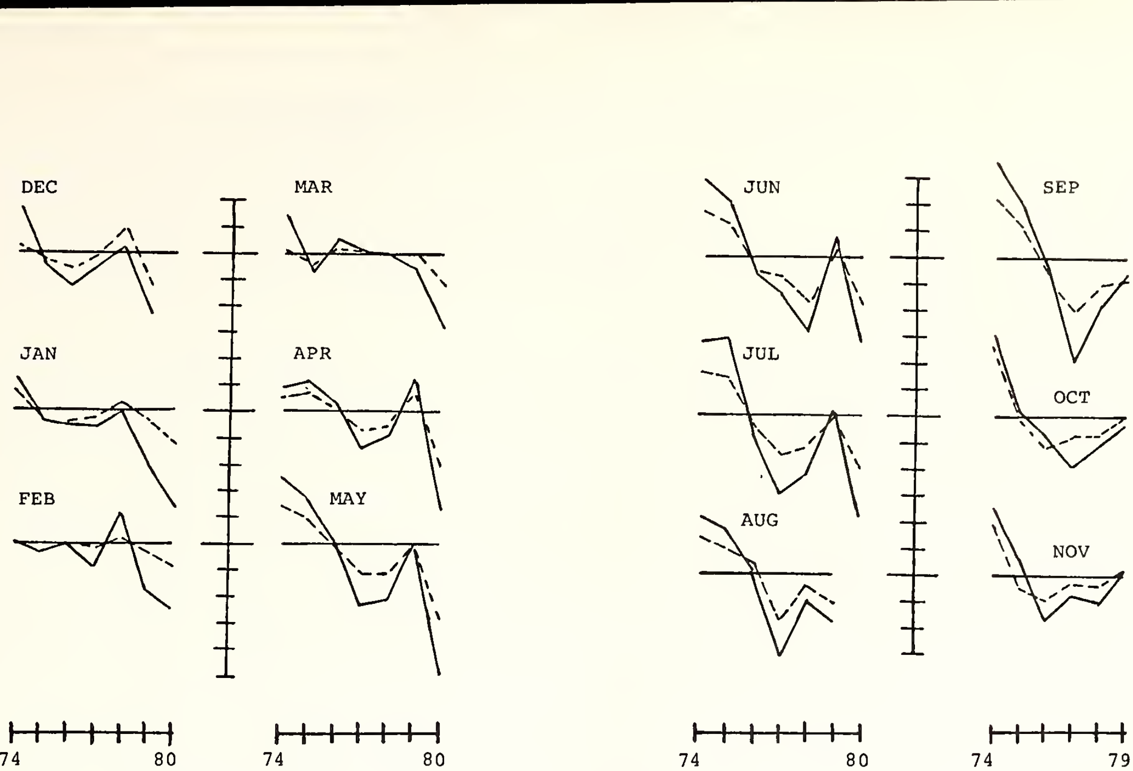

Fig. 7. Average monthly departure from the 1974-78 means of total Southern Hemisphere ice extent in concentrations above 1/10 or 1/8 including polynyas (solid line) and of the surface reflectivity index south of 30°S (dashed line). Scale in units of .5 million km^2 and .5% surface reflectivity.

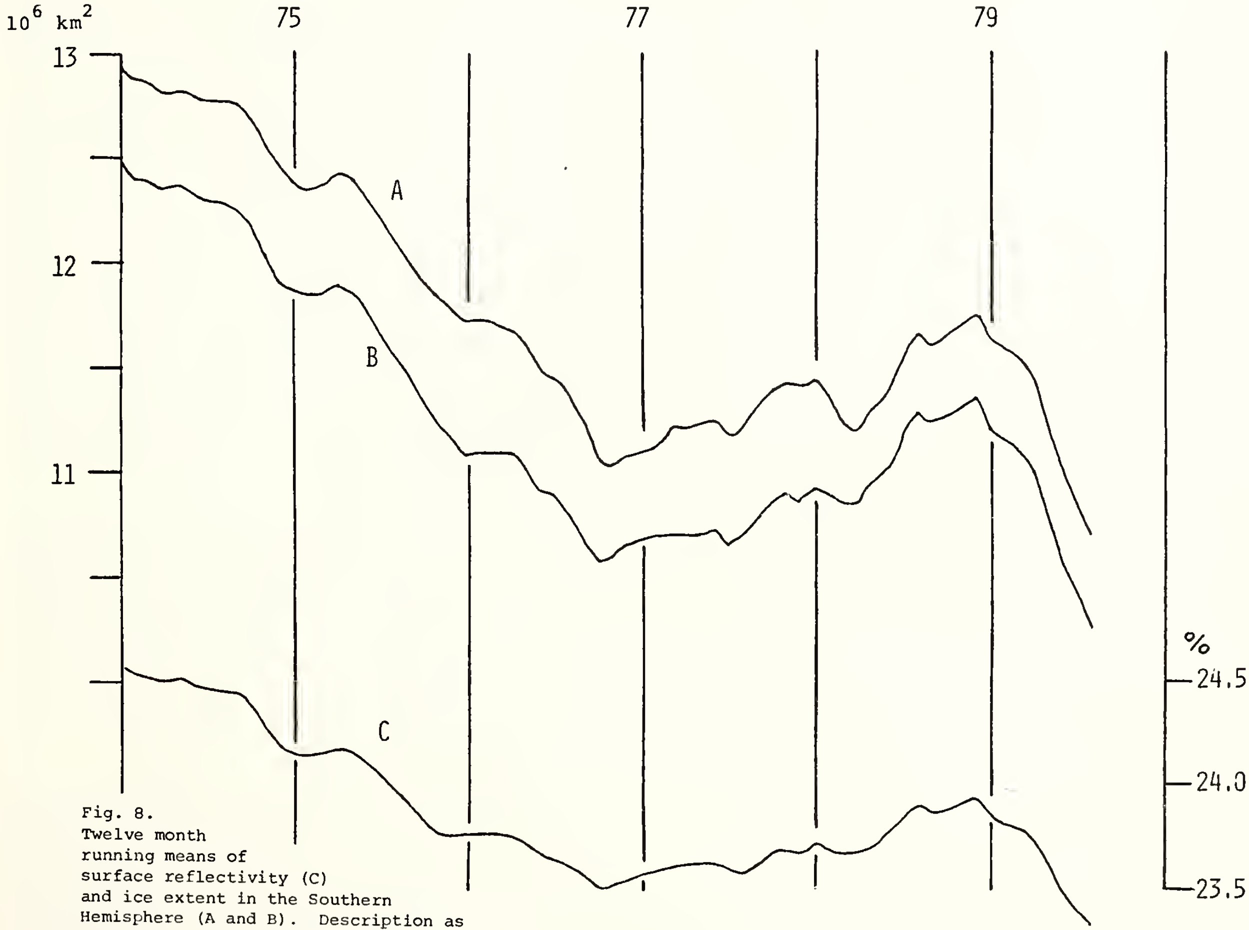

Fig. 8.
Twelve month running means of surface reflectivity (C) and ice extent in the Southern Hemisphere (A and B). Description as in Figure 5. Observe the record lows ending July 1980 in all three variables.

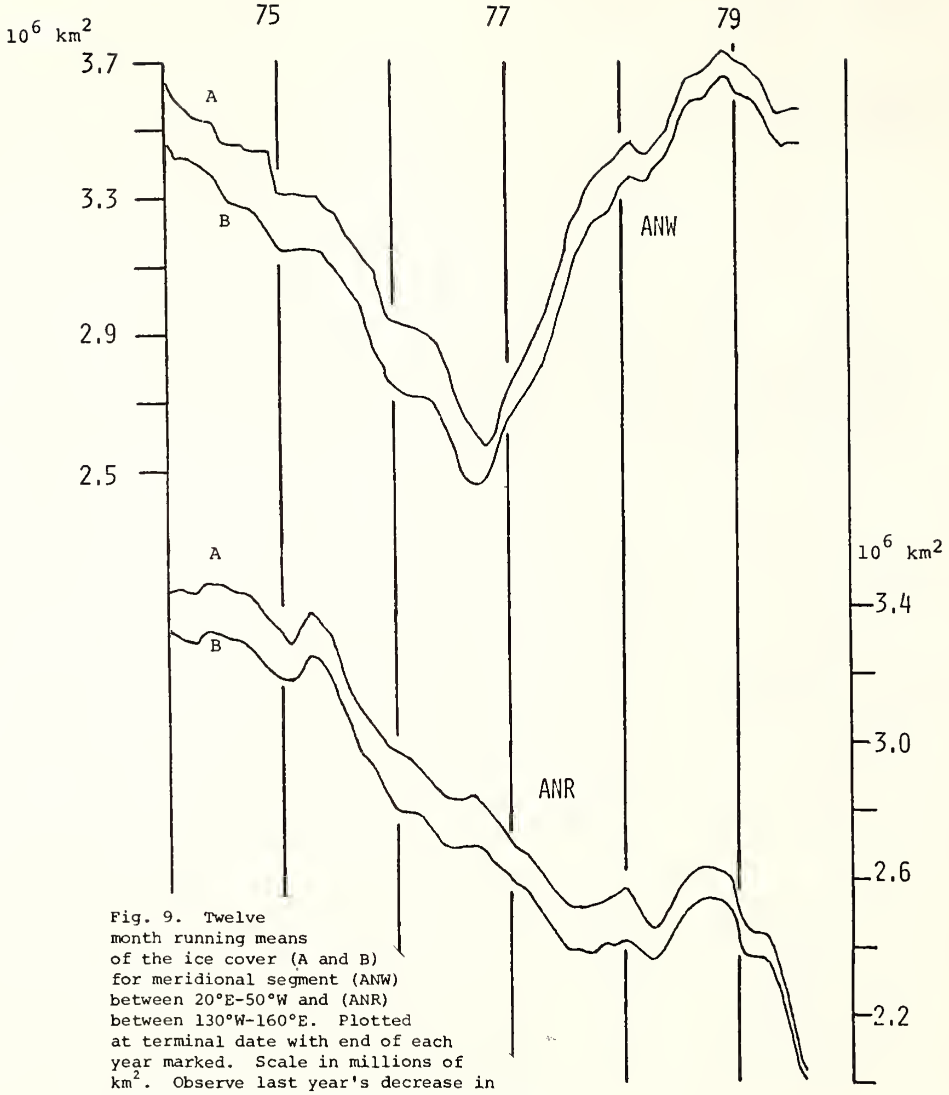

Fig. 9. Twelve month running means of the ice cover (A and B) for meridional segment (ANW) between 20°E-50°W and (ANR) between 130°W-160°E. Plotted at terminal date with end of each year marked. Scale in millions of km^2. Observe last year's decrease in both areas which is especially pronounced in the Ross Sea segment (ANR)

The tropical circulation during 1980 and its relation to that of recent years

Arthur F. Krueger
Climate Analysis Center
NMC/NWS/NOAA
Washington, D. C. 20233

For the fourth winter in a row the South Pacific anticyclone has remained weaker than normal. This anomaly originated with a major change in circulation over the tropical Pacific that began back in 1976. One index of this prolonged weakness of the South Pacific circulation is the anomaly of the Easter minus Darwin pressure difference shown at the top of figure 1. This time series was above normal during 1975-76. It dropped abruptly during the first half of 1976 and has essentially remained negative ever since. The other time series shown in figure 1 behaves in a similar manner although there are some significant differences after mid-1976. This is especially true of the two 850 mb tradewind indices. At 140 W the trades remained weak during most of 1976 and 1977 but recovered during 1978. At 170 E however - except for the 1976-77 winter - they have been weak during northern winter with even westerly flow occurring.

At the bottom of figure 1 is a time series for the longwave radiation anomaly at the Equator and 180°. The maximum occurring during 1975-76 indicates that the equatorial Pacific dry zone extended well west of normal at this time and is rather typical of a strong tradewind regime over the equatorial Pacific. As the trades weakened during 1976, cloudiness extended east of the dateline and the longwave cooling decreased. It has remained low ever since.

The nature of these changes in longwave radiation and cloudiness over the tropical Pacific can be seen in figure 2. Here the past five winters, with 1976 at the top and 1980 at the bottom, are shown. Note the extent of the equatorial Pacific dry zone during the 1976 winter. The 275 W m^{-2} contour is a good measure of this and it extends westward to the dateline during the season. During the following winters it receded to the east as cloudiness (and rainfall) moved into the Central equatorial Pacific. In particular, note how far east the 275 W m^{-2} contour was during the 1978 winter. Near the dateline the longwave radiation was now less than 225 W m^{-2} which represents a decline of 50 W m^{-2} since the 1976 winter. This represents an eastward extension of the Southern Indo-Pacific convergence during these winters, and as would be expected it was also accompanied by an extension of the surface equatorial westerlies to the east of the dateline.

It is interesting that the equatorial Pacific dry zone began to extend slightly westward again during this past winter (1980). Note that the western terminus of the 275 W m^{-2} contour was located near 170° W. Despite this, the tropical circulation during this season essentially represents a continuation of the regime that characterized the previous three winters. Again the Southern Indo-Pacific convergence stretched eastward from Africa into the central tropical Pacific and from here extended toward higher southern latitudes.

Because of frequent transient disturbances these regions of low outgoing radiation are characterized by a large interdiurnal variability. The standard deviation (sigma) of the twice daily observations about the seasonal mean is a measure of this and is shown in figure 3 for the winters of 1980 (top) and 1976 (bottom). Although in many respects similar, there are nevertheless important differences. In particular, the Southern Indo-Pacific convergence experienced larger variability during the 1980 winter than during that for 1976. Note the larger areas of 40 W m-2 over both the Pacific and Indian Oceans. At the Equator and 180° sigma increased from 20 to 35 W m^{-2} while over the eastern Pacific, in contrast, it continued low. It is interesting that the variability over the Southern Hemisphere, particularly the South Pacific, was greater during the 1980 season. This suggests a greater amount of storminess during that austral summer than during 1976 and this in turn contributed to the maintenance of a weaker South Pacific anticyclone.

The weakness of the South Pacific anticyclone during this 1980 season relative to that for 1976 is shown at the bottom of figure 4. This is the streamfunction of the 1000 mb vector wind difference between the 1980 winter and that for 1976. The actual streamfunction for winter 1980 is shown above. Heavy dots on both of these maps locate stations over the South Pacific that are often used to compute a Southern Oscillation Index. In the lower figure note the relative cyclonic rotation that is very nearly located over the South Pacific anticyclone shown above. The greatest reduction in tradewind strength appears in the central equatorial Pacific - note the relative westerly flow here. Westerly flow - indicated by the shaded areas in the upper figure - extended eastward from Africa across the Indian Ocean toward Polynesia. Over the North Pacific in contrast, some increase in tradewind strength is indicated near 10° latitude (fig. 4, bottom).

This strengthening of the northern trades was also accompanied by a stronger than normal subtropical jetstream over the North Pacific (fig. 5, lower). Essentially this jetstream elongated from the western Pacific downstream to about 150 W. Note the extent of the shaded area over the Pacific which represents speeds greater than 40 m s^{-1} (fig. 5, upper). Concurrently the 200 mb anticyclone, normally located east of the Philippines, also extended eastward as did the 275 w m^{-2} maximum in longwave radiation (figure 2). Figure 3 indicates that this was a persistent feature of the circulation during this season as sigma in turn decreased here (compare with that for 1976 at the bottom of figure 3).

The most striking feature of the upper tropospheric flow over the Tropics was the continued weakness of the equatorial westerlies east of 180°. Figure 1 compares the time series of these 200 mb equatorial westerlies with several other indices. In the lower part of figure 5 also note the relative easterly flow over the equatorial Pacific with anomalous subtropical westerlies north and south. Figure 6 indicates that stronger subtropical westerlies over both the North and South Pacific appear to be typical features of the circulation during periods of weak equatorial westerly flow.

The relation of sea surface temperatures in the eastern tropical Pacific to the time series shown in figure 1 is not a simple one. Four such series are shown in figure 7. The ocean warming indicated during 1976 is especially noteworthy and corresponds with the major change in tropical circulation noted earlier and indicated in figure 1. During 1977 however, temperatures in the equatorial current (the two center curves in figure 7) dropped rapidly, while they remained above normal at 10° N and S (top and bottom curves). Since 1978 the equatorial current has warmed again and recently has even averaged slightly above normal. South of the Equator (10 S, 140 W) temperatures have essentially continued above normal since late 1976 while at 10 N, 110 W they have dropped to near normal which is still close to 28° C.

The contrast in the two most recent summer tropical circulations is also noteworthy. While the 1979 Asian monsoon was weak, that for 1980 was stronger than normal. A comparison of the outgoing longwave radiation for these two summer regimes indicates a large area of 225 W m^{-2} or less over southeast Asia and the western Pacific during 1980 (fig. 8, upper). It also covered much of the Indian subcontinent in contrast to 1979 when only the eastern Bay of Bengal was covered (fig. 8, lower). The lower values of the longwave radiation during 1980 were accompanied by a stronger high level anticyclone over southeast Asia and the western Pacific (fig. 9). Accordingly 200 mb wind speeds in the easterly tropical jetstream were also stronger with speeds above 20 m s^{-1} over the Arabian Sea. Across the Equator in the winter hemisphere the westerlies were stronger east of Australia during 1980 than during 1979. (The shaded areas in figure 9 represent either easterly winds of 10 m s^{-1} or more or Southern Hemisphere westerly winds of 40 m s^{-1} or more.)

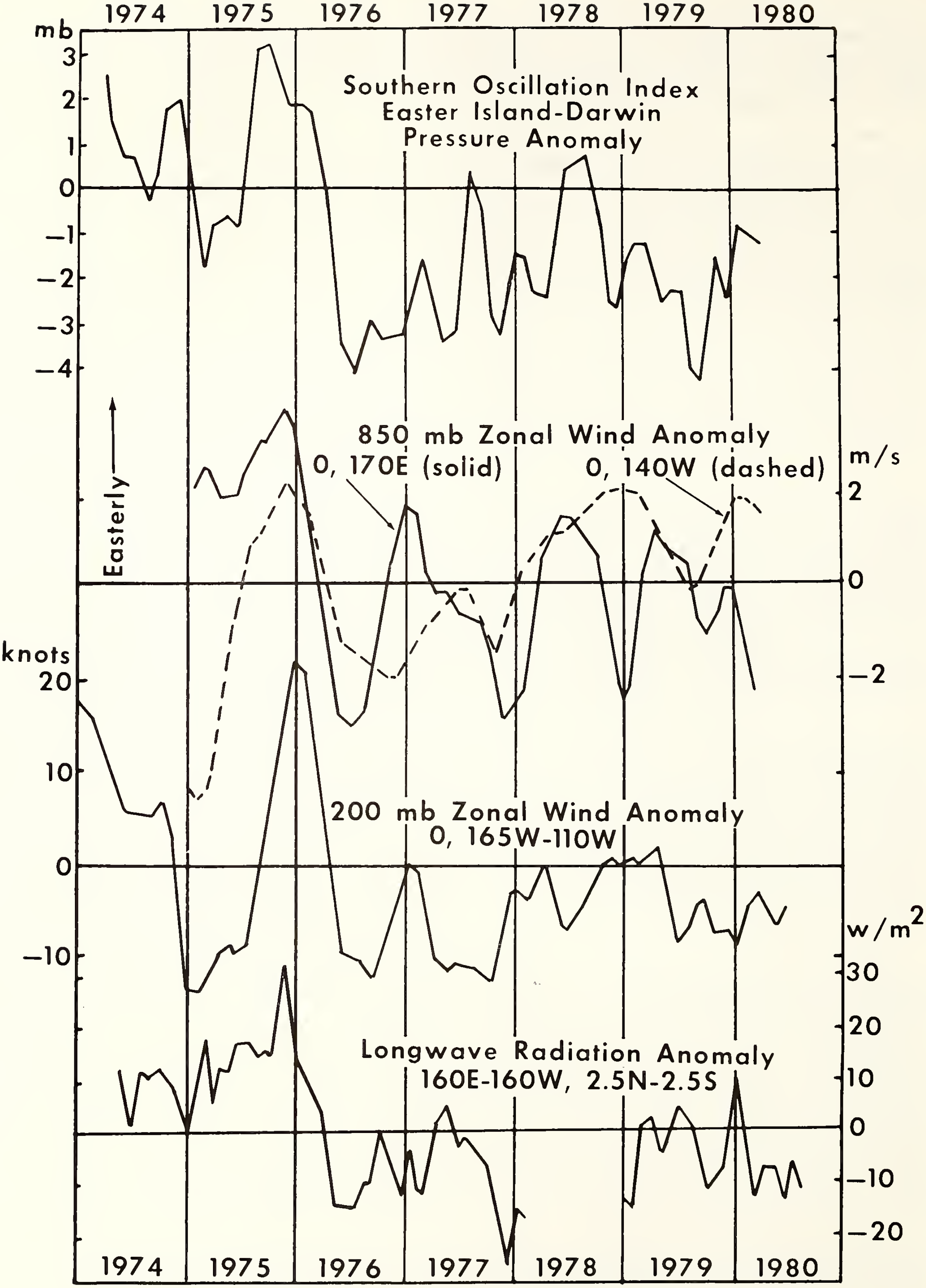
1974
1975
1976
1977
1978
1979
1980
mb
3
2
1
0
−1
−2
−3
−4
Southern Oscillation Index
Easter Island-Darwin
Pressure Anomaly
Easterly
850 mb Zonal Wind Anomaly
0, 170E (solid)
0, 140W (dashed)
m/s
2
0
−2
knots
20
10
0
−10
200 mb Zonal Wind Anomaly
0, 165W-110W
w/m2
30
20
10
0
−10
−20
Longwave Radiation Anomaly
160E-160W, 2.5N-2.5S

Figure 1

Outgoing Longwave Radiation for the Tropics

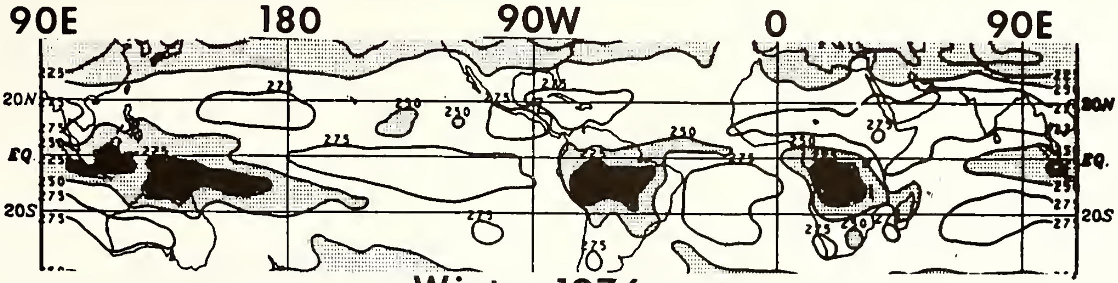

Winter 1976

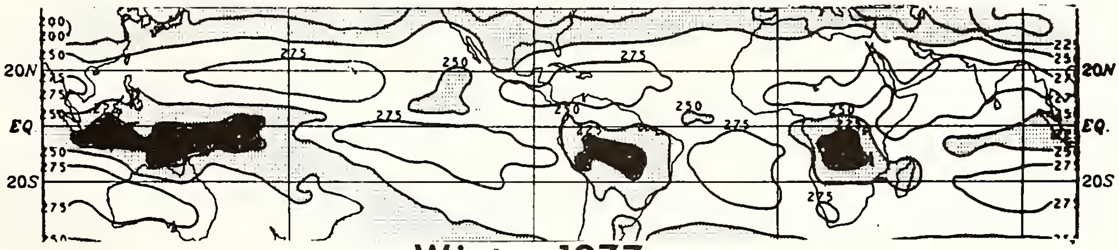

Winter 1977

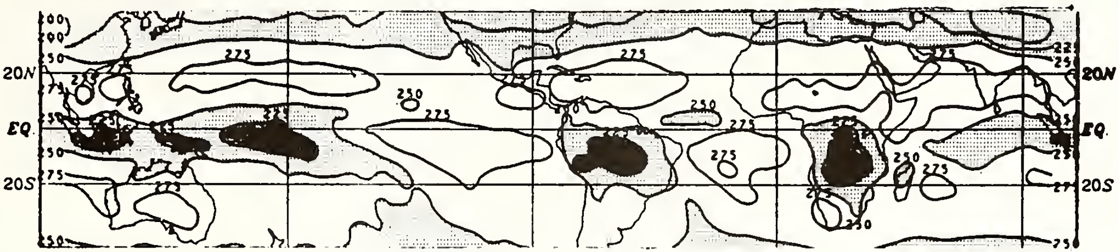

Winter 1978

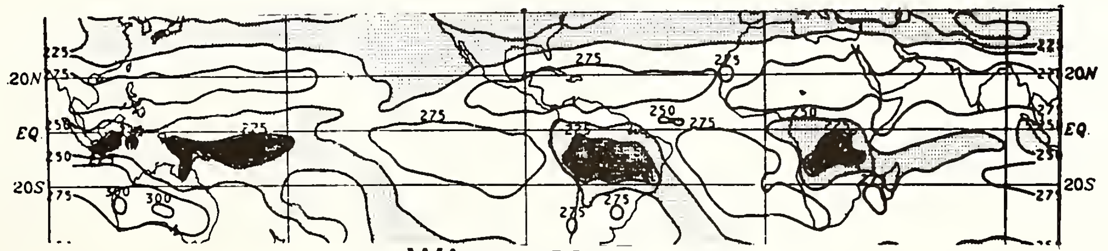

Winter 1979

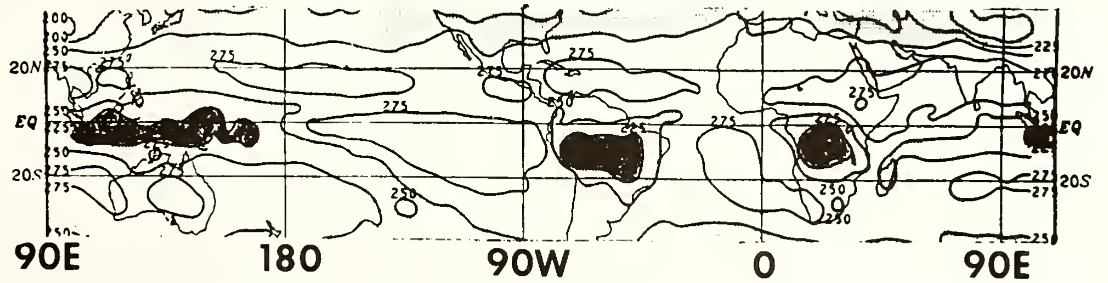

Winter 1980

Figure 2

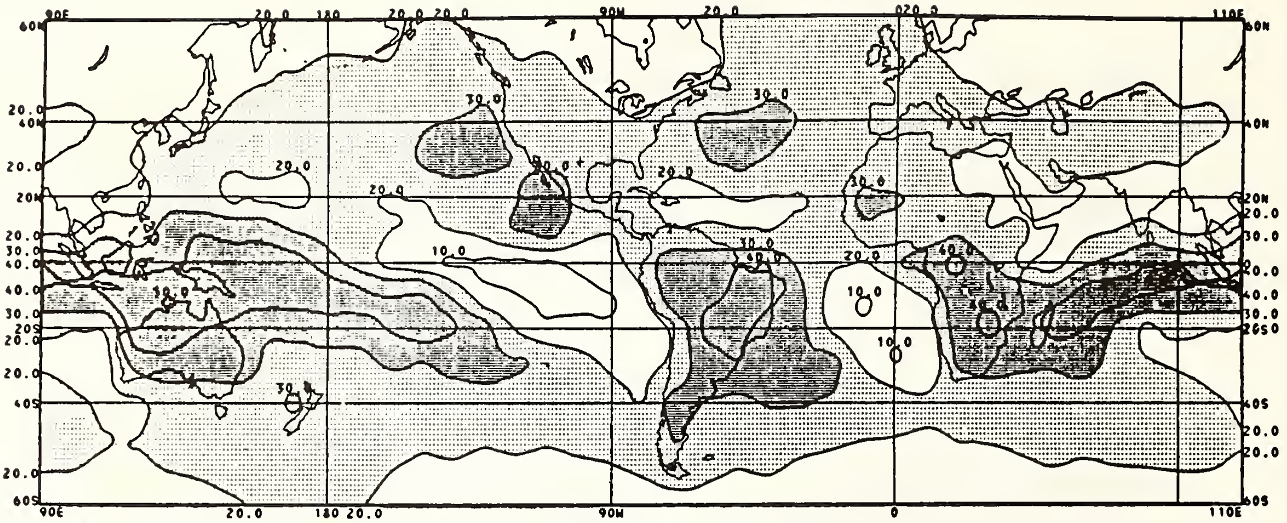

176 DAY AND NIGHT OBSERVATIONS FROM DEC 1, 1979 TO FEB 27, 1980
STANDARD DEVIATIONS OF OUTGOING LONGWAVE RADIATION

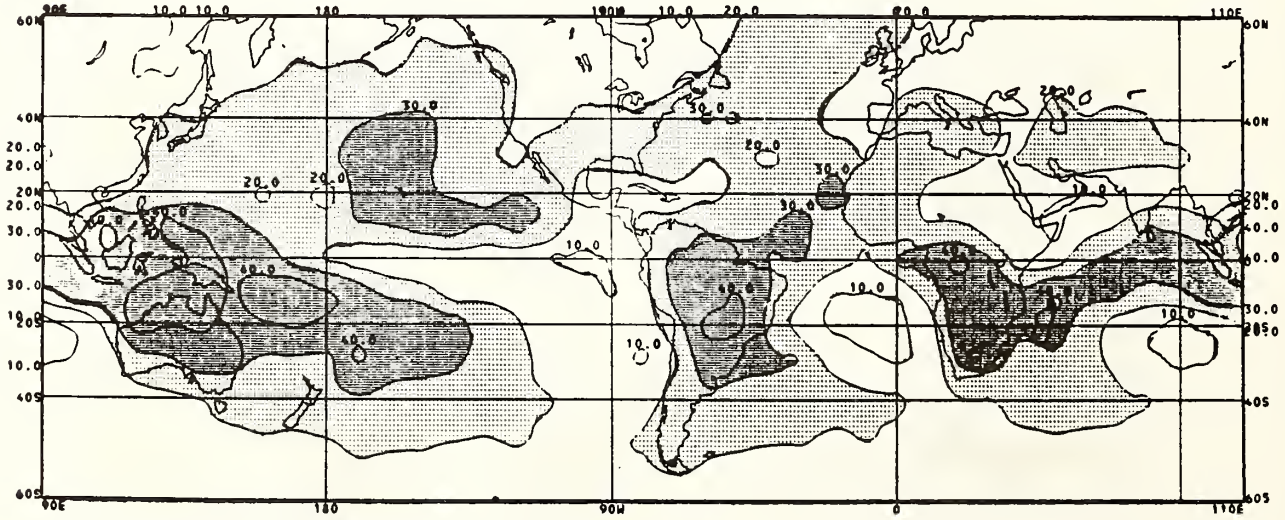

182 DAY AND NIGHT OBSERVATIONS FROM DEC 1, 1975 TO FEB 28, 1976
STANDARD DEVIATIONS OF OUTGOING LONGWAVE RADIATION

Figure 3

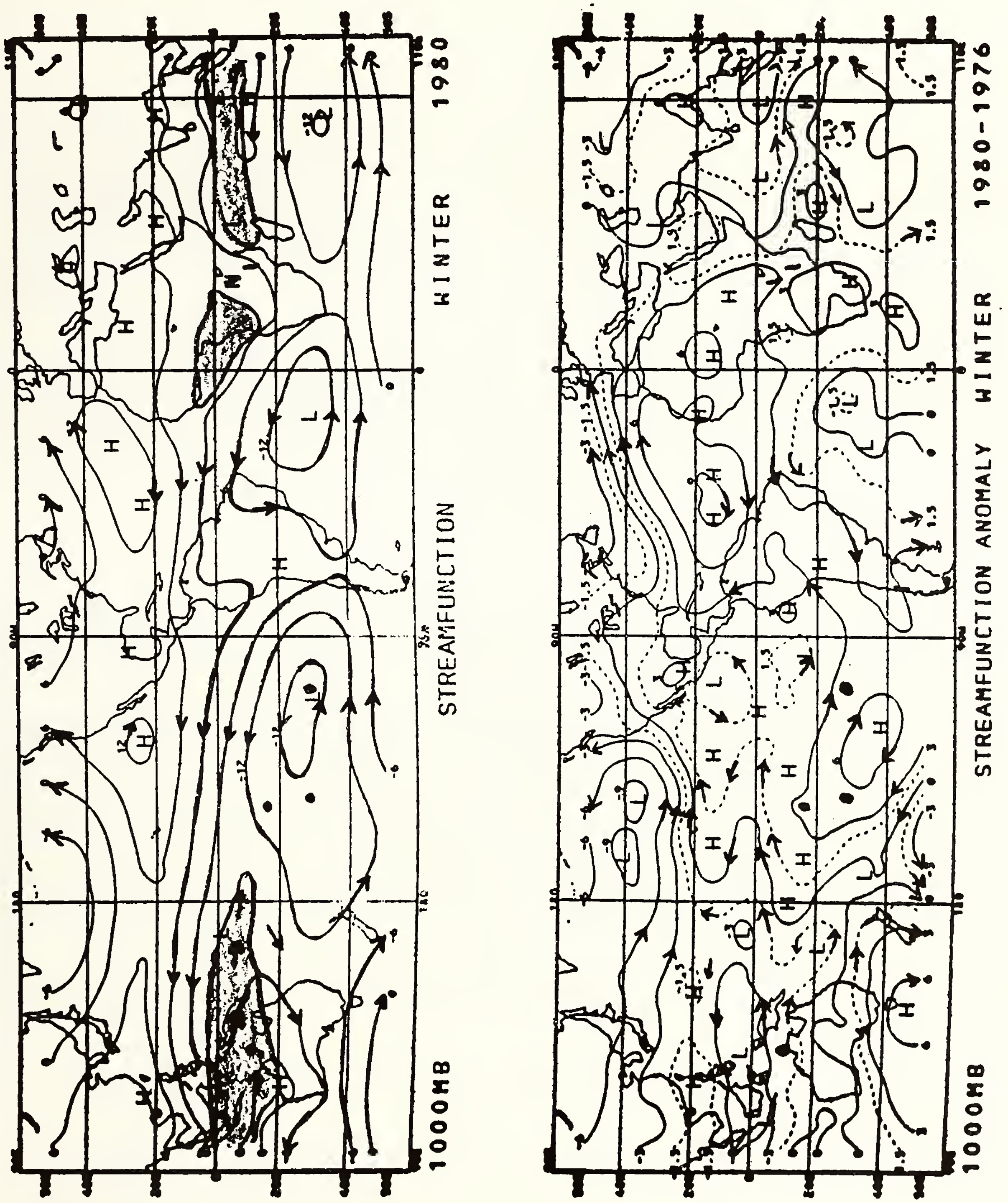
1000MB STREAMFUNCTION WINTER 1980

1000MB STREAMFUNCTION ANOMALY WINTER 1980-1976

Figure 4

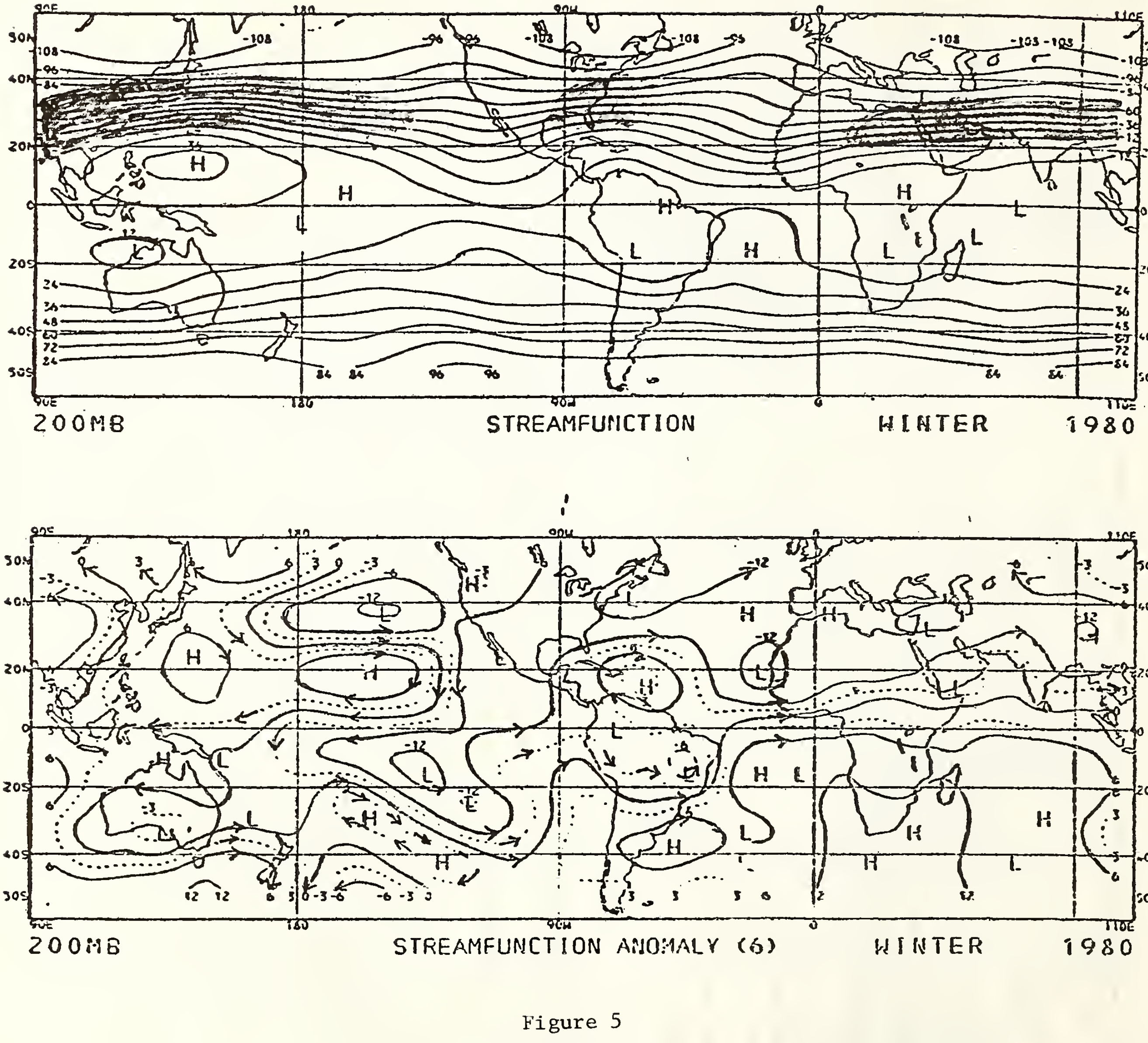
200MB STREAMFUNCTION WINTER 1980
200MB STREAMFUNCTION ANOMALY (6) WINTER 1980
90E
180
90W
0
110E
50N
40N
20N
0
20S
40S
50S
H
L

Figure 5

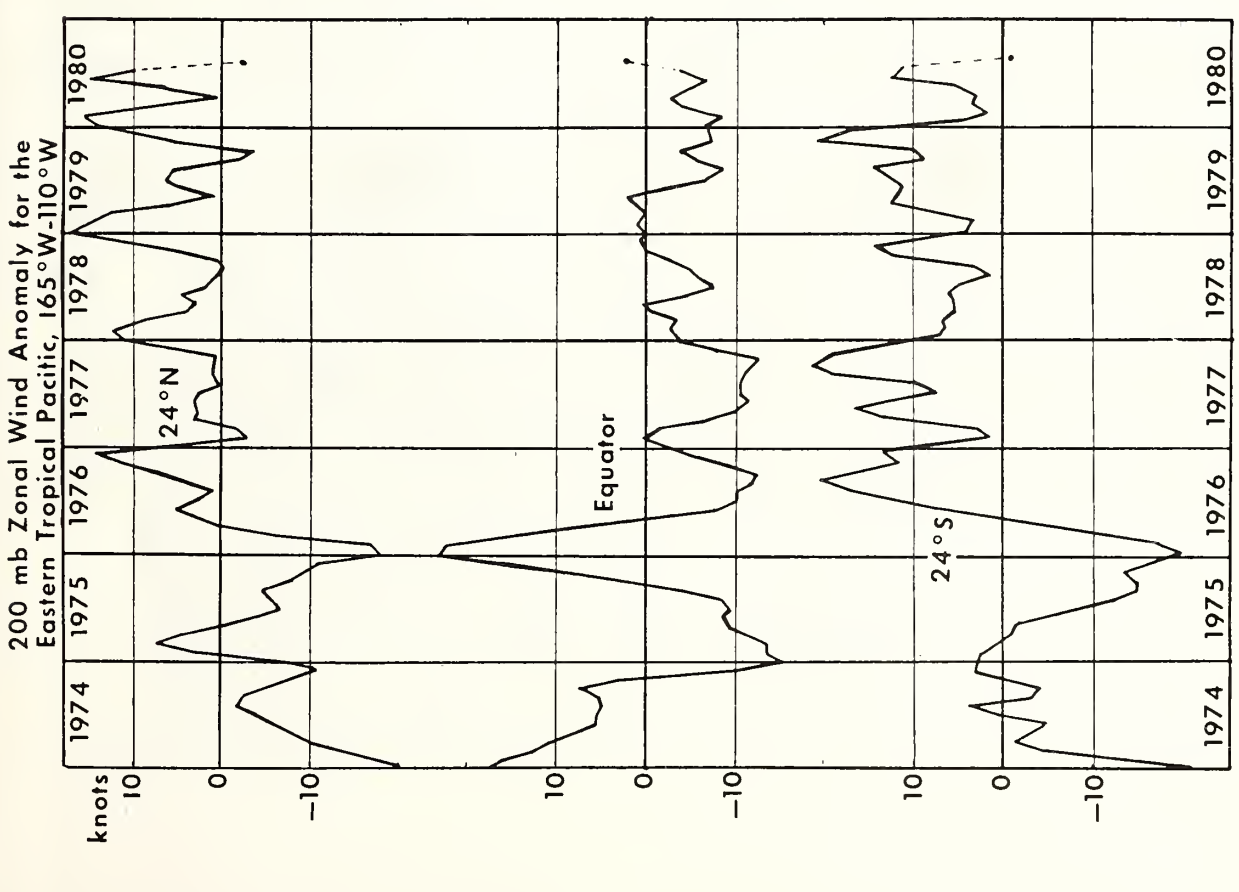

200 mb Zonal Wind Anomaly for the Eastern Tropical Pacific, 165°W-110°W

Figure 6

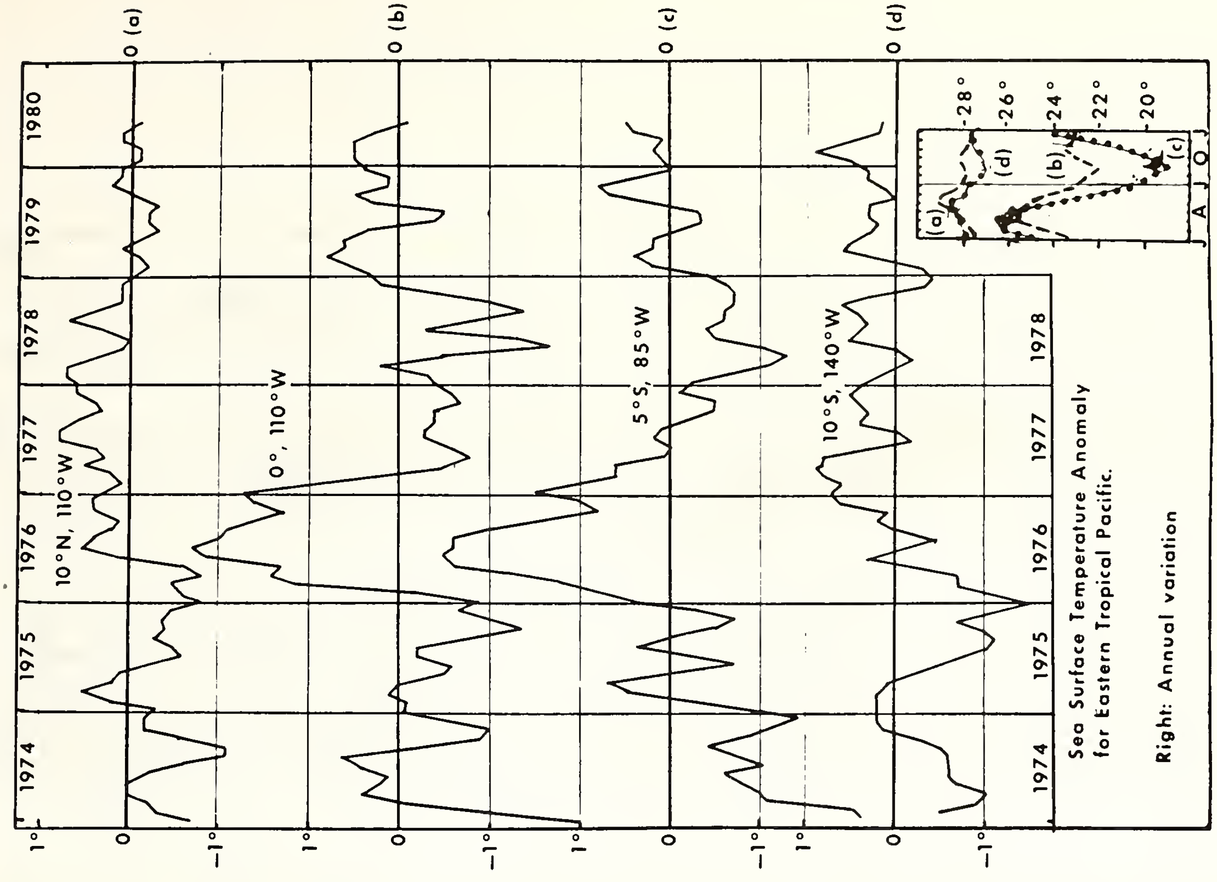

Sea Surface Temperature Anomaly for Eastern Tropical Pacific.

Right: Annual variation

Figure 7

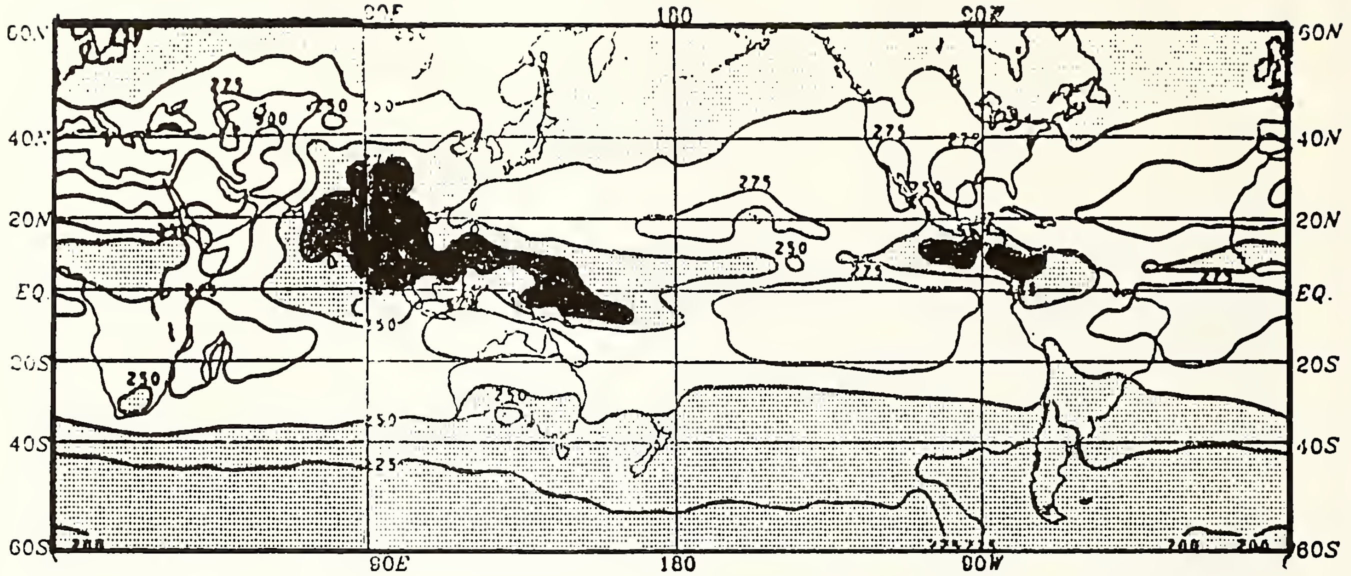

OUTGOING LONGWAVE RADIATION

SUMMER 1980

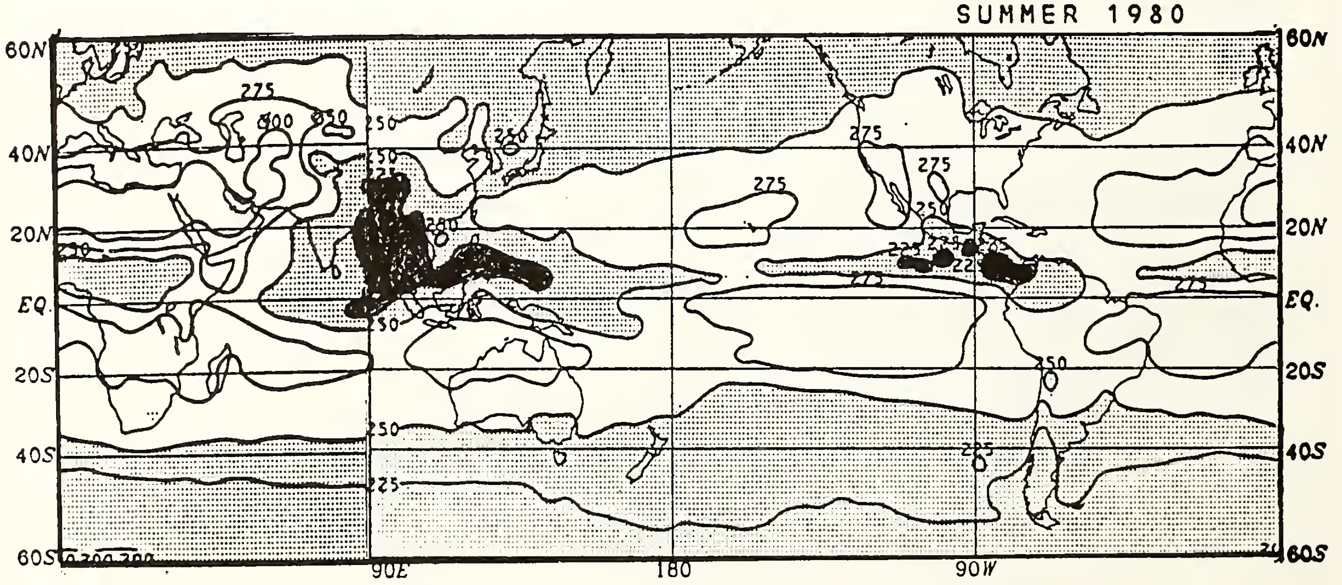

OUTGOING LONGWAVE RADIATION

SUMMER 1979

Figure 8

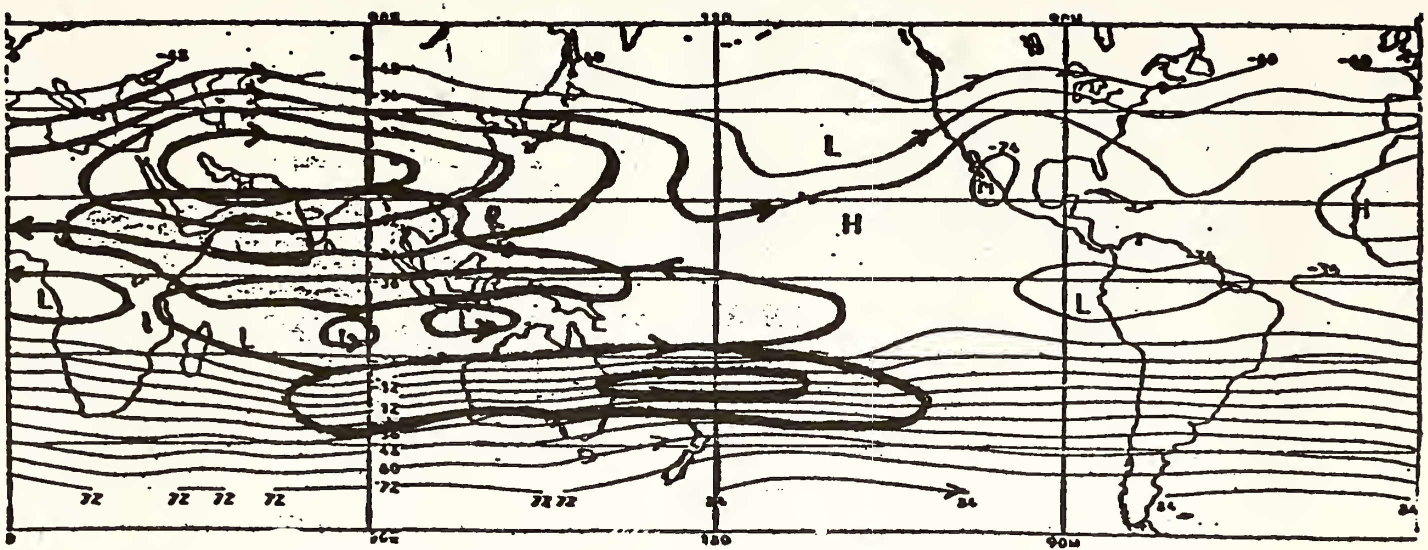

200MB STREAMFUNCTION SUMMER 1980

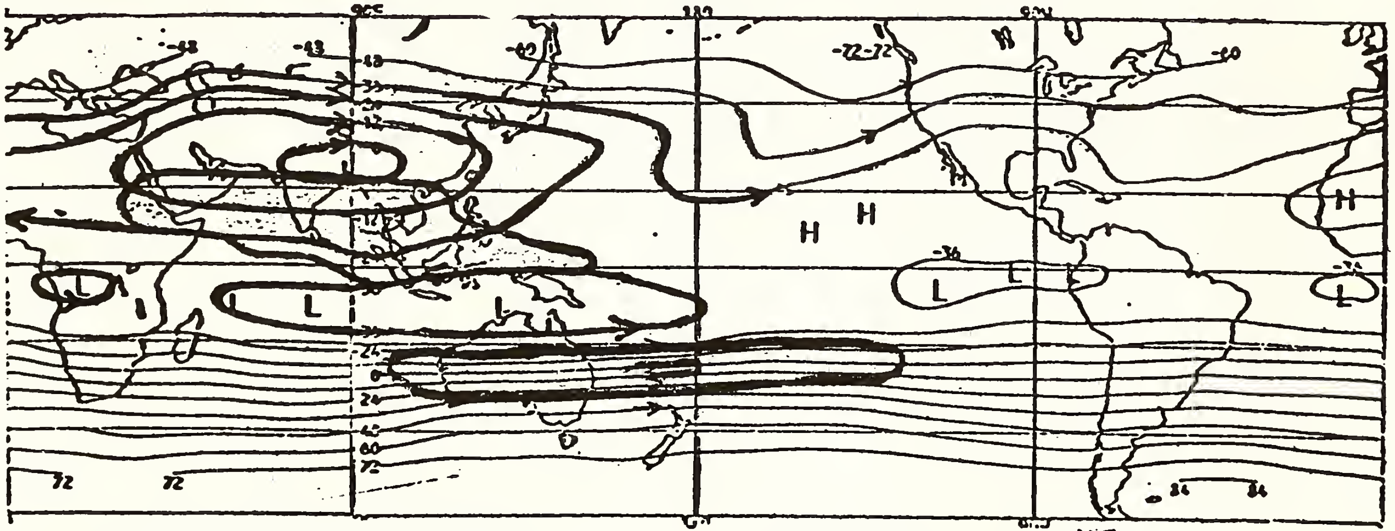

200MB STREAMFUNCTION SUMMER 1979

Figure 9

Atlantic and Eastern Pacific Tropical Cyclones in 1980 and Some Relations with the Large-Scale Circulation

Carl O. Erickson
Climate Analysis Center
NMC/NWS/NOAA
Washington, D. C. 20233

A. Brief Account of Historical Record.

Figure 1 is a computer plot of all North Atlantic tropical cyclone tracks over the 92-year period 1886-1977. A crude parabolic configuration, with a concentration of activity over the western portions of the ocean basin, is apparent.

North Atlantic averages for an 80-year period of relatively reliable data beginning in 1899 are given in Table 1, line 2. Averages for a shorter 13-year period, 1966-78, are given in line 3. This recent shorter period includes both a period of above-average activity, 1968-71, and a period of below-average activity, 1972-77, thus reducing the possibility of overall bias within that 13-year period. Comparison with the longer 80-year period indicates no apparent trend. However, the extreme years of 1914 and 1933 (lines 4 and 5) show the great fluctuations that have occurred in interannual activity.

Statistics for the current year, 1980, show the North Atlantic as having a near-average number of tropical cyclones but an above-average number of cyclone days (two hurricanes in existence on the same day equals two hurricane days, etc.). The latter is a better measure of overall tropical cyclone activity.

Over the last four years, 1977-1980, there has been a general uptrend in North Atlantic tropical cyclone activity. Figure 2 shows storm tracks for 1977 -- an unusually inactive year in which there were no storms over the central and eastern Atlantic or the eastern Caribbean. Unfavorable large-scale circulation patterns, including weaker-than-normal subtropical anticyclones and above-average vertical wind shear at low latitudes, have been cited as being at least partly responsible for the lack of tropical activity in that year. By contrast, 1979 was a year of near normal activity, including a return to some Cape Verde type tropical cyclones. Major hurricanes David and Frederick were of this type (see paper by Wagner).

For the eastern North Pacific, relatively reliable statistics exist only for about the last two decades -- the era of the meteorological satellite. Table 1 shows that, for the period 1966-78, the average number of eastern Pacific storms and hurricanes has been greater than for the North Atlantic. There is reason to believe that the same disparity probably has existed for a much longer period. In 1980, eastern Pacific storms numbered near their 13-year average.

B. Atlantic Tropical Cyclones in 1980.

North Atlantic tropical cyclone activity in 1980 continued the uptrend of the previous two years (see Table 2). In July, before the first storm of the season had formed, a large-scale circulation pattern broadly favorable for tropical cyclone development was in existence. This included the "3-wave" pattern of stronger-than-normal anticyclones over the eastern Pacific, U. S., and North Atlantic (see paper by Dickson), permitting a relatively broad easterly current over the Tropics. Additionally, the sea-surface temperatures (not shown) were near or slightly above normal over much of the tropical Atlantic.

Despite the seemingly favorable environment, only one Atlantic tropical cyclone occurred before mid-August. However, that one hurricane -- Allen -- was a record-breaker. It became the second most intense Atlantic hurricane of record (central pressure 899 mb) while traversing the northwestern Caribbean, being exceeded in intensity only by the 1935 Labor Day hurricane in the Florida Keys. Within the Caribbean itself, Allen is the most intense hurricane of record. One must caution that these statistics are not absolute, as the intensities of some storms during the earlier years of this century are not well documented.

Figure 3 shows the track of Allen together with the mean flow for August 1980 for the mid-tropospheric layer 700-300 mb. Numbers beside directional arrows are layer-mean wind speeds (m s^{-1}). A large anticyclone is centered near 26N, 35W, with broad easterly flow to the south. The track of Allen agrees very well with the implied steering.

The mid-August to mid-October portion of the North Atlantic hurricane season (figure 4) was quite different from the early season. Whereas the early season featured one super-hurricane, traversing the entire width of the Atlantic basin, the succeeding period had no less than 8 cyclones, all much less intense, and most moving northward in the central Atlantic. None affected the Eastern U. S. Although the Atlantic mean anticyclone was weaker in September than in August, it is not obvious why such a large proportion of the storms followed northward paths in mid-ocean. The mean mid-ocean flow at 40W did have a weak southerly component at all latitudes between 15N and 40N, but the flow was so weak that this can be only a partial explanation.

It is noteworthy that the two tropical cyclones that entered Texas in 1980 (Allen, and a much weaker storm -- Danielle) together accounted for a large fraction of the total summer rainfall over that state. Otherwise, Texas was afflicted by heat and drought (see paper by Dickson).

C. Eastern North Pacific Tropical Cyclones in 1980.

Up to mid-August 1980, while the North Atlantic was having one exceptional hurricane, the eastern North Pacific was experiencing a succession of 9 storms of weak or moderate intensities (Figure 5). An upper-tropospheric anticyclonic anomaly over Mexico and the adjacent Pacific (Figure 6) plus warm water at low latitudes evidently favored storm formation, but layer-mean steering toward the northwest (Figure 7) soon carried most cyclones into an environment of lower SST (Figure 8). Consequently, the usual cyclone life cycle during this particular 1980 period was characterized by rapid formation, a short track toward the northwest, and relatively rapid dissipation over an increasingly cooler ocean.

Although the sea-surface temperature analysis of Figure 8 is for only one day (near the midpoint of the period), the overall pattern of relatively large SST gradient toward the northwest was a persistent summer feature and is similar to the climatological mean pattern for the area. Numerous ship observations off the Mexican west coast lend confidence to the analysis.

The northwestward steering in the tropical cyclone area (Figure 7) is seen to be a peripheral part of the very large and strong continental anticyclone centered over Oklahoma. That persistent anticyclone was also very influential in the maintenance of the 1980 summer heat wave over the U. S. (see paper by Dickson).

Eastern North Pacific cyclone tracks during the period Aug 15-Oct 15, 1980, are shown in Figure 9. As in the North Atlantic, a rather pronounced change in overall activity is noticed by comparison with the preceding period. However, in the eastern Pacific the change is toward fewer storms with more zonally-oriented tracks, whereas the North Atlantic change was in the opposite sense toward more numerous storms with more meridionally-oriented tracks. Over both oceans, small but perhaps significant changes in the overall mean steering flow seem to have been influential.

REFERENCES

Gunther, Emil B., 1980: "Eastern North Pacific Tropical Cyclones of 1979," Monthly Weather Review, Vol. 108, No. 5, pp. 631-641.

Lawrence, Miles B., 1978: "Atlantic Hurricane Season of 1977," Monthly Weather Review, Vol. 106, No. 4, pp. 534-545.

Neumann, Charles J., George W. Cry, Eduardo L. Caso, and Brian R. Jarvinen, 1978: Tropical Cyclones of the North Atlantic Ocean, 1871-1977, U. S. Government Printing Office, Washington, D. C., 170 pp.

Table 1. --Historical summaries of North Atlantic and eastern North Pacific tropical cyclones.

	North Atlantic				Eastern North Pacific	
	No. of Hurricanes	No. of Storms & Hurricanes	No. of Hurricane Days	No. of Storm & Hurricane Days	No. of Hurricanes	No. of Storms & Hurricanes
1886-1898	5.4	8.5	---	70.8		
1899-1978 (80 years)	4.8	8.3	21.5	47.7		
1966-1978	5.7	10.0	20.6	46.8	7.5	14.8
	(Extreme Years)					
1914	0	1	0	5		
1933	9	21	50	138		
	(Current Year)					
1980	7	9	(34) *	(58) *	7	14

* preliminary estimate (1980 tabulation does not include November and December)

Table 2. --Tropical cyclone statistics for each of the last four years.

	North Atlantic				Eastern North Pacific	
	No. of Hurricanes	No. of Storms & Hurricanes	No. of Hurricane Days	No. of Storm & Hurricane Days	No. of Hurricanes	No. of Storms & Hurricanes
1977	5	6	9	17	4	8
1978	5	11	13	44	12	18
1979	5	8	21	48	6	10
1980	7	9	(34)	(58)	7	14

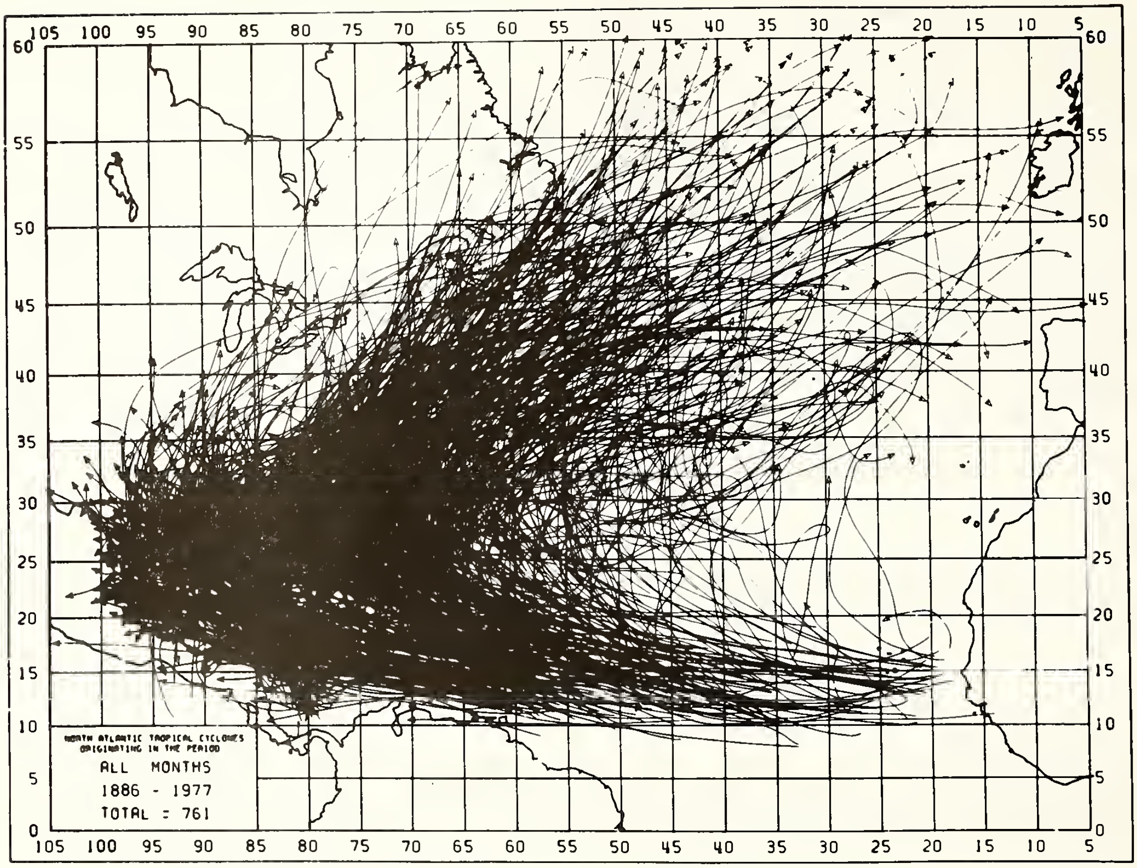

Figure 1. --Computer plot showing the tracks of the 761 known Atlantic tropical cyclones reaching at least tropical storm intensity over the 92-year period 1886-1977 (from Neumann et al., 1978).

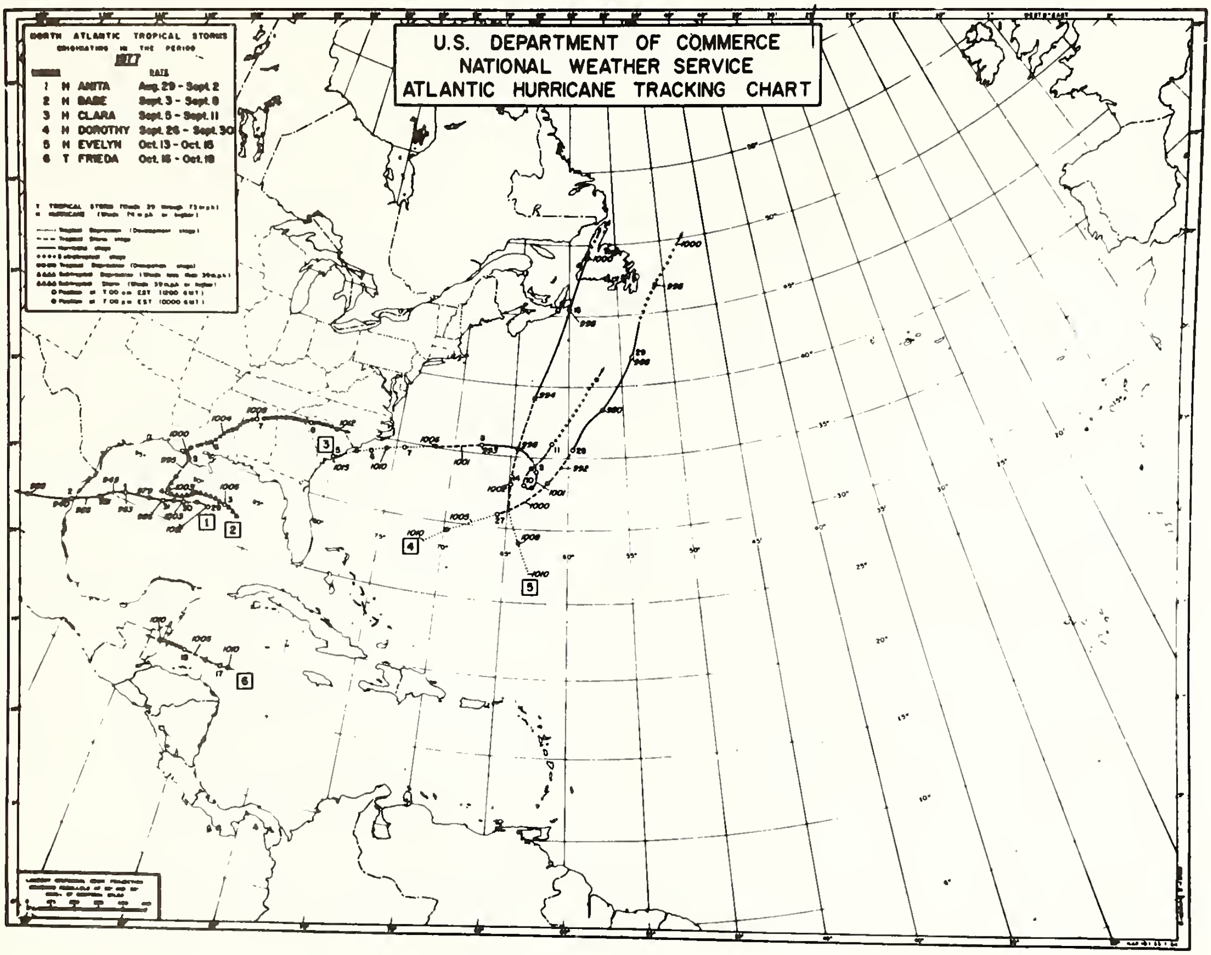
U.S. DEPARTMENT OF COMMERCE
NATIONAL WEATHER SERVICE
ATLANTIC HURRICANE TRACKING CHART
NORTH ATLANTIC TROPICAL STORMS
ORIGINATING IN THE PERIOD
1977
DATE
1 H ANITA Aug. 29 - Sept. 2
2 H BABE Sept. 3 - Sept. 8
3 H CLARA Sept. 5 - Sept. 11
4 H DOROTHY Sept. 26 - Sept. 30
5 H EVELYN Oct. 13 - Oct. 15
6 T FRIEDA Oct. 16 - Oct. 19
1
2
3
4
5
6

Figure 2. --Tracks of North Atlantic tropical cyclones in 1977 (from Lawrence, 1978).

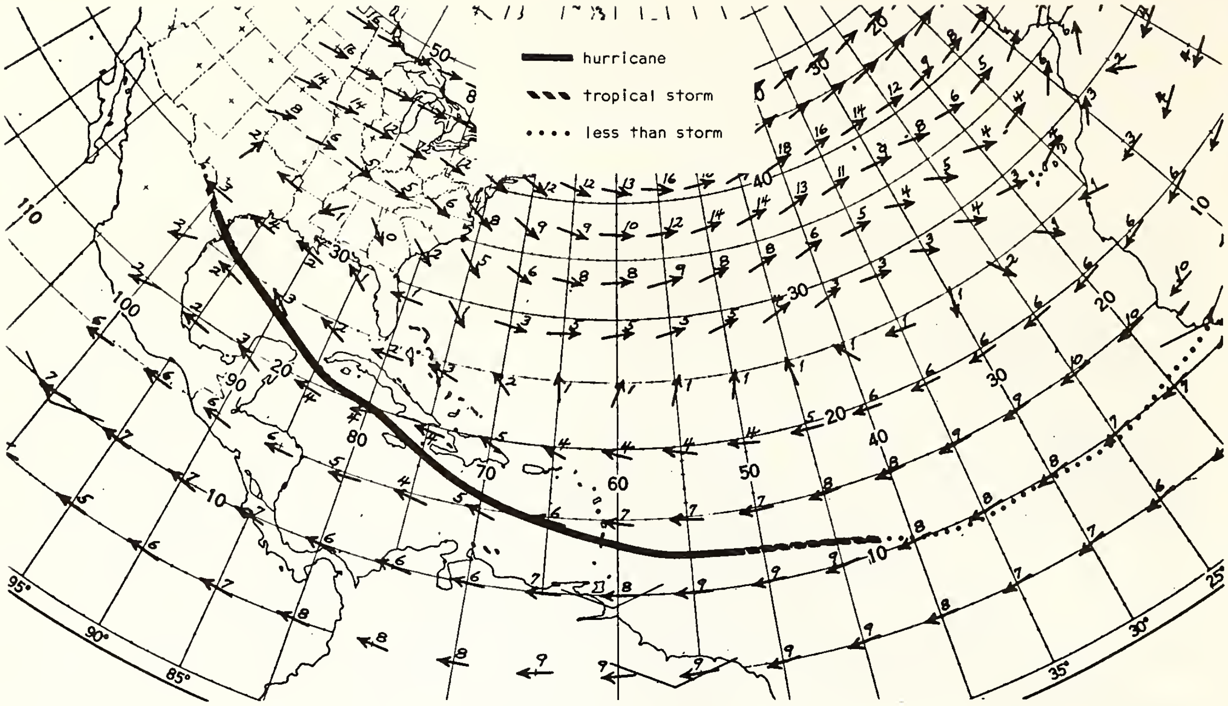

Figure 3. --Track of hurricane Allen, early August 1980, including eastern Atlantic portions of less than hurricane intensity. Arrows and plotted numbers represent monthly mean flow (m s^{-1}) for August 1980 for the mid-tropospheric layer 700-300 mb.

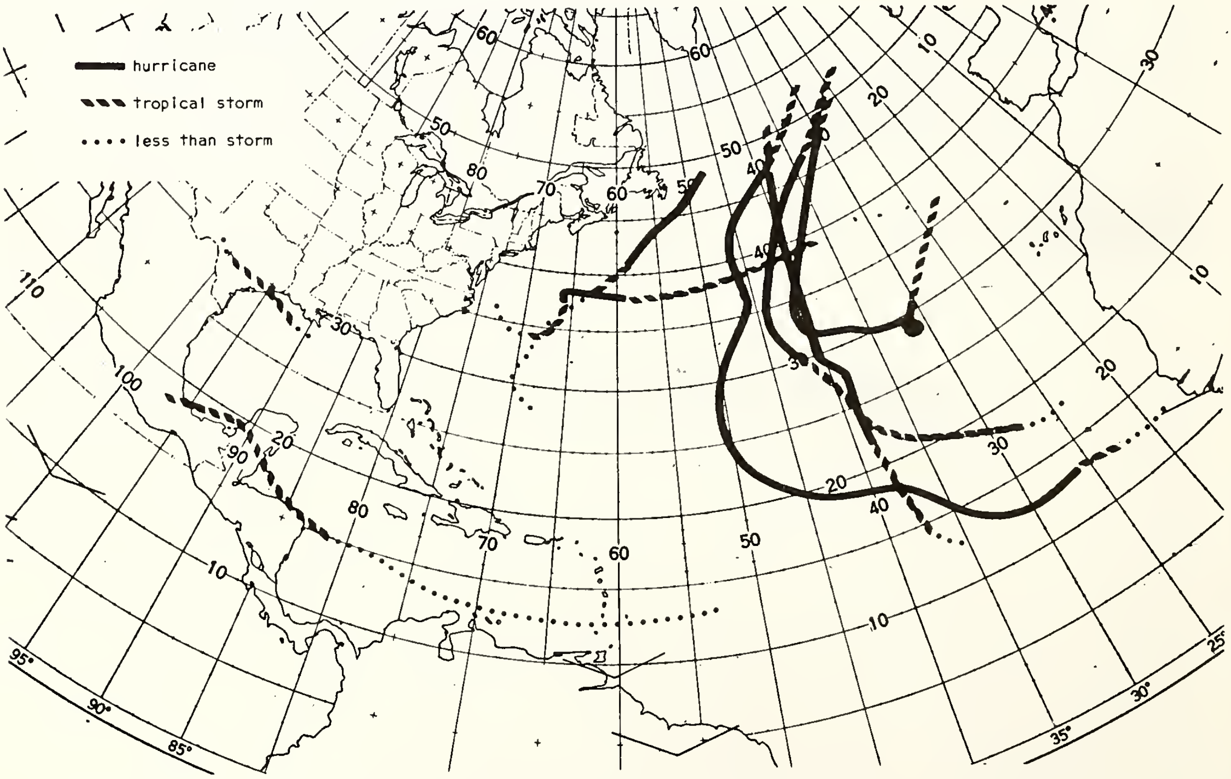

Figure 4. --Tracks of Atlantic tropical cyclones for the period August 14 - October 15, 1980.

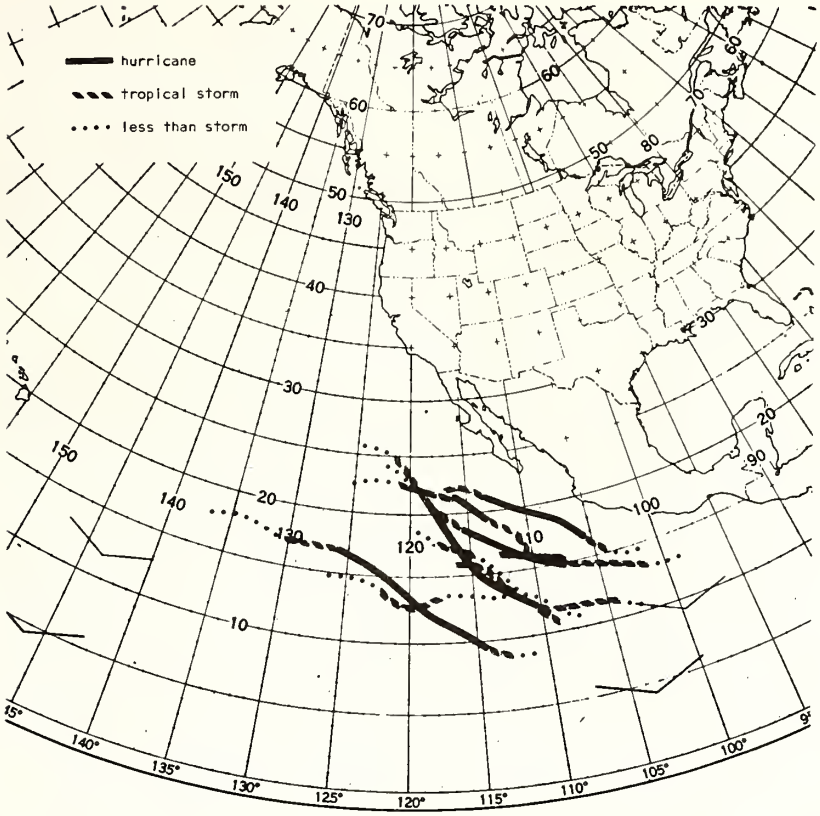

Figure 5. --Tracks of eastern North Pacific tropical cyclones, June 1 - August 15, 1980.

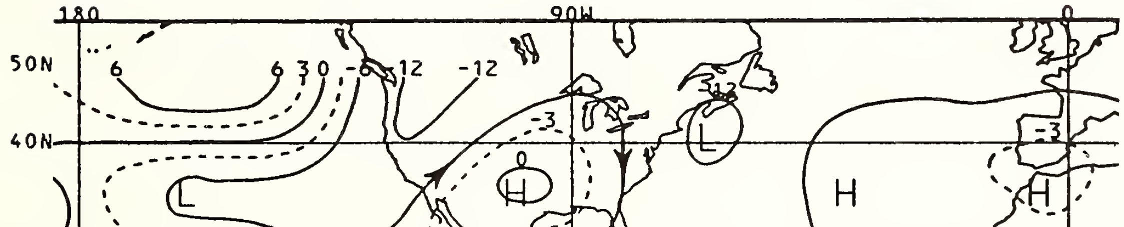

Figure 6. --Streamfunction anomaly at 200 mb for summer (Jun-Jul-Aug) 1980. Anomaly is based on summer data for the 6-year period 1968-1973.

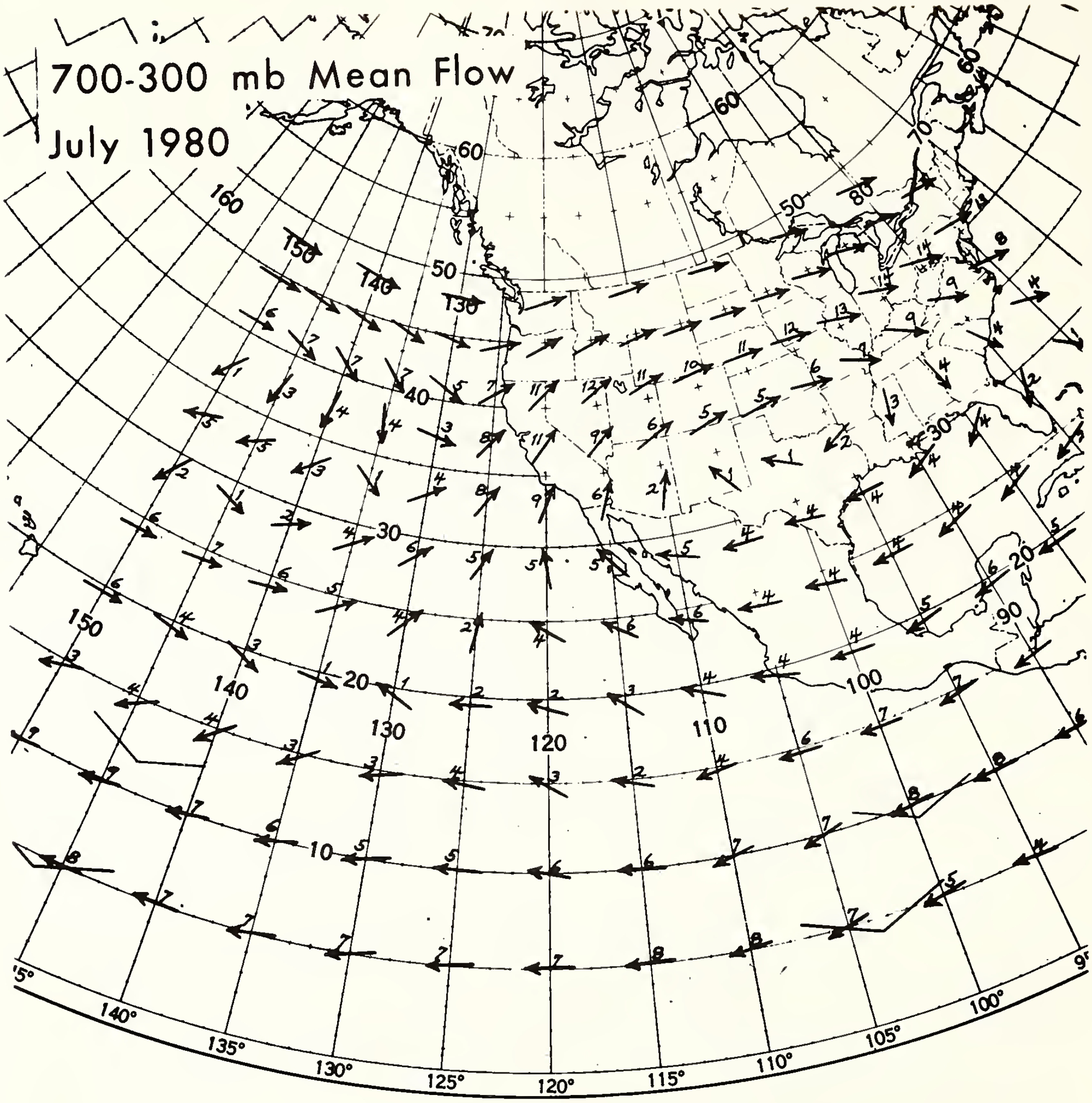

Figure 7. --Monthly mean flow (m s^{-1}) for the mid-tropospheric layer 700-300 mb for July 1980.

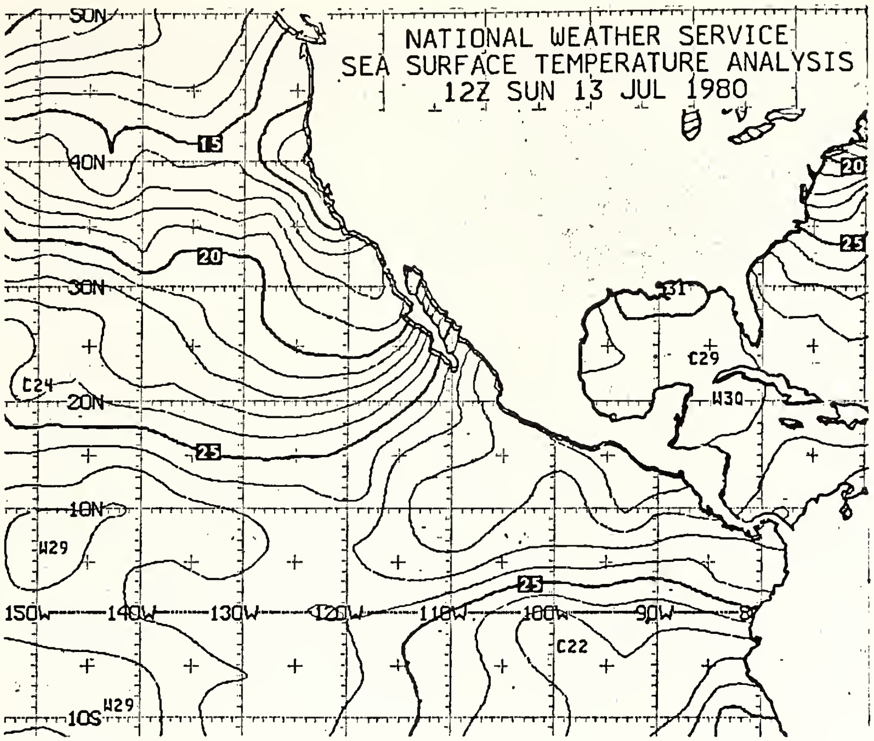

Figure 8. --Sea-surface temperature analysis for 13 July 1980.

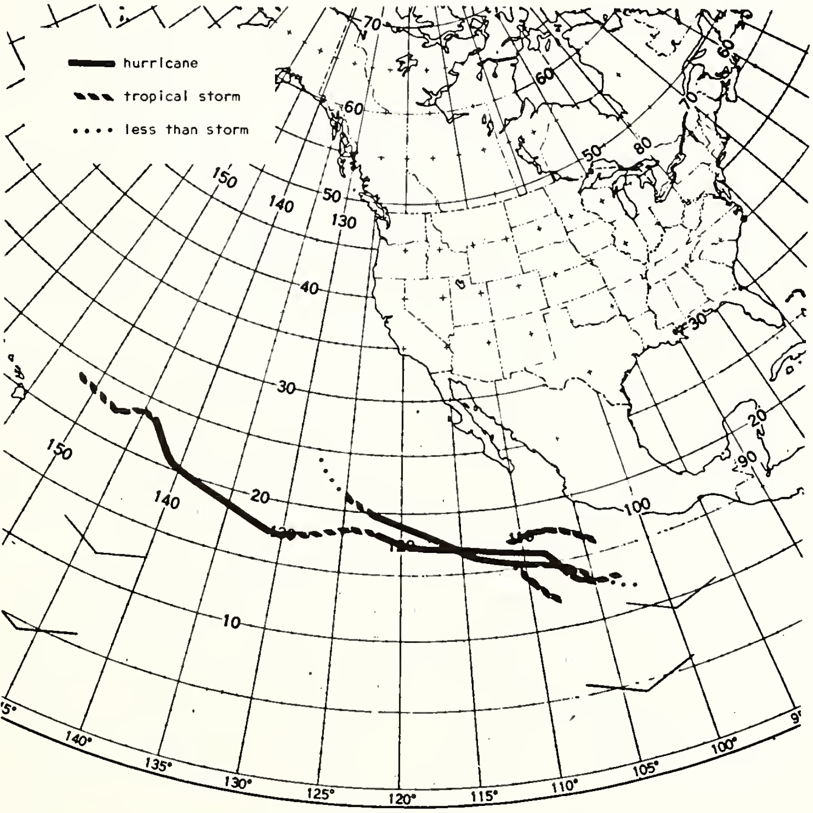

Figure 9. --Tracks of eastern North Pacific tropical cyclones, August 15 - October 15, 1980.

A rotated principal component analysis of the interannual variability of the 500 mb height field

John D. Horel
Department of Atmospheric Sciences
University of Washington
Seattle, Washington 98195

Principal component and rotated principal component solutions derived from time series of monthly mean 500 mb height are compared. The set of 111 gridpoint time series is based on the December, January, and February monthly means of twice-daily NMC gridded analyses from 1962-63 through 1976-77; this is the same data set used by Wallace and Gutzler (1980, 1981) (hereafter referred to as WG). The spatial patterns (eigenvectors or empirical orthogonal functions) associated with the principal components are computed from the matrix of cross-correlations between all 111 normalized time series. The principal components that satisfy the Kaiser criterion by explaining more than one unit of total normalized variance are linearly transformed (rotated) using the varimax method to obtain the rotated principal components.

While the principal components are the best general factors to describe the original time series, the rotated principal components have several advantages, including: they emphasize the relatively few strong relatonships among the time series and, hence, describe more regional scale patterns; while they are temporally uncorrelated, their spatial patterns (or loading vectors) are allowed to be spatially correlated and are simpler to interpret; their spatial patterns resemble the observed regional anomaly fields during those months when the components have large values; and they are less dependent upon the domain of the analysis. A drawback of the rotated principal component solution is its lack of uniqueness. Experiments with the data set used in the present study suggest reasonable changes in the analysis procedure do not noticeably affect the results.

The percent of the normalized variance explained by each of the 19 principal components that satisfy the Kaiser criterion and by each of their 19 rotated counterparts is shown in Table 1. Note that the total variance explained by all 19 rotated principal components and principal components is the same; the variance has just been redistributed so that the rotated modes explain more variance locally.

The eigenvectors associated with the first four principal components derived from the above data set have been shown by WG and are repeated here in Fig. 1. The eigenvectors are quite complicated, each one explaining some variance in many different regions, compared to the loading vectors of the first four rotated principal components shown in Fig. 2. The first rotated mode is not greatly different from the first principal component except the dominant relationship, a "seesaw" in the west Pacific, is enhanced while the marginal correlations near Hudson Bay and west Africa are reduced. The second rotated mode exhibits a "wavetrain" type pattern with one center of action in the subtropics and additional centers of action downstream first to the north and then to the east. The third rotated mode represents a north-south "seesaw" in the Atlantic while the fourth primarily describes the variability of 500 mb height near the North Pole.

Fig. 3 summarizes the spatial patterns of the first 10 rotated principal components. From Fig. 3 it is apparent that rotated principal components 1, 2, and 3 describe strong regional standing oscillations while the others primarily represent either weaker "seesaws" or modes with only one center of action. Modes 1, 2, and 3 are also very similar to the West Pacific, Pacific/North American (or East Pacific) and East Atlantic patterns determined by WG using the negative extrema method. The weaker pattern of mode 5, complicated to interpret because its center of action overlaps with those of modes 2 and 6, is similar to the West Atlantic pattern of WG.

Advantages of the rotated principal component model compared to the negative extrema method employed by WG are the relative computational convenience and objectivity of the rotated principal component solution. In a single computer run the spatial patterns and time series of the rotated principal components can be obtained at a cost which is not greatly increased from that required to calculate the unrotated components. In contrast, the negative extrema method is quite laborious, and requires several computer runs to adequately identify the standing oscillations.

Wallace, J. M., and D. S. Gutzler, 1980: Horizontal teleconnections during the Northern Hemisphere winter season. Proc. Fourth Ann. Clim. Diag. Wrkshp., 296-306.

1981: Teleconnections in the geopotential height field during the Northern Hemisphere winter. Submitted to Mon. Wea. Rev.

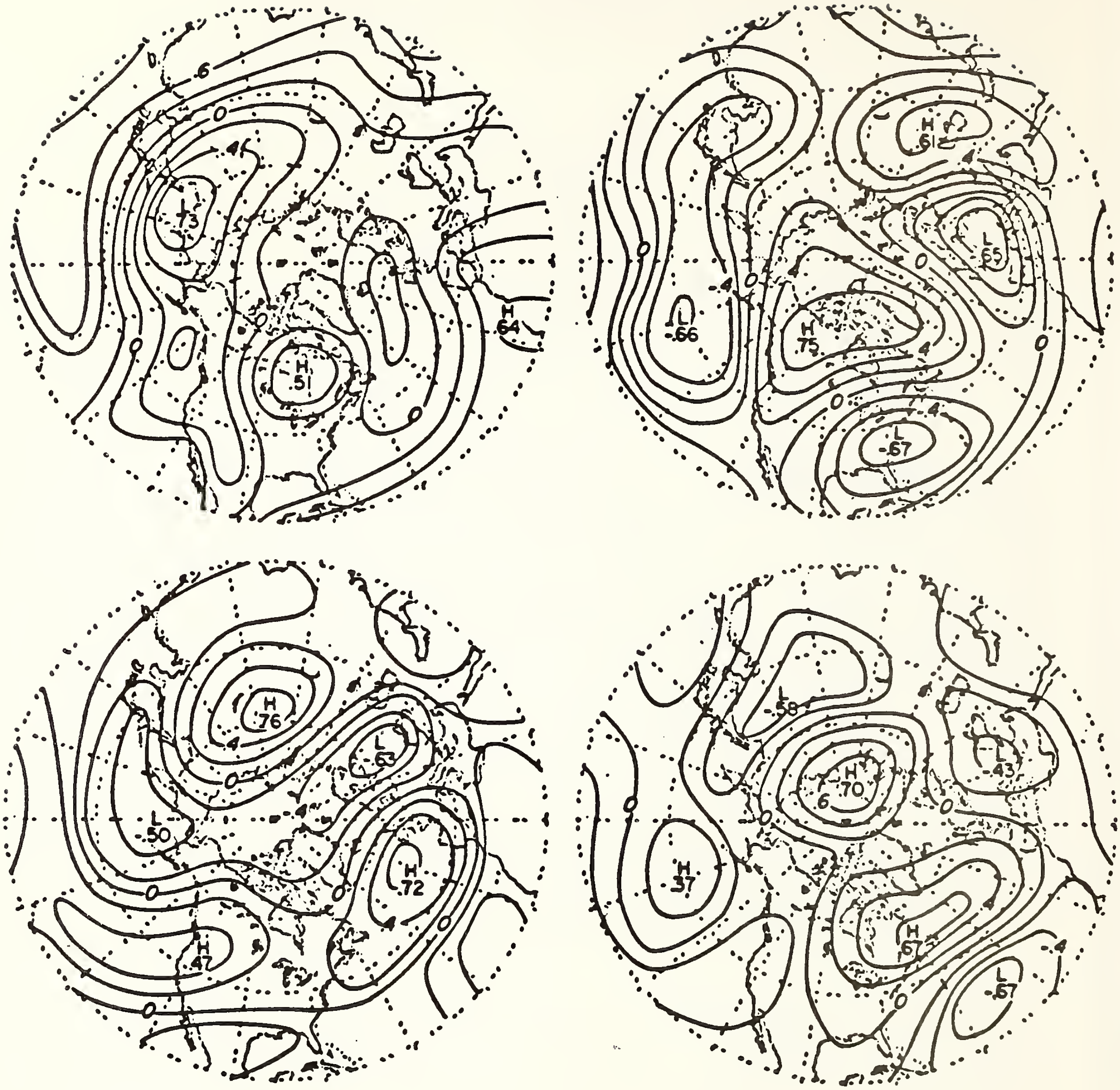

Figure 1. Eigenvectors of the first four principal components derived from 500 mb height time series consisting of 45 winter months. The value of the k^{th} eigenvector at any location represents the temporal correlation between the k^{th} principal component and the time series of local 500 mb height. The sign convention is arbitrary. Contour interval 0.2.

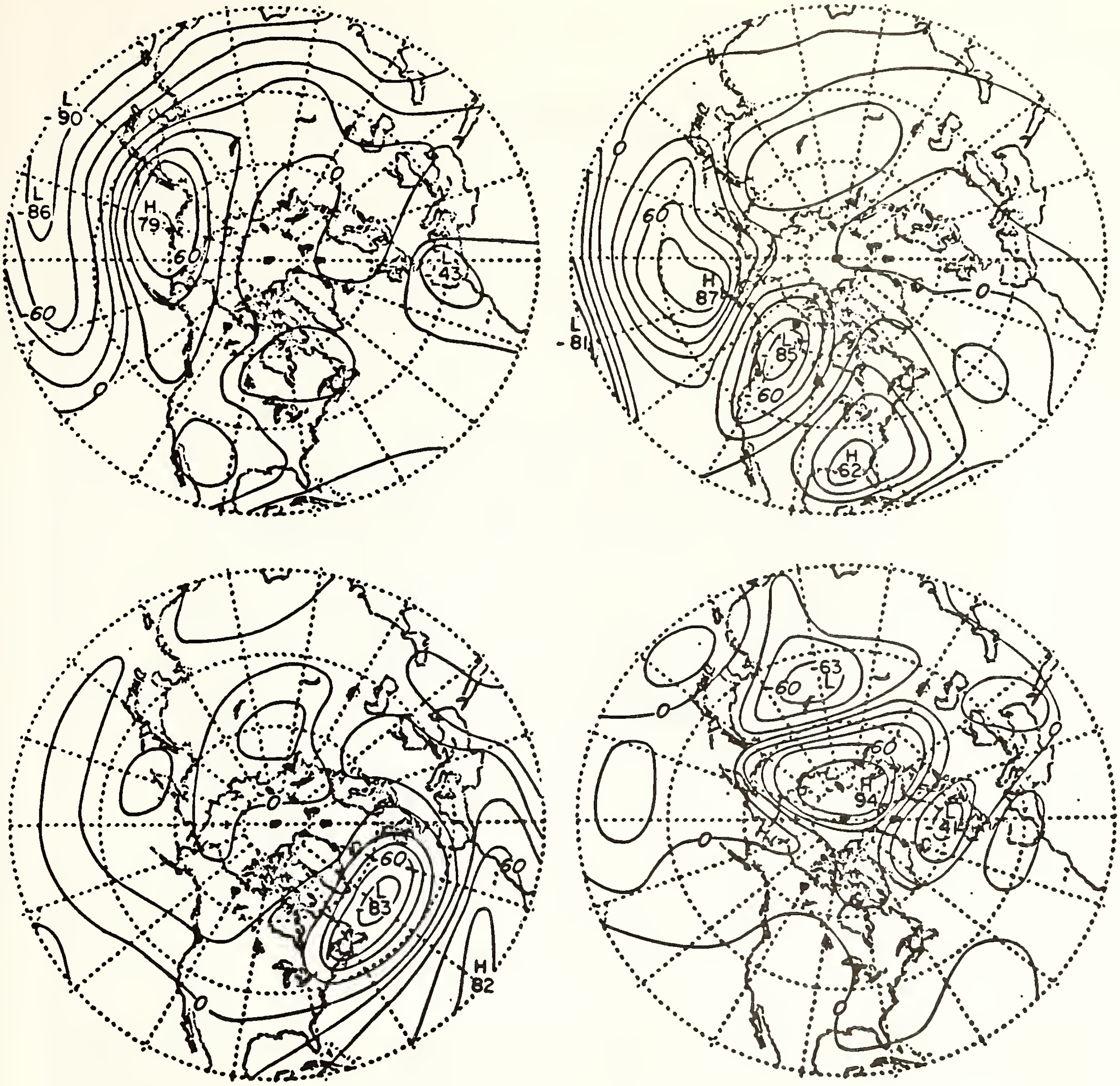

Figure 2. Loading vectors of the first four rotated principal components derived from the same data set and principal components described in Fig. 1. The rotated principal components are a varimax rotation of the 19 principal components whose first four spatial modes are shown in Fig. 1. The value of the kth loading vector at any location represents the correlation between the kth rotated principal component and local 500 mb height. Contour interval 0.2.

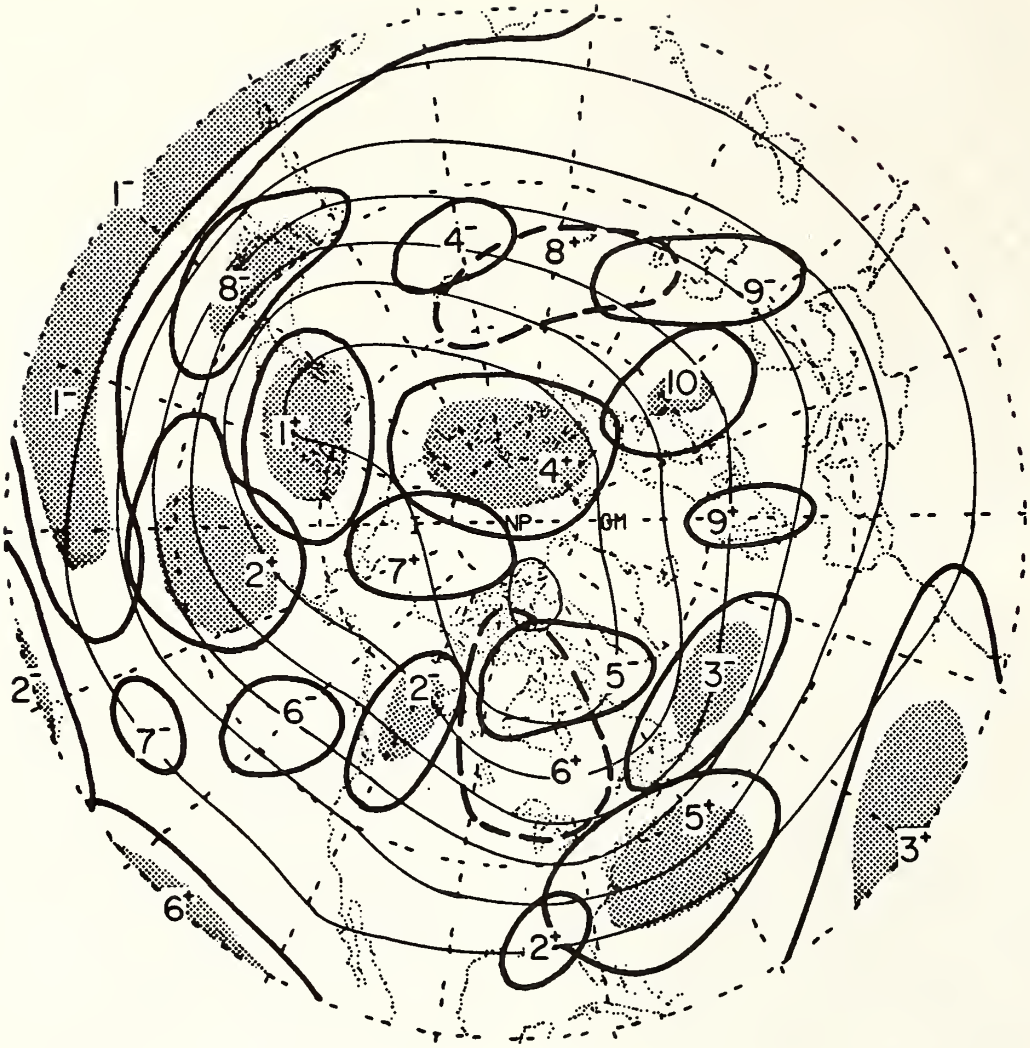

Figure 3. Summary map of the loading vectors associated with the first ten rotated principal components, derived from the same data set and principal components described in Fig. 1. The summary map has been superimposed on the wintertime mean 500 mb height contours (light lines), contour interval 120 m. The ± 0.6 isopleths (heavy lines) of correlation coefficient between each of the ten rotated principal components and local 500 mb height are shown; correlations exceeding ± 0.75 are shaded. Dashed lines denote the ±0.4 for selected rotated principal components. Labels in each center of action indicate the number of the rotated principal component and the sign of the correlation at the location of strongest correlation.

Time Evolution of Teleconnection Patterns

Harold J. Edmon, Jr.
Department of Atmospheric Sciences
AK-40, University of Washington
Seattle, Washington 98195

Cross-correlation analysis of wintertime 500 mb heights has revealed the existence of several "teleconnection patterns" over the Northern Hemisphere. Modelling results suggest that some of these patterns develop in the Tropics and propagate into mid-latitudes. This paper is an examination of lag cross-correlations using the centers of one teleconnection pattern to see if there is evidence of such a propagation.

The data used in this study consists of five-day contiguous means of twice-daily NMC octagonal grid analyses for November through March for thirty winters from 1948-49 to 1979-80. The winters of 1959-60 and 1960-61 were not used due to data problems during 1960. Seasonal and interannual variability was eliminated by fitting a quadratic to each individual winter and then subtracting it out. Individual cross-correlation maps consist of correlations between 500 mb height at a fixed base grid point and 500 mb height at every grid point over the hemisphere five days earlier (-1 lag), simultaneously (0 lag) or five days later (+1 lag). The base grid points chosen are the four centers of the Pacific-North American pattern derived by Gutzler and Wallace (1981) from monthly mean data: 20°N, 160°W; 45°N, 165°W; 55°N, 115°W; 30°N, 85°W. Five-day means were used since they eliminate baroclinic instabilities and because model results suggest a propagation time of two days from one center to the next.

Figure 1 shows the 0 lag pattern for the western two points of the pattern. These reveal the four point teleconnection pattern over the east Pacific and North America, with only small correlations elsewhere. Figure 2 shows the -1 lag pattern for these points. This map indicates how the heights over the hemisphere five days ago are correlated to the "current" height values at these points. The patterns show that these two base points are connected to themselves and each other, with smaller correlation elsewhere. Figure 3 shows the +1 lag pattern for these points. This map indicates how heights five days ago at the points are correlated with the "current" hemispheric heights. Both of these maps show the complete four point pattern, whereas Fig. 2 did not. The Aleutian point shows correlations with the eastern two points that are nearly as high in Fig. 3 as the 0 lag correlations in Fig. 1. The correlations in Fig. 2 are much weaker. This asymmetry between Figs. 2 and 3 indicates that the downstream points are preferentially influenced by heights in the Aleutians five days earlier, suggesting propagation of the centers.

Figures 4, 5, 6 show the 0, -1, +1 lag patterns respectively for the eastern two points. In these figures the four point pattern occurs best in the 0 and -1 lag maps, indicating that the heights at these points are influenced preferentially by past height changes to the west, again indicating possible propagation of these patterns. Maps of -2 and +2 lags (not shown) were also calculated for these points, but they showed no correlations outside the range of ±0.2. The time scale of this propagation agrees with modelling results performed by Brian Hoskins in which he placed a vorticity source in the Tropics and arrived at a height pattern similar to the Pacific-North American teleconnection pattern after a week, with new centers appearing every two days from west-to-east. More work is planned in this area, including the study of other teleconnection patterns and the inclusion of height data below 20°N.

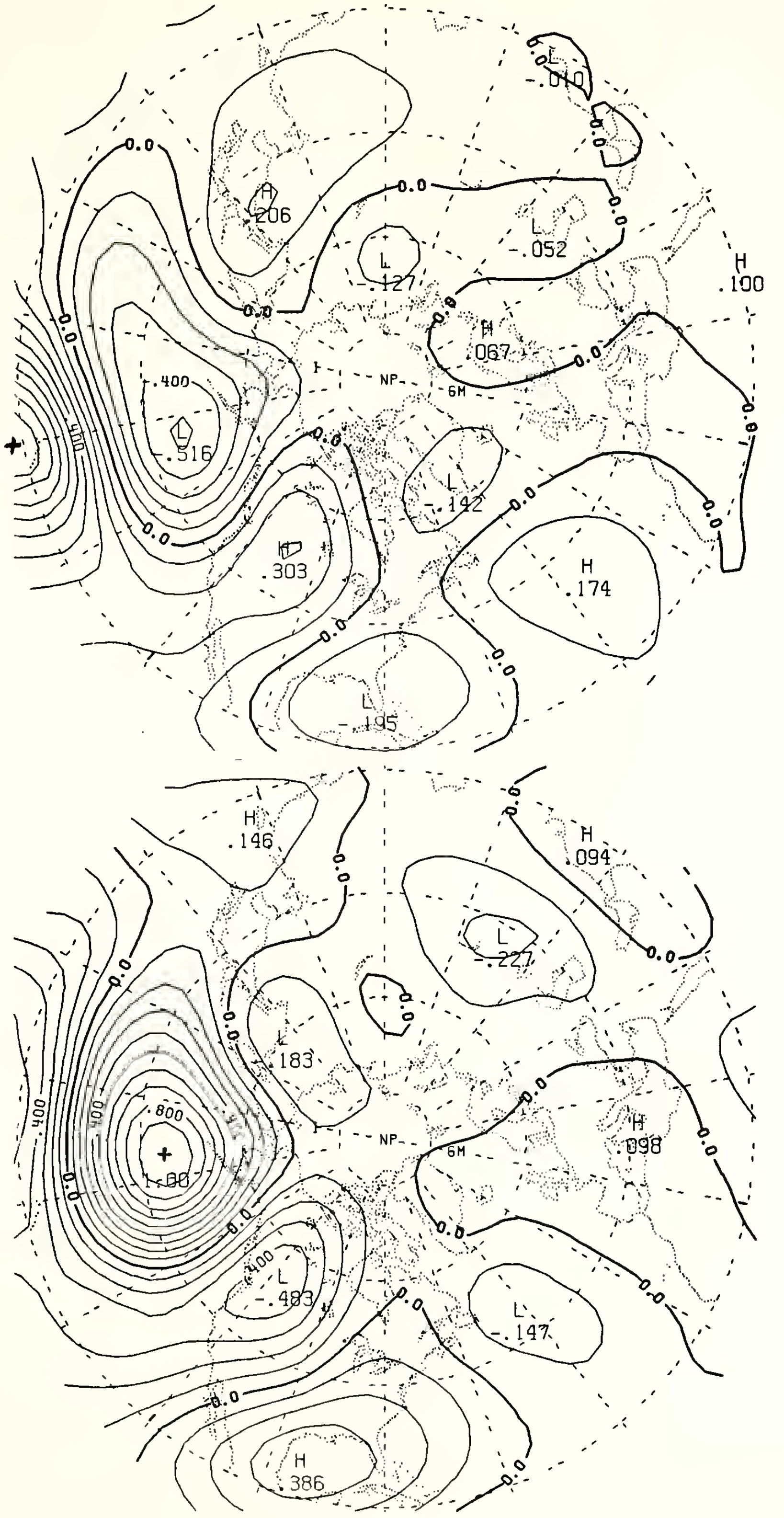

Fig. 1. 0 lag cross-correlation maps for western points. Base points are indicated by a cross. Contour interval is 0.1.

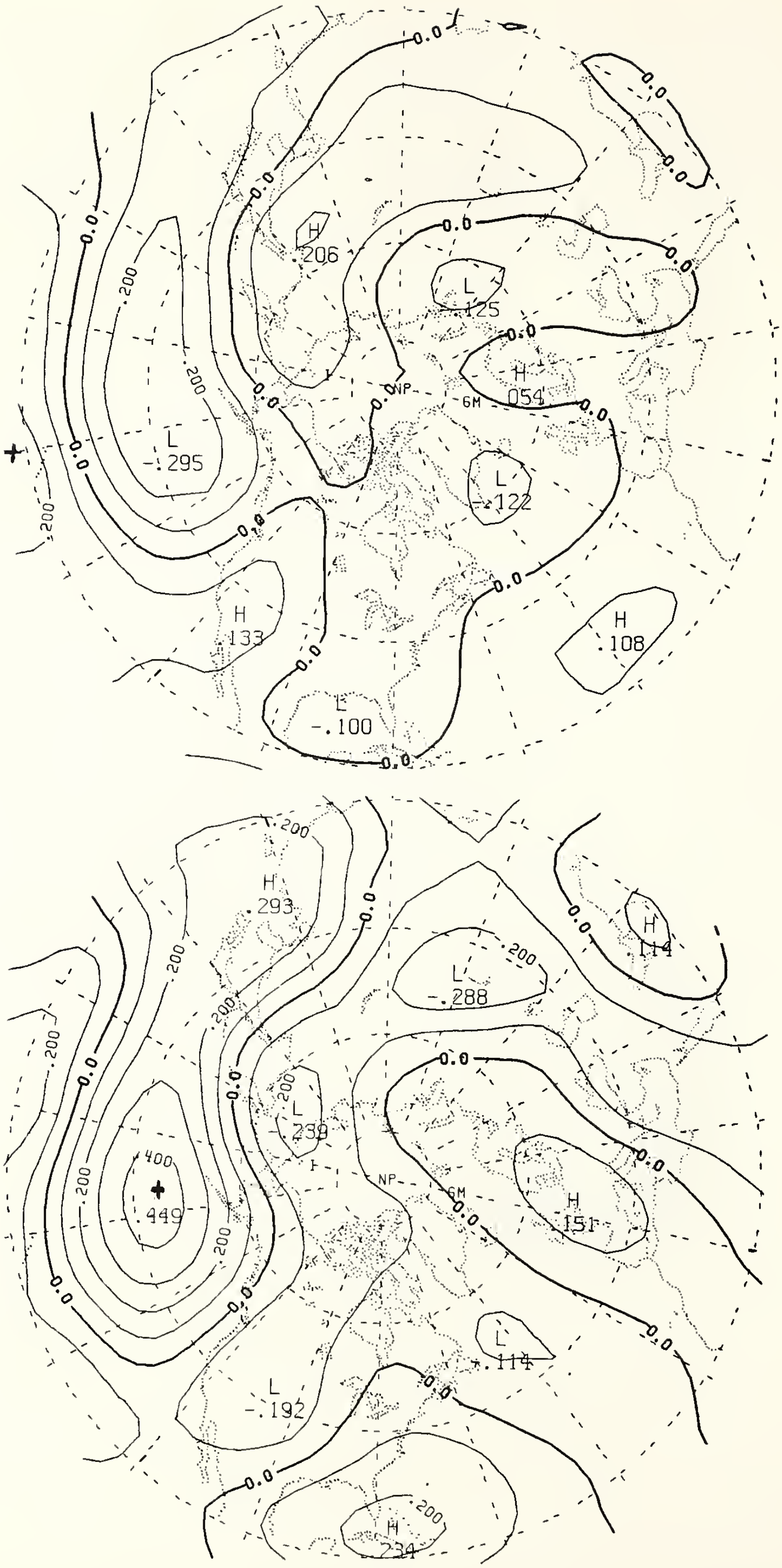

Fig. 2. Same as Fig. 1 for -1 lag.

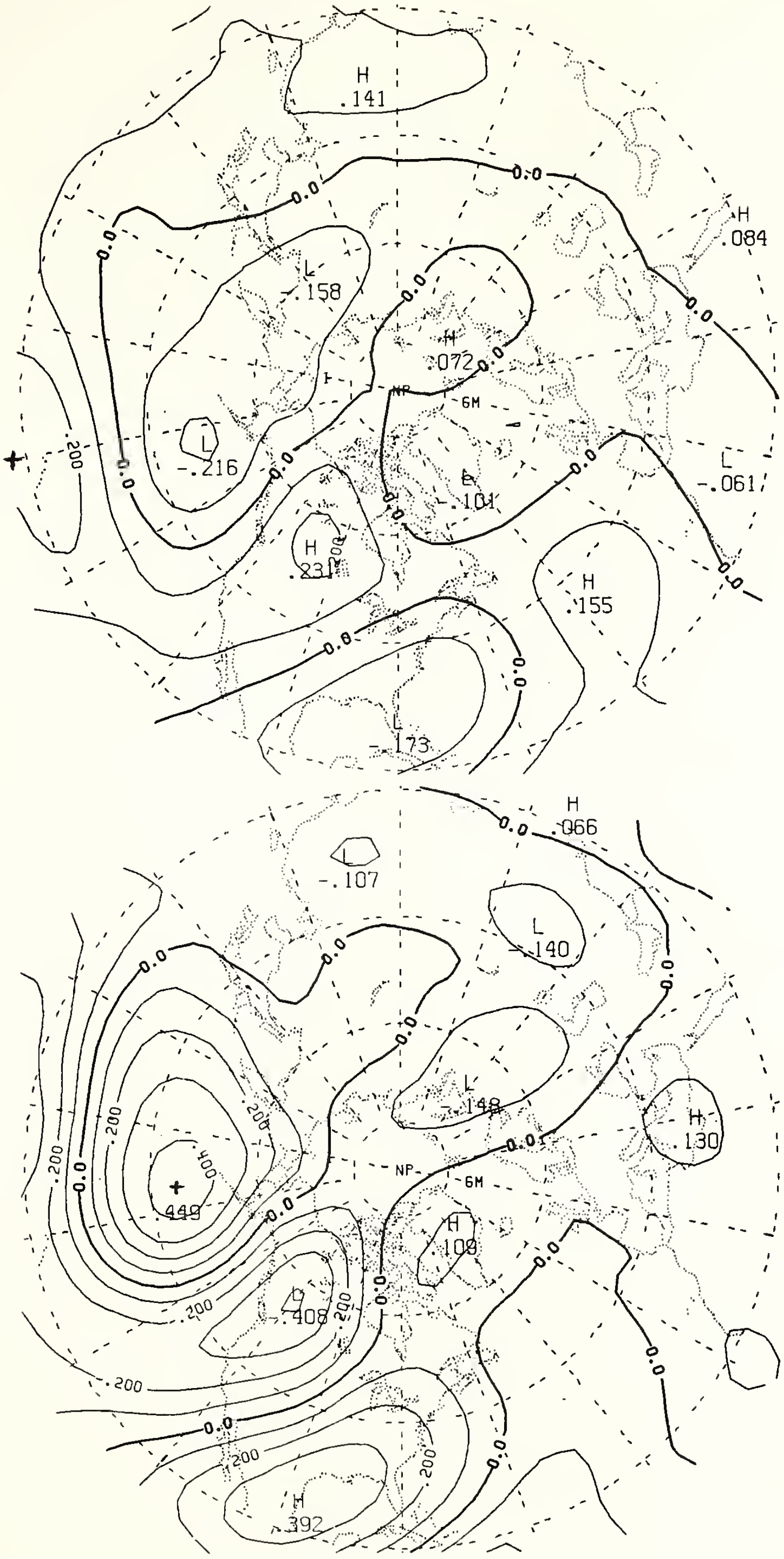

Fig. 3. Same as Fig. 1 for +1 lag.

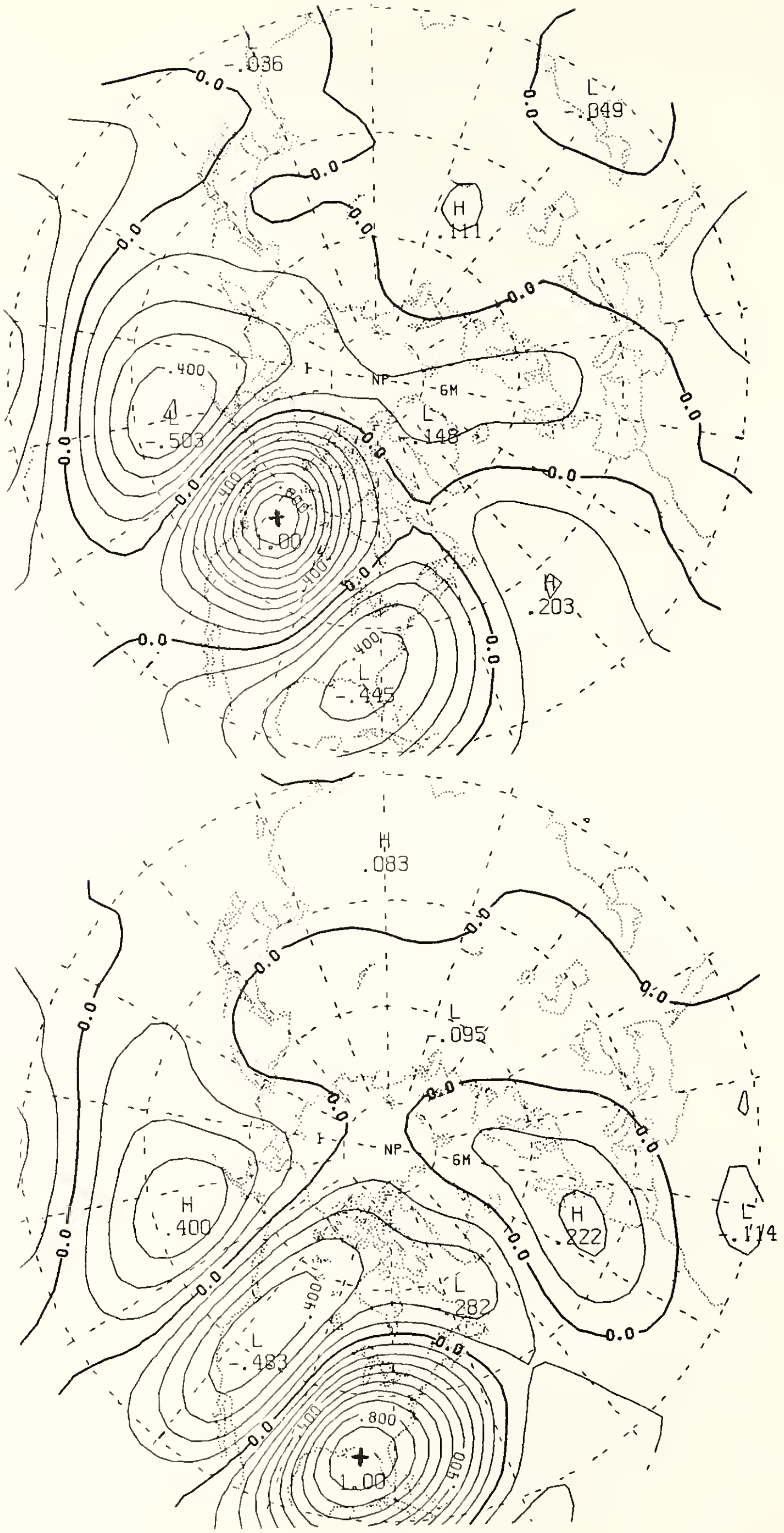

Fig. 4. Same as Fig. 1 for eastern points.

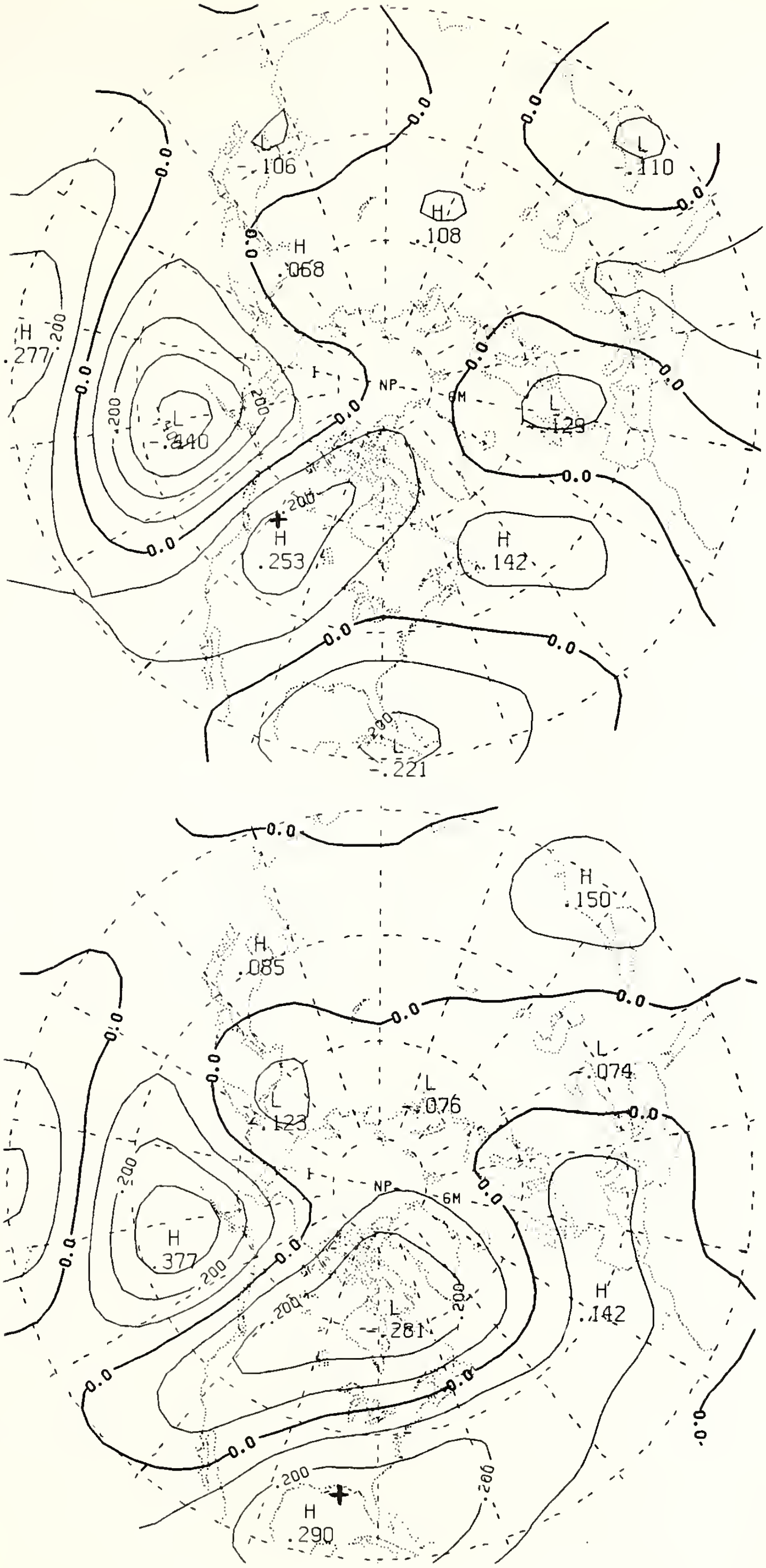

Fig. 5. Same as Fig. 4 for -1 lag.

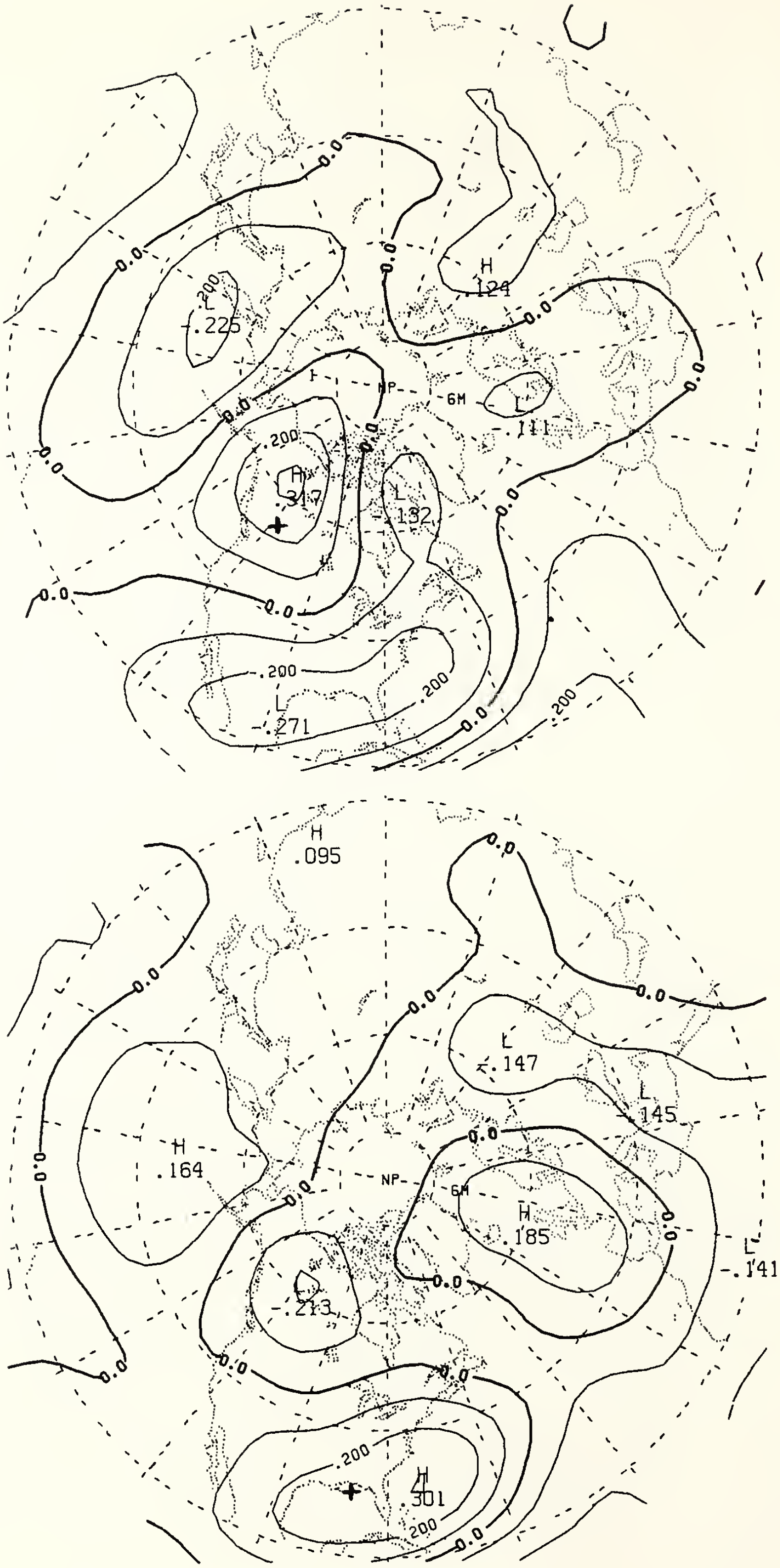

Fig. 6. Same as Fig. 4 for +1 lag.

Low frequency circulation modes as revealed by eigenvector analysis of the 250-mb and 850-mb wind fields

Klaus M. Weickmann and John E. Kutzbach
Center for Climatic Research and
Department of Meteorology
University of Wisconsin
Madison, Wisconsin 53706

Large-scale shifts in the atmospheric circulation occur on interannual, seasonal, and intraseasonal time scales. An important aspect of the medium-to long-range forecasting problem is the documentation and ultimate understanding of these large-scale, low-frequency fluctuations. Previous studies of the time averaged wintertime circulation (Blackmon et al., 1977; Lau, 1978) suggest a link between large-scale ageostrophic mass circulations, the seasonal mean jets and distributions of diabatic heating and topography. The possible low-frequency variability of these connections and the implications for weather patterns have not been determined. This study documents the spatial and temporal characteristics of the wintertime circulation variability through eigenvector (EV) analysis of the 850-and 250-mb wind field.

NMC objective analysis data for the period NOV-MAR of 1974-75 through 1979-80 forms the basic data set. The domain of analysis covers the region 30°S-85°N. Spatial resolution is 5° lat. by 10° long., while 5-day averages of twice daily data comprise the time resolution. The EV analysis is performed on the 250-and 850-mb wind field simultaneously. Thus, each EV represents an anomaly pattern at 250 and 850 mb, while the EV coefficients represent the time variation of the pattern. The eigenvectors are computed relative to the time mean patterns at 250 and 850 mb; these 6-year means are shown in Figure 1.

Figure 2 displays the time series of coefficients for EV's 1-3. The shape of the first (top) time series suggests that EV 1 is related to the seasonal cycle. The amplitude of the seasonal cycle is seen to vary interannually, e.g., it is large in 76-77 and small in 78-79. The second time series shows a flip in the sign of the EV coefficient from 75-76 to 76-77. This change coincides with a major warming of sea surface temperatures (SST) in the equatorial Pacific and a concurrent increase in cloudiness in the same region. Intraseasonal fluctuations are also apparent in the series, e.g., the oscillation in 79-80 coincides with a major index cycle as reported by Wagner (1980). The third time series shows mainly intraseasonal variations which are particularly well defined during the FGGE year, 1978-79.

The spatial pattern corresponding to EV1 is shown in Figure 3. At 250 mb (Fig. 3a) the main features (corresponding to a positive coefficient) are: 1) intensified westerlies in the Northern Hemisphere middle latitudes, 2) presence of mid-oceanic troughs over the eastern Pacific and the Atlantic Ocean, 3) northward directed outflow from tropical land masses, and 4) intensified easterlies (or weakened westerlies) in the Southern Hemisphere. Related features are also evident at 850 mb (Fig. 3b). The 850-mb westerlies from the Indian Ocean to the central Pacific in the Southern Hemisphere are a particularly strong feature.

The second eigenvector at 250 mb and 850 mb is shown in Figure 4. For a positive coefficient this pattern represents an expansion and intensification of the middle latitude (ML) westerlies over both oceans. The subtropical anomalies tend to be out of phase with those in ML. As evidenced by comparing the 250-mb and 850-mb patterns, the features tend to be equivalent barotropic in middle latitudes. However, in the Southern Hemisphere tropics around 160°W anomalous westerlies at 850 mb become anomalous easterlies at 250 mb (with a positive coefficient), implying fluctuations in intensity of the Walker Circulation.

An alternate, more easily interpreted presentation of the EV analysis is obtained by utilizing the mean pattern. Consider the equation

$$\underset{\sim}{\zeta} = \underset{\sim}{\bar{\zeta}} + c_i \underset{\sim}{e}_i$$

where $\underset{\sim}{\bar{\zeta}}$ is the mean pattern (Figure 1), c_i is a representative maximum positive or negative value of the EV coefficient (Figure 2), and $\underset{\sim}{e}_i$ is an EV. The $\underset{\sim}{\zeta}$ vector then represents the EV plus the mean (EPM) with EPMi^+ denoting the pattern of the ith EV with a positive coefficient, while EPMi^- is the ith EV with a negative coefficient. This form of presentation is advantageous because (1) the patterns associated with + and - EV coefficients can be seen explicitly and (2) the changes in familiar circulation features can be seen.

Figure 5 shows EPM2$^+$ at 250-and 850-mb while Figure 6 shows EPM2$^-$ at these levels. Large differences between the EPM's are evident over the tropical central Pacific at 250 mb. EPM2$^-$ shows well developed mid-oceanic troughs in this region while EPM2$^+$ has anticyclones straddling the Equator. Anticyclones over all three tropical land masses are also shifted northward in EPM2$^+$. The subtropical jet streams (STJ), located in the eastern Pacific and the Atlantic Ocean sector, are well developed in EPM2$^-$, while the ML jets are stronger in EPM2$^+$. Strong equatorial westerlies in the Pacific go with weak equatorial westerlies in the Atlantic in EPM2$^-$ and vice-versa in EPM2$^+$. Contrasting the patterns at 850 mb EPM2$^+$ displays stronger and expanded oceanic westerlies (note Rex-type blocking patterns over both oceans), a ridge versus a trough on the west coast of the U.S., an eastward extension of the monsoonal low in the Indonesian region and a shift southward of maximum easterlies upwind from South America.

EV3 is pictured at 250 mb and 850 mb in Figure 7. In contrast to EV2, the ML anomalies of EV3 at 250 mb are out of phase between the Pacific and Atlantic Oceans. Thus with a positive (negative) sign for the coefficient the jet over the Atlantic (Pacific) is strong and expanded, while the jet over the Pacific (Atlantic) is shifted north. The anomalies in the STJ are out of phase with the ML anomalies over the same ocean. Another significant feature is the cross-equatorial flow in vicinity of 180°W in the Pacific. The anomalies again display an equivalent barotropic structure in middle latitudes (compare the 850- and 250-mb patterns). In the equatorial western Pacific anomalous westerlies at 850 mb (with a positive coefficient) extend from New Guinea to past the dateline.

A clearer picture of the implications of the EV3 anomalies can be obtained by considering the EPM's. Figure 8 shows EPM3$^+$ at 250 mb and 850 mb, while Figure 9 shows EPM3$^-$ at these levels. At 250 mb EPM3$^+$ has a STJ with roots near 20°N, 180°W merging into a strong E-W ML jet over the Atlantic, while EPM3$^-$ shows a STJ with roots near 15°N, 60°W merging into a strong ML jet east of Asia. Cross-equatorial flow of 4 m/s is present near 170°W in EPM3$^+$. Concurrently, the anticyclones in the western Pacific and Indonesian-New Guinea region are shifted westward and extend to the Indian Ocean. At 850 mb EPM3$^-$ shows a strong Aleutian and Icelandic Low while in EPM3$^+$ the Icelandic Low is shifted southward and the Aleutian Low is shifted westward. A trough dominates the U.S. west coast in EPM3$^+$ with ridging (blocking) extending from western Canada to north of Alaska. In contrast, a ridge dominates the U.S. west coast in EPM3$^-$. A significant shift eastward of the monsoonal low over northern Australia is also visible in EPM3$^+$.

In summary, this analysis has documented near global anomaly patterns which have intraseasonal, seasonal, and interannual time scales. Diagnostic study of these circulation modes is planned with particular emphasis on the mass circulations in vicinity of the three tropical land masses, e.g., how do the mass circulations fluctuate in intensity and northward extent? Characterization of the intraseasonal oscillations shown in the coefficient time series will also be pursued.

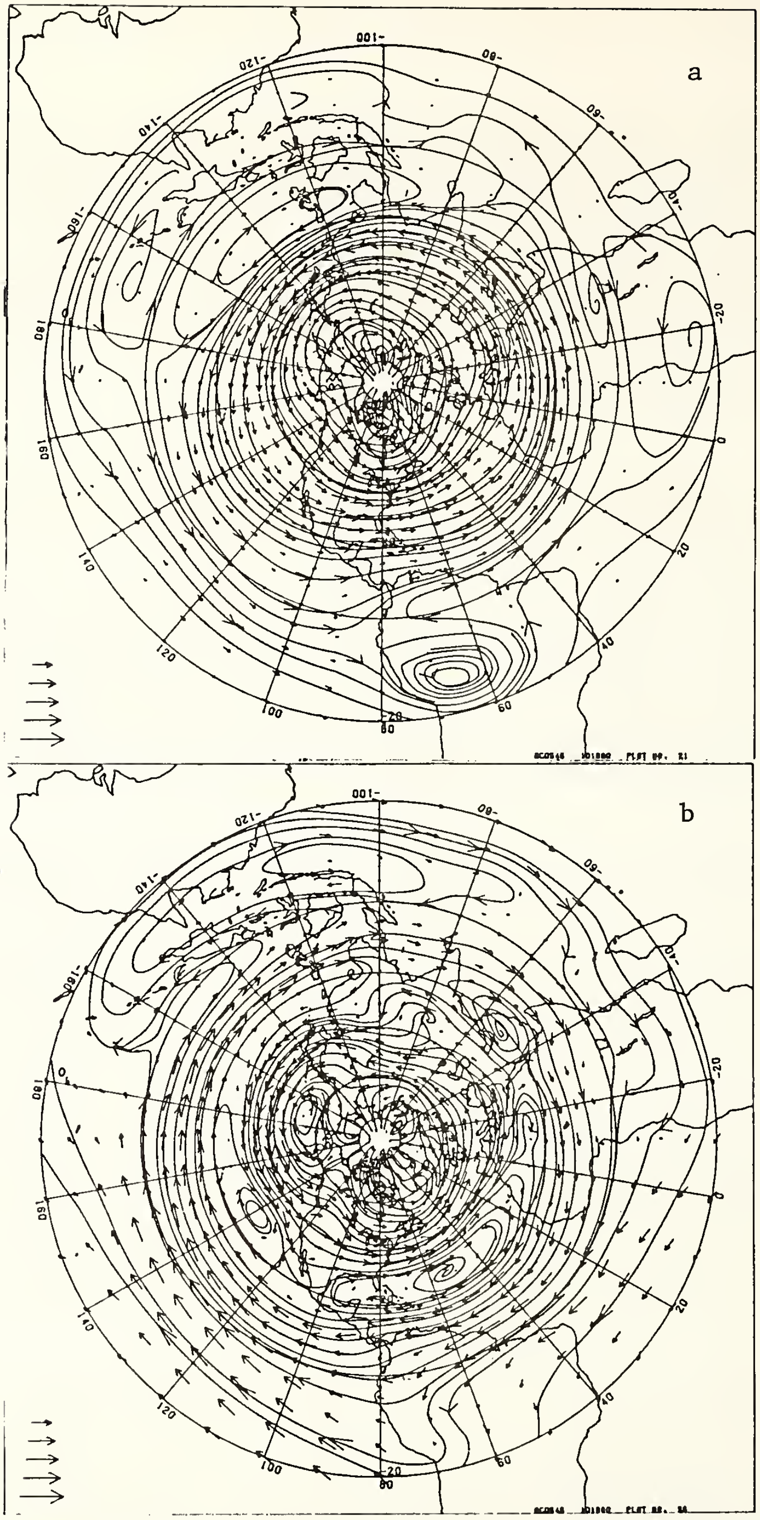

Figure 1. The 6-year mean wind field at 250 mb (a) and 850 mb (b). In this and all subsequent figures the arrows are scaled by the maximum speed on the map. Arrows are also scaled as a function of latitude with the scaling depicted at the lower left. The scale shows the arrow length corresponding to the maximum speed for the latitudes 0° (lower arrow), 20°N, 40°N, 60°N, and 80°N. Note that the outer latitude circle is 20°S.

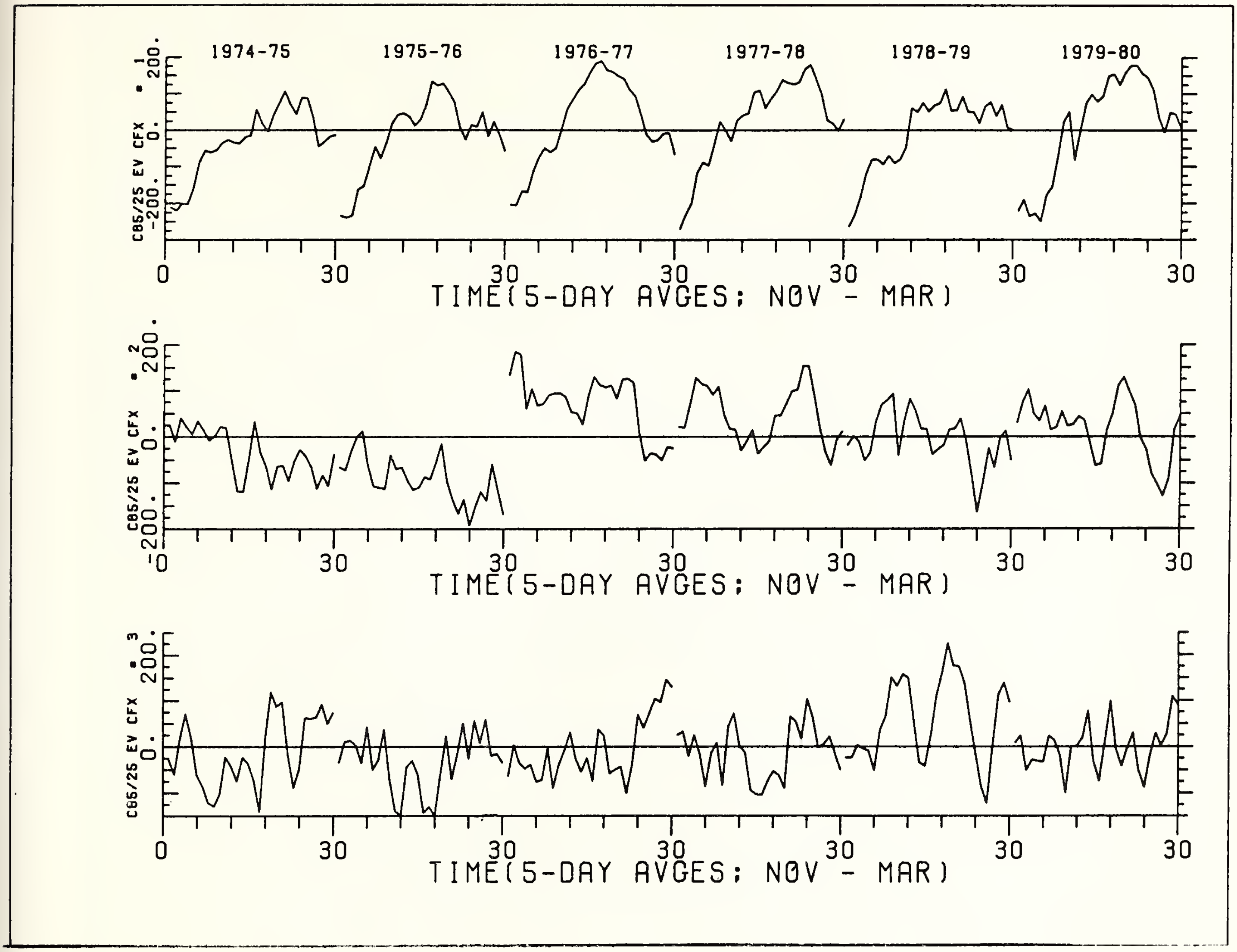

Figure 2. The time series of coefficients for eigenvectors 1, 2 and 3.

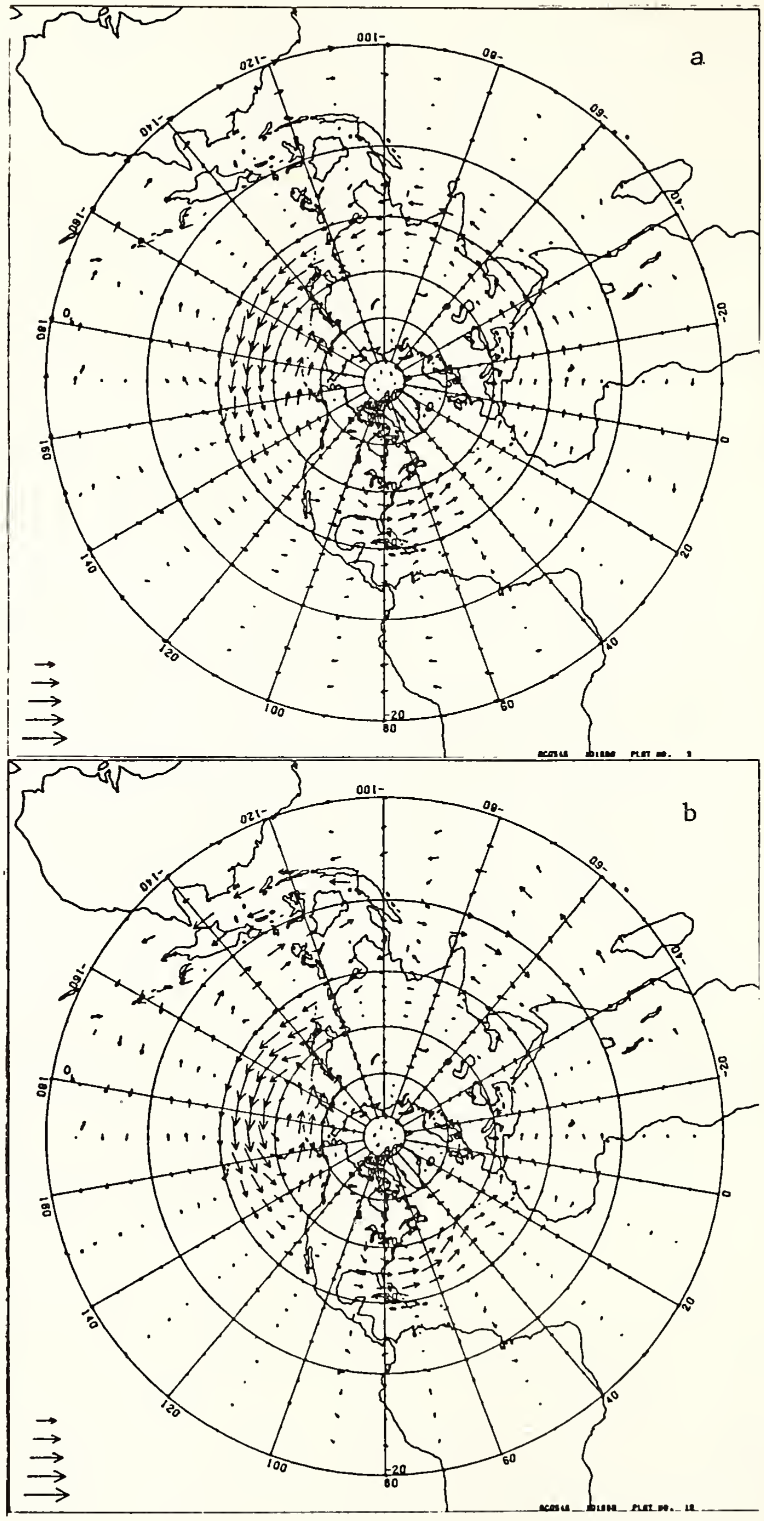

Figure 3. Eigenvector 1 at 250 mb (a) and 850 mb (b).

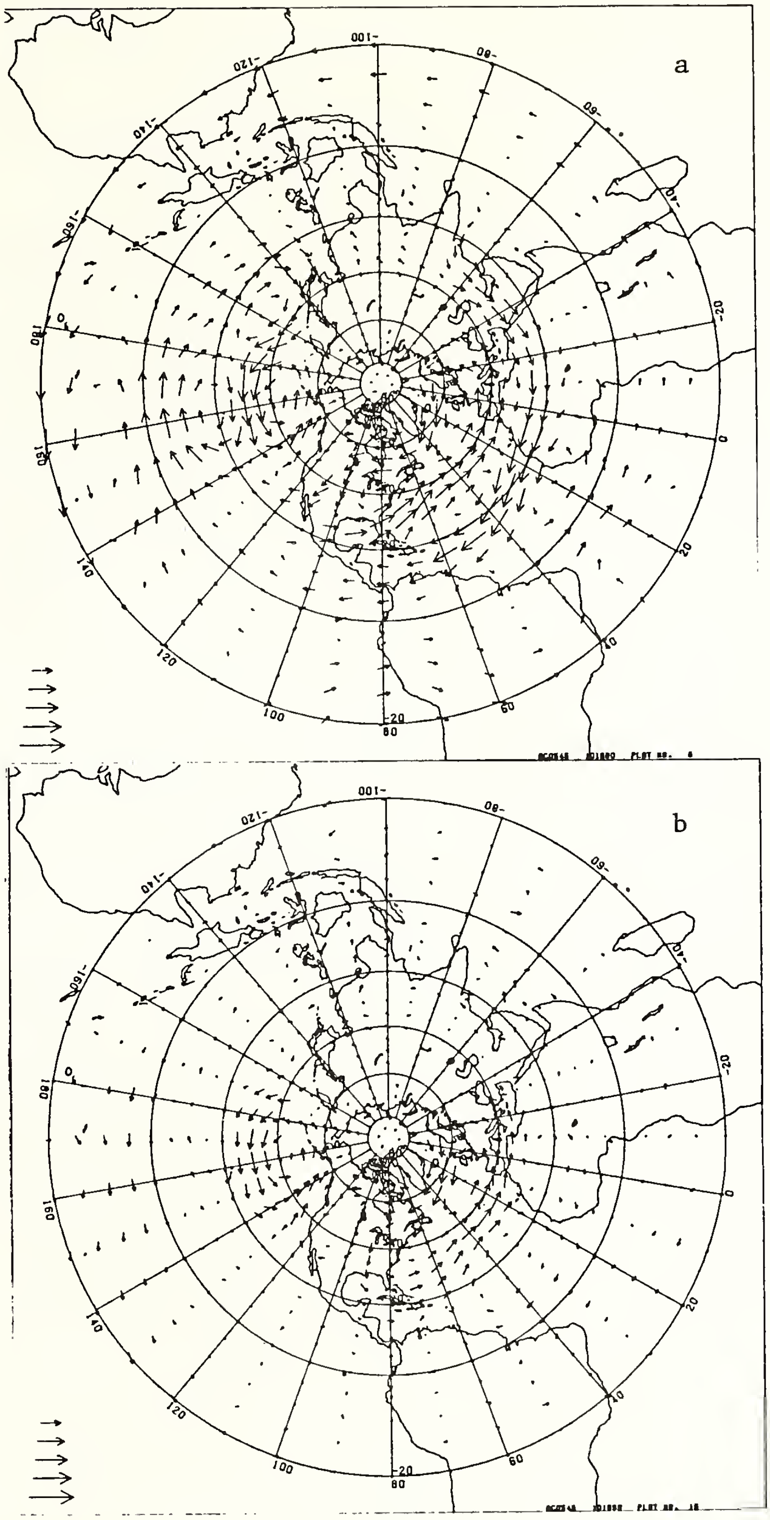

Figure 4. Eigenvector 2 at 250 mb (a) and 850 mb (b).

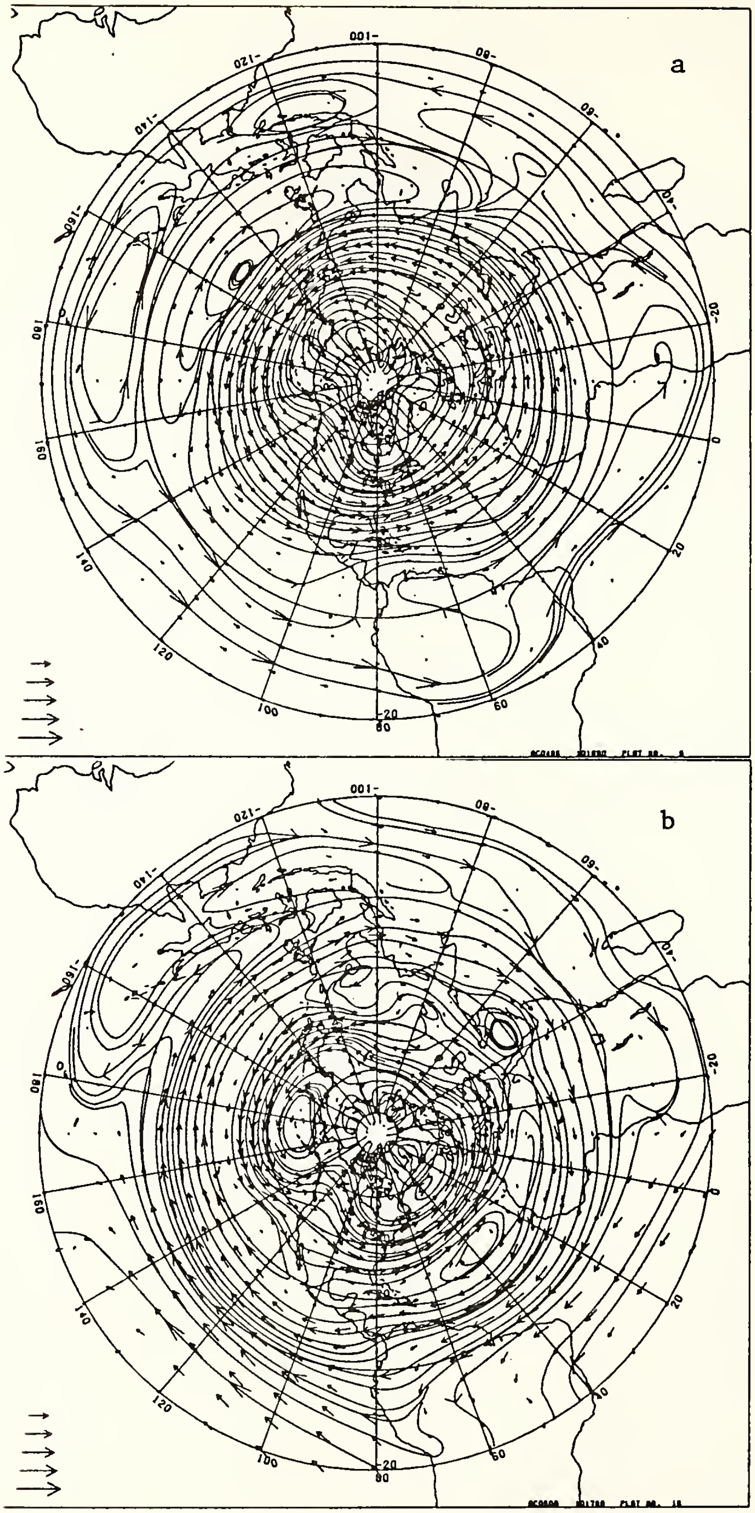

Figure 5. Streamline analysis of EPM2$^+$ (see text) at 250 mb (a) and 850 mb (b).

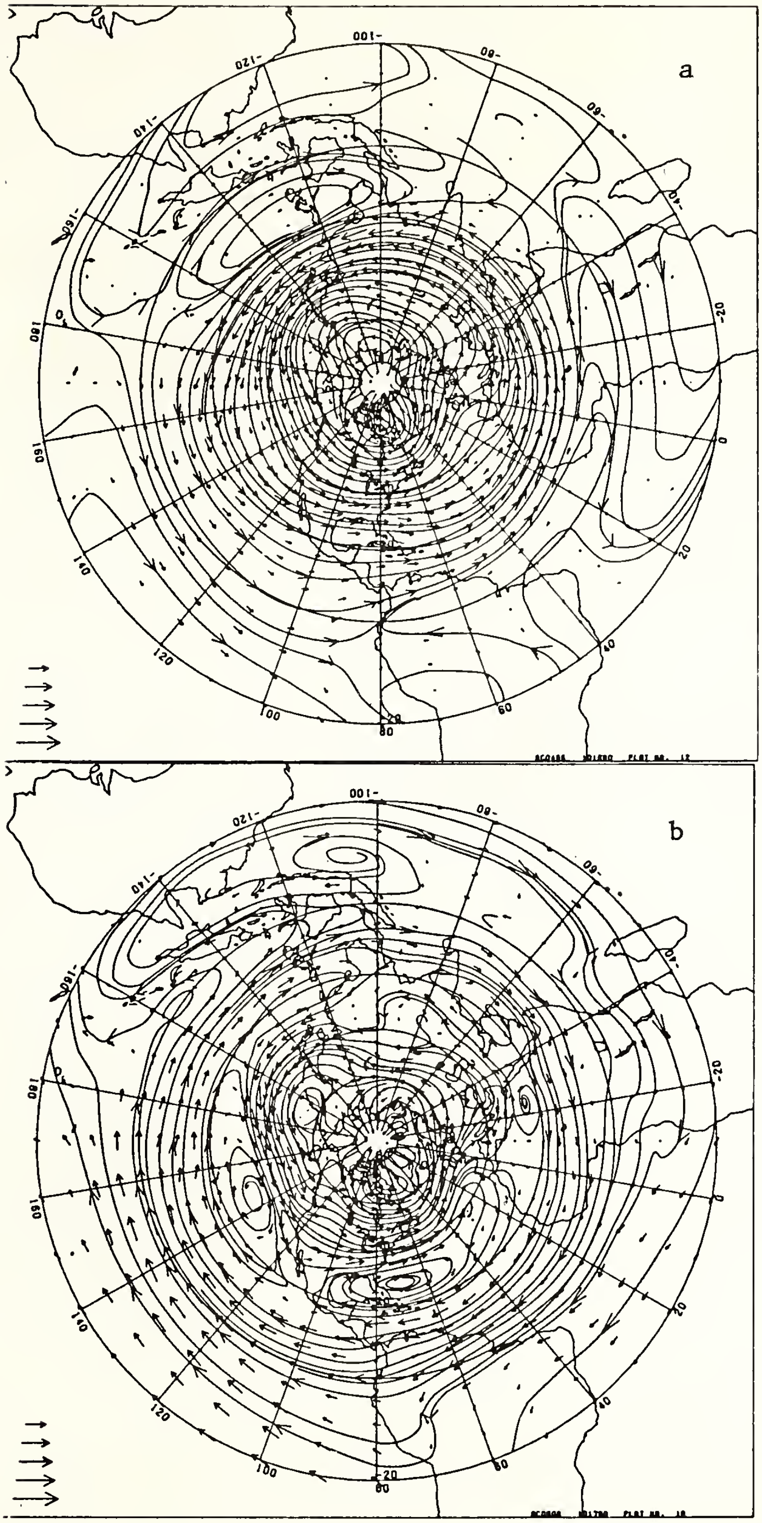

Figure 6. Streamline analysis of EPM2$^-$ (see text) at 250 mb (a) and 850 mb (b).

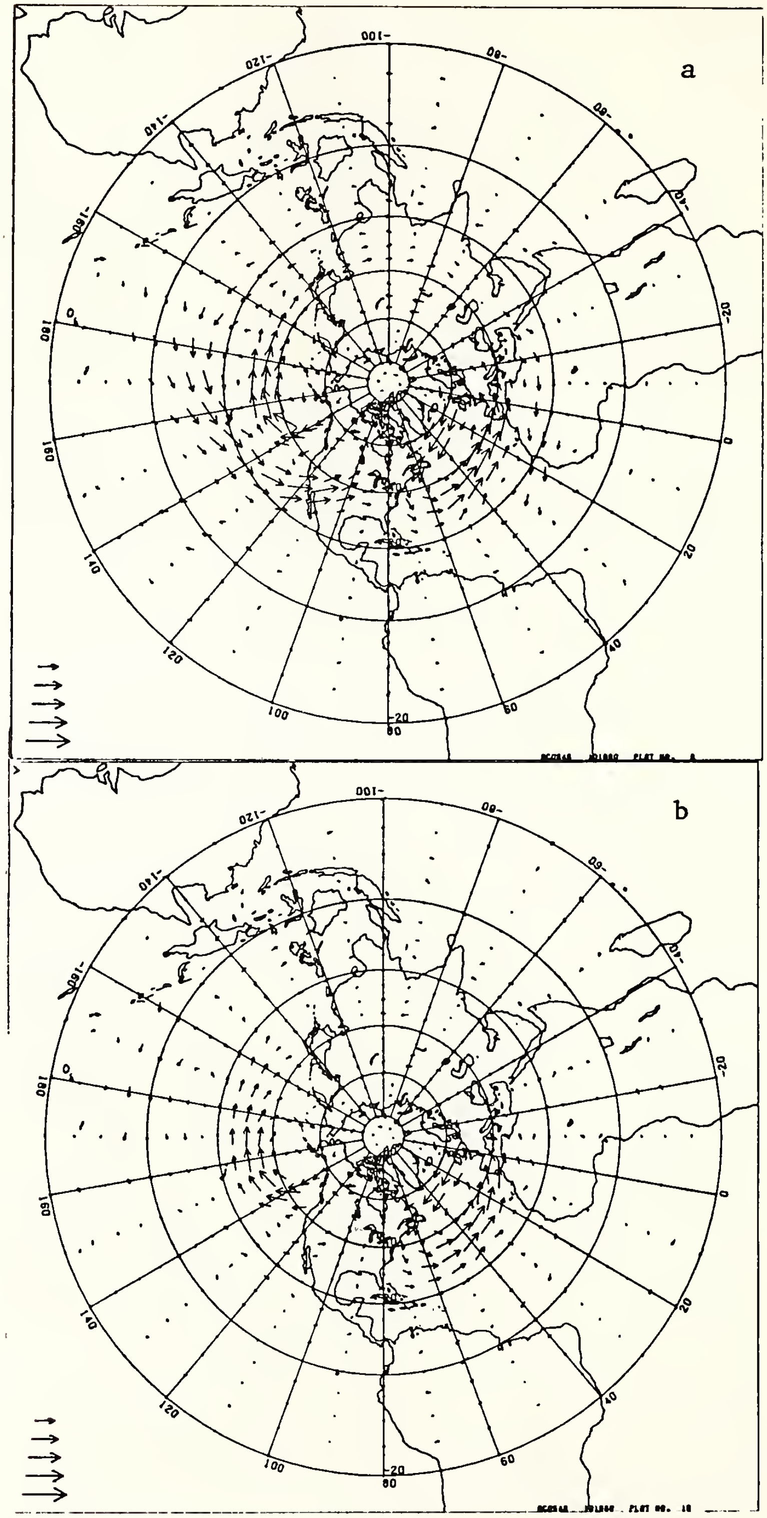

Figure 7. Eigenvector 3 at 250 mb (a) and 850 mb (b).

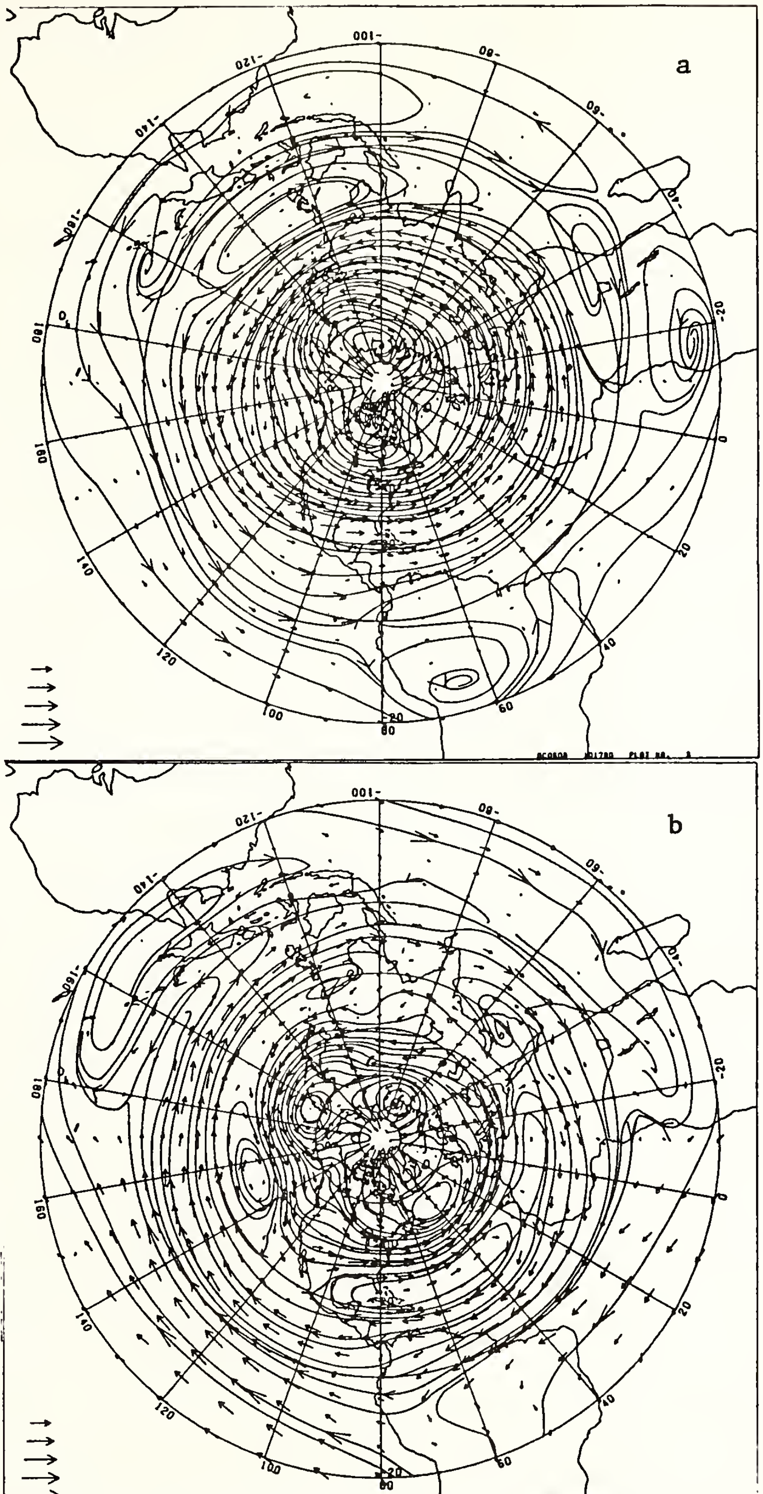

Figure 8. Streamline analysis of EPM3$^+$ (see text) at 250 mb (a) and 850 mb (b).

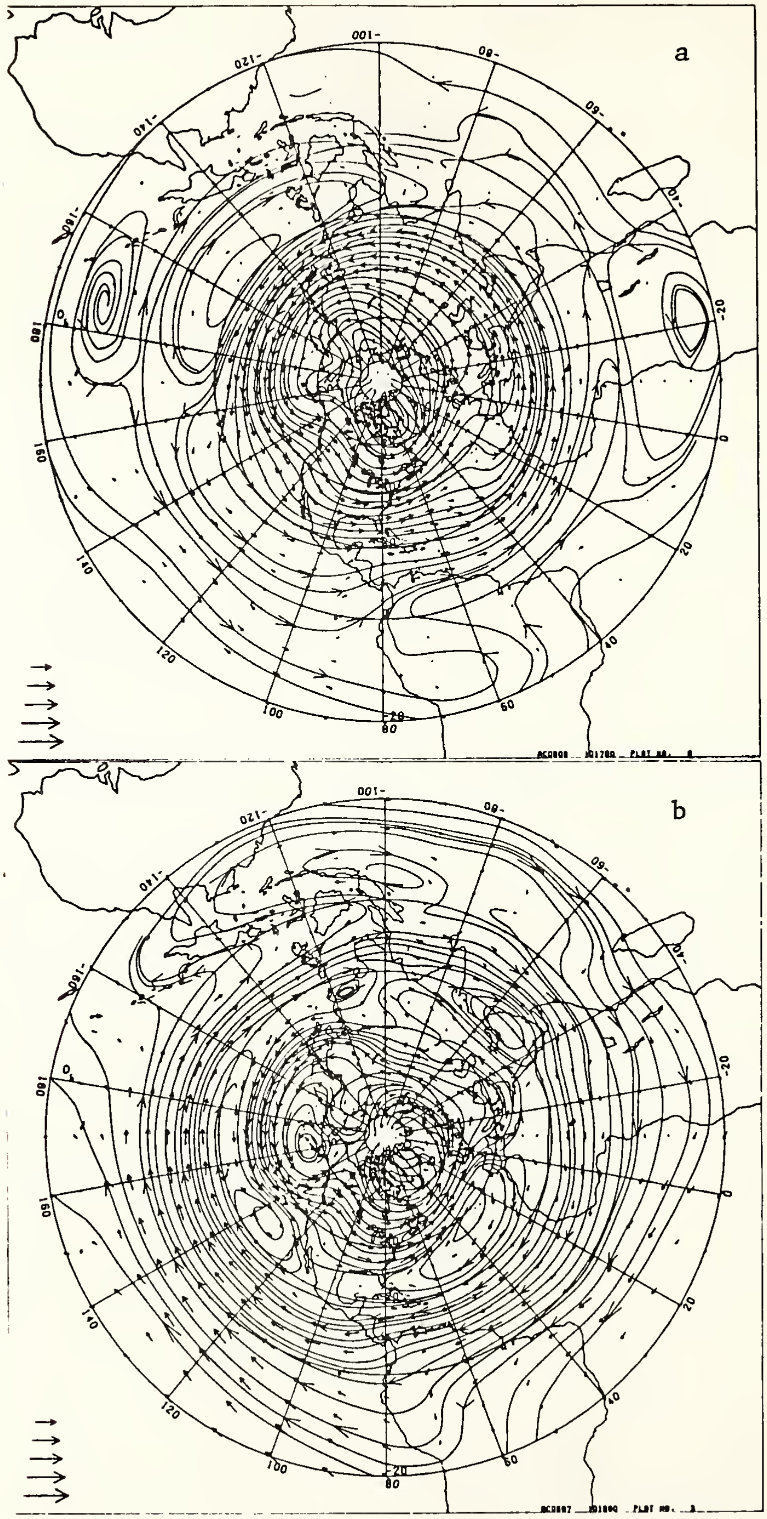

Figure 9. Streamline analysis of EPM3¯ (see text) at 250 mb (a) and 850 mb (b).

OROGRAPHIC INFLUENCE OF THE ROCKY MOUNTAINS ON THE WINTER CIRCULATION OVER THE CONTIGUOUS UNITED STATES

PART I: LARGE-SCALE ASPECTS

by

Steven W. Lyons and Takio Murakami

Department of Meteorology
University of Hawaii
Honolulu, Hawaii 96822

Abstract

The winter mean circulation over and around the North American continent, including the Rocky Mountains, was investigated by using twice-daily wind, temperature, and geopotential height data at eight standard pressure levels for the period of 1 December 1978 through 28 February 1979. Surface pressures, temperatures, and winds were estimated over a 2.5° latitude by 2.5° longitude resolution smoothed topography, as determined by Berkofsky and Bertoni (1955).

Winter mean surface winds near 45°N, 120°W tend to split into northward and southward currents which flow around the high American Rocky Mountains (refer to Fig. 1, bottom). However, a significant part of these low-level winds also flow over the highest mountains and surrounding lower topographies. Boundary layer frictional effects, which result in significantly reduced wind speeds, extend upward through the 700-mb level over a limited area of the highest American Rockies (Fig. 1, top).

At 300 mb, a strong jet stream south of the American Rockies at approximately 28°N is characterized by pronounced eastward acceleration, which is primarily associated with winter mean, nongeostrophic southerly winds (Fig. 2, top). Conversely, momentum flux convergence due to transient disturbances (Fig. 3, top) is the major factor in maintaining a less pronounced-300 mb polar

jet stream near 50°N and 120°W, which is associated with northerly winds and slight eastward acceleration.

A pronounced thermally direct (indirect) vertical circulation occurs south (north) of 30°N along the west coast of the U.S. (Fig. 4). Topographic enhancement of the descending branch of the direct Hadley cell is evident over the southeastern corner of the American Rockies (35°N, 105°W). Off the east coast of the U.S. at around 60°W, indirect (direct) vertical circulations are found to the north (south) of the jet stream axis (38°N), but are only weakly defined as compared to the vigorous overturnings along the U.S. west coast.

At 700 mb, winter mean temperatures are colder over the American Rockies than over the surrounding areas to the east and west (Fig. 5, top). From the surface through 500 mb, significant northward sensible heat fluxes due to transient eddies are observed over the following three regions: (1) from the Gulf of Alaska to northern Alaska; (2) from the warm northeast Pacific, over the American Rockies, into the central northern U.S. and Canada; and (3) from the Gulf of Mexico coast into the northeastern U.S. (refer to Fig. 5, top).

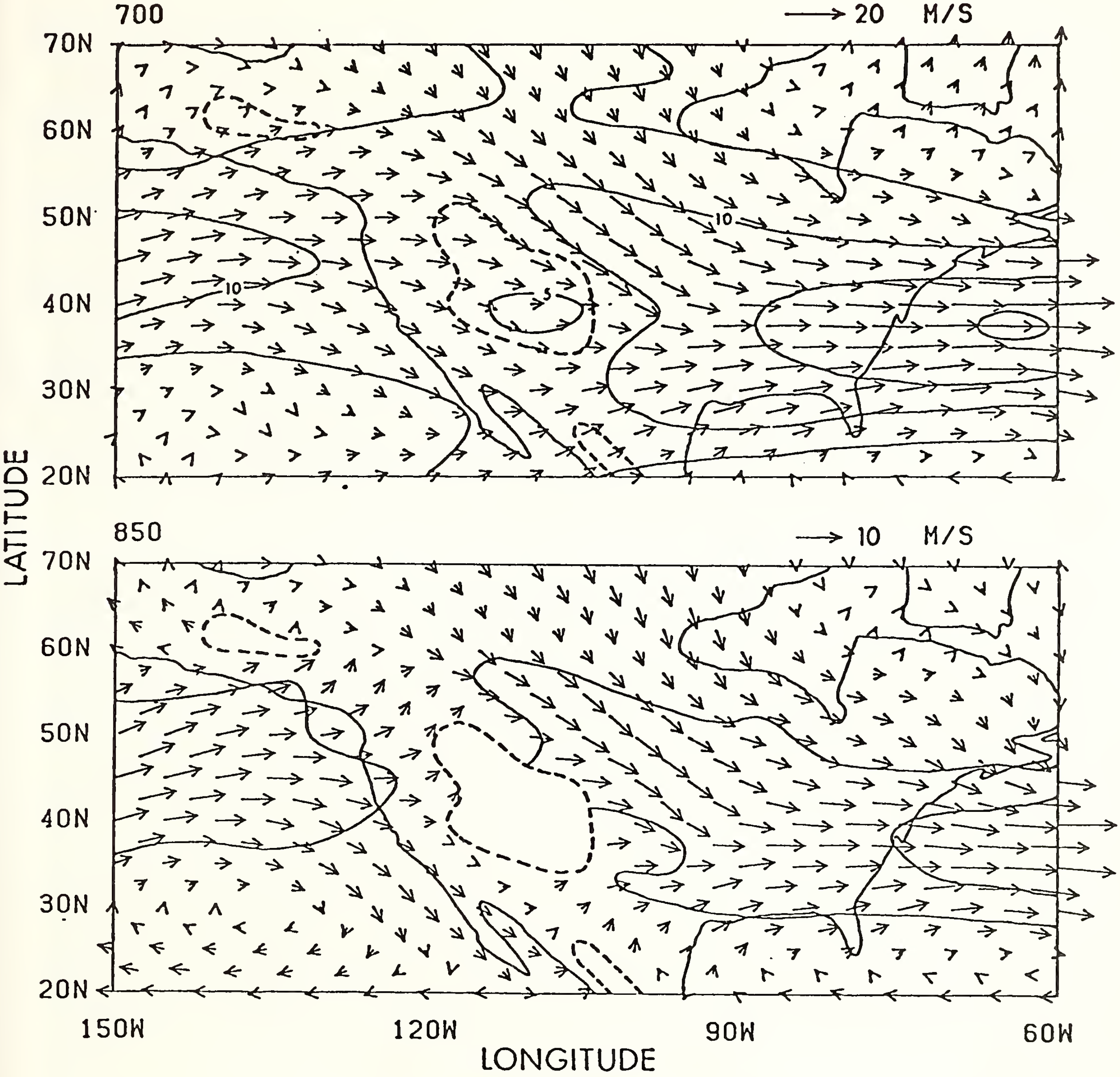

Figure 1. Winter mean wind vectors (arrows) at 700 mb (top; 20 m s^{-1} unit) and 850 mb (bottom; 10 m s^{-1} unit). Isotachs (solid lines) are shown at 5 m s^{-1} intervals. Dashed lines are 1500 m smoothed topographic height contours.

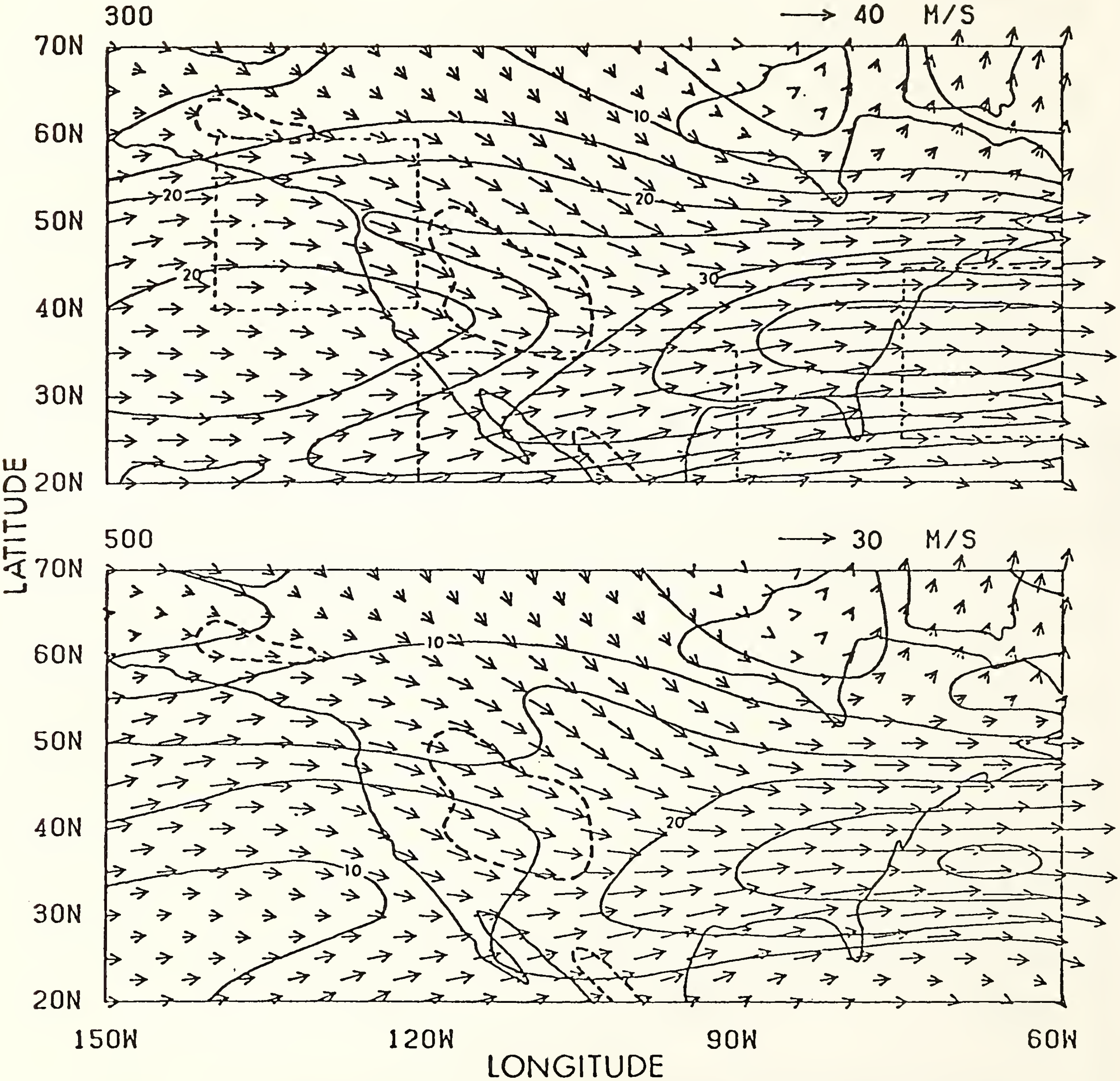

Figure 2. As in Fig. 1, except for 300 mb (top; 40 m s^{-1} unit) and 500 mb (bottom; 30 m s^{-1} unit).

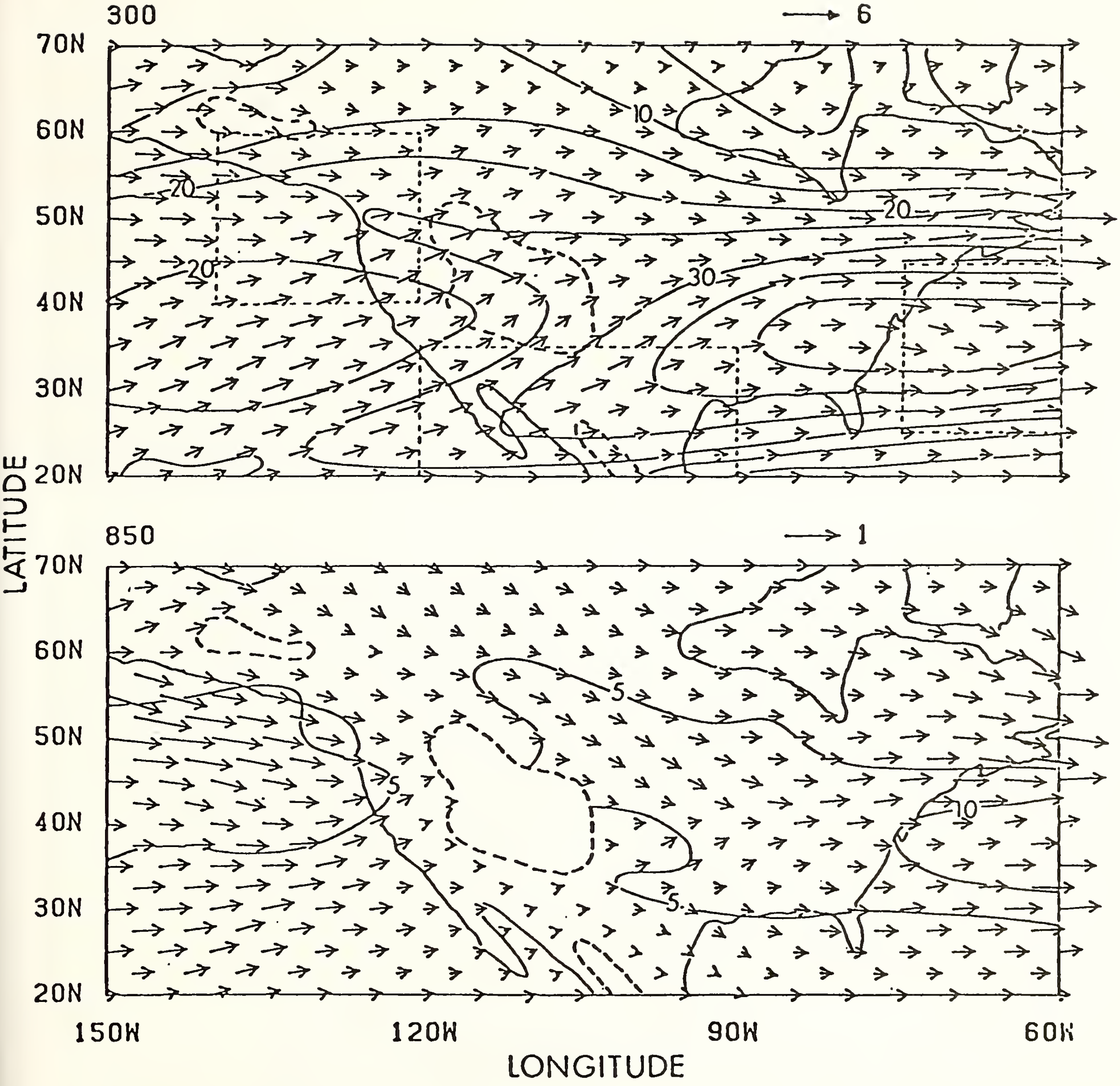

Figure 3. Winter mean momentum flux vectors of $\overline{u'u'}$ and $\overline{u'v'}$ (arrows) due to transient disturbances at 300 mb (top; 600 m^2 s^{-2} unit) and 850 mb (bottom; 100 m^2 s^{-2} unit). Isotachs (solid lines) for winter mean winds are drawn at 5 m s^{-1} intervals.

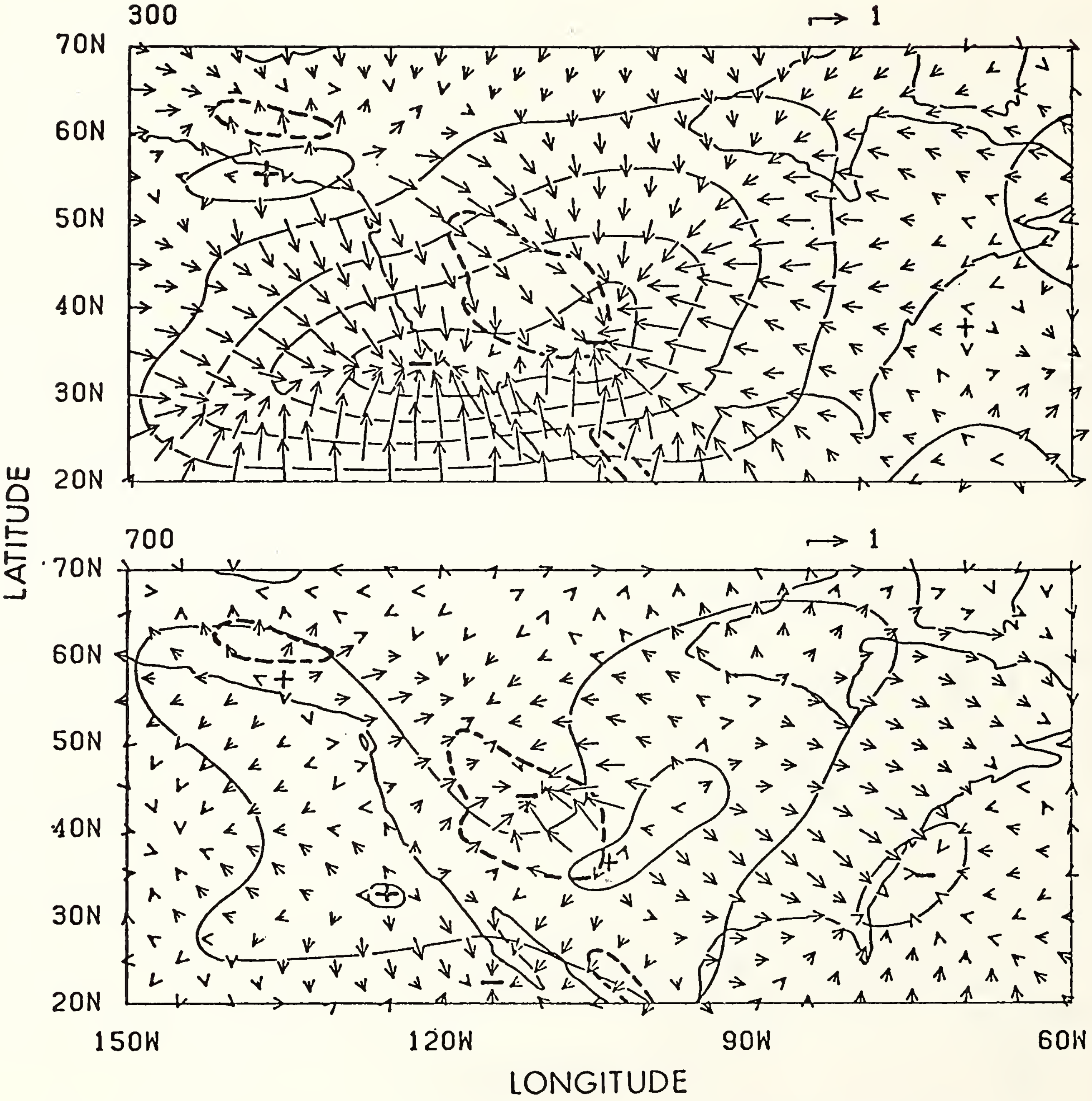

Figure 4. Winter mean divergent wind vectors (arrows; 1 m s^{-1} unit) and velocity potential fields (solid lines; 4 x 10^5 m^2 s^{-1} intervals) at 300 mb (top) and 700 mb (bottom).

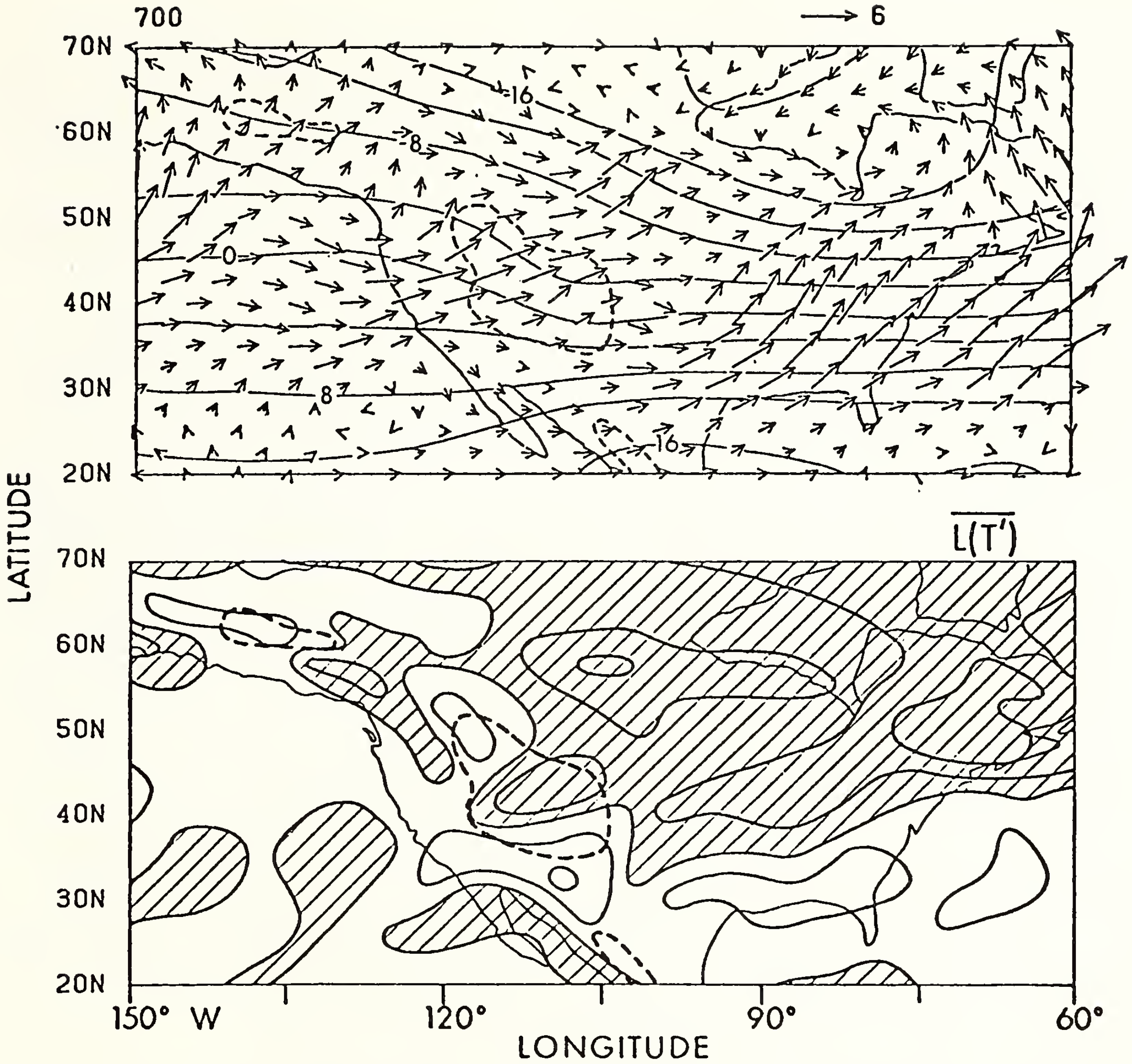

Figure 5. Top: Winter mean $(\overline{u'T'}, \overline{v'T'})$-vector fluxes (arrows; 60 °C m s^{-1} unit) due to transient eddies, and winter mean temperatures (solid lines; 4 °C intervals) at 700 mb. Bottom: Heat flux divergence and/or convergence due to transient eddies at 700 mb. Intervals are 2 x 10^{-5} °C s^{-1}. Hatching indicates areas of flux convergence.

INTERANNUAL VARIABILITY OF VACILLATING PLANETARY-SCALE WAVES

James P. McGuirk
Meteorology Department
Texas A&M University
College Station, TX 77843

Calculations of the so-called Lorenz energy cycle have been performed for a daily basis for 14 years of data (Fall 1963 through Spring 1977) using the NMC-gridded height and temperature fields from the surface to 100 mb. Fig. 1(a) and (b) show the series of January averages of the four energy modes. Although these series indicate a substantial interannual variability, they are not necessarily good representations of entire winter seasons. For example, the two dots on fig. 1(a) occurred during intense stratospheric sudden warming periods--January 15 to February 15, 1971, and January 1977, and thus are more representative of those specific events and not of the whole winter season. Daily time series (figs. 2 and 3) or spectra of many seasons of data (fig. 4) indicate a strong, highly significant (in excess of 99.9% probability of non-random occurrence) oscillation between the zonal modes and the eddy modes.

Table 1 summarizes the statistics of the oscillation for zonal available potential energy for the 14 cold seasons (the oscillation, termed vacillation, disappears during the summer months). In a typical cold season, nine oscillations are observed with a mean periodicity of 24 days and a peak-to-peak amplitude, varying between 2 and 5 x 10^5 J/m^2. Maximum random short-term fluctuations in zonal available potential energy seldom exceed 10 x 10^5 J/m^2.

Bandpass-filtered series of the energy modes for several years (figs. 5 and 6) illustrate key features of vacillation:

1. The almost uninterrupted persistence in amplitude and period during the entire cold season.
2. The almost exact out-of-phase relationship between zonal available potential energy and the eddy energy modes.
3. The disappearance of the oscillation in summer.
4. The breaks in the oscillation of zonal kinetic energy.
5. The breaks in the available potential energy cycle in the anomalous winter 1976-1977 (intermittancies of this sort are not observed in any of the other 13 years).

Because of the oscillation between zonal and eddy modes, the vacillation has been equated to a zonal index cycle. Whereas the vacillation contributes to zonal index variations, other processes do also (such as the January-February sudden warming--fig. 2); therefore, the vacillation is not synonymous with the zonal index cycle. On the other hand, when differences in jetstream level winds are formed between individual maximum and minimum periods of eddy amplitude associated with vacillation, a statistically significant variation in westerly geostrophic wind speed is detected between 50 and 60°N (fig. 7).

The vacillation is dominated by planetary-scale wave oscillations, primarily zonal wave numbers 2 and 3. Fig. 8 shows a decomposition of the total eddy available potential energy into zonal wave number components one through four for the 1970-71 cold season. The vacillation in this year was dominated by a very steady planetary wave number 2 oscillation which actually exceeded the total eddy oscillation during December and January. During this season the wave number 3 oscillation was large and persistent as well.

Fourier-analyzed wave number 2 data for the 500-mb height field are presented in fig. 9 for two successive eddy minima and maxima. Variations in wave amplitude between about 100 m (at eddy minima) and 250 m (at eddy maxima) are typical and result in a meridional geostrophic velocity fluctuation of about 10 m/sec at 500 mb. It is observed that the meridional mode of the wave (the number of positive and negative height peaks at a fixed longitude) is not constant for either eddy maxima or eddy minima. Comparisons of Fourier-analyzed heights at 500 mb and at 700 mb at latitude 55°N show that the planetary wave number 2 at 500 mb lags the same wave at 700 mb by about 7° of longitude. However, although the mean wave is observed to tilt westward with height, the tilt fluctuates periodically with an amplitude of ± 6° in phase with the vacillation (fig. 10) and the wave is occasionally observed to tilt to the east. When the wave amplitude is largest, the tilt is smallest (most barotropic) and when the amplitude is smallest the wave tilt is greatest (most baroclinic). The wave tilt through geostrophic theory can be interpreted as an efficiency factor for the northward transport of sensible heat.

If one compares the observed data with pre-existing theories of vacillation, one observes that Pedlosky's weakly nonlinear, baroclinically unstable, single-wave model is the most consistent.

TABLE 1.

AVERAGE WINTERTIME BEHAVIOR OF VACILLATION IN ZONAL AVAILABLE POTENTIAL ENERGY

YEAR	NO. OF PERIODS	START* DATE	END* DATE	MEAN PERIOD (DAYS)	STANDARD DEVIATION (DAYS)	MEAN AMPLITUDE ($10^5 j/m^2$)	STANDARD DEVIATION ($10^5 j/m^2$)
1963-64	7	NOV 19	APR 23	24	3.5	1.8	.7
1964-65	7.5	SEPT 26	MAR 14	24	3	1.6	.5
1965-66	6.5	NOV 4	MAR 23	23	1.5	2.0	.6
1966-67	8	OCT 25	APR 6	22	3.3	1.7	.7
1967-68	7	DEC 26	JUN 23	27.5	4.5	1.8	1.0
1968-69	12	SEPT 10	JUN 20	24.5	3	1.9	.8
1969-70	12	AUG 26	MAY 21	23	4	1.0	.4
1970-71	9	AUG 20	MAR 15	24	2	2.5	.7
1971-72	10	OCT 25	MAY 12	21	4.5	1.6	.8
1972-73	9.5+			25.6	2.5	1.4	
1973-74	10			22	4	1.5	
1974-75	9			22.3	3.1	2.1	
1975-76	6			24.7	5.1	2.0	
1976-77	9.5+			22.5	5.7	1.2	

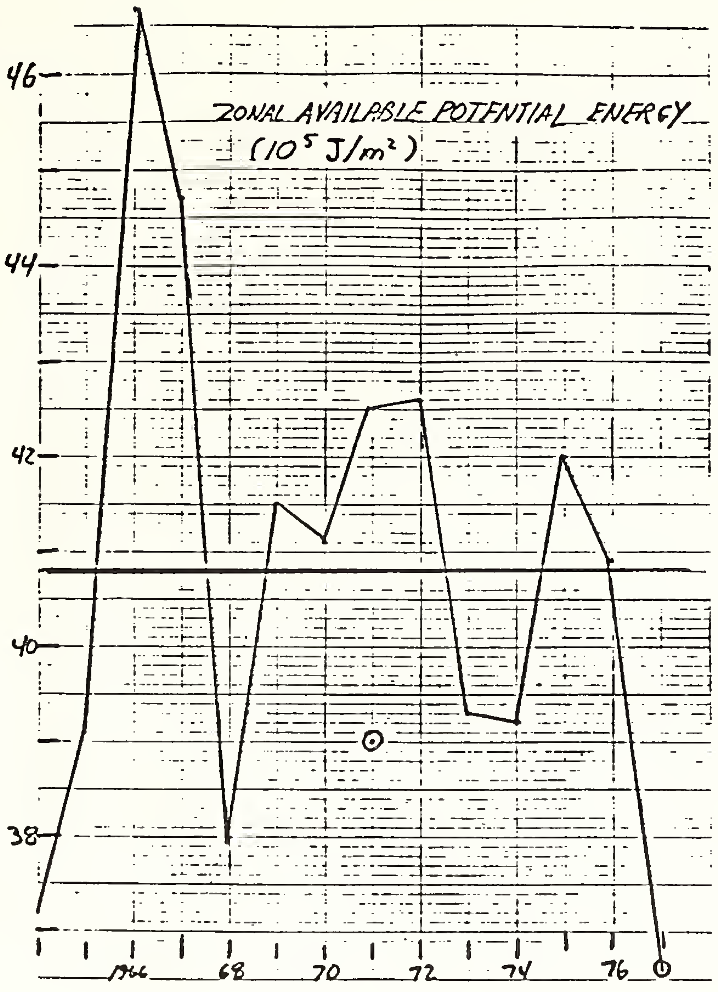

Fig. 1 (a) January averages of zonal available potential energy (1000-100 mb and north of 20°N). The two circles refer to periods of intense stratospheric sudden warming, the first one being an average from 15 January - 15 February. (Units in 10^5 J/m^2)

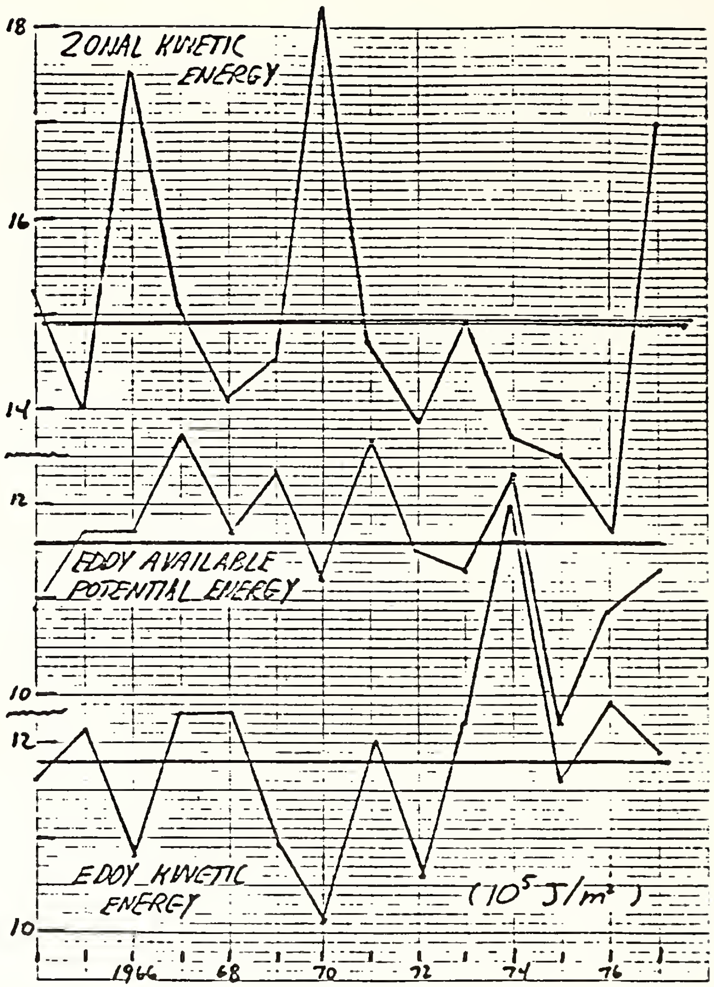

Fig. 1 (b) Same as Fig. 1 (a) except for zonal kinetic energy, eddy available potential energy and eddy kinetic energy.

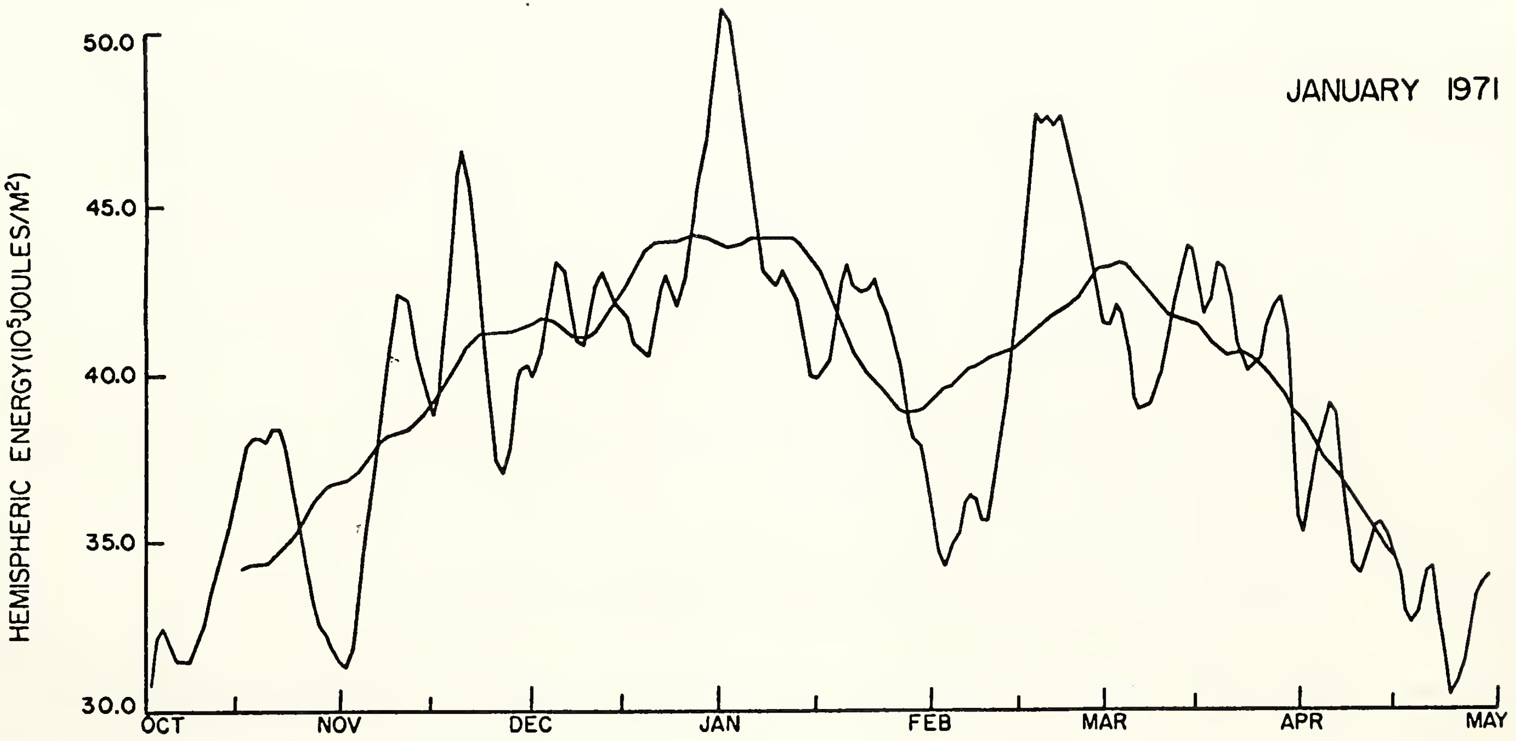

Fig. 2 Thirty-one day running mean (smooth curve) and 3-day running mean of zonal available potential energy for the 1970-71 cold season. Both vacillation peaks and stratospheric sudden warming signature are apparent in this figure.

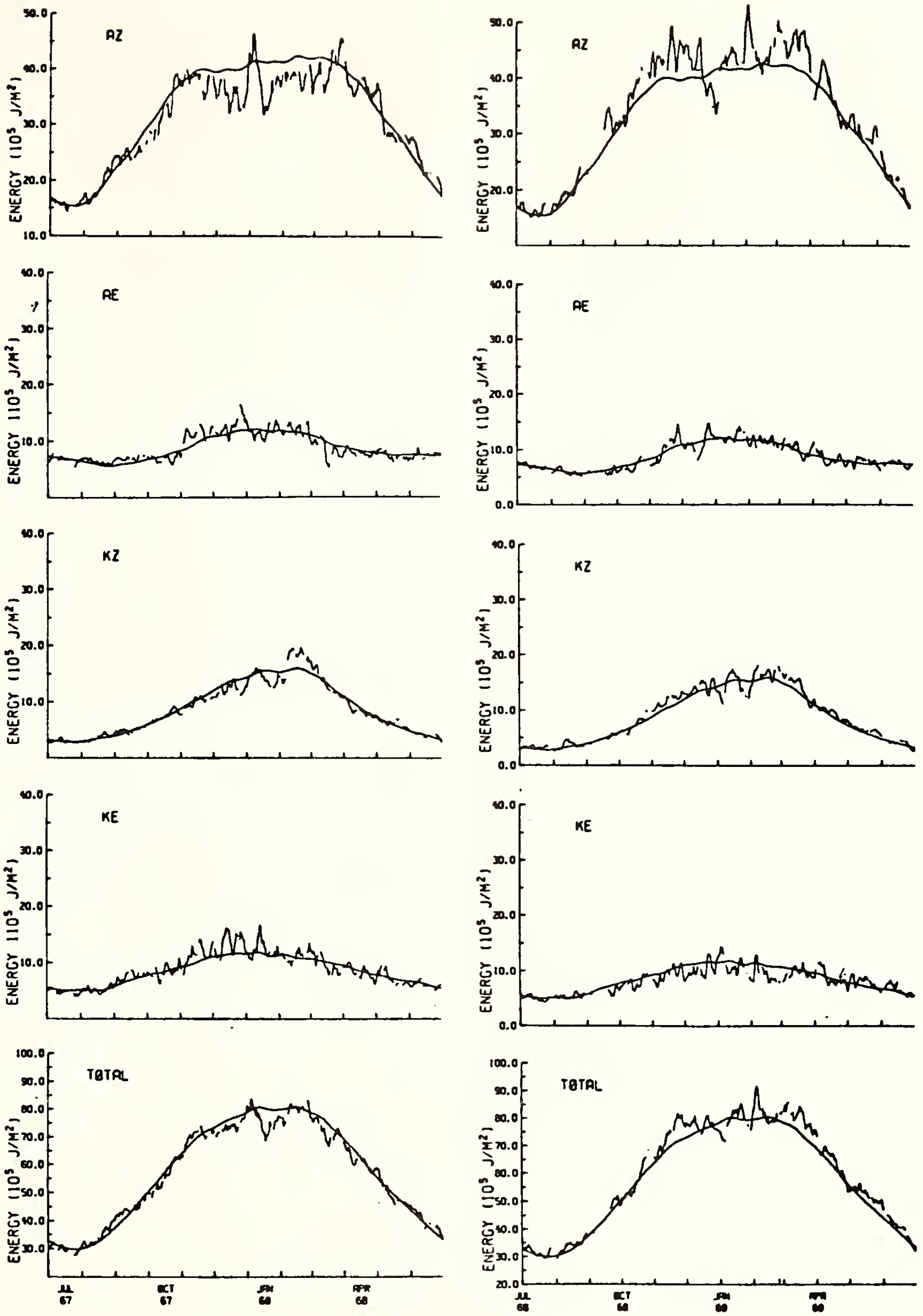

Fig. 3 Daily zonal and eddy available potential and kinetic energies and summation of all four modes for 1967-68 (left) and 1968-69 (right). Smoothe line gives binomially-smoothed nine-year average. Both short term and interannual variability are apparent.

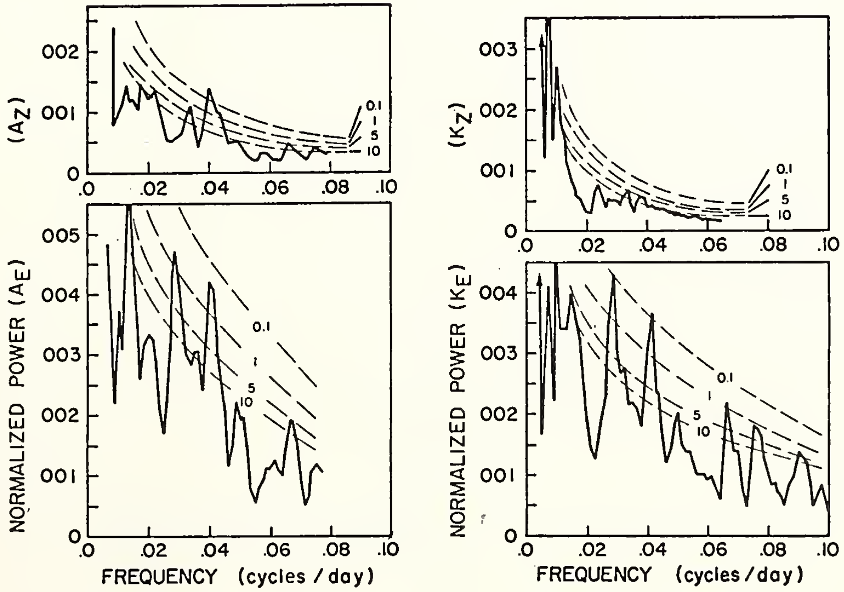

Fig. 4 Spectral estimates of nine years of daily energy data, by mode. Dashed lines give chi-squared confidence limit for an assumed red-noise spectrum. Significant peaks at about 0.04 cycles/day are evident. The spectra include summer seasons and, thus, underestimate the strength of vacillation.

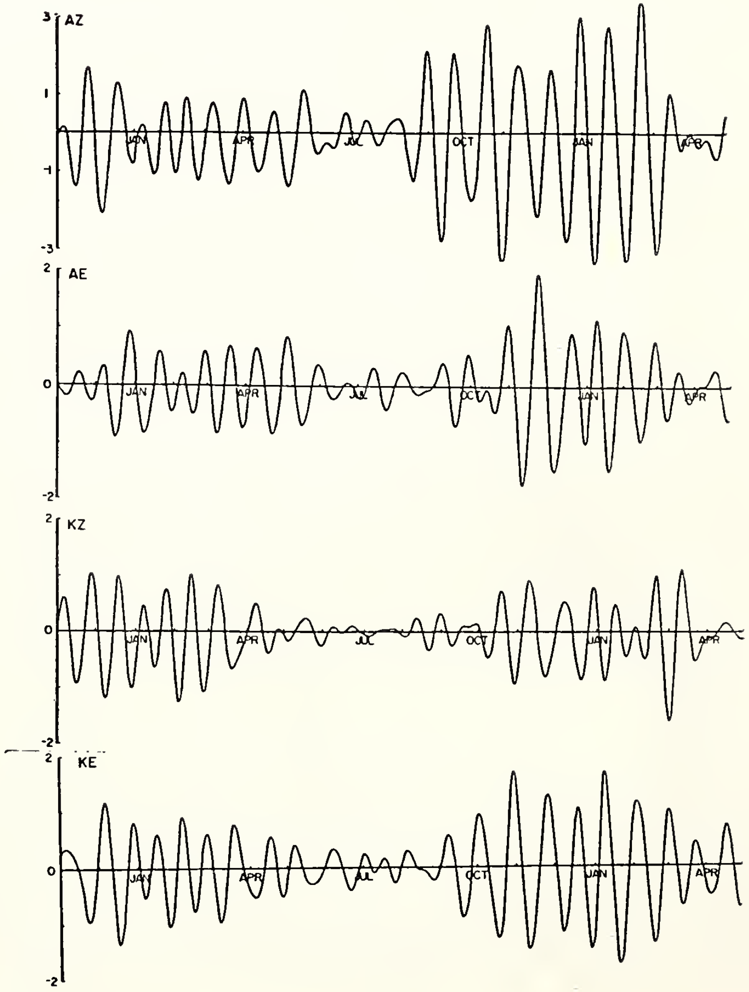

Fig. 5 Bandpass-filtered energy mode data for two winter seasons (October 1969 - April 1971). The filter is centered on a periodicity of 22 days. (Units in 10 J/m.)

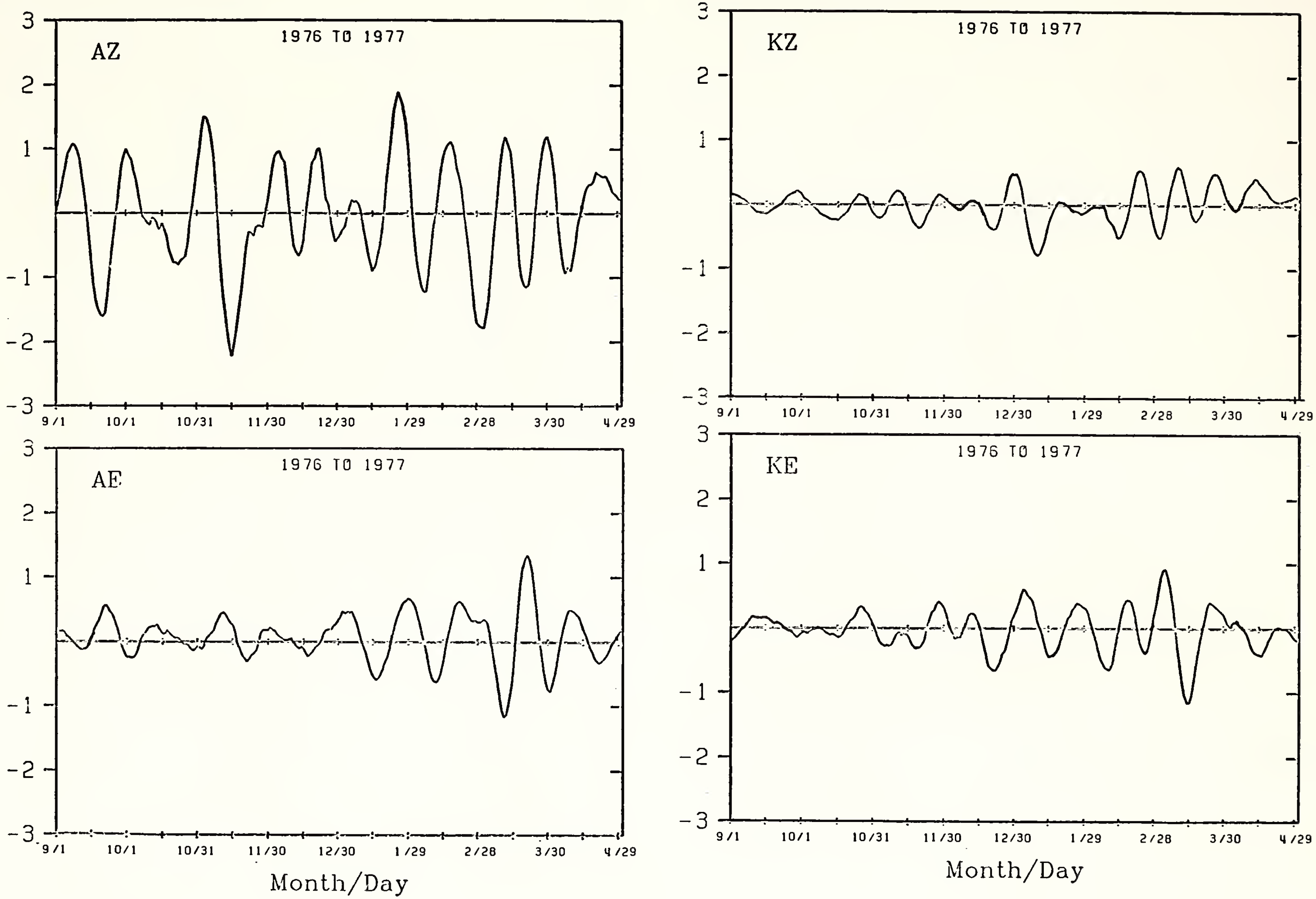

Fig. 6 Same as Figure 5 except for the anomalous cold season 1976-77.

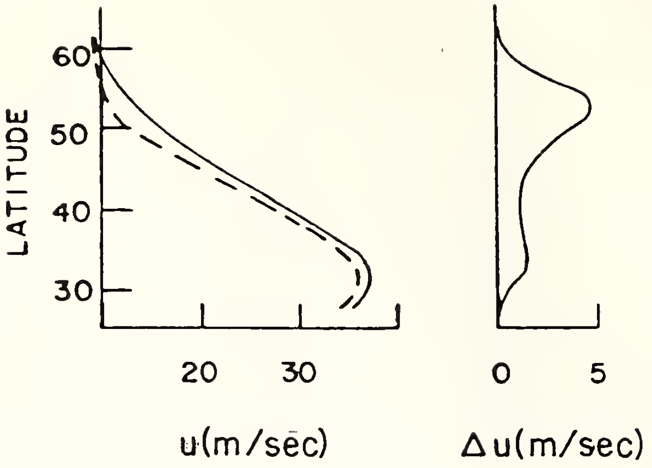

Fig. 7 Composite profiles (left) of the mean zonal geostrophic wind at 250 mb for two years of days of eddy energy minima (solid line) and eddy energy maxima (dashed line). The difference in the two profiles appears at the right. A t-test shows the peak wind difference to be non-random with a confidence exceeding 99%.

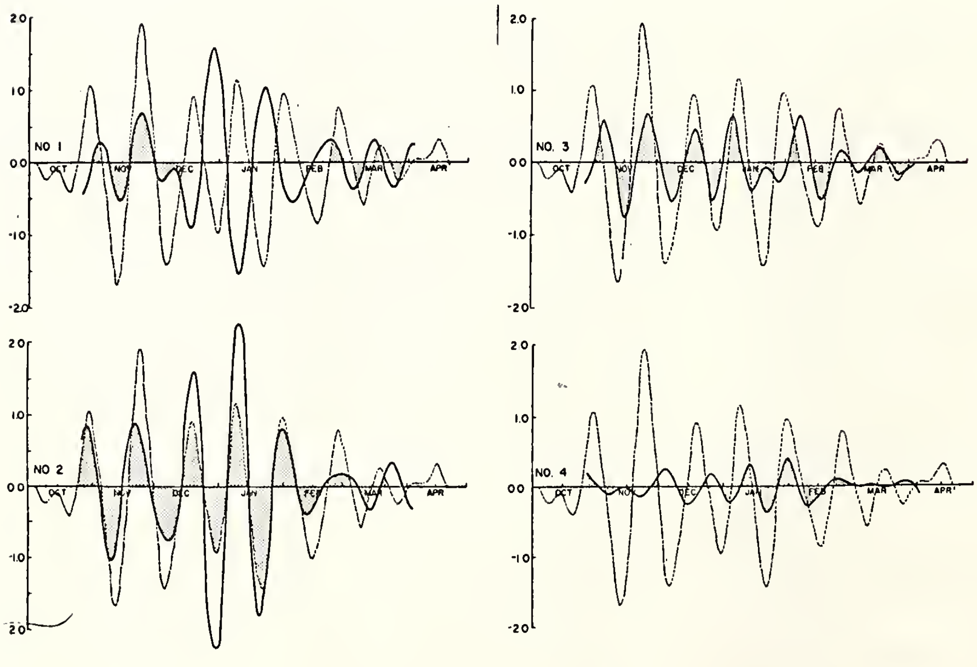

Fig. 8. Bandpass-filtered potential energy associated with zonal wave numbers one through four for the 1970-71 cold season (solid lines). Dashed lines show the filtered eddy available potential energy due to all waves for reference.

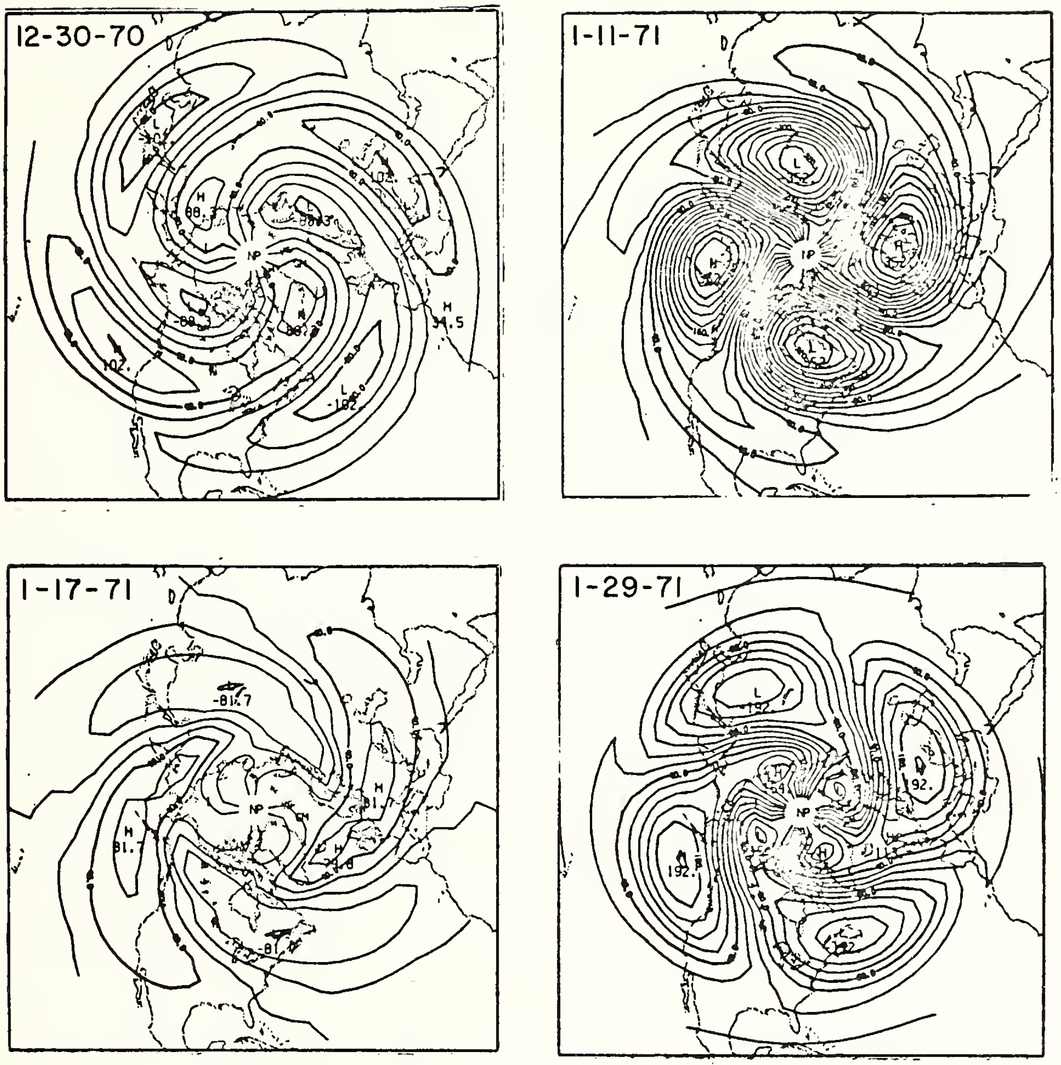

Fig. 9 500 mb height fields, Fourier-analyzed around latitude circles for wave number two. Two successive periods of maximum (right) and minimum (left) eddy amplitude are shown. (Contour interval = 40m.)

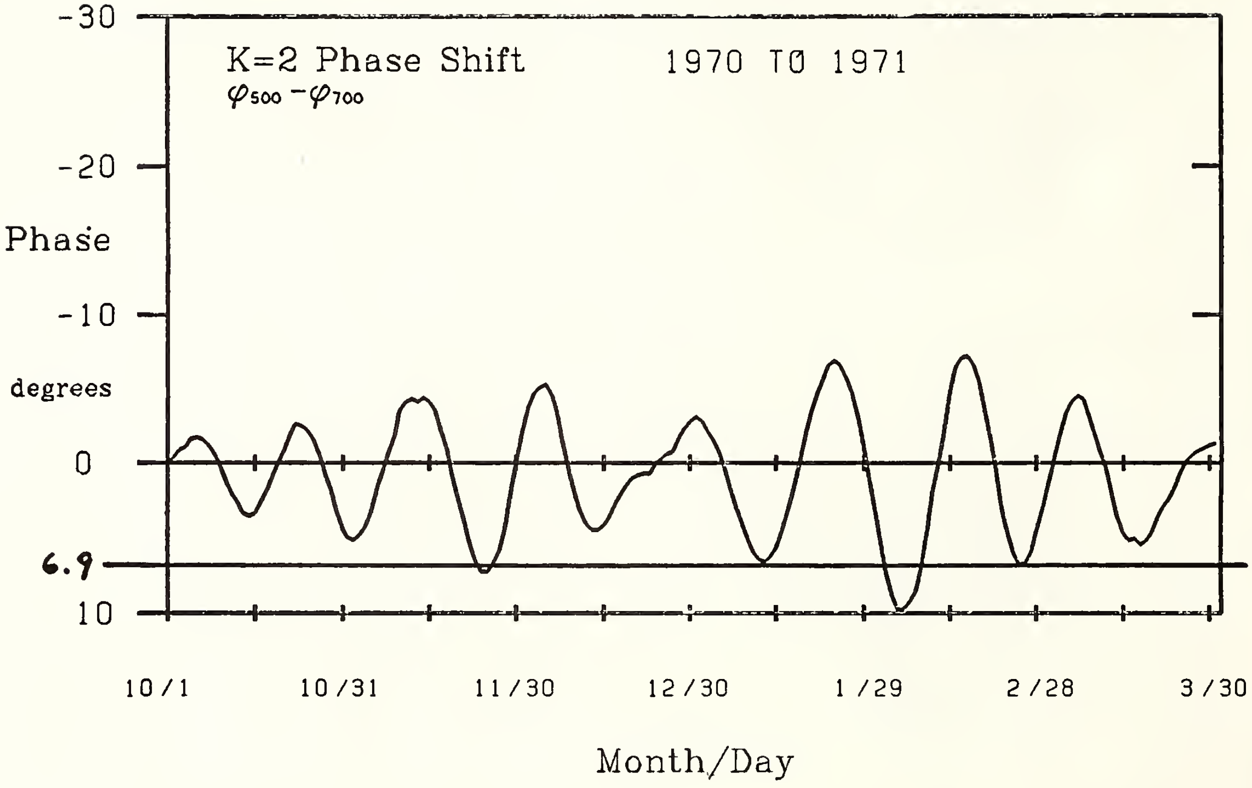

Fig. 10 Bandpass-filtered phase difference, in degrees longitude, between the 500 mb and 700 mb zonal wave number two height fields at 55°N. The heavy straight line gives the wintertime average phase lag of -6.9° of longitude.

INTERANNUAL CLIMATIC ANOMALIES: DO THEY PROPAGATE?

W. H. Quinn, S. K. Esbensen and D. B. Enfield
Oregon State University

In earlier work (presented at the Third Annual Climate Diagnostics Workshop, 1978) Dr. Kirby Hanson applied a low-pass filter to Northern Hemisphere monthly zonal averages of 700-mb height departures from normal (DN's) for the period 1965-70 and noted an apparent continuous phase propagation of positive and negative height anomalies from the subtropical to polar latitudes (Fig. 1). His analysis of regional distributions of 700-mb height DN's over this period indicated that three regions were contributing to the zonally averaged anomalies -- the Eastern Pacific, the Atlantic, and central Asia. Our interest has been to extend this study over a 33-year record of 700-mb data obtained from the NOAA/NWS Climate Analysis Center to determine whether or not similar anomaly patterns recur, and the cause for their development. Also, since the DN's appeared to originate in lower latitudes, there was an interest in determining whether or not they were related to the interannual changes found in the Equatorial Pacific. (The Northern Hemisphere 700-mb data does not extend south of 15°N latitude.)

The low-pass filtered DN time series for the extended period from January 1947 to January 1980 are shown in Fig. 2. Although a qualitative inspection reveals some tendency for poleward propagation in middle and high latitudes, the systematic propagation of the anomalies from tropical to subpolar latitudes which Hanson noted from 1965-70 is not a ubiquitous feature of the longer period. For example, during the period 1971-78 a standing oscillation appears to be a more appropriate interpretation, with the mid-latitudes (35-55°N) fluctuating out of phase with the subtropical (15-30°N) and high latitudes (60-70°N).

Fig. 3 compares the response of the 13-month running-mean filter used by Hanson with the four-pole tangent-Butterworth filter used to smooth the extended series. The tangent-Butterworth filter has a half-power point of 0.4 cycles per year (cpy) and effectively eliminates variability at frequencies of 1 cpy or more.

To quantitatively summarize the features of the DN time series in Fig. 2 we have analyzed the coherence and phase structure between the low-pass filtered DN's at the various latitudes. The spectral analyses were performed using the fast fourier transform method for the time period January 1951 - January 1980, on all series pairs from 15°N-80°N. The 349 monthly values in each series were interpolated to 512 (= 2^9) points and linearly detrended. The spectral estimates were band averaged to yield a bandwidth of 0.21 cpy and 12 degrees of freedom. The coherence-squared (henceforth γ^2) estimates in the 0.09-0.30 cpy (3.4-11.6 years) band were arranged in a matrix format and contoured to show the coherence pattern (Fig. 4.a). The diagonal line corresponds to γ^2=1.0 and zero separation (i.e., each zonal band with itself). The line of points parallel and adjacent to the diagonal is for station pairs separated by 5° of latitude, and so forth to the maximum separation of 65° at the lower left corner of the matrix. The shading indicates $\gamma^2 \geq 0.4$, which is significant between the 90% and 95% confidence level. It is clear that coherence is high ($\gamma^2 > 0.6$) at separations of 5°-15°. Then there is a trough of mostly insignificant coherence corresponding to separations of 10°-20°. A secondary maximum occurs for separations of 15°-45°. The coherence again becomes insignificant at larger separations until a third maximum of marginal significance is reached at the largest separations (60°-65°). This complex coherence structure runs contrary to what one would expect of a system dominated by simple, linear propagation.

The corresponding matrix of phase estimates (degrees) is shown in Fig. 4.b (estimates for which $\gamma^2 < 0.3$ are not given). Positive values indicate propagation in a poleward sense, and the corresponding phases in months can be approximated by assuming a nominal periodicity at mid-band of about 64 months (e.g., +30 degrees implies a poleward lag of about 5 months). The shaded areas indicate four groupings for which coherence is high and phase is relatively uniform:

Group 1 consists of latitude pairs close to the diagonal having high coherence ($\gamma^2 > 0.6$). The phases indicate poleward propagation with lags of 1-8 months for separations of 5°-15° of latitude.

Group 2 consists of tropical latitudes (20°-25°) lagging the opposite phase in temperate latitudes (45°-55°) by 2-5 months for separations of 20°-35° of latitude.

Group 3 consists of temperate latitudes (40°-55°) which predominantly lead the opposite phase in polar-subpolar latitudes (≥65°) by 4-6 months for separations of 15°-40°.

Group 4 consists of tropical (15°-20°) and polar (75°-80°) latitudes fluctuating approximately in phase for separations of 55°-65°.

Other phases between the "significant groups" are intermediate in value, spatially non-uniform and/or correspond to marginal values of γ^2.

Except for group 1 (small separations) there is not so much a suggestion of propagation as of zonal bands that tend to fluctuate in phase or in opposite phase with other bands, the phases being relatively separation independent within each group. This, combined with the non-monotonic decrease of coherence with increasing separation, leads us to disfavor a propagation hypothesis. It is interesting to note that the first mode of an empirical orthogonal function (EOF) analysis of the filtered data explains 75% of the total variance in the non-normalized time series, and puts tropical and polar latitudes in phase with each other and in opposite phase to temperate latitudes, in agreement with the cross spectral analysis and with the results of Van Loon (1980: in this volume). Note, however, that groups 2 and 3 involve phase shifts to either side of a perfect opposite-phase relationship, indicating that care must be taken in future analyses of the data.

Hanson's regional analysis of low-pass filtered gridpoint data indicated that the apparent poleward movement of the anomalies in the zonally averaged fields results from the poleward movement of three separate anomaly centers -- one in the Eastern Pacific, one in the Atlantic and one over Asia -- each having somewhat similar poleward movements over a three and a half year period. Our analysis generally supports Hanson's analysis as far as which regions have the most intense anomaly activity. However, our preliminary analysis suggests that the apparent propagation is a result of the intensification of regional anomalies which are part of large-amplitude standing oscillations (or teleconnections). One of these teleconnection patterns is related to the Southern Oscillation and has a large center of action over the Northeast Pacific. As seen in Figs. 5.a and 5.b, when heights are abnormally high over the middle-latitude northeastern Pacific, the heights have a tendency to be high over middle-latitude zones in the eastern United States, the Atlantic, Europe, and western Asia. At the same time, the heights at high latitudes and low latitudes tend to be abnormally low. The patterns in Figs. 5.a and 5.b are reversed when the middle-latitude eastern Pacific heights are abnormally low. It is our interpretation that the variability in the position, timing, and strength of the anomalies contributing to these regional correlation patterns, sometimes gives the appearance of propagation from one center of action to another as the phase of these standing oscillations reverses.

In Fig. 2 from 1965 on (when the lower latitude data, 15°-30°N, were more reliable) a close correspondence is noted between the tropical and subtropical zonal 700-mb height DN peaks and troughs and the El Niño and anti-El Niño type troughs and peaks respectively in the Southern Oscillation index anomalies. Although periodicities between comparable features are the same, there usually appears to be a substantial lead on the part of the index changes. However, sea surface temperature and rainfall anomaly peaks and troughs for central and western equatorial Pacific sites, which have also been noted to lag several months behind associated index features, seem to occur nearer the time of the zonal 700-mb height DN peaks and troughs in the 15°-30°N latitude band. This indication, that these 700-mb height DN's are associated with changes occurring in the equatorial Pacific, caused us to look in detail at equatorial and near-equatorial upper air data over the central and western Pacific where the anomalous changes are very large.

The only equatorial Pacific data record suitable for studying changes in the overlying troposphere in relation to sea surface temperature (SST) was that for Canton Island (2° 46'S, 171° 43'W). Canton had an 18-year record for SST, surface weather observations and upper air data (1950-1967). Since there appeared to be inconsistencies between computations of 1000-mb heights for earlier years (1949-57) as compared to later years (1958-67), and also since heights of higher pressure levels are obtained by adding successive increments from below, it appeared best to use thicknesses between pressure levels rather than heights of the pressure surfaces to represent atmospheric changes. Data taken at 03Z and 00Z showed consistently greater thicknesses between levels than data taken at 15Z and 12Z (Table 1). The average overall diurnal variation in this case is 31.8 m. One can be misled when using upper air data from "Monthly Climatic Data for the World," if the diurnal shift isn't taken into account, for periods when published data times were shifted from 00Z (or 03Z) to 12Z (or 15Z).

Fig. 6 shows separate plots of 850-1000 mb thickness data for the two time periods in relation to SST data for Canton. Using the average monthly values, no lag is noted between SST changes and the low level thickness changes; and, for both cases correlation coefficients exceeded 0.8. Fig. 7 shows plots of the low-pass filtered Rapa-Darwin sea level pressure index anomalies, Canton I. SST anomalies, Canton I. 850-1000 mb thickness anomalies, and Canton I. 200-500 mb thickness anomalies. The index changes show in general a lead of several months over all other variables. Table 2 shows the lead/lag relationships between variables and indicates that the thermal changes are initiated at the surface and penetrate upward with time. Similar tropospheric changes were noted in the upper level data for other low latitude sites. Fig. 8 shows plots of the low-pass filtered Majuro Island (07° 05'N, 171° 23'E) 200-850 mb thickness anomalies and the Easter-Darwin sea level pressure index anomalies. Although there is only a short period of overlap between Canton I. and Majuro I. data, conformance in thickness fluctuations was noted; and, by reference to the Southern Oscillation indices this conformance record can be extended over a 30-year period. In each case the index changes precede the thickness changes by several months (Tables 2 and 3).

In the Southern Hemisphere we have been concerned with the El Niño/anti-El Niño type climatic changes taking place along the west coast of South America. Fig. 9 and Table 4 show the time relation between SST changes at the central equatorial Pacific locations (Canton I., Christmas I.) and sites along the coast of Peru (Talara, Puerto Chicama, and Don Martin I./La Punta). This three to five month lag of equatorial Pacific changes behind the coastal Peruvian changes is similar to the lag of the Darwin component changes behind those of the subtropical high components of the Southern Oscillation indices. In other words, what happens in the eastern South Pacific ties in closely with the changes occuring in the South Pacific subtropical high; whereas, what happens in the central and western equatorial Pacific ties in closely with changes in location and intensity of the Indonesian equatorial low.

Our report at the 1979 Climate Diagnostics Workshop indicates a close relation between El Niño/anti-El Niño type situations and the coastal sea and weather conditions of tropical and subtropical Chile. Table 5 indicates that Chilean rainfall categories and rainfall amounts at Santiago and Valparaiso also relate reasonably well to these El Niño/anti-El Niño type conditions. All 13 of the wet (P) and very wet (TP) years between 1875 and 1930 coincided with years when significant El Niño events were setting in or occurring. Although there were four cases where El Niño occurred without an accompanying classification of wet (P) or very wet (TP) conditions, in two of these cases (1884 and 1930) there were relatively large rainfall amounts at Santiago and/or Valparaiso. Fig. 10 shows a plot of the low-pass filtered 200-850 mb thickness anomalies for a recent record of Antofagasta data. Here again we note the El Niño/anti-El Niño type changes in thickness and a lag behind the Easter-Darwin index anomalies similar to what we found at Majuro.

Based on our investigation up to this point, it appears that the features in the zonally averaged 700-mb height DN's are due primarily to standing oscillations in geographical regions which are limited in longitude as well as latitude. We have found that the 700-mb zonal height DN's from 15°N to 30°N are clearly related to the El Niño/anti-El Niño type fluctuations noted in the Southern Oscillation indices and to other atmospheric variables throughout the tropical and subtropical troposphere of the Pacific region. We conclude that understanding of the low-level zonally averaged features on interannual time scales will most likely be obtained from a detailed examination of the structure and evolution of regional features and teleconnections.

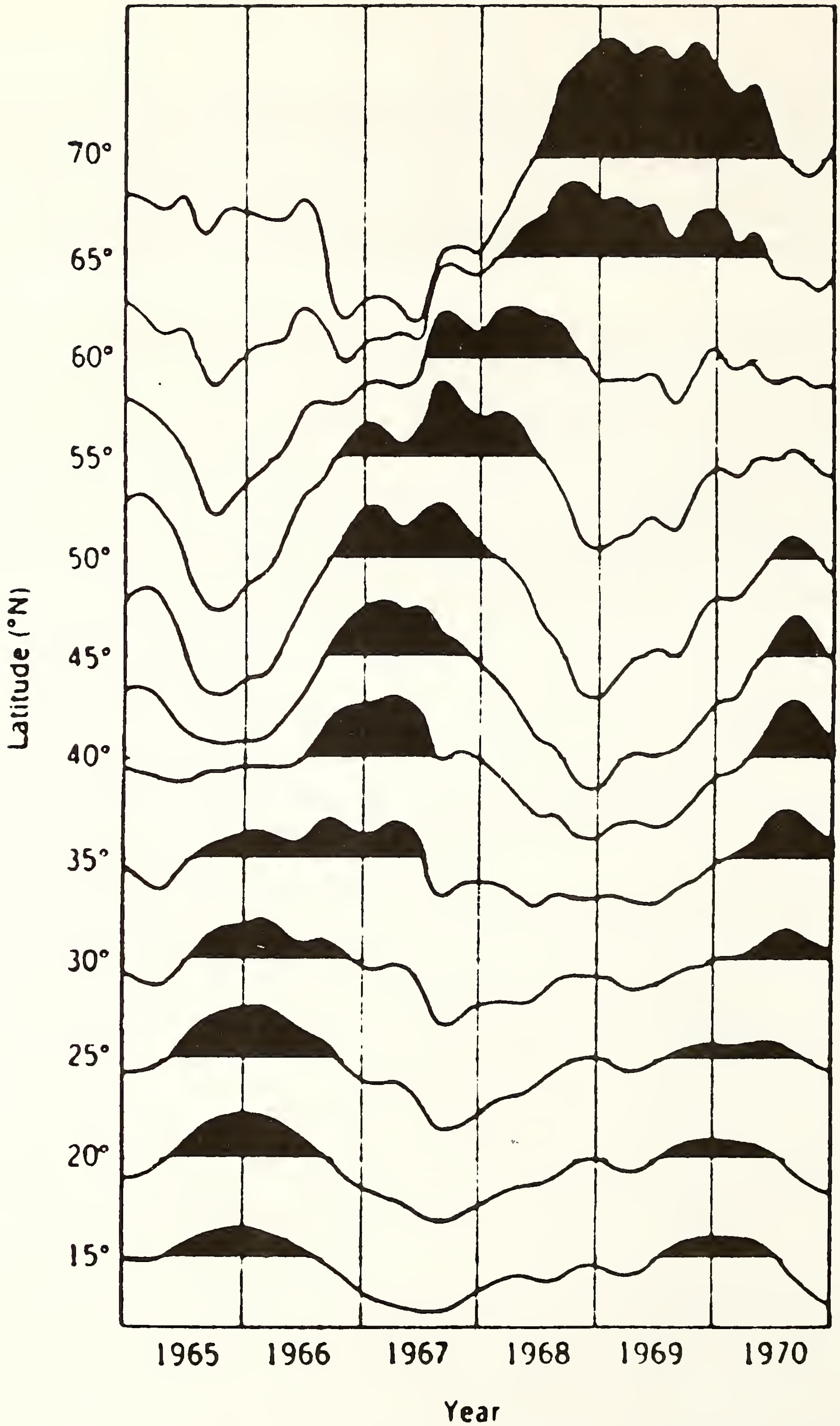

Fig. 1. Time variation of low-pass filtered, zonally averaged 700 mb geopotential height anomalies (from Hanson, 1978). The filter used is a 13-month running mean (see Fig. 3).

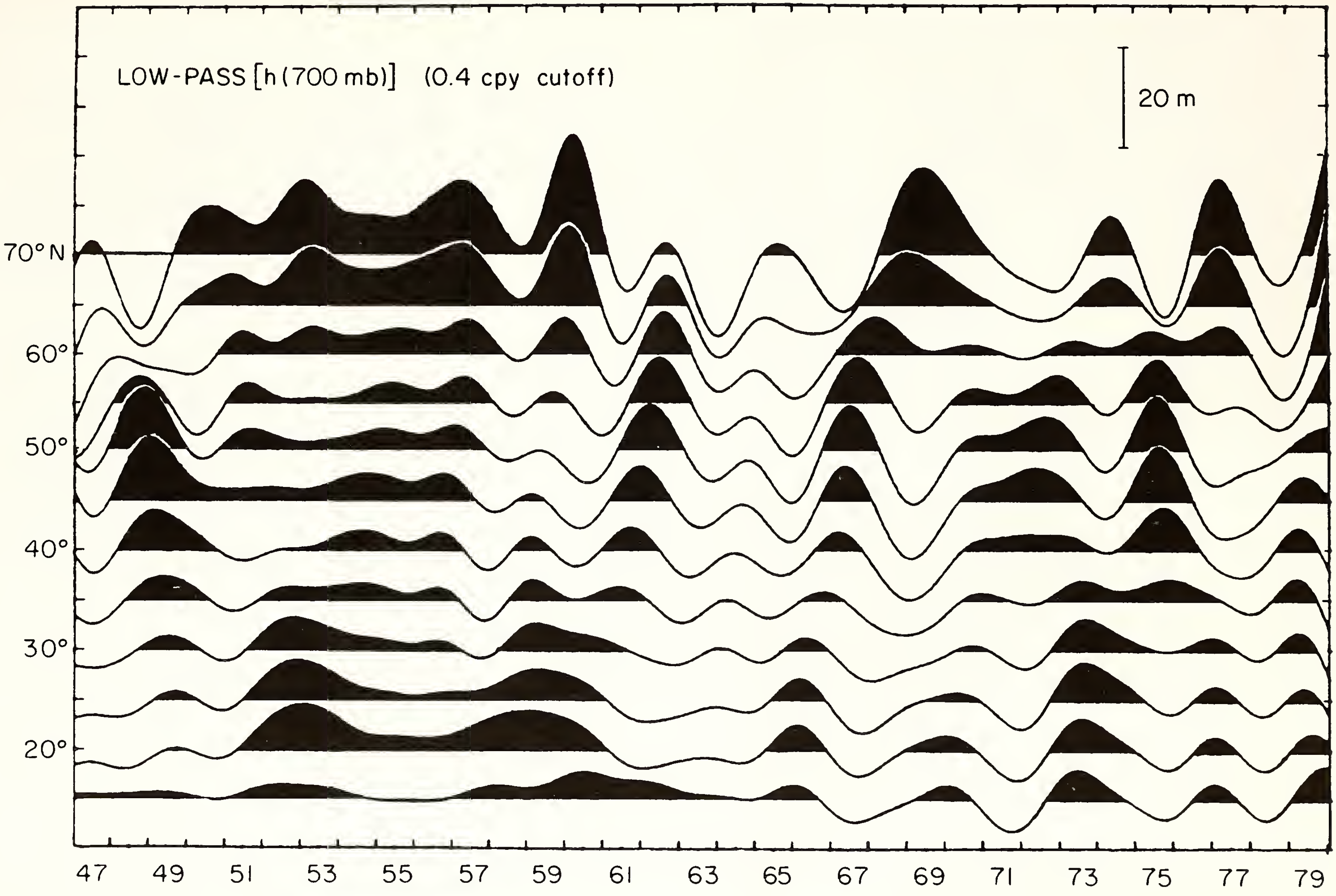

Fig. 2. Time variation of low-pass filtered, zonally averaged 700 mb geopotential height anomalies. The filter used is a four-pole, tangent-Butterworth filter (see Fig. 3).

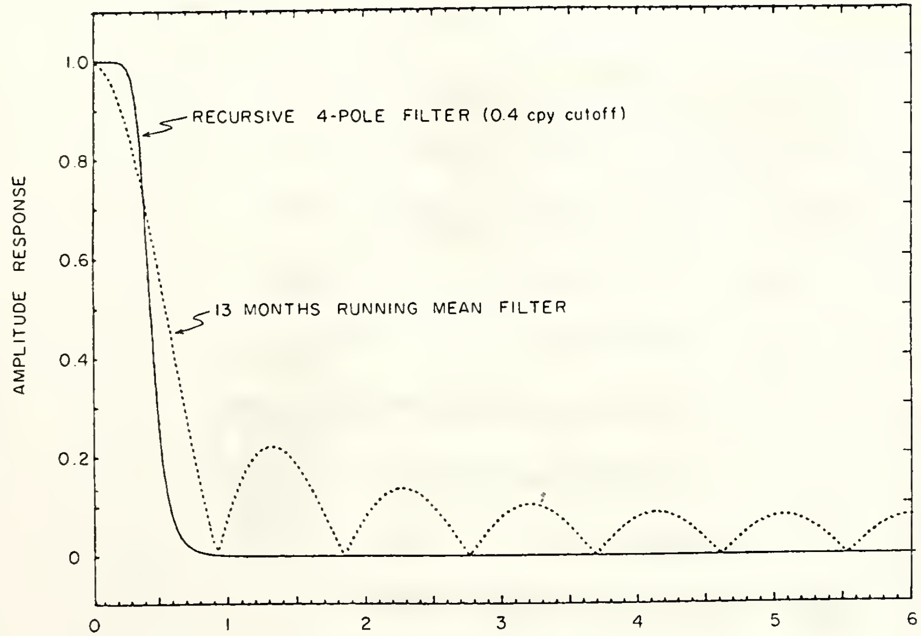

Fig. 3. Amplitude response functions of the four-pole, tangent-Butterworth and 13-month running-mean low-pass filters. The half-power point of the tangent-Butterworth filter is 0.4 cycles per year.

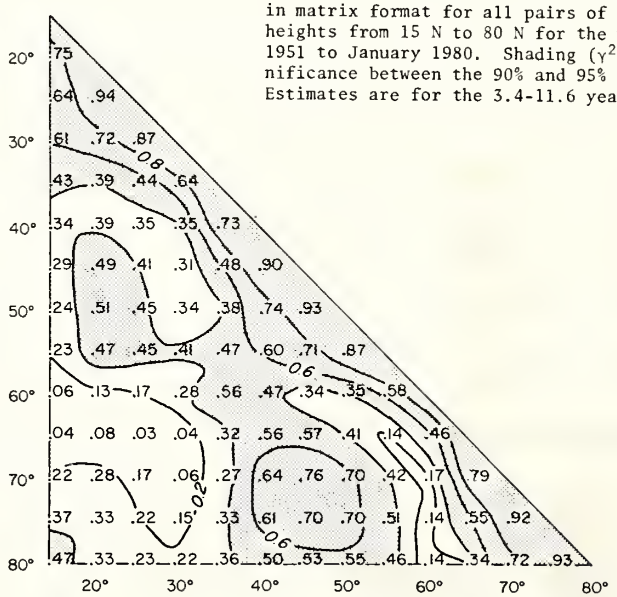

Fig. 4a. Values and contours of coherence-squared are arranged in matrix format for all pairs of global band 700 mb heights from 15 N to 80 N for the period from January 1951 to January 1980. Shading ($\gamma^2 \geq 0.4$) indicates significance between the 90% and 95% confidence levels. Estimates are for the 3.4-11.6 year band.

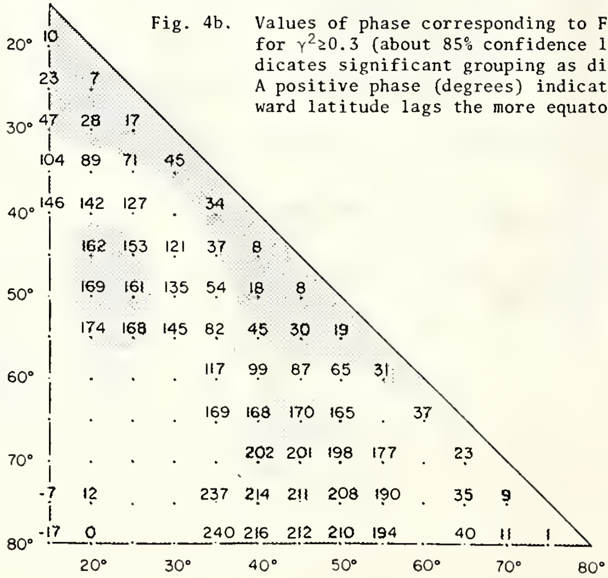

Fig. 4b. Values of phase corresponding to Fig. 4a. are shown for $\gamma^2 \geq 0.3$ (about 85% confidence level). Shading indicates significant grouping as discussed in the text. A positive phase (degrees) indicates that the more poleward latitude lags the more equatorward latitude.

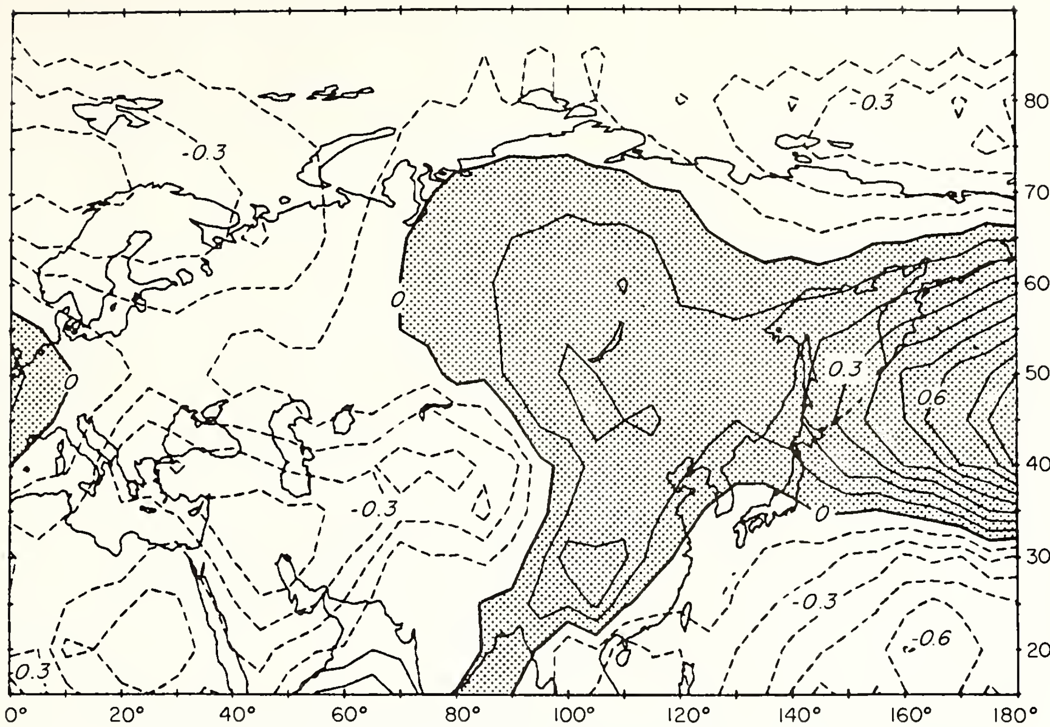

Fig. 5a. Time-correlations of low-pass filtered 700 mb geopotential heights with the filtered heights in the eastern North Pacific Ocean (165°W, 45°N) for winters from 1949-50 to 1976-77.

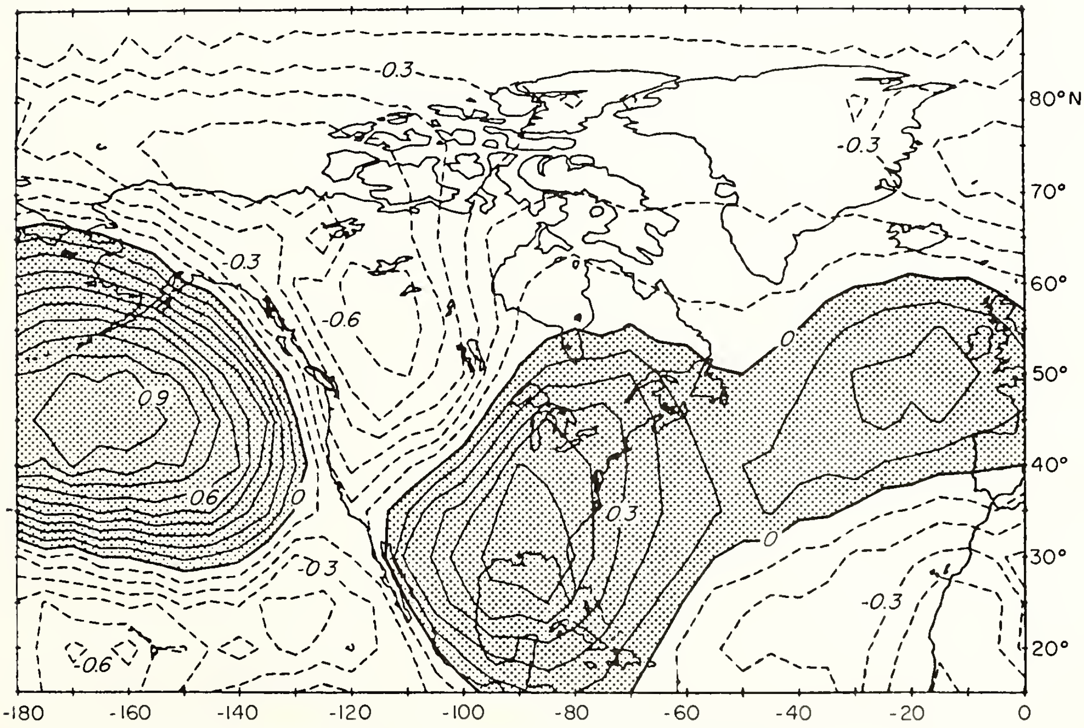

Fig. 5b. Time-correlations of low-pass filtered 700 mb geopotential heights with the filtered heights in the eastern North Pacific Ocean (165°W, 45°N) for winters from 1949-50 to 1976-77.

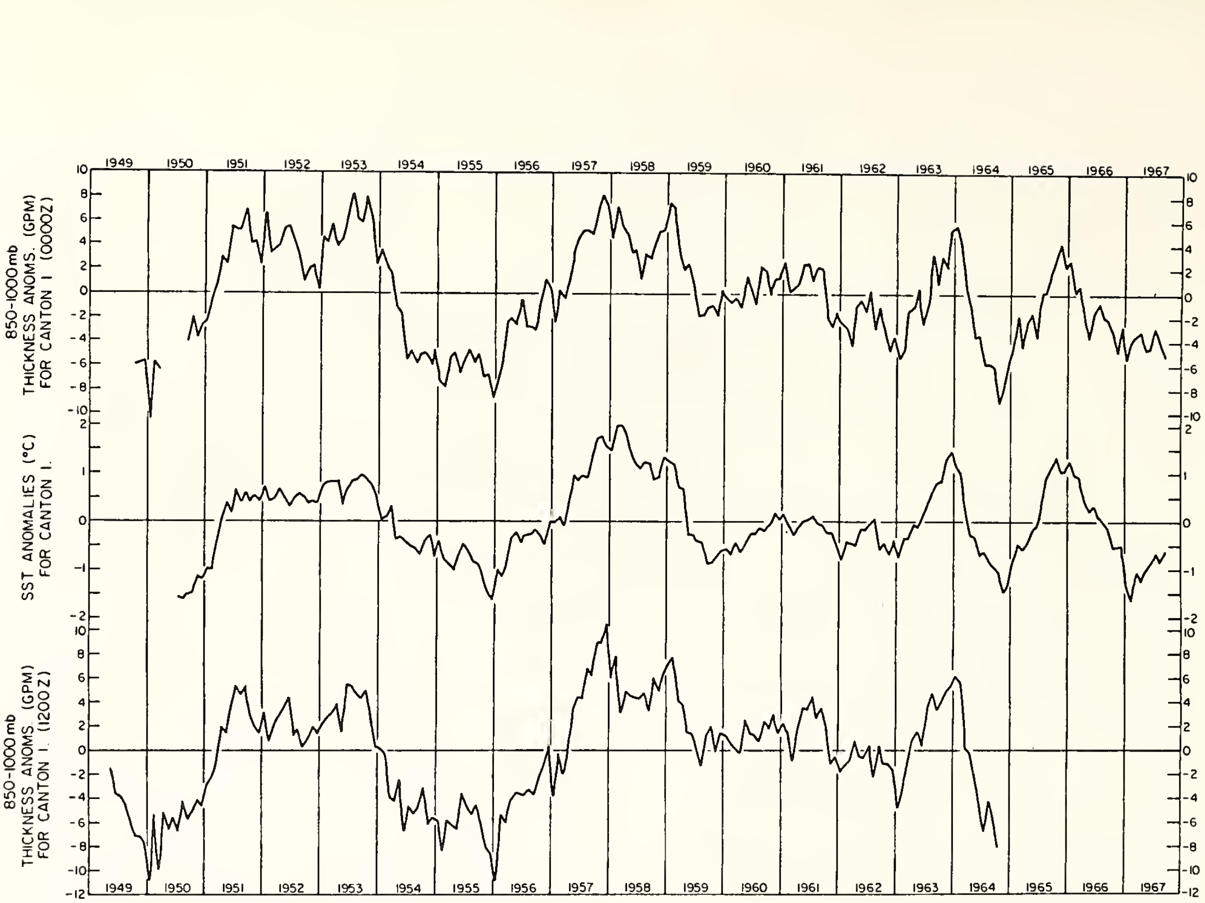

Fig. 6. Plot of anomalies of monthly sea surface temperature in relation to anomalies of monthly 850-1000 mb thickness in geopotential meters for 0000Z and 1200Z at Canton I. (2° 46'S, 171° 43'W) for 1949-67.

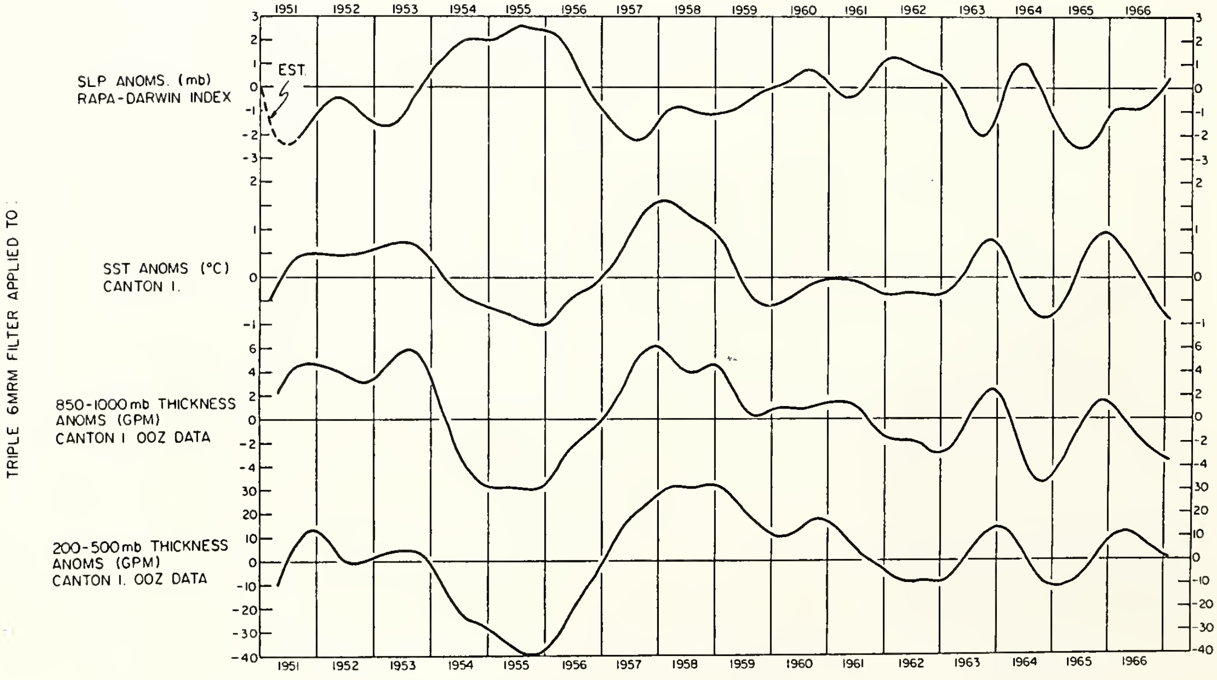

Fig. 7. Triple 6-month running mean plot of anomalies of the difference in sea level pressure (mb) between Rapa I. (27° 37'S, 144° 20'W) and Darwin (12° 26'S, 130° 52'E), anomalies of sea surface temperature (°C) for Canton I. (2° 46'S, 171° 43'W), anomalies of 850-1000 mb thickness in geopotential meters (GPM) for Canton 0000Z data, and anomalies of 200-500 mb thickness in GPM for Canton 0000Z data for 1951-66.

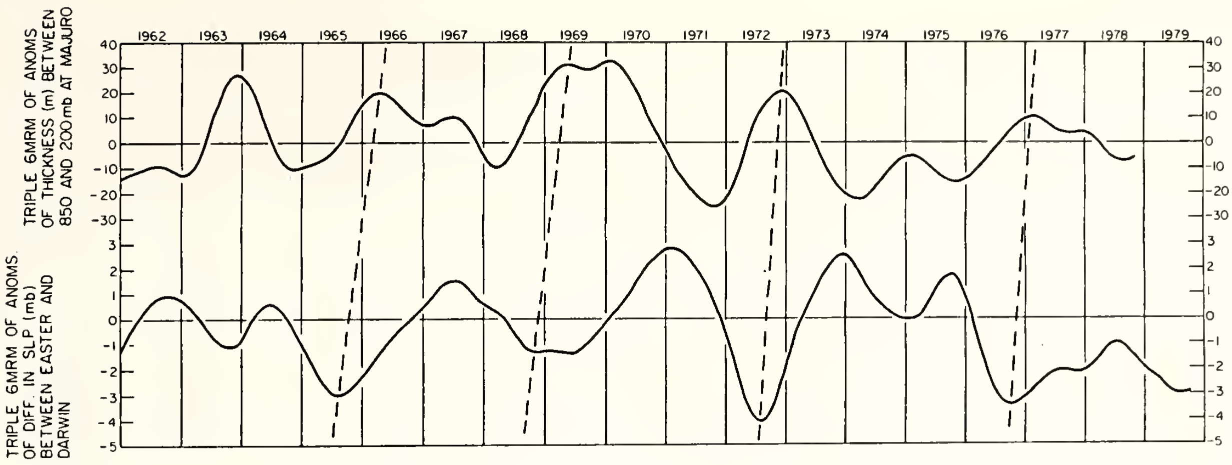

Fig. 8. Triple 6-month running mean plot of anomalies of 200-850 mb thickness in geopotential meters for Majuro I. (7° 05'N, 171° 23'E), and anomalies of the difference in sea level pressure (mb) between Easter I. (27° 10'S, 109° 26'W) and Darwin (12° 26'S, 130° 52'E) for 1962-79.

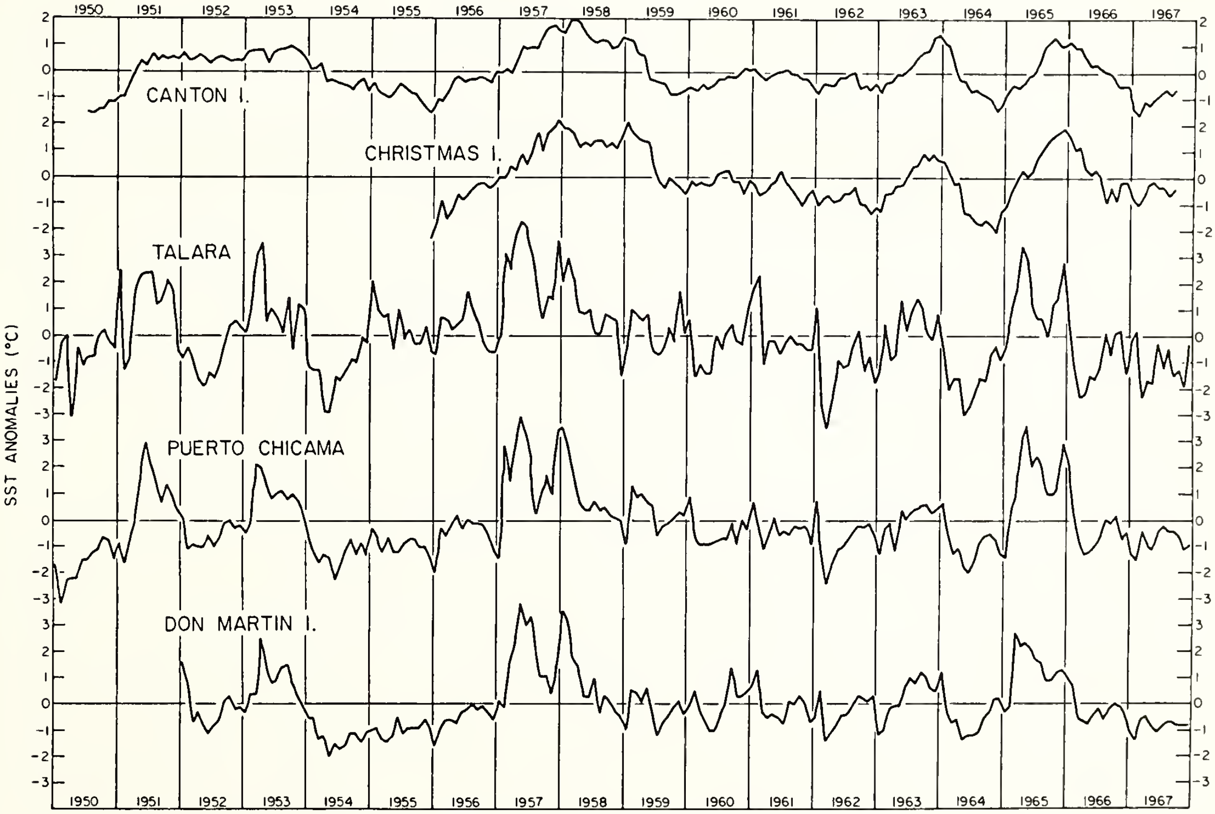

Fig. 9. Plot of anomalies of monthly sea surface temperatures (°C) for Canton I. (2° 46'S, 171° 43'W), Christmas I. (1° 59'N, 157° 28'W), Talara (4° 30'S, 81° 17'W), Puerto Chicama (7° 42'S, 79° 27'W), Don Martin I. (11° 02'S, 77° 41'W) for 1950-67.

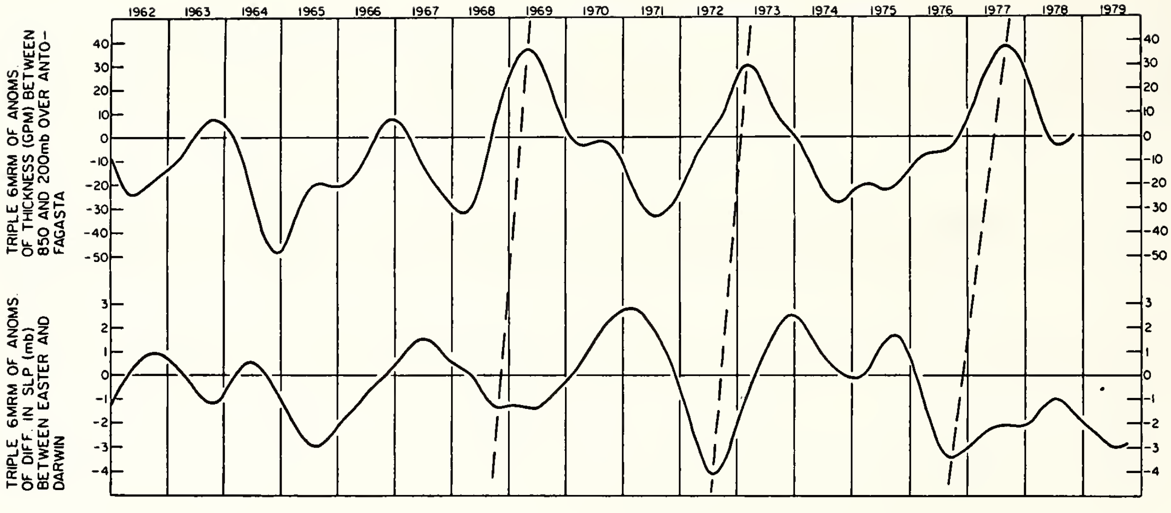

Fig. 10. Triple 6-month running mean plots of anomalies of 200-850 mb thickness in geopotential meters for Antofagasta (23° 28'S, 70° 26'W), and anomalies of the difference in sea level pressure (mb) between Easter I. (27° 10'S, 109° 26'W) and Darwin (12° 26'S, 130° 52'E) for 1962-79.

Table 1. Monthly differences in thickness obtained by subtracting the 200-850 mb thickness values for 1200/1500Z from the 200-850 mb thickness values for 0000/0300Z.

	J	F	M	A	M	J	J	A	S	O	N	D
1950									26	25	39	30
1951	13	28	33	30	33	36	20	26	31	36	44	33
1952	30	33	28	29	25	25	25	32	24	34	29	35
1953	35	30	29	23	18	27	25	30	39	47	55	48
1954	42	40	59	44	33	28	27	22	27	21	53	40
1955	26	34	33	43	25	20	28	27	31	31	34	27
1956	39	39	57	47	27	42	41	32	36	45	41	34
1957	44	33	36	39	41	34	37	30	34	32	45	17
1958	37	29	41	30	36	44	22	31	38	35	38	38
1959	32	42	33	25	39	40	33	36	32	31	41	42
1960	41	32	27	31	35	25	44	39	32	36	33	33
1961	27	39	57	24	21	24	22	22	24	18	31	23
1962	25	26	21	16	28	21	26	34	29	21	21	26
1963	16	20	22	20	19	16	21	29	21	29	35	30
1964	26	29	35	29	27	40	50	41	35	30		

The average thickness difference between the two time periods is about 32 GPM.

Table 2. Lag/lead correlation coefficients between the Rapa-Darwin index and the following: Canton sea surface temperature (SST), Canton 850-1000mb thickness, Canton 200-500mb thickness.

Lag/lead in months	R-D vs. SST Correl. Coeffs.	R-D vs. 850-1000Th. Correl. Coeffs.	R-D vs. 200-500Th. Correl. Coeffs.
-1	-.496	-.503	-.444
0	-.559	-.557	-.493
1	-.609	-.609	-.525
2	-.640 Index	-.649 Index	-.573
3	-.649 leads	-.677 leads	-.606
4	-.644	-.673	-.629 Index
5	-.623	-.648	-.636 leads
6	-.583	-.597	-.629
7	-.527	-.536	-.623
8	-.461	-.461	-.590
9	-.394	-.396	-.547
10	-.328	-.334	-.481
Period of record	1951-1967	1951-1967	1951-1967

Table 3. Lag/lead correlation coefficients between the Rapa-Darwin and Easter-Darwin indices and the 200-850 mb thickness for Majuro.

Lag/lead in months	R-D vs. 200-850Th. Correl. Coeffs.	E-D vs. 200-850Th. Correl. Coeffs.
0	-.334	-.262
1	-.369	-.307
2	-.404	-.346
3	-.436	-.380
4	-.467 Index	-.397 Index
5	-.488 leads	-.401 leads
6	-.487	-.397
7	-.457	-.386
8	-.395	-.357
9	-.322	-.290
10	-.250	-.206
Period of record	1960-1979	1960-1979

Table 4. Lag/lead correlation coefficients between Canton Island sea surface temperature (SST) and the following: Talara SST, Puerto Chicama SST and La Punta SST.

Lag/lead in months	Canton vs. Talara SST Correl. Coeffs.	Canton vs. Puerto Chicama SST Correl. Coeffs.	Canton vs. La Punto SST Correl. Coeffs.
-9	.499	.489	.524
-8	.549	.560	.606
-7	.588	.623	.678
-6	.614 Talara	.673	.734
-5	.623 leads	.702	.774
-4	.610	.715 Puerto Chicama	.792 La Punta
-3	.577	.715 leads	.793 leads
-2	.530	.703	.778
-1	.477	.677	.747
0	.416	.634	.690
1	.342	.568	.616
2	.249	.478	.526
Period of record	1950-1967	1950-1967	1956-1967

Table 5. Precipitation classification by year for Chile with the addition of precipitation in mm for Santiago (33°16'S, 70°50'W) and Valparaiso (33°01'S, 71°39'W) (from Taulis, 1934. Classification categories are very dry (TS), dry (S), normal (N), wet (P) and very wet(TP). Strong (S) and moderate (M) El Niño (EN) occurrences (from Quinn et al., 1978) are included.

	Class.	Santiago	Valparaiso	El Niño Occurrences
1875	N	238.7	301.0	
76	S	126.7	329.0	
77	TP	650.4	847.0	EN(S) 77-78
78	N	401.4	510.0	
79	S	165.5	322.0	
80	TP	652.7	915.0	EN(M) 80
81	N	441.0	398.0	
82	N	303.5	436.0	
83	N	365.0	581.0	
84	N	387.1	664.0	EN(S) 84-85
85	N	397.5	415.0	
86	TS	109.7	222.0	
87	P	563.6	695.0	EN(M) 87-88
88	TP	693.3	967.0	
89	N	229.6	306.0	
90	N	222.3	362.0	
91	TP	614.6	822.0	EN(S) 91
92	S	123.4	120.0	
93	N	238.5	412.0	
94	N	242.0	312.0	
95	N	293.3	350.0	
96	N	263.1	463.0	EN(M) 96
97	N	355.3	523.0	
98	N	498.4	848.0	
99	TP	773.2	1,196.0	EN(S) 99-00
1900	TP	819.5	1,345.0	
01	N	384.3	530.0	
02	P	505.8	724.0	EN(M) 02
03	S	194.7	389.0	
04	TP	686.2	1,087.0	
05	TP	615.7	1,077.0	EN(M) 05
06	N	293.3	414.0	
07	N	269.0	663.0	
08	N	202.3	274.0	
09	S	183.9	326.4	
10	N	271.2	492.4	
11	S	169.9	249.9	EN(S) 11-12
12	N	291.1	500.1	
13	N	268.0	324.6	
14	TP	700.5	1,173.2	EN(M) 14
15	N	236.8	407.4	
16	N	225.3	246.0	
17	N	203.8	359.7	
18	N	376.8	491.8	EN(S) 18-19
19	TP	649.5	943.2	
1920	N	290.2	291.2	
21	N	435.3	707.6	
22	N	447.7	700.5	
23	N	366.6	505.9	
24	TS	66.3	61.8	
25	N	259.0	397.4	EN(S) 25-26
26	TP	760.8	879.0	
27	N	405.7	547.0	
28	N	341.0	481.0	
29	N	354.0	423.0	EN(M) 29-30
30	N	500.0	639.0	

Digitization of the NOAA/NESS Continental Snow Cover Data Base

by

Michael Matson and Marylin S. Varnadore
NOAA/National Earth Satellite Service
Washington, D.C. 20233

The NOAA/NESS Northern Hemisphere continental snow cover data base is approaching its 15th data year and, although not a climatology by strict definition, is being incorporated more frequently into climate modelling and diagnostic studies. In an effort to facilitate this integration, NESS, in conjunction with the University of Nebraska-Lincoln, has undertaken the digitization of the continental snow cover data base from 1966-1980. The Northern Hemisphere Weekly Snow and Ice Cover Chart (see figure 1) is being digitized using a NMC I, J box grid overlaid on a polar stereographic map. The grid selected is the same as that used for the satellite-based earth radiation budget atlas of Winston et al. (1979). After establishing the appropriate geography into the data base (see figure 2), each grid box is designated snow-covered (non-snow-covered) if the grid box has 50 percent or more snow cover (50 percent or less snow cover). The reflectivity classes are not digitized. An example of the computer printout display of a Northern Hemisphere snow cover map is shown in figure 3. Since latitude-longitude information is also provided for each grid box, it is possible to determine the true Earth surface area of each box and in turn the snow-covered area of each continent (Table 1) or a region of the continent. To enhance the display of snow cover on the computer printout a microfilm product has been developed which allows the snow-covered areas to be displayed on an appropriate background geography (see figure 4). Although not shown here, a color microfilm map has also been developed with water as blue, land as green, and snow as gold. Archival of the digitized continental snow cover data will not only be on microfilm, but will include punch cards and computer-compatible tape. Complete documentation will be provided for all archived products and repositories of the archives will be the Environmental Data and Information Service (EDIS) of NOAA and World Data Center-A. Archival should be completed by Spring 1981.

Operational digitization of the Northern Hemisphere Weekly Snow and Ice Cover Chart is now being performed by the Synoptic Analysis Branch of NESS using the same grid and procedure as that used for the historical data. Therefore the archival of digital continental snow cover will continue in the future, providing climate researchers with a format for analyzing snow cover compatible with other climate data bases.

Reference

Winston, J.S., A. Gruber, T.I. Gray, M.S. Varnadore, C.L. Earnest, and L.P. Mannello, 1979: Earth-Atmosphere Radiation Budget Analyses Derived from NOAA Satellite Data June 1974-February 1978, Vols. 1 and 2, U.S. Dept. of Commerce, NOAA.

TABLE 1

NORTH AMERICA SNOW COVER AREA

Year	Week	Area (x 10^7 km^2)	% of continent covered
1967	1	1.677	79.2%
1967	14	1.338	63.2%
1967	36	0.347	16.4%
1971	10	1.635	77.2%

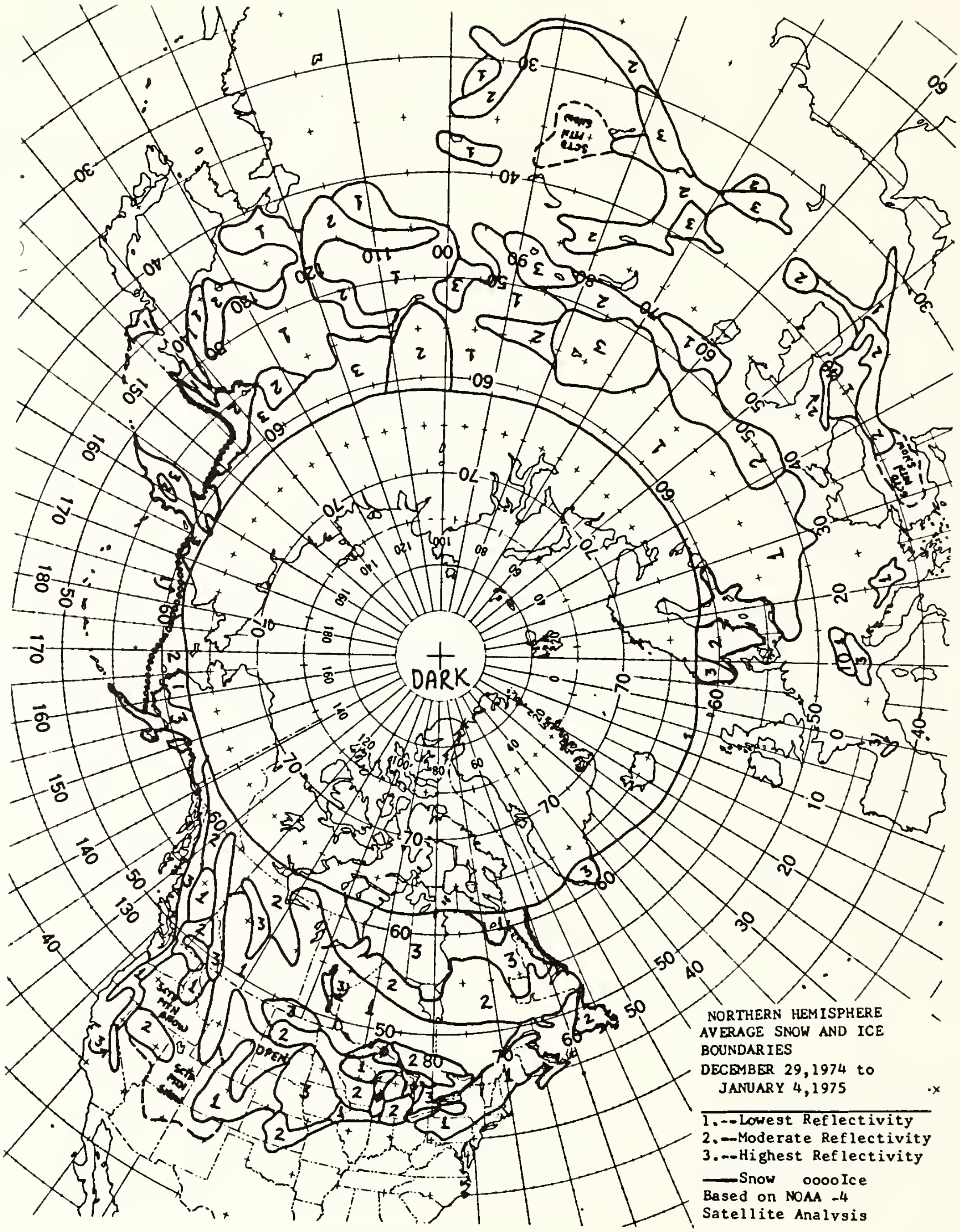

Fig. 1. Snow and ice chart of the Northern Hemisphere for the 7-day period 29 December 1974 through 4 January 1975 prepared by NOAA/NESS. Note the several classes of reflectivity and the areas of scattered mountain snow. Also note the "dark" area where visible data cannot be collected during the polar night.

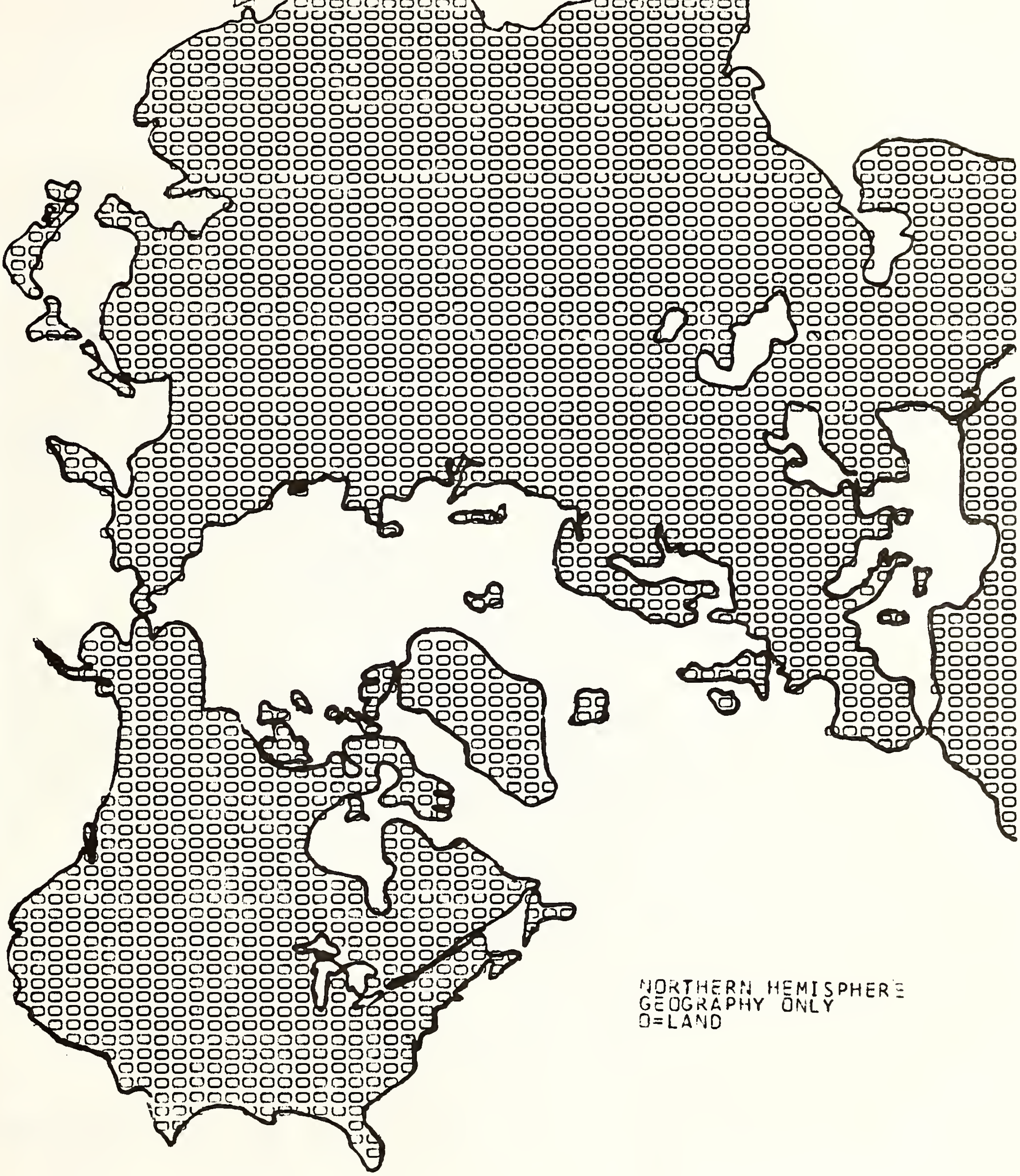

Fig. 2. The digitized Northern Hemisphere geography.

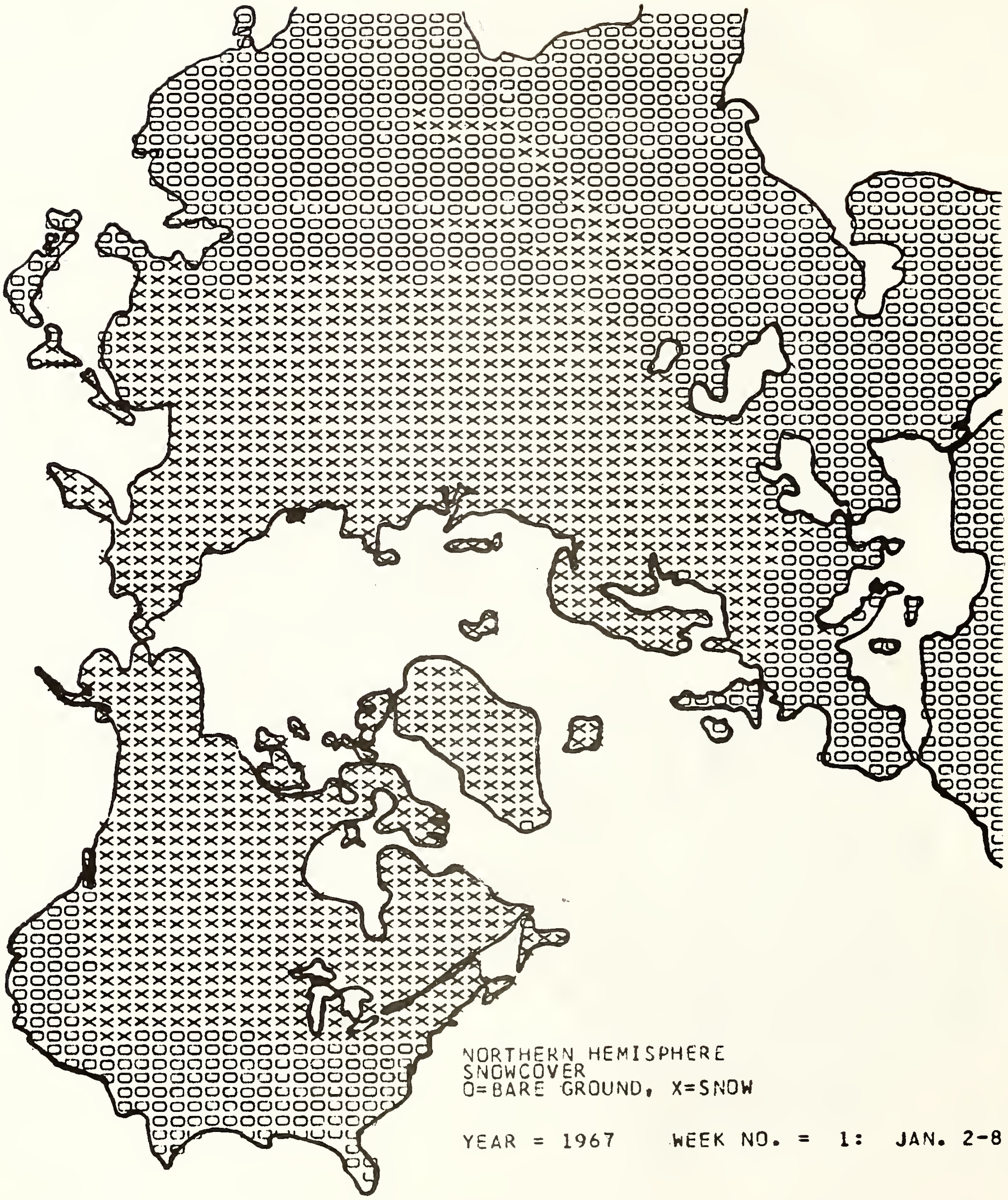

Fig. 3. A digitized Northern Hemisphere snow cover chart for the period 2-8 January 1967.

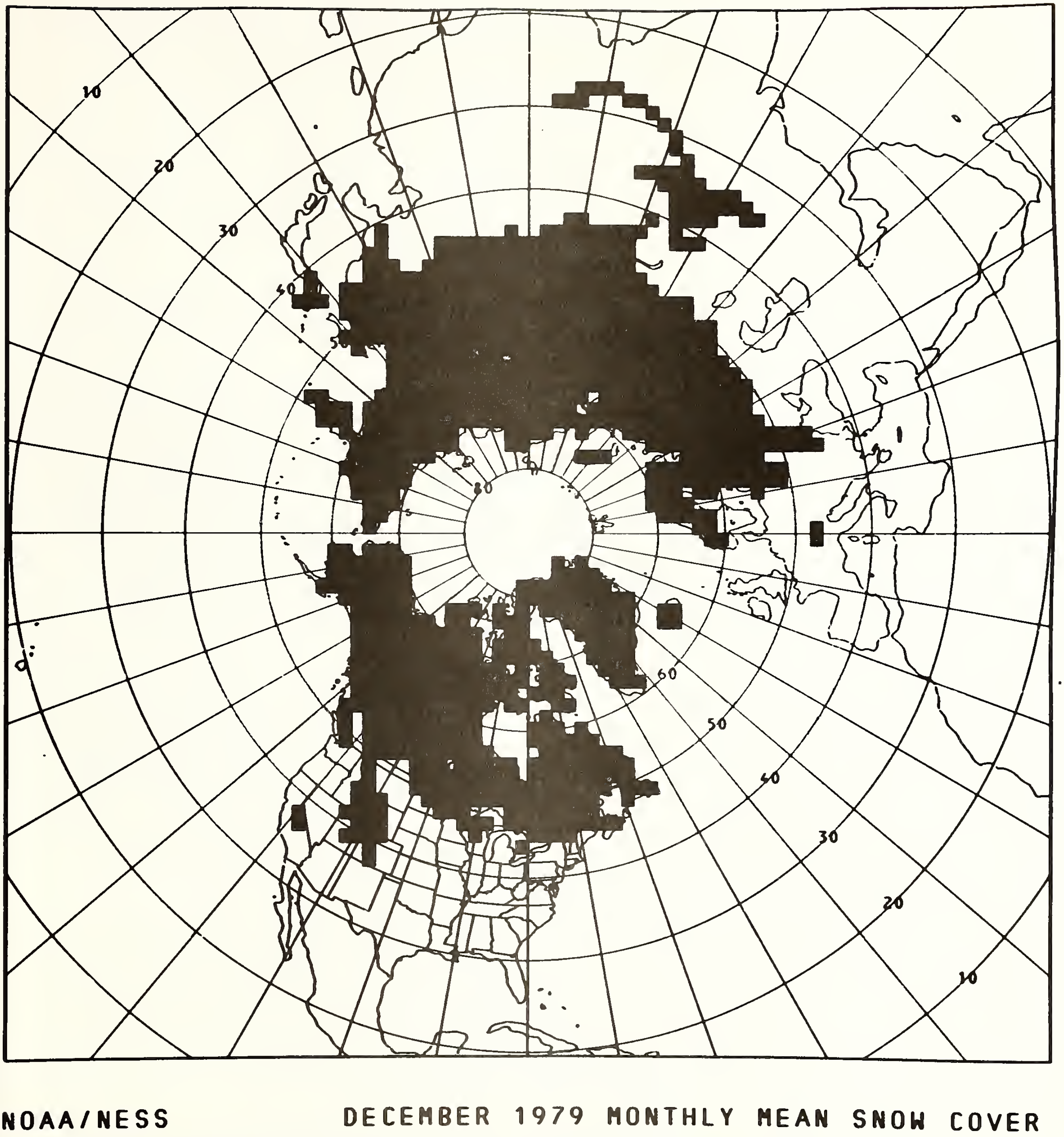

Fig. 4. A microfilm product displaying Northern Hemisphere snow cover for December 1979. The snow cover shading can also be displayed as various gray tones rather than black.

Normals of Monthly Surface Northern Hemisphere Albedo*

William L. Donn

Lamont-Doherty Geological Observatory of Columbia University
Palisades, N. Y. 10964

and

Julian Adem

Centro de Ciencias de la Atmosfera y Facultad de Ciencias,
UNAM, Mexico 20, D.F.
and
Lamont-Doherty Geological Observatory of Columbia University,
Palisades, N. Y. 10964

The results described here were developed for application in the thermodynamic model of Adem, (e.g. 1979). The model generated forecasts of monthly anomalies of temperature and precipitation and uses anomalies of surface snow and ice as one of the three input variables. Current NOAA-NESS charts of weekly snow and ice cover provide the data for this purpose. However, these charts give reflectivity according to these scale values: 1, 2, and 3. According to G. Kukla who has studied these maps as well as actual satellite photographs for many years, the indexes 1, 2, and 3 can be treated as average reflectivity centered on albedo values 30, 45, and 65, respectively.

As the normal values available heretofore in regions of snow and ice are based on different scaling as well as on leaner observations, we could not derive valid albedo anomalies for application in the model. Consequently the laborious task of generating new normals was undertaken. According to Kukla (personal communication) scaling interpretations in snow-ice charts prior to 1974 were not reliable enough for our purpose. The normals for snow and ice presented here are thus based on observations from January 1974 through June 1980. We will try to update these results each year.

Values of surface albedo were determined from each chart for the grid points used in the model. To do this, a transparent overlay was matched to each snow-ice chart after correcting for size scale differences. Because the model uses a coarse mesh grid, we averaged the albedo in a standard box centered on each grid point. Beyond the region of snow and ice we used the values of Posey and Clapp (1964) whose values appear intermediate between those of Hummel and Reck (1979) and Preuss and Geleyn (1980).

Resulting means are available in polar projections for the Northern Hemisphere with values given at each of the 512 grid points. Because we use the albedo of the last week in the month to generate a forecast for the following month, the values (and maps) refer to the mean of the last week of each month rather than a true mean of the entire month. By simple graphical interpolation one can obtain the actual mean for each point, assuming a significant difference exists. Data can also be provided by latitude and longitude as well as for grid points.

---

*Lamont-Doherty Geological Observatory of Columbia University Contribution Number 3067.

The contoured mean maps from January to July, plus the annual average map, present the results in a more visual form, although they may suffer in some details from normal contour smoothing and interpretation. Contours are drawn at intervals of 10 percent from 65 to 15 percent and then at smaller intervals where geographic change is small.

References

Adem, J. (1979), Low resolution thermodynamic grid models. *Dyn. Atmos. Oceans*, 3, 433-351.

Hummel, J. and R. Reck (1979), A global surface albedo, *J. Appl. Meteorol.* 18, 239-252.

Posey, P. and P. Clapp (1964), Global distribution of normal surface albedos, *Geofisica Internl.* 4, 38-48.

Preuss, H. and J. Geleyn (1980), Surface albedos derived from satellite data and their impact on forecast models, *Arch. Met. Geoph. Biokl. Ser. A.* 29, 345-356.

Acknowledgments

This work was supported by NOAA Grant NA-79-AA-D-00066. The laborious data reduction essential to the project was carried out by Robert Towsley. The Goddard Institute for Space Studies generously provided time for all computation on their IBM 360/95 digital computer.

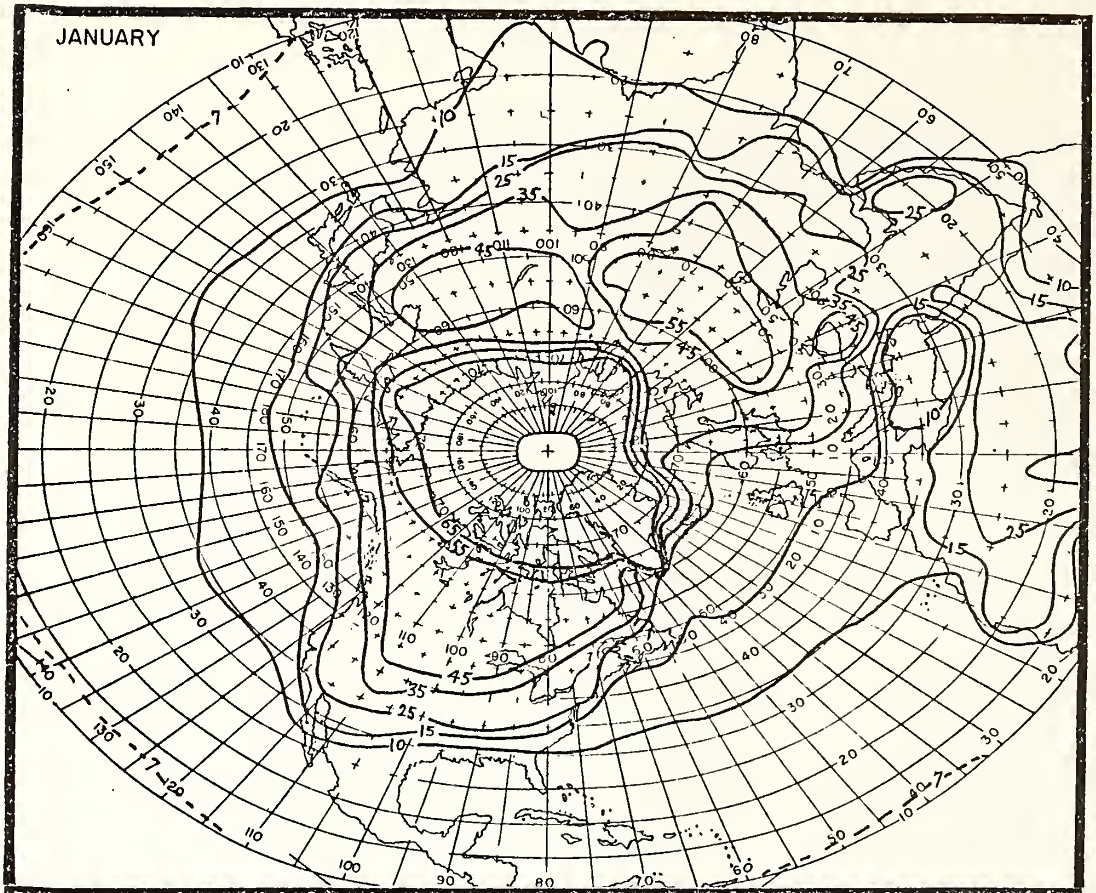
JANUARY
7
10
15
25
35
45
55
65
70

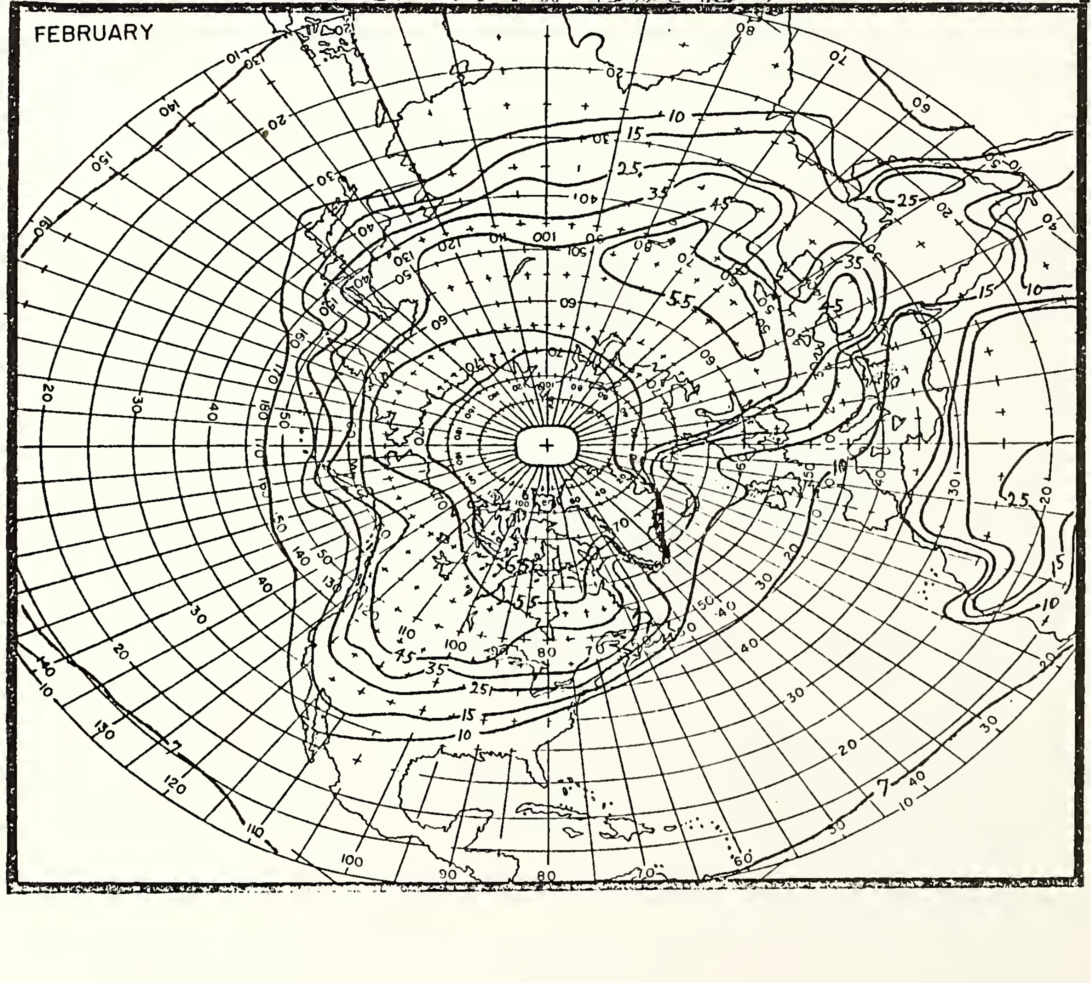
FEBRUARY
7
10
15
25
35
45
55
65
70

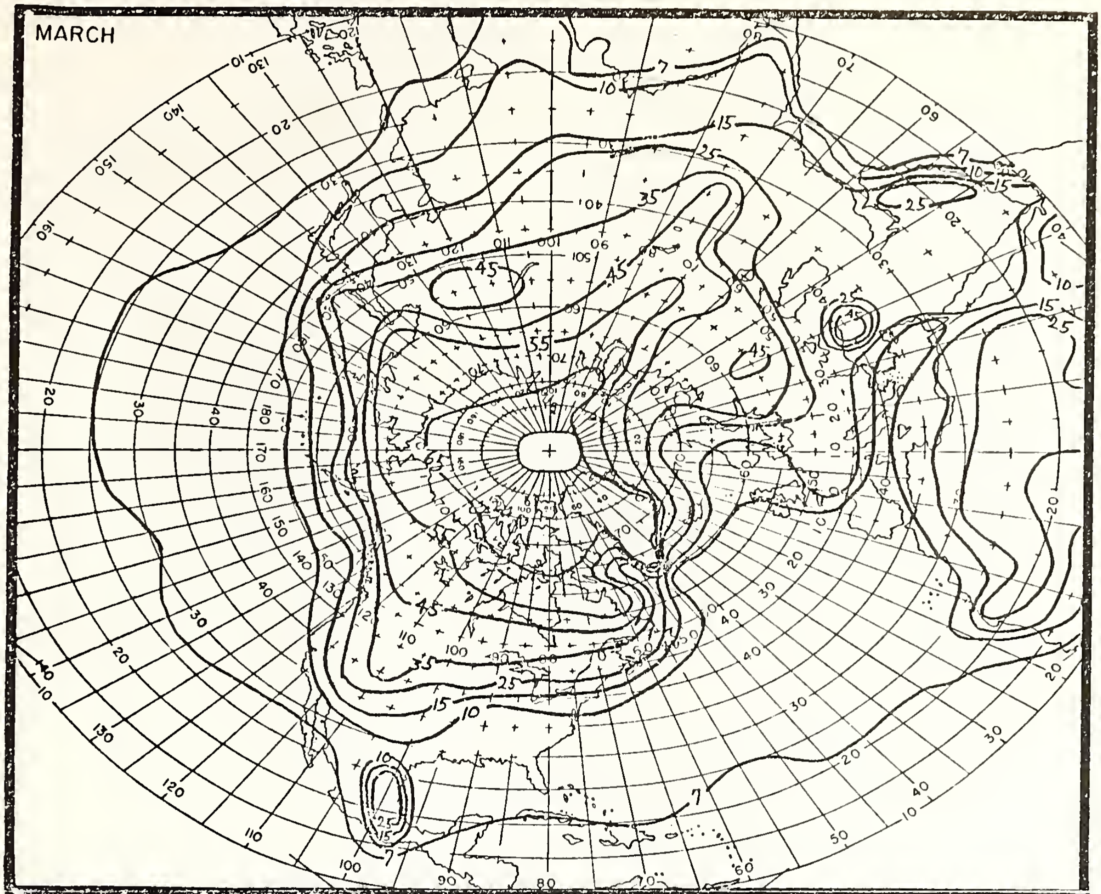
MARCH
7
10
15
25
35
45
55
10
15
25
35
45
10
15
25
7
20
30
40
50
10
20
30
40

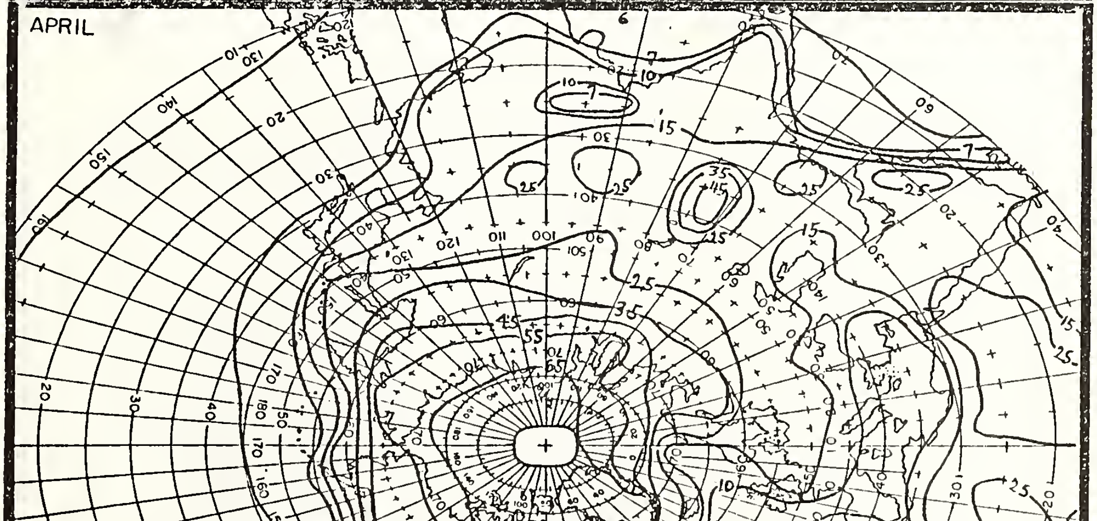
APRIL
6
7
10
15
25
35
45
55
65
10
15
25
35
45
55
7
10
15
25
6
20
30
40
50

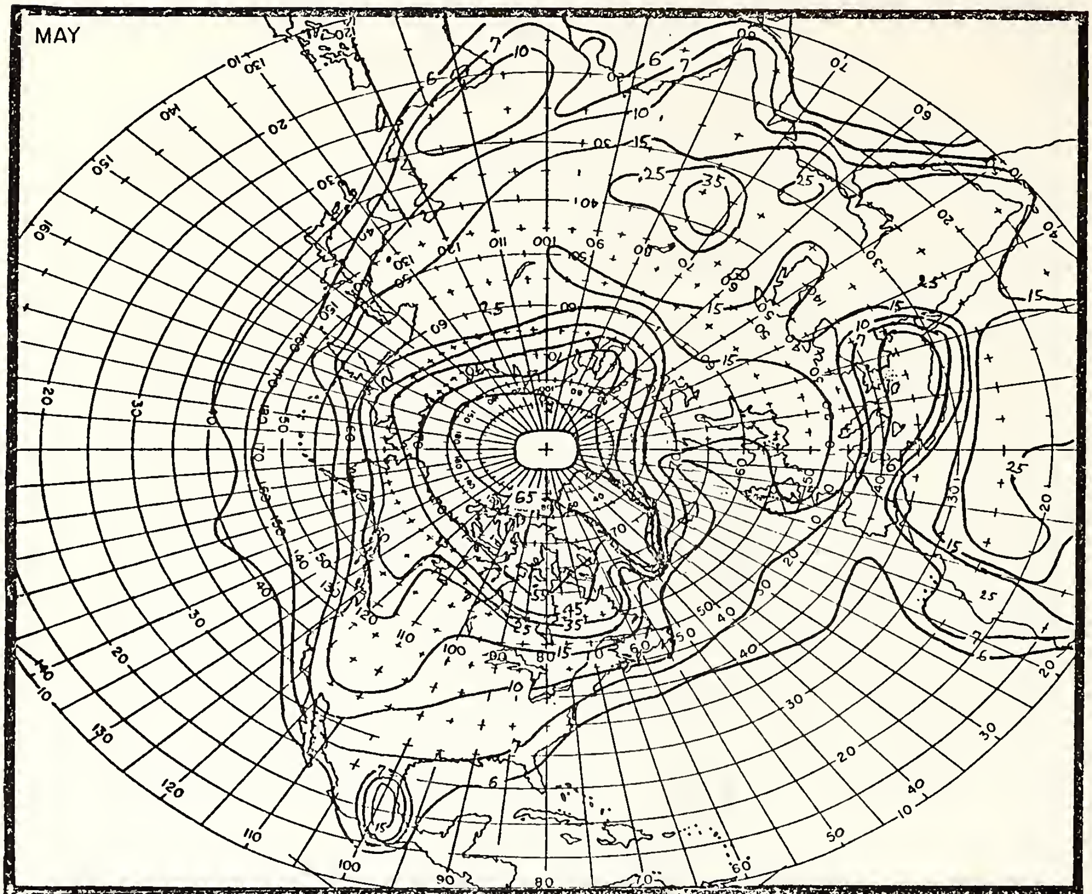

MAY

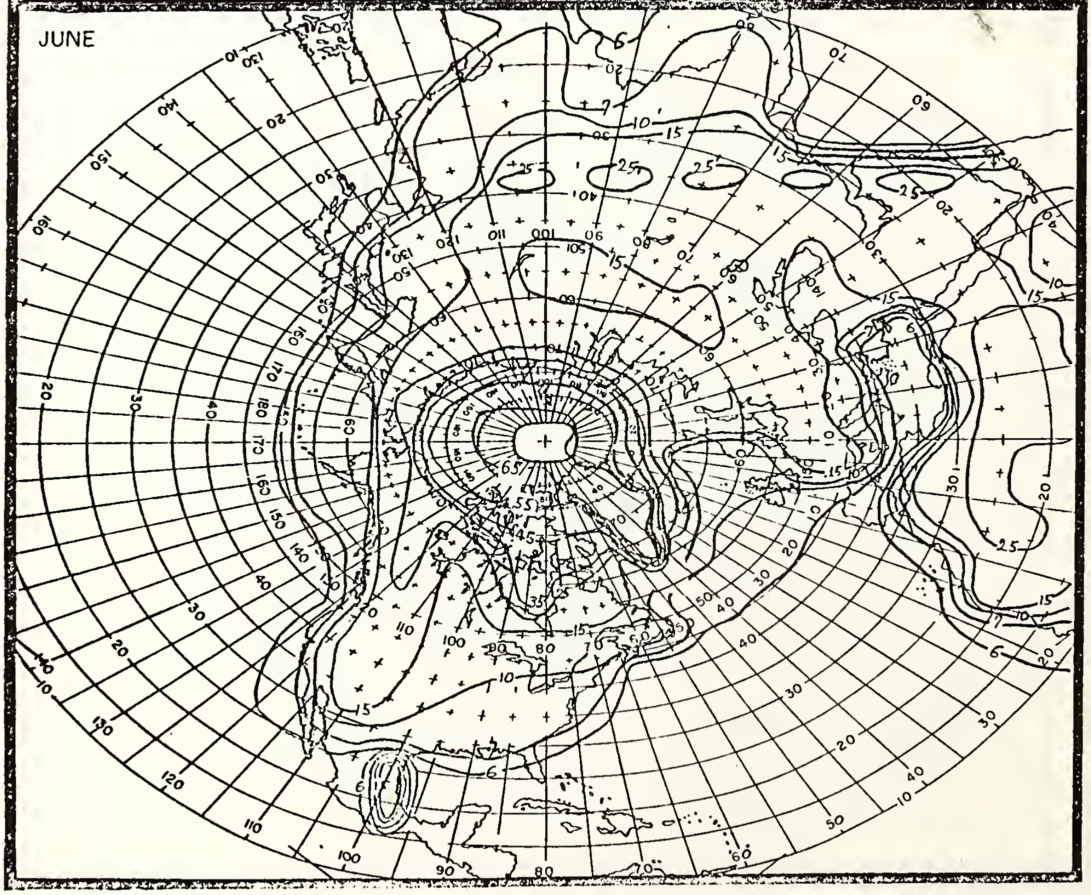

JUNE

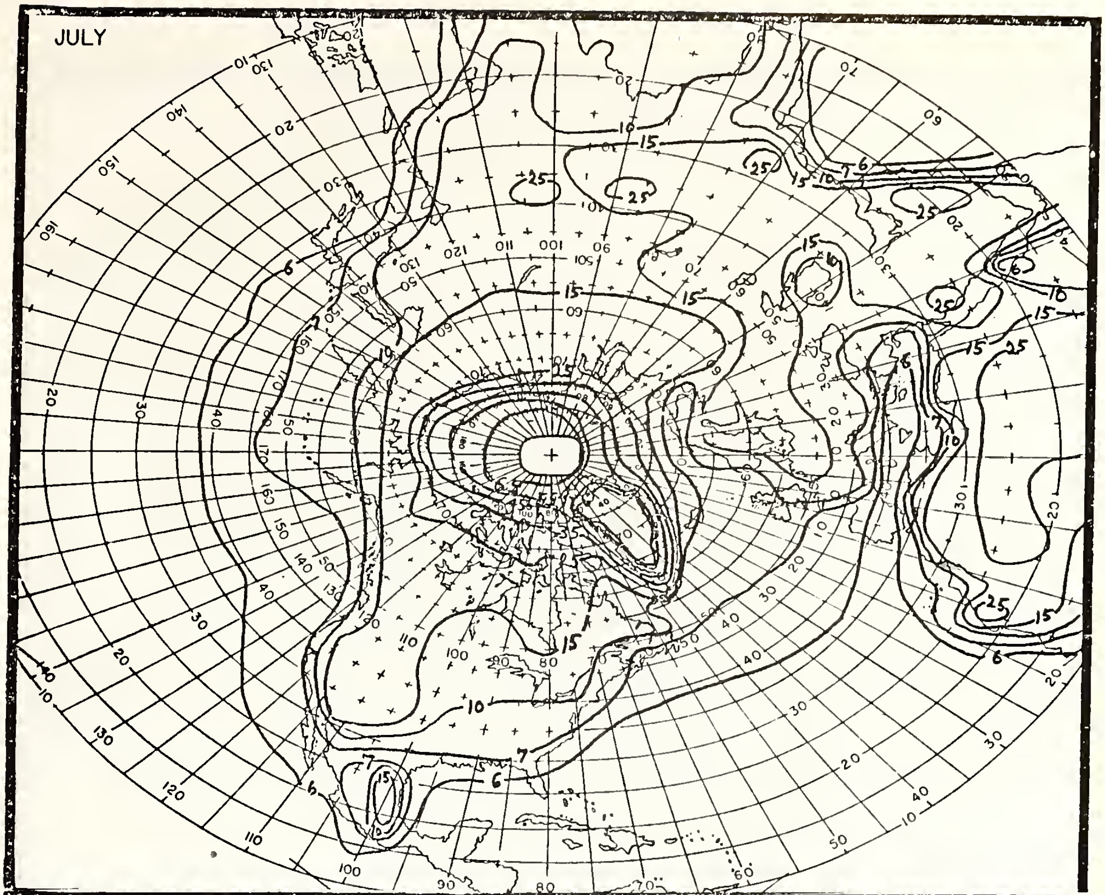

JULY

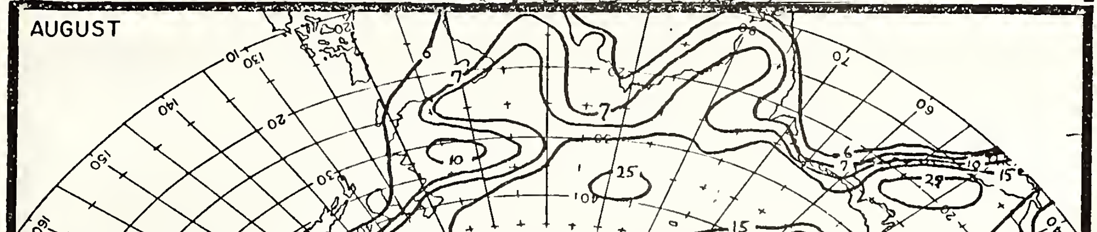

AUGUST

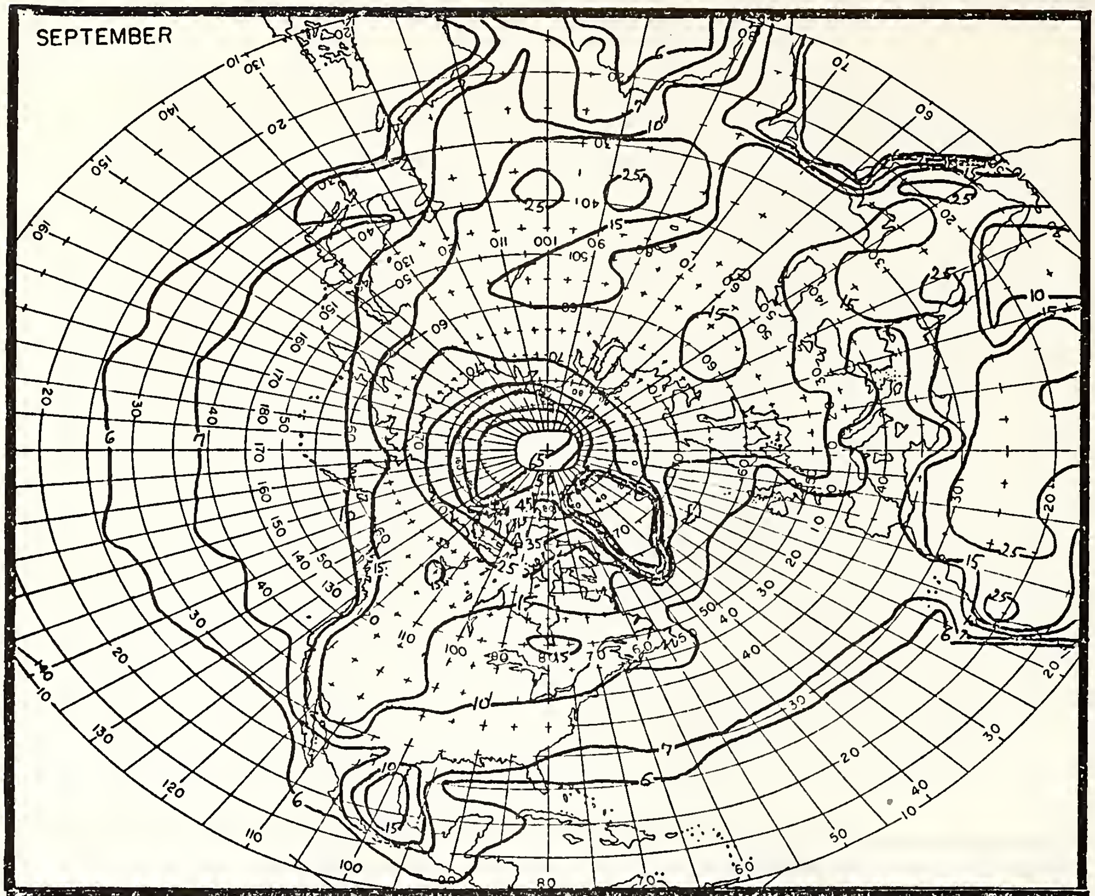
SEPTEMBER

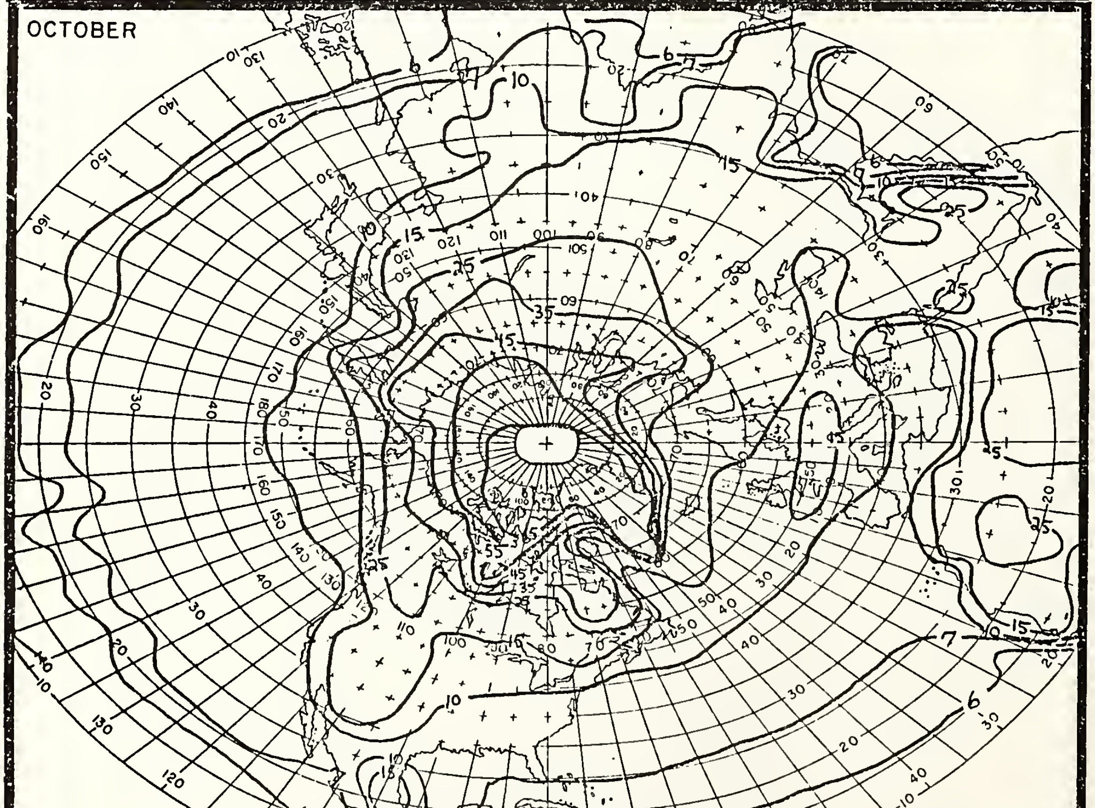
OCTOBER

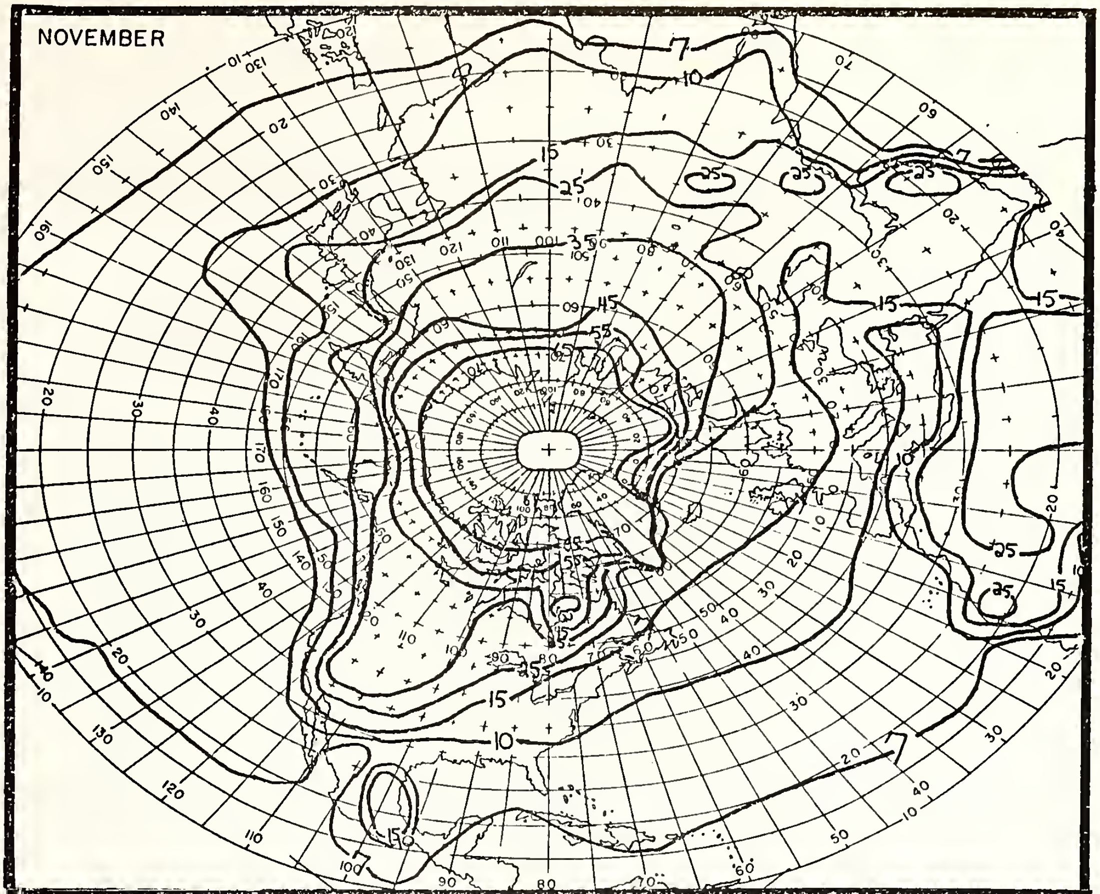

NOVEMBER

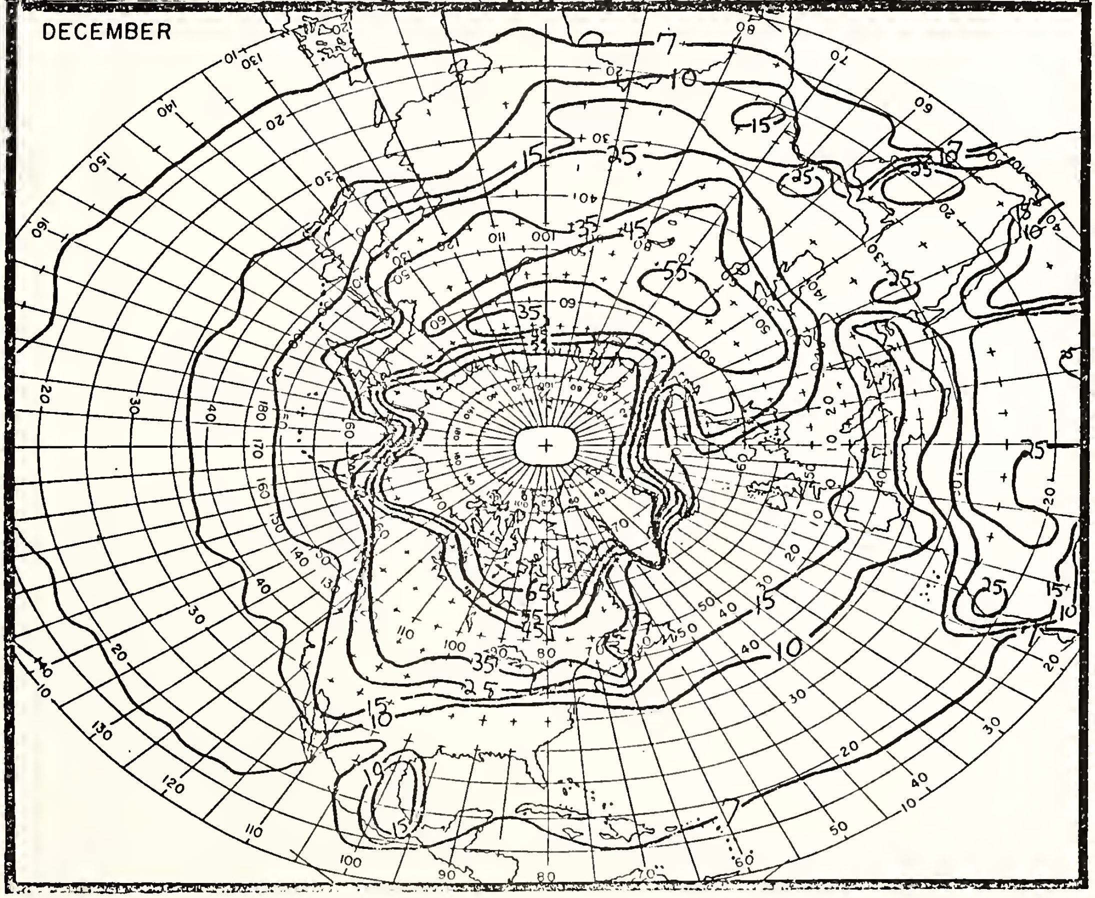

DECEMBER

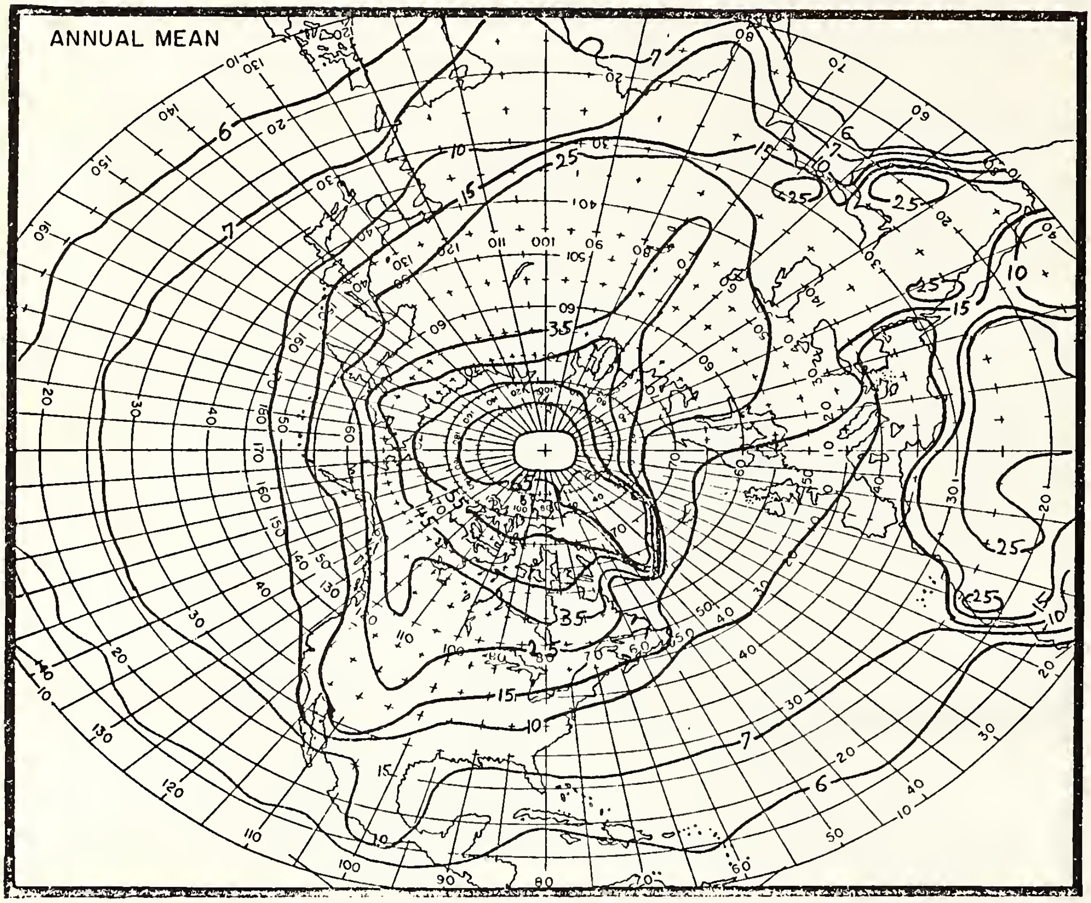
ANNUAL MEAN
6
7
10
15
25
35

The Air Force operational global snow-ice data set as a possible source for studies of short-term climate fluctuations

Philip F. Clapp and Thomas H. Carpenter
Climate Analysis Center
NMC/NWS/NOAA
Washington, D. C. 20233

The U. S. Air Force Global Weather Central at Offutt Air Force Base, Omaha, Nebraska, prepares an automated, operational data set for snow and ice over both hemispheres (Luces, et al., 1975), available at the National Climatic Center, Asheville, N. C., in a 5-year archive, 1976 to date. Snow is updated at 00 GMT each day and ice for each week. This high resolution in time is matched by an equally fine resolution in space, the grid spacing being 1/8 of the standard NMC 200 nm grid.

Snow (at land gridpoints only)is given in 6 depth categories, from less than 2 inches to 10 inches or more. Ice (at water gridpoints only) is indicated as present if a point falls within the ice boundary, the coordinates of which are sent to Offutt each week from the Navy-NOAA Joint Ice Center at Suitland, Md. No depth or ice concentration (fraction of ice-covered water at the gridpoint) are given. The snow depths are based on surface-synoptic observations aided by an elaborate snow-depth climatology. Data from the military satellites are used only to eliminate snow from those sub-satellite gridpoints where the surface brightness is less than a prescribed snow threshold.

Approximately 2 years of these data were acquired from NCC by the Meteorological Satellite Laboratory of NESS, and were made available to the authors to evaluate their usefulness in monitoring short-term climate fluctuations. To date, the total areas of snow and ice were separately computed for each 10-degree longitude sector in the Northern Hemisphere, from November 1978 to January 1980. The total areas of snow covering Eurasia and North America were also determined for the same period. In the following examples only monthly-mean values will be discussed.

Fig. 1 shows the snow areas (above) and ice areas (below) for each 10-degree sector plotted as a function of longitude for December 1978 (solid lines with dots) and, where significantly different, for December 1979 (dashed, crosses). Snow areas in 1979 were considerably smaller than those in 1978 in Europe, western Asia, and central and western North America; and higher than 1978 in central Asia. This finding is in agreement with other studies (e.g. NOAA-NESS snow charts; Matson, et al., 1979). Ice areas as a function of longitude show peaks in the regions of Baffin Bay - Hudson Straight, Greenland Sea, and Okhotsk - Bering Seas, where the ice is not restricted by continents to the south. Corresponding areas for December 1979 also changed from December 1978 but the differences were too small to be shown at the scale of the figure.

Fig. 2 shows the total area of snow over Eurasia (above) and North America (below) for each month from November 1978 to January 1980. The Air Force data (AFGWC, solid line with dots) may be compared to the NOAA-NESS data (dashed, crosses) for the same months. (Continental areas are defined in the same way.) It is to be expected that the Air Force data will show larger areas, since they include snow depths less than 2 inches. This is true for Asia, but not for North America. In particular, the 2-month difference in the location of the minima has not been explained.

Fig. 3 shows a similar plot of ice areas, for all Arctic seas (above), the Okhotsk - Bering Seas (middle) and the North Atlantic region (below). The ice areas in all Arctic seas are compared with 25-year monthly averages (1953 to 1977) computed by Walsh and Johnson (1979). The latter are expected to be smaller, because Walsh and Johnson accounted for the ice concentration at each gridpoint.

The annual changes in ice and snow cover from 1978-79 to 1979-80 for the months November, December, and January are shown in Table 1. The signs of the snow-cover changes computed from the Air Force data agree with those of NOAA-NESS (with the glaring exception of November) but are much smaller. The changes in both snow and ice cover for the entire Northern Hemisphere are negative, except for snow in November. The 700-mb height anomalies (Fig. 4) reveal changes from December 1978 to December 1979, which are consistent with the decrease in snow cover, but it is more difficult to explain the decrease in Arctic ice cover. Perhaps the anomalous cyclonic circulation in the North Atlantic caused ice to be advected out of Davis Strait and to be driven and packed into a smaller area in the north Greenland Sea.

The next steps should include examination of the entire 5-year record of the Air Force snow-ice data for both hemispheres; with special emphasis on possible trends and on comparison with other sources. Then further study should be made of the relationship between snow and ice cover and weather for selected regions with and without lag.

References

Luces, S. A., S. J. Hall, and J. D. Martens, 1975: The AFGWC snow cover analysis model. AFGWC Tech. Memo. 75-1, Air Weather Service, U. S. Air Force, Air Force Global Weather Central, Offutt AFB, NE 68113

Matson, M., D. A. Wiesnet, C. P. Berg, and E. Paul McClain, 1979: New data and new products: the NOAA-NESS continental snow cover data base. Proc. Fourth Annual Climate Diagnostics Workshop, Oct. 16-18, 1979, U. Wis., Madison, Wis., pp. 351-364.

Walsh, J. E. and C. M. Johnson, 1979: An analysis of Arctic sea ice fluctuations, 1953-1977. J. Phys. Oceano., 9, 3, pp. 580-591.

Table 1: Annual change in snow and ice cover for the months November, December, and January 1978-79 to 1979-80.

SNOW COVER CHANGE ($10^6 KM^2$)

	NOVEMBER		DECEMBER		JANUARY	
	AFGWC	NESS	AFGWC	NESS	AFGWC	NESS
EURASIA	+3.3	-2.6	-0.9	-6.3	-0.1	-4.1
NORTH AMERICA	-0.4	-2.7	-1.5	-3.1	-1.6	-1.3
NORTHERN HEMISPHERE	+2.9	-5.3	-2.4	-9.4	-1.7	-5.4

ICE COVER CHANGE ($10^6 KM^2$)

	AFGWC DATA		
	NOVEMBER	DECEMBER	JANUARY
BERING SEAS	0	+0.2	+0.3
NORTH ATLANTIC	-0.5	-0.5	-0.6
ALL ARCTIC SEAS	-0.5	-0.3	-0.5

Fig. 1 SNOW AREAS BY 10 DEGREE LONGITUDE SECTORS

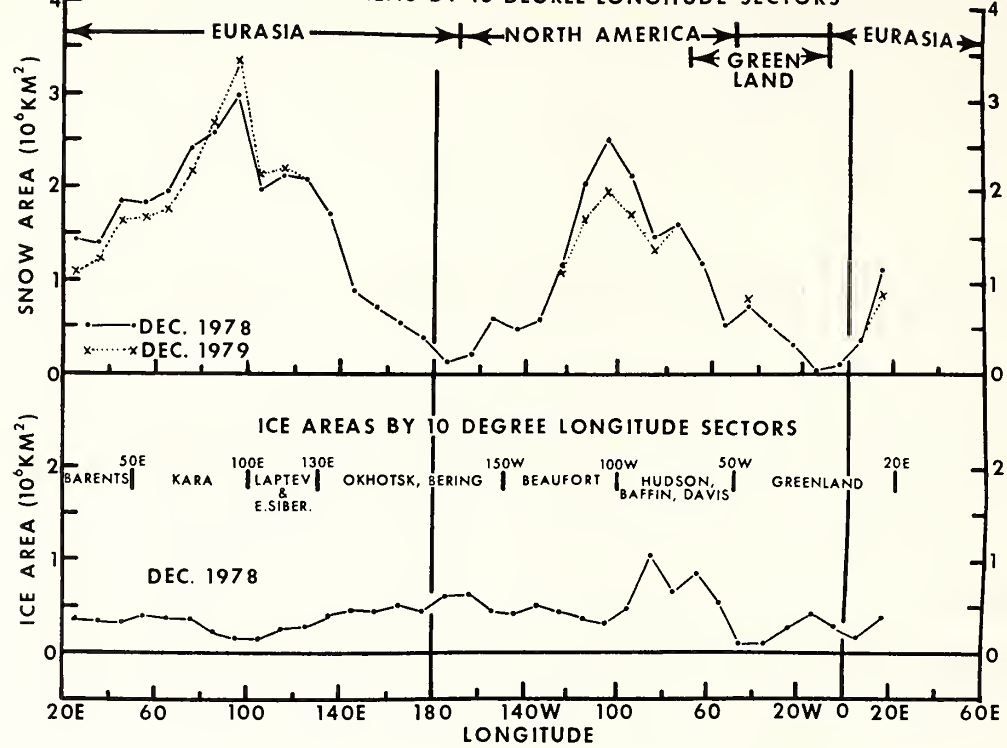

Fig. 2 CONTINENTAL SNOW COVER - NORTHERN HEMISPHERE

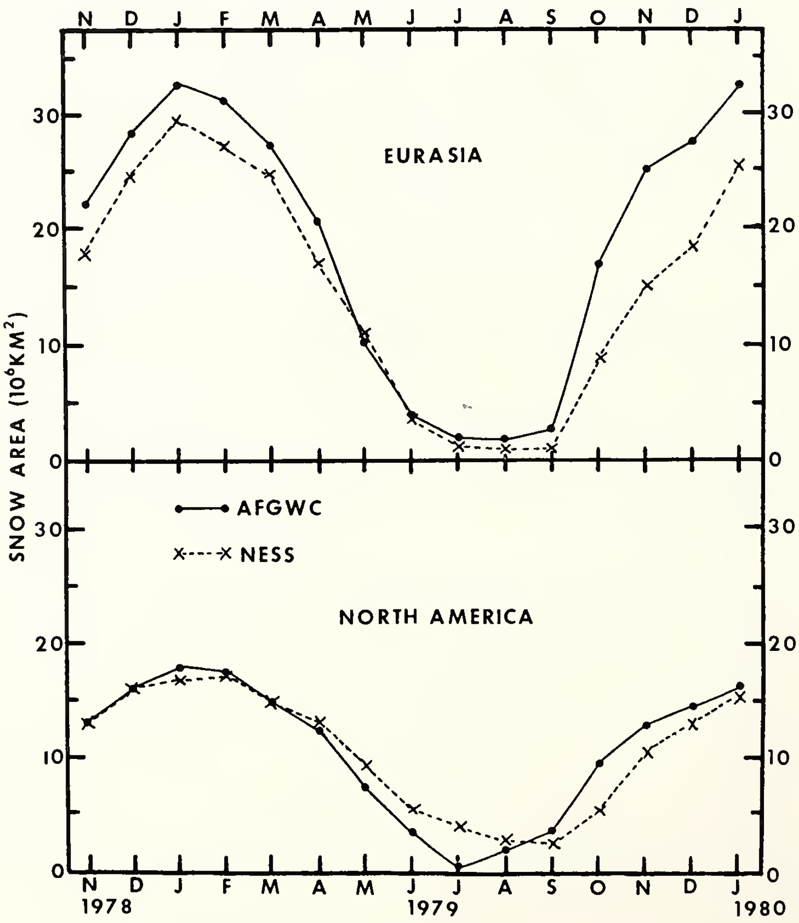

Fig. 3 ICE COVER IN ARCTIC SEAS

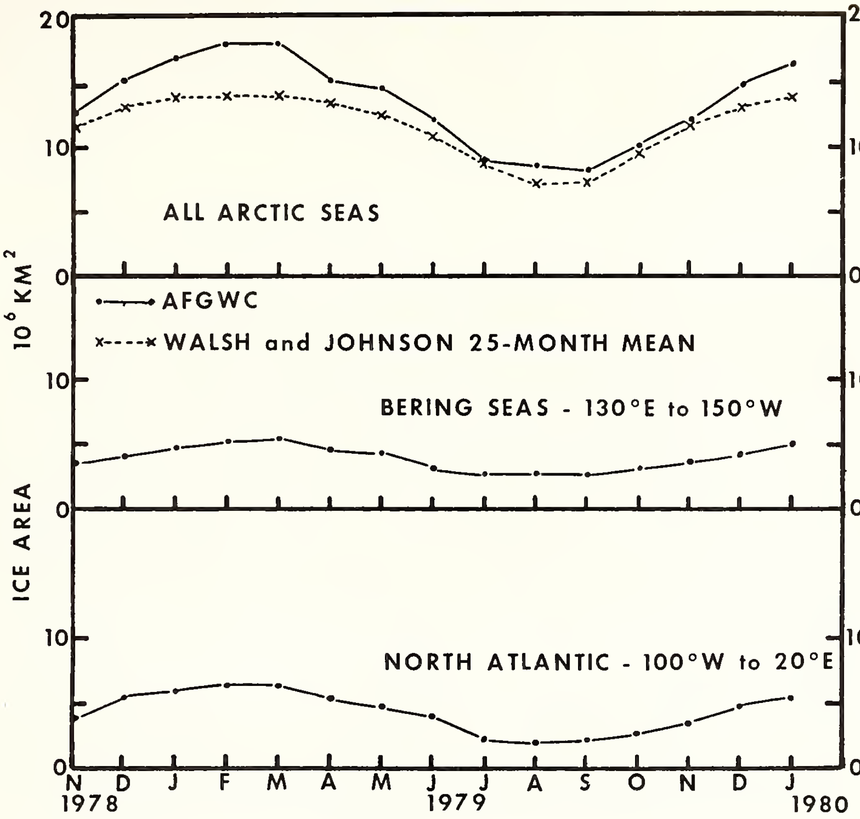

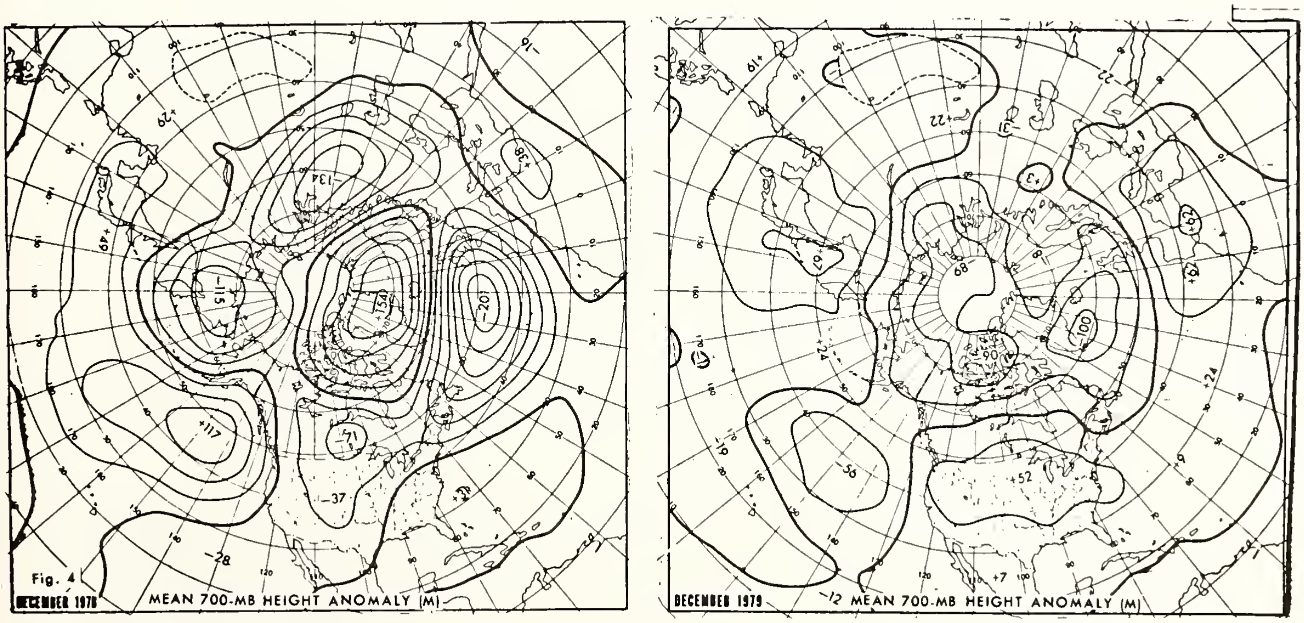

Fig. 4

Application of Near Real-Time Water Budgets in Monitoring Climate-Related Events

P.Y.T. Louie and W.I. Pugsley
Canadian Climate Centre
Atmospheric Environment Service
Downsview, Ontario

Introduction

It is possible to infer from the basic synoptic observations over a region, answers to such questions as: Where is there a drought situation? Where is the soil already saturated? Where is there a flooding potential? However, by integrating the basic observed synoptic fields using a water budget concept, answers to such questions are more apparent and they can be provided in greater detail. The purpose of this paper is to describe a framework in which near real-time water budgets are computed on a national scale in Canada using minimum synoptic data as input. Application of the resulting water budget products to identify and monitor significant climate-related events is discussed.

The Water Budget Model

The term water budget can have many meanings depending on the scale in which it is being considered. In this application, the term water budget will be defined as the short term accounting of the moisture conditions at a given location. Methods for computing water budgets at a location were advanced in the 1940's by the works of C.W. Thornthwaite in the U.S., H.L. Penman in England and M.I. Budyko in the U.S.S.R. There have since been numerous modifications to these three basic methods.

The choice of a water budget model for a particular application is determined in part by the input data available. Although synoptic network stations now observe a wide range of variables suitable as input for water budgets, models requiring minimum input data are the most practical for operational purposes. A simple model requiring minimum input data will maximize the number of stations for which water budgets can be computed. Furthermore, the problems with estimating values for missing data, which are unavoidable when working with real-time data, are also minimized.

The water budget model chosen for this application is the climatic water balance technique developed by Thornthwaite and Mather in 1955. This model is well known and widely used; thus its applications and limitations are well documented. Its input requirements are modest requiring only screen temperatures, precipitation, latitude, and an estimate of the soil water holding capacity. These variables are readily available. Soil moisture water holding capacities for the synoptic station locations were estimated based on soil texture classification by Agriculture Canada. Water holding capacities ranged from 100 mm for sandy loam to 280 mm for heavy clays. Because snow is an important variable in the Canadian climate, a simple snow budget routine was added to the original Thorthwaite and Mather model. This routine accumulates and melts snow depending on the daily screen temperature and provides a better accounting of the snow pack than the original model. A simplified flow chart of the model depicting its major components is given in figure 1.

Operational Procedure

A simplified flow chart of the data inputs and the computer routines used in the processing of the water budgets is shown in figure 2. At the present time, 225 Canadian synoptic stations are being processed. There are plans to include in the near future, approximately 100 northern U.S. synoptic stations to provide continuity across the international border. The time-step for these water budget computations is one day. This was chosen primarily to satisfy the requirement for the snowmelt computations. Present applications of the water budget products do not require such frequent time steps and in fact, it is unlikely that the simple water budget model used can provide this temporal resolution. Processing is therefore simplified by storing the daily input data in a eight day file and processing the water budgets every seven days. Only the seven day averages and accumulations of the water budget components are then analyzed. The computing time for all the processing shown in figure 2 is relatively small and should present no problems for any large main frame computer. The weekly output products include maps of selected fields, tabulations and a station file containing the current and the previous four weeks' water budget components for all stations. The latter is useful not only for providing the week to week changes (i.e. trends) in the water budget components, but it also provides the initial values for the next week's budget computations. Another important feature to note is the use of a normal weekly water budget component file of all the stations. This file was generated by applying the water budget model on the daily climatic normal temperature and precipitation data at each station. The weekly deviation from normal values can then be easily calculated for each water budget component at each station.

Application of Products

Table 1 lists the twelve water budget components tabulated weekly for each synoptic station. Selected components, their week to week change and their deviation from normal are mapped and their spatial patterns analyzed. Two components which have been found particularly useful for identifying and monitoring significant climate-related events are the snow storage and the soil moisture estimates.

The snow storage term computed at the end of each period represents an estimate of the snow water equivalent in the snow pack at a location. By mapping this term as shown in figure 3, an estimate of the spatial distribution of the water storage in the snow pack is obtained on a large spatial scale. Such maps should be an improvement over the mapping of snow depth values since the snow storage term is computed from actual gauge snow water equivalent measurements. On the other hand, because of the large spatial scale, these snow water equivalent estimates are not meant to compete or be comparable with the finer resolution snow survey measurements made for specific water basins. Mapping the week to week change of the snow storage term have also been found to be very informative. Figure 4 shows a map of the 14 day change in the snow storage from April 17 to 30, 1979. Three centers indicating snow pack depletion in excess of 100 mm can be easily identified. These centers coincided well with the widespread flooding experienced during that period in the Peace River, the Red River Valley, the Sturgeon River, the Ottawa River and the Saint John River. It is suggested that by monitoring the week to week change in the snow storage term, it is possible to identify potential flood regions and assess their severity.

The soil moisture term, because it simultaneously accounts for the precipitation and antecedent moisture availability and the evaporative demand of the atmosphere, has been found to be a useful indicator of drought and forest fires. Figure 5 is a map of the estimated soil moisture deviation from normal for May 26, 1980. The 30 per cent below normal isoline delineates well the areas in Saskatchewan, Manitoba and Northern Ontario experiencing drought conditions at that time. Figures 6 to 9 are maps of soil moisture estimates in per cent of the soil water holding capacity for the last weeks of May to August respectively. On each of these maps are also located the forest fire starts within each of those months. It can be seen that with a few exceptions, most of the forest fire starts for each month are located within areas with soil moisture estimates of less than 40 per cent of the soil water holding capacity.

Discussion

The application of a simple water budget model on basic synoptic data in effect increases the useful information from the basic input fields. However, the limitations of the model and the approximations involved in extending the point estimates from the model to the large spatial scale being considered should be stressed. It is not expected that the absolute values of the derived component fields are accurate. These component estimates should therefore be used only as indices and the emphasis is on the deviation of these components from their normal values and their week to week trends. The applications given in the previous section illustrates the use of the deviation from normal and weekly trend fields in identifying and monitoring significant climate-related events.

Reference

Thornthwaite, C.W. and Mather, J.R. (1955): The Water Balance. Publication in Climatology, Vol. 8, No. 1. Drexel Institute of Technology, Centerton

SIMPLE WATER BUDGET AT A LOCATION

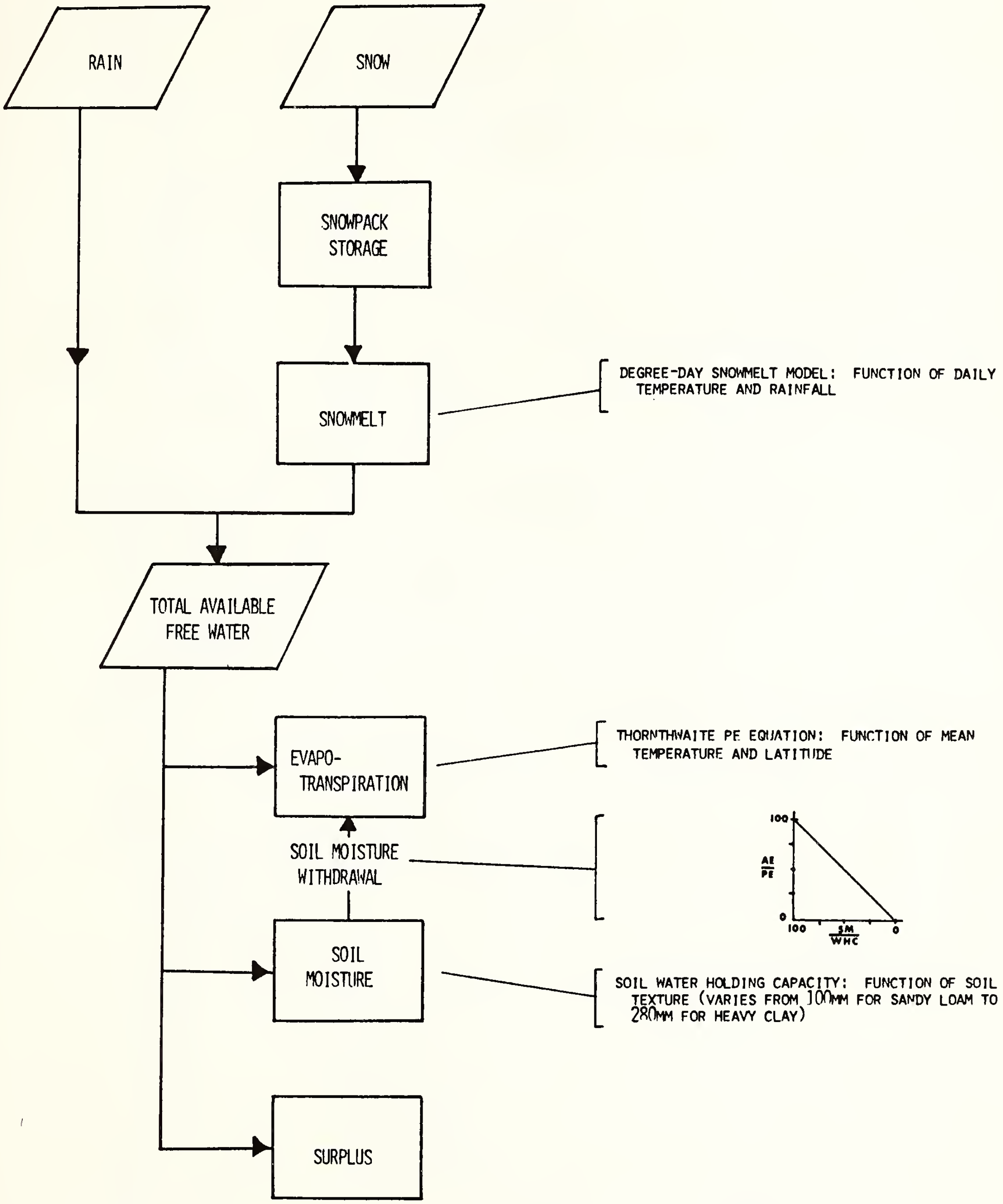

DEGREE-DAY SNOWMELT MODEL: FUNCTION OF DAILY TEMPERATURE AND RAINFALL

THORNTHWAITE PE EQUATION: FUNCTION OF MEAN TEMPERATURE AND LATITUDE

SOIL WATER HOLDING CAPACITY: FUNCTION OF SOIL TEXTURE (VARIES FROM 100MM FOR SANDY LOAM TO 280MM FOR HEAVY CLAY)

FIGURE 1

DATA FLOW FOR NEAR REAL-TIME WATER BUDGETS

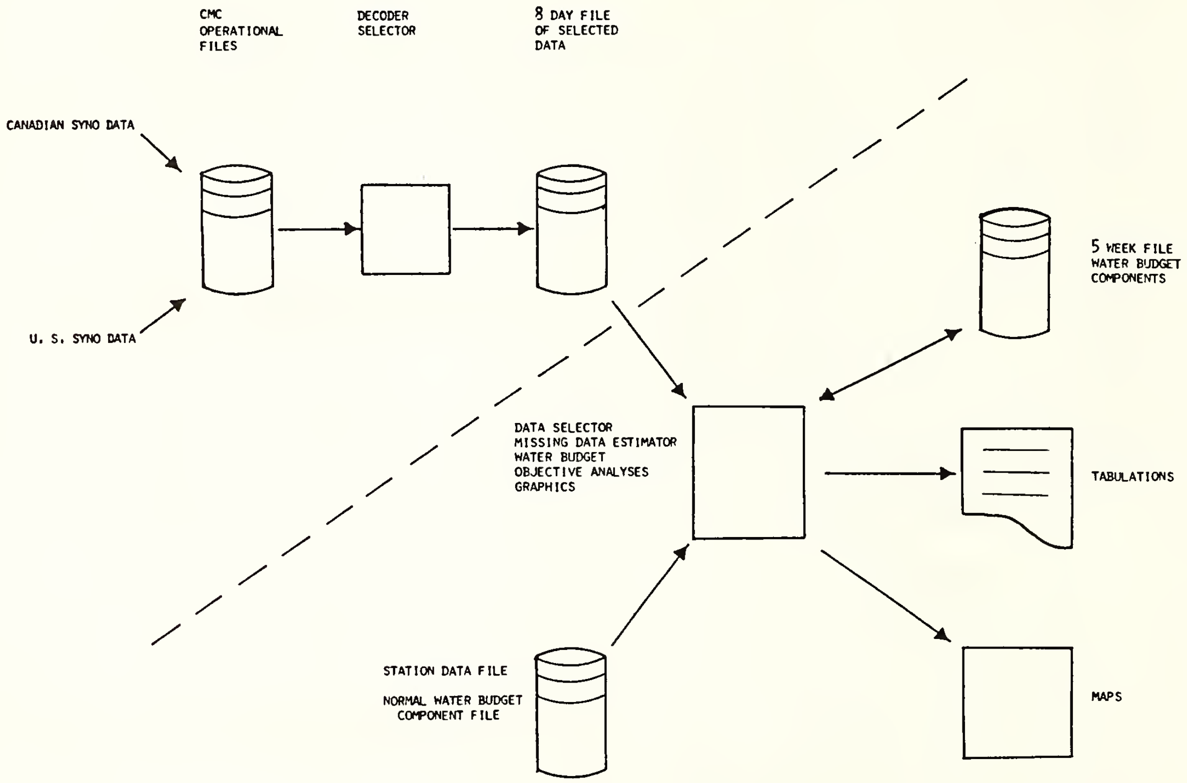

FIGURE 2

ACCUMULATED SNOW WATER EQUIVALENT ESTIMATES (MM)
FOR THE PERIOD ENDING 30 APRIL 1979

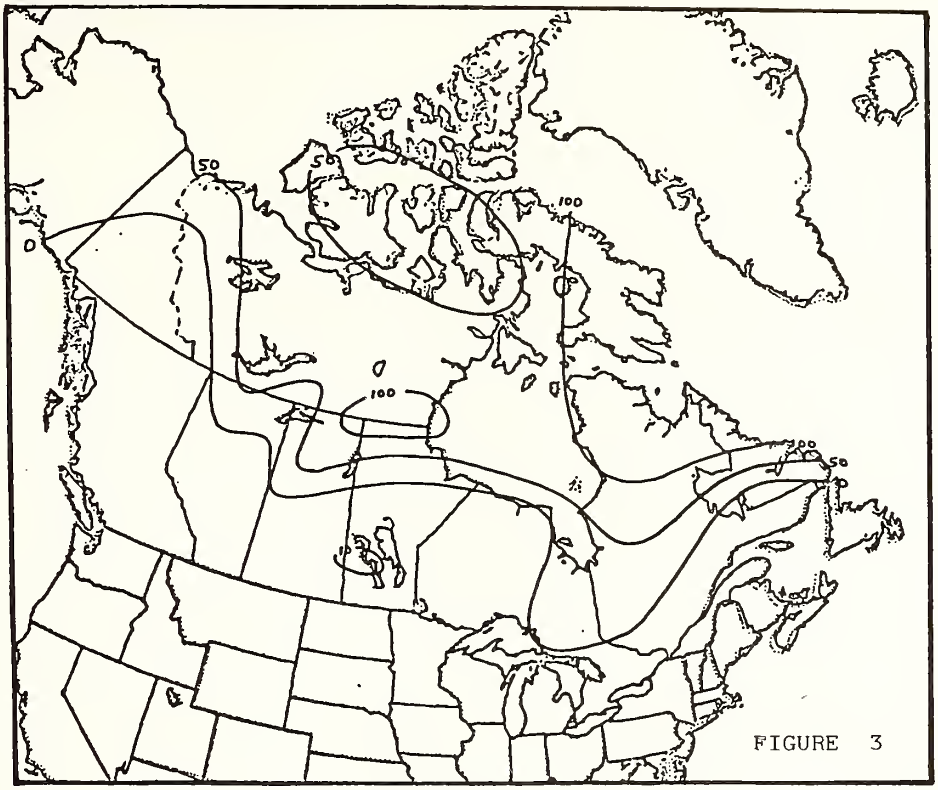

FIGURE 3

14-DAY CHANGE IN SNOW WATER EQUIVALENT ESTIMATES (MM)
FROM 17 APRIL 1979 TO 30 APRIL 1979

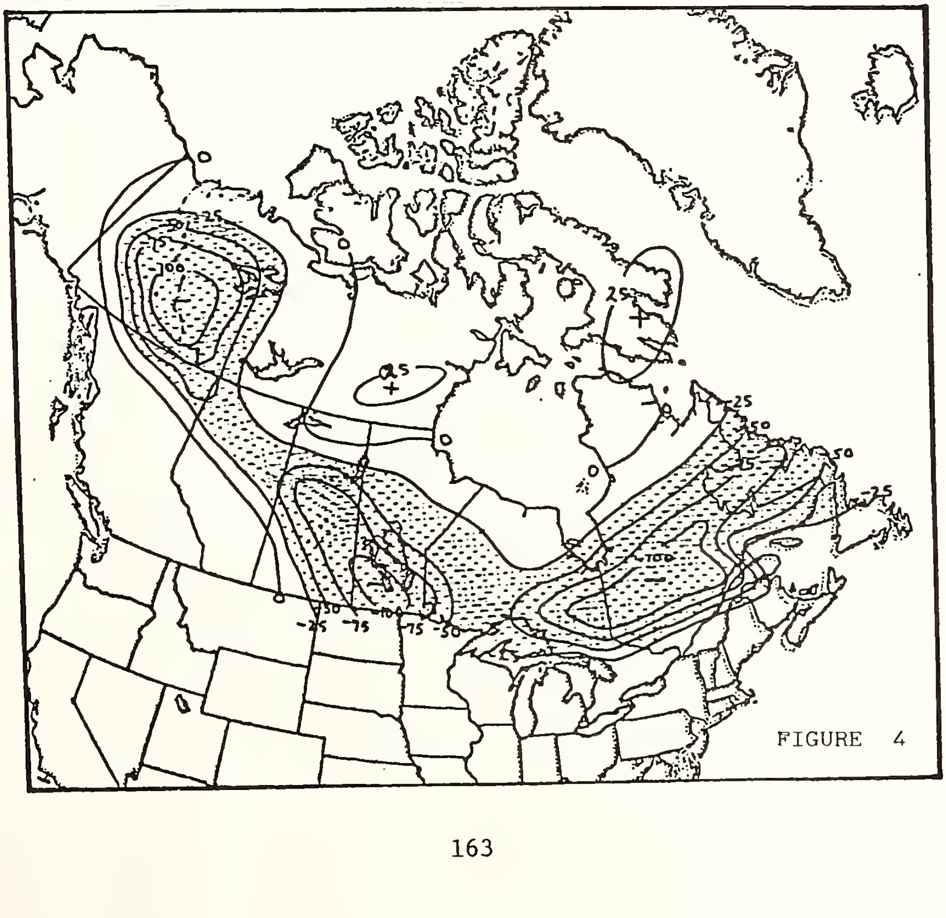

FIGURE 4

Table 1

Tabulated Water Budget Components For 7-Day Periods

1.	TEMPERATURE	- mean daily temperature for period (°C)
2.	RAIN	- total rainfall for the period (mm)
3.	SNOW	- total snowfall water equivalent for the period (mm)
4.	PRECIPITATION	- total rainfall plus snowfall water equivalent for the period (mm)
5.	ACCUMULATED PRECIPITATION	- total accumulated precipitation at the end of the period from the beginning of the water year (Oct. 1)
6.	SNOW STORAGE	- accumulated water equivalent of snow pack at the end of the period (mm)
7.	SNOW MELT	- total snow melt for the period (mm)
8.	POTENTIAL EVAPOTRANSPIRATION	- total potential evapotranspiration for the period (mm)
9.	ACTUAL EVAPOTRANSPIRATION	- total actual evapotranspiration for the period (mm)
10.	SOIL MOISTURE	- soil moisture storage at the end of the period (mm)
11.	DEFICIT	- total water deficit for the period (mm)
12.	SURPLUS	- total water surplus for the period (mm)

SOIL MOISTURE ESTIMATES DEVIATION FROM NORMAL IN PERCENT

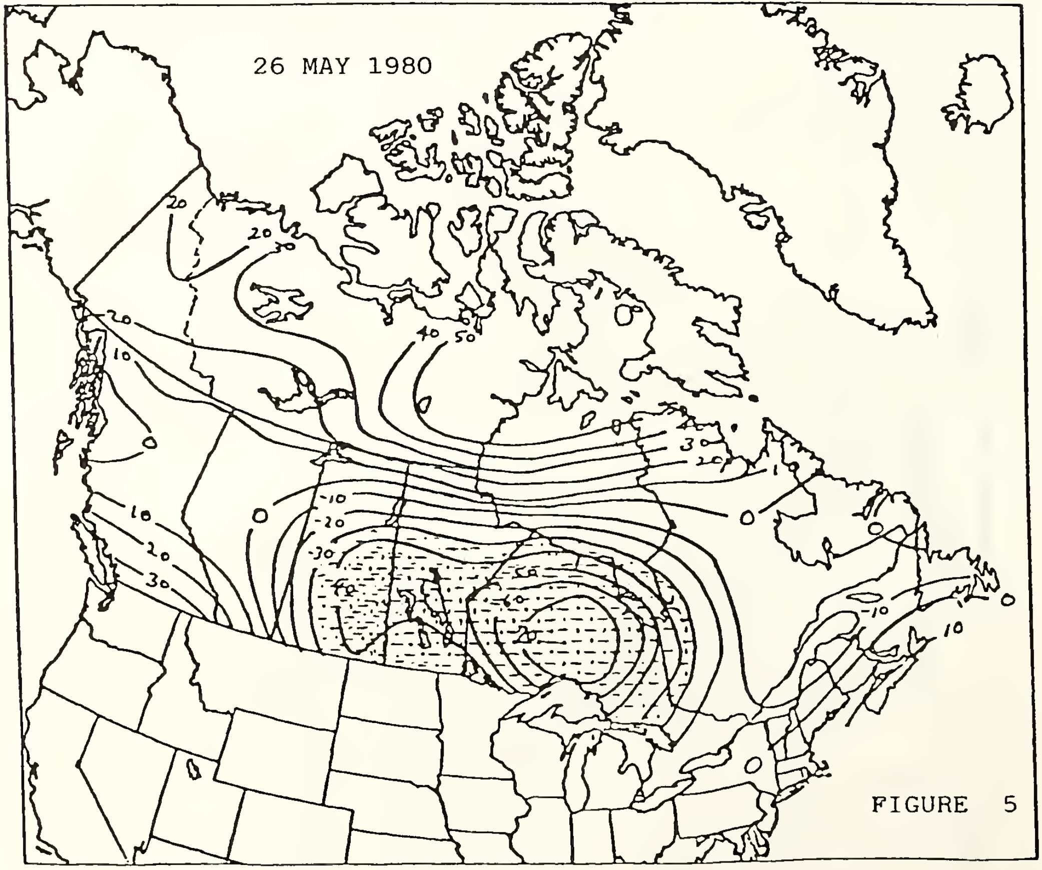

FIGURE 5

SOIL MOISTURE ESTIMATES IN PERCENT OF WATER HOLDING CAPACITY

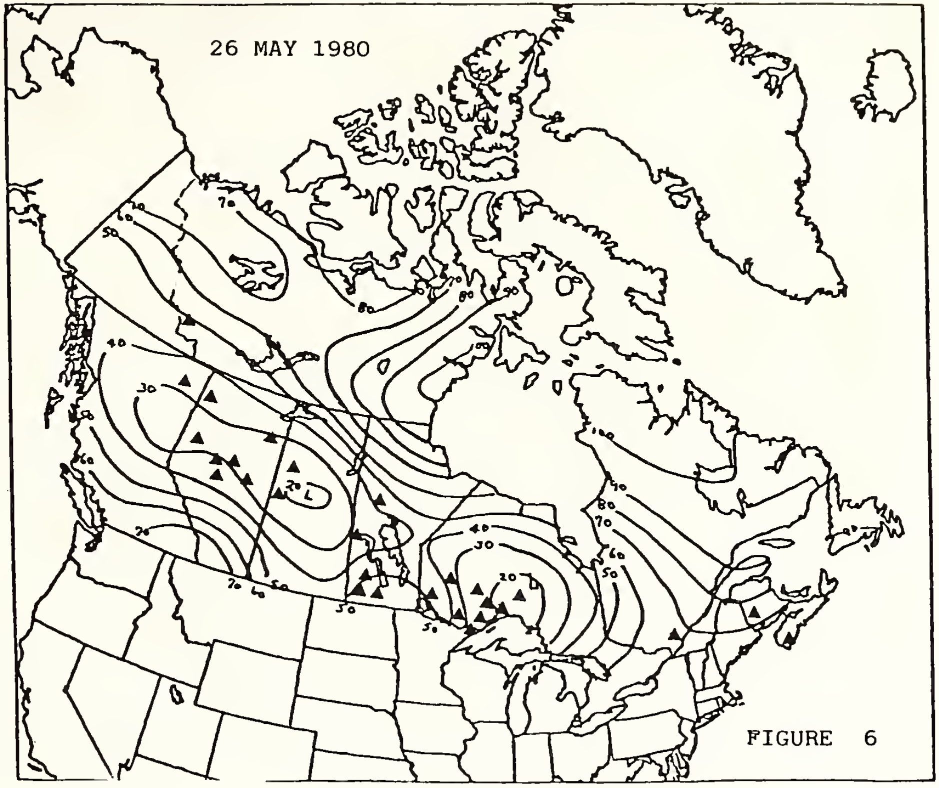

FIGURE 6

▲- FOREST FIRE LOCATIONS

SOIL MOISTURE ESTIMATES IN PERCENT OF WATER HOLDING CAPACITY

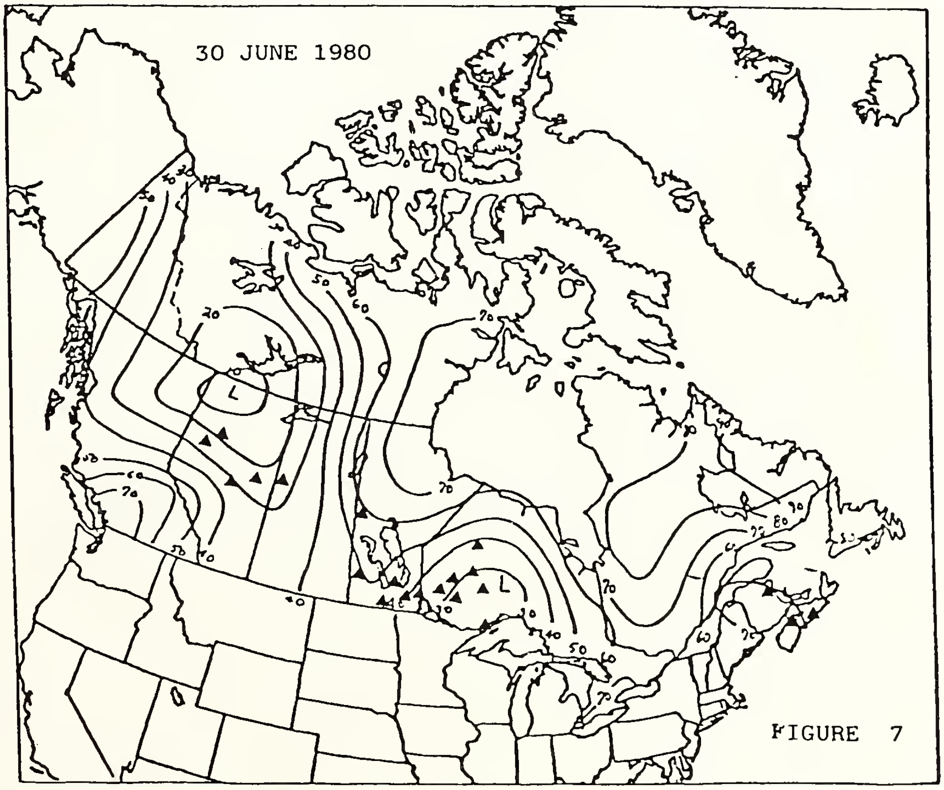

FIGURE 7

SOIL MOISTURE ESTIMATES IN PERCENT OF WATER HOLDING CAPACITY

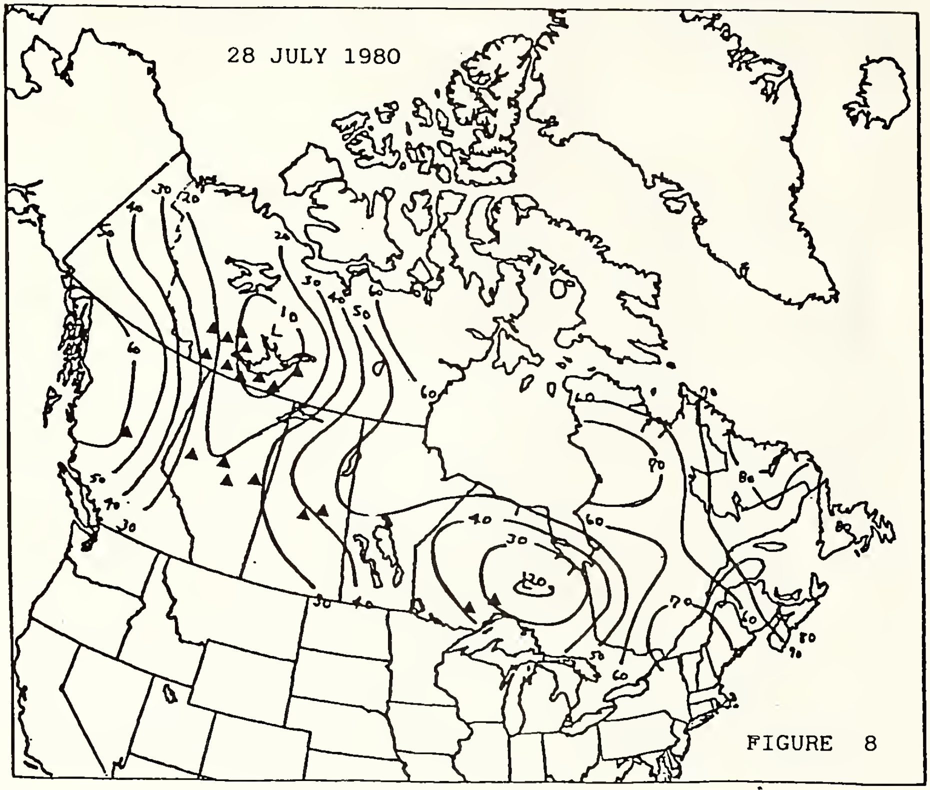

FIGURE 8

▲- FOREST FIRE LOCATIONS

SOIL MOISTURE ESTIMATES IN PERCENT OF WATER HOLDING CAPACITY

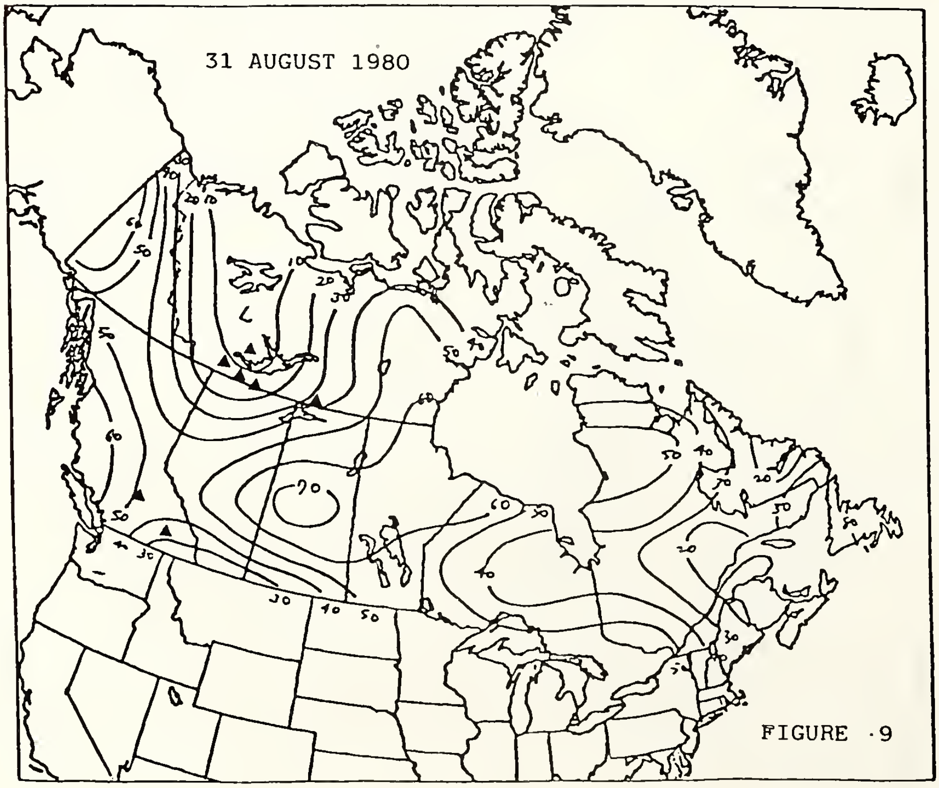

FIGURE ·9

Modeling Mean Annual Stratospheric Aerosol Loading in the Northern Hemisphere due to Large Volcanic Activity

Brian M. Goodman
Center for Climatic Research
Institute for Environmental Studies
University of Wisconsin
Madison, Wisconsin 53706

The goal of this study is to estimate the average annual contribution by "large" volcanic eruptions to the stratospheric aerosol load (SAL) over the Northern Hemisphere middle latitudes between 1883 to 1976. A "large" volcanic eruption is defined as one which directly injects material into the stratosphere. The degree of influcence an individual eruption has on the SAL depends upon its location, time of year, and magnitude, which determine the amount, vertical distribution, and atmospheric transport of the injected material (Figure 1).

A normalized synthetic mean annual SAL time series is constructed from the Hirschboeck volcano chronology by applying a simple time profile for the fraction of material (sulfur and ash) which remains suspended after an eruption to each date of eruption and integrating over the appropriate calendrical years. The Hirschboeck chronology lists the location and date of an eruption, and also a crude measure of its magnitude. Unfortunately, only her type 2 classification satisfies the criteria defined for a "large" eruption, such that in the model all "large" eruptions are assumed to be equal.

Neglecting transport processes, a simple time profile for the fraction of sulfur in the form of a 75% aequeous solution of H_2SO_4 is a function of the in situ gas-to-particle production rate and the gravitational fallout rate (Figure 2). For conditions prevailing in the lower stratosphere a conversion time constant of ≈115 days is used. From the literature a concensus height for the level of maximum H_2SO_4 concentration is taken to be 18 km for a "large" eruption, which corresponds to a mean residence time of ≈400 days. Similarily, the fraction of ash particles which remain suspended is only a function of the gravitional fallout rate (Figure 3). Again from the literature a consensus height for the level of maximum ash concentration ($r \leq 1$ μm) is taken to be 14 km, which corresponds to a mean residence time of ≈90 days. The H_2SO_4 and ash time profiles are combined (Figure 4) with a 2:1 weighting, respectively, and are normalized such that the total amount of material injected is set equal to one.

The normalized synthetic time series is separated into three latitude bands (50N $\leq$ Subpolar, 50N $<$ Middle Latitude $<$ 20 N, and 20N $\leq$ Equatorial $\leq$ 10S, Figures 5-7) and a multiple regression is performed against a time series of the mean annual aerosol optical depth composited from several middle latitude observations. The three latitude bands correspond to the three main circulation zones and also coincidentally to the three main belts of volcanic activity, such that the multiple regression coefficients will implicitly include any systematic differences between the average annual optical depth contributed by "large" eruptions in these three latitude bands due to differences in the atmospheric transports or in the eruptions themselves.

Over the entire period 1883 to 1976, the multiple regression coefficients (Figure 8) show that the subpolar eruptions contribute approximately twice as much to the mean annual middle latitude SAL, as a middle latitude or equatorial eruption, which is approximately the same amount as is always present in the background-constant. Note that on an annual time scale the contribution by an equatorial eruption would be divided half and half between the two hemispheres, such that the initial output of an equatorial eruption is probably equal to that of a subpolar eruption, and both contribute more than a middle latitude eruption. This result is in agreement with the observation that the largest eruption during the last few centuries have occurred at either subpolar or equatorial latitudes.

The mean annual SAL contributed by each latitude band according to the model is shown in Figure 9. Note that the total contribution to the SAL depends not only on the size of the eruption, but also upon the number of eruptions. The combined contribution by all the latitude bands according to the model is compared to the observed composite time series in Figure 10. Although the model statistically explains about 77% of the observed variance at the 99% significance level, there are some time periods where the agreement is not very good.

In the early part of the period, some of the discrepancies may be due to the poor quality of the data. But it also seems that the assumption that all "large" eruptions are equal is not valid, and that these differences need to be taken into account in more realistic time profiles. Also weaker eruptions may be contributing significant amounts of gaseous material to the stratosphere and their variations need to be considered. Towards both these ends work is currently in progress to improve both the aerosol optical depth data base as well as the volcano chronology data base. Improvements are also being made in the time profiles to include seasonal variations in the residence times and variations in the initial eruption cloud heights and water vapor content.

Figure Captions

Figure 1. Factors influencing the development of a volcanic aerosol veil.

Figure 2. Normalized fraction of total suspended H_2SO_4 aerosol. The small dashed line is the gas-to-particle production, the large dashed line is the gravitational fallout, and the solid line is the convolution of the two.

Figure 3. Normalized fraction of total suspended ash particles.

Figure 4. Fraction of total suspended ash and H_2SO_4 aerosol. The small dashed line is the H_2SO_4 time profile, the large dashed line is the ash time profile, and the solid line is the normalized 2:1 weighting combination of H_2SO_4:ash.

Figure 5. H_2SO_4 and ash aerosol loading by "large" subpolar eruptions.

Figure 6. Same for "large" middle latitude eruptions.

Figure 7. Same for "large" equatorial eruptions.

Figure 8. Multiple regression coefficients.

Figure 9. Volcanic contribution to aerosol optical depth by the three latitude bands. The lower clear area is the equatorial band eruptions, the solid area is the middle latitude band eruptions, and the upper clear area is the subpolar band eruptions.

Figure 10. The regression model for aerosol optical depth compared to the observations. The dashed line is the regression model results and the solid line is the observed values.

FACTORS INFLUENCING THE DEVELOPMENT OF A VOLCANIC AEROSOL VEIL

A. VOLCANIC AEROSOL INJECTION
    1. ASH
    2. GAS-TO-PARTICLE CONVERSION
        A. SULFATES
        B. CHLORIDES

B. VOLCANIC AEROSOL HEMISPHERIC DISTRIBUTION
    1. HORIZONTAL TRANSPORT
        A. MEAN FLOW
        B. EDDY DIFFUSIVITY

C. VOLCANIC AEROSOL OUTFLOW
    1. GRAVITATIONAL FALLOUT
    2. CROSS-EQUATORIAL FLOW
    3. VERTICAL TRANSPORT
        A. HADLEY CELL CIRCULATION
        B. JET CORE ACTIVITY
        C. CHANGES IN TROPOPAUSE HEIGHT
        D. EXTRA-TROPICAL CYCLONES

FIGURE 1

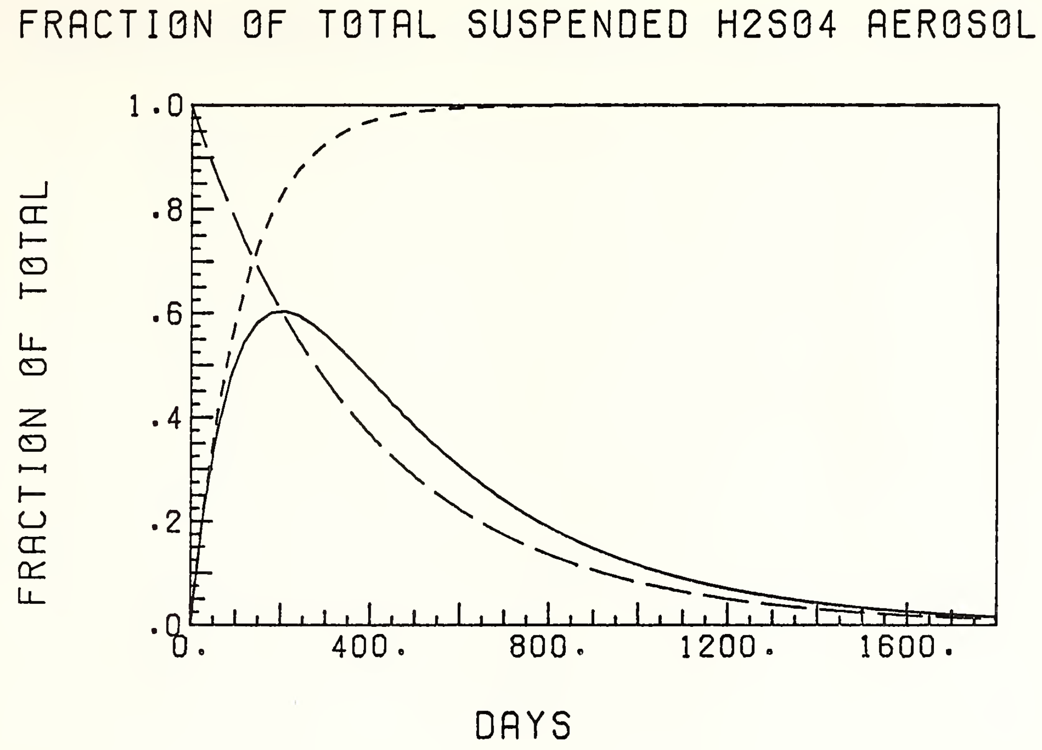

FIGURE 2

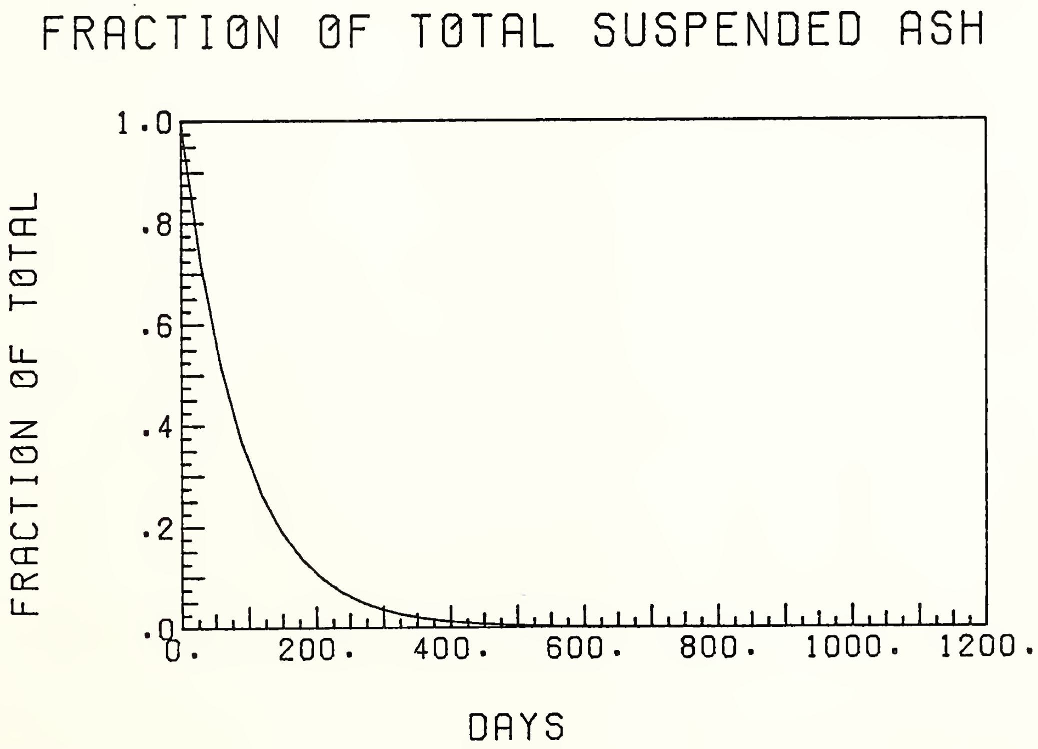

FIGURE 3

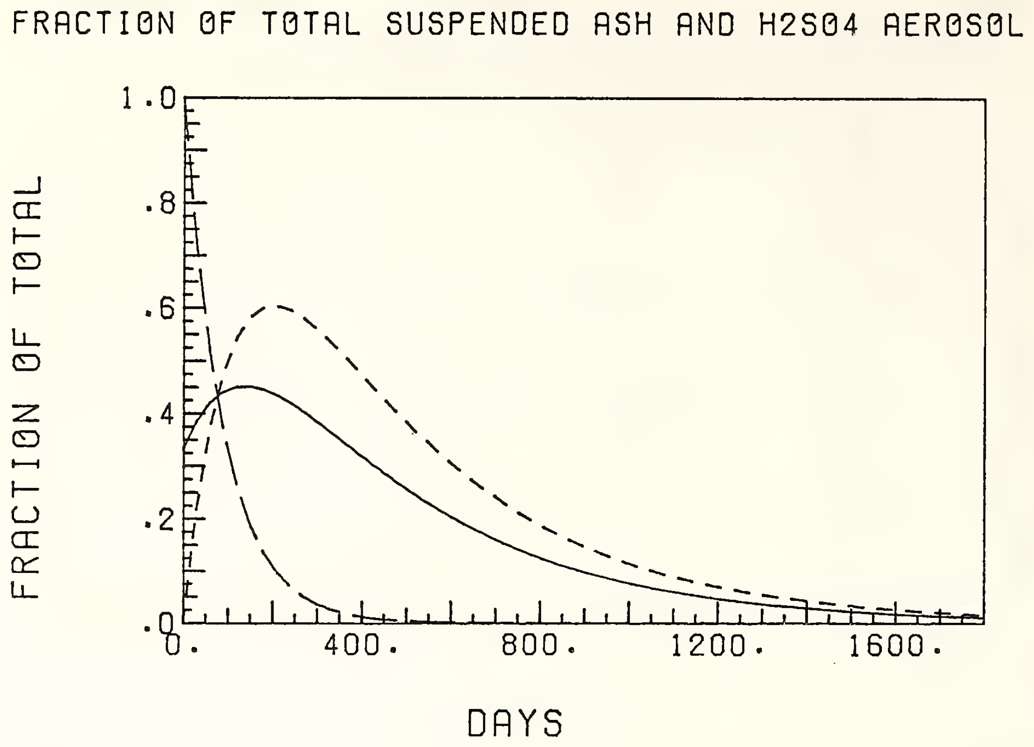

FIGURE 4

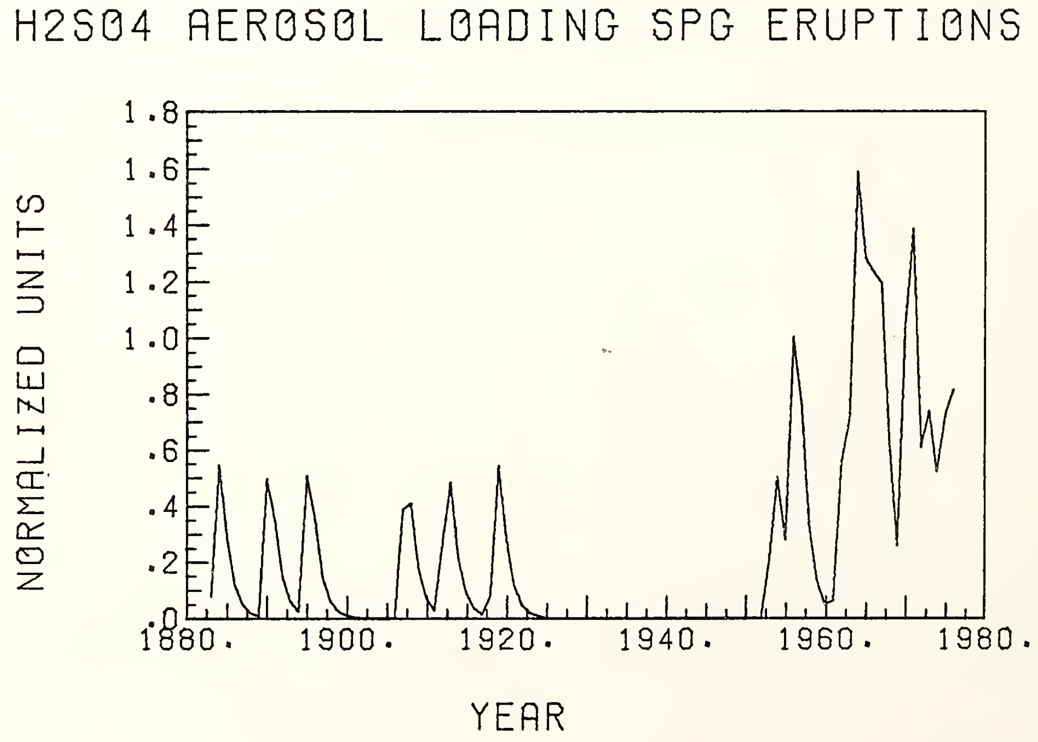

FIGURE 5

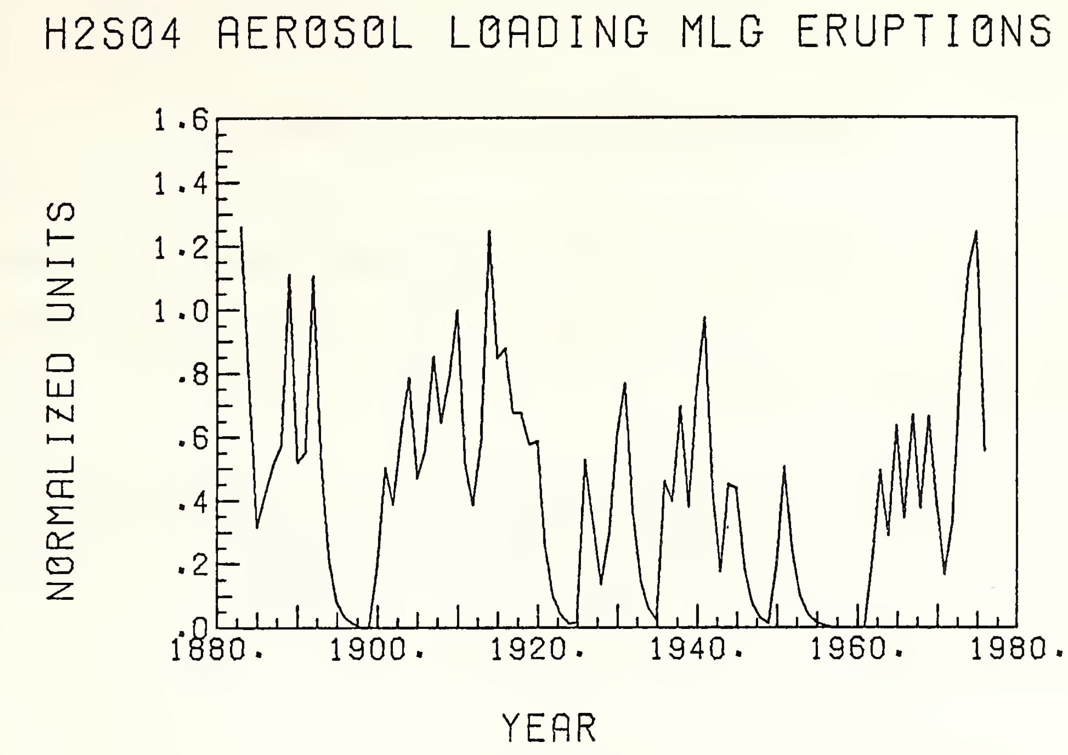

FIGURE 6

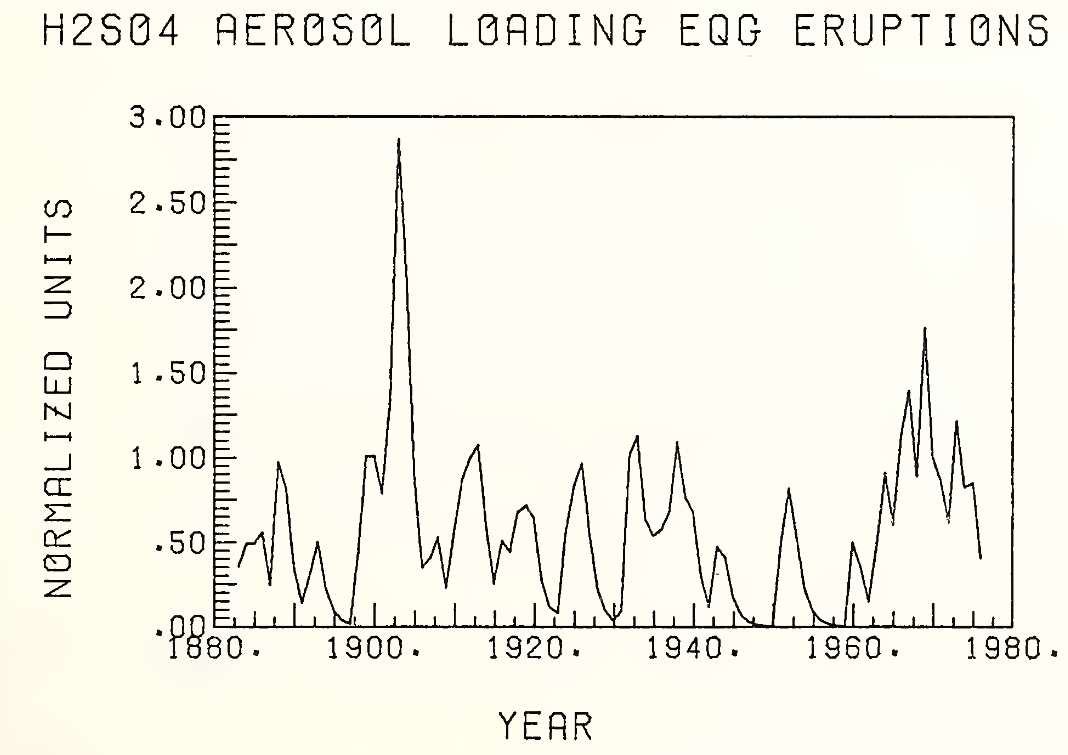

FIGURE 7

MULTIPLE REGRESSION COEFFICIENTS

THE MULTIPLE REGRESSION COEFFICIENTS REPRESENT THE AVERAGE ANNUAL CONTRIBUTION BY A SINGLE ERUPTION TO THE MEAN ANNUAL AEROSOL OPTICAL DEPTH.

MODEL I - REGRESSION OVER THE ENTIRE PERIOD 1883-1976

SUBPOLAR	0.030 ±0.004
MIDDLE LATITUDE	0.014 ±0.004
EQUATORIAL	0.016 ±0.003
CONSTANT	0.031 ±0.002

$R = +0.876$

$R^2 = 0.767$ (SIGNIFICANT AT THE 0.0010 LEVEL)

$SE = \pm 0.016$

FIGURE 8

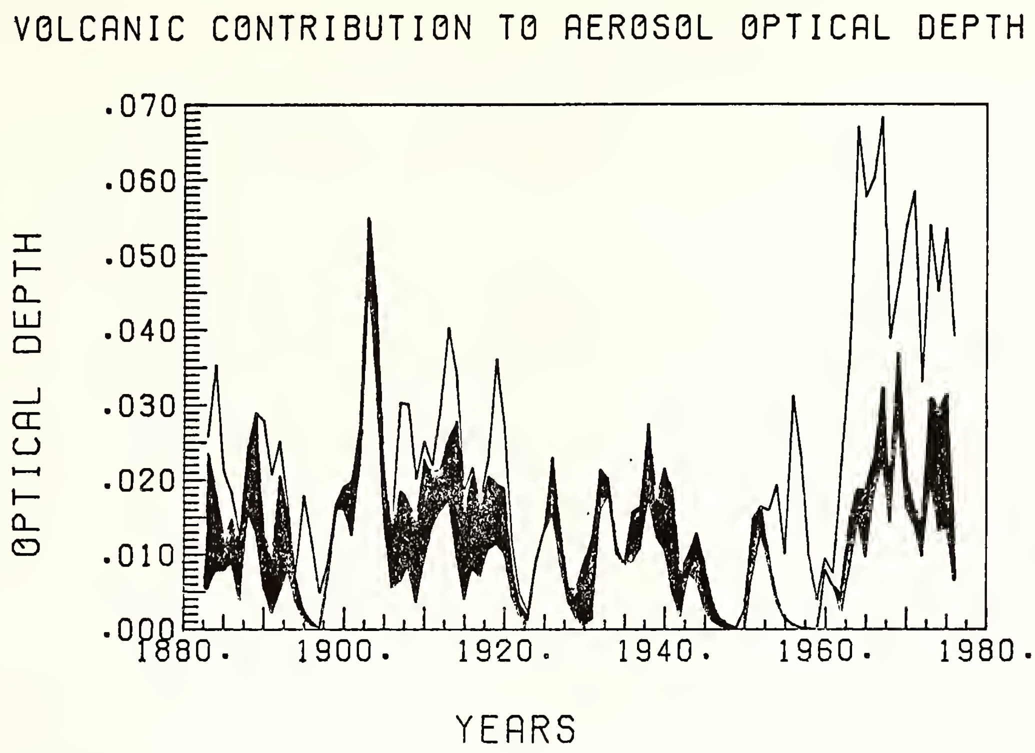

FIGURE 9

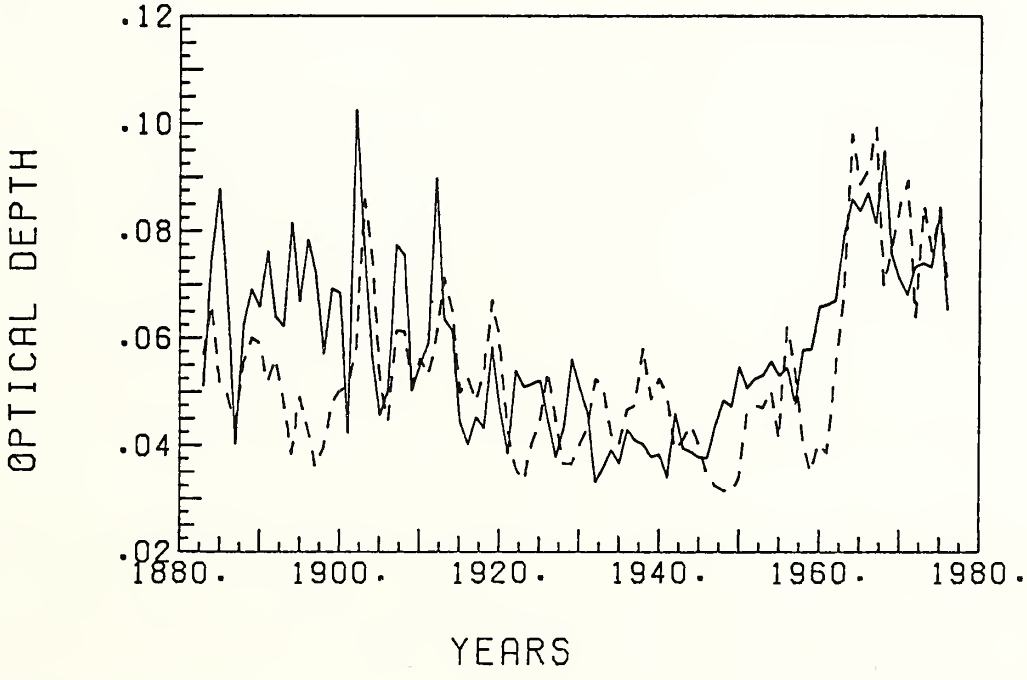

FIGURE 10

The Southern Oscillation and Global Anomalies in December, January, February

Harry van Loon
National Center for Atmospheric Research
Boulder, Colorado 80307

We defined the northern winters between 1899/1900 and 1977/78 when the Southern Oscillation (SO) reached extremes. These extremes we called HIGH/DRY and LOW/WET (H/D, L/W) according to the level of pressure in the tropical South Pacific Ocean and amount of rainfall in the equatorial Pacific. We averaged the sea level pressure on the Northern Hemisphere at grid points in the H/D and the L/W winters and subtracted the average of H/D from that of L/W. The residual is shown in Fig. 1 where the sign then is in the sense of the anomalies in L/W winters. Noteworthy are the west-east change of sign in the Pacific Ocean and the south-north change in the Atlantic Ocean, and the tendency for the Aleutian and Icelandic lows to be out-of-phase in position or intensity, or both.

We performed the same operation with the much lower number of years analyzed on the Southern Hemisphere. The map of the differences between L/W and H/D, Fig. 2, shows not only the well-known tendency for opposite pressure anomalies at lower latitudes in the area around Australia and in the South Pacific Ocean, but also a tendency for higher pressure in the South Pacific low and lower pressure in the westerly belt of the Indian and Atlantic Oceans during L/W than H/D years.

During the period when pressure-heights and temperatures at grid points are available at 700 mb on the Northern Hemisphere there were 9 L/W and 8 H/D winters. Figure 3 shows the difference, L/W minus H/D, in various quantities at this pressure level. The top curve demonstrates that the poleward flux of sensible heat in the quasi-stationary eddies was stronger at its peak in middle latitudes in the L/W winters. Consequently, the heat divergence south of 50°N was stronger in L/W years, the temperature (second curve) was lower over the region where the divergence was stronger, and the south-north contrast of temperature was larger south of 50°N and smaller north of 50°N in the L/W than in the H/D winters. The 700-mb height contrasts followed a similar pattern, as evidenced by the height differences in the third curve; and the zonal geostrophic wind, fourth curve, was thus stronger in L/W years south of 45°N and weaker north of 45°N than in H/D years. The flux of sensible heat in the transient eddies tended to be stronger in L/W than in H/D winters south of 45°-50°N where the latitudinal temperature contrasts were larger and the cyclonic shear more intense, and weaker north of 50°N.

The last illustration, Fig. 4, indicates that the stronger zonal wind in the subtropics and weaker wind at higher latitudes in December-January-February during L/W than during H/D, are found in both hemispheres (4 L/W and 3 H/D at 500 mb were used on the Southern Hemisphere; and 9 L/W, 8 H/D on the Northern Hemisphere). This points to a change in the meridional cells from one extreme of the SO to the other.

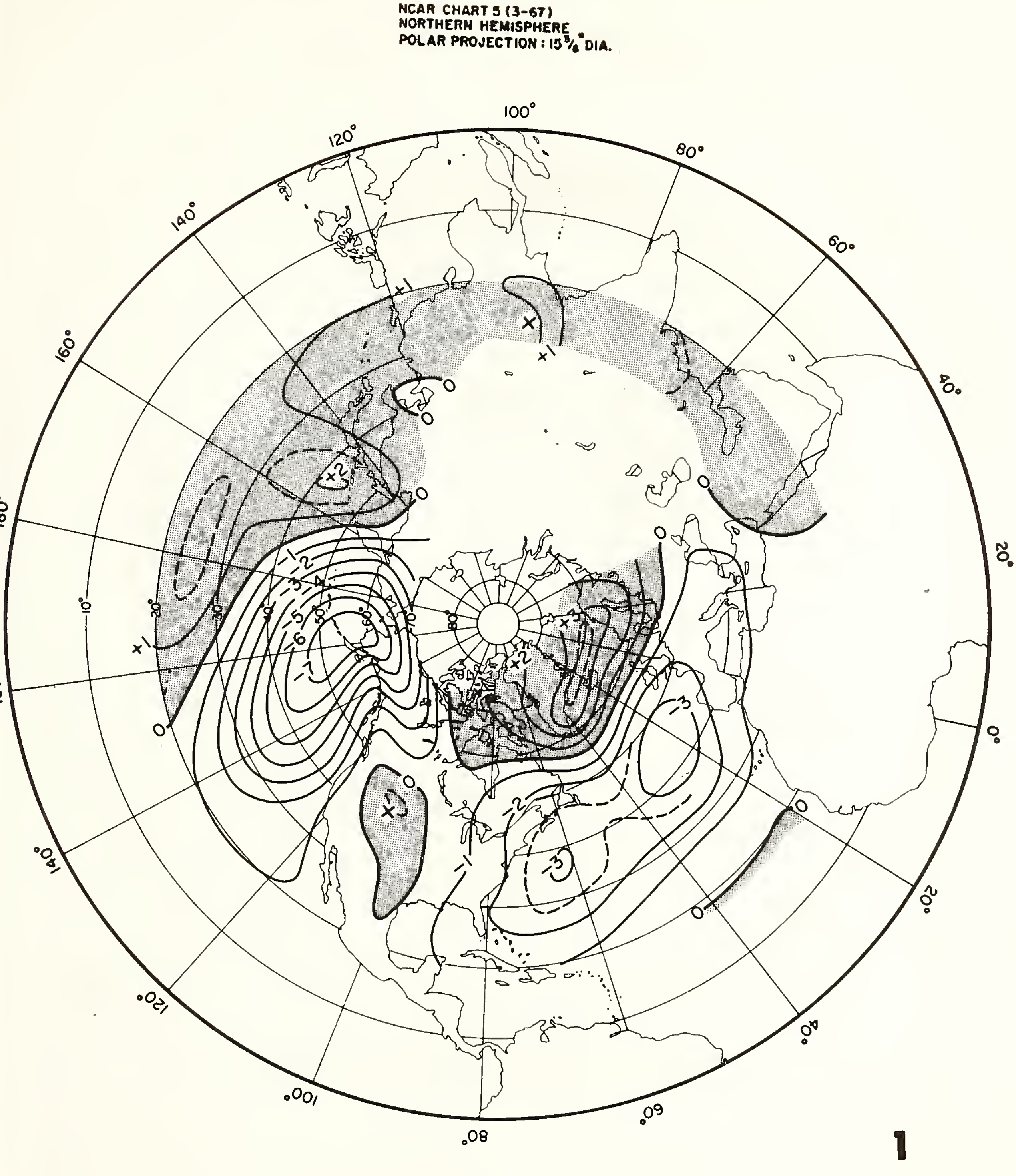

1

DIFFERENCE (mb) BETWEEN
LOW/WET (21 WINTERS) &
HIGH/DRY (19 WINTERS)

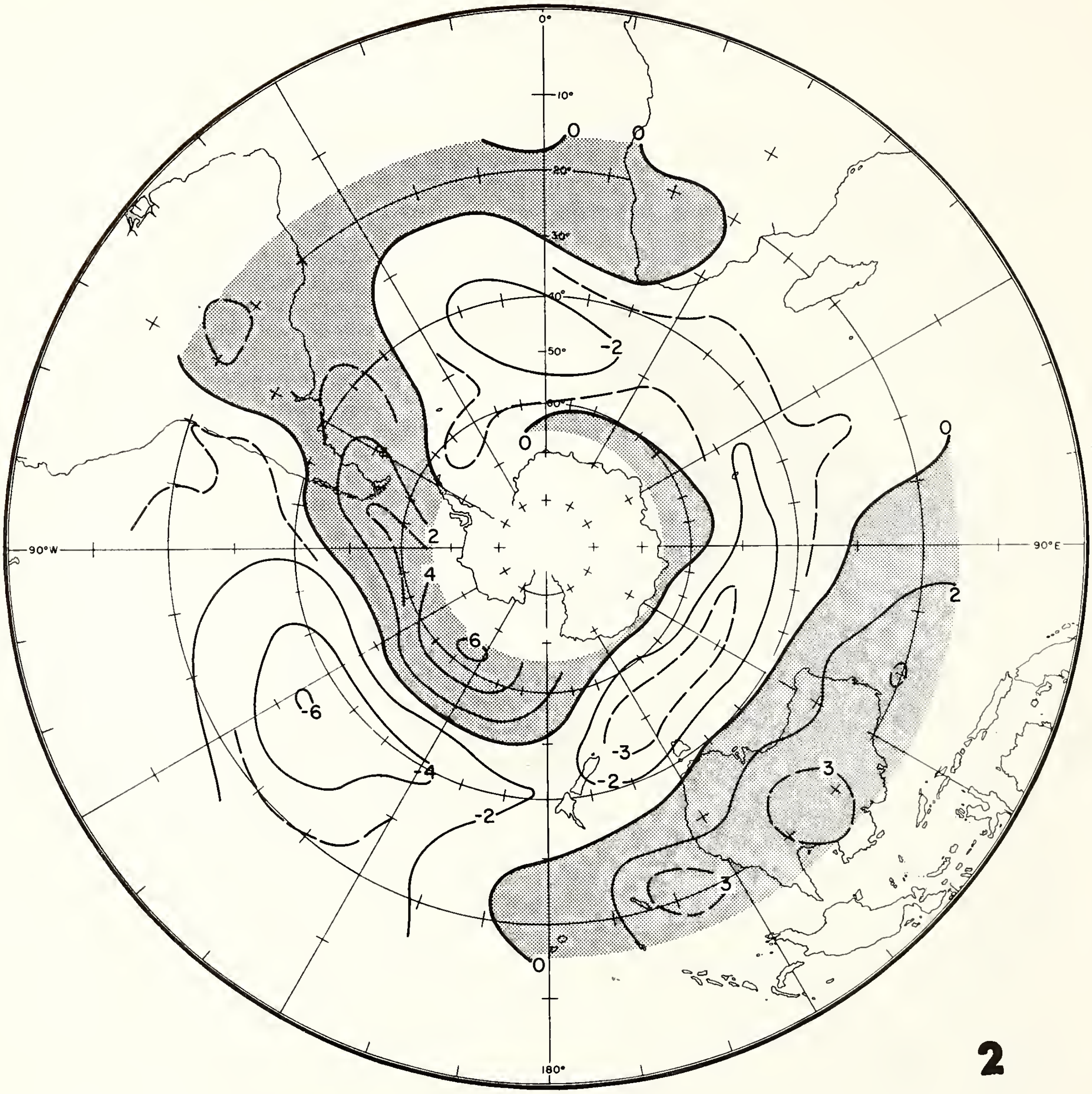

2

DIFFERENCE (mb) BETWEEN LOW/WET (5 summers)
AND HIGH/DRY (4 summers)

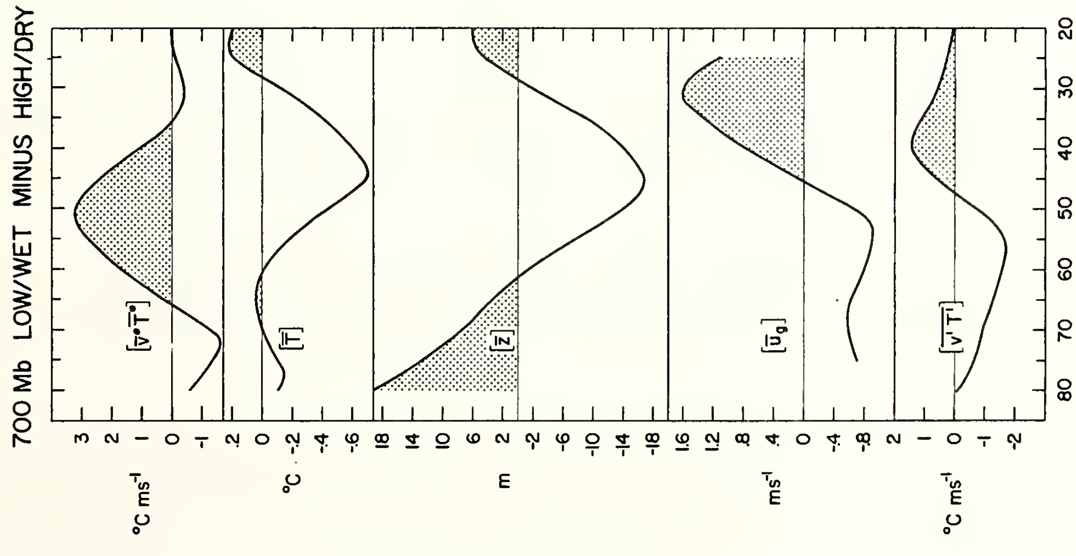
700 Mb LOW/WET MINUS HIGH/DRY
°C ms⁻¹
3
2
1
0
-1
[v̄*T̄*]
°C
.2
0
-.2
-.4
-.6
[T̄]
m
18
14
10
6
2
-2
-6
-10
-14
-18
[z̄]
ms⁻¹
1.6
1.2
.8
.4
0
-.4
-.8
[ū_g]
°C ms⁻¹
2
1
0
-1
-2
[v'T']
80
70
60
50
40
30
20
NORTH LATITUDE

3

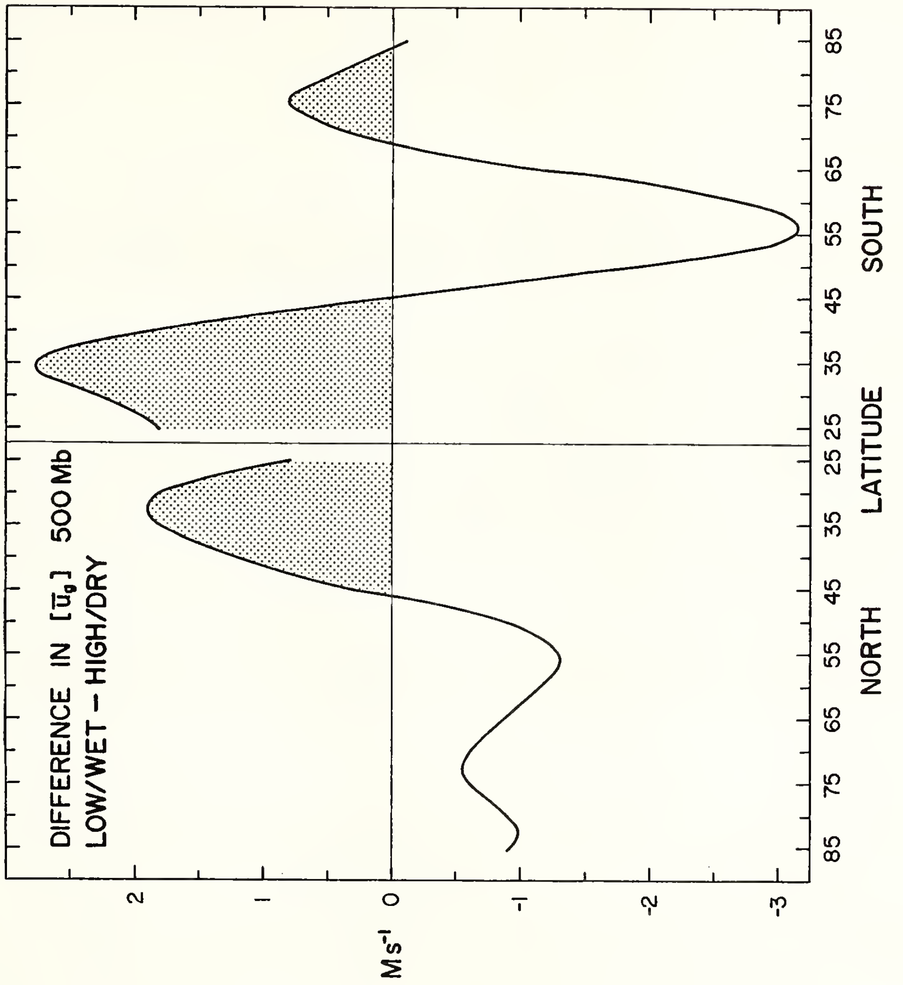
DIFFERENCE IN [ū_g] 500 Mb
LOW/WET − HIGH/DRY
Ms⁻¹
2
1
0
-1
-2
-3
85
75
65
55
45
35
25
25
35
45
55
65
75
85
NORTH
LATITUDE
SOUTH

4

Fluctuations in Mid and Upper Troposphere Flow Associated with the Southern Oscillation

P.A. Arkin, W.Y. Chen and E.M. Rasmusson
Climate Analysis Center
NMC/NWS/NOAA
Washington, D. C. 20233

1. Introduction

Variations in the 700-mb and 200-mb circulation associated with the Southern Oscillation (SO) are documented using Empirical Orthogonal Functions (EOF's), lagged cross-correlation, and composite analysis.

The analyses are derived from operational grid-point data. 700-mb data consist of departures from long term monthly mean height values for the period 1951-79 for the area north of 20°N. The 200-mb data consist of departures of wind component values (U, V) from mean monthly values for the period 1968-79 extracted from the NMC operational tropical analysis which spans the latitude band 48.6°N-48.6°S. A subarea of this grid, extending from 48.6°N-37.2°S and from 110°E through 180° to 150°W was used in the data analysis in order to exclude areas of questionable data quality.

The SO was defined by Southern Oscillation Index (SOI), consisting of the difference in normalized mean monthly surface pressure anomalies (unsmoothed) at Tahiti and Darwin.

2. 200-mb analyses

The first EOF (EOF 1) of the zonal wind component, derived from data for all months, is shown in Fig. 1. The most prominent feature of this EOF, which explains 16 percent of the total nonseasonal variance, is the three elongated areas of maximum variability centered over the Pacific. Note that variations near the Equator are out of phase with those in the northern and southern subtropics, a feature of the circulation previously noted by Chiu and Lo (1979) and Krueger and Winston (1979). Note also the eastward extension of these features into the Atlantic.

A link between EOF 1 and the SO is suggested by the equatorial Pacific cell which resembles the upper branch of the Walker circulation as hypothesized by Bjerknes (1969). The similarity of the time series associated with EOF 1 and the SOI (Fig. 2), which have a linear correlation of 0.66, reinforces the link.

Figure 3 shows the spatial distribution of the linear correlation coefficient (teleconnections) between the SOI and 200-mb U and V components. The U pattern resembles EOF 1. The V component pattern indicates confluence near the Equator between 140°E and 170°W and diffluence between 130°W and 90°W associated with high SOI.

The teleconnection statistics for the case of SOI leading the winds by four months (Fig. 4) show a similar pattern, but the eastward extension is more pronounced, with substantial areas of the Americas and the Atlantic having higher correlations than zero lag.

Teleconnection statistics have also been computed for the four individual seasons. These show significant variations from season to season, although the patterns all exhibit the same broadscale appearance of out of phase variations between Equator and subtropics. Composite analysis yield similar results, with the interesting feature that the eastward extensions of the three major centers of variability appear to be strongest in the high SOI case.

3. 700-mb analysis

Seasonal composites were constructed for both large positive and negative anomalies of SOI. The strongest SO signal appears in the winter composites when 700-mb anomalies lag the SOI by two seasons (Fig. 5). The pattern over the Pacific-North America-Atlantic sector of the midlatitudes is similar to that shown by Bjerknes (1972), Namias (1976), and Horel and Wallace (1981). Note particularly the pattern of low/high departures in the Gulf of Alaska, high/low departures over western North America, and low/high departures over the Eastern North America-Western Atlantic area associated with low/high SOI. The pattern of correlations between SOI and surface temperature anomalies presented by Wright (1977) closely agrees with that which would be expected from this anomaly pattern. An interesting feature is again the tendency for more pronounced Atlantic anomalies associated with the high SOI composite. This is particularly well illustrated by the existence of a broad area exceeding the 95 percent confidence value for the high SOI composite over the eastern North America/Western Atlantic area, while no point in this area exceeds the 95 percent limit for the low SOI composite.

Similar composites for the other three seasons, for zero lag, are shown in Figs. 6 and 7. The autumn pattern is similar to the winter pattern, with the Gulf of Alaska anomaly particularly well developed. The lag 1 and 2 signals are relatively weaker than their winter counterparts. The spring and summer signal is significantly weaker.

References

Bjerknes, J., 1969: Atmospheric teleconnections from the equatorial Pacific. Mon. Wea. Rev., 97, 163-172.

_________, 1972: Large-scale atmospheric response to the 1964-65 Pacific equatorial warming. J. Phys. Ocean., 2, 212-217.

Chiu, W. and A. Lo, 1979: A preliminary study of the possible statistical relationship between the tropical Pacific sea surface temperature and the atmospheric circulation. Mon. Wea. Rev., 107, 18-25.

Horel, J.D. and J.M. Wallace, 1981: Planetary scale atmospheric phenomena associated with the interannual variability of sea surface temperature in the equatorial Pacific. To be published in Mon. Wea. Rev.

Krueger, A and J. Winston, 1979: Further analysis of recent fluctuation in circulation and cloudiness (rainfall) over the tropics. Proceedings of the Fourth Annual Climate Diagnostics Workshop, October 16-18, 1979, Madison, Wisconsin, NOAA, U.S. Department of Commerce.

Namias, J., 1976: Some statistical and synoptic characteristics associated with El Nino. J. Phys. Ocean., 6, 130-138.

Wright, P.B., 1977: The Southern Oscillation: Patterns and mechanisms of the teleconnections and the persistence. Rep. HIG 77-13, Hawaii Institute of Geophysics. University of Hawaii, 107 pp.

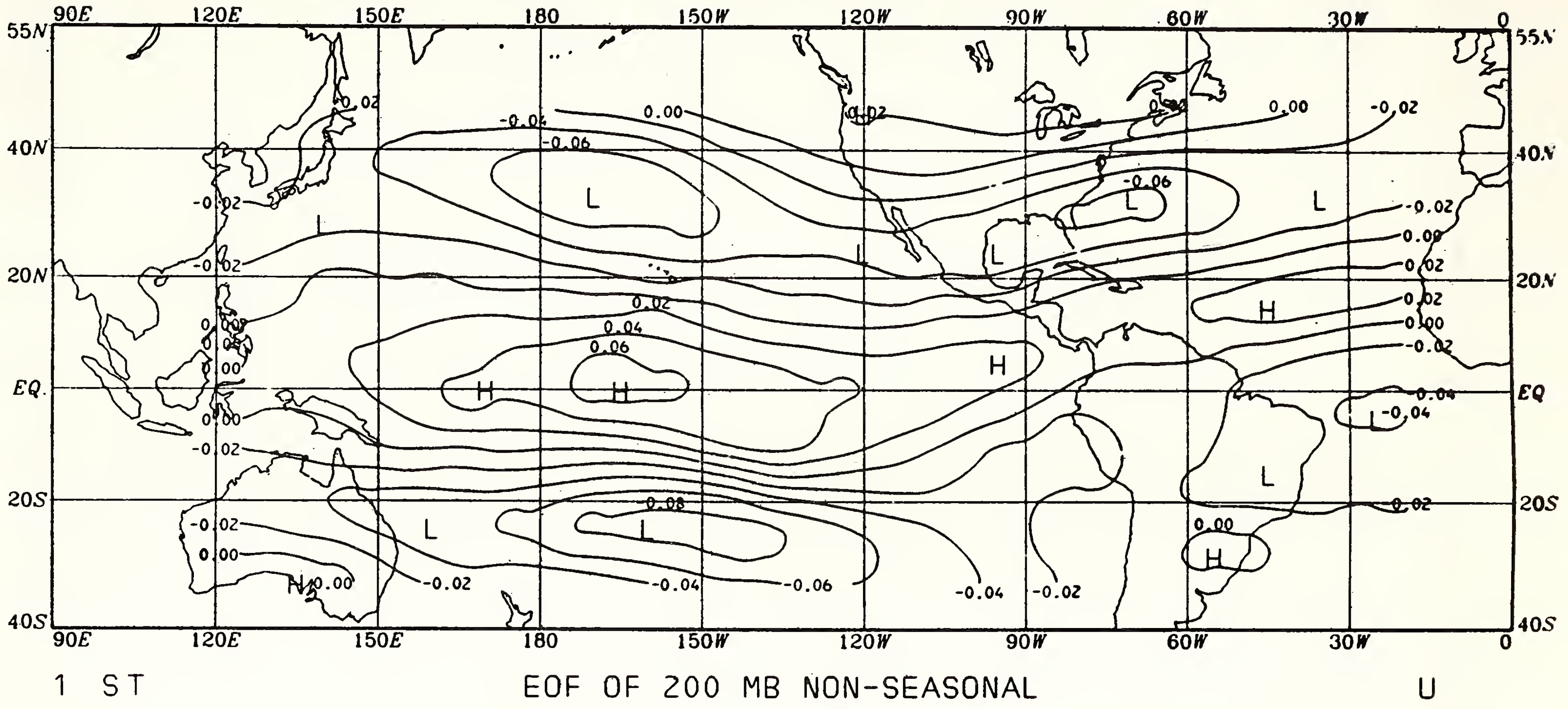

Fig. 1 First EOF (EOF 1) of departures from 200 mb mean monthly zonal winds.

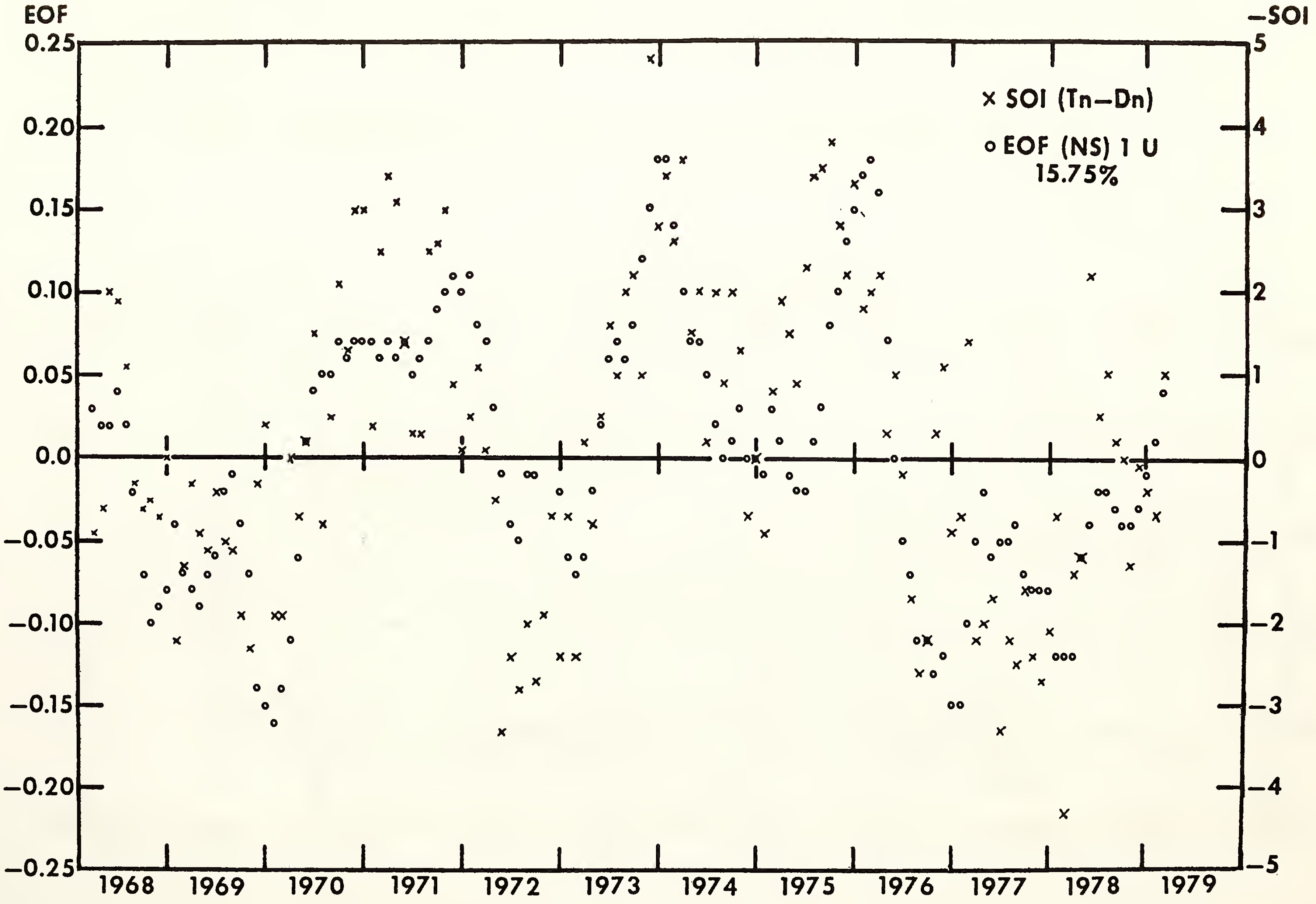

Fig. 2 Time series associated with EOF 1 (circles) plotted with SOI (crosses). Peak correlation of 0.66 occurs for SOI leading by 1 month.

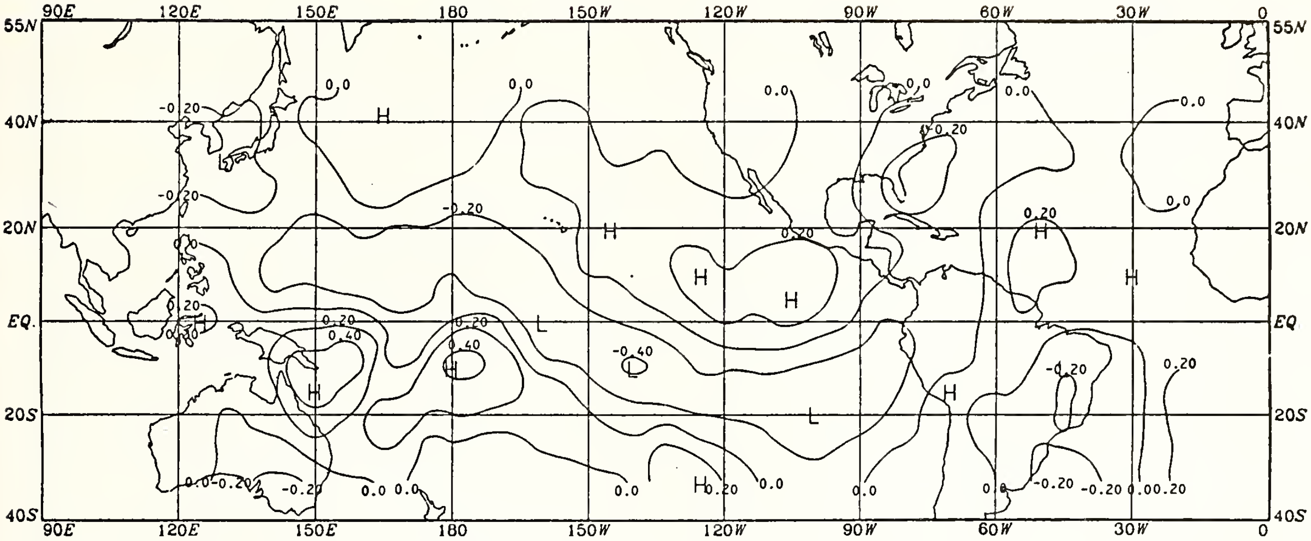

0 LAG CORRELATIONS OF SOI-U OR V V-TD

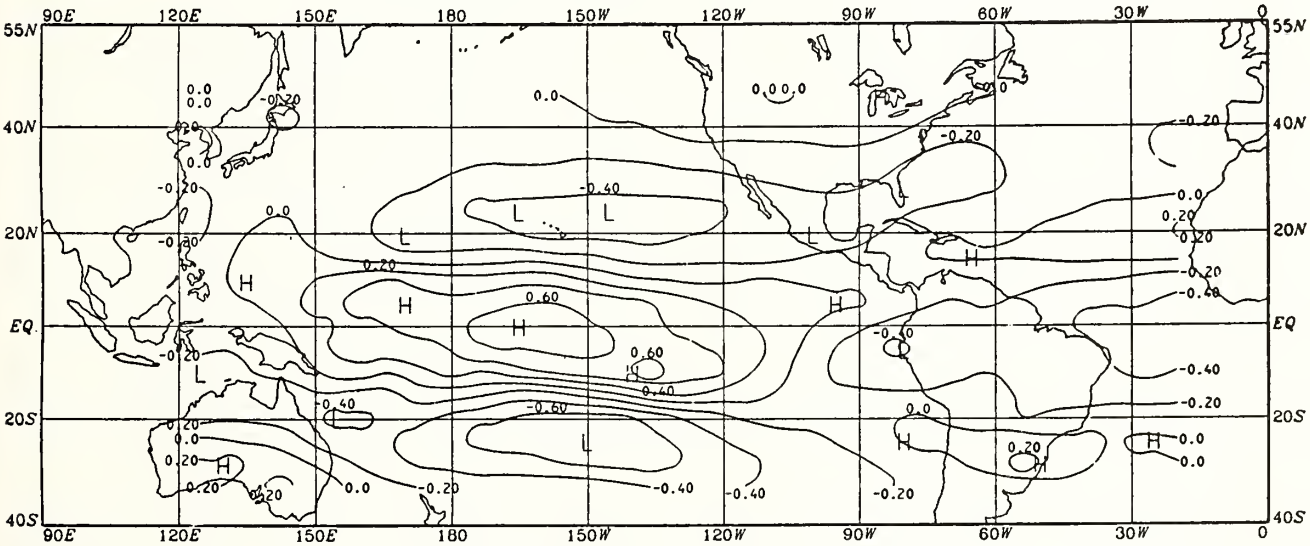

0 LAG CORRELATIONS OF SOI-U OR V U-TD

Fig. 3 Teleconnections (linear correlation at each grid point) between the 200 mb U 2(top) and V (bottom) component departures from monthly mean values and the SOI.

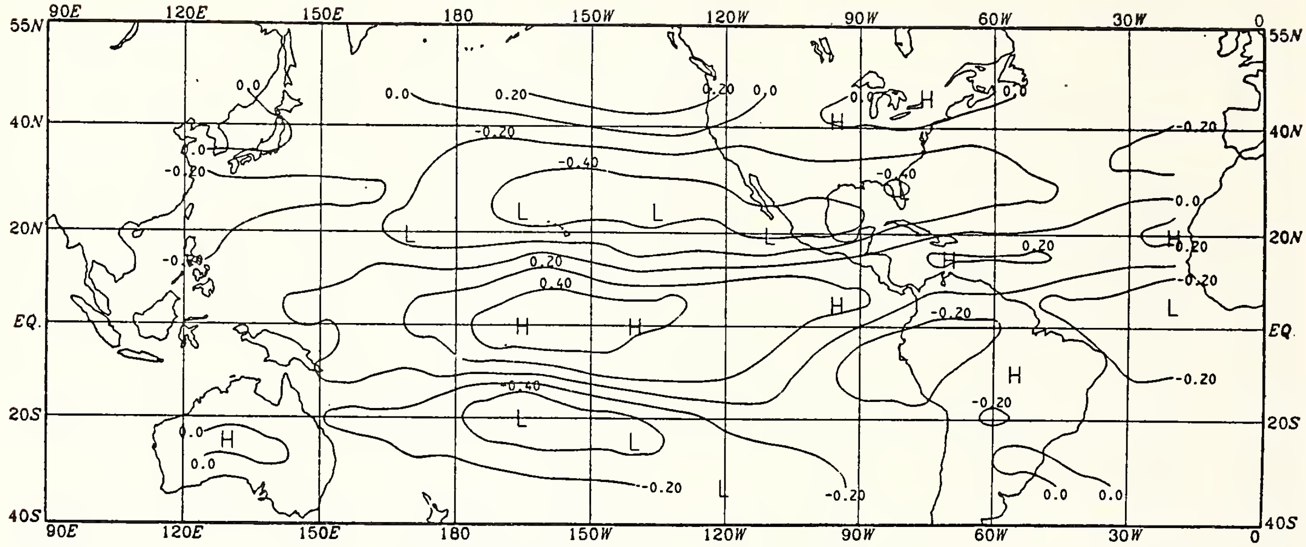

+4 LAG CORRELATIONS OF SOI-U OR V U-TD

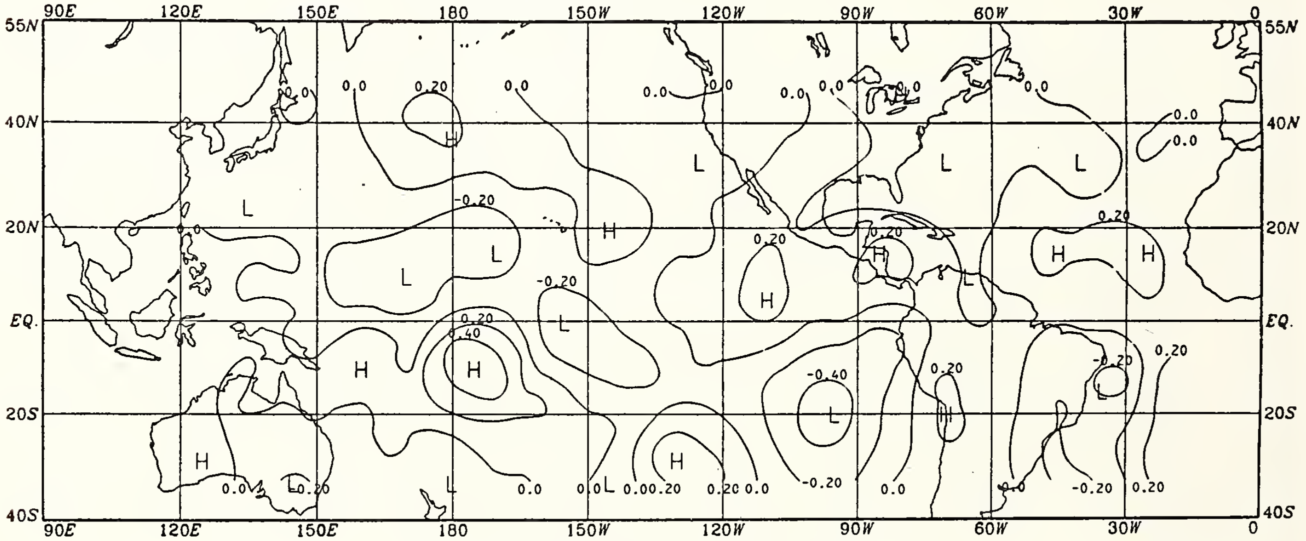

+4 LAG CORRELATIONS OF SOI-U OR V V-TD

Fig. 4 As in Fig. 3 but with the SOI leading by 4 months.

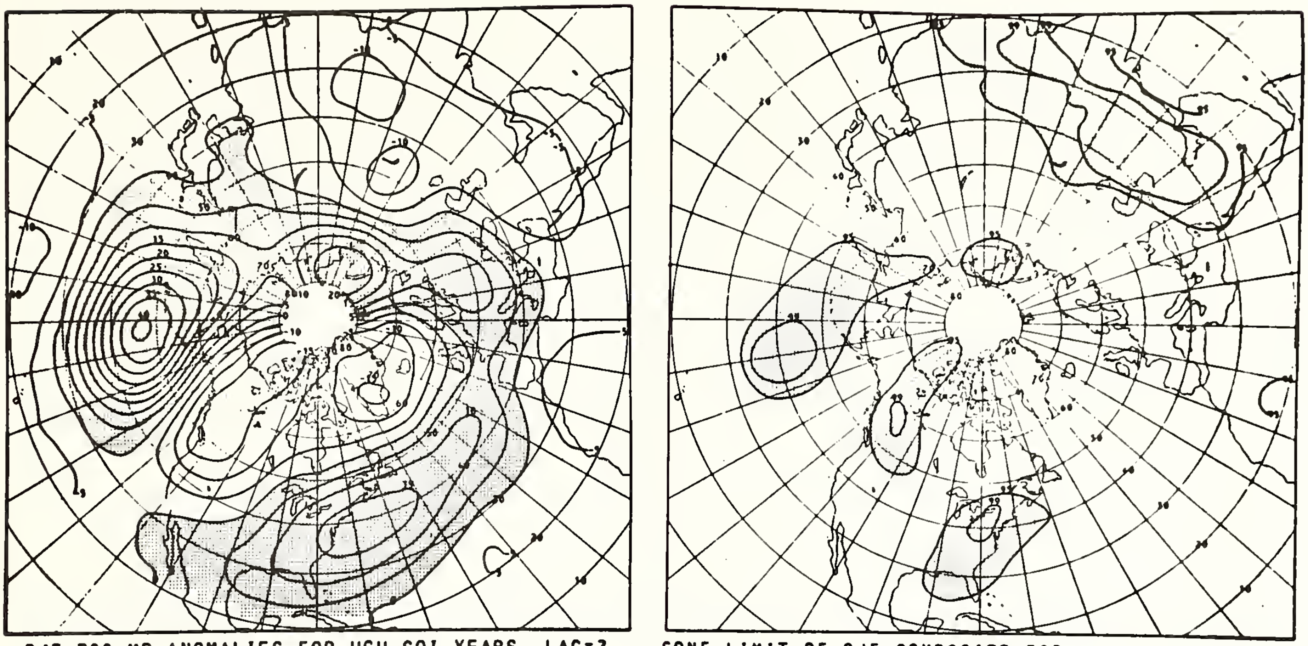

DJF 700 MB ANOMALIES FOR HGH SOI YEARS, LAG=2

CONF.LIMIT OF DJF COMPOSITE FOR HGH SOI YRS,LAG=2

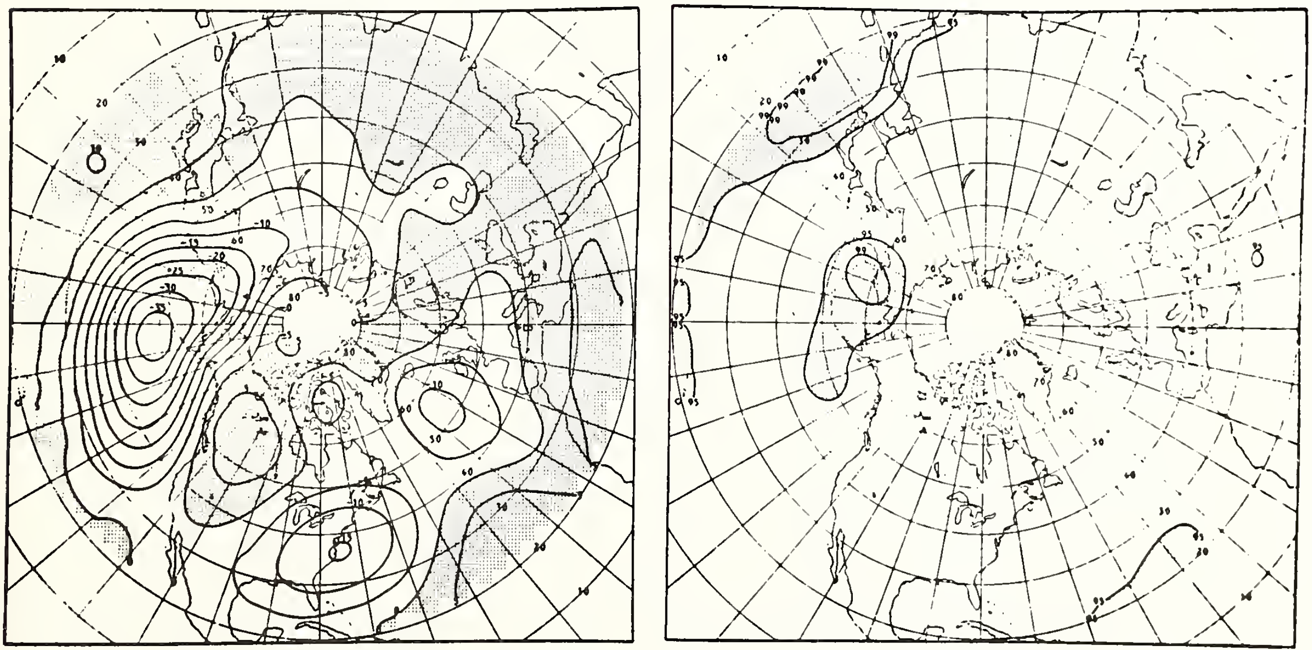

DJF 700 MB ANOMALIES FOR LOW SOI YEARS, LAG=2

CONF.LIMIT OF DJF COMPOSITE FOR LOW SOI YRS,LAG=2

Fig. 5 Winter composites of 700 mb height anomalies for high SOI values (upper) and low SOI values (lower), with SOI leading height field by two seasons.

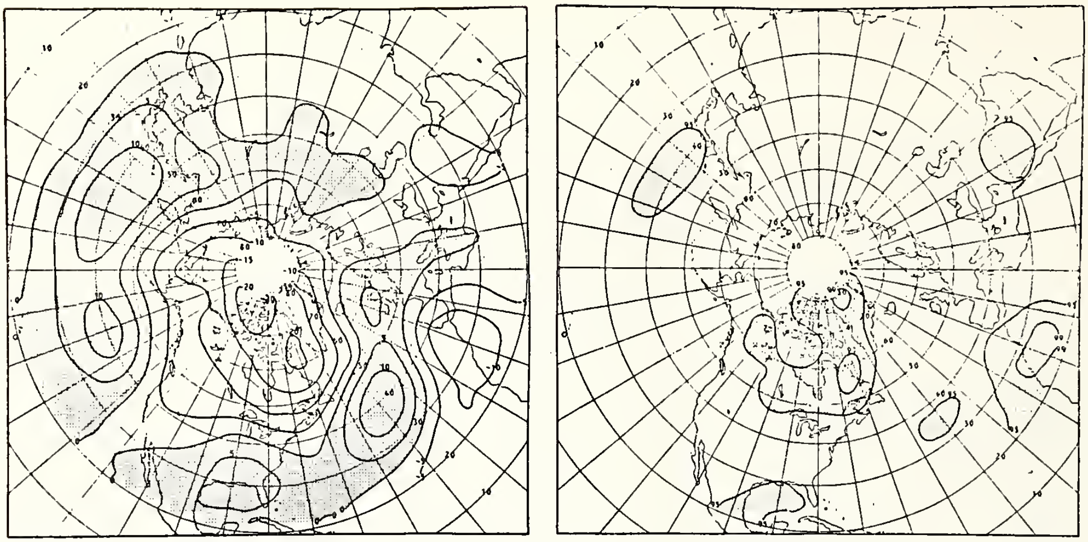

MAM 700 MB ANOMALIES FOR HGH SOI YEARS, LAG=0

CONF.LIMIT OF MAM COMPOSITE FOR HGH SOI YRS,LAG=0

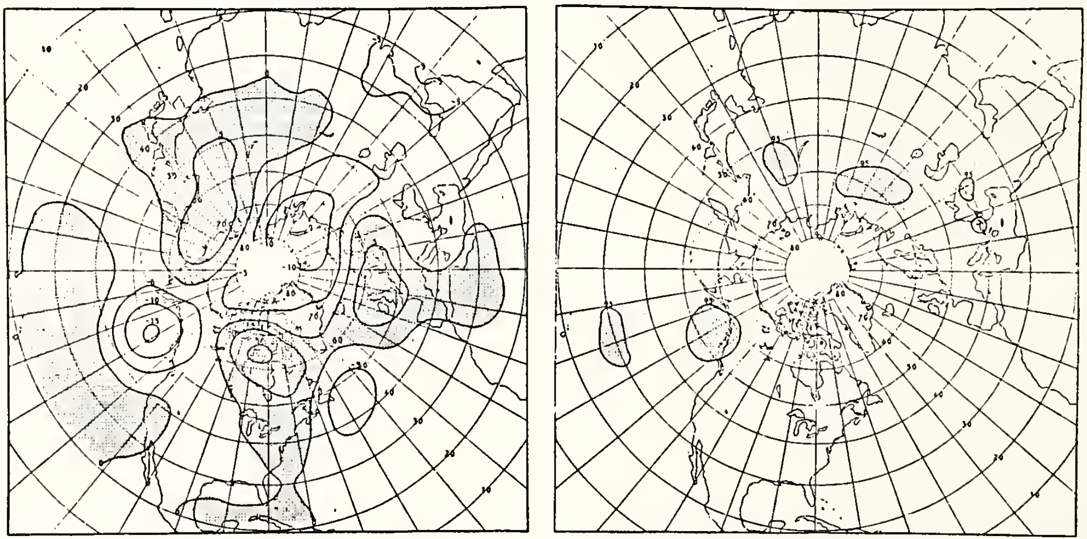

JJA 700 MB ANOMALIES FOR HGH SOI YEARS, LAG=0

CONF.LIMIT OF JJA COMPOSITE FOR HGH SOI YRS,LAG=0

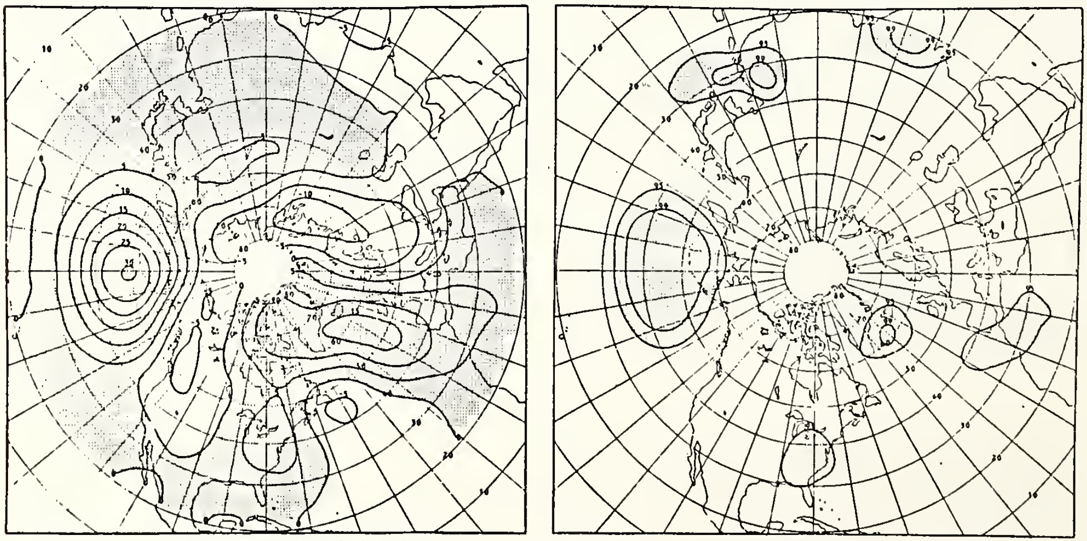

SON 700 MB ANOMALIES FOR HGH SOI YEARS, LAG=0

CONF.LIMIT OF SON COMPOSITE FOR HGH SOI YRS,LAG=0

Fig. 6 Composites for other three seasons, with zero lag, for high SOI values.

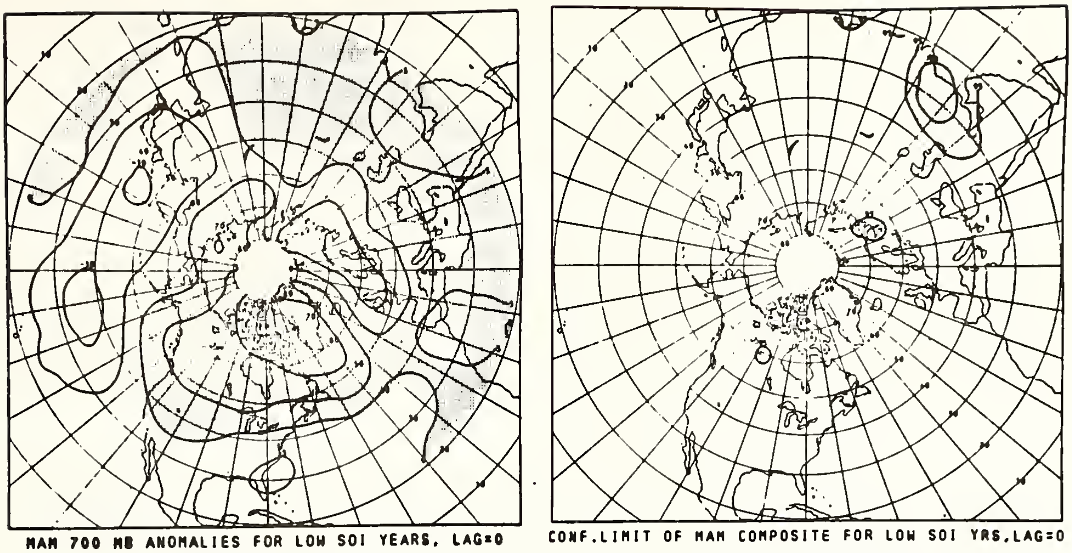

MAM 700 MB ANOMALIES FOR LOW SOI YEARS, LAG=0

CONF.LIMIT OF MAM COMPOSITE FOR LOW SOI YRS,LAG=0

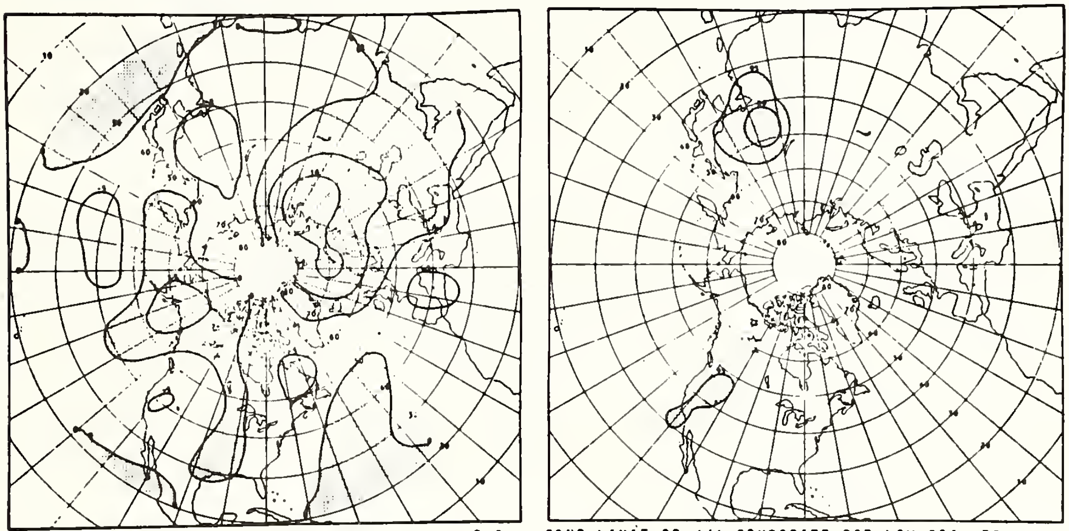

JJA 700 MB ANOMALIES FOR LOW SOI YEARS, LAG=0

CONF.LIMIT OF JJA COMPOSITE FOR LOW SOI YRS,LAG=0

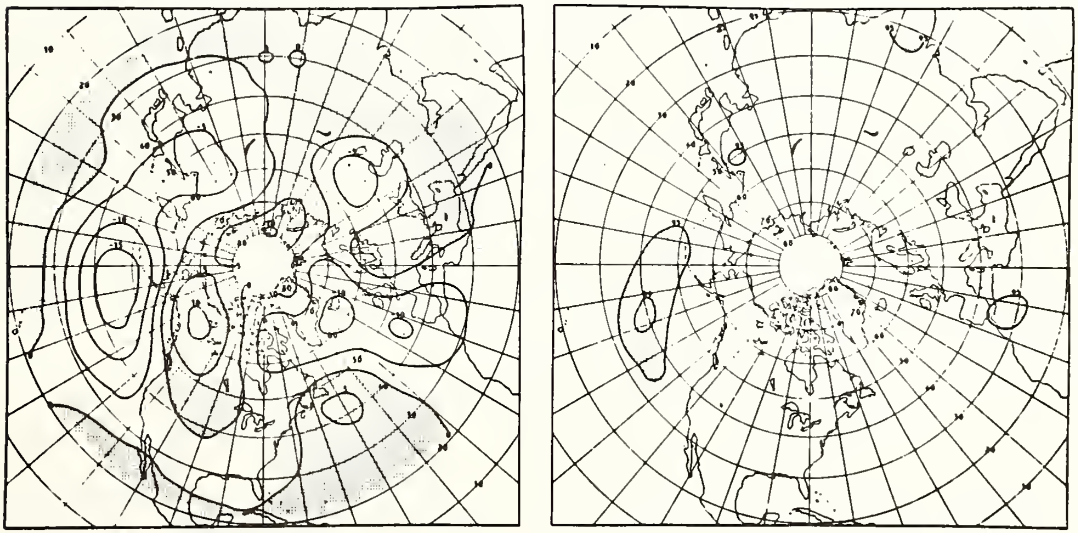

SON 700 MB ANOMALIES FOR LOW SOI YEARS, LAG=0

CONF.LIMIT OF SON COMPOSITE FOR LOW SOI YRS,LAG=0

Fig. 7 As in Fig. 6, but for low SOI values

El Niño and Variations in the Atmosphere Over the Tropical Pacific Ocean

Bryan C. Weare
Department of Land, Air and Water Resources
University of California
Davis CA 95616

Every few years an approximately year-long episode occurs when anomalously warm ocean surface water covers the eastern equatorial Pacific. This anomaly is often referred to by its local name of El Niño. This phenomenon has been hypothesized to be the response to and the stimulus of very large-scale ocean atmospheric interactions covering the entire Pacific basin and beyond.

Marine weather observations for the entire tropical Pacific Ocean for the period 1957-76 have been used to explore the spatial character of this interaction. From these individual observations obtained from the Fleet Numerical Weather Central, we have calculated individual monthly means of a number of basic meteorological parameters as well as derived parameters such as heat and momentum surface fluxes. The latter have been derived from the use of the data together with the so-called bulk formulae.

January mean data were stratified by averaging Januaries which preceded known El Niño events and separately averaging those Januaries which directly followed those events. El Niño events were characterized by the time coefficients of the dominant function of an empirical orthogonal analysis of Pacific Ocean surface temperatures between 50°N and 20°S. Fig. 1 shows that series, and indicates by hatching, the major and minor El Niño events. Minor events, which were not included in the averages which follow, are shown by more vertical hatching. The Januaries preceding and following El Niños are indicated by vertical lines.

The differences between tropical Pacific conditions towards the beginning of and towards the end of El Niño events will be illustrated in terms of the differences between the average of Januaries preceding minus the average of the Januaries following. For instance in Fig. 2, it may be seen that sea temperatures in the Januaries before El Niño are cooler than those at the end of El Niño throughout the eastern Pacific north of 15°S. The stippling on Fig. 2, as on all of the following figures, indicates those 5° by 5° grids for which the differences are greater than would be expected at the 95% confidence level following a Student t-test. Fig. 3 shows that there are similar differences in surface humidity.

Fig. 4 and 5 show the differences in zonal and meridional wind stresses. In general in the equatorial region zonal westerlies (easterlies) are stronger (weaker) preceding versus following El Niño events. However, north of 10° N the reverse is generally the case. The most significant differences in the meridional stresses are in the central northern Pacific in which southerly momentum fluxes are stronger preceding the events.

Fig. 6 shows the difference in the net surface heating of the ocean. This net heating is the solar radiative flux into the ocean minus the sum of the infrared radiation, latent heat, and sensible heat fluxes out of the ocean surface. Significantly greater fluxes into the ocean in the eastern region occur during the Januaries preceeding El Niños. Since these differences are generally between 30 and 60 W/m^2, this suggests that a substantial portion of the heating or cooling phase of an El Niño event is related to local surface heating changes. Fig. 7 indicates that the pattern of the net heating change is very similar to that of the negative of the loss of latent heat from the surface. Preceding El Niños relatively less heat is removed in the eastern region. Fig. 8 and 9 illustrate that changes in solar heating and infrared cooling largely cancel each other. This is because both are closely related to cloudiness changes.

This analysis suggests that not only ocean dynamical changes related to wind stress but ocean surface heating variations may be important to the development and/or decay of warm water events in the eastern Pacific Ocean. Other analyses using minor as well as major events and December and February averages as well as January means tend to verify this conclusion.

Figure 1

TIME SERIES OF COEFFICIENTS OF PACIFIC SST EOF I

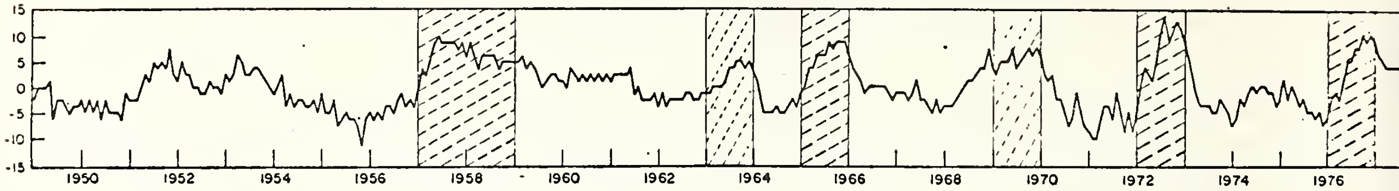

Figure 2

PRE - POST EL NINO YEARS JANUARY MEAN

T_s SEA TEMPERATURE (°C)

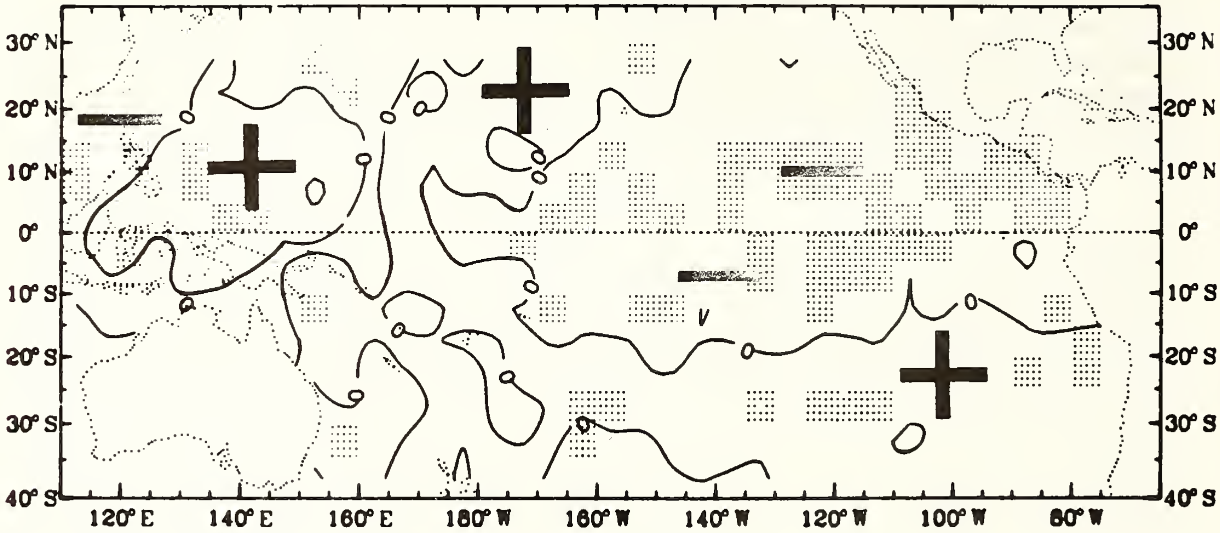

Figure 3

PRE - POST EL NINO YEARS JANUARY MEAN

q_a AIR HUMIDITY (g/kg)

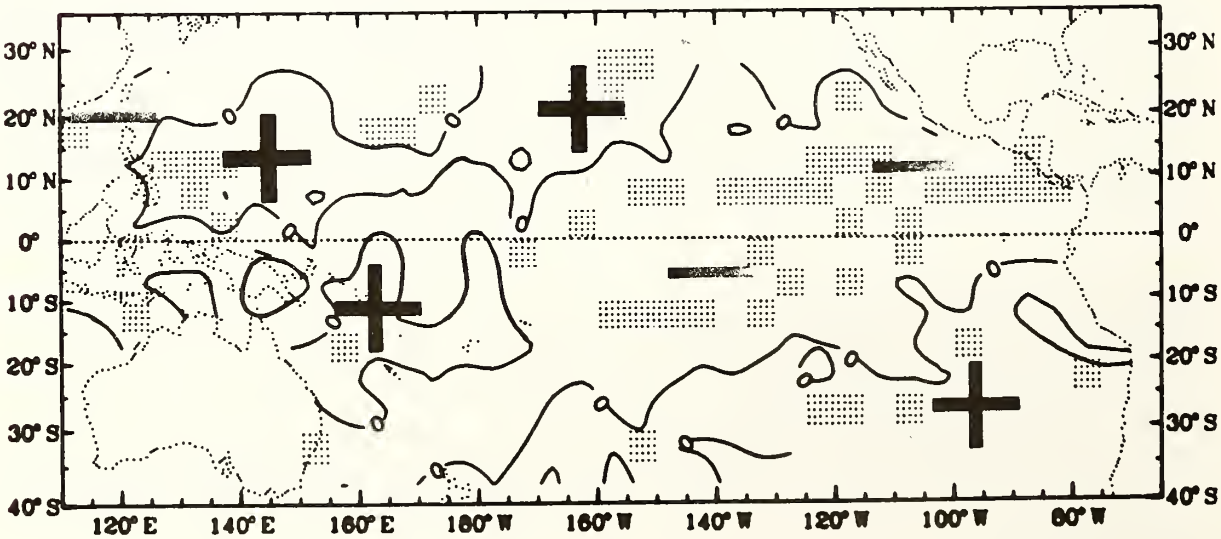

Figure 4

PRE - POST EL NINO YEARS JANUARY MEAN
1000 X τ_x ZONAL WIND STRESS (Nt/m^2)

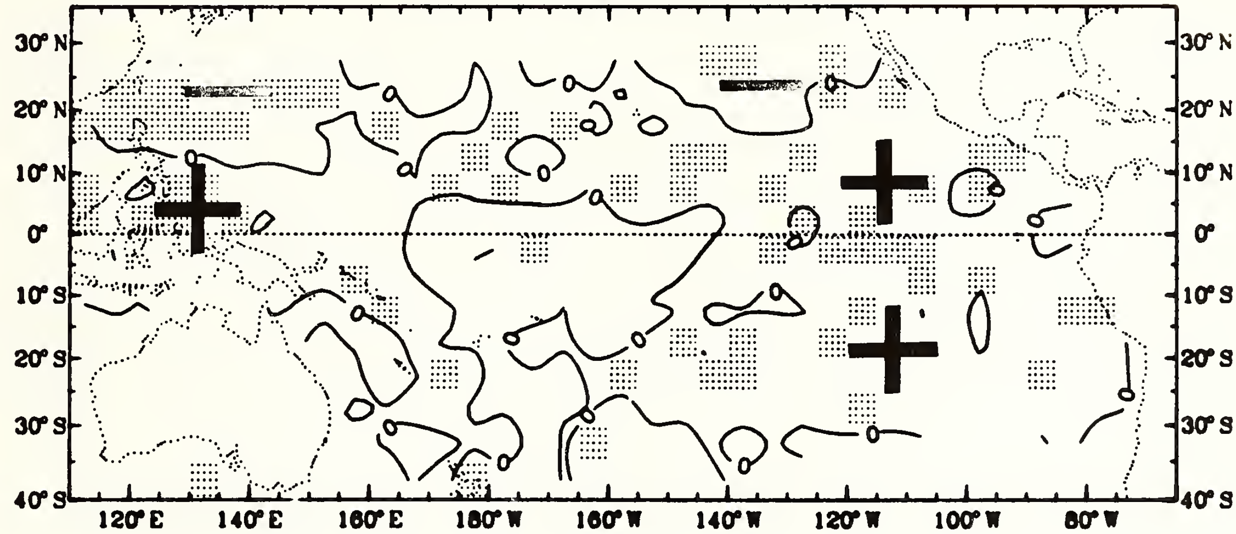

Figure 5

PRE - POST EL NINO YEARS JANUARY MEAN
1000 X τ_y MERIDIONAL WIND STRESS (Nt/m^2)

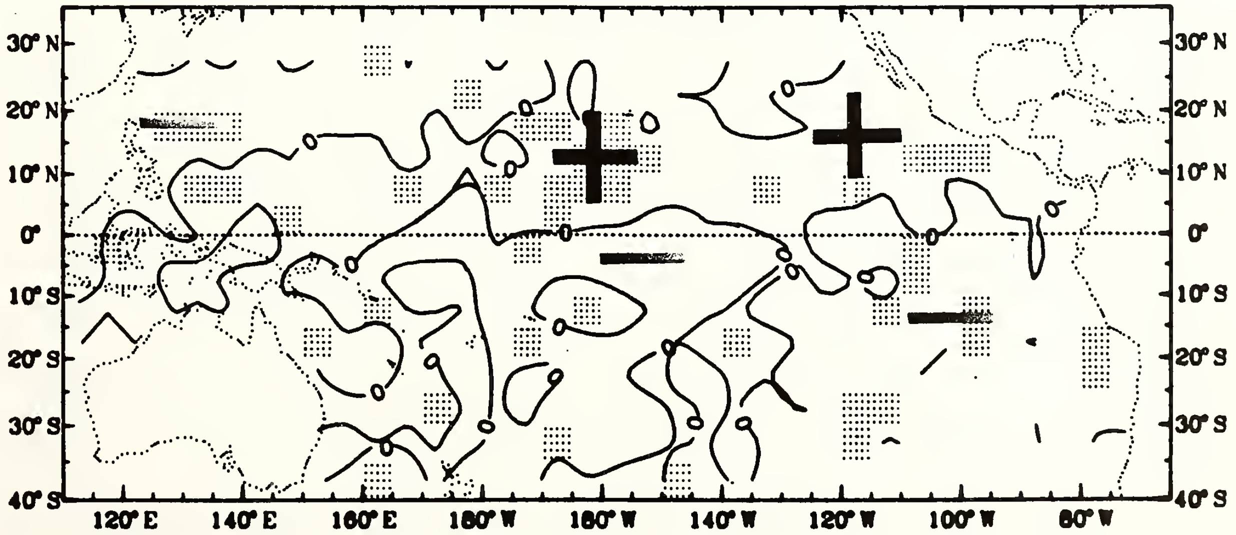

Figure 6

PRE - POST EL NINO YEARS JANUARY MEAN

$Q_S-Q_B-Q_L-Q_I$ NET HEATING (W/m^2)

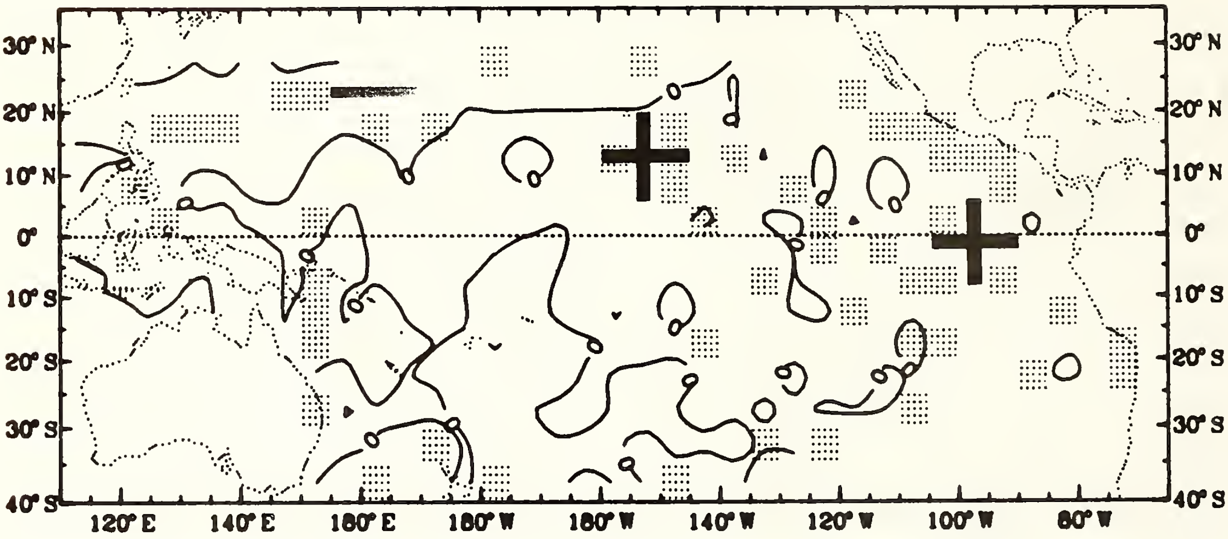

Figure 7

PRE - POST EL NINO YEARS JANUARY MEAN

Q_L LATENT HEAT FLUX (W/m^2)

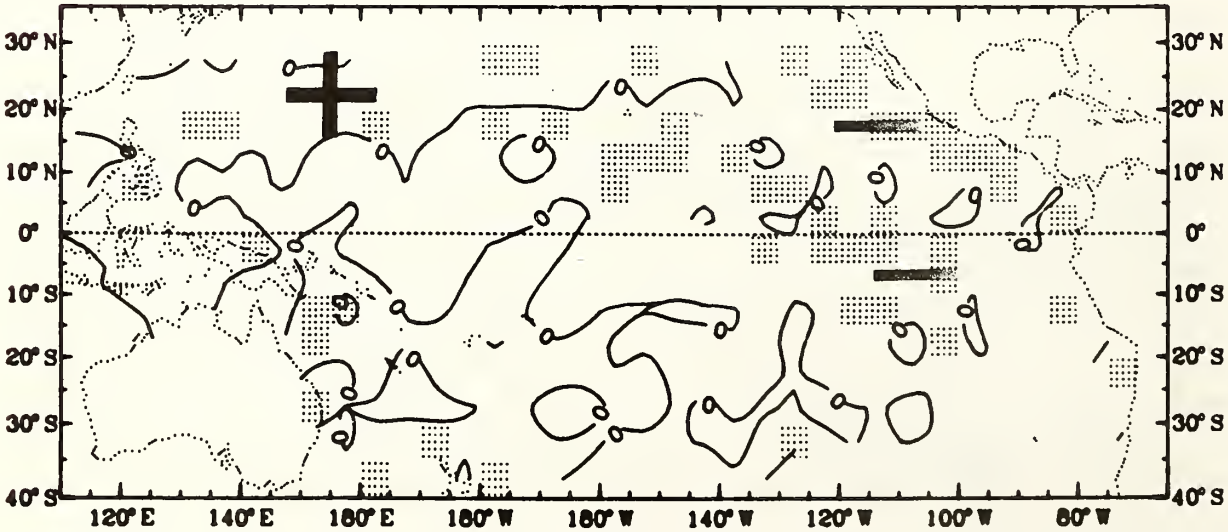

Figure 8

PRE - POST EL NINO YEARS JANUARY MEAN
Q_s SOLAR RADIATION (W/m^2)

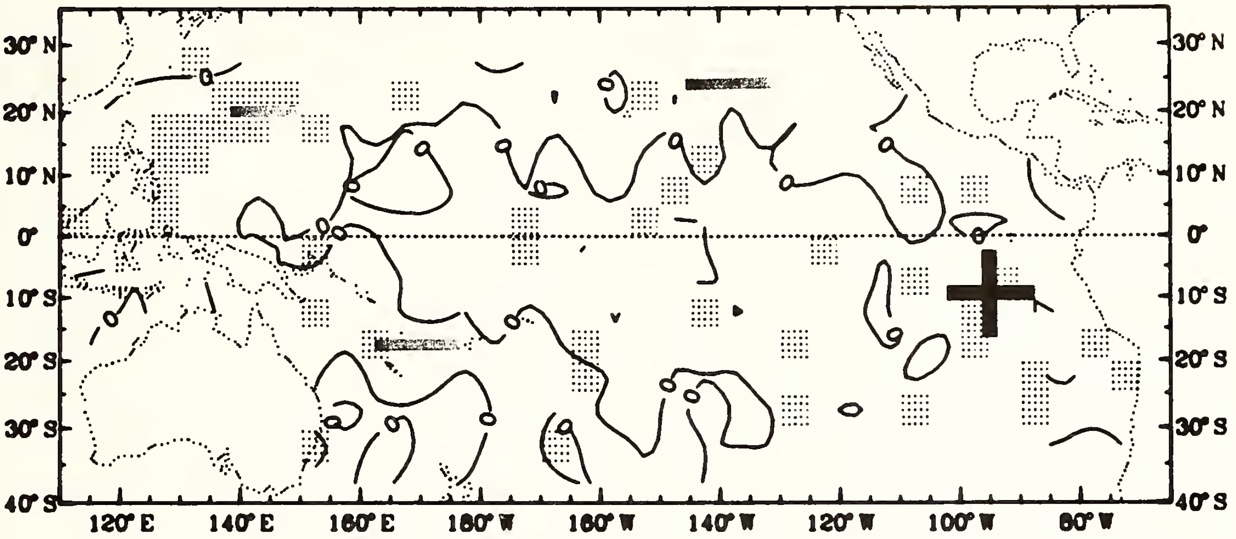

Figure 9

PRE - POST EL NINO YEARS JANUARY MEAN
Q_l NET BACK LONG WAVE RADIATION (W/m^2)

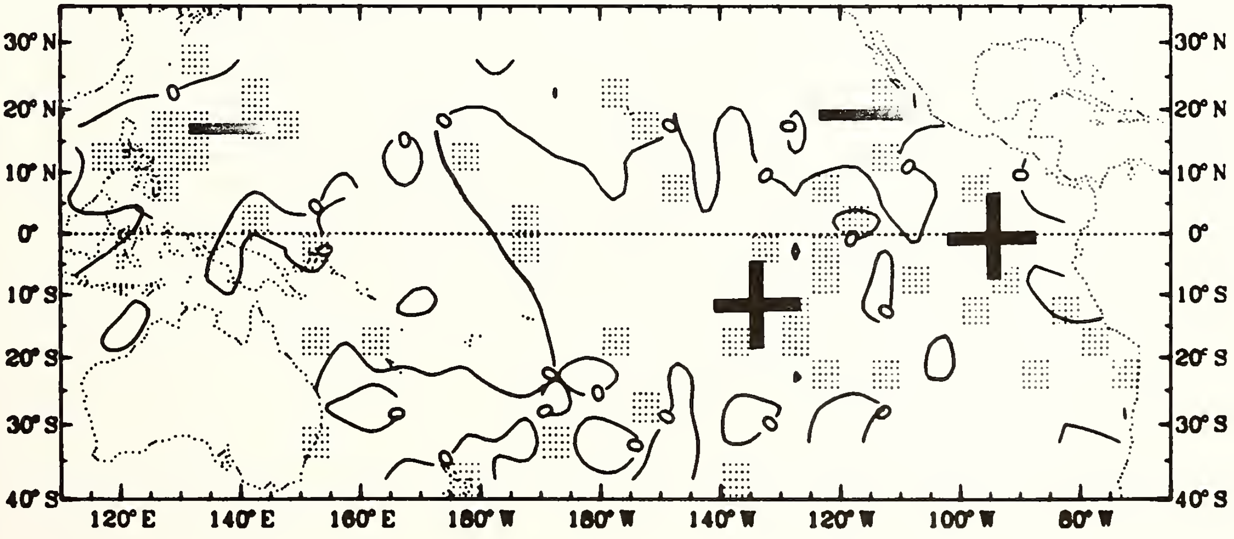

Correlation between the easterly wind stress and the zonal sea surface temperature variance in the eastern tropical Pacific.

Cho-Teng Liu
Joint Institute for Study of the Atmospheres and Ocean
University of Washington/NOAA
Seattle, Washington 98195

The monthly mean wind stress in the region of 100°W-140°W and 2°S-2°N was cross-correlated with the zonal sea surface temperature (SST) variation in the region 80°W-143°W and 2°S-2°N. The high correlation between the two, as seen in Figure 3, suggests that the wind stress plays an important role in the generation of the equatorial long waves, which was first observed by Legeckis with GOES-EAST satellite images.

The wind stress data used in this study are calculated from ship-reported wind. The zonal SST variation was computed from the SST-field which was derived from the objective analysis of ship SST observations. One example of the analyzed SST-field for July 1-15, 1979, is shown in Figure 1. During this half month, Legeckis has observed westward propagating equatorial SST fronts. We located SST observations from the research vessel *Oceanographer* that was cruising along 110°W for S. Hayes of NOAA/PMEL. Figure 2 is the SST section along 110°W. The locations of SST fronts in both figures agree with those observed by Legeckis using satellite pictures. One quick conclusion is that the monthly mean SST analysis will not be able to describe the equatorial SST variations, because both the data are too sparse and the averaging period is too long to depict these SST fronts (notice the large frontal movement in just 10 days). Any spotty observations in this region are subject to up to 2°C error from the monthly mean values.

Although the exact causes of the equatorial fronts are still debatable, we would like to explore the most potential one, the wind stress. If the wind stress is the primary driving force behind the equatorial long waves, one should be able to find some cross-correlation between them. Unfortunately the equatorial long waves have never been tracked by any ship. All we have are sparsely and randomly distributed SST observations. Statistically, when the equatorial wave fronts appear in the eastern Pacific, one should be able to find increased temporal and spatial variation of SST. Therefore, we cross-correlate the wind stress and the zonal variation of SST field derived from these randomly distributed SST observations. As in Figure 3 the time series of zonal SST variation (not SST itself) is correlated with the zonal wind stress on the time scale of three months or longer. Therefore the wind stress is a potential candidate in generating the equatorial SST fronts.

Figure 1. Sea surface temperature analysis of July 1-15, 1979. The objective analysis used 911 ship radio weather reports.

Figure 2. Sea surface temperature fronts at 2.5°N and 4.0°N, along 110°W in July 2-3, 1979, and at 1.2°N and 5.6°N, along 110°S in July 12-13, 1979.

Figure 3. The cross-correlation between the wind stress (upper curve, 100°W-140°W and 2°S-2°N) and the zonal variation of sea surface temperatures (lower curve, 80°W-143°W and 2°S-2°N).

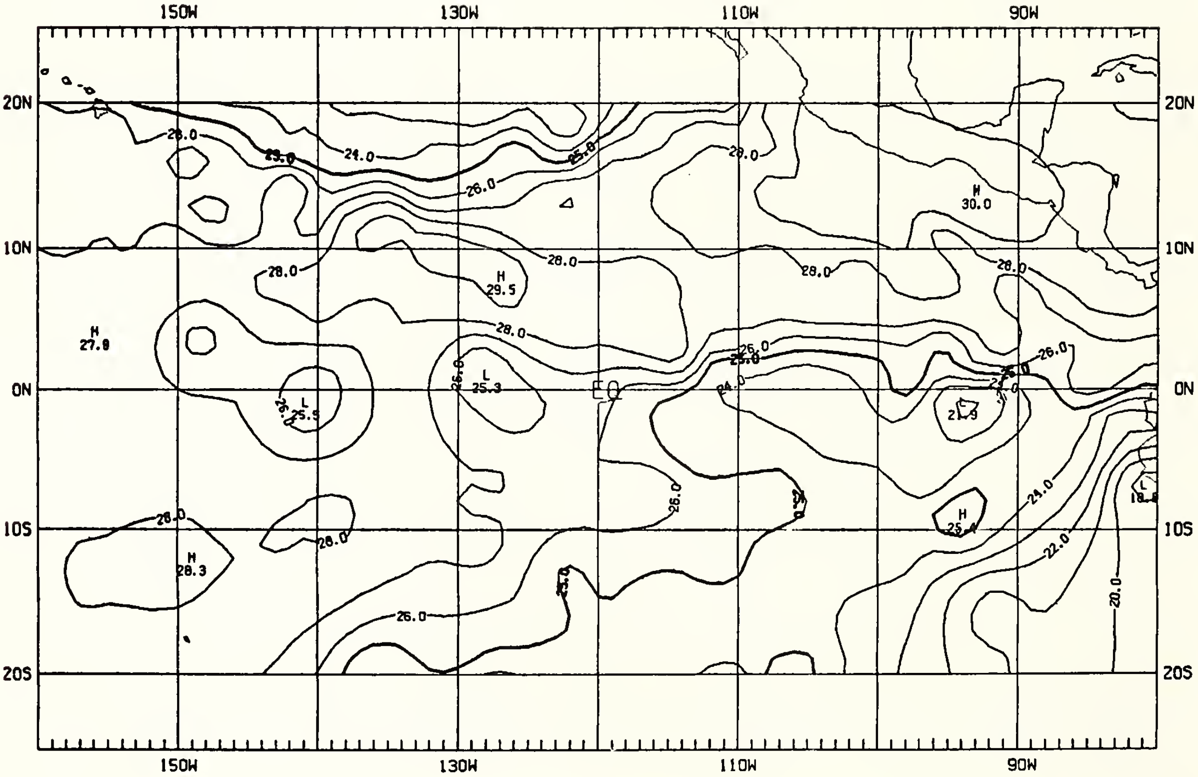
150W
130W
110W
90W
20N
10N
0N
10S
20S
EQ
28.0
24.0
26.0
H
30.0
H
29.5
H
27.8
L
25.5
L
25.3
L
21.9
H
25.4
H
28.3
22.0
20.0
L
18.8

Figure 1

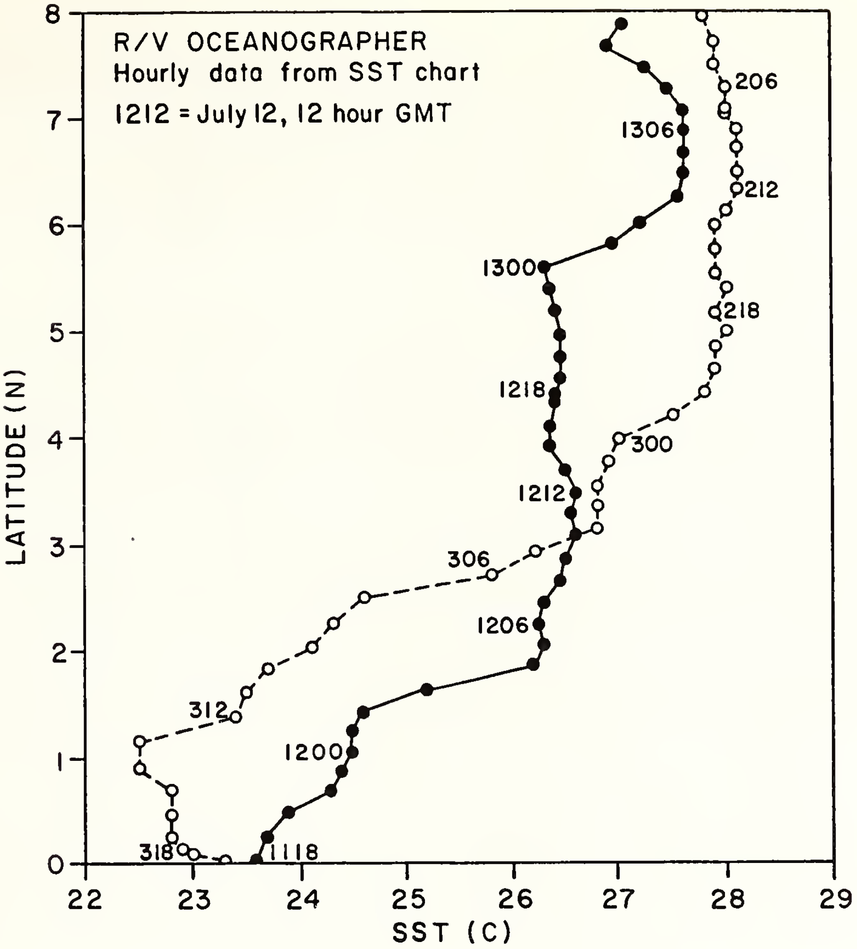

Figure 2

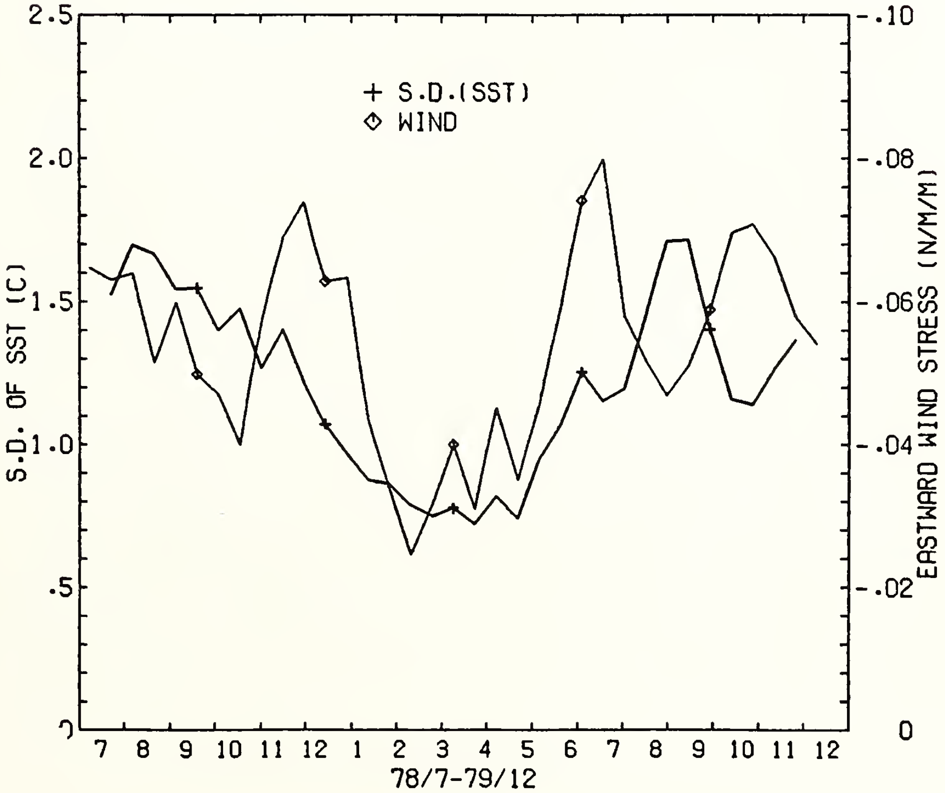

Figure 3

Pacific Trade Wind Fluctuations and the Southern Oscillation Index

Stephen Pazan and Gary Meyers
University of California
Scripps Institution of Oceanography
La Jolla, California 92093

Introduction

Interannual surface wind fields in the tropical Pacific fluctuate in a complex way with the southern oscillation. Interannual fluctuations in sea level and temperature seem to be closely associated with these surface wind field fluctuations. The ocean is certainly driven by the wind; it may be that the wind and the atmosphere are also driven in feedback by the ocean. Critical to an understanding of the relationship between ocean and atmosphere is an understanding of the spatial structure of the interannual variations.

There have been three previous studies of surface wind interannual variations in the Pacific which have used essentially the same dataset to study the spatial structure of interannual variations. These are:

1) A study of wind variations and the El Nino (Wyrtki, 1976). Wyrtki found that the El Nino warming in the eastern Pacific off Peru was preceded by a collapse of the tradewind system in the central Pacific.
2) Orthogonal eigenfunction analyses of bimonthly wind fields (Barnett, 1977). Principal modes of the wind fields are determined by seasonal changes. Modes of the interannual anomalies have very large spatial scales with important centers in the western equatorial Pacific and the vicinity of the ITCZ.
3) A study of the interannual behavior of Hadley cell circulation using zonally averaged Pacific marine winds (Reiter, 1978). The meridional velocity fluctuations were discovered to have distinct structure (Reiter, 1978).

The present study is a preliminary effort to determine the spatial structure of that part of the surface wind field which is in harmony with the southern oscillation index. Winds from marine observations have been monthly averaged from 1947 to 1972,and the months have then been seasonally averaged to produced seasonal mean winds. Averages were made over rectangles 2 degrees in latitude by 10 degrees in longitude The resulting mean winds were arrayed on a 17 by 30 grid extending from 30°S to 30°N and 110°E to 70°W. Peter Wright's(1977) southern oscillation index modified to include more Pacific Ocean data used to calculate regression coefficients of the wind against southern oscillation index. This southern oscillation index was computed as the first orthogonal eigenfunction of surface pressures at: Bombay, India; Darwin, Australia; Apia, Samoa; Tahiti; and Easter Island. In this way it was hoped to eliminate spatial biases which might arise from merely taking the difference in sea level pressure at two stations. The regression equation was

$$(\vec{V}-\overline{\vec{V}})=\vec{\Gamma}(SOI)$$

which has the virtue of providing an $\vec{r}$ which is like a wind anomaly if the southern oscillation index (SOI) is properly normalized. In fact, inspection of the southern oscillation index (Figure 1) shows that the minima at strong El Nino years 1958, 1966, and 1972 were very nearly -2 mb. What this means in terms of interpreting the regression coefficients will be explained later.

December-January-February seasonal regression coefficients were plotted in Figure 2. Recollecting that the southern oscillation index was -2 during strong El Nino years, it can be seen that the figure represents an anomaly wind field at about one-half the strength of a strong El Nino. Features in this figure can be readily identified with interannual fluctuations in the December-January-February wind field, such as: 1) weakened East Asian monsoon; 2) weakened and reversed easterlies west of 180 degrees and south of the Equator ; 3) a shift of the ITCZ to the south from 120°W to the dateline; 4) and a strong increase in northerly winds north of Hawaii. However, all of these features are obscured and confused by the high meridional wavenumber noise. In order to reduce the 'jitter' of the vectors, a hanning filter (1/4, 1/2, 1/4) was used in the meridional direction.

Before the results of this filtering are examined, another question of confidence in the regression coefficients will be addressed. Regression coefficients of the wind on the southern oscillation index only reflect random noise when the wind is not correlated with the southern oscillation index. In Figure 3a, correlation coefficients greater than 0.5 of the zonal component of wind vs. the southern oscillation index are hatchured, and the zonal component of the regression coefficients are contoured. It is evident that the hatchured area is coincident with the areas of greatest regression coefficient, i.e. greatest the southern oscillation index 'anomaly' activity. Similarly, Figure 3b is hatchured in the area where correlation coefficient of meridional wind component is greater than 0.5. It is also evident that in this latter the greatest meridional coefficients are very nearly coincident with the hatchured zones of greatest confidence. For the period of record, 26 years, there would be better than 15 degrees of freedom, since there are at least 15 out of 26 seasons with data for each plotted vector. The hypothesis that the winds are correlated with the southern oscillation index within the hatchured areas will fail less than 5% of the time with these many degrees of freedom assuring that the regression coefficients do reflect a variation in the wind field with the southern oscillation index.

The filtered December-January-February regression coefficient vectors are shown in Figure 4a, demonstrating the effectiveness of the hanning filter in removing the 'jitter' of the unfiltered plot while retaining most of the information. Features of the wind field are clearer, particularly in indicating the small shift of the ITCZ and in delineating the character of the extra-equatorial west Pacific flow. In the west Pacific, the regression coefficient vectors indicate a converging flow upon the Southern Hemispheric near equatorial convergence. This flow seems to be connected with weak easterlies in the Northern Hemisphere and an eddying or wavelike flow in the Southern Hemisphere east of Australia. The eddy flow is indicated by dotted lines and has been seen in IR satellite images.

March-April-May regression coefficient vectors are shown in Figure 5a and are much like the December-January-February pattern albeit less intense. The anomaly north of Hawaii is now a westerly and there is less confusion in vectors near the ITCZ east of]30°W, indicating that changes that are not in phase with the southern oscillation index during the December-January-February are in phase in March-April-May.

Any effect of the southern oscillation on the south east Asian monsoon is too weak to identify, but the near equatorial convergence is nearly as strong from 160°E to 160°W as during December-January-February. Once again, an eddy or standing wave phenomenon is observed from 170°E to 160°W south of 10°S.

June-July-August regression coefficient vectors (Figure 6a) have shifted five to ten degrees north in the western Pacific, a change which is paralleled in the seasonal climatology (Figure 4b and 6b) from March-April-May to June-July-August. The southward shift of the ITCZ during periods of negative the southern oscillation index is strongly apparent in the western Pacific in this season. A broad band of westerly flow in the Southern Hemisphere from 170°E 120°W and at 95°W would reverse flow between 20°S and 30°S. (Figure 6b) and possibly reflects a northward shift in the Southern Hemispheric middle latitude circulation. The anomalous flow is no longer north of Hawaii but the 'standing wave' seen in December-January-February and spring is quite strong east of Australia.

September-October-November regression coefficient vectors (Figure 7a) follow the June-July-August pattern, with an even stronger reversal of flow in the western Pacific, as can be seen by comparing with climatology (Figure 7b). The ITCZ has a strong shift equatorward from climatology, as in June-July-August. The westerly southeast Asian monsoon is strengthened slightly, just as the December-January-February easterly southeast Asian monsoon was also strengthened. Strong standing wave or eddy flow patterns are observable in the southwest Pacific in this season also.

Conclusions

Major interannual variations of the trade wind system are visible in linear regression coefficients against a the southern oscillation index. In particular, westerlies in the western Pacific trades reflect a weakening of the Walker circulation during the southern oscillation index less than 0. An equatorward shift of the ITCZ is observed in all seasons, being strongest in June-July-August and fall. Since the ITCZ shifts south in the climatological December-January-February months, the seasonal shifts in the ITCZ are weakened during periods of negative the southern oscillation index. The southward ITCZ shift from March to August may decrease the momentum exported to the Southern Hemisphere circulation via Hadley cell teleconnections, thus creating the strong southern hemispheric westerly trade wind anomalies seen in June-July-August. No converse response is seen in December-January-February to shifts in the ITCZ during September-October-November.

An eddy or standing wave pattern is observed in the southwest Pacific in all seasons. A similar pattern can be seen in IR satellite observations. This pattern may reflect a teleconnection with the Southern Hemisphere.

REFERENCES

Barnett, T. P., 1977: The principal time and space scales of the Pacific trade wind fields. Journal of the Atmospheric Sciences, 34, #2, 221-236.

Reiter, E. R., 1978: Long-term wind variability in the tropical Pacific, its possible causes and effects. Monthly Weather Review, 106, 324-330.

Wyrtki, K., 1975: El Nino - the dynamic response to the equatorial Pacific Ocean to atmospheric forcing. Journal of Physical Oceanography, 5, 572-584.

Wyrtki, K., 1976: The trade wind field over the Pacific Ocean. Journal of Applied Meteorology, 15, 698-704.

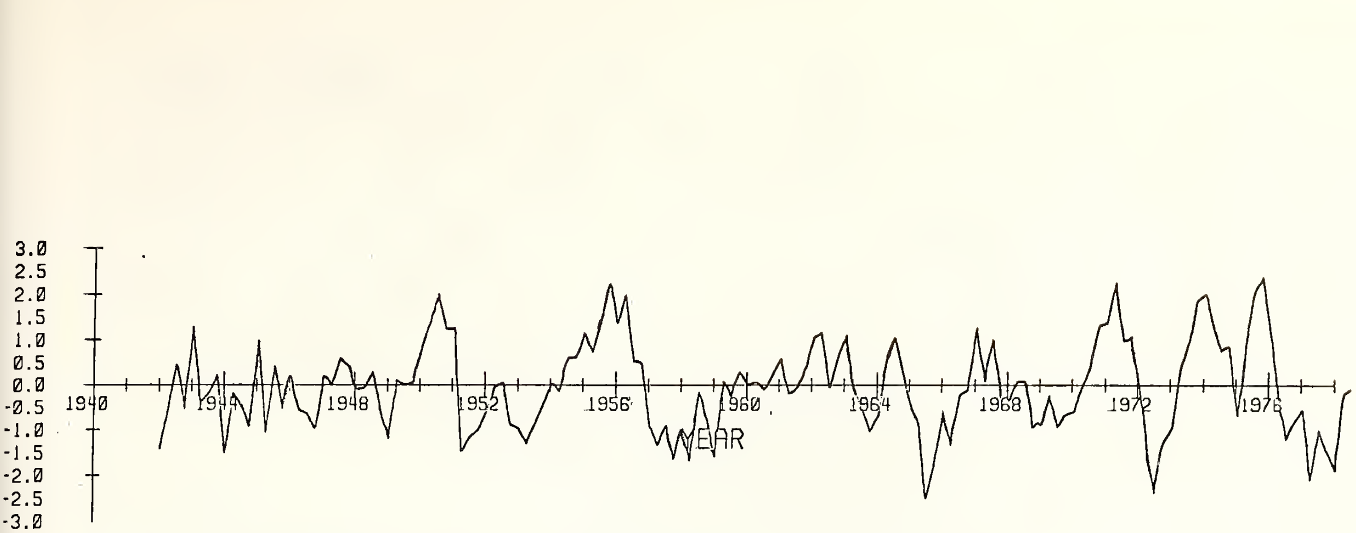

Figure 1. Peter Wright's Southern Oscillation index. This is the first orthogonal eigenfunction of sea surface pressures at Darwin, Australia; Bombay, India; Apia, Samoa; Tahiti; and Easter Island.

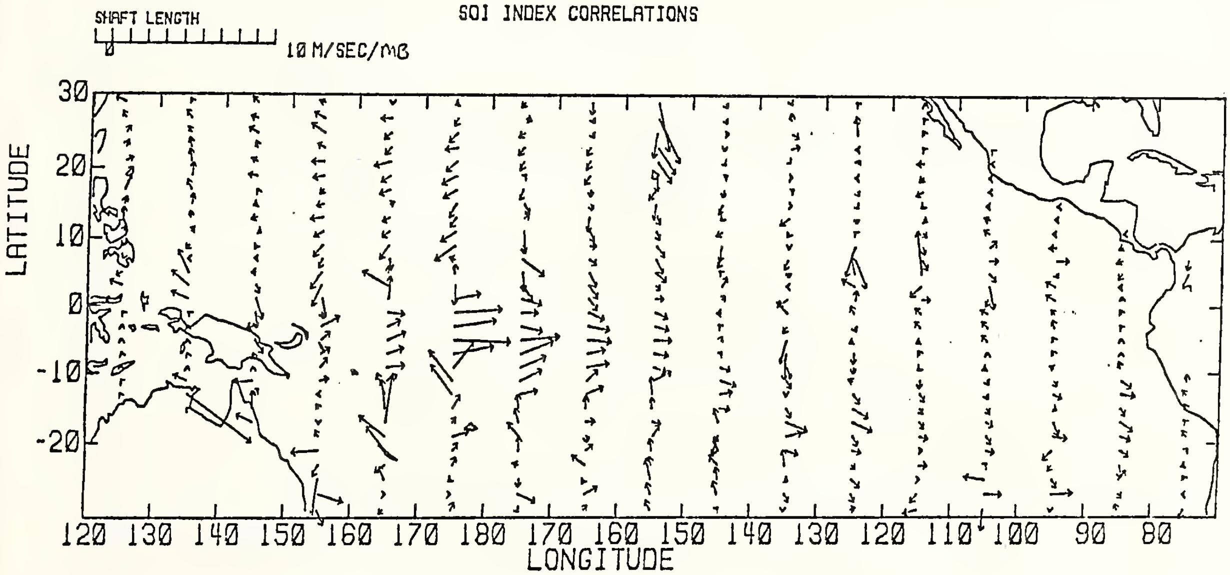

Figure 2. December-January-February seasonal regression coefficients of surface wind against Peter Wright's southern oscillation index.

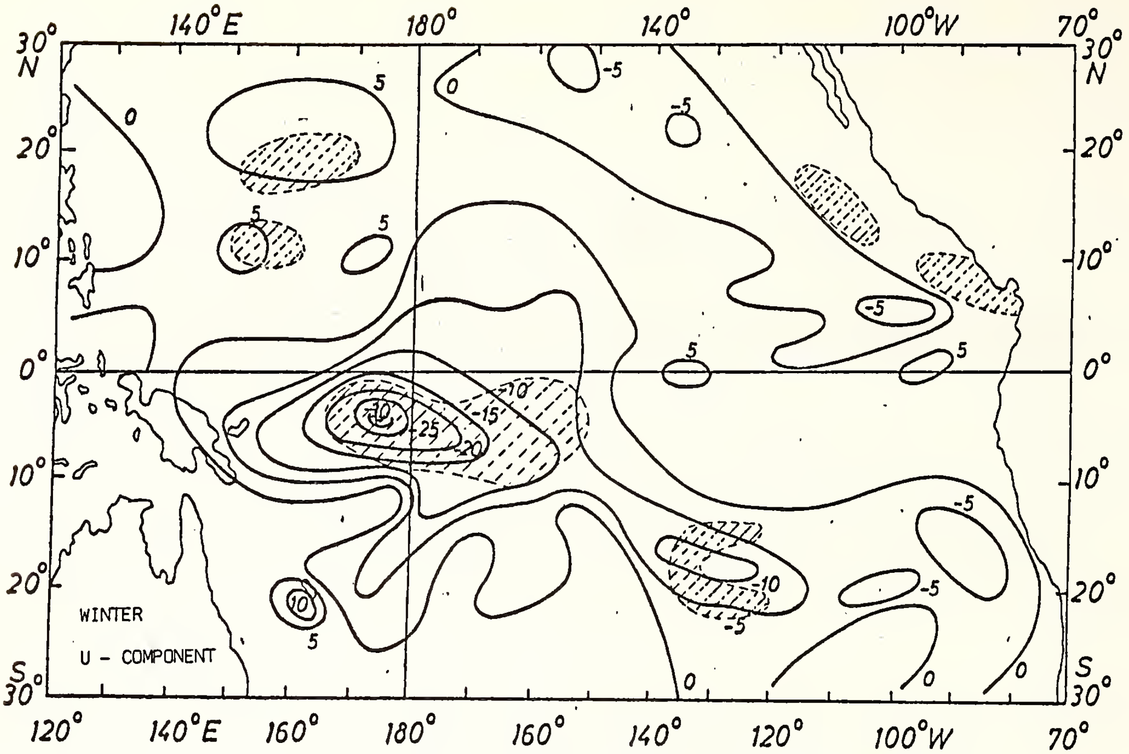

FIGURE. 3A. CONTOURS OF THE ZONAL COMPONENT OF WIND REGRESSION COEFFICIENTS. AREAS IN WHICH THE CORRELATION COEFFICIENTS OF THE ZONAL WIND AND THE SOUTHERN OSCILLATION INDEX EXCEED 0.5 ARE HATCHURED.

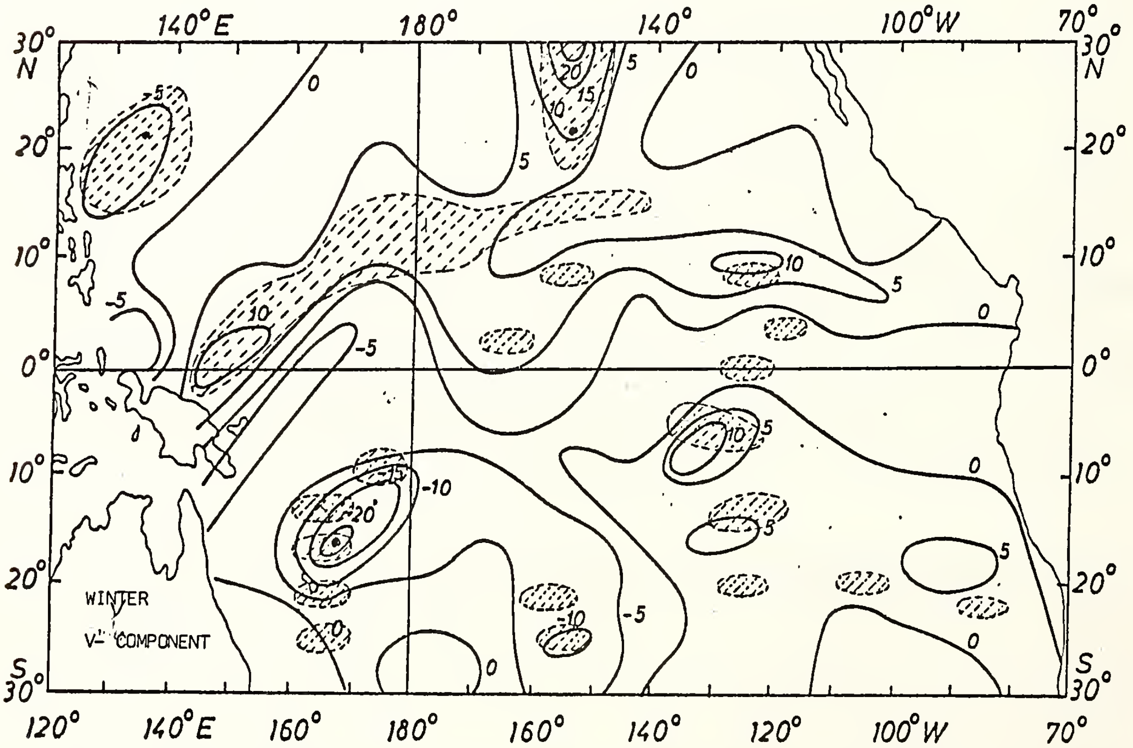

FIGURE 3B. CONTOURS OF THE ZONAL COMPOENNT OF WIND REGRESSION COEFFICIENTS. AREAS IN WHCIH THE COERRLATION COEFFICIENTS OF THE ZONAL WIND AND THE SOUTHERN OSCILLATION.INDEX EXCEED 0.5 ARE HATCHURED.

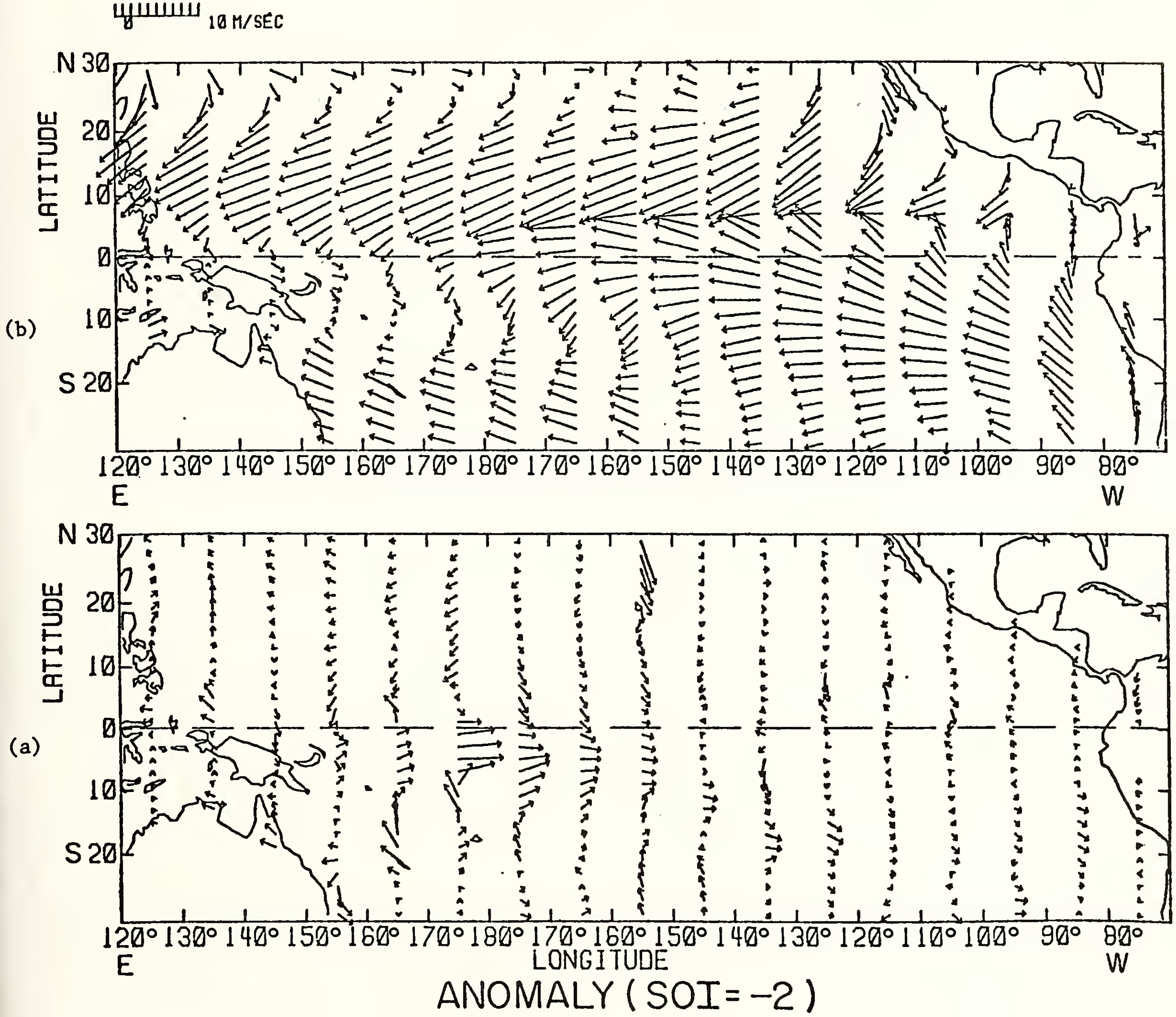

SOUTHERN OSCILLATION
TRADE WIND ANOMALIES
DECEMBER, JANUARY, FEBRUARY

MEAN (1947-1973)

ANOMALY (SOI= -2)

Figure 4

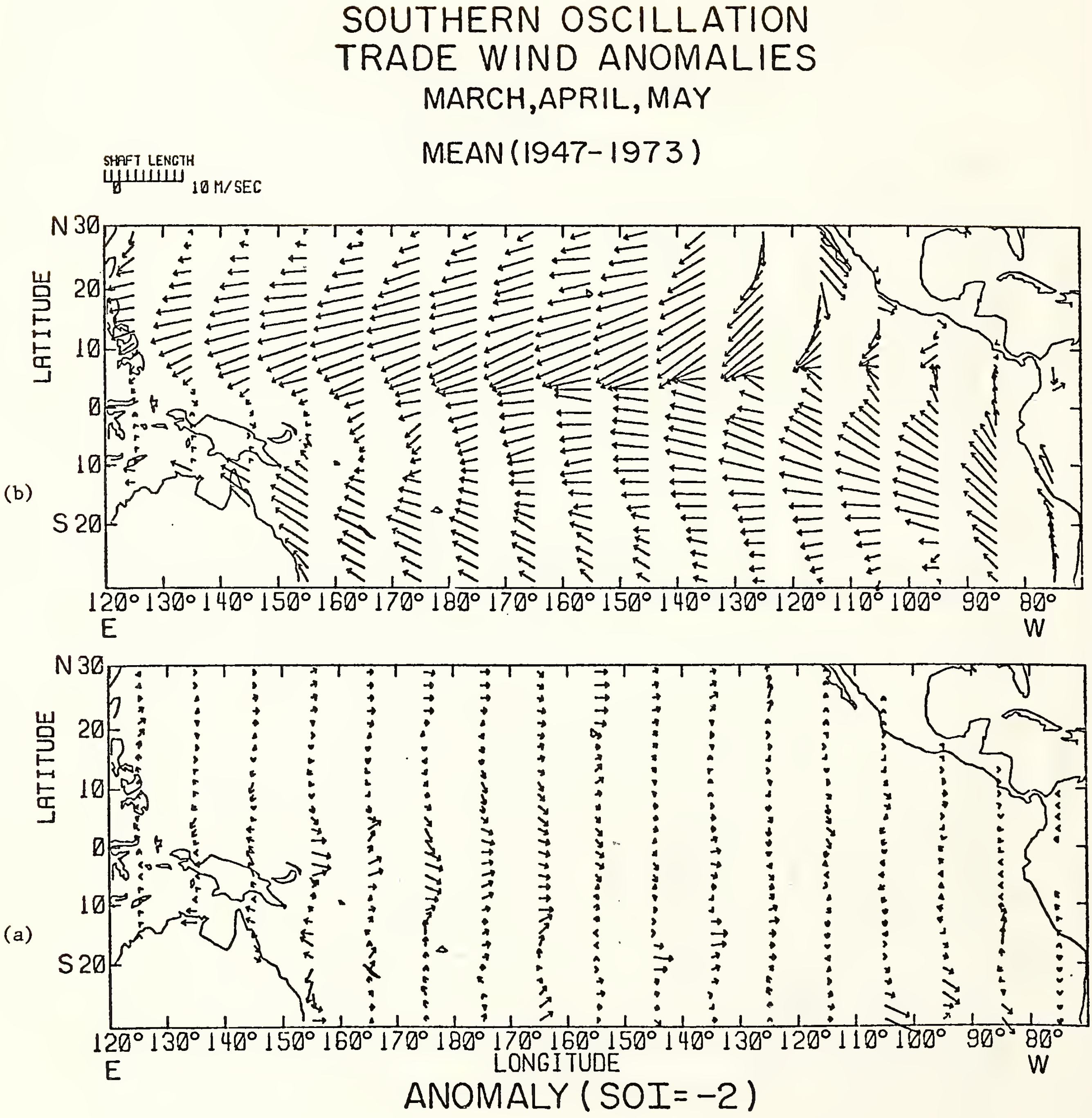
SOUTHERN OSCILLATION
TRADE WIND ANOMALIES
MARCH, APRIL, MAY
MEAN (1947-1973)
SHAFT LENGTH
0
10 M/SEC
N 30
20
10
0
10
S 20
LATITUDE
(b)
120° 130° 140° 150° 160° 170° 180° 170° 160° 150° 140° 130° 120° 110° 100° 90° 80°
E
W
N 30
20
10
0
10
S 20
LATITUDE
(a)
120° 130° 140° 150° 160° 170° 180° 170° 160° 150° 140° 130° 120° 110° 100° 90° 80°
E
LONGITUDE
W
ANOMALY (SOI=-2)

Figure 5

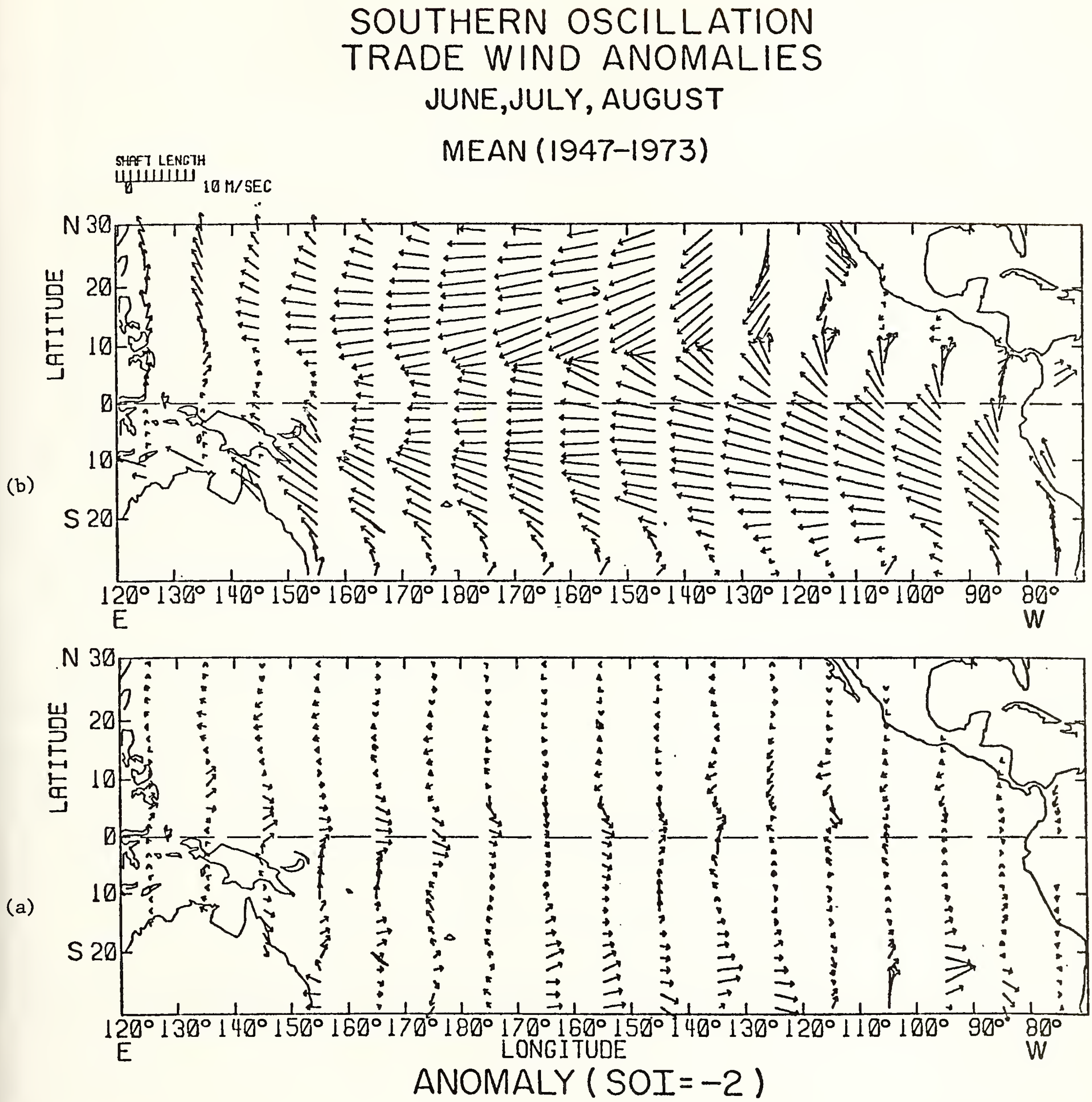

SOUTHERN OSCILLATION
TRADE WIND ANOMALIES
JUNE, JULY, AUGUST

MEAN (1947-1973)

ANOMALY (SOI=-2)

Figure 6

SOUTHERN OSCILLATION
TRADE WIND ANOMALIES
SEPTEMBER, OCTOBER, NOVEMBER

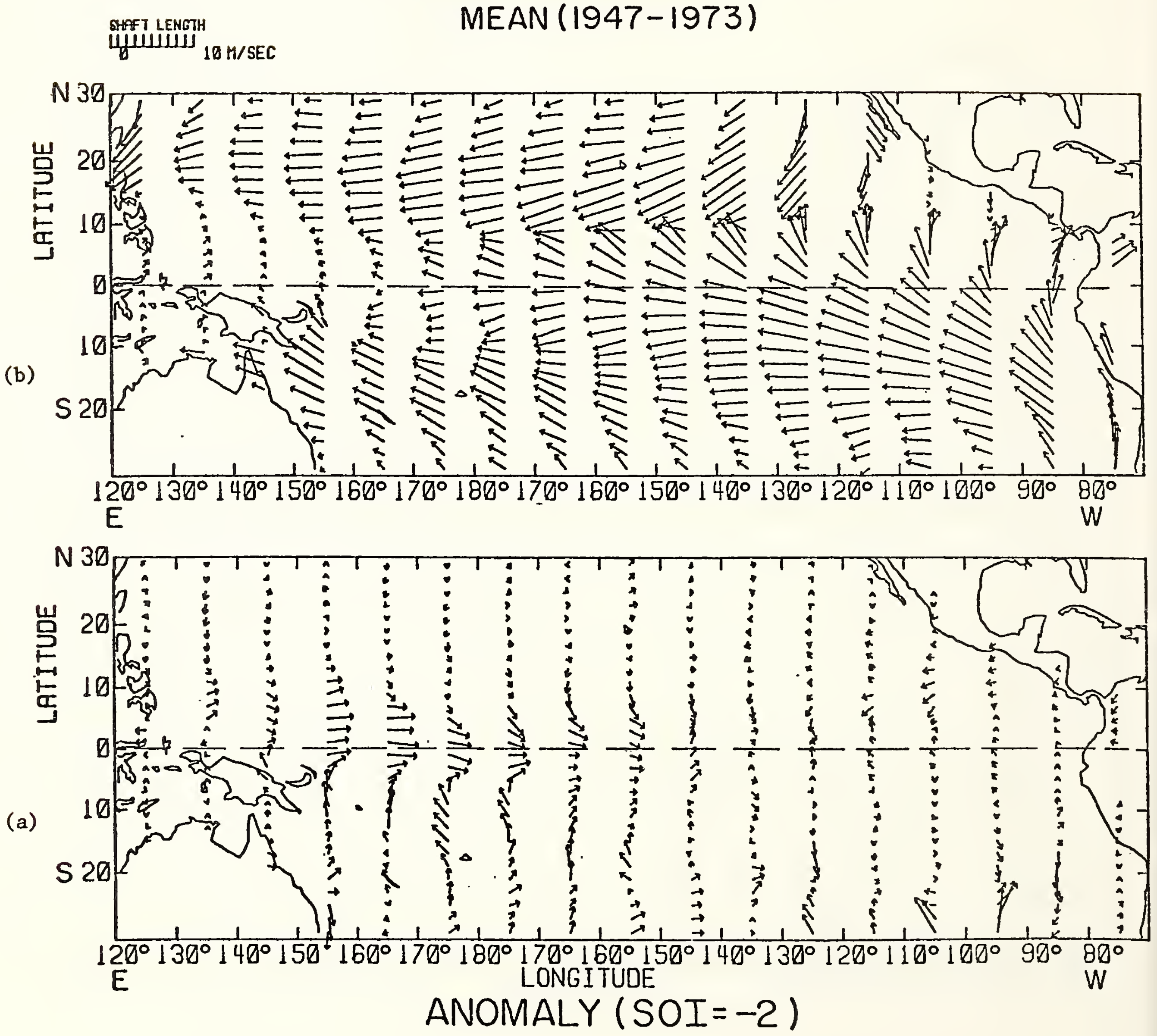

MEAN (1947-1973)

ANOMALY (SOI=-2)

Figure 7

Comparison of Four Equatorial Wind indices over the Pacific and El Nino Outlook for 1981

Klaus Wyrtki
University of Hawaii

Indices of climatological parameters are much needed tools for the study of the interannual variations of the ocean atmosphere system. A wind index for the equatorial Pacific Ocean is needed for the analysis and prediction of El Nino (Wyrtki, 1975; Barnett and Hasselmann, 1979). At present four wind indices are being prepared for the equatorial Pacific Ocean and it is the goal of this study to determine how well they agree. Since two of the indices are based entirely or in part on satellite observations it will also be of interest to note how well they compare with conventional surface wind observations.

The NORPAX index is based on ship observations derived from the climate data file (Wyrtki and Meyers, 1976, and updated by Pazan in 1980). The index gives both the average wind vector and the wind stress for each month of the period 1947 to 1978 for the area from 4°N to 4°S and from 140°W to 180°. Stresses were computed from individual observations, and averaged for areas of two degrees of latitude and 10 degrees of longitude. Sixteen such fields were averaged for the index. The number of observations used for the index varied between 40 and 100 per month with an average of about 70.

A similar index is being computed by the National Marine Fisheries Service, (NMFS) (Miller, personal communication). This NMFS index is based on ships' radio reports, covers the period 1961 to 1979, and gives monthly mean vector winds. Averaging is performed for five degree areas and 16 such areas are averaged for the index, which covers the area from 5°N to 5°S and from 140°W to 180°. The number of observations in this area is typically between 30 and 90 and the average is about 60. The NORPAX index and the NMFS index are using essentially the same data base.

An index based entirely on satellite wind vectors has been developed by Sadler (personal communication). Vectors of low-level cloud motion are averaged for areas of 2.5 degrees of latitude and 10 degrees of longitude, and both the monthly mean vector winds and the wind stress are being computed. The index covers the period 1975 to 1980 and the area from 5°N to 5°S and from 140°W to 180°. The index is based on 700 to 1600 observations per month.

The tropical wind analysis by the National Environmental Satellite Service (NESS) is also being used to derive a wind index. A daily computer analysis of the tropical wind field at 1000 mb using pressure, wind, and satellite wind observations as input, is a basis for a computation of monthly mean wind vectors at grid points five degrees apart (Krueger, personal communication). These wind vectors have been used to determine a monthly wind index for the area 7.5°N to 7.5°S and 140°W to 180° for the period 1976 to 1980.

These four wind indices of somewhat different design and origin (Table 1) can now be compared and time series of the indices are shown in Figures 1 to 6. Correlation coefficients between them are listed in Table 2.

The NORPAX and the NMFS index compare very favorably, both in terms of the monthly values as well as with regard to the 12-month running mean. This is not surprising since they are based on virtually the same data set. The correlation coefficient between the two indices of 0.74 is unexpectedly low; this is due to the high variability of the wind field, which is inadequately sampled by only about 60 observations per month. The standard deviation of the difference between the NORPAX and the NMFS winds is 0.9 m/s^{-1}.

The satellite wind index by Sadler compares well with either the NORPAX or the NMFS ships wind index, and the correlation coefficient of 0.66 and 0.61 are not significantly different. They are, however, less than the correlation between the two indices based on ships' observations. Remarkable is that the standard deviation of the satellite winds (0.9 m/s^{-1}) is less than that of the ship winds (1.2 m/s^{-1}); this is also obvious from a visual inspection of Figures 1 to 3. The lower variability of the satellite winds exists despite the fact that the mean satellite wind of 8.4 m/s^{-1} is substantially stronger than the mean surface wind of 4.9 m/s^{-1}. This indicates that the trade winds at cloud level are much more regular than the winds at sea level, and that projecting satellite observed winds to the sea surface may be a rather difficult procedure.

The NESS wind index compares very well with the NORPAX index ($r = 0.73$), but much less favorably with the NMFS index ($r = 0.53$). This may be partly due to the rather short period of comparison, but is more likely due to the somewhat large number of observations included in the NORPAX index.

The Sadler index, using satellite wind observations exclusively, and the NESS index, which uses the same satellite winds, but projects them through a computer analysis and a boundary layer model to the sea surface, correlate only with $r = 0.57$, indicating problems in the analysis. The actual satellite observations and the ships' observations correlate better.

A comparison between the zonal components of the wind stress as derived from the ships' observations and from the satellite winds (Figs. 5 and 6) shows, as expected, a larger variance of the monthly values but the same low-frequency signal. The correlation is only 0.57, less than that for the zonal wind.

No corresponding analysis was made for the meridional component of the wind, which is generally small over this area and is a present not required as an index.

In conclusion it can be stated that all four wind indices give approximately the same low-frequency signal. In individual months they differ considerably, which is due to the small number of observations for the two indices based on ship reports, and due to the limited ability to project cloud motion vectors through the atmospheric boundary layer to the ocean surface for the indices based on satellite winds. The indices are in general satisfactory for the purpose of long term climate analysis, but their precision and utility on the monthly time scale could be considerably improved if the number of ship weather reports in the area could be increased to about 200. Until that is accomplished, the untempered satellite wind index is probably the best.

According to observations and theory El Nino is preceded by the accumulation of unusually large masses of warm water in the western equatorial Pacific Ocean. This documents itself in higher sea level and in a depression of the thermocline, both produced by stronger than normal trade winds over a period of many months. El Nino is subsequently triggered by the relaxation of the trade winds.

Since the 1976 El Nino the trade winds over the central equatorial Pacific have not been above normal for extended periods. The ships' observations (Fig. 1) show very weak winds in 1977 and 1978. An index of satellite winds derived by Sadler (Fig. 3) shows that equatorial trade winds in 1979 and early 1980 were still somewhat below normal. Consequently no accumulation of warm water could occur in the western Pacific.

Sea level records at Malakal and Yap in the Philippine Sea (Fig. 7) display a normal annual cycle in 1977, 1978, and 1979. Sea level is low during the north hemispheric winter, rises in spring, and has a maximum in summer. In 1980 the spring rise of sea level does not occur and sea level remains low at least until August. Consequently the most important precondition of the occurance of El Nino, namely high sea level in the western equatorial Pacific, is not given. The failure of sea level to rise seasonally in the spring of 1980 may be caused partially by the weak equatorial winds (Fig. 3) and partially by the winds over the western equatorial Pacific, but information on winds west of the date line are not available to me at this time.

On the basis of this analysis it may be stated that a moderate or strong El Nino is not possible in 1981, because sea level in the western Pacific is not above normal, which is the most important precondition for its occurance.

References:

Barnett, T. P., Rev. Geosphys. and Sp. Phys., 17, 949-968, 1979.

Wyrtki, K., J. Phys. Oceanogr., 5, 572-584, 1975.

Wyrtki, K. and G. Meyers, J. Appl. Meteor., 15, 698-704, 1976.

Table 1. The four wind indices in the equatorial Pacific.

	DATA	PARAMETERS	PERIOD	AREA
NORPAX	SHIPS, LOG	U, TAUX	1947 - 78	4N-4S, 140W-180
NMFS	SHIPS, RADIO	U,	1961 - 79	5N-5S, 140W-180
SADLER	SATELLITE	U, TAUX	1975 - 80	5N-5S, 140W-180
NESS	ANALYSIS	U,	1975 -80	7.5N-7.5S, 140W-180

Table 2. Corellation coefficients between the four wind indices. Number of months in brackets. Upper right half for wind speed indices, lower left for wind stress indices.

WIND

	NORPAX	NMFS	SADLER	NESS
NORPAX		0.74 (92)	0.66 (44)	0.73 (39)
NMFS	----		0.61 (54)	0.53 (49)
SADLER	0.57 (44)	----		0.57 (55)
NESS	----	----	----	

WIND STRESS, TAUX

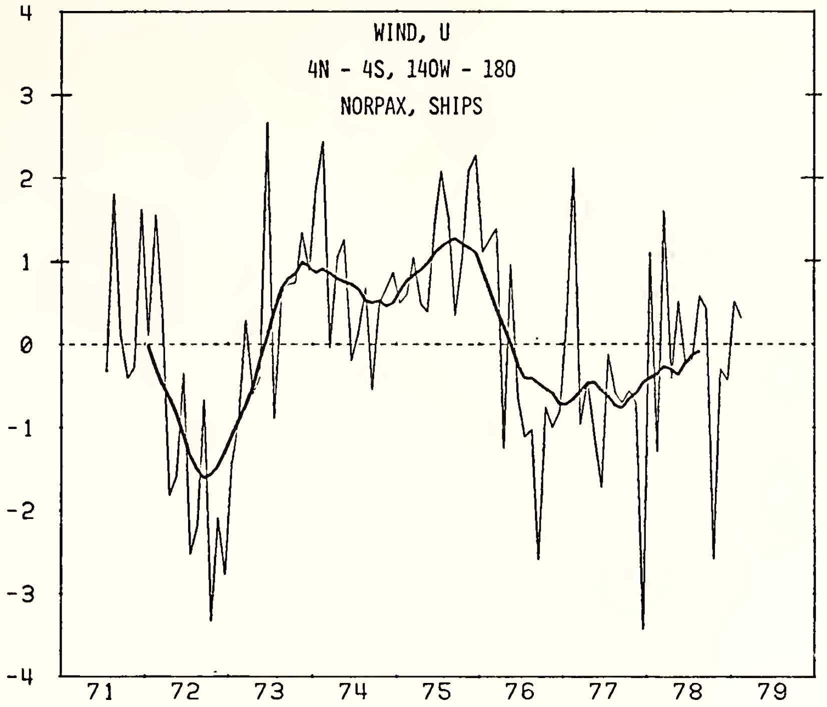

Fig. 1. NORPAX index. Zonal component (m s^{-1}, westward positive) of the equatorial wind based on ship observations. The thin line gives individual monthly means, the heavy line the 12 month running mean. The mean is 4.9 m s^{-1}.

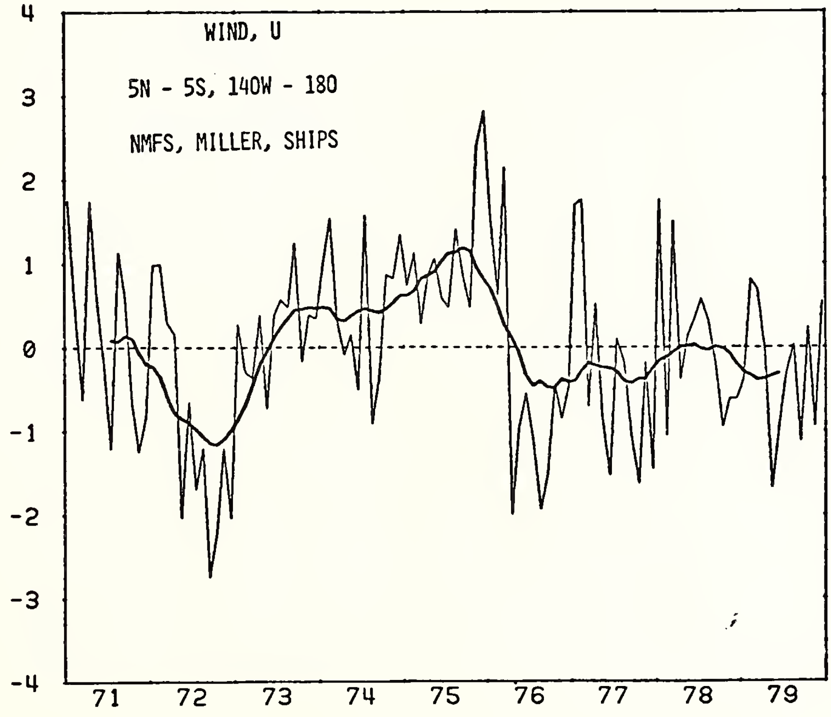

Fig. 2. National Marine Fishery Service index. Zonal component (m s^{-1}, westward positive) of the equatorial wind based on ships radio reports. The thin line gives individual monthly means, the heavy line the 12 month running mean. The mean wind is 4.4 m s^{-1}.

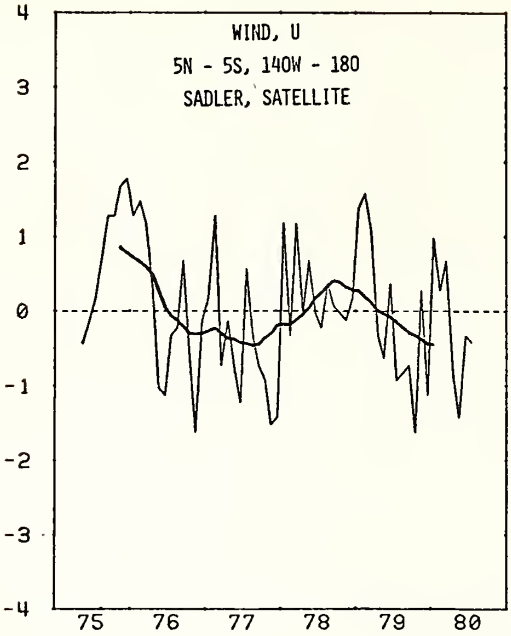

Fig. 3. Satellite wind index. Zonal component (m s^{-1}, westward positive) of the equatorial wind based on low level cloud motion vectors. The thin line gives individual monthly means, the heavy line the 12 month running mean. The mean wind is 8.4 m s^{-1}.

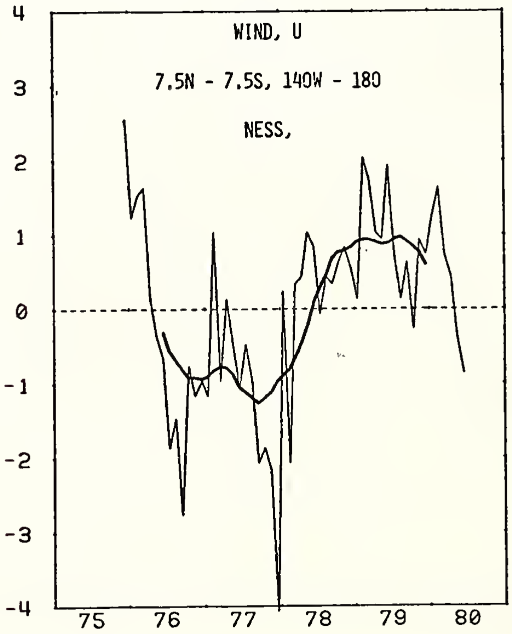

Fig. 4. National Environmental Satellite Service Index. Zonal component (m s^{-1}, westward positive) of the equatorial wind based on the daily tropical wind analysis. The thin line gives individual monthly means, the heavy line the 12 month running mean. The mean wind is 4.6 m s^{-1}.

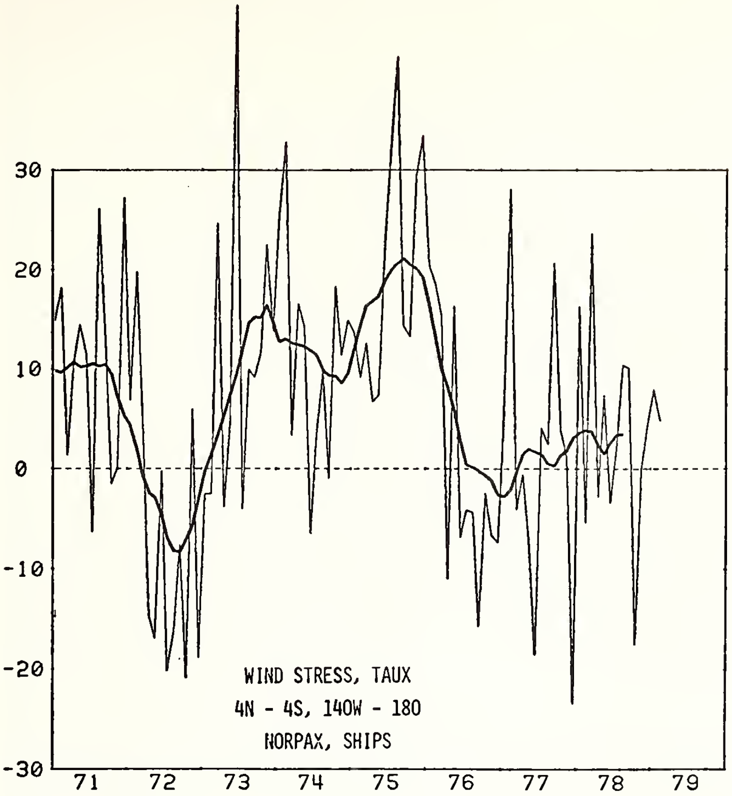

Fig. 5. NORPAX wind stress index. Westward component of the equatorial wind stress ($m^2 s^{-2}$) based on ships wind observations The thin line gives individual monthly means, the heavy line the 12 month running mean.

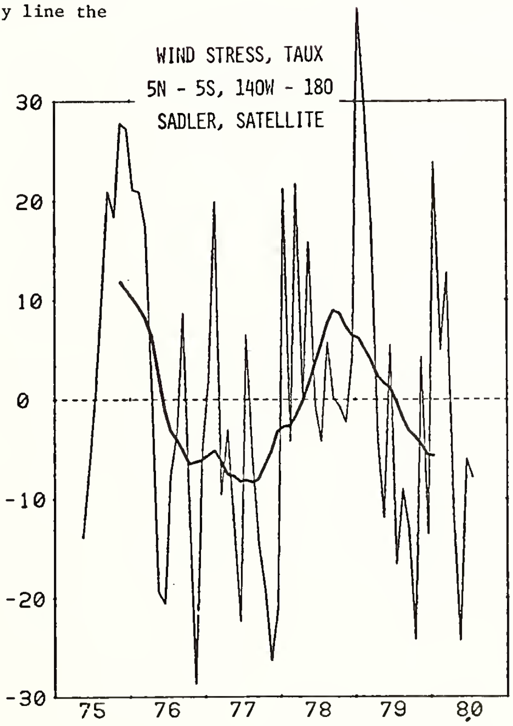

Fig. 6. Satellite wind stress index. Westward component of the equatorial wind stress ($m^2 s^{-2}$) based on low level cloud motion vectors. The thin line gives individual monthly means, the heavy line the 12 month running mean.

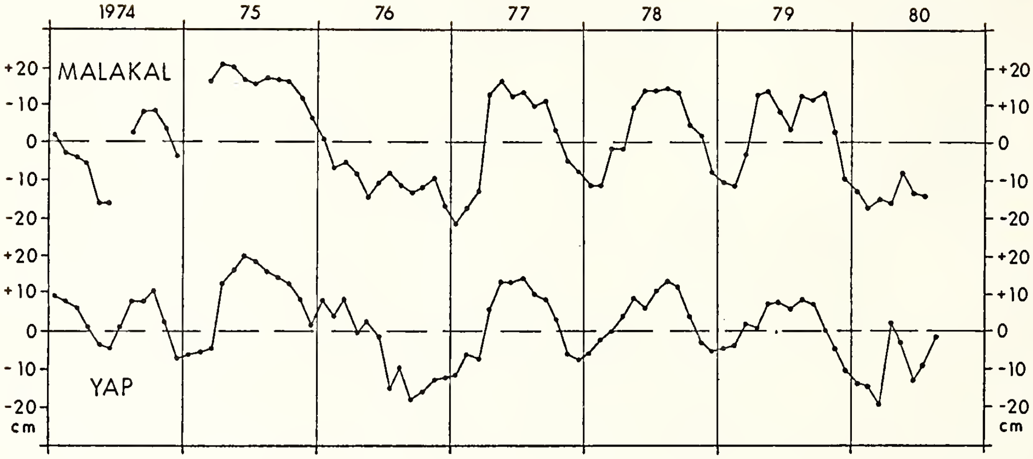

Fig. 7. Monthly mean sea level (cm) at Malakal (7N, 134E) and Yap (9N, 138E) from 1974 to 1980.

SYNOPTIC PROCESSES OVER THE SOUTH PACIFIC OCEAN DURING YEARS OF CONTRASTING EQUATORIAL CIRCULATION AND SST ANOMALIES

Richard A. Keen

Cooperative Institute for Research in Environmental Sciences
University of Colorado
Boulder, Colorado 80309

This paper discusses the role of synoptic-scale systems, both tropical and extratropical, in the larger-scale atmospheric circulation variability known as the Southern Oscillation (S. O.). The usual low-level winds over the equatorial Pacific are characterized by dry easterlies. Occasionally - particularly over the Western Pacific during November, December, and April - this flow reverses. Equatorial westerlies are associated with active convection.

Examples of the interannual variability of the distribution of active convection over the Central and Western Tropical Pacific, as measured by the frequency of Highly Reflective Clouds (HRC) on satellite imagery, are shown in Fig. 1. In December 1973, dry easterlies extended along the Equator as far west as Indonesia, with only 5 mm precipitation at Canton Island (172^{o}W, 3^{o}S). Wet equatorial westerlies crossed the date line during December 1972 and 1977; respective Canton Island precipitation totals were 427 mm and 522 mm.

The synoptic sequence shown in Fig. 2 is typical of heavy rain events at Canton Island, and occurred twice during each of the seasons 1957-58 and 1977-78. On 10 November, equatorial easterlies extend across the date line; a cold front is penetrating into tropics from the southwest. By 23 November, the cold front (as analysed on NMC charts) stalls; a cyclonic development near the date line initiates equatorial westerlies. A second low forms north of the Equator on 26 November, and the westerlies reach Canton Island. By 5 December, the northern low moves poleward as a tropical storm, but a broad trough remains south of the Equator, maintaining equatorial westerlies. In this particular case the southern low pressure region generated two tropical storms. Most of these heavy rain episodes at Canton Island have resulted in tropical storm development, usually in both hemispheres. The climatology of these disturbances can easily be extended by considering named tropical pairs.

The interrelationships between cyclone pairs, equatorial convection and SST's, and the S. O. are summarized in Figure 3. There is a good correlation between the S. O. index (Tahiti minus Darwin pressures) and the eastward equatorial extent of 29^{o}C surface water. However, the longitudes of warm water and equatorial convection (defined by HRC = 3, see Figure 1) agree interannually but not on an annual cycle. The longitudes are about the same during southern summers, but differ by 40^{o} during southern winters. This implies that the link between SST and convection is not a simple direct one. Cyclone pairs occur during southern summer only, and provide the dynamical link between warm surface water and convection on the Equator. In general, the longitude of the cyclone pairs follows those of high SST's and convection from summer to summer;

the exception was 1974-75 when, in spite of warm SST's near the date line, no cyclone pair developed. The apparently developing S. O. anomaly collapsed early in 1975. Also apparent in Fig. 3 is a feedback between the occurrence of cyclone pairs and extent of warm water. Five events when warm SST's extended east after development of a pair are October 1972, December 1976, March 1977, December 1977, and December 1979. The SST changes for these five events are composited in Figure 4. In all five, a SST warming occurred in an area just south of the Equator, apparently due to advection or reduced upwelling associated with the surface westerlies between the paired cyclones.

Extratropical storm tracks for high and low S. O. winters are compared in Figures 5 and 6. Low S. O. is eastward extension of the equatorial anomaly (rain events at Canton Island). The parameter shown is the magnitude of 500-mb positive vorticity flux, computed from daily Australian gridded 500-mb heights and summed over a month or season. Relative vorticity is computed; to isolate cyclonic regions only positive values are taken, and are multiplied by geostrophic wind to get the flux. The resulting magnitudes are related to the number and intensity of upper short waves passing over each grid point. During low S. O. winters cyclonic activity is weaker across Australia but stronger over the central South Pacific, apparently weakening the western flank of the subtropical anticyclone.

Vorticity fluxes for high and low S. O. Decembers are compared in Figures 7 and 8. An expansion of the circumpolar vortex during low S. O. is apparent in both vorticity flux and 500-mb height changes. The greater flux over the Tasman Sea indicates more "digging" troughs during low S. O.; more detailed displays of the data show a northward spur along the date line. Data for individual Novembers and Decembers associate relatively high fluxes near the date line with cyclone pair development, supporting the implication suggested by cold fronts on the synoptic sequence in Figure 2 that extratropical systems may trigger some cyclone pairs. The absence of date line cyclone pairs during 1974-75 may have been related to the lack of low-latitude extratropical disturbances (i.e. very small vorticity fluxes near the date line).

In summary, the suggested role of synoptic systems in the S. O. is:

1) Cross-equatorial cyclone pairs provide the link between warm surface water and equatorial convection in the Central Pacific.

2) These systems generally vary in longitude with the S. O. anomaly, but appear to play a feedback role in maintaining or extending the warm equatorial sea surface temperature anomaly.

3) South Pacific extratropical storm activity is generally stronger and displaced equatorward during low S. O. seasons.

4) These low-latitude extratropical systems may help initiate formation of date-line cyclone pairs.

5) The occurrence (or absence) of a single synoptic system may influence the outcome of an entire Southern Oscillation anomaly.

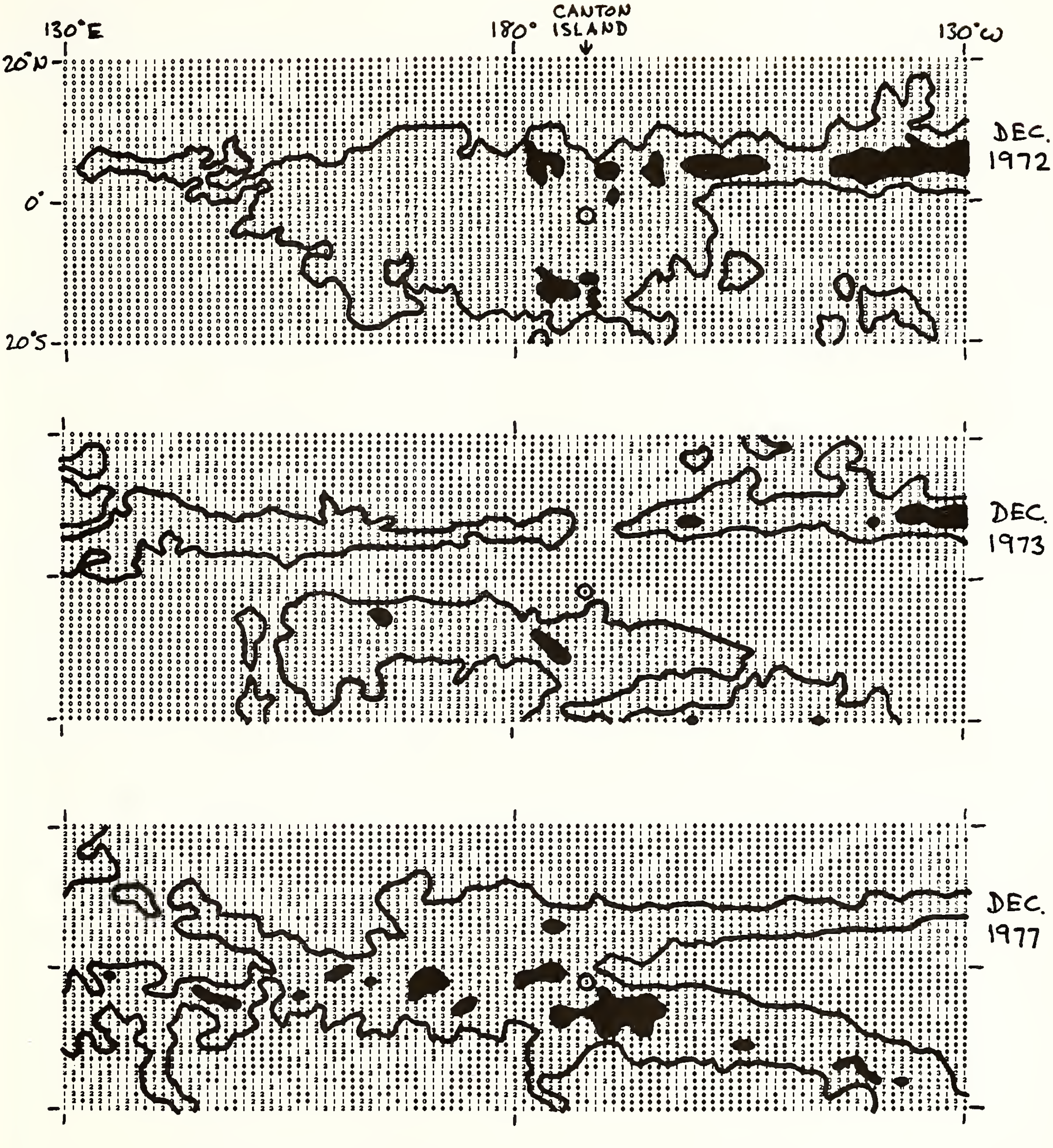

Fig. 1. Monthly number of days per 1-degree square with Highly Reflective Clouds (HRC) over the central and western tropical Pacific, December 1972, 73, and 77. Areas with HRC frequencies of 3 or more are outlined, and frequencies of 10 or more are shaded. Data courtesy of O. Garcia, JIMAR.

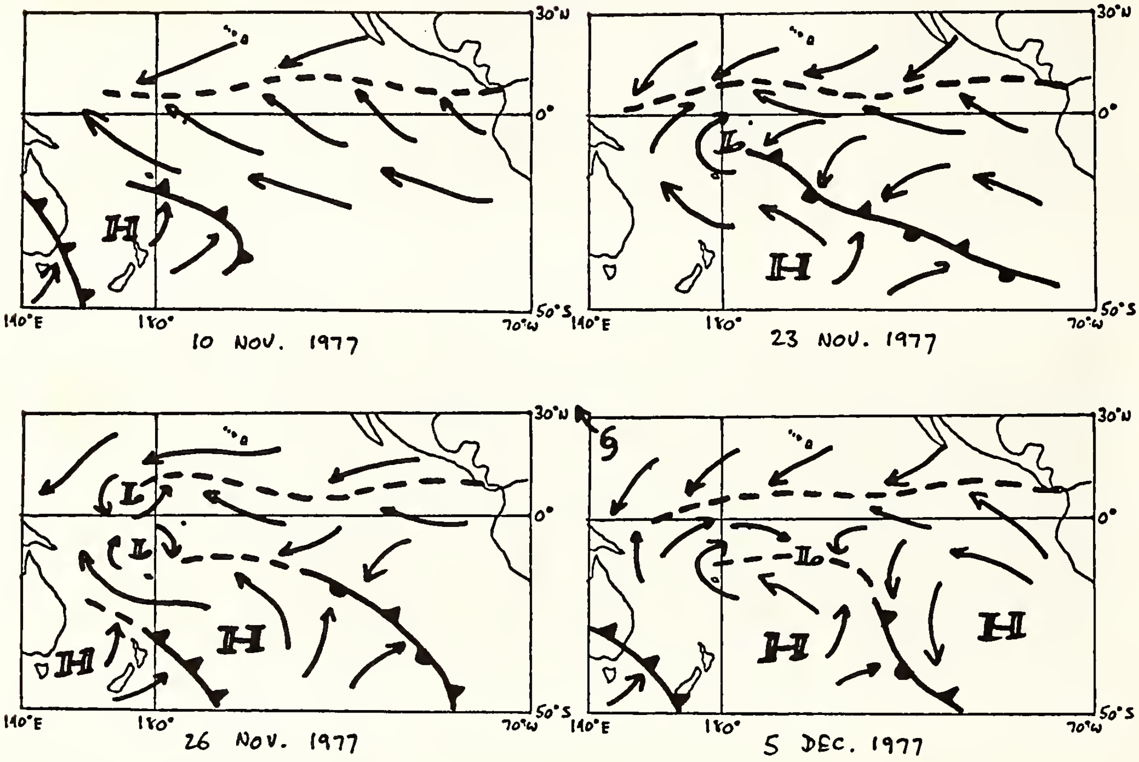

10 NOV. 1977

23 NOV. 1977

26 NOV. 1977

5 DEC. 1977

Fig. 2. Surface synoptic analyses during the evolution of an equatorial westerly disturbance, November-December, 1977.

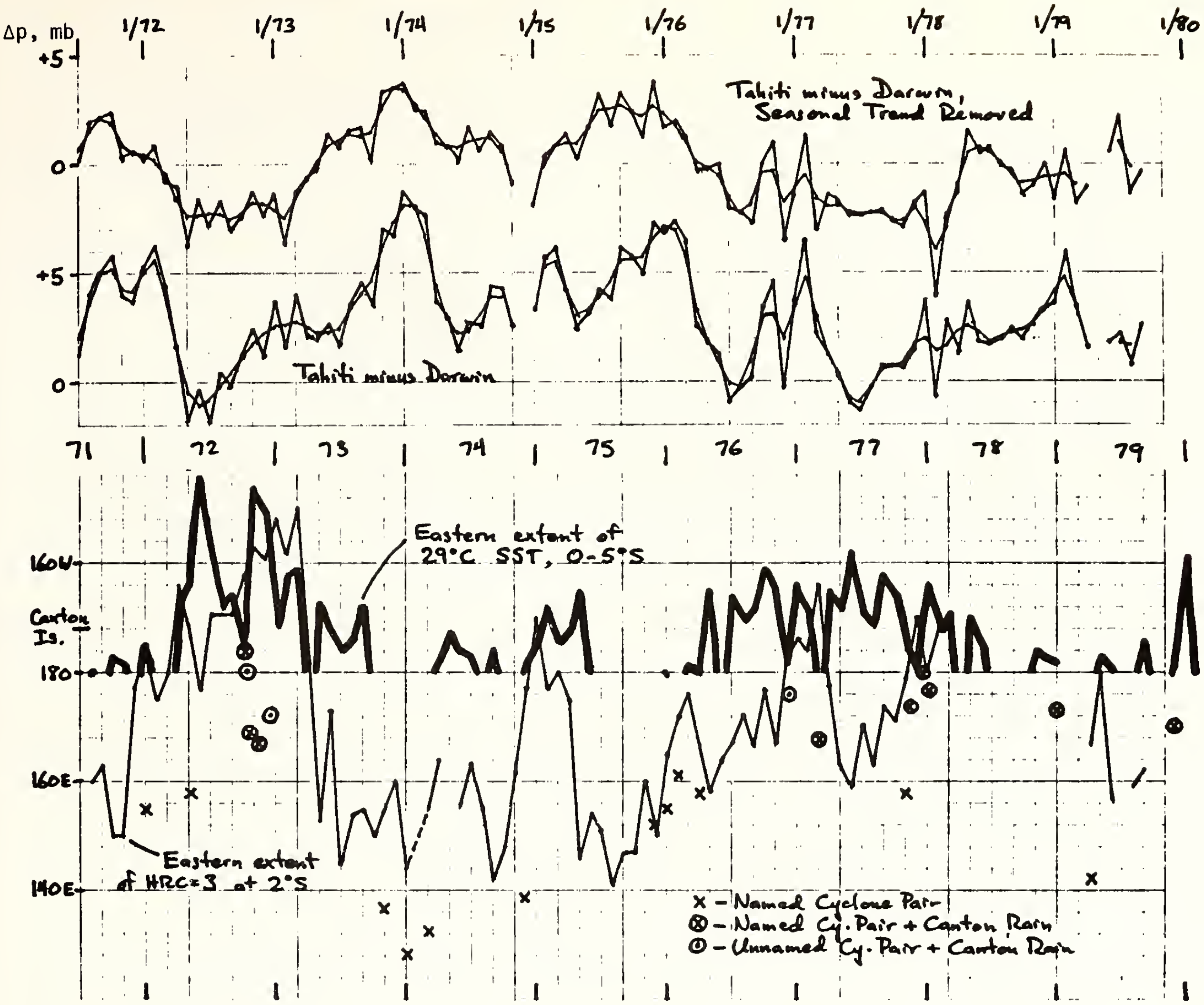

Fig. 3. Top: Monthly mean sea-level pressure differences between Tahiti and Darwin.
Bottom: Longitudes of the easternmost equatorial extents of 29^{0}C SST's and active convection, and of cross-equatorial cyclone pairs.

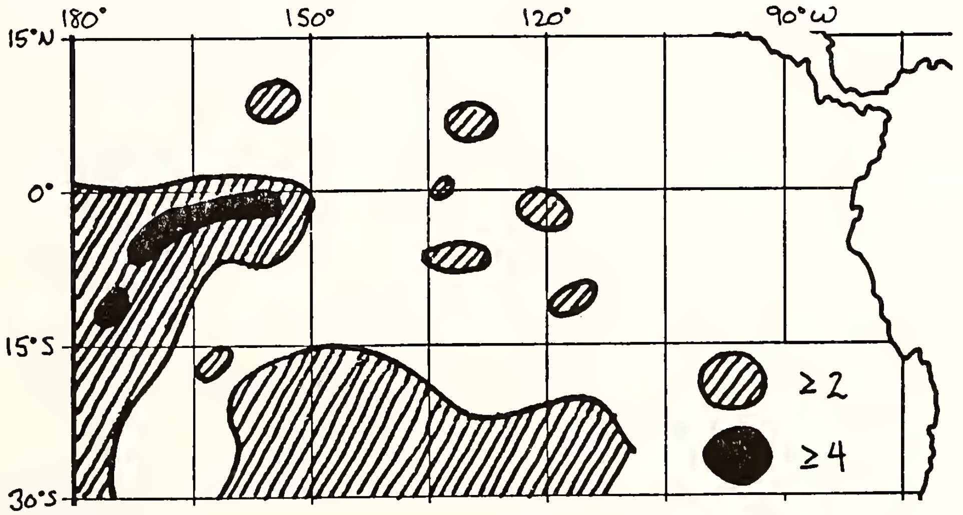

Fig. 4. Number of occurrences (out of 5 events) that SST rose by 1^{0}C or more between the central month of a date line cross-equatorial cyclone pair (Canton Island heavy rain event) and the following month.

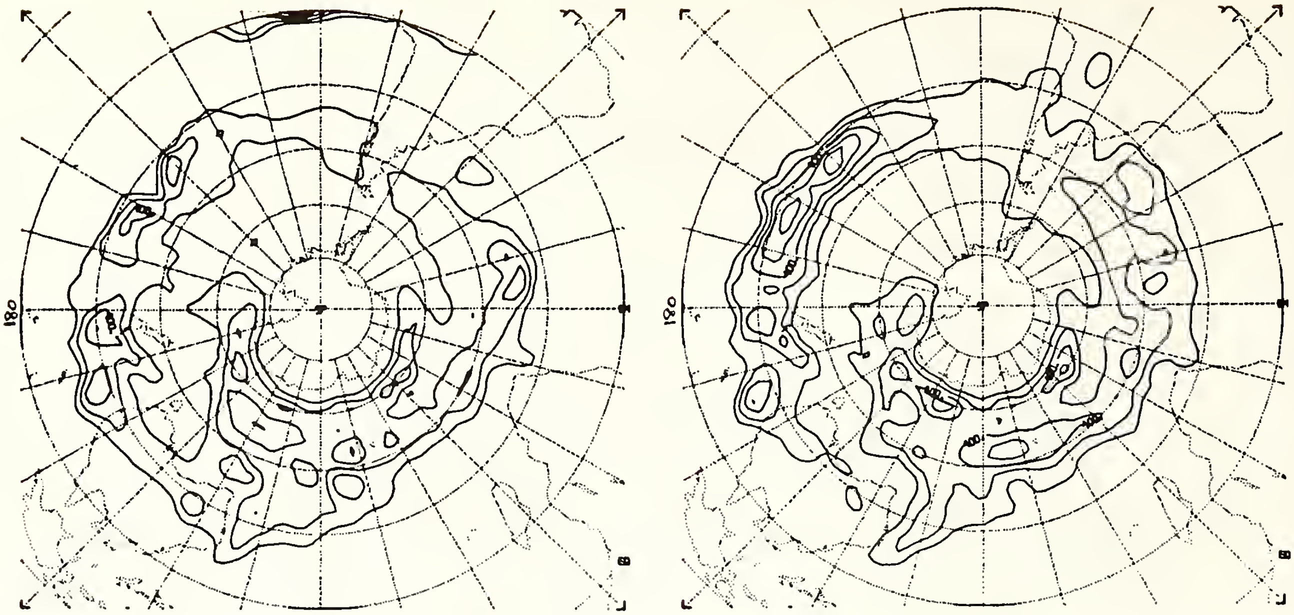

Fig. 5. (left) Magnitude of positive relative vorticity flux, composited for three high Southern Oscillation winters (June-September), 1973, 74, and 75. Contour interval, 100 x 10^{-6} m/sec^2; zero and 100 contours omitted for clarity.
(right) As above, but composited for three low Southern Oscillation winters, 1972, 76, and 77.

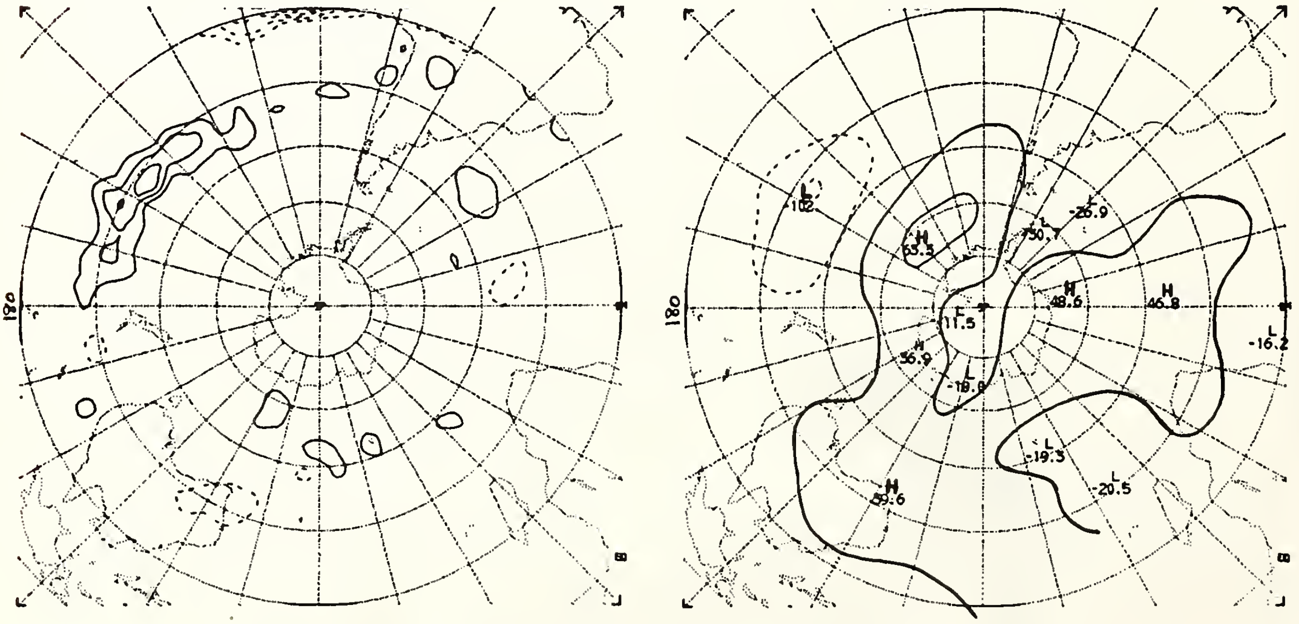

Fig. 6. (left) Vorticity flux difference between the low and high Southern Oscillation winters (low minus high) in figure 5. Contour interval, 100 x 10^{-6} m/sec^2; zero contour omitted for clarity; negatively valued contours dashed.
(right) Mean 500mb height difference between low and high Southern Oscillation winters (low minus high). Contour interval, 50m; negatively valued contours dashed.

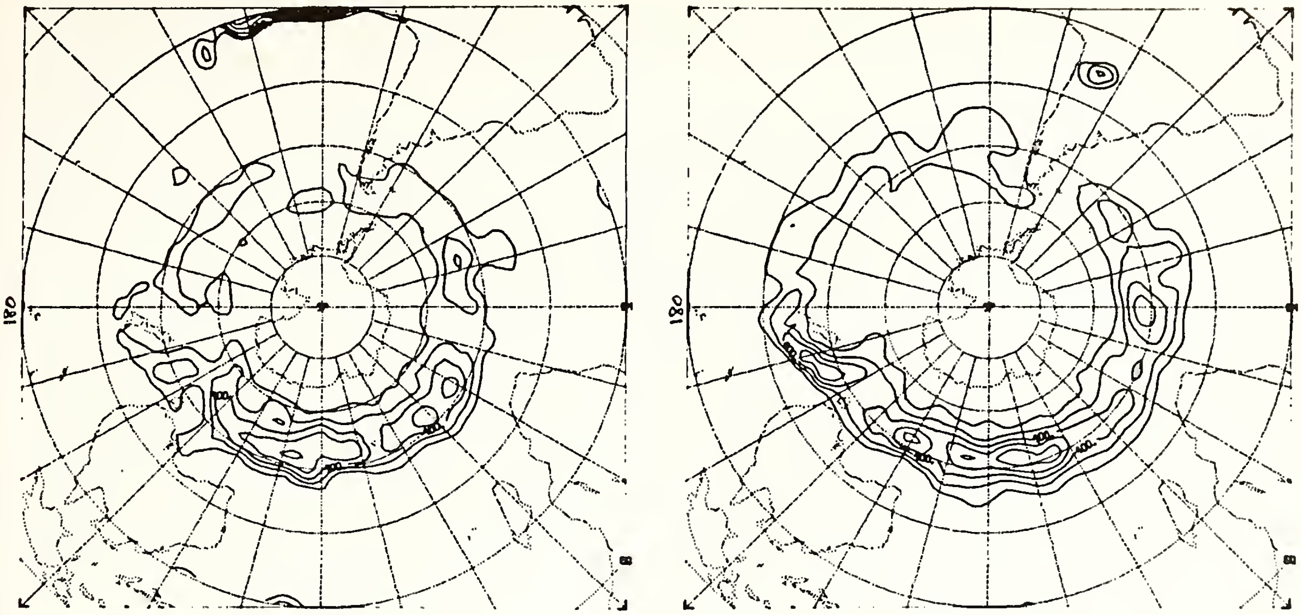

Fig. 7. (left) As in fig. 5, except vorticity flux is composited for three high Southern Oscillation Decembers, 1973, 74, and 75.

(right) Vorticity flux composited for three low Southern Oscillation Decembers, 1972, 76, and 77.

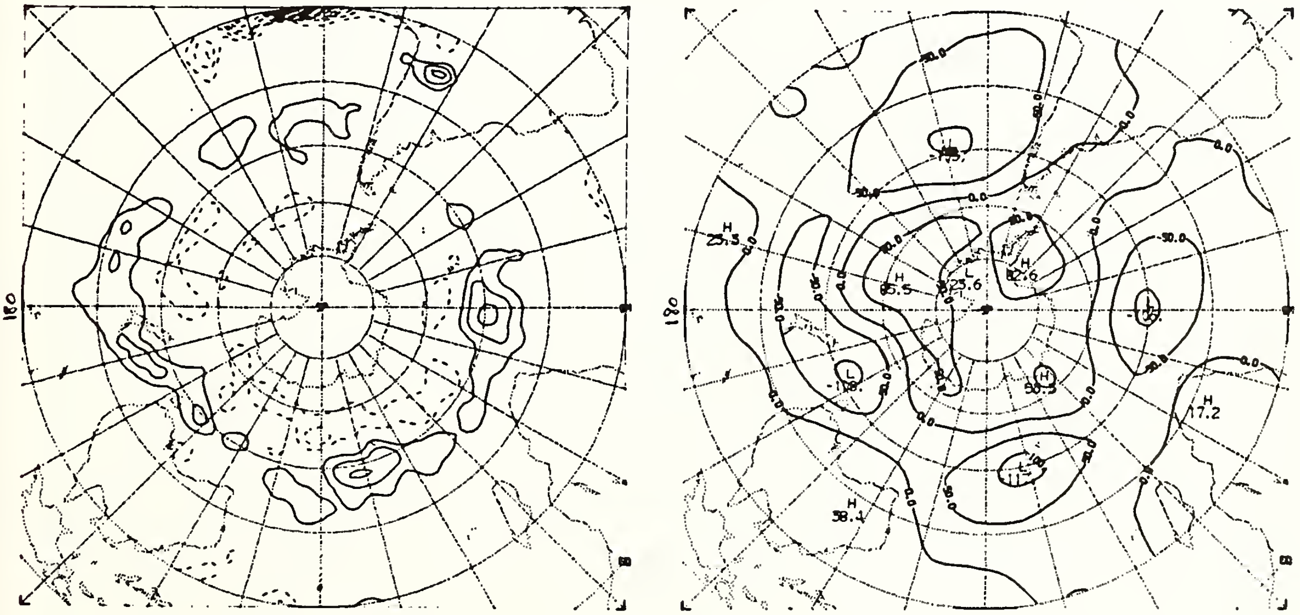

Fig. 8. (left) As in fig. 6, except differenced between the low and high Southern Oscillation Decembers (low minus high) in fig. 7.

(right) Mean 500mb height difference between low and high Southern Oscillation Decembers (low minus high). Contour interval, 50m.

An Analysis of Seasonal Trade Wind Divergence in the Pacific and Its Relationship to Circulation in Higher Latitudes

by

Robert Harnack

Department of Meteorology & Physical Oceanography
Rutgers - The State University
New Brunswick, New Jersey 08903

The 25-year monthly Pacific trade wind data set assembled by Wyrtki and Myers by 2° latitude by 10° longitude quadrangles was used to compute horizontal velocity divergence for each standard season in the period 1948-73. In order to increase the number of observations available for analysis, data of adjacent quadrangles were aggregated so that data points were 4° latitude and 10° longitude apart. Individual monthly means were also aggregated into standard season means. Horizontal velocity divergence was then computed for each season, using a 4° latitude - 10° longitude grid.

Long-term means were computed and mapped for each season. Figures 1 and 2 show the maps for winter (Dec-Feb) and summer (June-Aug), respectively. These each indicate the zonally extensive area of convergence centered near 6°N in winter and near 8°N in summer. Divergence anomalies were also computed for each season -- a partial analysis of which is shown in Figure 3. This indicates that most of the interannual variability is found in the Northern Hemisphere tropics. No obvious relationship between trade divergence anomaly and the occurrence of El Nino events (e.g., 1951, 1953, 1957, 1963, 1965, 1969, 1972) is seen by examination of this figure.

The divergence field for each season was subjected to empirical orthogonal function (EOF) analysis. Explained variances by EOF number are seen in Table 1. The analyses showed that 15 to 18 percent of the total variance was accounted for by the first function. Monte Carlo testing indicated that at least six EOF's probably represent a climatic signal. Figures 4 and 5 show an analysis of the spatial coefficient pattern for EOF1 in winter and summer, respectively. These patterns appear to represent mainly the north-south gradient of divergence, and therefore their amplitudes mainly represent north-south shifts of zones of divergence, especially for summer. Zonal coherence is also indicated over the entire eastern tropical Pacific, especially north of the Equator in summer. A more complex pattern is noted in winter. The time varying amplitudes for EOF1 in winter and summer are graphed in Figure 6.

The first several seasonal trade wind divergence EOF's were correlated with each of 15 seasonal zonal circulation indices at 700 mb using -4 to +4 season lags. The domains and names of the 12 regional zonal indices are indicated in Figure 7. Each of the three additional indices used cover the entire hemisphere and correspond to each of the three indicated latitude belts. Figures 8 - 11 show contemporaneous relationships (0 season lag) between trade divergence EOF1 and the zonal indices for each season. Only a few correlation coefficients were determined to be significant at the 5 percent level (indicated by underlining of the values). The most interesting correlations were found between trade divergence EOF1 in a season and the following winter season zonal indices.

One-season lag relationships for autumn trade wind EOF1 preceding the zonal indices for winter is shown in Figure 12. Several statistically significant relationships are indicated. Two-, three-, and four-season lag relationships are shown in Figures 13 - 15, respectively. Each gives relationships between winter zonal indices and antecedent trade divergence EOF1. With the exception of the three-season lag relationship (Figure 14), each map shows many significant relationships involving the Pacific, North American, and Atlantic sectors. These suggest that the Pacific trade wind field may be used to foreshadow mid- and high-latitude circulation regimes in winter up to four seasons in advance. An advance indication of winter season blocking in the North Atlantic and North Pacific sectors may accrue also.

Figures 16 - 21 show graphs of selected correlation functions for the relationships between trade divergence EOF1 and zonal indices at -4 to +4 season lag. Large dots on the graphs indicate relationships deemed significant at the 5 percent level. These serve to further illustrate that most of the significant correlations occur only when winter zonal circulation is involved in such a way that trade divergence EOF1 leads the zonal index. Some carry-over of large correlations to spring zonal circulation is also noted. Only apparently random relationships were seen in this study when other trade wind EOF's or other combinations of seasonal zonal indices and lag amounts were used.

The determination of a physical explanation for the correlations cited is proceeding.

Fig. 1. Long-term mean Pacific trade wind divergence ($\times 10^{-6}$ sec^{-1}) for winter (1948-73).

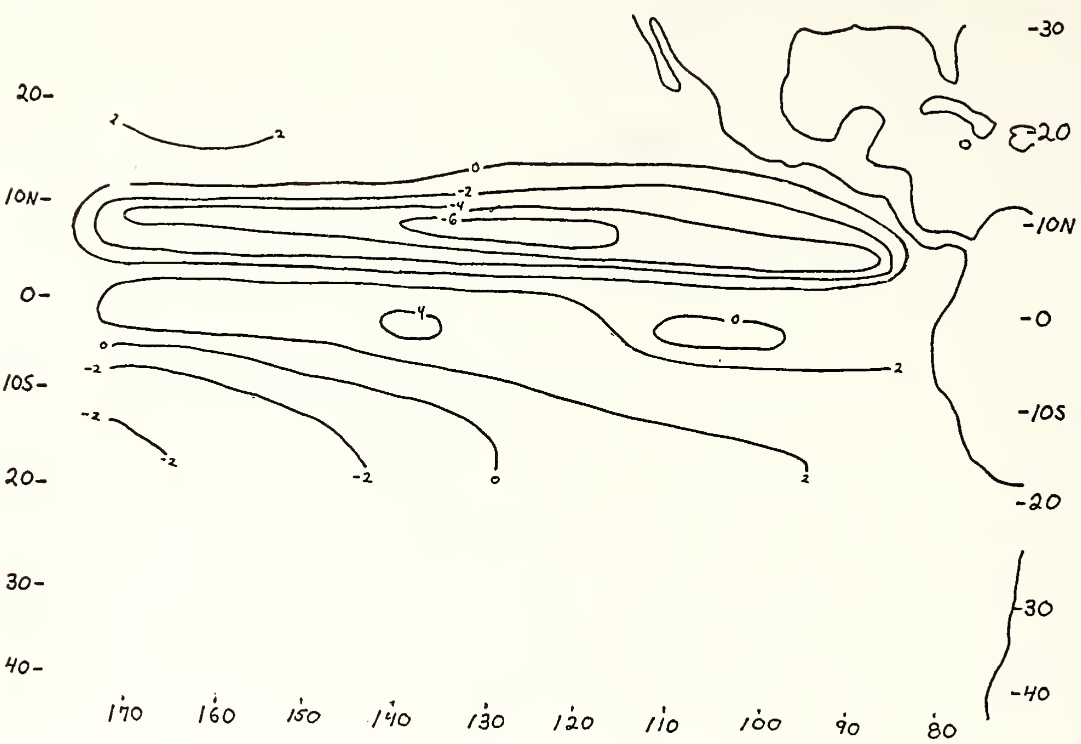

Fig. 2. Long-term mean Pacific trade wind divergence ($\times 10^{-6}$ sec^{-1}) for summer (1948-73).

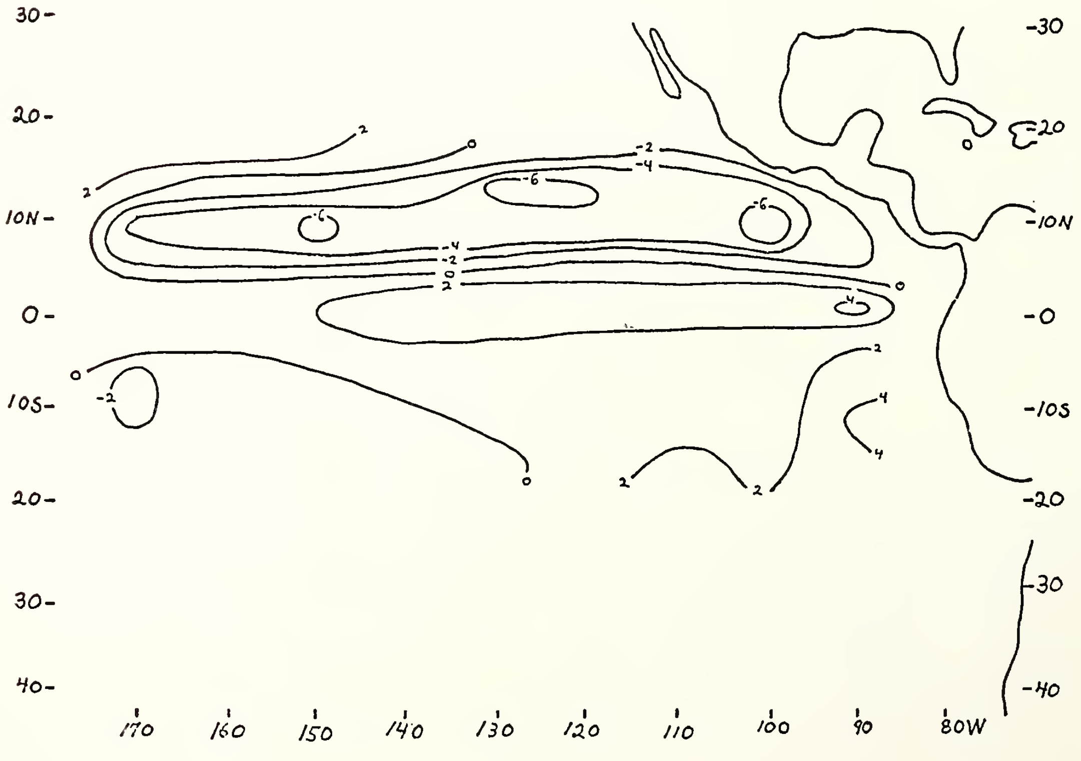

Fig. 3. Time versus latitude map of zonally averaged seasonal Pacific trade wind divergence anomaly in period 1949-73. Isopleths for +2 units ($\times 10^{-6}$ sec^{-1}) shown as solid and -2 units shown as dashed have been extracted from a fully analyzed map.

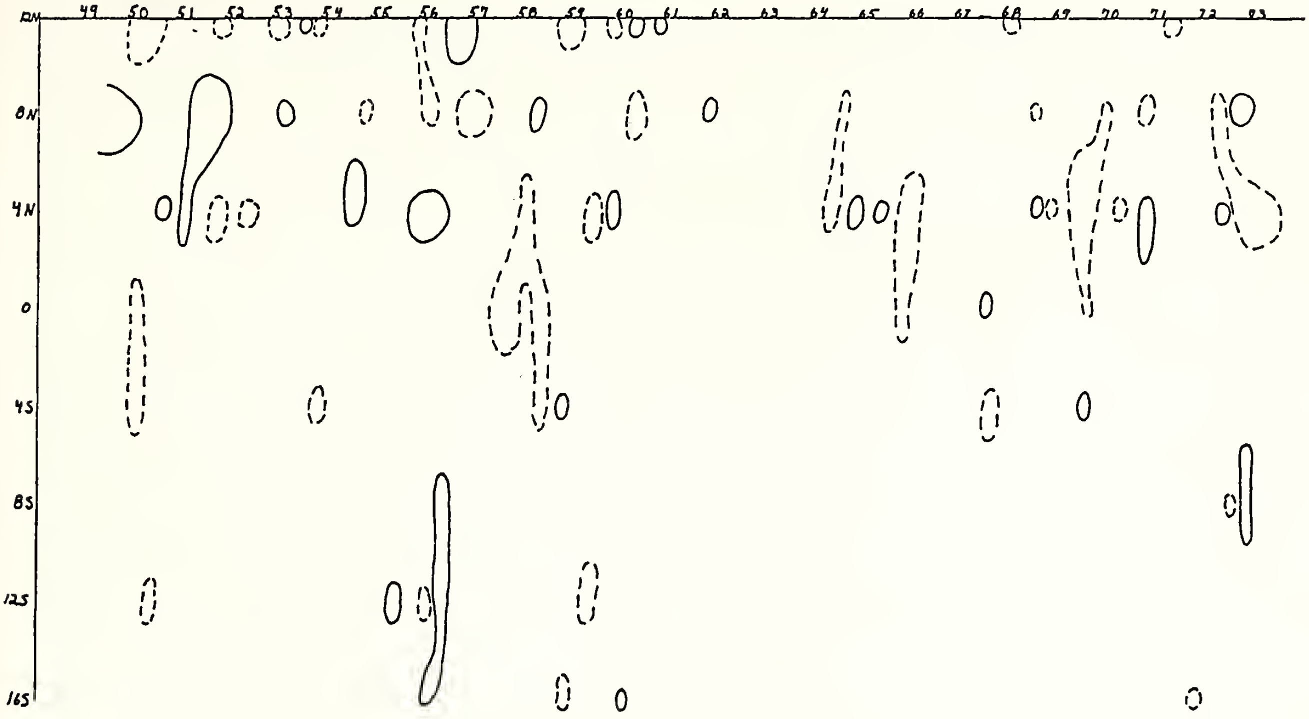

Table 1. Explained variances for seasonal Pacific trade wind divergence EOFs.

EOF No.	Explained Variance			
	Summer	Fall	Winter	Spring
1	18	15	16	18
2	11	13	13	12
3	9	10	12	10
4	9	9	9	9
5	8	7	8	9
6	8	7	7	7

Fig. 4. Spatial coefficient pattern for winter Pacific trace wind divergence EOF1.

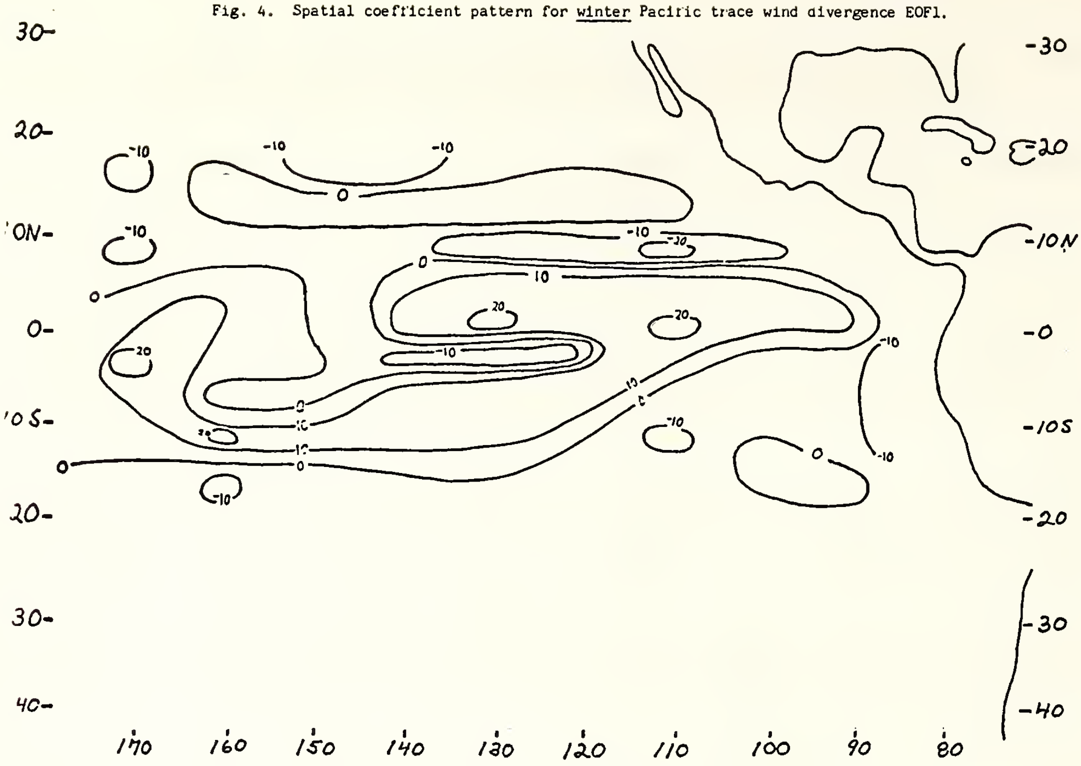

Fig. 5. Spatial coefficient pattern for summer Pacific trade wind divergence EOF1.

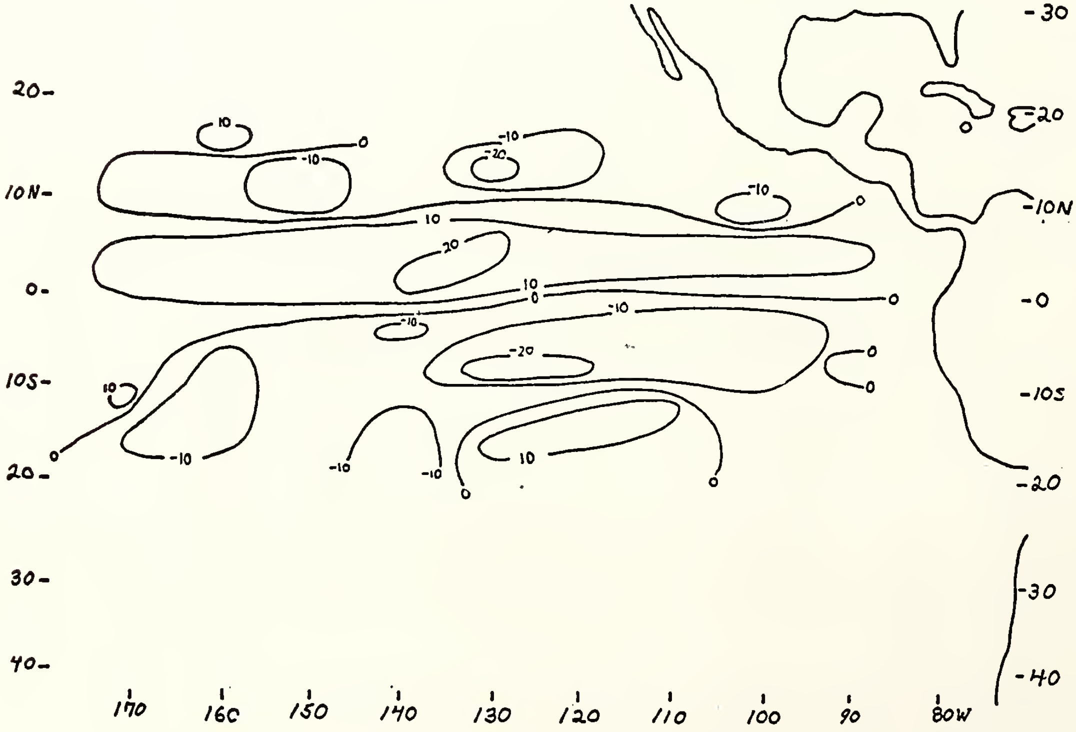

Fig. 6a. Amplitudes of winter Pacific trade wind divergence EOF1 in period 1948-73.

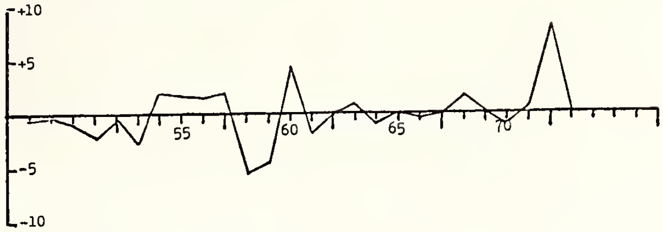

Fig. 6b. Amplitudes of summer Pacific trade wind divergence EOF1 in period 1948-72.

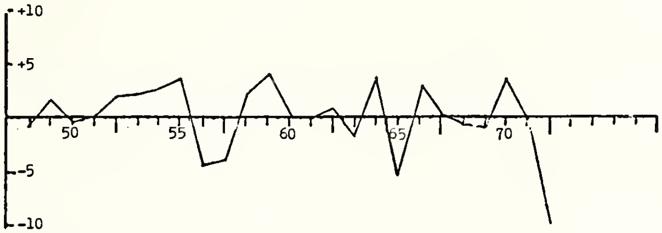

Fig. 7. Zonal circulation indices at 700 mb used in correlation studies.

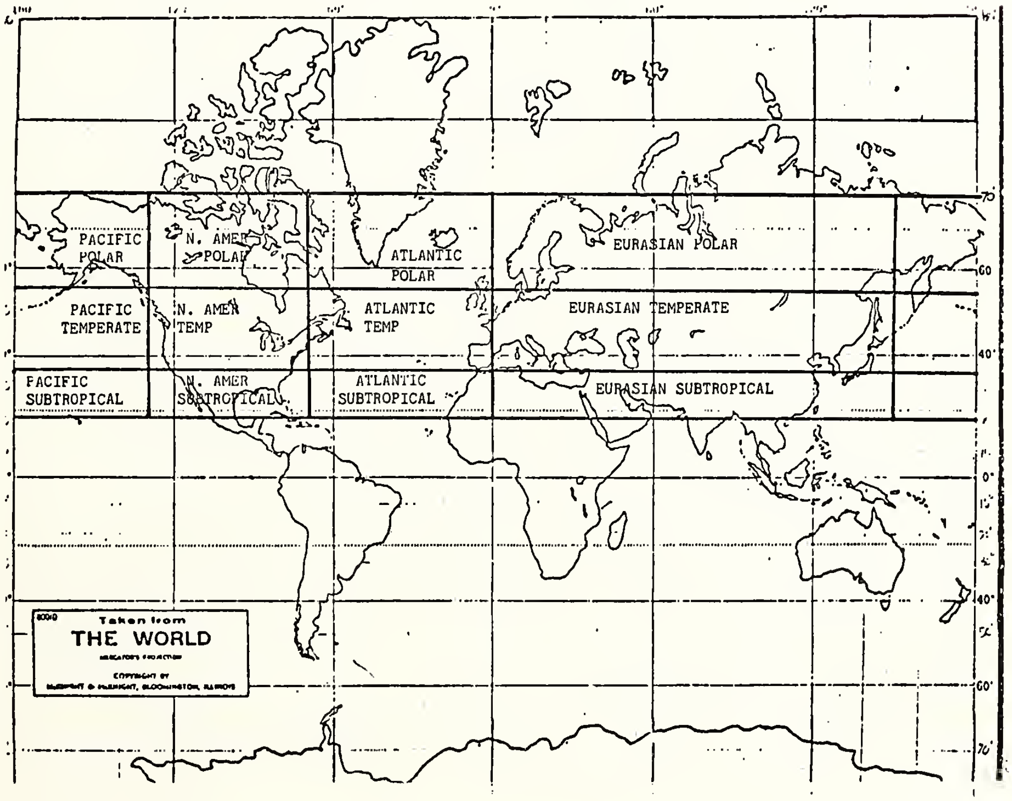

Fig. 8. Distribution of correlation coefficients for the contemporaneous relationship between winter Pacific trade wind divergence EOF1 and zonal indices (0 season lag).

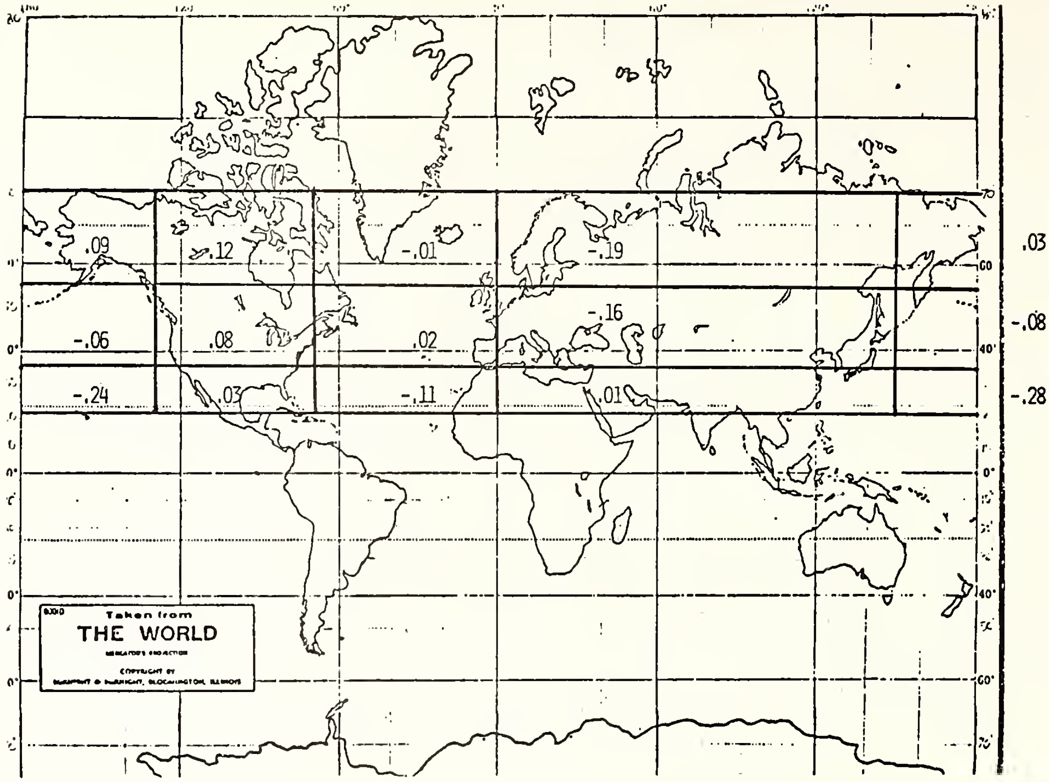

Fig. 9. Distribution of correlation coefficients for the contemporaneous relationship between spring Pacific trade wind divergence EOF1 and zonal indices (0 season lag).

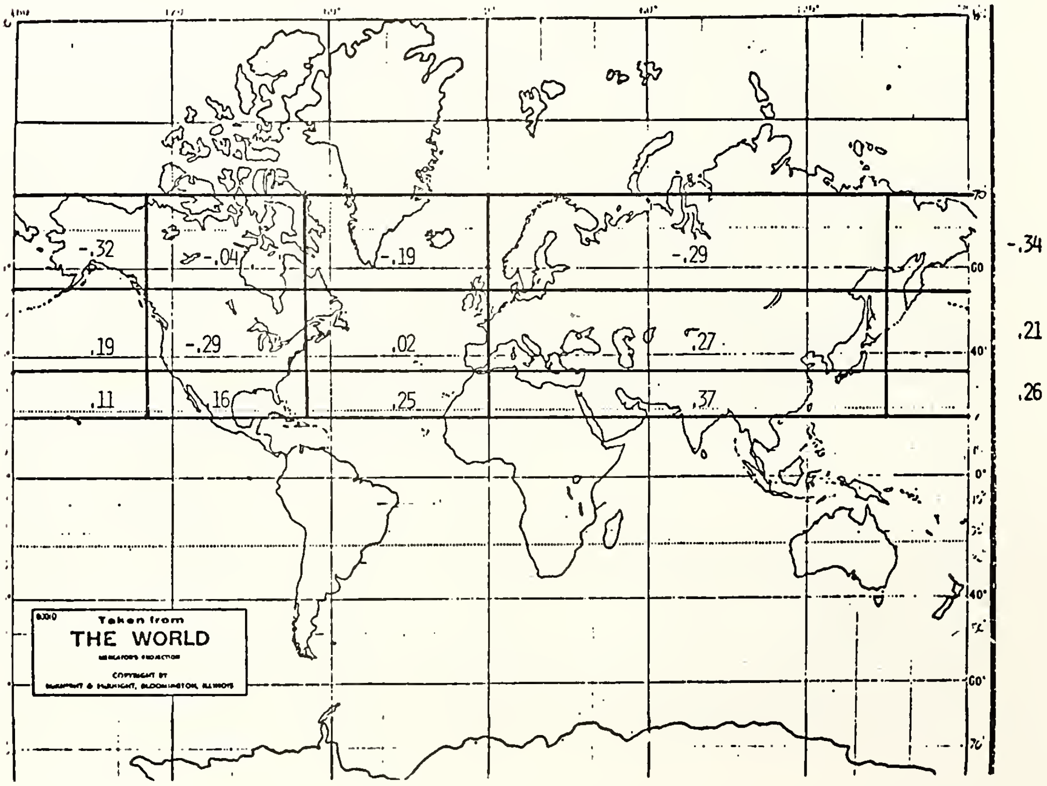

Fig.10. Distribution of correlation coefficients for the contemporaneous relationship between summer Pacific trade wind divergence EOF1 and zonal indices (0 season lag).

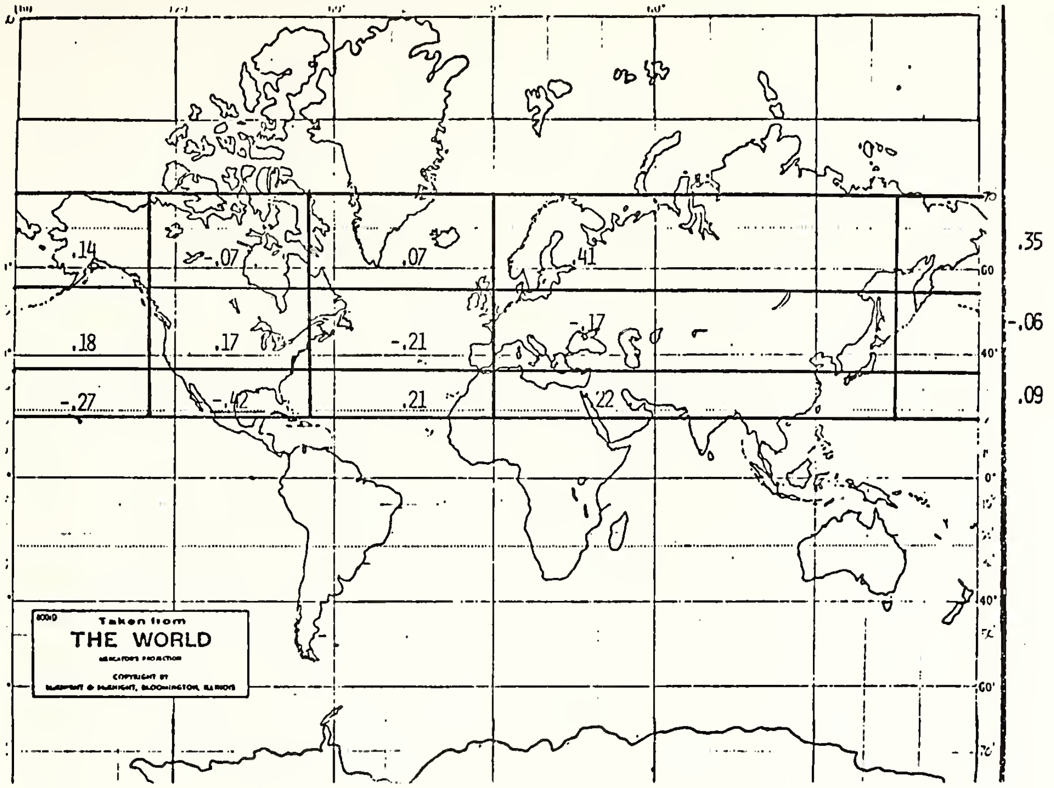

Fig.11. Distribution of correlation coefficients for the contemporaneous relationship between autumn Pacific trade wind divergence EOF1 and zonal indices (0 season lag).

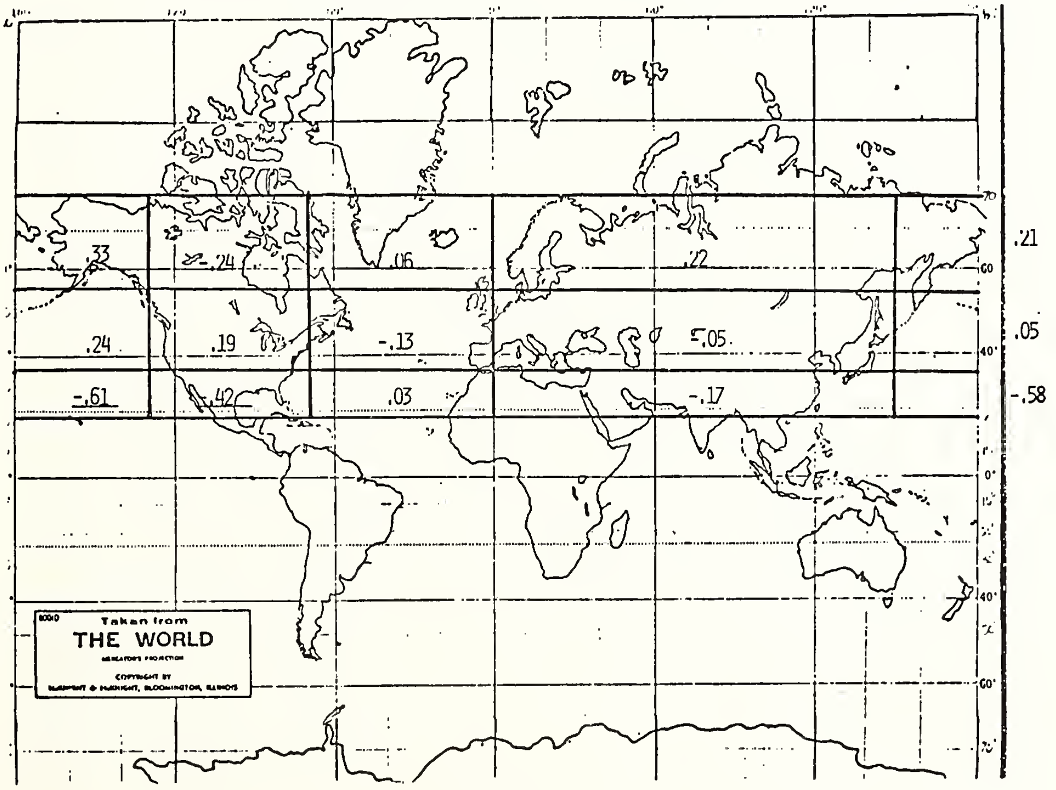

Fig. 12. Distribution of correlation coefficients for the relationship between autumn Pacific trade wind divergence EOF1 and the following winter zonal indices (1 season lag).

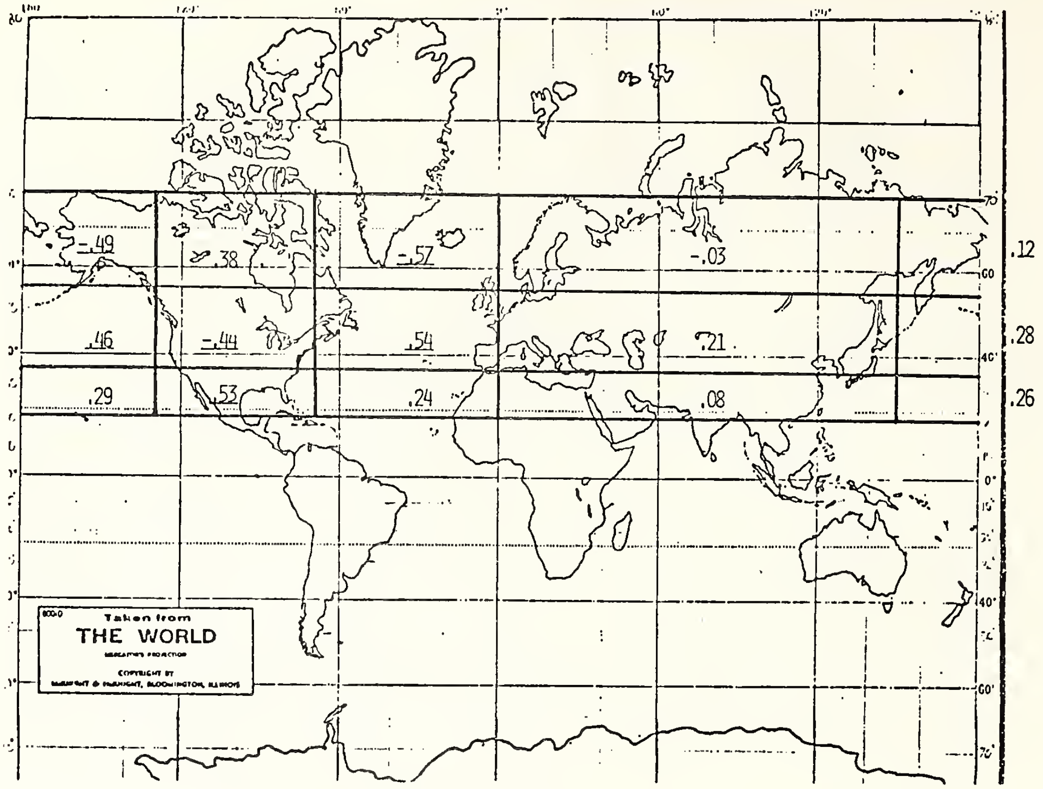

FIG. 13. Distribution of correlation coefficients for the relationship between summer Pacific trade wind divergence EOF1 and the following winter zonal indices (2 season lag).

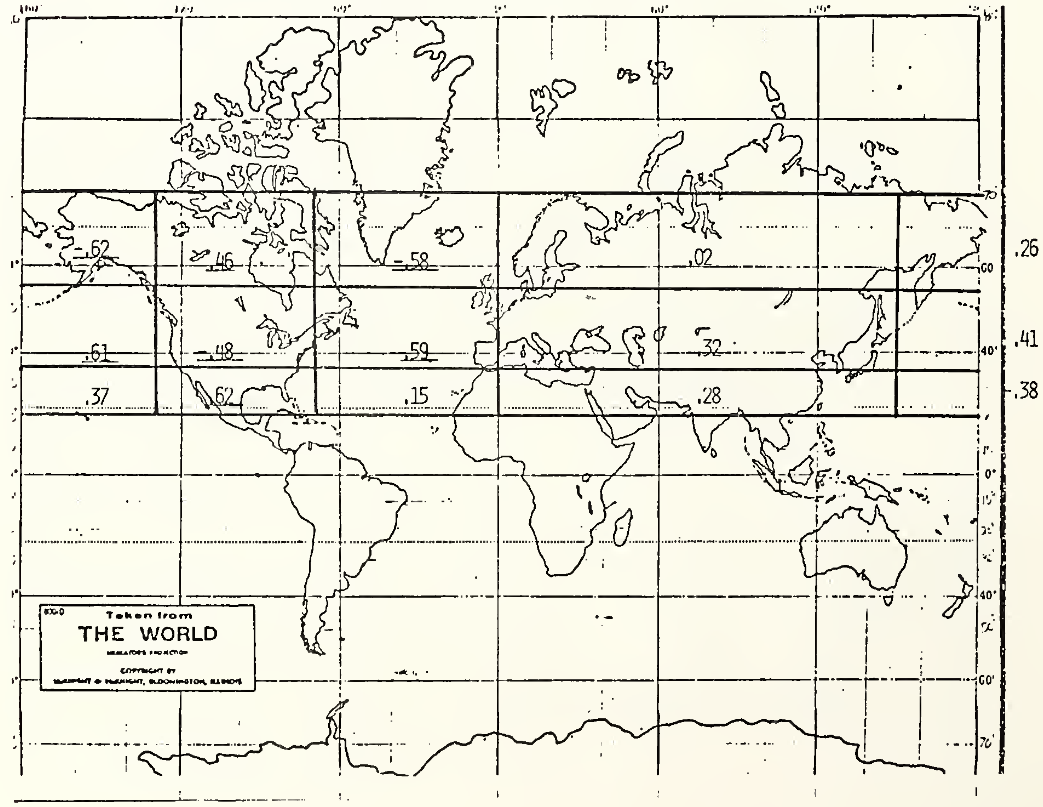

Fig. 14. Distribution of correlation coefficients for the relationship between spring Pacific trade wind divergence EOF1 and the following winter zonal indices (3 season lag).

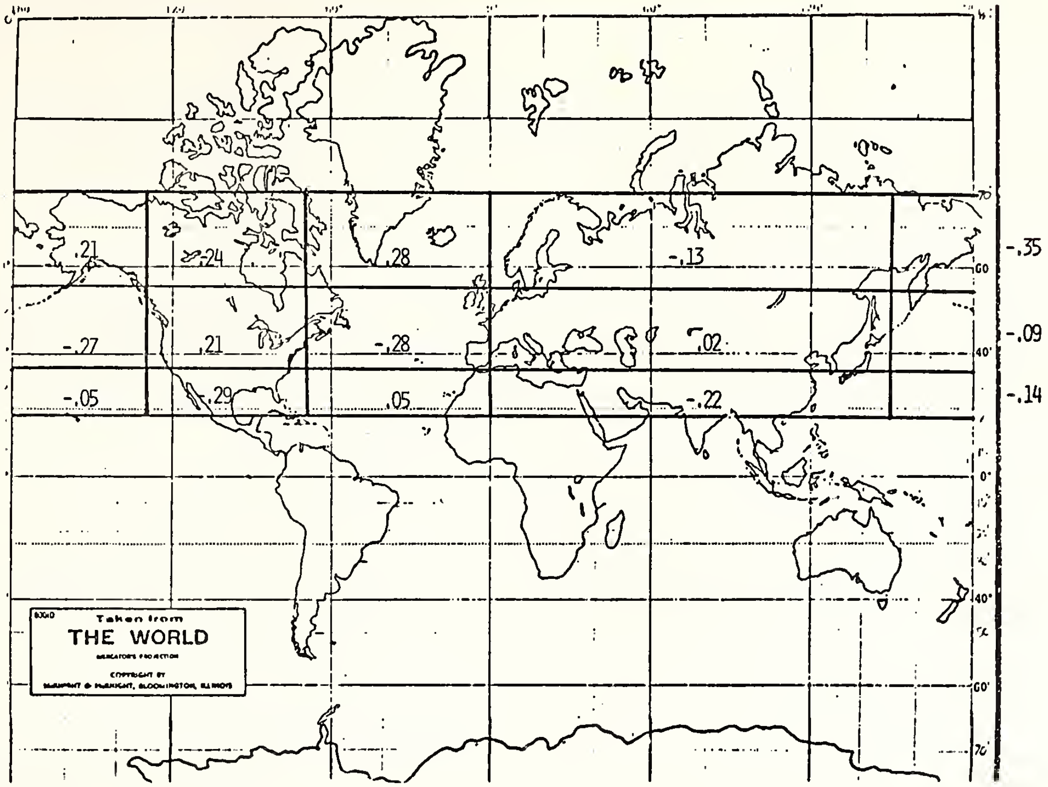

Fig. 15. Distribution of correlation coefficients for the relationship between winter Pacific trade wind divergence EOF1 and the following winter zonal indices (4 season lag).

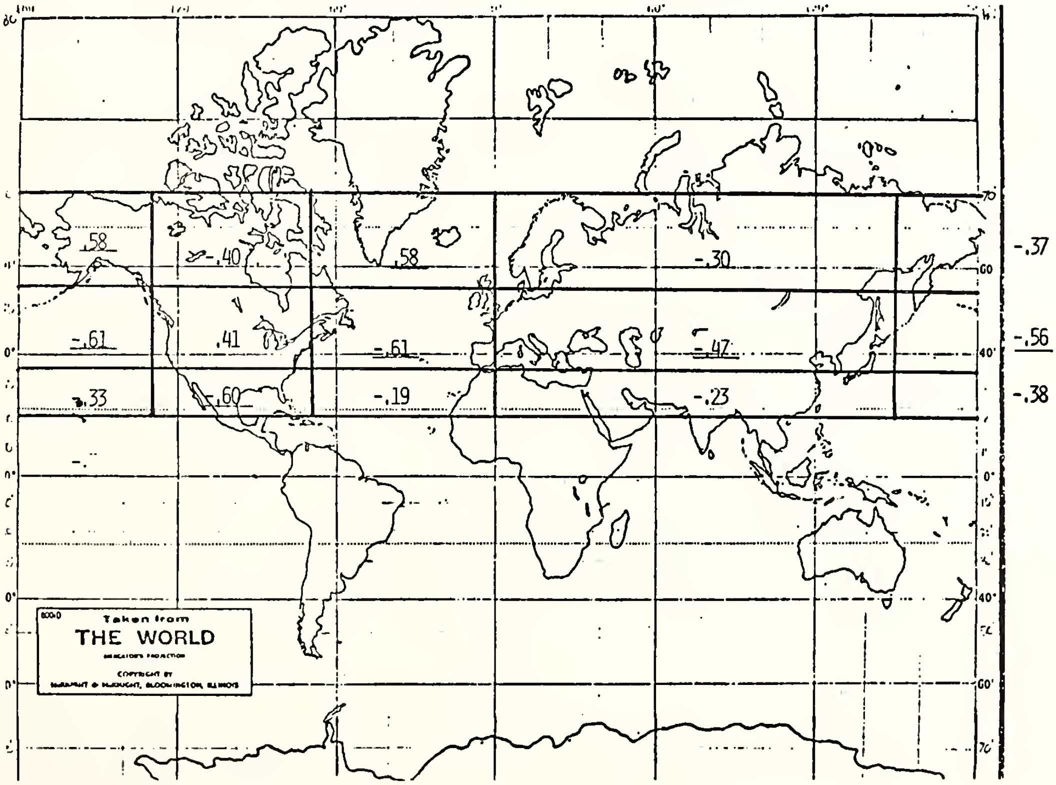

Fig. 16.

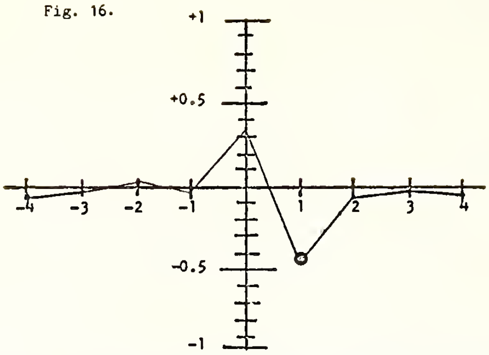

Simple correlations for autumn Pacific trade wind divergence EOF1 leading (positive lag) and lagging (negative lag) the Pacific polar (55-70N) zonal index by 1-4 seasons.

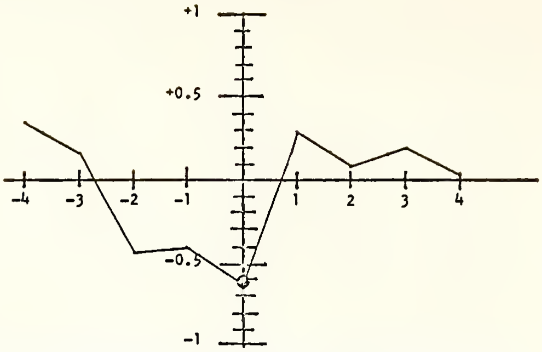

Simple correlations for autumn Pacific trade wind divergence EOF1 leading (positive lag) and lagging (negative lag) the Pacific subtropical (20-35N) zonal index by 1-4 seasons.

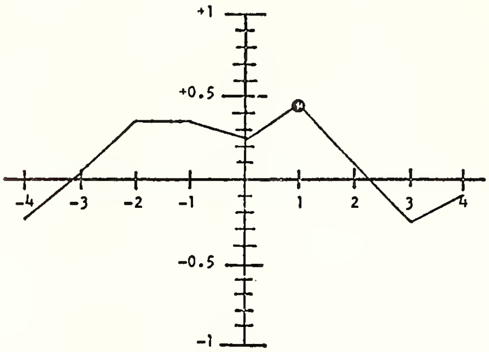

Simple correlations for autumn Pacific trade wind divergence EOF1 leading (positive lag) and lagging (negative lag) the Pacific temperate (35-55N) zonal index by 1-4 seasons.

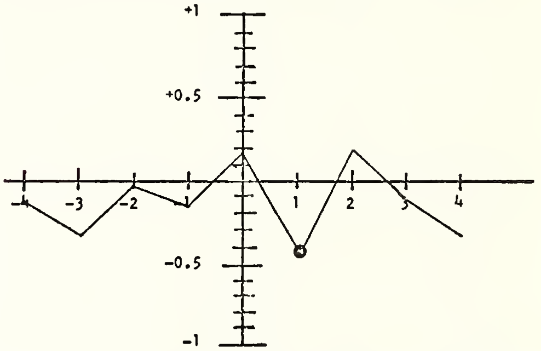

Simple correlations for autumn Pacific trade wind divergence EOF1 leading (positive lag) and lagging (negative lag) the North American temperate (35-55N) zonal index by 1-4 seasons.

Fig. 17.

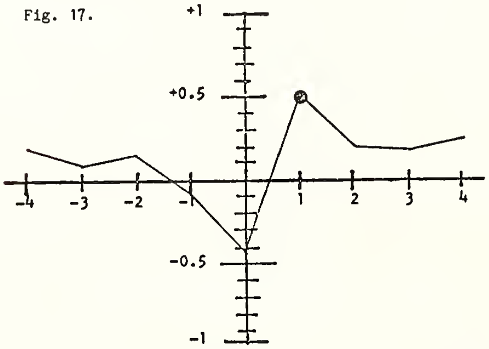

Simple correlations for autumn Pacific trade wind divergence EOF1 leading (positive lag) and lagging (negative lag) the North American subtropical (20-35N) zonal index by 1-4 seasons.

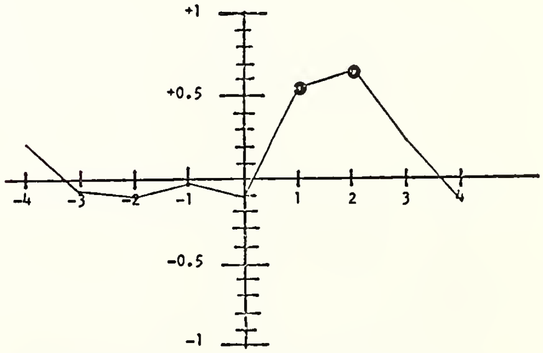

Simple correlations for autumn Pacific trade wind divergence EOF1 leading (positive lag) and lagging (negative lag) the Atlantic temperate (35-55N) zonal index by 1-4 seasons.

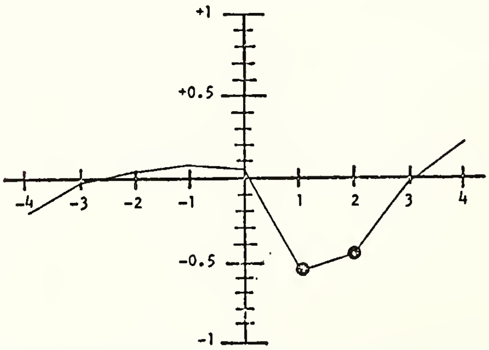

Simple correlations for autumn Pacific trade wind divergence EOF1 leading (positive lag) and lagging (negative lag) the Atlantic polar (55-70N) zonal index by 1-4 seasons.

Fig. 18.

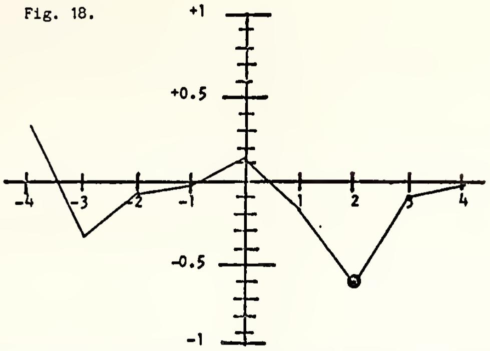

Simple correlations for summer Pacific trade wind divergence EOF1 leading (positive lag) and lagging (negative lag) the Pacific polar (55-70N) zonal index by 1-4 seasons.

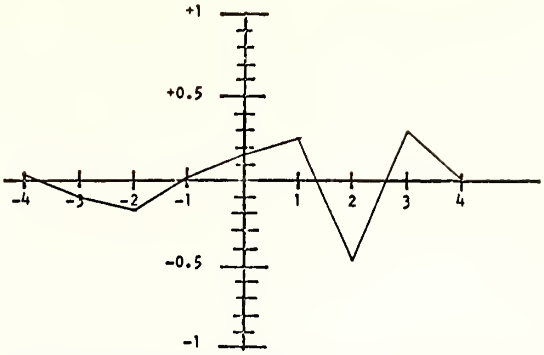

Simple correlations for summer Pacific trade wind divergence EOF1 leading (positive lag) and lagging (negative lag) the North American temperate (35-55N) zonal index by 1-4 seasons.

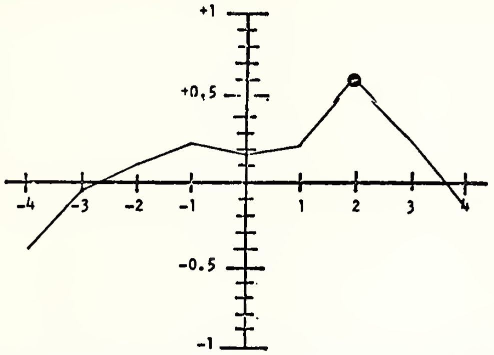

Simple correlations for summer Pacific trade wind divergence EOF1 leading (positive lag) and lagging (negative lag) the Pacific temperate (35-55N) zonal index by 1-4 seasons.

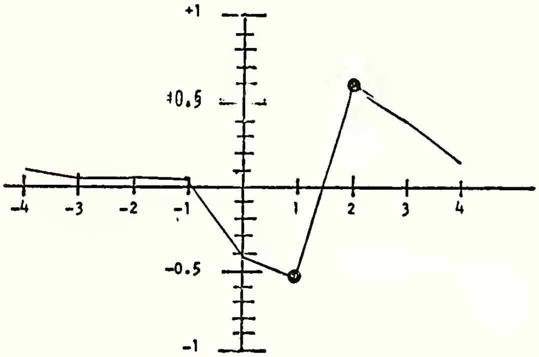

Simple correlations for summer Pacific trade wind divergence EOF1 leading (positive lag) and lagging (negative lag) the North American subtropical (20-35N) zonal index by 1-4 seasons.

Fig. 19.

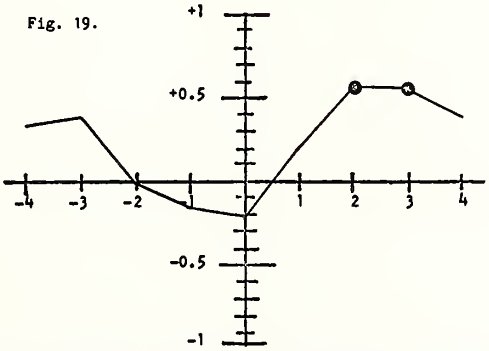

Simple correlations for summer Pacific trade wind divergence EOF1 leading (positive lag) and lagging (negative lag) the Atlantic temperate (35-55N) zonal index by 1-4 seasons.

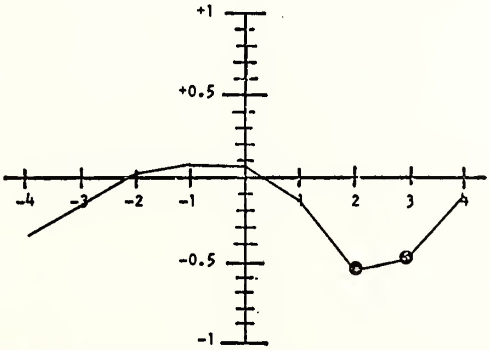

Simple correlations for summer Pacific trade wind divergence EOF1 leading (positive lag) and lagging (negative lag) the Atlantic polar (20-35N) zonal index by 1-4 seasons.

Fig. 20.

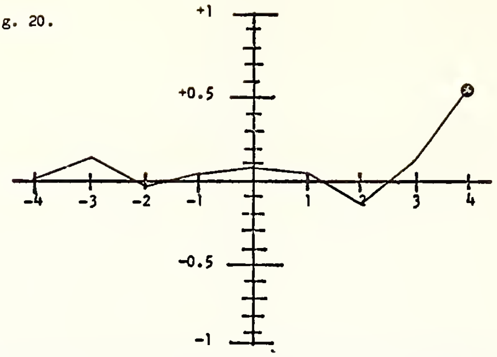

Simple correlations for winter Pacific trade wind divergence EOF1 leading (positive lag) and lagging (negative lag) the Pacific polar (55-70N) zonal index by 1-4 seasons.

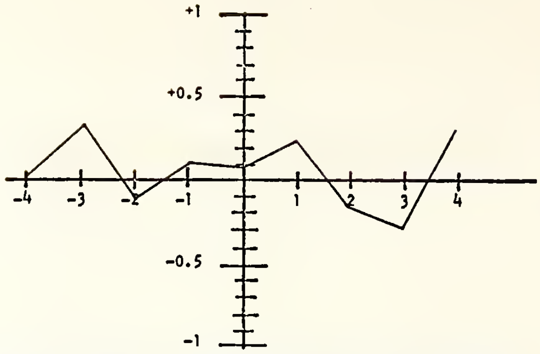

Simple correlations for winter Pacific trade wind divergence EOF1 leading (positive lag) and lagging (negative lag) the North American temperate (35-55N) zonal index by 1-4 seasons.

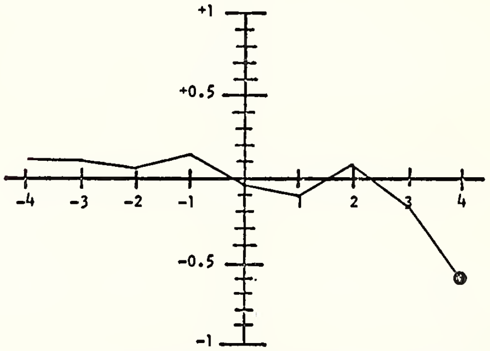

Simple correlations for winter Pacific trade wind divergence EOF1 leading (positive lag) and lagging (negative lag) the Pacific temperate (35-55N) zonal index by 1-4 seasons.

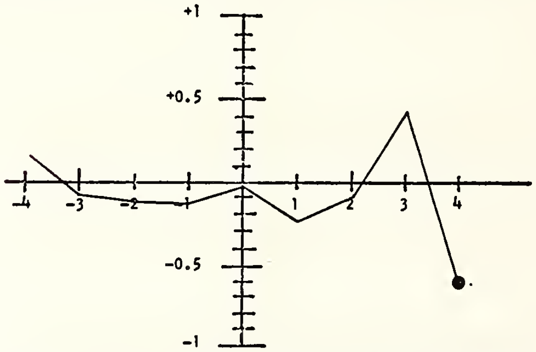

Simple correlations for winter Pacific trade wind divergence EOF1 leading (positive lag) and lagging (negative lag) the North American subtropical (20-35N) zonal index by 1-4 seasons

Fig. 21.

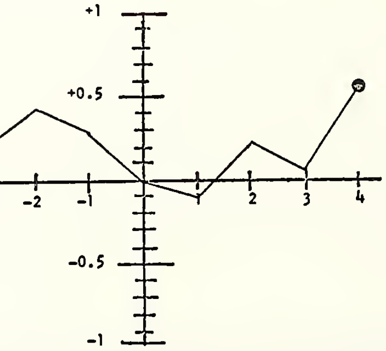

Simple correlations for winter Pacific trade wind divergence EOF1 leading (positive lag) and lagging (negative lag) the Atlantic polar (55-70N) zonal index by 1-4 seasons.

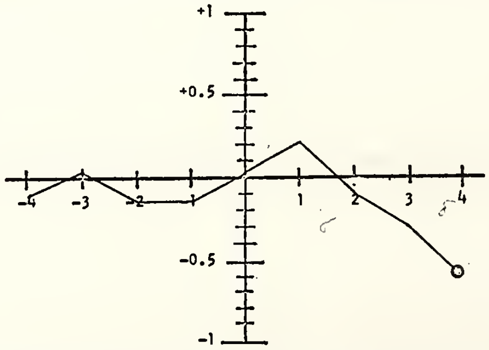

Simple correlations for winter Pacific trade wind divergence EOF1 leading (positive lag) and lagging (negative lag) the Atlantic temperate (35-55N) zonal index by 1-4 seasons.

On the Influence of Warm Equatorial Conditions in the Central Pacific on Climatic Patterns in the United States: 1977-80

Arthur V. Douglas
Climate Research Group
Scripps Institution of Oceanography
La Jolla, California 92093

Over the past three winters, precipitation in the Southwest has averaged up to 300% of normal (Figure 1). Each year the heavy rains and mountain snows began in January and lasted into March, with the strongest departures being located near the lower Colorado River valley. The average 700-mb height departures for January through March of these years indicate that the eastern North Pacific was characterized by strong troughing (Figure 2). During this period the anomalous 700-mb flow pattern into the Southwest was from the eastern tropical Pacific. An examination of satellite film loops indicates that a number of the heavy precipitation events were associated with tropical cloud masses moving northeastward from the central equatorial Pacific.

Over the past few years heavy rainfall events in the central equatorial Pacific have been recorded by stations indicated in Figure 3. Composite 700-mb height anomaly maps for wet and dry periods at these equatorial stations are shown in Figure 4. High rainfall index years (El Niño years) show strong troughing in the eastern North Pacific (Figure 4) and this 700-mb pattern is remarkably similar to that of the past three winters (Figure 2). A plot of rainfall at Fanning Island (Figure 5) clearly indicates that the past three years have been relatively wet in the central equatorial Pacific, but these anomalies have not approached those of "true" El Niño years (e.g., 1972-73 and 1976-77).

While the eastern equatorial Pacific was not particularly warm during this past wet winter (Figure 6), the extreme eastern tropical Pacific was unusually warm. The SST anomaly pattern in Figure 6 is very similar to that found in past El Niño winters (e.g., 1957-58 and 1976-78). In fact, the past three winters have been characterized by this pattern of cold waters in the central North Pacific and warm waters in the eastern tropical Pacific. Satellite data reveal a strong subtropical jet stream in the eastern North Pacific in March 1980, with a band of cloudiness extending northeastward into Baja California (Figure 7). The subtropical jet stream and attendant cloud bands crossed the warmest water off Baja California (Figures 6 and 7). This is in contrast to an anti-El Niño case, March 1976, when the subtropical jet stream was located in a similar position but when warm water conditions and advection of tropical moisture were not apparent across the extreme eastern North Pacific (Figures 8 and 9).

The average 700-mb height departures for the falls preceding the heavy precipitation events are shown in Figure 10. The anomalies depicted in this figure are not significant, indicating that diagnosis of the upcoming rains was probably not possible using 700-mb data. However, the SST departures in the falls preceding the heavy rains were more persistent (Figure 11).

Based on correlation analysis, the observed fall SST patterns foreshadowed abnormal lowering of 700-mb heights in the eastern North Pacific: cold central Pacific waters in the fall indicating below normal heights in winter and above normal SST's near 30°N/140°N being indicative of below normal 700-mb heights in the subsequent winter months (upper map Figure 11). The SST anomaly pattern during the past three falls is typified by enhanced baroclinicity in the eastern North Pacific—a pattern which would be transferred to the overlying atmosphere, whereby storms approaching from the southwest might intensify before striking land. Part of the intensification process included the advection of warm moisture air ahead of the storms as illustrated in Figure 7. The SST departure prior to and near the end of the heavy rainfall events indicate an intensification of the SST gradients during the winter. While strong interaction between the tropics and mid-latitudes in 1976 probably resulted in the initiation of the current SST pattern, the perpetuation of the anomalous SST pattern appears strongly linked to events in the North Pacific during the winters of 1978, 1979, and 1980.

FIGURE CAPTIONS

Figure 1. Percentage of normal precipitation, January through March 1978, 1979, and 1980. Departures are based on long term means 1941-70.

Figure 2. Average 700-mb height departures for the period January through March of 1978, 1979, and 1980. Note the anomalous southwest flow into the West Coast from the eastern Tropical Pacific.

Figure 3. Location of the central equatorial Pacific Islands with long term rainfall records. Heavy rainfall at the islands are often associated with El Niño events off South America. A typical location for the 200-mb jet is indicated based on satellite-derived winds.

Figure 4. Composite 700-mb height departure maps for years with high rainfall or low rainfall at the islands indicated in Figure 3. High rainfall years are generally associated with El Niño conditions. Note the strong similarity between the upper map and Figure 2.

Figure 5. Percentage of the median precipitation for Fanning Island, 1970-1980. Note the heavy rainfall events during the falls and winters (circled values) of two recent El Niño years, 1972-73 and 1976-77.

Figure 6. Sea surface temperature departures for March 1980 based on the long term mean of 1947-72. Note the near normal conditions along the Equator and anomalously strong gradient in the eastern North Pacific between 130°W and 150°W.

Figure 7. Outgoing long-wave radiation for March 1980, with 200-mb jet maximum indicated by arrows. In the tropics lowest values indicate region of cloudiness.

Figure 8. Sea surface temperatures for March 1976 based on the long term mean of 1947-76. Note the cold water along the Equator and reversal of gradients in the North Pacific compared to March 1980 (Figure 6).

Figure 9. Outgoing long-wave radiation for March 1976. Note the decreased cloud activity in the eastern tropical Pacific and central equatorial Pacific compared to March 1980 (Figure 7).

Figure 10. Average 700-mb height departures for the Falls of 1977, 1978, and 1979. Anomalies are based on the long term means 1947-72.

Figure 11. Upper map shows the correlation between North Pacific SST's in fall and subsequent 700-mb height departures in winter. Bottom map shows the average SST departures for the falls of 1977, 1978, and 1979. Visual inspection of the two charts would indicate below normal heights would have been expected from 45°N/160°W to 30°N/135°W in the winters of 1977, 1978, and 1979.

Figure 12. Average SST departures for December 1977, 1978, and 1979. These Decembers were relatively storm free in the Southwest.

Figure 13. Average SST departures for March 1978, 1979, and 1980. Note the strengthening of the SST anomalies and gradients in the eastern North Pacific.

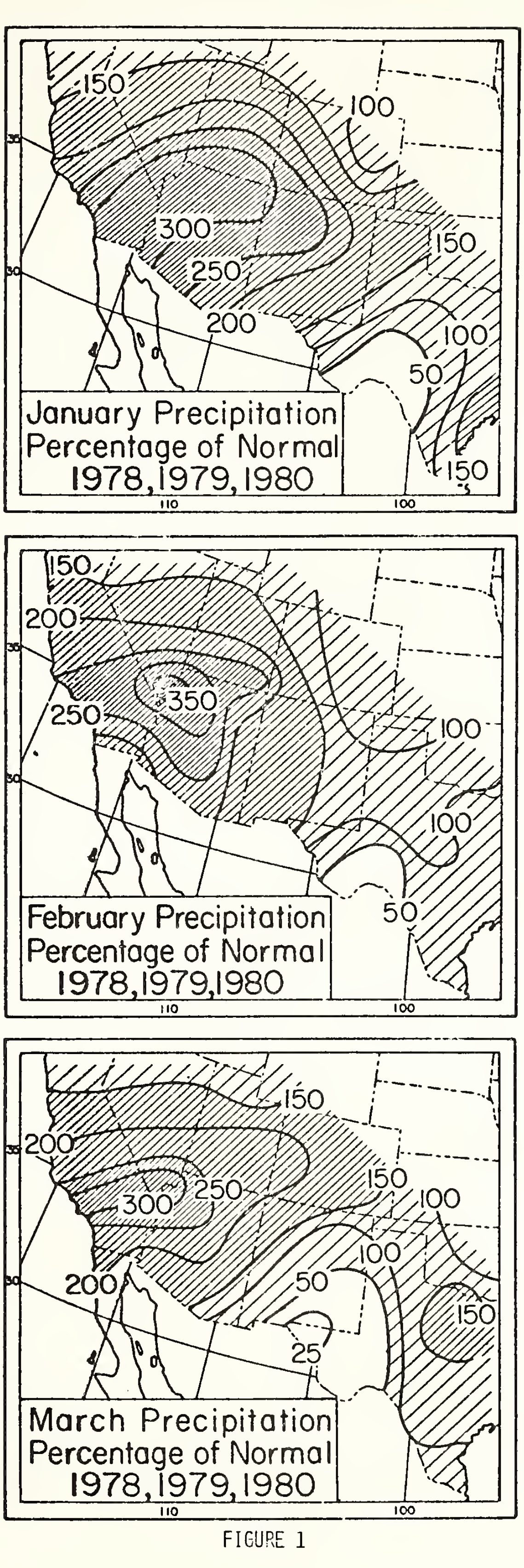
January Precipitation Percentage of Normal 1978, 1979, 1980

February Precipitation Percentage of Normal 1978, 1979, 1980

March Precipitation Percentage of Normal 1978, 1979, 1980

FIGURE 1

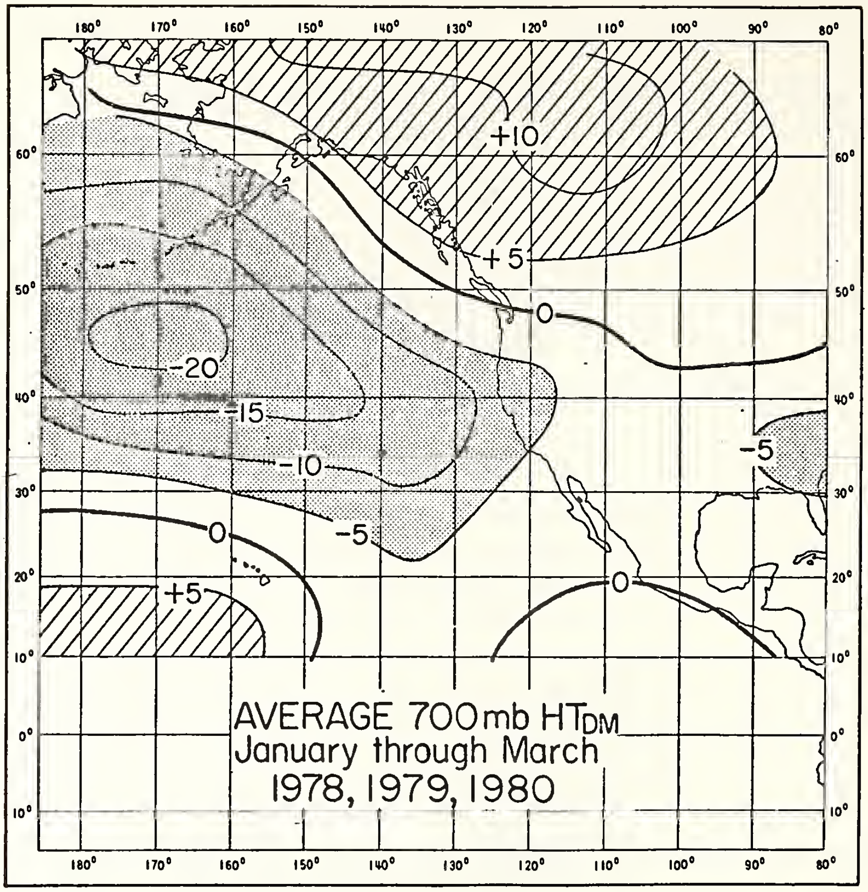

FIGURE 2

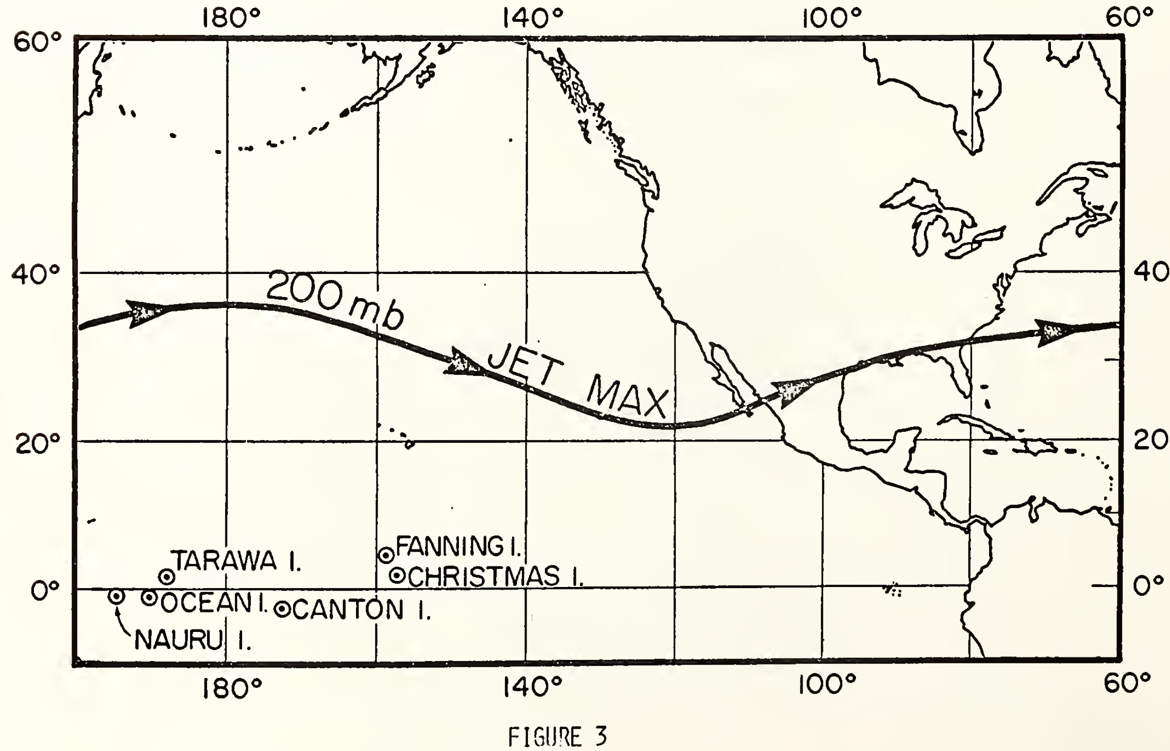

FIGURE 3

700mb HT.$_{DM}$

Winters with High Rainfall Index 1958, 64, 66, 73, 77, 78

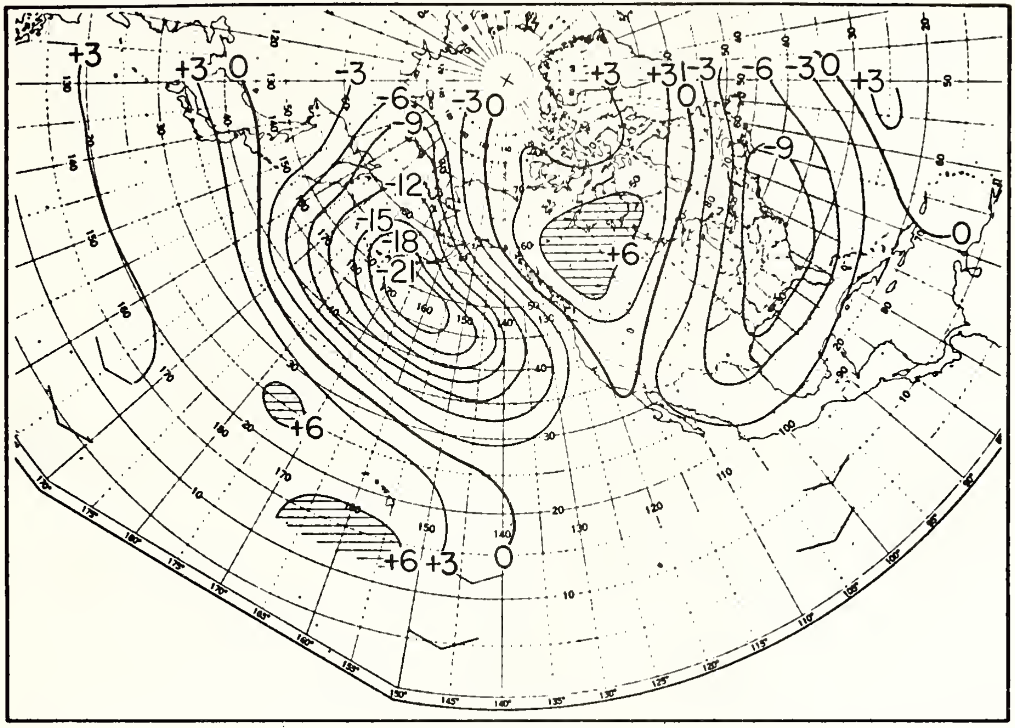

700mb HT.$_{DM}$

Winters with Low Rainfall Index 1950, 51, 55, 71, 74, 76

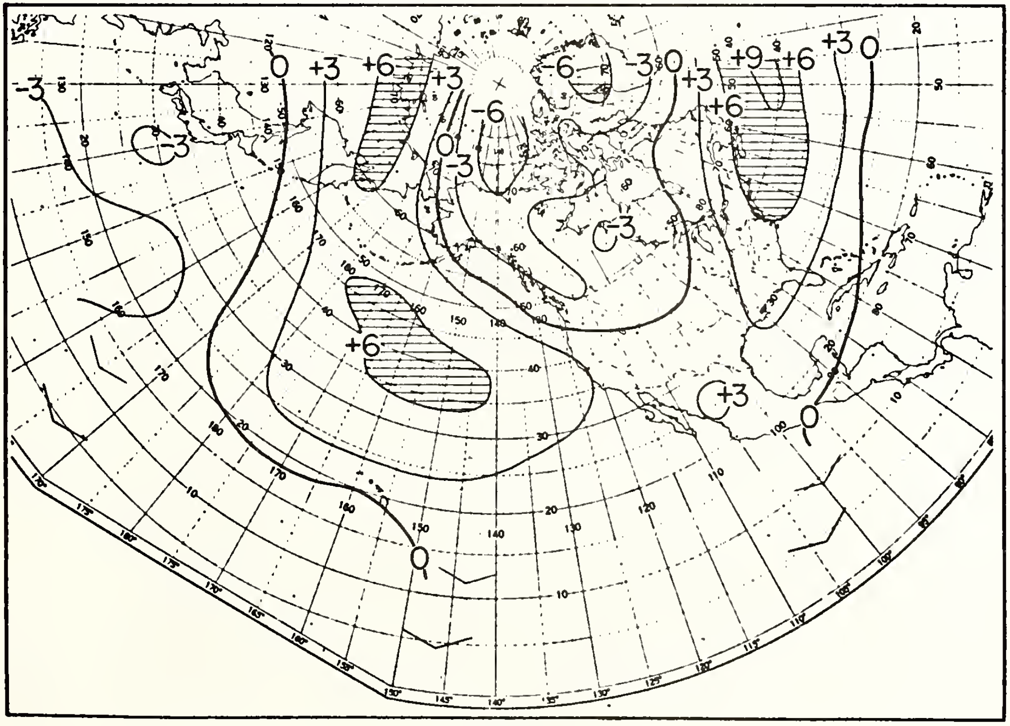

FIGURE 4

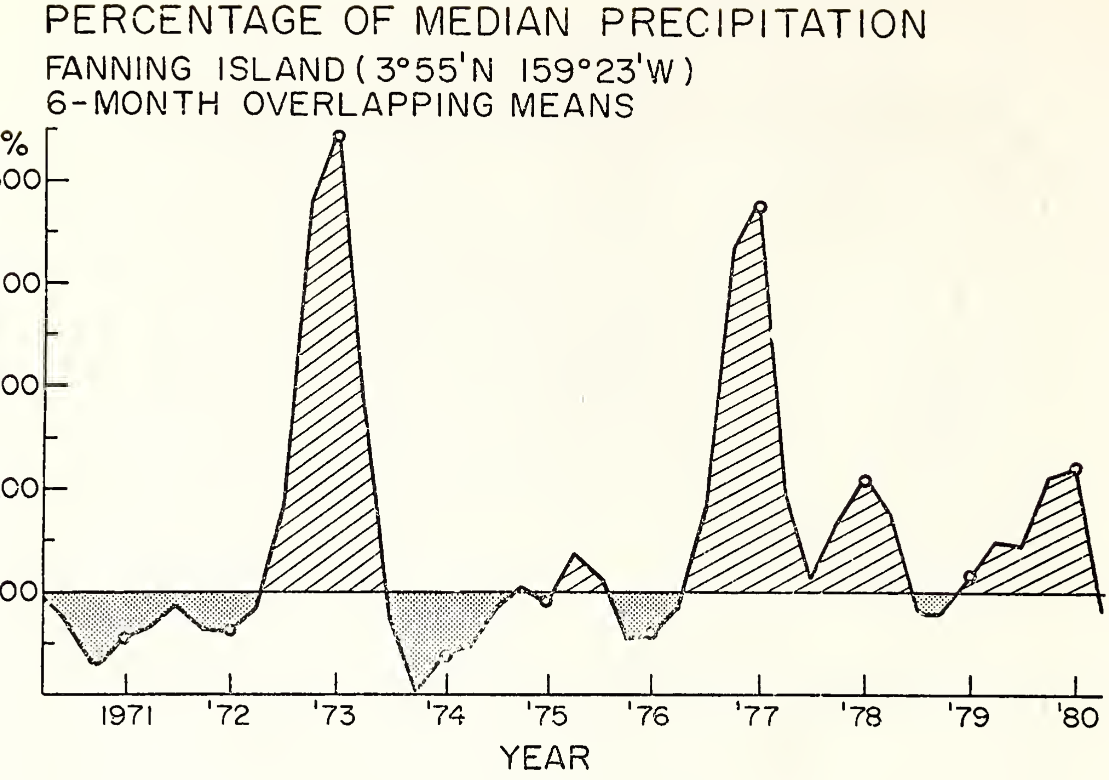

FIGURE 5

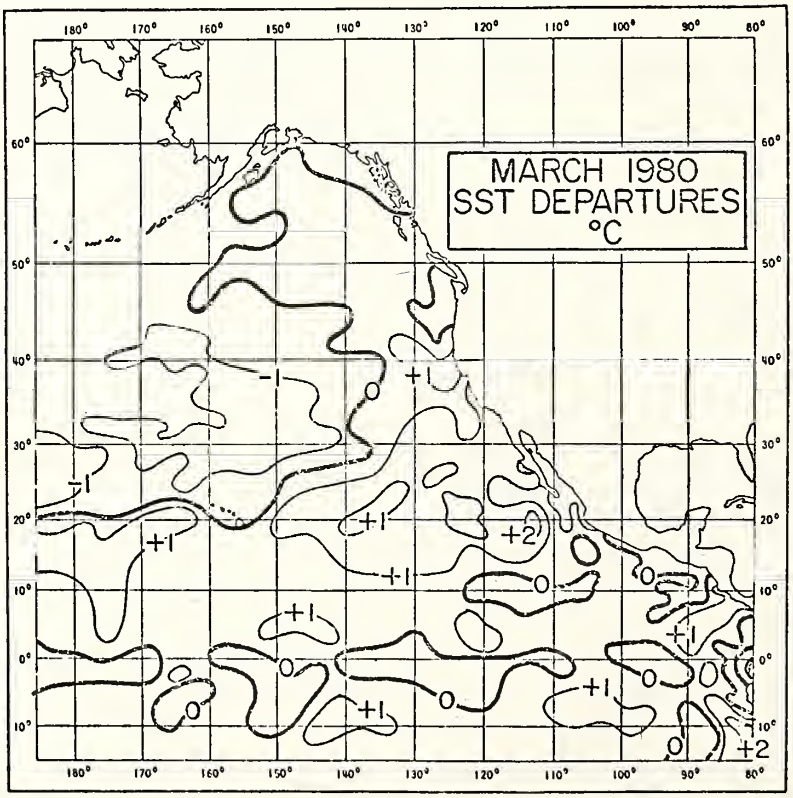

FIGURE 6

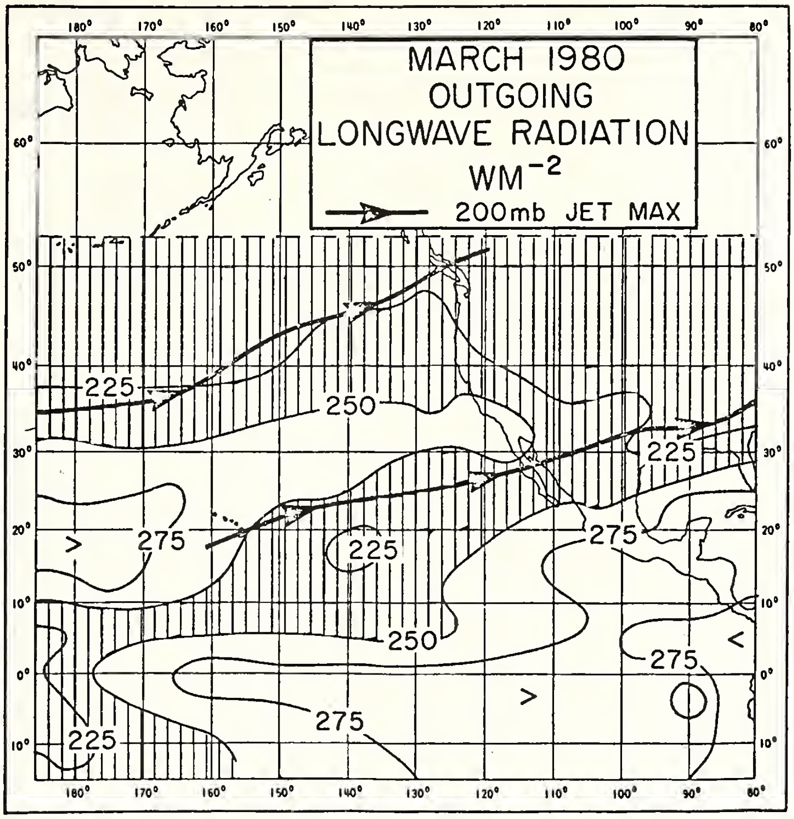

FIGURE 7

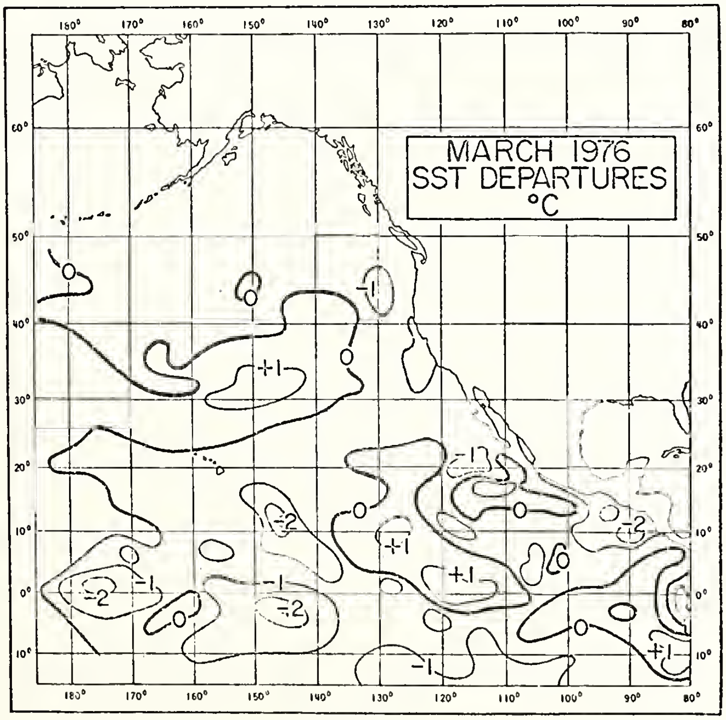

FIGURE 8

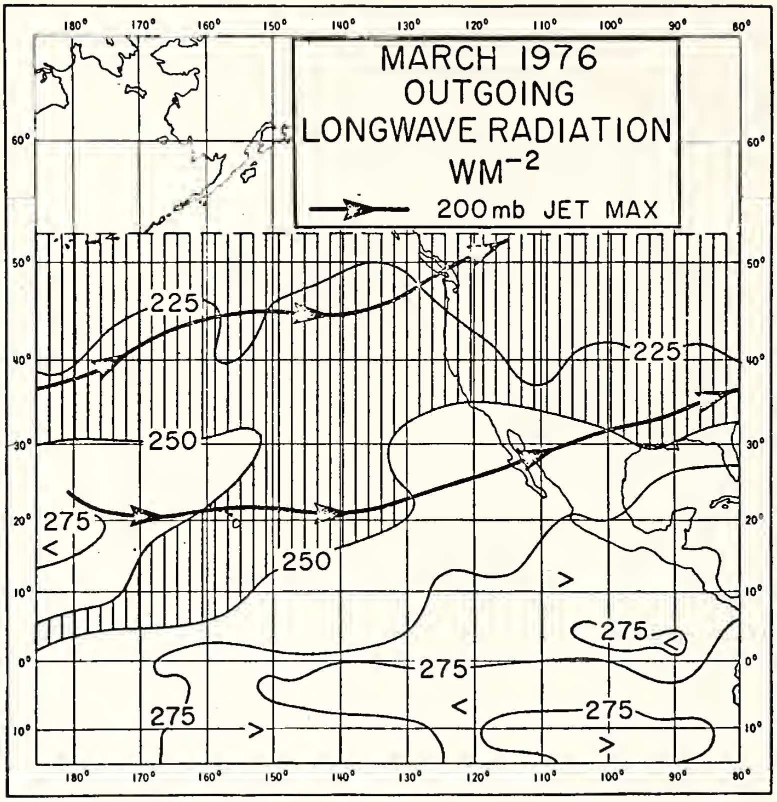

FIGURE 9

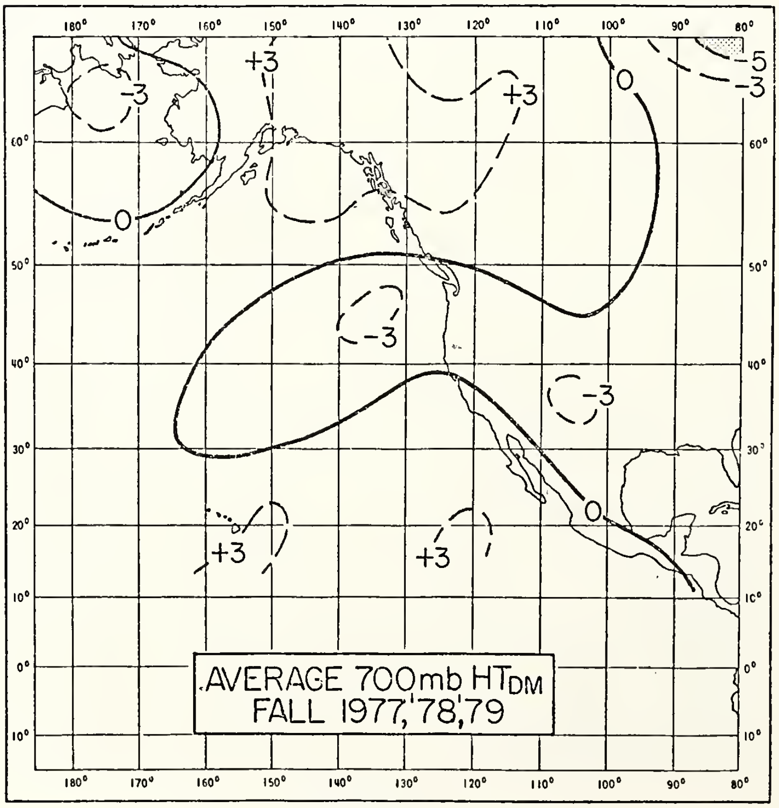

FIGURE 10

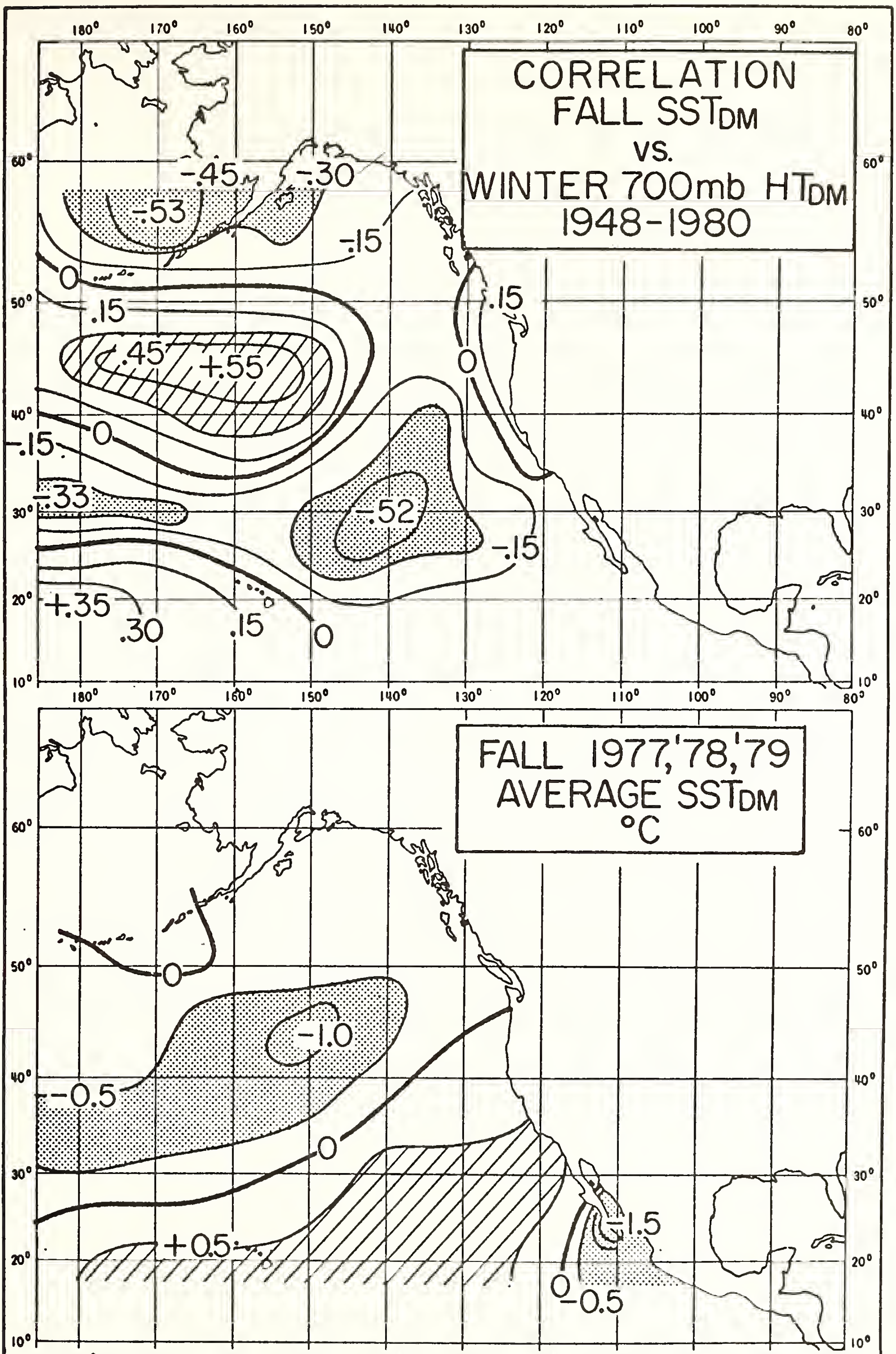
CORRELATION
FALL SST$_{DM}$
VS.
WINTER 700mb HT$_{DM}$
1948-1980
-.45
-.30
-.53
-.15
0
.15
.45
+.55
0
-.15
-.33
-.52
-.15
+.35
.30
.15
0
FALL 1977,'78,'79
AVERAGE SST$_{DM}$
°C
0
-1.0
-0.5
0
+0.5
-1.5
0
-0.5
180°
170°
160°
150°
140°
130°
120°
110°
100°
90°
80°
60°
50°
40°
30°
20°
10°

FIGURE 11

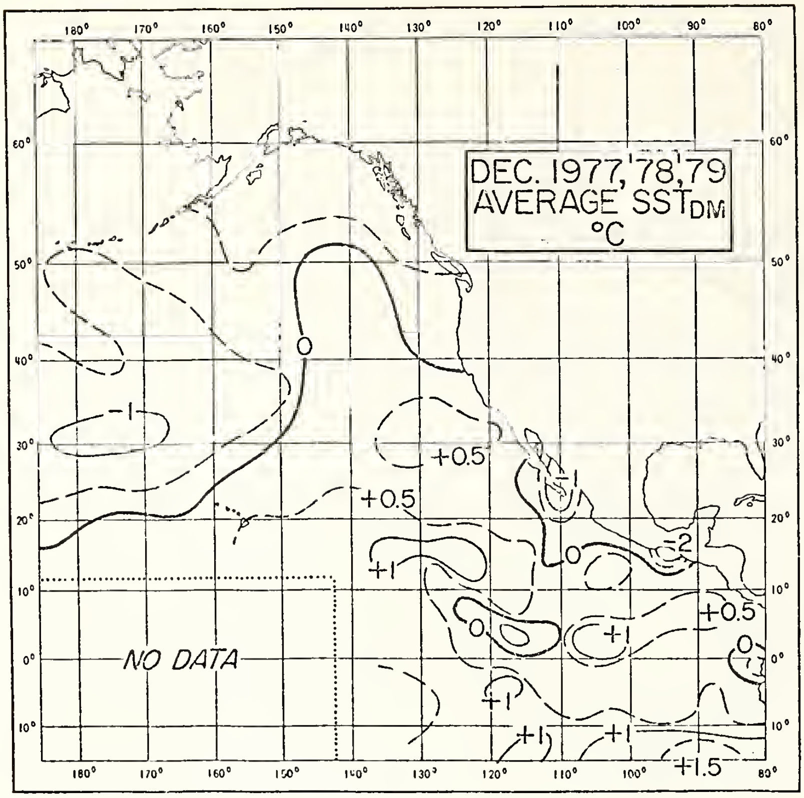

FIGURE 12

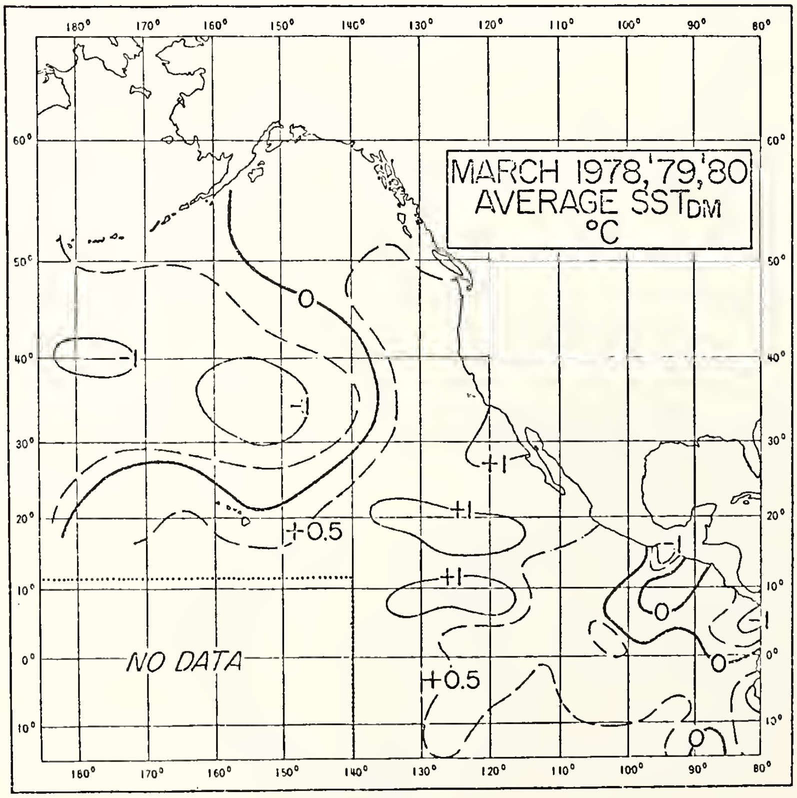

FIGURE 13

THE RESPONSE OF THE ATMOSPHERIC BOUNDARY LAYER TO SEA SURFACE TEMPERATURE ANOMALIES

Siri Jodha Singh Khalsa *
CIRES Climate Program
NOAA/ERL
Boulder, Colorado 80303

The atmospheric boundary layer (ABL) is the interface between the ocean and the rest of the atmosphere; it is through this layer that all interactions between these two systems must take place. The lack of a clear understanding of the mechanisms behind large scale "teleconnections" and the failure of GCM's to realistically reproduce observed atmospheric responses to sea surface temperature anomalies (SSTA's) point to the need for a better understanding of the ABL in its role as intermediary between the ocean and the large scale atmospheric flow.

We have been examining the data in the 1972-1973 El Niño atlas produced at the University of Hawaii. The 26 months of data encompass a major El Niño event and the anti El Niño (cold equatorial waters) which followed. The area covered by the atlas is the coastline of the Americas to the date line and 30°S to 20°N.

In Figure 1 zonal averages of latent plus sensible heat flux from the ocean surface (computed with the bulk aerodynamic method), sea surface temperature, and surface wind speed are plotted as difference values, August 1972 minus August 1973. In zone 1 (dateline to 150°W) and zone 2 (150°W to 120°W) positive SST differences on the Equator are due to positive SST anomalies during the El Niño year and negative SSTA's in the anti El Niño year. The warm water off South America during El Niño is evident in zone 3 (120°W to the Americas).

The behavior of estimated latent plus sensible heat flux, Q_T, relative to SST is different for all three longitude zones in Figure 1. In zone 1 Q_T difference is negative almost everywhere that the SST difference is positive. In zone 2 the Q_T and SST maxima coincide at the Equator. In zone 3 the Q_T difference is also positive almost everywhere but north of 10°S the two curves show no correlation.

Wind speed accounts for the behavior in zone 1. There a negative wind speed difference results in a negative Q_T difference. In zone 2 the wind speeds were the same in the 2 months so SST exerted the dominant influence. In zone 3 the wind speed difference is near zero from 15°S to 5°N and thus cannot account for the sharply lower Q_T difference in the vicinity of 2.5°N.

To fully understand the behavior of Q_T it is necessary to examine the upstream history of the air flow. In Figure 2a it can be seen that the southeasterlies off the South American coast flow over steadily increasing SST. In 1972 (Figure 2b) the southeasterlies which eventually cross the Equator in zone 1 pass over a broad region of cool water. In passing over this region the air-sea differences in temperature and humidity, ΔT and Δq, become small. As the flow crosses the Equator, it encounters a sharp rise in SST. ΔT and Δq increase sharply producing values of Q_T which exceed those for the same region in 1972, although in 1973 SST was 2°C lower. A similar analysis of zone 2 shows that in 1972 the Q_T maximum was on the Equator where the SST gradient was largest, although the highest SST was to the north. Again, north of the Equator there is a point where Q_T is larger in 1973, although the SST is cooler by 2°C compared with 1972.

The most common assumption concerning the manner in which positive equatorial SSTA's are able to affect large scale atmospheric circulations is that they produce enhanced convection. Highly reflective cloud (HRC) has been shown to be a good indicator of rainfall over the tropical oceans. In Figure 3b HRC and SST differences are plotted for the same months as in Figure 1. Little correspondence is seen. By contrast Figure 3a shows a generally good agreement between HRC and surface wind convergence ($-\nabla\cdot\overline{V}$). An examination of the individual months revealed that SST and HRC maxima coincided nearly perfectly. The maxima in zones 1 and 2 of Figure 3a are offset because surface wind was divergent along the Equator in 1973. Figure 4a provides another striking example of the correlation between HRC and $-\nabla\cdot\overline{V}$.

Work currently in progress involves following streamlines from the trades into the convergence zone while recording changes in winds, fluxes, precipitation, SST and other parameters along the path. Hopefully this will provide additional insights into the question of what determines the observed patterns of fluxes and precipitation. The goal is to provide a basis for more realistic modelling of the atmospheric response to equatorial SSTA's.

*NRC Research Associate

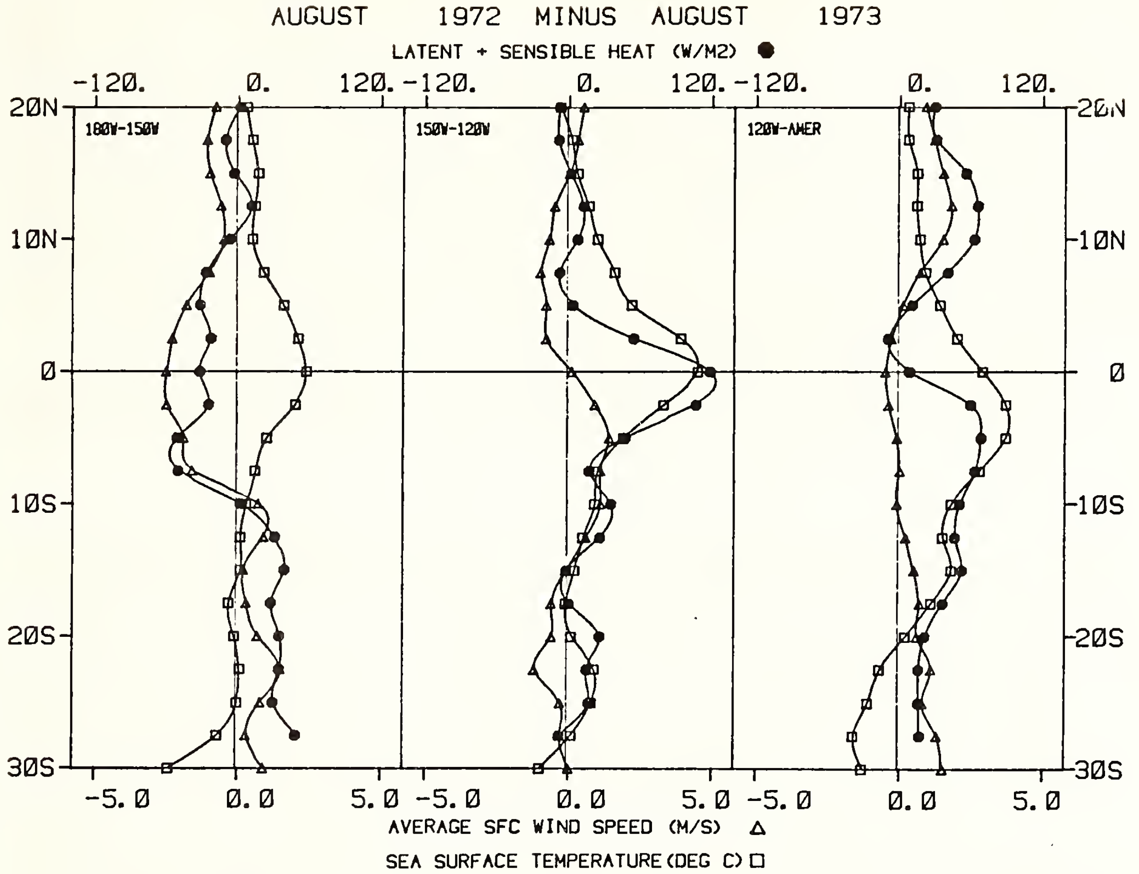

Figure 1. Latent plus sensible heat flux, surface wind speed, and sea surface temperature zonally averaged and expressed as differences between August 1972 and August 1973.

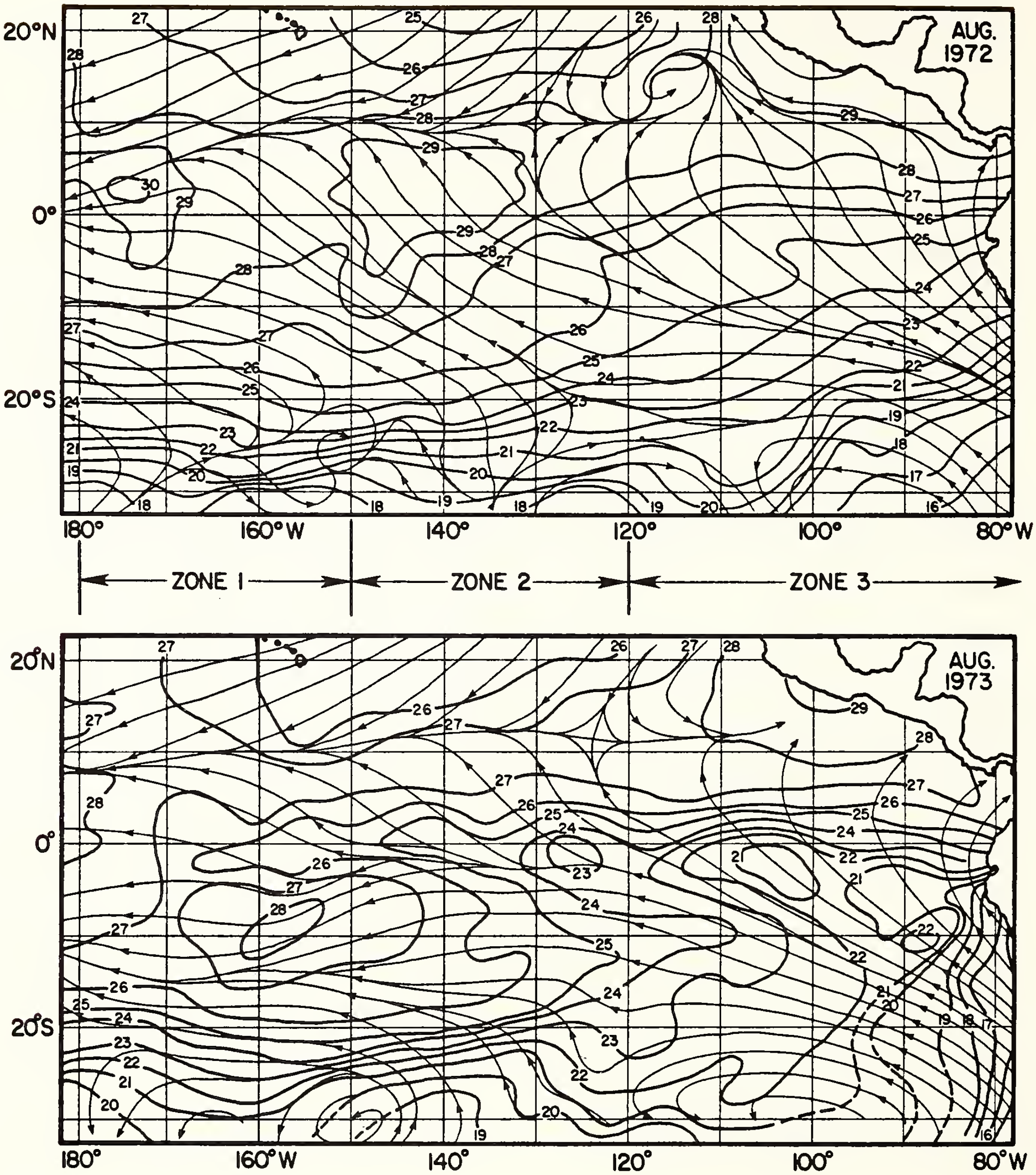

Figure 2. Surface wind streamlines and sea surface temperature isotherms for a) August 1972 and b) August 1973.

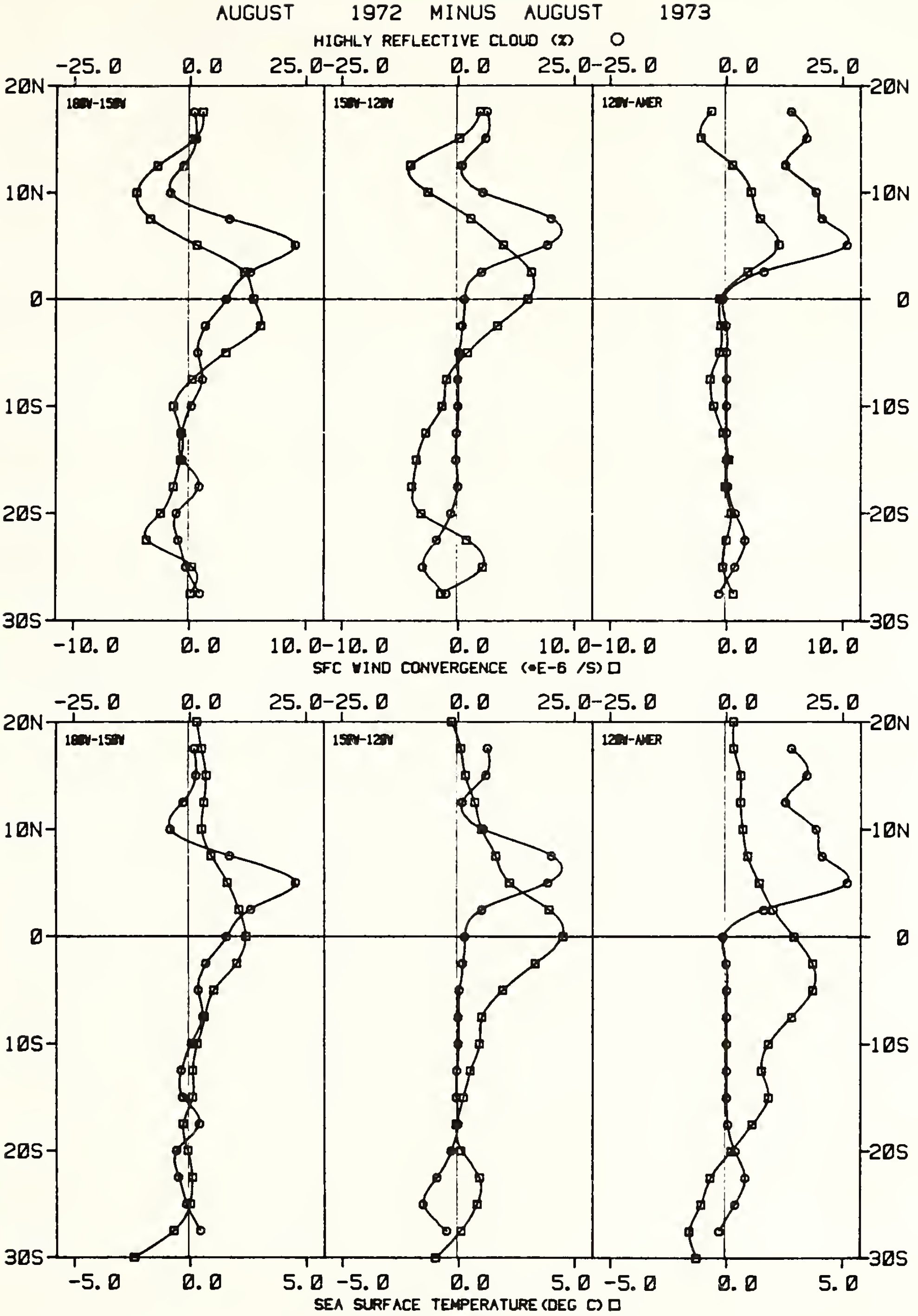

Figure 3. Highly relective cloud frequency compared with: a) surface wind convergence ($-\nabla\cdot\bar{V}$), and b) sea surface temperature, differenced for the same months as in figure 1.

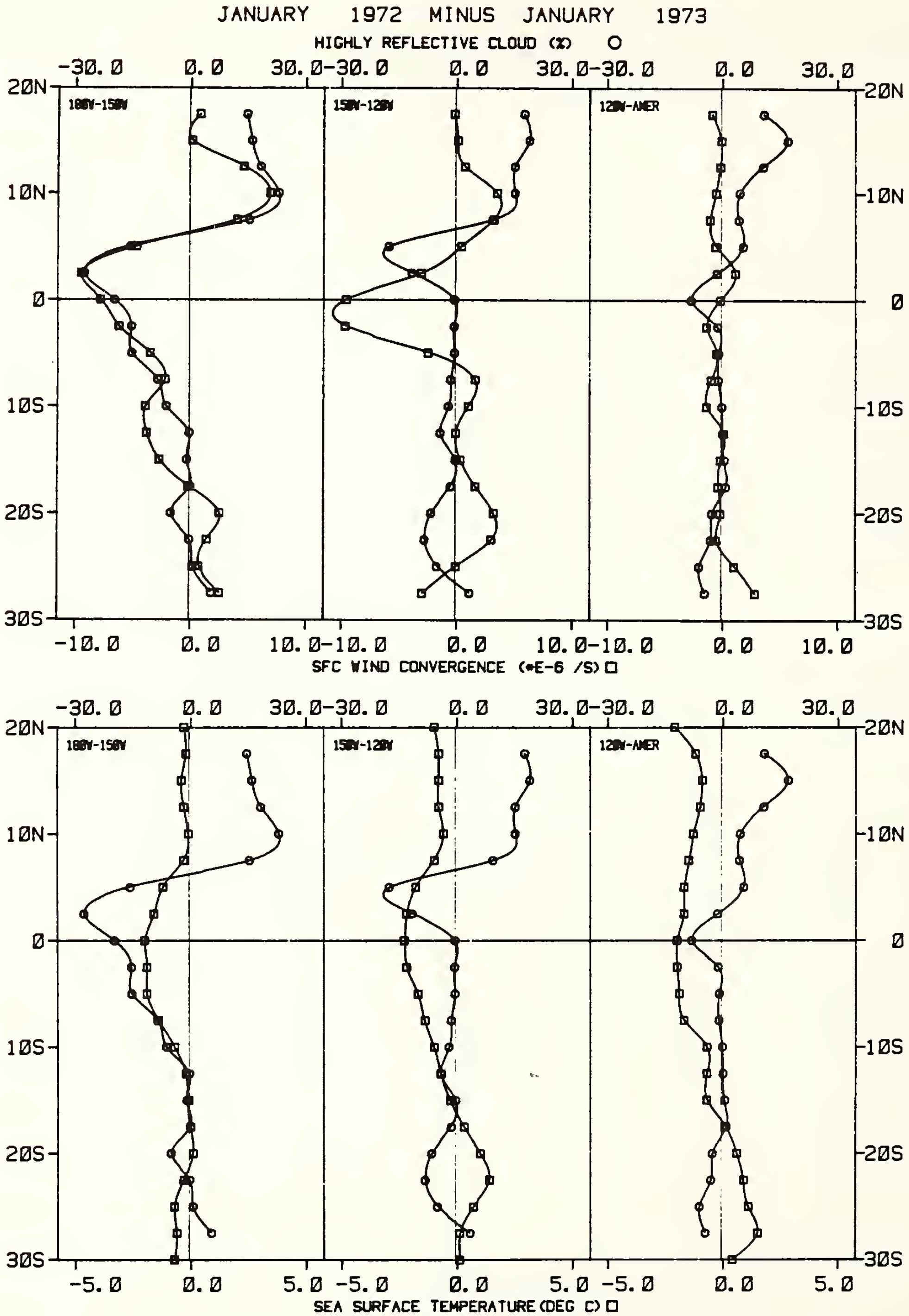

Figure 4. Same as Figure 3 except for January 1972 (pre el Nino) minus January 1973 (el Nino).

Droughts in Northeast Brazil

A. D. Moura[1] and J. Shukla
Goddard Laboratory for Atmospheric Sciences
NASA/GSFC, Greenbelt, Maryland 20771 USA

It is proposed that a possible mechanism for the occurrence of severe droughts over northeast Brazil is the establishment of a thermally direct local circulation which has its ascending branch at about 10°N and its descending branch over northeast Brazil and adjoining oceanic region. The driving for this anomalous circulation is provided by warming due to enhanced moist convection associated with warmer sea surface temperature anomalies over the northern tropical Atlantic, and cooling associated with colder sea surface temperature anomalies in the southern tropical Atlantic. The combined effects of thermally forced subsidence and reduced evaporation and moisture flux convergence produce severe drought conditions over northeast Brazil.

We have examined the monthly mean sea surface temperature anomalies over tropical Atlantic and rainfall anomalies over two selected stations (Fortaleza, 3°46'S,38°31'W and Quixeramobim, 5°12'S,39°18'W) for 25 years (1948-1972). Figure 1 shows the correlation between March SST anomalies and normalized rainfall departures. It is found that the most severe drought events are associated with the simultaneous occurrence of warm sea surface temperature anomalies over north and cold sea surface temperature anomalies over south tropical Atlantic. Simultaneous occurrences of warm sea surface temperature anomaly at 15°N, 45°W and cold sea surface temperature anomaly at 15°S, 5°W were always associated with negative anomalies of rainfall, and vice versa. This is illustrated in Fig. 2 which presents the 25-year rainfall deviations plotted as a function of SST anomaly in the 15°N, 45°W area (abcissa) and the mean of SST anomalies in the 15°S, 5°W and 5°S, 25°W areas (ordinate). These areas contain the highest correlation coefficients. It is striking that in the lower right quadrant of Fig. 2 all the rainfall departures are negative with the highest values being farthest away from the origin. In the upper left quadrant all rainfall departures are positive. Looking at the actual monthly mean SST anomaly maps for extremely dry and extremely wet years in northeast, we find that the composite SST patterns seem to appear also on an individual basis (droughts in 1951, 1953, 1958 and wet years in 1964, 1967).

A simple primitive equation model was also used to calculate the frictionally controlled and thermally driven circulation due to a prescribed heating function in a resting atmosphere. The heating function was designed to simulate a heat source to the north and a heat sink to the south of the Equator. This prescribed thermal forcing produced a thermally direct circulation with ascending motion to the north and descending motion to the south. The analytical solutions agreed well with the results of numerical experiments carried out with a multilevel global general circulation model.

---

[1] Permanent affiliation: Instituto de Pesquisas Espaciais, CNPq/INPE, Sao Jose dos Campos, Sao Paulo, Brazil.

We have also carried out a series of numerical experiments to test the sensitivity of the GLAS (Goddard Laboratory for Atmospheric Sciences) model to prescribed sea surface temperature anomalies over tropical Atlantic.

The model was first integrated for 90 days with climatological sea surface temperature. The initial conditions were taken from the observations of January 1, 1975. Then the SST anomaly shown in Fig 3 was superimposed over the climatological sea surface temperature, and the SST anomaly was assumed to be constant for 90 days. Starting from the atmospheric initial conditions identical to the first run, the model was integrated again for 90 days. We would refer to these two integrations as the 'control run' and the 'anomaly run', respectively.

Figure 4 shows the 15-day running mean time series of daily rainfall averaged over the areas A and B (shown in Figure 3) for control and anomaly runs. Although the spatial resolution is not adequate to resolve small scale phenomena, the natural variability of the model shows spatially inhomogeneous structure and therefore it is necessary to average the daily rainfall over sufficiently large spatial areas. Area B contains the northeast Brazil region and the neighboring oceans with colder SST anomaly. Area A includes the region of warm SST anomaly. The rainfall over area A increases due to warm SST anomaly and shift of ITCZ from area B in the control run to area A in the anomaly run. In the anomaly run the mean rainfall in area A remains larger than the control run for all the 90 days. The rainfall in control and anomaly runs is comparable for the first 10 days, but for days 20-60, the anomaly run has less rainfall than the control run. Although 60-day or 90-day mean rainfall for area B is smaller for the anomaly run compared to the control run, the difference is not systematic after 60 days. Internal model adjustments make the two rainfll series indistinguishable during days 60-90.

Figure 5 shows the 60-day mean rainfall differences between the anomaly and the control run. The differences were smoothed by a 5-point smoother except along 2°N and 2°S where no averaging was done across the latitudes. There is a clear increase in the rainfall over warm SST anomalies to the north and decrease in the rainfall over cold SST anomalies to the south. Most of the northeast Brazil region shows a decrease in the rainfall. Although the maximum reduction of the rainfall occurs over the oceans adjacent to northeast Brazil, the differences over the land are large enough to support the basic proposed mechanism. Although there is not sufficient observed rainfall data over the oceans to document this phenomena, it is our conclusion, based on these numerical and analytical results, that the drought over northeast occurs in association with a reduction in the rainfall over a larger region adjacent to northeast Brazil. An increase in the rainfall over northern South America, in association with droughts over northeast, is consistent with earlier observational findings.

Figure 6 shows the difference of the first 60-day mean meridional circulation averaged between 50°W and 5°E. The anomalous meridional circulation shows an ascending branch with maximum vertical motions between 5° and 10°N and a descending branch to the south of Equator. It is this descending motion over northeast Brazil region which is one of the most important factors in producing the drought. We have not explained here that why a SST anomaly over north Atlantic produces a meridonal circulation whose scale is about 2000 km; however, it is comparable to the Rossby radius of deformation for equatorial motions. Descending motion to the south of Equator reduces the vertically integrated moisture flux convergence, which, coupled with reduction in evaporation over the ocean, reduces rainfall in northeast Brazil region.

This study suggests that the SST anomalies in low latitudes can change the large scale Hadley- and Walker-type circulations which are otherwise stable with respect to dynamic instabilities. It can be speculated that the interannual variability of the location and intensity of the subtropical highs can be related to the variability of the tropical heat sources.

Figure 7 shows the differences between the anomaly run and the control run for 30-day mean geopotential heights at 850 mb. The difference field has similar structure at 500 mb and 300 mb, suggesting the barotropic nature of response. The natural variability of monthly means during the northern hemispheric winter is usually larger at middle latitudes; however the observed changes are larger than the natural variability of the model. These results seem to confirm the earlier suggestions that extratropical general circulation in Atlantic may be related to tropical variability. The present study suggests that the tropical heat sources are the primary driving mechanisms for the observed teleconnections.

Since the sea surface temperature anomalies over tropical Atlantic persist for several months. (Fig. 8), the proposed mechanism could provide guidance for predicting droughts over northeast Brazil.

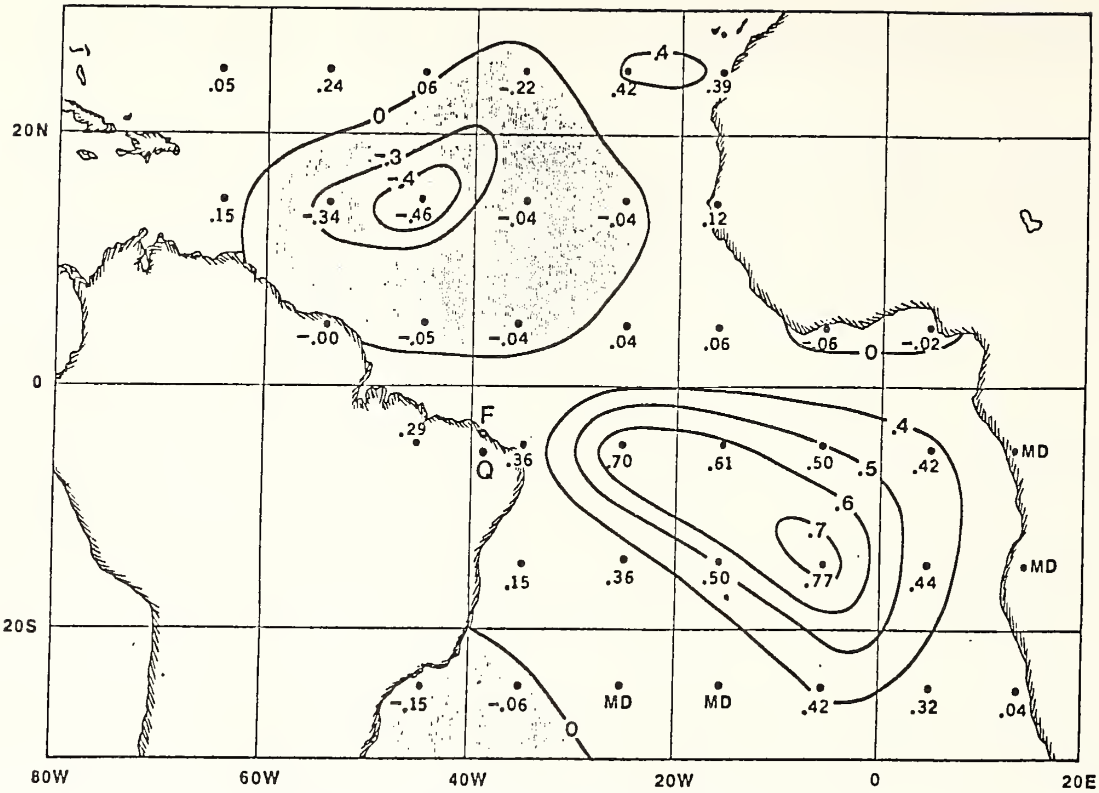

Fig 1. Correlation coefficients between sea surface temperature over Atlantic and average rainfall for Fortaleza and Quixeramobim.

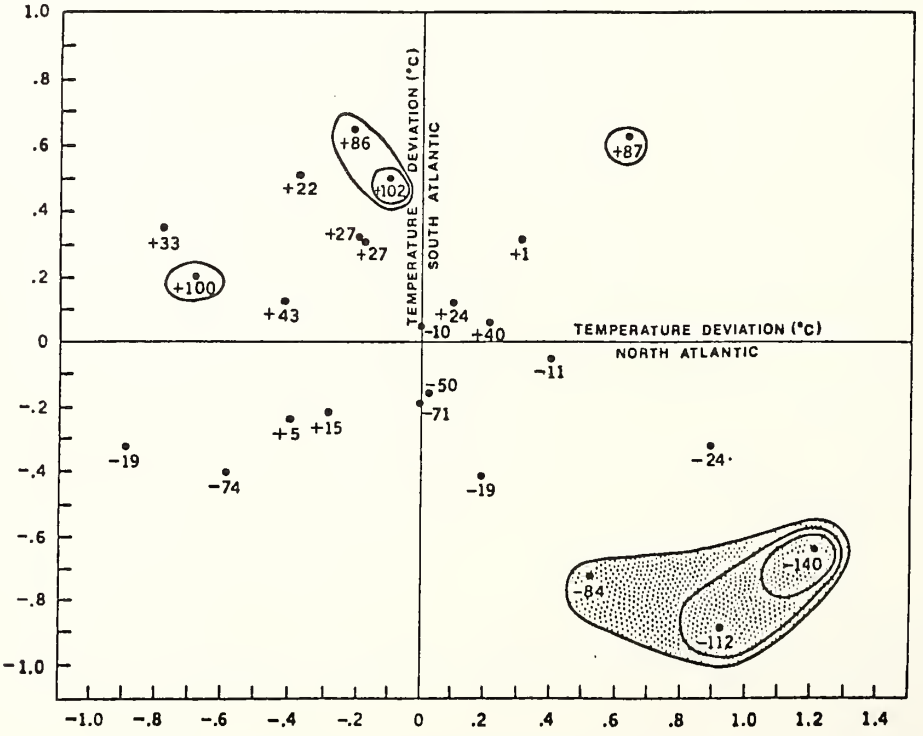

Fig 2. Average of March, April, May rainfall departures (mm) at Fortaleza and Quixeramobim in relation to SST anomaly at 15°N, 45°W (absissa) versus average of SST anomaly at 15°S, 5°W and 5°S, 25°W (ordinate).

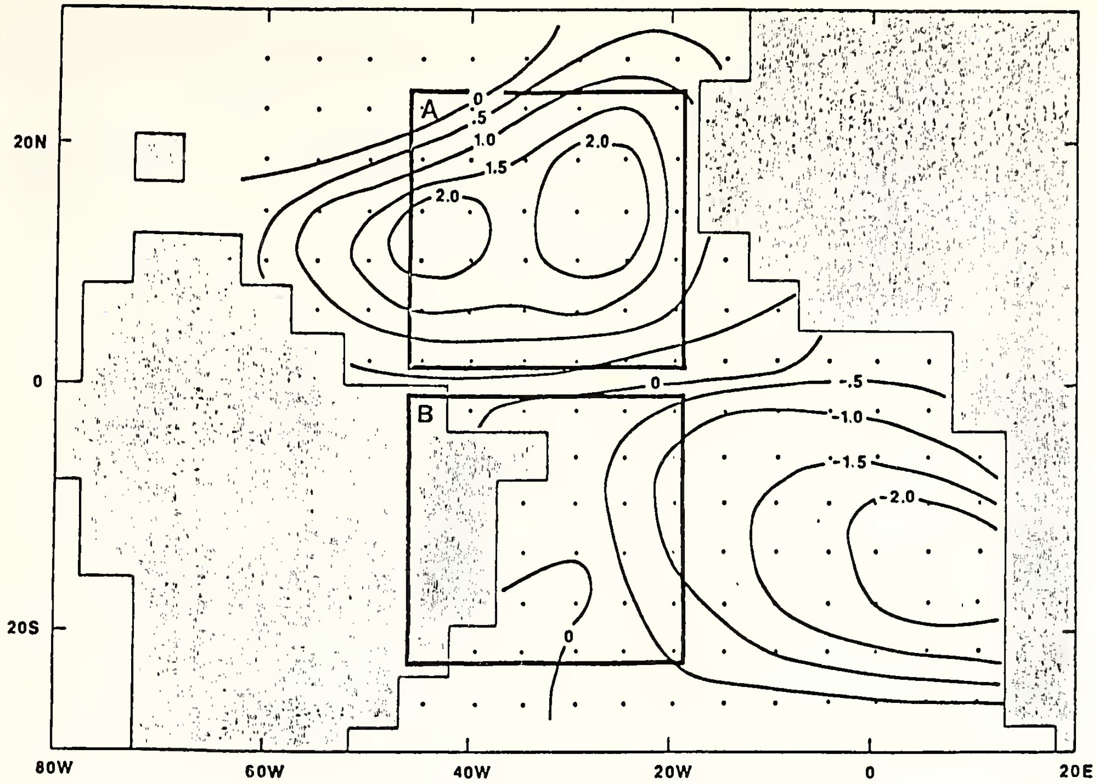

Fig 3. Sea Surface temperature anomaly (°c) for the anomaly run. Thick lines enclose area A (upper) and area B (lower).

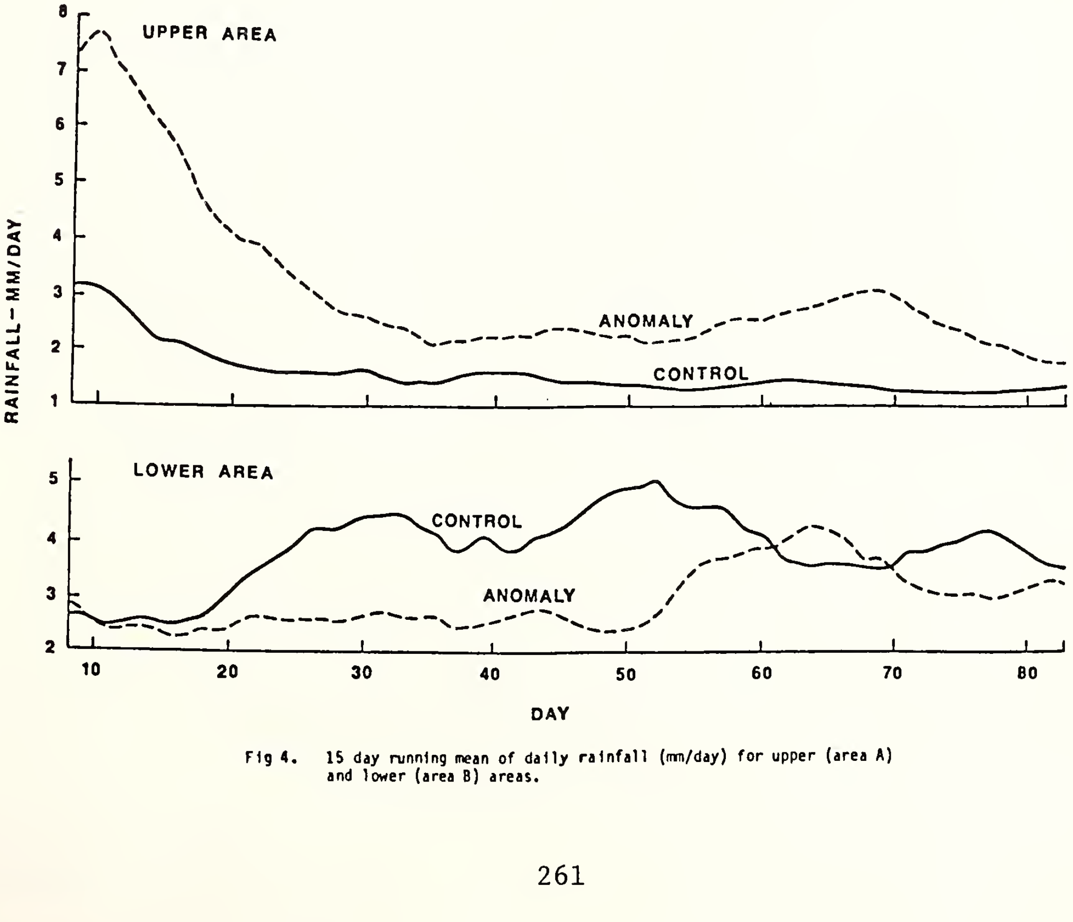

Fig 4. 15 day running mean of daily rainfall (mm/day) for upper (area A) and lower (area B) areas.

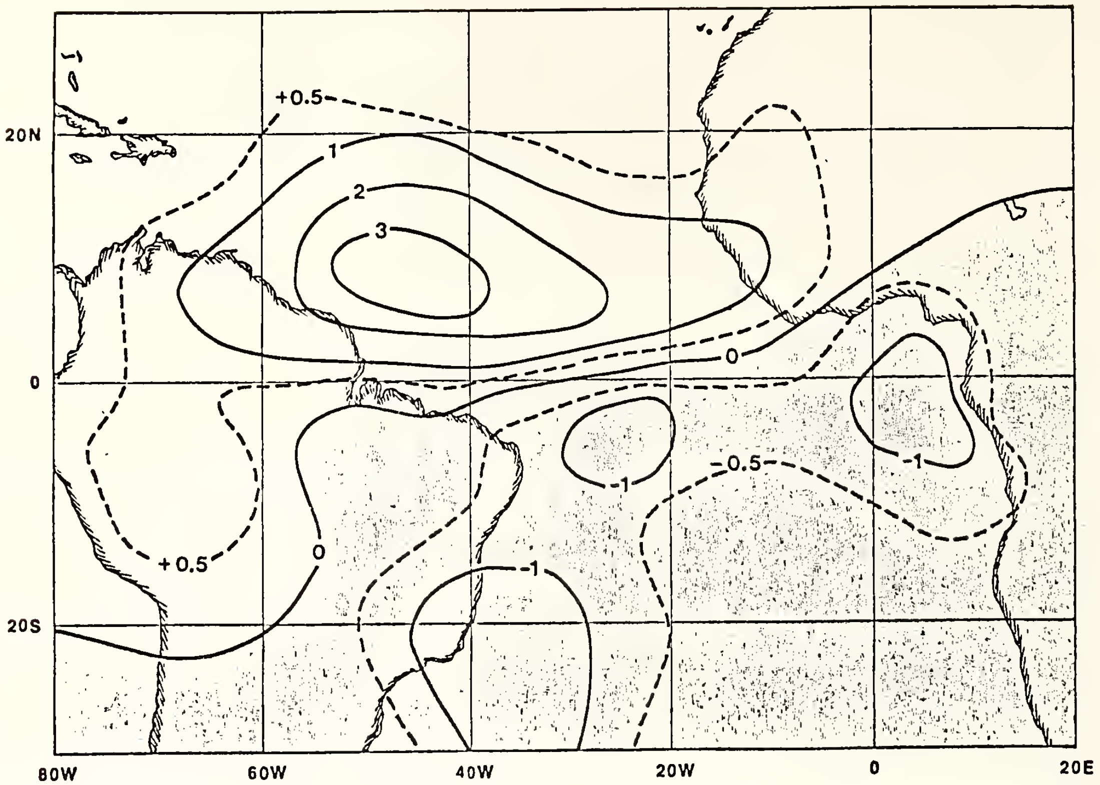

Fig 5. Difference (anomaly-control) of 60 day mean rainfall (mm/day).

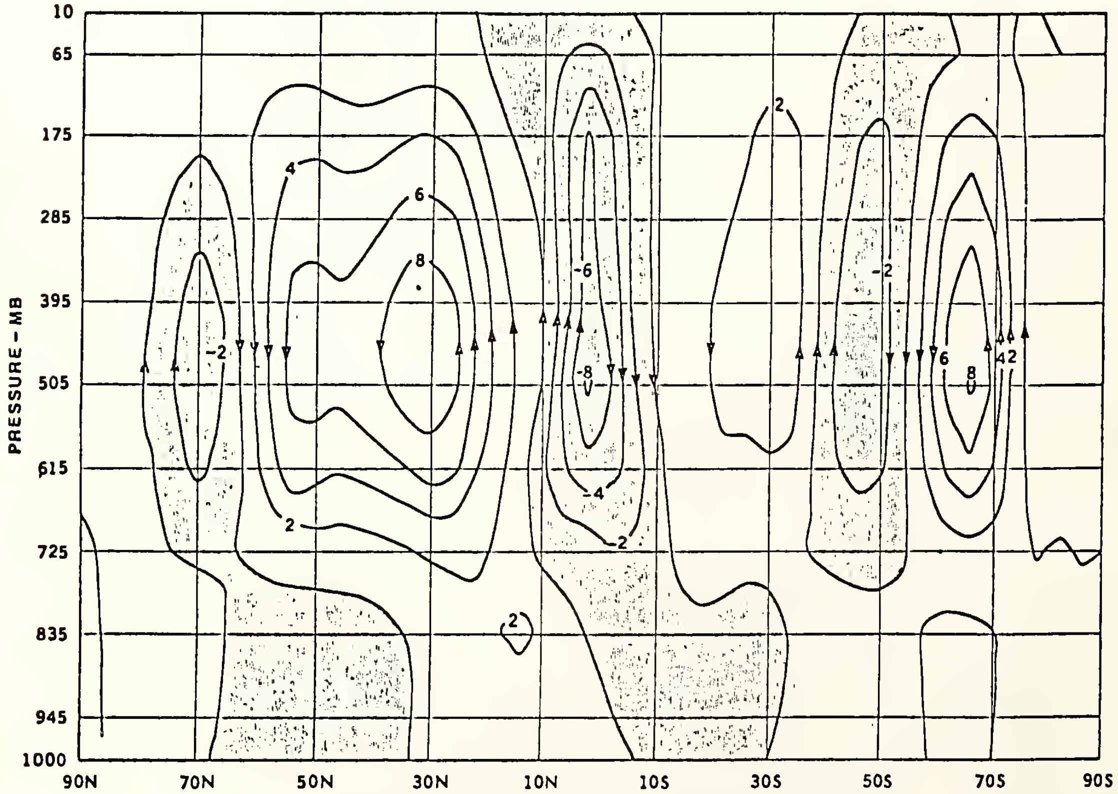

Fig 6. Difference of 60 day mean meridional circulation (10^{13}gm/sec) averaged between the longitudes 50°W and 5°W.

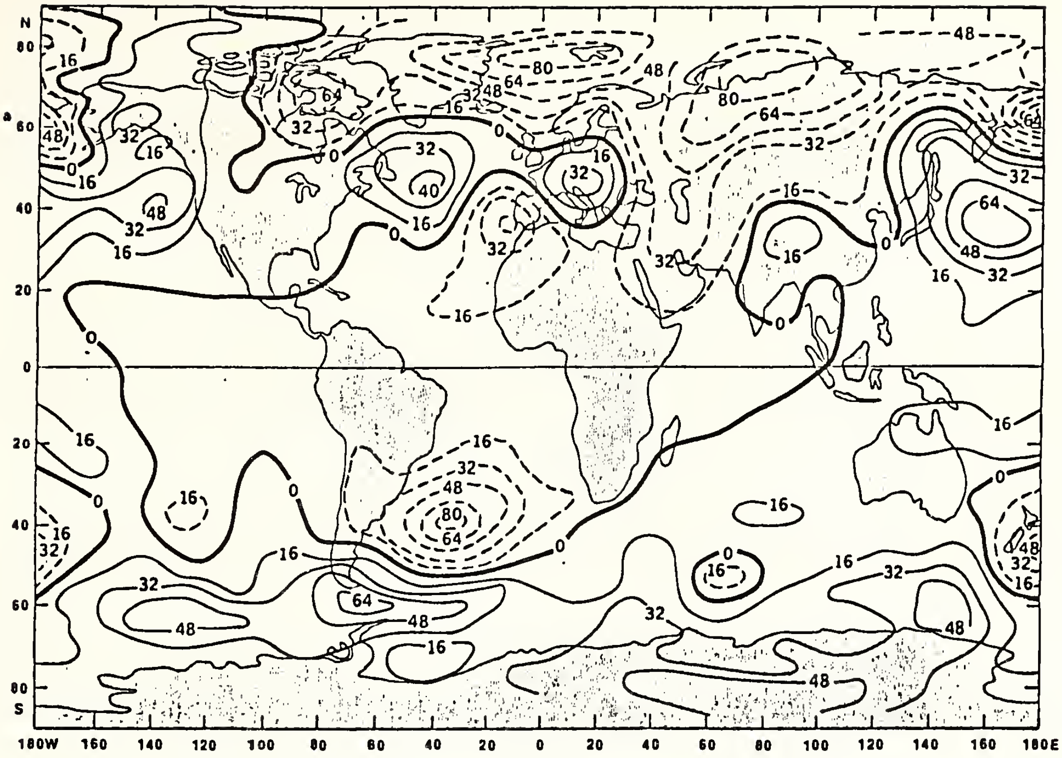

Fig 7. Differences (anomaly-control) of 30 day mean geopotential height (gpm) at 850 mb.

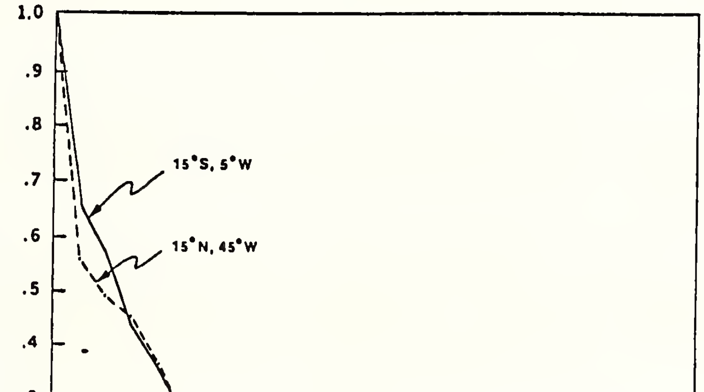

Fig 8. Lag correlation function for monthly mean SST anomaly at 15°S, 5°W and 15°N, 45°W.

Relation of Ocean Currents to Wind in the Southern Hemisphere

Richard B. Wearn, Jr. and D. James Baker, Jr.
Applied Physics Laboratory and Department of Oceanography
University of Washington
Seattle, Washington 98195

The recent work of Namias and Fletcher has shown that changes in the sea surface temperature distribution are associated with climate fluctuations on interannual and interdecadal time scales, and there is a suggestion in the data that processes at high southern latitudes may play some special role in the changes which occur. These results have stimulated interest in understanding what processes affect the distribution of ocean properties. However, we do not yet have information about what changes in currents or deep ocean properties (e.g. heat storage) may be associated with the observed climate changes.

The Southern Ocean plays a central role in the world ocean. The major exchanges between ocean basins occur there, and large heat exchanges between ocean and atmosphere lead to formation of water masses which dominate the deep water properties of much of the world ocean. The strong Southern Hemisphere westerlies drive the largest of all ocean current systems, the Antarctic Circumpolar Current (ACC). This current system forms the boundary between Antarctic surface waters and warmer, more northern waters.

We have begun a program to monitor the strength of the Antarctic Circumpolar Current and to determine how it is related to wind and other atmospheric forcing.

Figure 1 shows the dynamic height of the sea surface relative to 1000 dbar calculated from mean hydrographic data. The contours shown correspond approximately to streamlines of mean surface geostrophic flow.

Fluctuations in strength of the ACC were monitored using pressure gauges at 500 m depth across the Drake Passage to estimate geostrophic downstream flow.

Wind stress over the Southern Ocean was calculated from the 12 hourly, gridded, sea-level atmospheric pressure data provided by the Australian Bureau of Meteorology. The three-year time mean of the zonal component of stress is shown in Fig. 2. The stress is large compared with those occurring elsewhere over the world ocean. The asymmetry in the stress distribution arises because the Antarctic continent is not centered on the pole. The wind stress maxima occur near 50° S in the Indian Ocean sector.

A comparison of the wind stress and pressure gauge measurements across the ACC is shown in Fig. 3. Data have been low-passed with a 28-day-running mean filter. A time series of the zonal component of wind stress averaged over the latitude band from 45° S to 63° S is shown. Considerable seasonal and interannual variability is seen. The pressure gauge measurement at the north and south sides of the Drake Passage are shown with tides removed. The observed fluctuations in the pressure difference across the passage correspond to barotropic transport fluctuations of 80 x $10^6 m^3 s^{-1}$, or about 65% of the estimated mean transport of the ACC. A strong similarity between wind stress and pressure gauge signals is seen.

Figure 4 shows the lagged cross-correlation between the circumpolar averaged wind stress and ACC transport and between the local Drake Passage wind stress and ACC transport. Transport fluctuations with periods longer than 30 days are highly correlated with fluctuations in zonal wind stress integrated over the Southern Ocean, with transport lagging wind by about 9 days. The rapid response means that transport fluctuations observed are largely barotropic. The magnitude and time lag of these fluctuations are consistent with the rate at which momentum is supplied to the current system by the wind.

We have demonstrated that ocean pressure gauges are useful tools for monitoring fluctuations of the ACC. However, we do not yet know how these fluctuations may be related to climate. For example, do changes in strength of the ACC cause changes in the distribution of sea surface temperature? Also, we do not yet know what the relation between wind and transport may be over longer time scales, when the baroclinic response of the ocean may become more important.

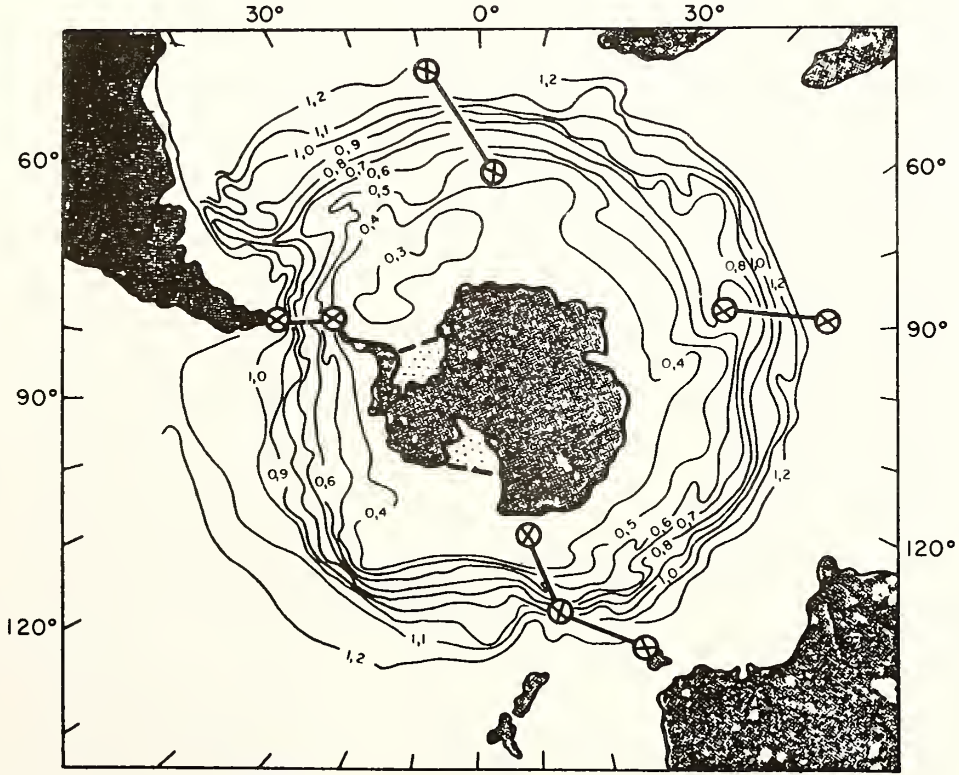

Figure 1. Sea surface dynamic height relative to 1000 dbars, showing the Antarctic Circumpolar Current. Four possible monitoring sections are shown.

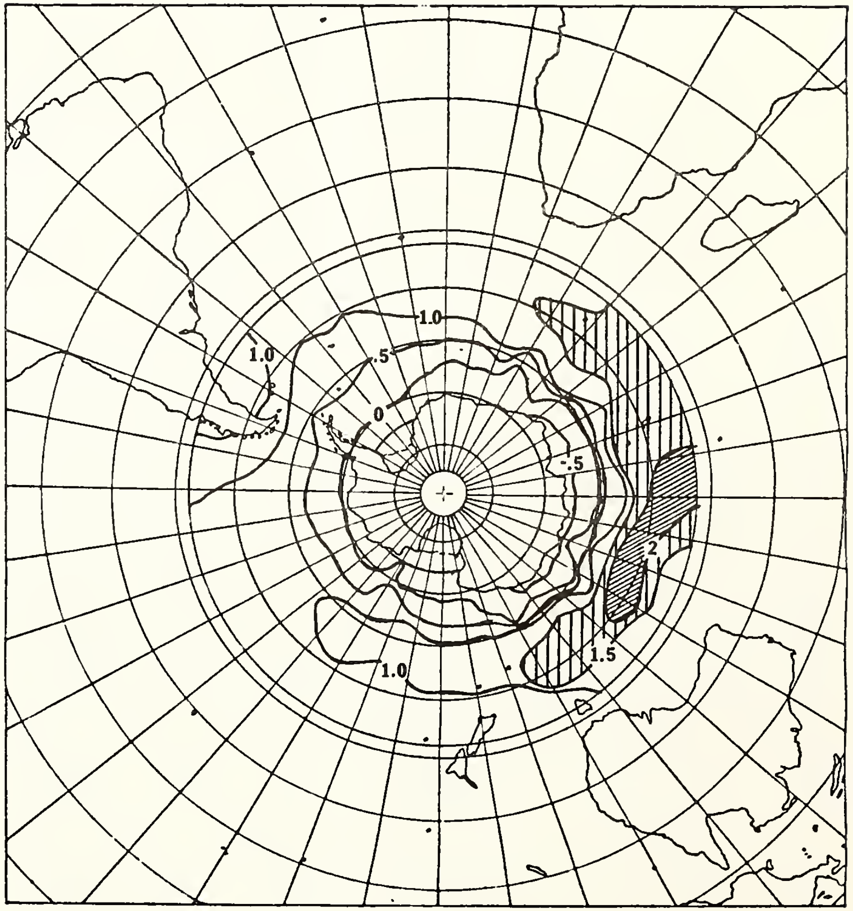

Figure 2. Distribution of three-year time mean zonal wind stress (dynes/cm^2) over the Southern Ocean.

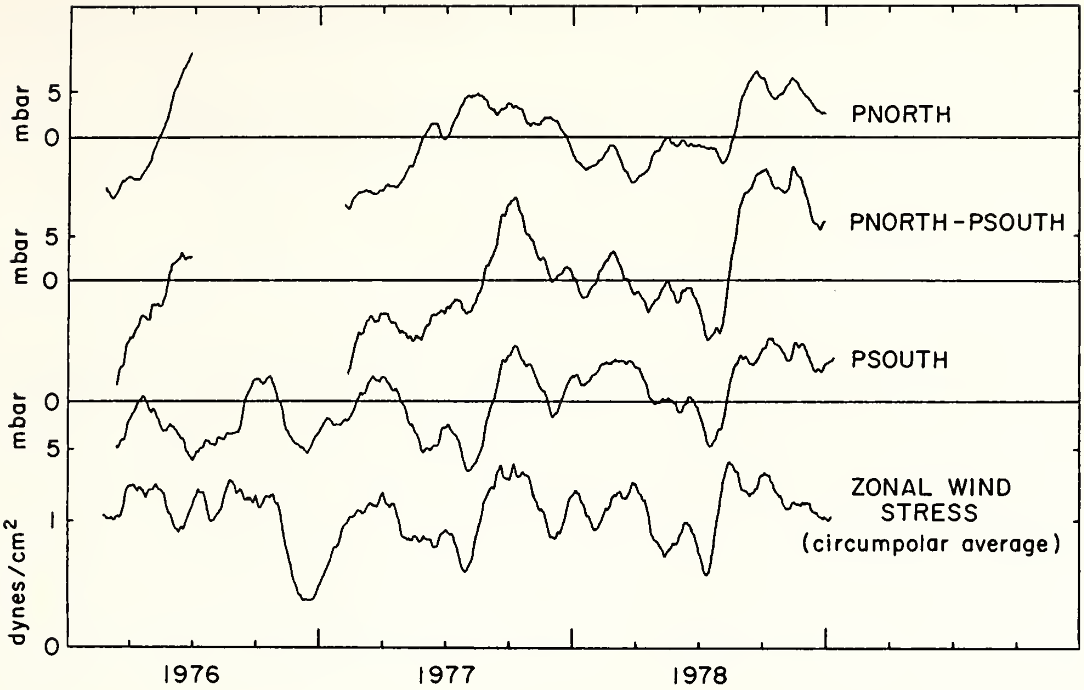

Figure 3. Low-passed ocean pressure gauge and wind data. Data have been detided and low-passed with a 28-day running mean filter. Psouth is shown inverted.

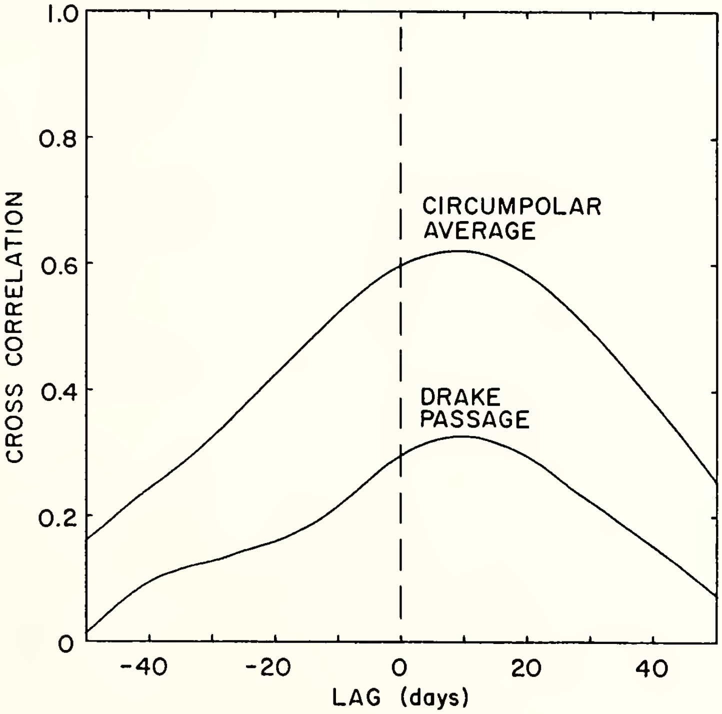

Figure 4. Crosscorrelations between circumpolar wind stress and Pnorth-Psouth and between Drake Passage wind stress and Pnorth-Psouth.

A First Estimate of the Annual Variation of Atlantic Ocean Heat Transport

Peter J. Lamb
Cooperative Institute for Marine and Atmospheric Studies
The University of Miami/NOAA, Miami, Florida, 33149
and
Climatology Section*, Illinois State Water Survey
Champaign, Illinois, 61820

The latitudinal variation of the "vertically integrated net meridional heat transport (VINMHT)" within the North and Tropical Atlantic Ocean (70°N-20°S, including the Gulf of Mexico and Caribbean Sea) is estimated on a bimonthly average basis. Previous investigations of the VINMHT by individual oceans have been restricted to an annual mean time-scale, due to the lack of access to subsurface temperature data. The only documentation of the annual cycle of oceanic VINMHT hitherto available is for the total Northern Hemisphere water body.

The present bimonthly estimates of the Atlantic VINMHT were obtained using an oceanic-residual method. The divergence of the VINMHT for each latitude zone was obtained as the difference between its rates of net surface heat gain [taken from computations by Bunker (Woods Hole Oceanographic Institution) and Hastenrath and Lamb (The University of Wisconsin Press, 1978)] and subsurface heat storage change (estimated from ∿234,000 temperature soundings). With the adoption of near-zero 70°N VINMHT boundary conditions calculated from Aagaard and Griesman (JGR, 1975; see present Table 1), successive southward integration converted these divergence values into VINMHT estimates for latitude circles 10° apart between 60°-30°N and 5° apart in the tropics. The results appear in Table 1. Their uncertainty increases southward from the 70°N boundary, due to the computational procedure employed, and becomes large in the tropics. This is also documented in Table 1. Because of uncertainty about the representativeness of the sub-250m annual temperature variations evident in the data set (only 54% and 20% of the soundings reached 300m and 500m, respectively), the VINMHTs were computed using storage change rates integrated over both the upper 300m and upper 500m. Table 1 shows that the two sets of results sometimes varied considerably, which suggests that the present limitation of the vertical integration to the upper 500m, due to the lack of data from greater depths, may constitute a further source of possible error. It could also be inherent in Oort and Vonder Haar's (JPO, 1976) monthly mean hemispheric VINMHT estimates, which are partially based on storage change rates computed for only the upper 275m.

It is evident from Table 1 that many of the bimonthly VINMHT estimates possess considerable uncertainty. This requires that they be treated with some caution. Table 1 suggests that northward transports may prevail throughout almost all of the study region during January-October. The most likely area of possible occurrence of southward VINMHTs during this period is south of the Equator in May-June. Substantial variations in the northward VINMHT are indicated to occur between January and October. The northward flux out of the Northern Tropics appears to be strongest during July-October, when (particularly in September-October) the northward VINMHT may also be largest at 20°S and the Equator. However, the latter result is much less certain than the former (Table 1). The foregoing pattern is strongly enhanced for September-October when the storage computations are extended to 500m. During July-October, the northward VINMHT evidently undergoes only a relatively small reduction in the Northern Tropics, whereas much more pronounced decreases are indicated for the 40°-50°N (July-August) and 30°-50°N (September-October) zones. May-June, in contrast, appears to be characterized by a northward VINMHT that is very weak at 20°S and the Equator, increases strongly between 0°-15°N, approaches that of July-August at 30°N, and then decreases uniformly to 50°N.

---

* Present affiliation.

A particularly prominent March-April result is the pronounced increase in the northward VINMHT suggested to occur between 5°S and the Equator (Table 1). This converts a moderate northward flux at 20°S into an equatorial one comparable to that of July-October. During this bimonthly period, the 0°-5°S zone experiences both a moderate positive net surface heat gain and pronounced cooling in the upper 300m of the water body. Table 1 indicates a progressive decrease of the March-April transport north of 5°N. In contrast to the remainder of January-October, the extension of the storage change estimates to 500m reduces the March-April northward VINMHT. Table 1 suggests January-February is characterized by a northward VINMHT that is quite small at 20°S, undergoes a moderate increase to 30°N, and may be stronger than other bimonthly periods at 50° and 60°N. The latter feature, along with the VINMHT relative maximum at 40°N, arise from the North Atlantic having a maximum negative net surface heat gain between 30°-40°N at a time when its cooling is strongly concentrated in the 40°-50°N zone. However, the comparative lack of winter subsurface temperature data for this region (only 40% of summer amount between 40°-60°N) may render the foregoing results somewhat suspect.

The November-December results are in marked contrast to those for the rest of the year. Table 1 suggests that the VINMHT may be directed southward throughout much or even all of the study region during this period, and could show a general increase in this direction to a maximum at 10°-20°S. This is particularly indicated by the estimates derived from 500m storage change integrals, which have substantial magnitude south of 40°N. Much weaker, and extremely uncertain, southward VINMHTs were yielded by the 300m storage change calculations, especially north of the Equator (Table 1). The pattern of the November-December results north of 10°N, that of southward transports increasing towards the south, arises from the oceanic cooling (particularly when estimated to 500m) exceeding the negative net surface heat gain. This characterized every zone except 30°-40°N (cf Table 1). The tendency for the foregoing VINMHT pattern to persist south of 10°N largely results from positive net surface heat gains coinciding with lesser oceanic warming or oceanic cooling.

Although the November-December results in Table 1 are rather surprising and therefore of some potential interest, there are several reasons why they should be regarded as highly tentative at present. First, there does not appear to be a fully acceptable rationale for the southward VINMHT currently available. Furthermore, the higher latitude storage change estimates for cooler months may be adversely affected by having a lesser data base than those for the rest of the year. The Bunker net surface heat gain results probably also contain this source of possible error. As explained earlier, the method used here renders the mid- and low-latitude VINMHTs partially dependent on the more northerly estimates of the net surface heat gain and subsurface storage change. In view of their potential interest and considerable uncertainty, Table 1's November-December results may serve as a challenge to theoreticians and further stimulus for the planned program to directly monitor the Atlantic VINMHT at about 25°N.

Table 1 also documents the latitudinal variation of the mean annual Atlantic VINMHT computed from the annual average net surface heat gain. These mean annual VINMHTs are very similar to those yielded by Table 1's bimonthly values, due to the annual average storage change being extremely close to zero for both the upper 300 and 500m. Previous investigations of the annual average Atlantic VINMHT did not have access to either or both of the present superior sea-air heat exchange data sets. The mean annual pattern in Table 1 is therefore briefly discussed here. The annual average VINMHT is directed northward throughout the study region, which is not surprising in view of Table 1's bimonthly values. It increases from 81 x 10^{13}W at 20°S to a broad 5°-25°N maximum of 111-115 x 10^{13}W, largely due to substantial enhancement between 5°S and the Equator. This latter feature is strongly dictated by the March-April pattern (Table 1). The maximum annual average VINMHT occurs at 15°N, and there is a pronounced decrease poleward of 30°N, especially between 30°-40°N. The general pattern of these results does not appear to be seriously threatened by the possible errors involved (Table 1). It is very similar to that recently obtained by Hastenrath (JPO, 1980), whereas earlier work variously found the mean annual VINMHT to have a northward maximum near 30°N, weak northward or near zero cross-equatorial values, and a southward direction throughout almost all of 0°-20°S. From 40°N southward, however, Hastenrath's northward VINMHTs are 40-60% larger than the present ones. This difference appears to primarily result from Hastenrath's 40°-50°N net surface heat gain (taken from Budyko's Atlas) being more negative than the Bunker value used here. Budyko failed to detect the warming of the Labrador current between Nova Scotia and Cape Hatteras identified by Bunker and Worthington (BAMS, 1976). The present annual average VINMHT for 25°N (+113 x 10^{13}W) is in good agreement with the values Bryden and Hall (Science, 1980) recently inferred from the same Bunker data set (+111 x 10^{13}W) and computed directly from oceanographic measurements (+110 ± 29 x 10^{13}W).

Table 1. Latitudinal variation of bimonthly average "vertically integrated net meridional heat transport (VINMHT)" within the North and Tropical Atlantic Ocean, including the Gulf of Mexico and Caribbean Sea (10^{13}W). Northward transports are positive; those for 70°N are boundary conditions computed from Aagaard and Griesman (1975). Vertical integrations to 300m and 500m depths are given separately. The domain treated has the following noncontinental lateral boundaries: Baffin Is. east coast, 64°W in Hudson Strait, 66°W in Gulf of St. Lawrence, 6°W in Strait of Gibraltar, and 8°E in Skagerrak Strait. The bimonthly uncertainties (10^{13}W) are based on possible errors of 15W m^{-2} in the rates of both net surface heat gain and subsurface storage change, and 5 x 10^{13}W in the 70°N boundary transports. The annual average VINMHTs listed are computed from annual average net surface heat gains; they are very similar to the annual means of the bimonthly VINMHTs cited, due to the annual average subsurface storage change rate being extremely close to zero. The annual uncertainties (10^{13}W) are based on possible errors of 10W m^{-2} in the annual average rate of net surface heat gain and 5 x 10^{13}W in the 70°N boundary transport.

	Jan-Feb		Mar-Apr		May-June		July-Aug		Sept-Oct		Nov-Dec		Bimonthly	Annual	
Lat.	300m	500m	300m	500m	300m	500m	300m	500m	300m	500m	300m	500m	Uncertainty	Average	Uncertainty
70°N	+ 07	+ 07	+ 07	+ 07	+ 07	+ 07	+ 15	+ 15	+ 15	+ 15	+ 09	+ 09	5	+ 10	5
60°	+ 85	+109	+ 18	- 02	+ 14	+ 22	+ 36	+ 54	+ 24	+ 27	- 06	- 39	14	+ 28	8
50°	+126	+171	+ 57	+ 32	+ 29	+ 40	+ 59	+ 78	+ 50	+ 73	- 15	- 86	26	+ 52	12
40°	+ 79	+ 83	+ 83	+ 58	+ 82	+117	+128	+162	+ 90	+139	- 31	-129	42	+ 73	17
30°	+101	+124	+107	+ 58	+126	+164	+148	+174	+151	+216	- 03	-106	63	+107	24
25°	+101	+136	+126	+ 81	+113	+147	+169	+185	+157	+230	- 05	-117	76	+113	29
20°	+ 85	+139	+137	+ 86	+118	+170	+187	+195	+152	+227	- 13	-148	90	+114	33
15°	+ 83	+125	+149	+101	+121	+172	+189	+194	+165	+256	- 33	-174	102	+115	37
10°	+ 90	+128	+197	+157	+ 75	+118	+180	+191	+162	+246	- 45	-181	114	+113	41
5°N	+ 86	+120	+226	+193	+ 27	+ 60	+180	+201	+163	+241	- 37	-168	123	+111	44
0°	+ 63	+ 79	+196	+164	+ 18	+ 61	+180	+203	+211	+295	- 77	-209	133	+102	48
5°S	+ 50	+ 65	+137	+100	- 04	+ 47	+170	+203	+253	+322	-107	-238	143	+ 86	51
10°	+ 59	+ 77	+138	+108	- 13	+ 35	+156	+194	+257	+319	-121	-256	152	+ 82	53
15°	+ 49	+ 76	+142	+121	- 14	+ 23	+150	+187	+257	+331	-106	-259	161	+ 83	57
20°	+ 57	+ 77	+111	+108	+ 01	+ 49	+152	+182	+260	+322	-115	-271	170	+ 81	60

A COMPARISON OF WINDS AND SST'S FROM FOUR PACIFIC MARINE DATA SETS

Ellen Steiner

Cooperative Institute for Research in Environmental Sciences
University of Colorado
Boulder, Colorado 80309

The proliferation of data sets for use in climate studies is making it important to determine whether these data are consistent. I have compared the four wind and sea surface temperature (SST) data sets listed in Figure 1. The data were interpolated onto comparable grids and time series were plotted for select areas. The locations of the grid boxes considered in this discussion are seen in Figure 2. Station 38 was chosen because it lies in the data-rich region on the shipping lanes from San Francisco to Hawaii, and Station 97 was chosen because of its possible importance as an indicator of climatic trends.[1]

Figure 3 shows the SST's in station 38. Before 1961, only the HSST and CPM had data; the RMS difference between them was 1°C. RMS errors for the cases discussed are summarized in Figure 10. After 1961, the HSST, CPM, and NMFS SST's all compared well. The RMS error then between the HSST and CPM data was .34°C. 1961 was the first year an update was added to the HSST data, and subsequent SST's included intake as well as bucket temperatures. As a result, the number of observations jumped from the 10's and 20's before 1961 to the 500's and 600's after. A consequence of this discontinuity is demonstrated in Figure 4, a graph of the mean latitudes of the monthly observations in Station 38. Because of the small number of observations, the uncertainty is large before 1961. The discontinuity affects the wind speed and direction as well as the SST's. Wyrtki and Meyers' and the CPM wind speeds agree well throughout (Figure 5), while the HSST wind speeds don't compare well with those data till after 1961. The wind directions of Wyrtki and Meyers' and CPM also correspond well (Figure 6). December - February show the most interannual variability in wind direction, and it is in those months that the HSST corresponds most poorly with the other data (before 1961, that is). After 1961, all three data sets are in good agreement.

Other general problems with the data were the following: All the data sets showed occassional outlying points. There was a 9-year wind data gap in the CPM data for one of the regions examined. In general, the correspondence between the data varied depending upon region and month.

Our group at CIRES is experimenting with adjustment techniques to the data. We have applied the first of these to the HSST sea surface temperatures in an attempt to correct them to the center of each grid box. The corrections were done in the following manner:

1) Latitudinal gradients and the normal seasonal trends of SST's were estimated for each grid square.

---

[1] Fletcher, J. O., Radok, U., Slutz, R., Climatic Signals of the Antarctic Ocean. Submitted to JGR.

2) For the temporal gradients, the HSST hundred-year monthly means were used assuming each mean to be at the middle of the month.

3) For latitudinal gradients, a Russian atlas[2] of SST's was used. Only mean seasonal winter and summer gradients were derived from the Russian atlas; these were applied to the winter and summer months while interpolated values were applied to the fall and spring months.

4) The observations were reduced to the center of each box and the middle of each month by linear interpolation.

From the graph of mean monthly latitudes in station 38 (Figure 4), it can be expected that the adjustment would make a bigger difference before 1961, when the latitudes were scattered widely throughout the box, than after 1961 when they were clustered near the center. This is in fact what happens (Figure 7). Note that in some months, such as December and January, the adjustment actually smoothed out or changed the interannual variability. This would make a significant difference in results derived from these data. In other months, such as June, there is hardly any difference. A scatter plot of the adjusted vs. nonadjusted data (Figure 8) shows that on the whole, the adjustment introduced a slight warm bias into the SST's.

In station 97, the CPM and HSST data agreed fairly well before the adjustment. There was no discontinuity in the HSST data in 1961. The latitudinal distribution of SST's in station 97 was scattered but centered at about 42.5°S, i.e., north of the center of the box. Thus without the correction to 45°S there was a systematic warm bias in the data (Figure 9). The RMS difference between the adjusted and non-adjusted data was 2°C in this case, more marked than that in Station 38. Since both the CPM and HSST must get their data from ships approaching New Zealand from the (warm) north, the adjusted data is probably more accurate than either the nonadjusted HSST or CPM data.

Adjustment techniques such as the one described may well be the way to improve and standardize different data. We are currently refining this technique by making longitudinal corrections where appropriate, and by using the HSST data itself to compute self-consistent gradients.

---

[2] Physico-geographical Atlas of the World, Academy of Science, Main Administration of Geodesy and Cartography, Moscow, 1964, pp. 44-45.

Data Sets	Source	Type of data	Time	Extent	Grid Scale
Historical Sea Surface Temperature summary product (HSST)	National Climatic Center	SST's and winds[1]	1861-1960 update; 1961-1976	Indian and Pacific Oceans Pacific	variable (see Figure 1)
Compacted Pacific Marine data set (CPM)	National Climatic Center and Center for Environmental Assessment Services	SST's and winds[2]	1946-1976	Pacific	2° x 2°
National Marine (NMFS) Fisheries Service		SST's	1961-1977	70°W-180° 40°S-60°N	5° x 5°
Wyrtki and Meyers		Winds	1947-1972	70°W-120°E 30°S-30°N	2°latitude x 10° longitude

All data are monthly averages from ship reports.

[1] HSST also includes air temperatures.

[2] CPM also includes temperature and momentum flux quantities.

Figure 1

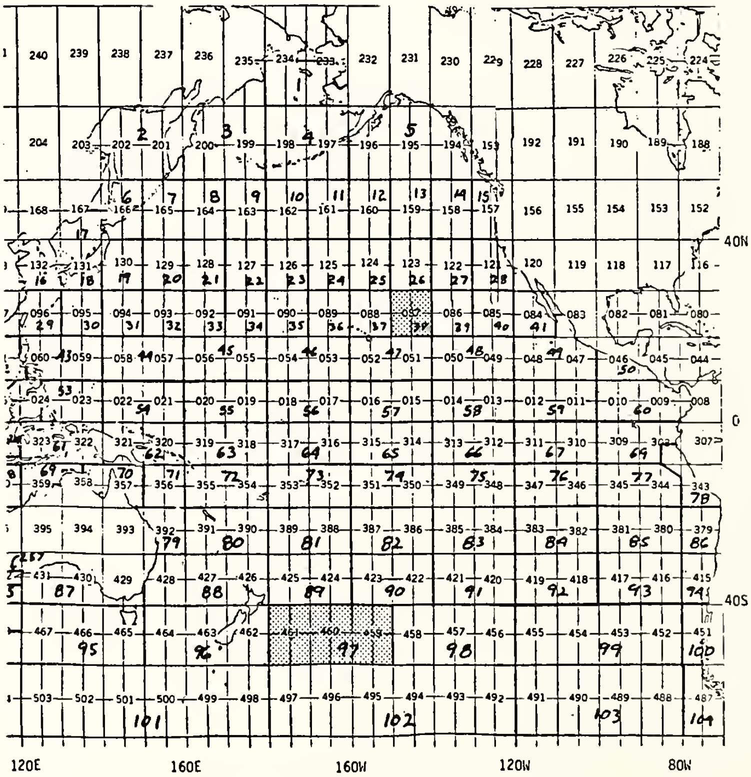

Figure 2. The handwritten numbers are the HSST Station numbers and the printed numbers are Marsden squares. The shaded areas are those discussed in this comparison.

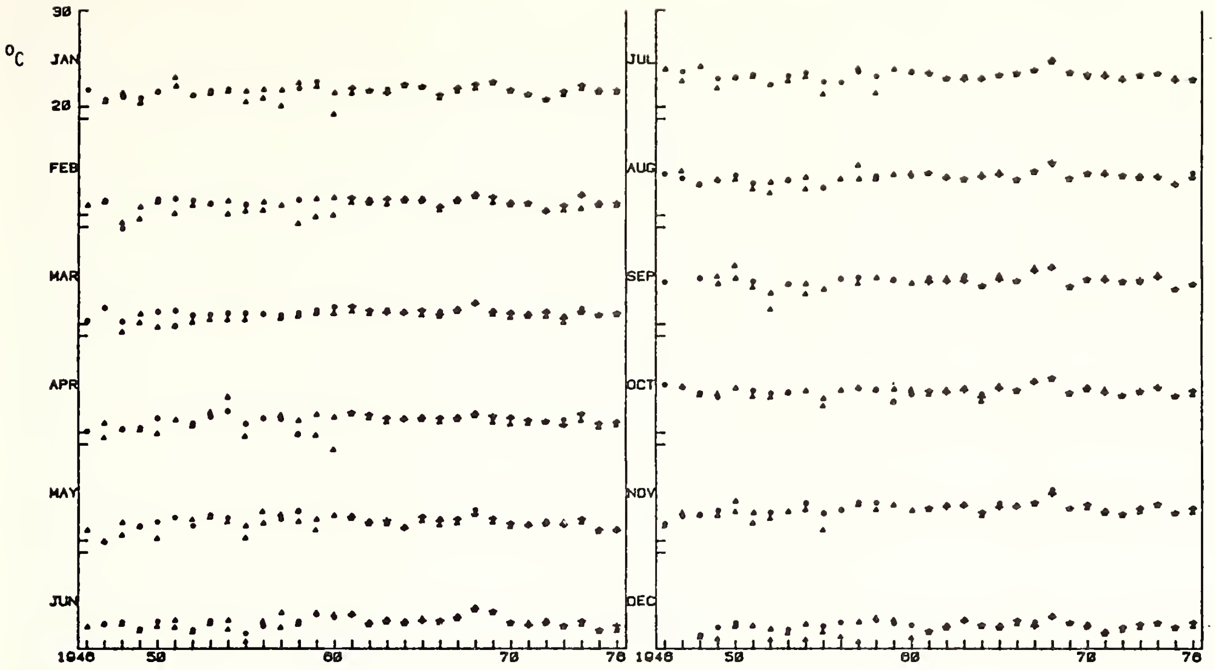

Figure 3. CPM (o), NMFS (+), and HSST(Δ) SST's in Station 38

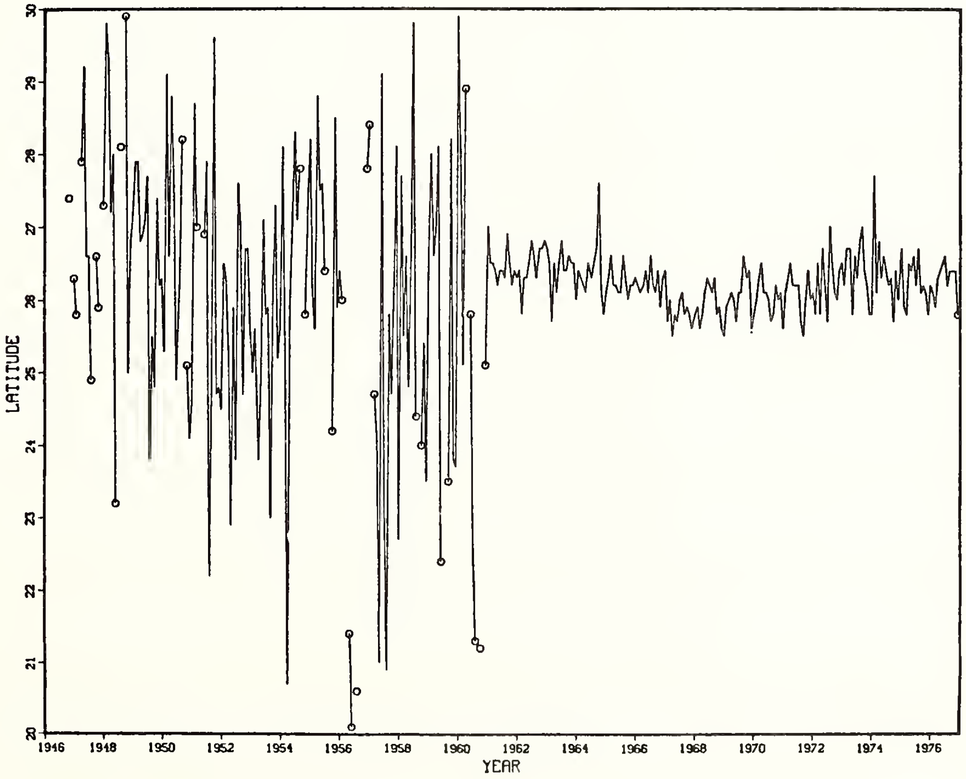

Figure 4. Monthly mean latitude of Observations in Station 38

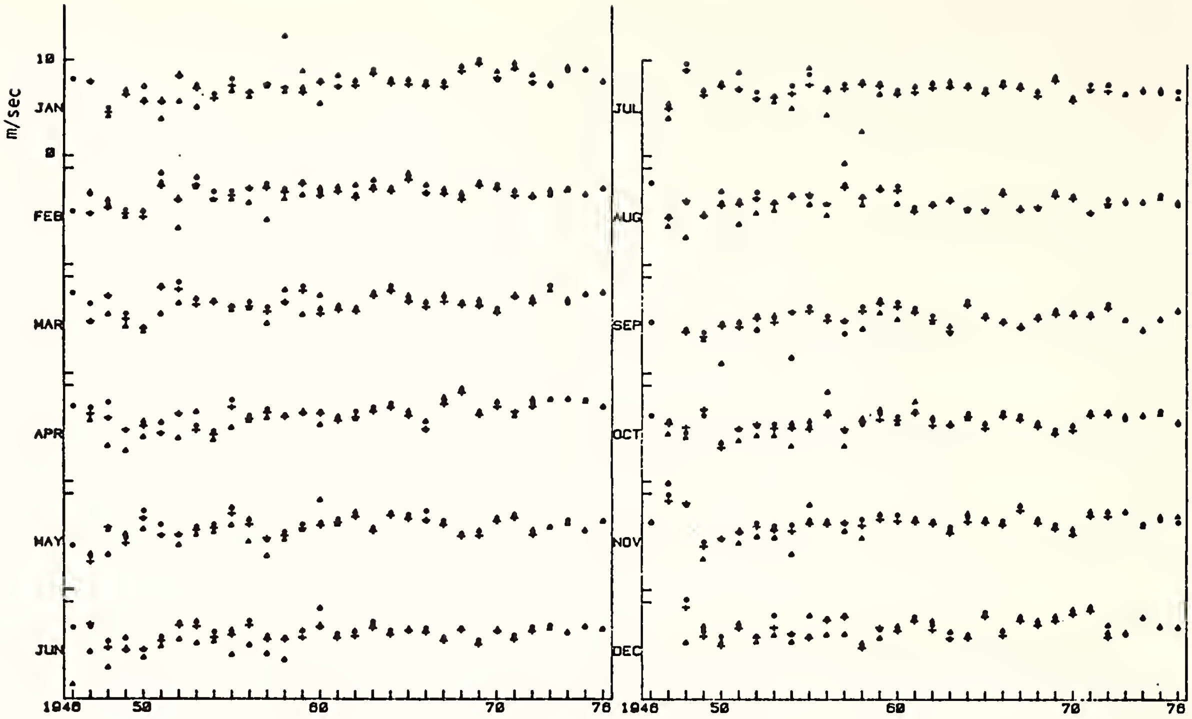

Figure 5. CPM (o), Wyrtki and Meyers' (+), and HSST (Δ) Wind Speeds in Station 38

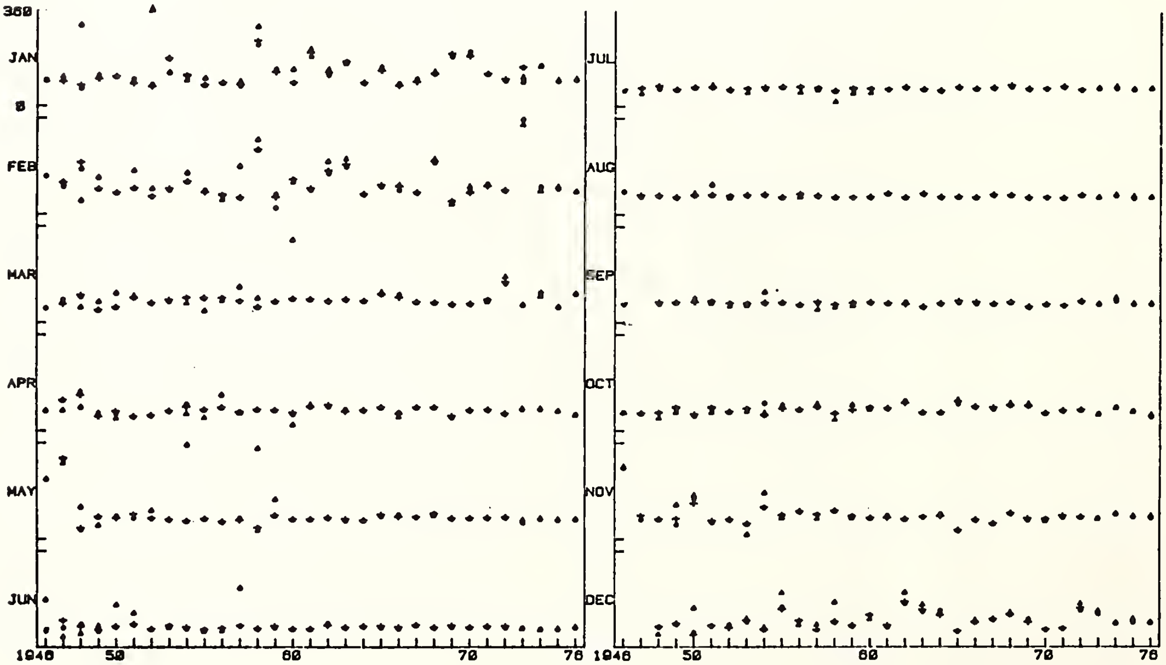

Figure 6. CPM (o), Wyrtki and Meyers' (+), and HSST Wind Direction in Station 38

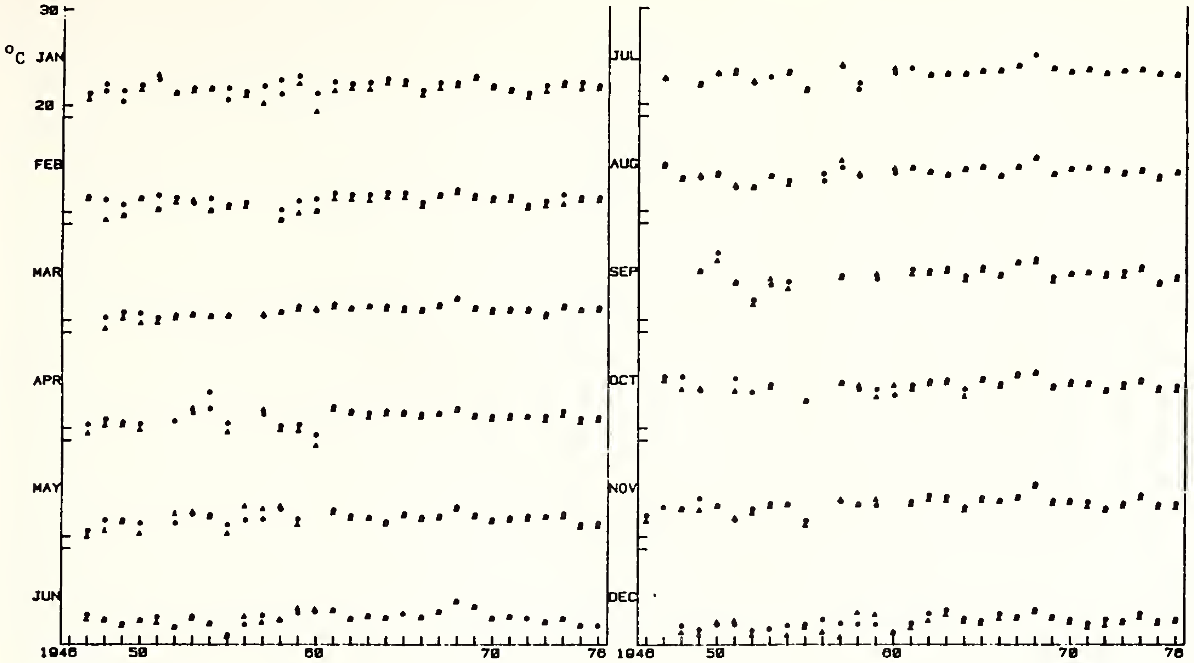

Figure 7. Adjusted HSST (o) and non-adjusted HSST (Δ) SST's in Station 38

Station 38

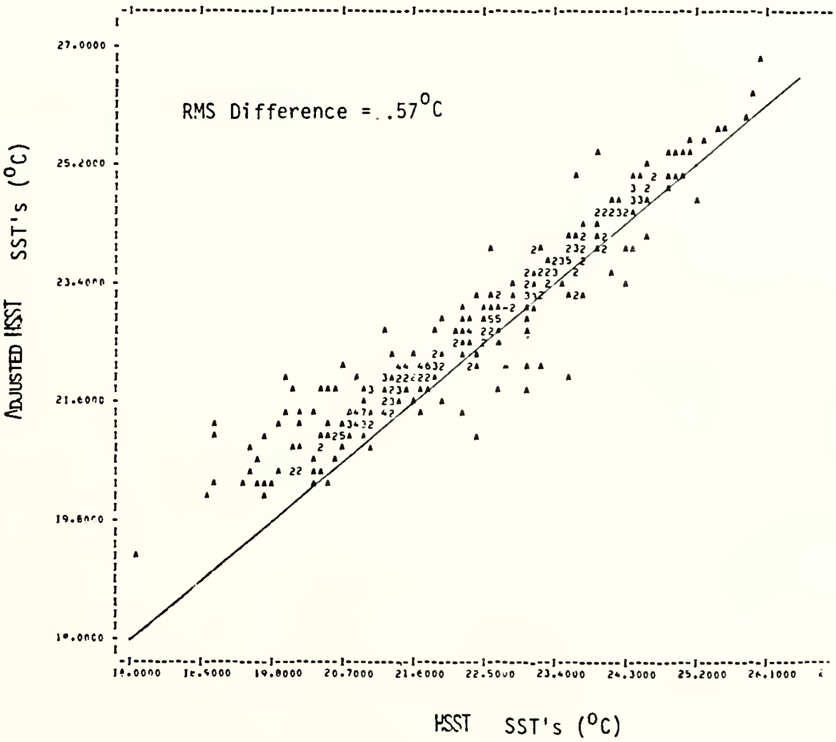

Figure 8

Station 97

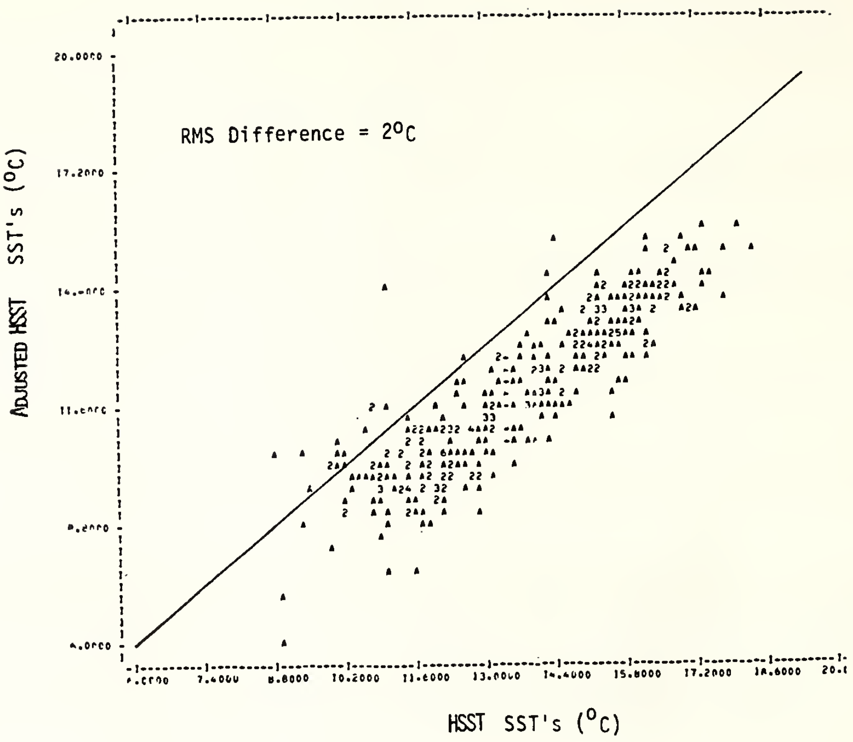

Figure 9

ROOT MEAN SQUARE DIFFERENCES

DATA	TIME PERIOD	SST	WIND SPEED	WIND DIRECTION
		STATION 38		
HSST vs. CPM	1946-76	.71°C	1.27 M/SEC	26.07°
	1946-60	1.00°C	1.85 M/SEC	37.74°
	1961-76	.34°C	.33 M/SEC	8.38°
ADJUSTED HSST vs. CPM	1946-76	.48°C		
ADJUSTED HSST vs. HSST	1946-76	.57°C		
HSST vs. FISHERIES	1961-76	.29°C		
CPM vs. FISHERIES	1961-76	.17°C		
HSST vs. WYRTKI AND MEYERS	1947-72		1.21 M/SEC	27.56°
CPM vs. WYRTKI AND MEYERS	1947-72		.47 M/SEC	5.55°
		STATION 97		
HSST vs. CPM	1946-76	.65°C		
ADJUSTED HSST vs. CPM	1946-76	1.77°C		
ADJUSTED HHST vs. HSST	1946-76	2.02°C		

FIGURE 10

COMPUTATION OF THE SEASONAL CYCLE OF THE SURFACE HEAT FLUX OVER THE GLOBAL OCEAN

Y.-J. Han, S.-W. Lee, S. Esbensen, Y. Kushnir
Climatic Research Institute
Oregon State University
Corvallis, Oregon

New estimates of the net surface heat fluxes over the global ocean have been obtained for all calendar months. The method used in the present calculation is patterned after Budyko (1963) and Bunker (1976). But further simplifications were made, following Haney (1971), to obtain a formula in the form $Q_s = Q_2(T_A^* - T_s)$, where Q_s is the net surface heat flux, T_s is the sea-surface temperature, T_A^* is the "apparent" atmospheric equilibrium temperature, and Q_2 is the proportionality constant. Here T_A^* and Q_2, derived from the original heat flux formulas, are functions of the surface meteorological parameters (e.g., surface wind speed, air temperature, dew point, etc.) and the surface radiation parameters. This particular formulation of the net surface heat flux, together with the necessary climatological atmospheric parameters, are intended to provide a realistic and computationally efficient upper boundary condition for oceanic climate modeling.

The basic climatological data set used to compute T_A^* and Q_2 was obtained from several sources. The surface atmospheric parameters were provided on a 5°x5° Marsden subsquare grid by the National Climatic Center. The surface insolation under the clear sky condition was taken from the table in Kondratiev (1969), but reduced by 10 percent at all latitudes to be consistent with more recent estimates (Bunker, 1976). The total cloud cover needed for both long- and short-wave radiation calculations was obtained from Miller and Feddes (1971), who estimated the monthly mean cloud cover from the satellite measurements.

The monthly mean values of T_A^* and Q_2 were computed over the global ocean for all calendar months, but only the annual mean values are shown in Fig. 1 and Fig. 2 to show the significant geographical dependence of these parameters. Although values are calculated in polar regions, the data density in both the Arctic and Antarctic Oceans is not large enough to provide stable climatological means. As a result, the computed T_A^* and

Q_2 fields near the climatological sea-ice boundaries are noisy even in the annual mean maps.

The annual mean net surface heat fluxes (Fig. 3) were computed and compared with the earlier estimates by Budyko (1963) for the world ocean and Bunker (1976) for the North Atlantic Ocean. The flux patterns were in good agreement at middle latitudes but some significant discrepancies were found at high and low latitudes. These discrepancies are also apparent in the zonal mean values shown in Fig. 4, where more recent estimates by Oort and Vonder Haar (1976) are also plotted for comparison. A more detailed comparison of each heat flux component shows that the major discrepancies are due to the estimates of the net radiation in the tropics and of the sensible heat fluxes in the high latitudes. We suspect that the solar insolation is somewhat overestimated in the present calculation mainly due to the use of the satellite inferred cloud data which, in the tropics, show systematically less cloud cover than the conventional ground observations (Fig. 5); the latter were used by both Budyko and Bunker. The relatively large heat fluxes in the high latitudes are probably due to the use of the heat transfer coefficient which are made to vary with the thermal stability and wind speed (Bunker, 1976).

In order to investigate the seasonal variability of the net flux, the monthly zonal mean values were computed and are shown in Fig. 6. The largest seasonal variabilities occur in the middle latitude oceans in both hemispheres. The relative magnitude of the variability, however, is greater in the northern oceans than in the southern oceans. This is consistent with the relatively stronger surface heat exchange processes in the northern ocean, especially in the vicinity of the major western boundary currents. For the purpose of comparison, the present result was checked with the independent calculations of Oort and Vonder Haar (1976). Their estimates of the net surface heat flux which was obtained as a residual of the vertically integrated atmospheric heat balance equation using satellite radiation measurements at the top of the atmosphere and conventional radiosonde data shows relatively less heating (~50 watts/m^2) during the summer half year and very much less cooling at the high latitudes during the winter. The relative accuracy of these two independent estimates, however, is difficult to judge because of many uncertainties involved in the methods and data used in each estimate.

The parameterization of the net surface heat flux by T_s, T_A^*, and Q_2 emphasizes the important role of sea surface temperature in determining the net surface heating of the oceans. The comparison between the heat fluxes obtained from model-simulated and observed sea-surface temperatures for the same T_A^* and Q_2 should give needed guidance for the development and verification of coupled ocean-atmosphere general circulation models.

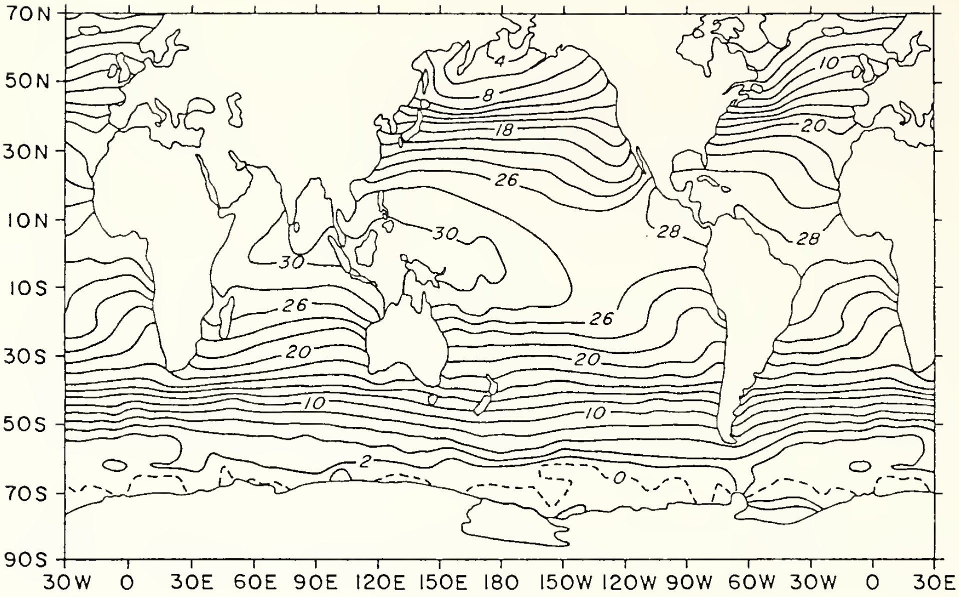

Fig. 1. Computed annual mean atmospheric equilibrium temperature (T_A^*). The isolines are drawn at 2°C intervals with the 0°C isotherm dashed.

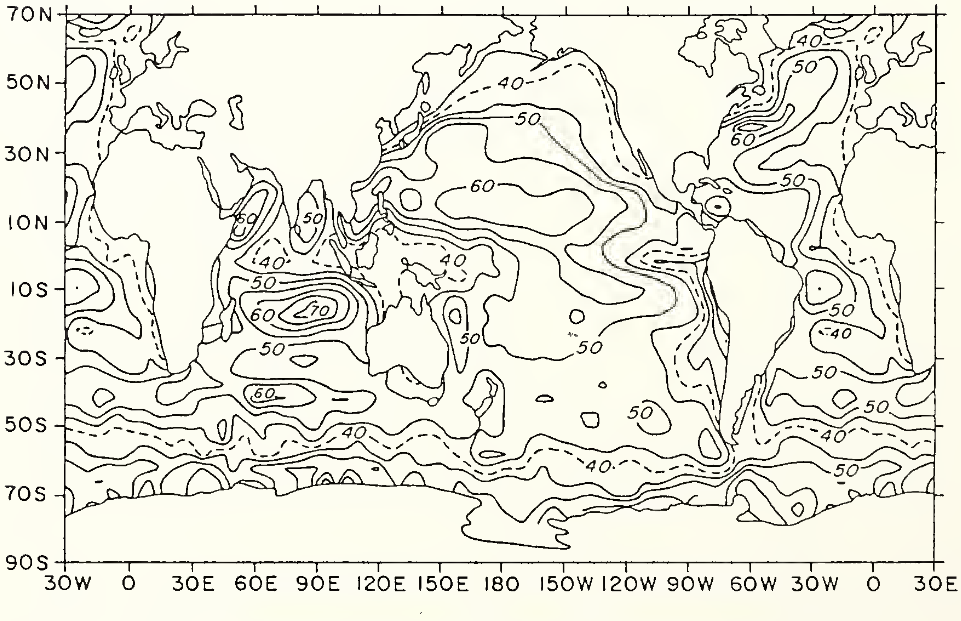

Fig. 2. Computed annual mean proportionality constant (Watts/m^2/°C). The isolines are drawn at 5 Watts/m^2/°C with the reference line (40) dashed.

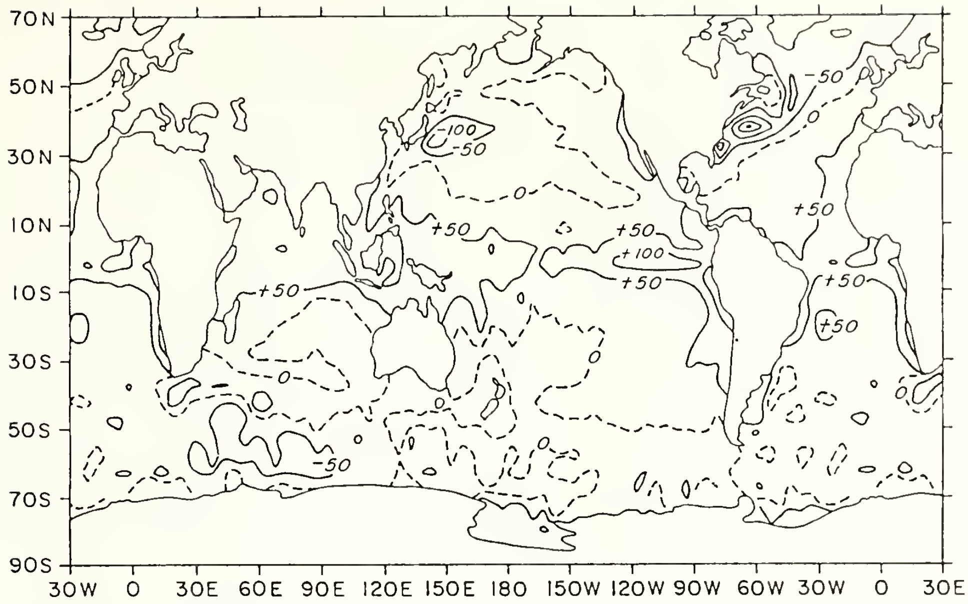

Fig. 3. Computed annual mean net surface heat flux (Watts/m^2). The isalines are drawn at 50 Watts/m^2 intervals with the reference line (0.0) dashed.

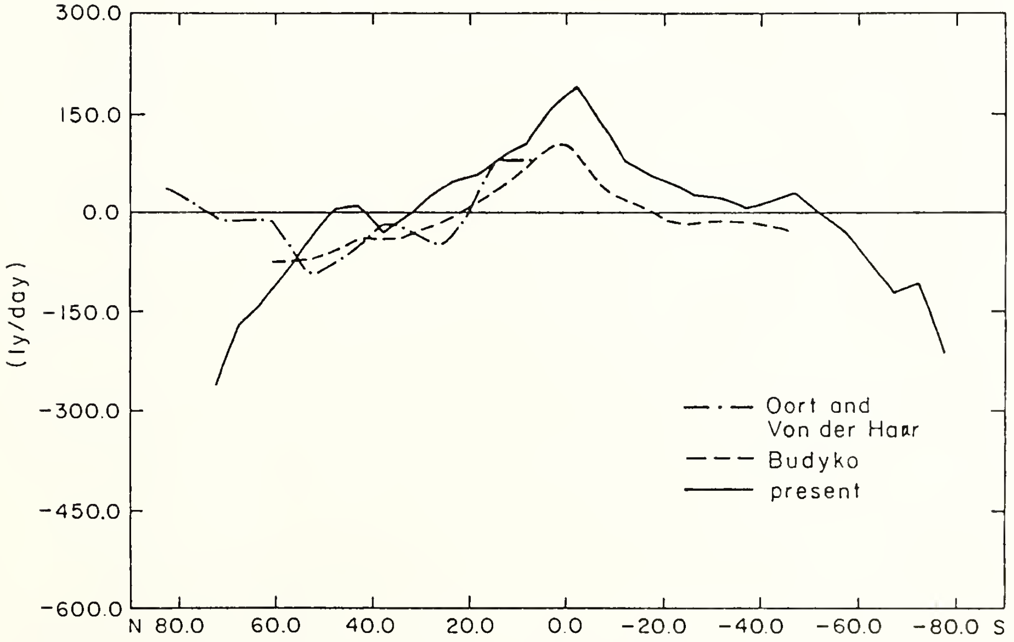

Fig. 4. Computed zonal mean of the annual mean net surface heat flux (ly/day).

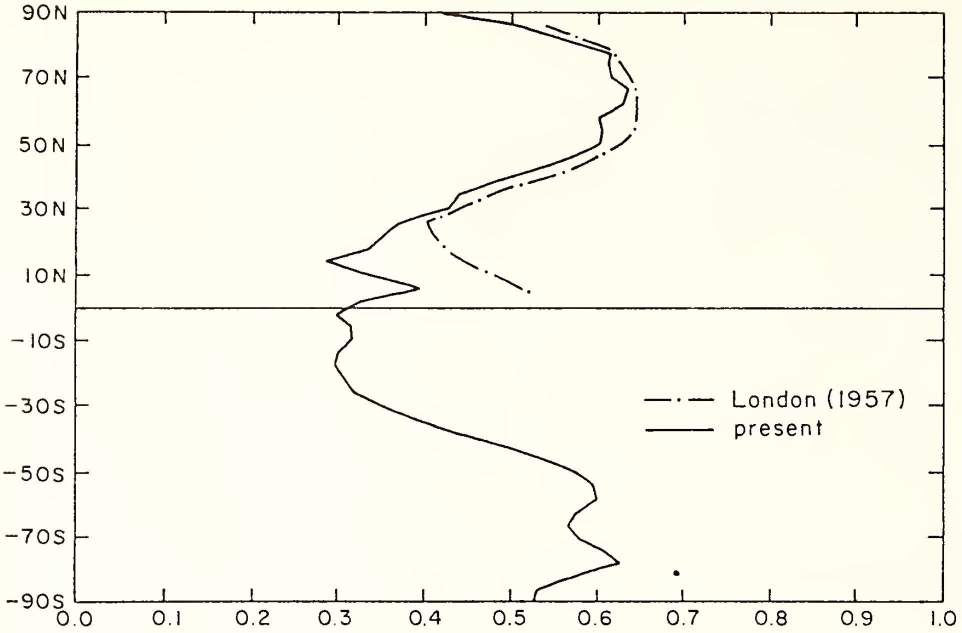

Fig. 5. Latitudinal distribution of the zonal mean of the annual mean cloud cover (fractions).

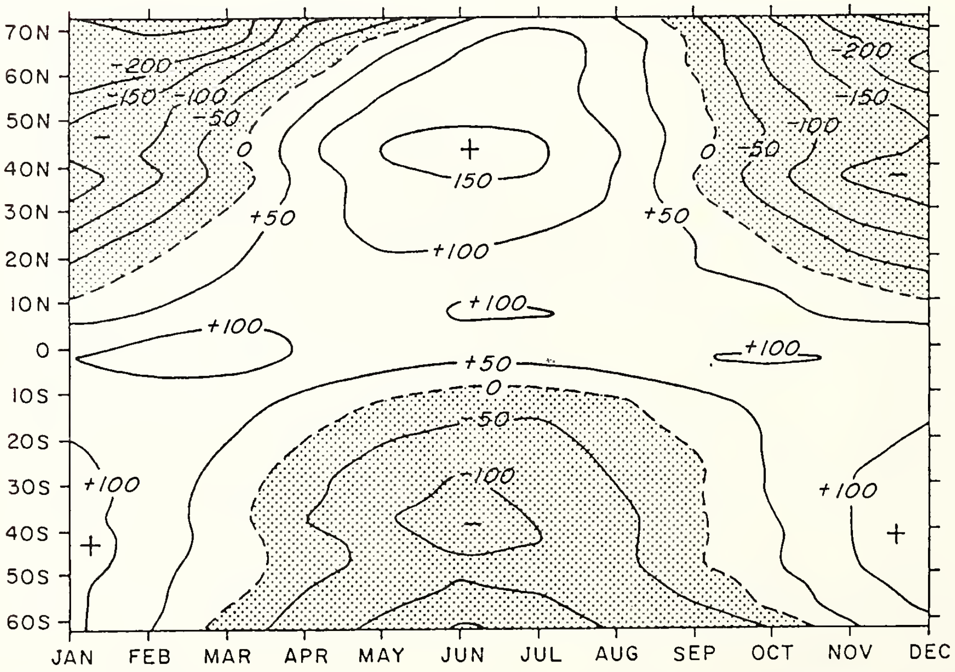

Fig. 6. Time latitude cross section of the zonal mean net surface heat flux (Watts/m^2). The isolines are drawn at 50 Watts/m^2 intervals with the zero line dashed.

Large scale heat exchange across the air-sea interface in the North Pacific Ocean during recent fall and winter seasons.

Nathan E. Clark
Scripps Institution of Oceanography
University of California, San Diego
La Jolla, California 92093

Comparison of fall and winter 700 mb. height anomaly fields with those of sensible and latent heat exchange between ocean and atmosphere shows that above (below)-normal heat flux over the entire eastern North Pacific Ocean is associated with below (above)-normal 700 mb. heights over the eastern North Pacific and western North America. Since below-normal height fields over these regions are related to heavy precipitation in the western U.S., the eastern North Pacific is operating as an important source of heat and moisture for storms moving out of the Gulf of Alaska and on to the North American coast.

The anomaly values of air-sea heat exchange used in this study were determined from marine weather data collected by ships-of-opportunity operating in the North Pacific Ocean from 1950 through 1979. The maps of 700 mb. height and anomaly values that were used in this initial qualitative comparison were obtained from the Climate Study Group at the Scripps Institution of Oceanography.

Figs. 1 and 2 show the 700 mb. height and anomaly values for the Northern Hemisphere during the winters of 1968-69 and 1976-77. These years were chosen to illustrate the differences in anomaly distribution over the eastern North Pacific Ocean and western North America during contrasting wet and dry winter seasons in the western United States. In Fig. 1 a trough in the 700 mb. height field is located along the west coast of North America, and below-normal values extend from the eastern North Pacific Ocean well into the western third of the continent. Associated with this trough were frequent storm systems that moved out of the Gulf of Alaska and dropped above-normal precipitation on the western states as they travelled inland. On the other hand, Fig. 2 shows a strong ridge in the 700 mb. height field located along the North American coast with above-normal values over the eastern North Pacific and western continental regions. This ridge prevented storm systems from entering the United States and drought conditions prevailed in the western states throughout the fall and winter seasons.

Figs. 3 and 4 show the anomaly values (actual seasonal values minus the long-term mean calculated from 1950 through 1979) of latent heat flux over the North Pacific Ocean north of 20° N. latitude for the fall seasons of 1968 and 1976 and the winter seasons of 1968-69 and 1976-77. In Fig. 3 both fall and winter seasons have above-normal evaporation and latent heat flux over the eastern North Pacific Ocean. These above-normal values occur in the same region as do the below-normal 700 mb. heights (Fig. 1) and are caused by the strong winds and cold, dry air on the western flanks of surface storm systems associated with the below-normal height field. In contrast to this situation, Fig. 4 shows below-normal evaporation and latent heat flux over the eastern North Pacific Ocean during fall 1976 and winter 1976-77, and these below-normal values occur in the same area as do above-normal 700 mb. height values (Fig. 2). The strong ridge of high pressure that persisted throughout these fall and winter seasons kept most storm systems out of the eastern North Pacific Ocean, and resultant light surface winds and more humid air diminished latent heat exchange between ocean and atmosphere.

Fig. 5 shows area averages of latent heat flux anomalies for fall and winter seasons from 1968 through 1978-79. Each of the area average values was determined for 5° by 5° seasonal anomaly values which were integrated over the region shown in outline on the maps in Figs. 1-4. If a comparison is made between the area averages of latent heat flux and winter seasonal anomaly maps of precipitation over the western United States (not shown), it shows that positive or above-normal area average latent heat flux corresponds to above-normal precipitation values and vice versa. It appears that the eastern North Pacific Ocean acts as an important source of heat and moisture for the storm systems that pass over it and eventually influences precipitation amounts in the western United States.

Figures

1. Seasonal mean 700 mb. height and anomaly values for winter 1968-69.

2. Seasonal mean 700 mb. height and anomaly values for winter 1976-77.

3. Anomalies or departures from the long-term mean (1950-79) of latent heat flux between the central and eastern North Pacific Ocean and overlying atmosphere for the fall of 1968 and winter of 1968-69.

4. Same as in Fig. 3 but for the fall of 1976 and winter of 1976-77.

5. Area averages of latent heat flux anomalies computed over the regions outlined in Figs. 1-4 for the fall and winter seasons of 1968 through 1978-79.

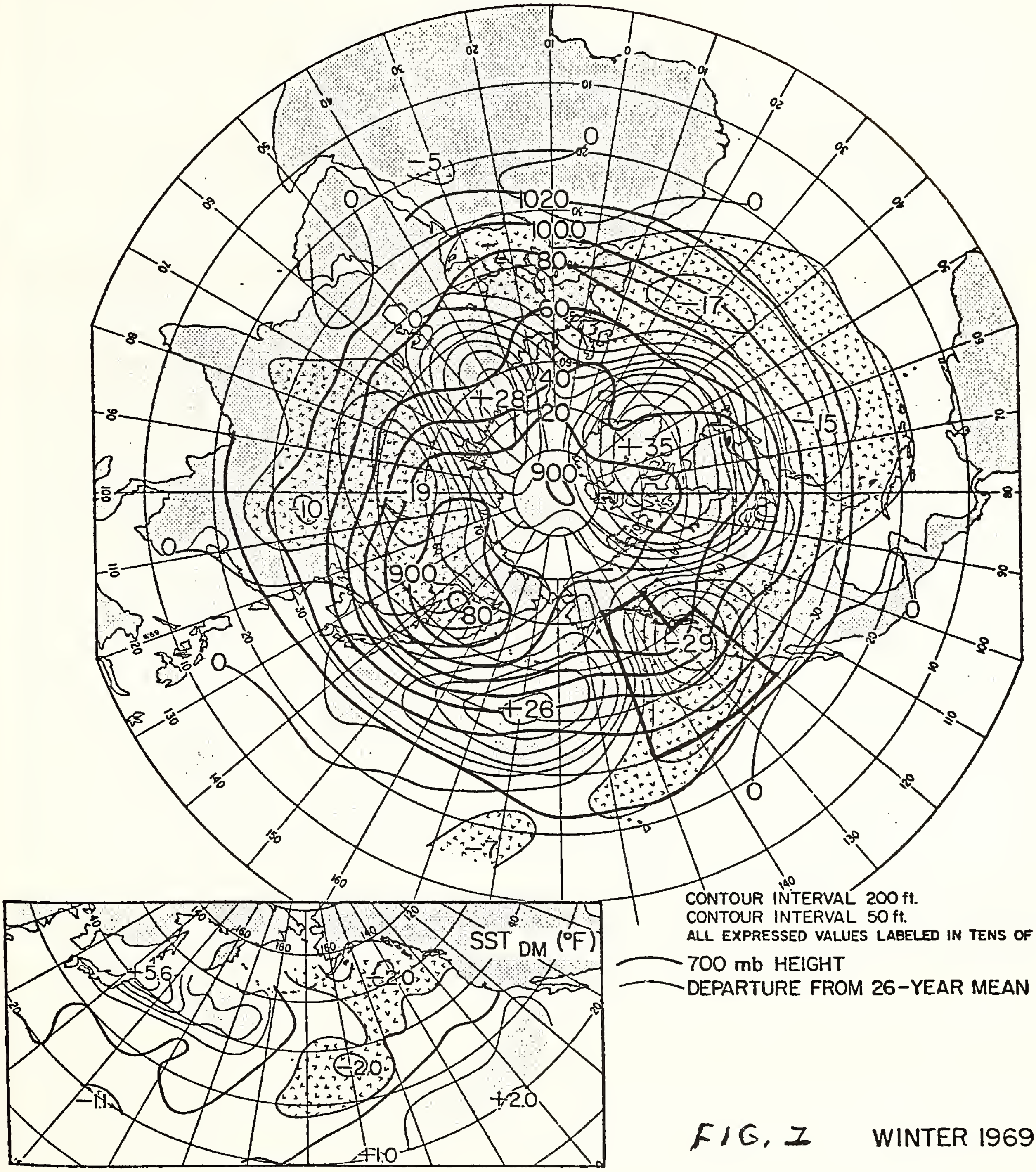

CONTOUR INTERVAL 200 ft.
CONTOUR INTERVAL 50 ft.
ALL EXPRESSED VALUES LABELED IN TENS OF FEFT
——— 700 mb HEIGHT
——— DEPARTURE FROM 26-YEAR MEAN

FIG. 2 WINTER 1969

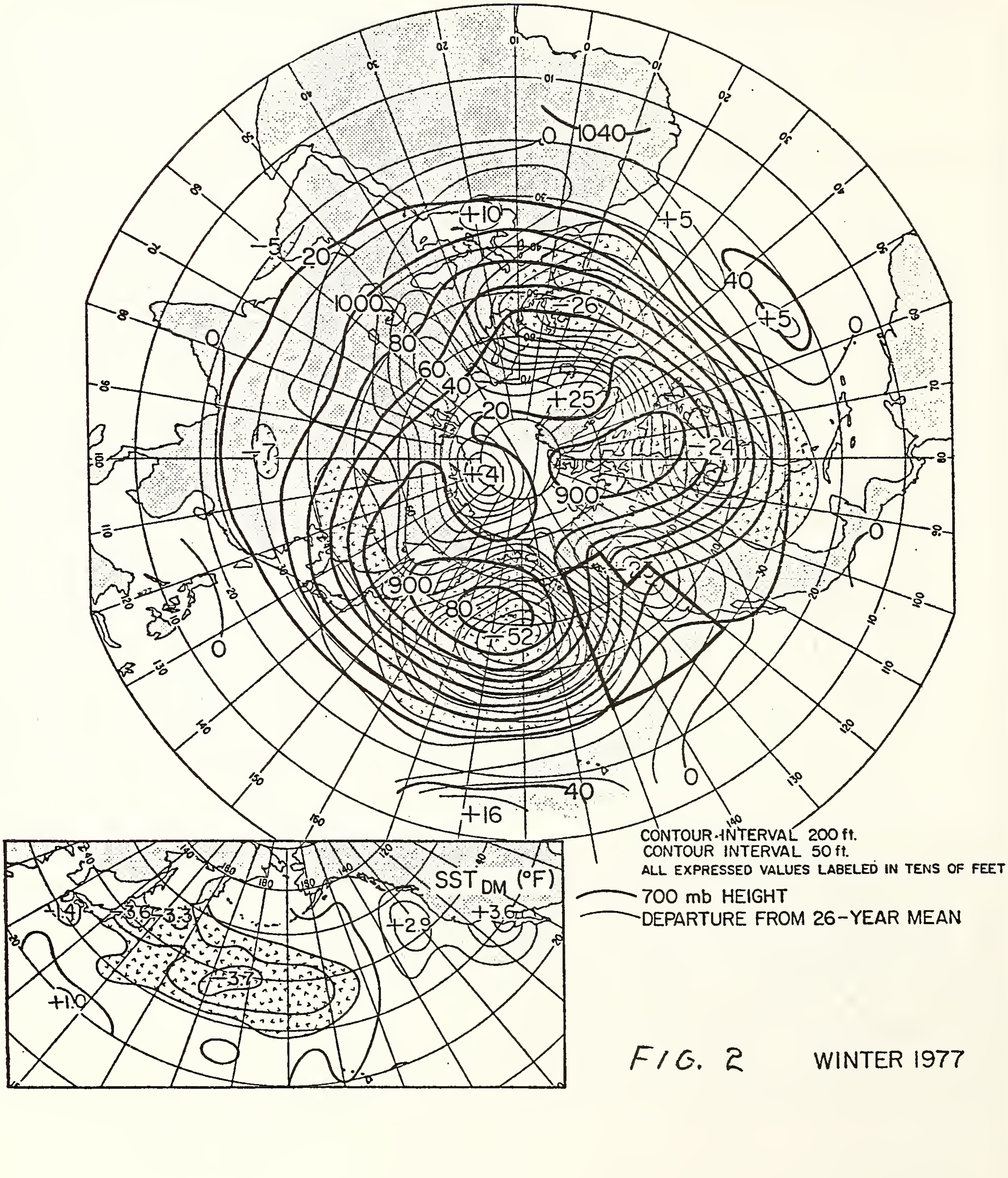

FIG. 2 WINTER 1977

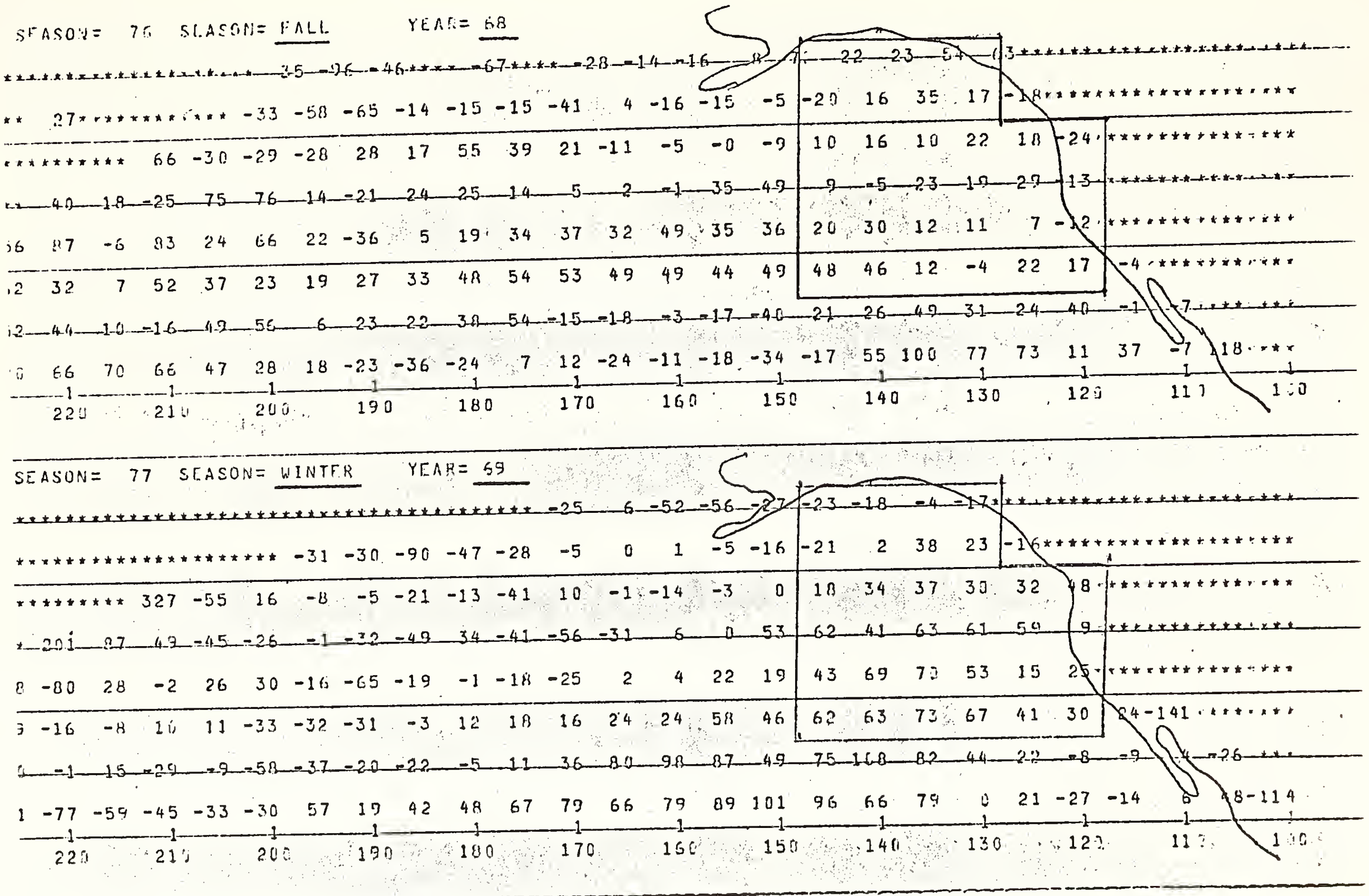

Fig. 3. Anomalies or departures from the long-term mean (1950-79) of latent heat flux between the central and eastern North Pacific Ocean and overlying atmosphere for the fall of 1968 and winter of1968-69.

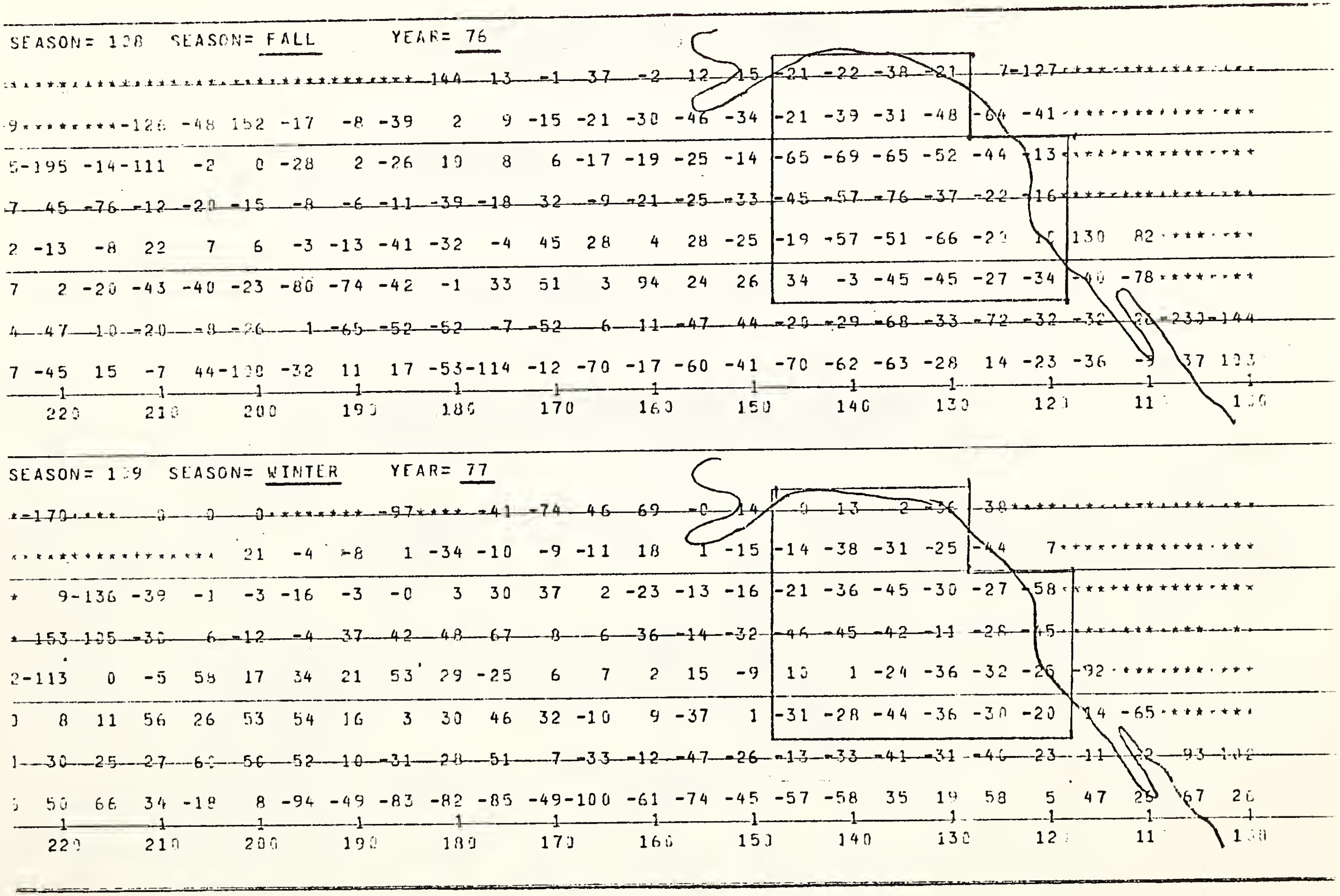

Fig. 4. Same as in Fig. 3 but for the fall of 1976 and winter of 1976-77.

AREA AVERAGE OF

LATENT HEAT ANOMALIES

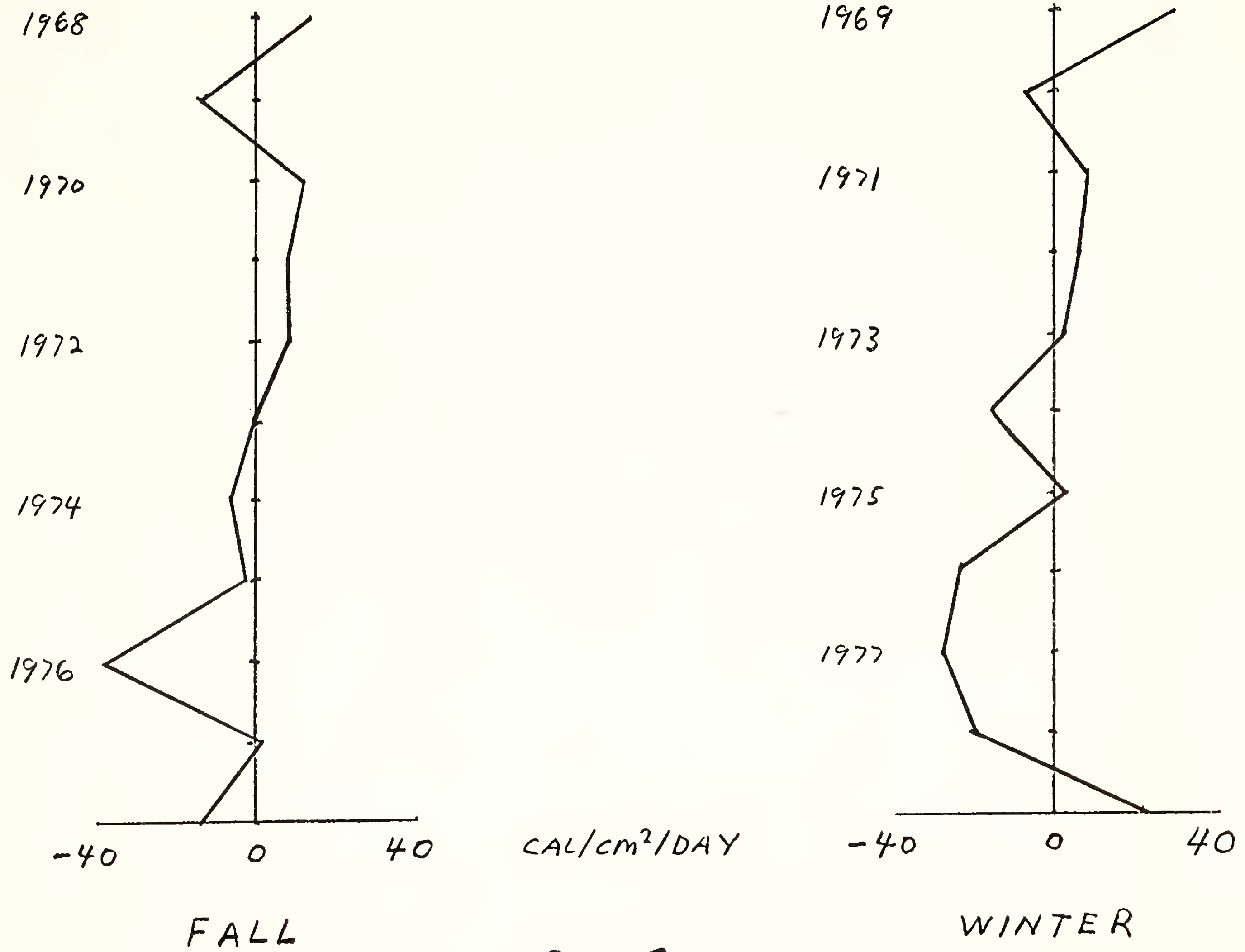

FIG. 5

On the Influence of Pacific Ocean Temperatures on Atmospheric Carbon Dioxide Concentration at Ocean Weather Station P

by

Kirby J. Hanson, James T. Peterson,
Geophysical Monitoring for Climatic Change
Environmental Research Laboratories, NOAA,
Boulder, Colorado 80303

Jerome Namias, Robert Born,
Scripps Institution of Oceanography,
University of California-San Diego,
LaJolla, California, 92093

C. S. Wong
Marine Carbon Research Center,
Institute of Ocean Sciences,
Dept. of Fisheries and Oceans,
P. O. Box 6000,
Sidney, B. C., Canada, V8L 4B2

The study presents an analysis of atmospheric CO_2 measurements at Ocean Weather Station P (50° N, 145° W) and sea surface temperatures over the North Pacific for the period 1974-1978. The results show that during 1976 and 1977 sea surface temperatures over the Northwest Pacific were significantly below normal and, coincidentally, atmospheric CO_2 levels at Station P were also lower than expected. This indirect evidence does not prove but suggests that the Northwest Pacific (40°-50°N) may have been a major sink for atmospheric CO_2 during 1976 and 1977 when sea surface tempratures over large areas of the Northwest Pacific were much below normal. However, a specific mechanism for this sink is not established. Direct observations of pertinent parameters obtained at appropriate times could establish the significance of the North Pacific as a sink for atmospheric CO_2 and lead to studies of the mechanism for such a sink.

Atmospheric CO_2 data from flask samples taken at Station P and analyzed at the Canadian Marine Carbon Research Center were used for this study. A time series plot of the Station P data (Fig. 1) for the individual days on which air flask samples were obtained shows the general features that are now well-known for a Northern Hemisphere ocean location: an intra-annual variation (at Station P about 15-18 ppm) with minimum in August-September, and a long term increase (for 1974-78) near 0.75 ppm/year). However, it is also evident that in a secular sense the CO_2 concentration does not follow a monotonic increase as would be expected if only CO_2 from fossil fuel sources were affecting the nonseasonal, long-term increase of atmospheric CO_2. During 1976 and early 1977, for example (Fig. 1), CO_2 concentrations are lower than for the same months in 1975.

North Pacific sea surface temperatures used in this study were provided by the Climate Research Group of Scripps Institution of Oceanography for a 5° x 5° latitude-longitude grid from 20° to 60° N and 130° E to 110° W in the form of monthly average departures from normal (DN). The normal was based on the period 1947-1979. The distribution over the North Pacific of the average temperature anomaly for the period 1974-78, Figure 2 (upper), shows a strong negative temperature departure in the central Pacific from 35-40° N centered near 180° longitude.

The standard deviation about the 5-year average computed from the monthly temperature DNs during the 1974-78 period, Fig. 2 (lower), shows that the variability during this period was highest on the north and northwest sides of the negative temperature DN and extended from northern Japan eastward across two-thirds of the Pacific between 40° and 45° N. This area of maximum variability includes the boundary between the warm Kuroshio current and the cold Oyashio current. The abnormally cold water over much of the North Pacific was produced largely by frequent strong cyclonic activity in and near the Aleutian Islands, which in turn led to strong winds and large heat extraction from the sea.

To study the relationship between Pacific sea surface temperature (SST) anomalies and CO_2 anomalies we have correlated, for each Pacific grid point, the monthly SST anomalies with the monthly CO_2 anomalies at Station P for the period 1974 through 1978. As indicated in Figure 3, the distribution of correlation maximum in the North Pacific is quite similar in pattern to that of the maximum variability of SST (lower Fig. 2) but is displaced about 5° farther north (45° - 50° N.) This correlation maximum has extensive east-west elongation but with highest values near 180° longitude. This extensive region is the so-called West Wind Drift region which places the entire area of high correlation upwind of Station P.

An area of secondary maximum in correlation is centered at 22.5° N and 165° W. The question of whether CO_2 anomalies detected at Station P originate in this area of secondary maximum is still open, but it is less likely to be a source region for CO_2 anomalies observed at Station P because of air trajectory considerations, alone.

In order to look at the question of how the correlation pattern may have varied from year to year, the secular variations of Station P CO_2 anomalies and SST anomalies at 45° N, 180° W are indicated in Figure 4. Clearly a large part of the high correlation comes from the coincidence of negative CO_2 anomalies and negative SST DNs during 1976 and the first half of 1977. There is no improvement in this correlation by lagging either data set.

The mean annual SST DNs year by year for 1975 through 1978 (Fig. 5) show that negative temperature anomalies were both geographically extensive and most intense in the North Pacific in 1976 and 1977. The SST DN pattern for the year 1976 is quite similar to the correlation based on 5 years of data (Fig. 3) which, again, suggests the importance of SST anomalies that year to the CO_2 anomalies at Station P.

Comparison of the annual correlation patterns of SST DNs vs. CO_2 DN in Figure 6 with the SST DNs in Figure 5 suggests there is a reasonably good correspondence between them. For example, the most geographically extensive and highest correlations were in 1976 and 1977, as were the SST DNs.

Some previous investigators have obtained correlations between time derivations of CO_2 and meteorological or oceanographical parameters. We have calculated time derivatives of the Station P CO_2 and SST using the month-to-month change as a basis for the derivative. Shown in Figure 7 are the values and positions of centers of correlation maximum for both time derivatives and for DNs. The latter are those indicated in Figure 6. Clearly the centers for both correlation methods are nearly collocated each year and are generally situated in the Northwest Pacific. It is also evident that correlations are slightly higher using the DN method than using the derivatives method, as indicated by the maximum correlation values in Figure 7.

We have also obtained an EOF analysis for (nonseasonal) SST DNs over the Pacific from 25°-55°N. As indicated in Table 1, analyses were obtained for the 5-year period 1974-1978 and for the 2-year period 1976-1977. The nonseasonal EOF component 1 for the 2-year period explained 31 percent of the variance. Its pattern (not shown) places highest values(> 0.2) at 45° N and 160°-170°E, a pattern quite similar to that for correlations of CO_2 anomalies and SST DNs for the years 1976 and 1977.

As with so many studies of natural phenomena, it is not possible to prove that the Northwest Pacific is the location of the cause of the CO_2 anomalies at Station P, because many things in nature are correlated without a cause-effect relationship. Yet the present study does delineate the area 40°-45°N and 160°-180° of the Northwest Pacific as having been a major sink for atmospheric CO_2 during 1976 and 1977. There are a number of possible mechanisms for such a sink, for example increased fixation of carbon by plants, temperature changes in the mixed layer, or combinations of these and other mechanisms.

The possible role of this area of the Pacific in modulating the global carbon cycle has not been evaluated. Through subsequent studies it may be possible to do this evaluation by examining atmospheric CO_2 data from other global-dispersed locations.

The present study suggests it may be useful to obtain direct sampling of atmospheric CO_2, pCO_2 in the ocean, primary productivity, and other parameters in this area of the Pacific, particularly during those periods in which SST DNs are negative. This would help to establish whether or not this area is at times a principal sink for atmospheric CO_2 as well as to establish the specific mechanism for that sink.

FIGURE LEGENDS

Figure 1. Atmospheric CO_2 concentration at Ocean Weather Station P for individual days on which air flask samples were obtained.

Figure 2. (Upper) sea surface temperature (SST) departure from normal (DN) in °F, and (lower) standard deviation of monthly SST DN in °F for the 1974-78 period.

Figure 3. Correlation of Station P CO_2 anomalies with SST DNs for the 1974-78 period.

Figure 4. CO_2 anomalies at Station P and SST DNs at 45° N, 180° W.

Figure 5. Mean annual SST DNs year by year for the period 1974-78. Shading indicates SST DNs colder than -1.5° F.

Figure 6. Correlations of Station P CO_2 DNs with SST DNs year by year for the period 1974-78. Shading indicates correlations greater than 0.6.

Figure 7. Correlation values and position of centers of maximum correlation for individual years 1974-78. Correlation by two methods are presented: CO_2 DN vs. SST DN; and CO_2 derivative and SST derivative.

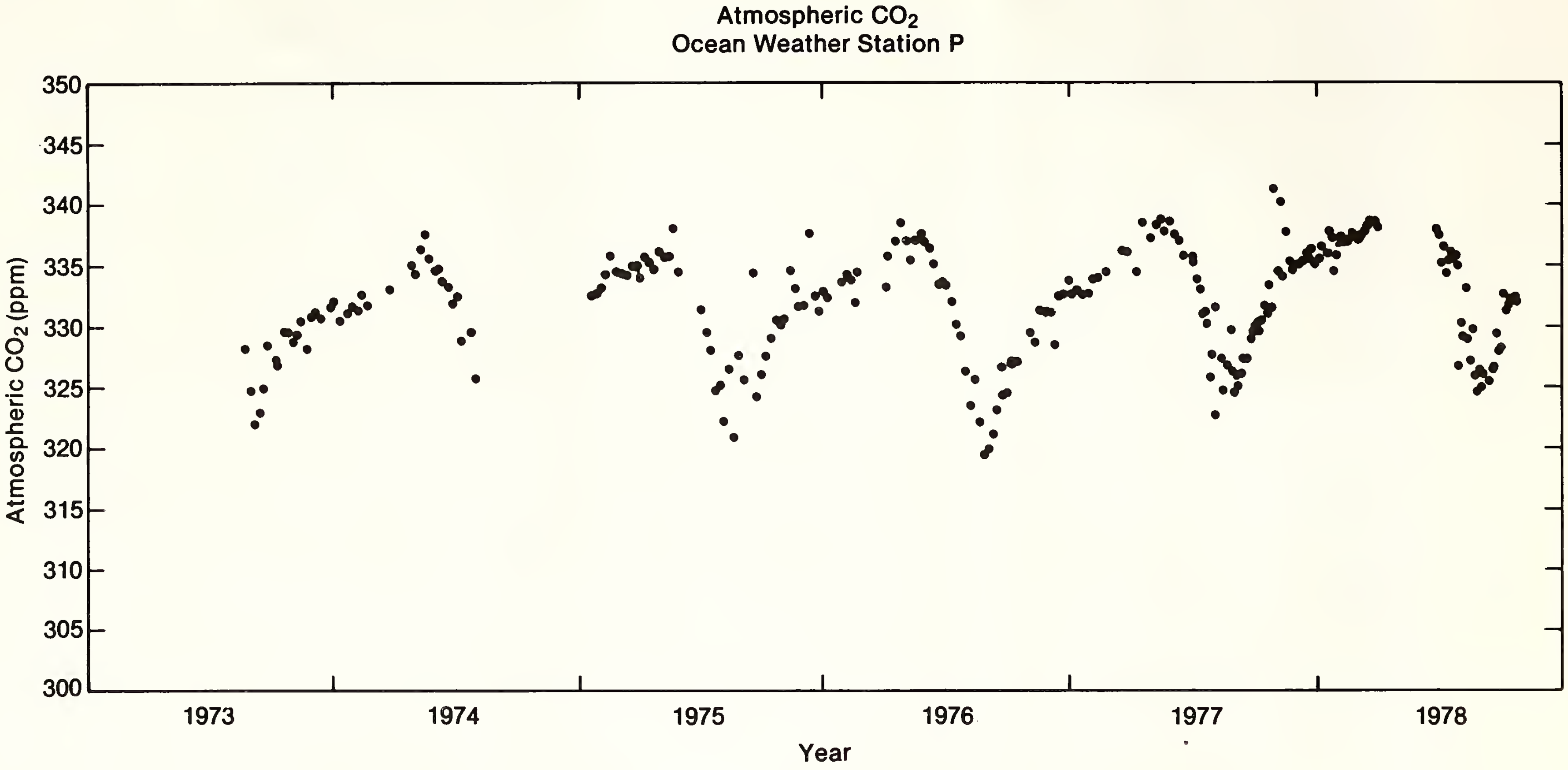
Atmospheric CO$_2$
Ocean Weather Station P

FIGURE 1

Temperature Departure from Normal (1974-78)
(°F)

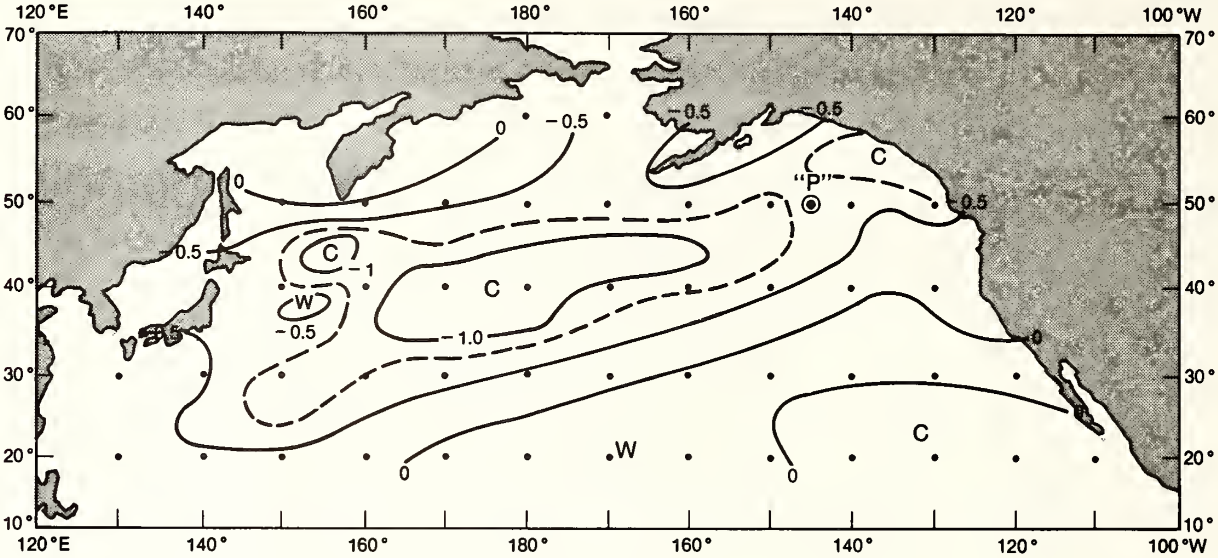

FIGURE 2(a)

Standard Deviation of SST D.N. (1974-78)
(°F)

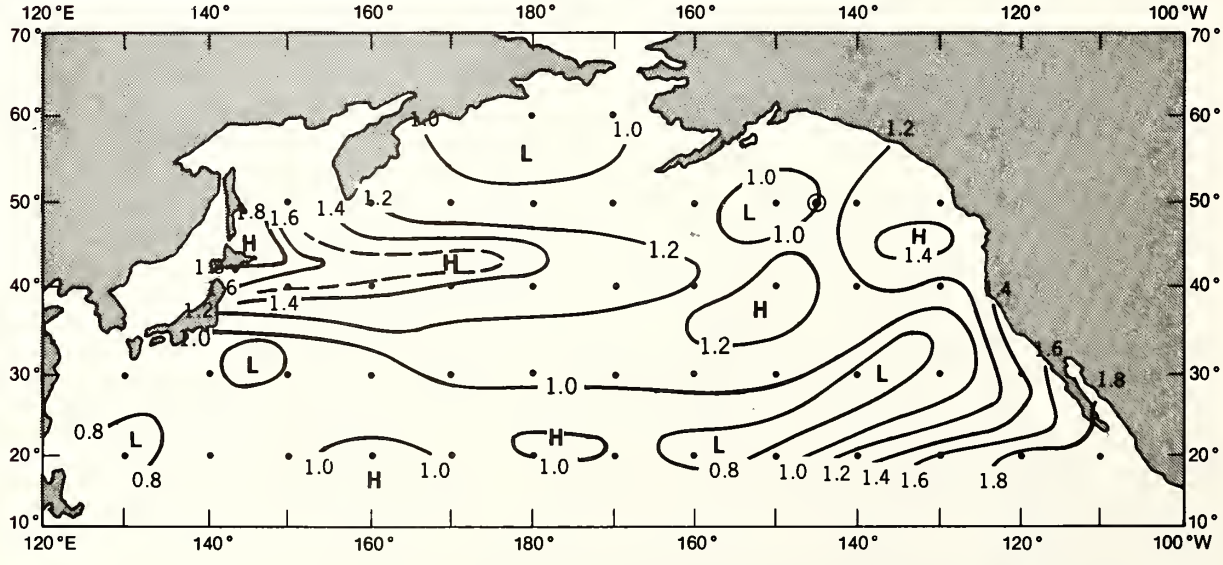

FIGURE 2(b)

Correlation: Station "P" CO_2 vs. Temperature D.N. (1974-78)

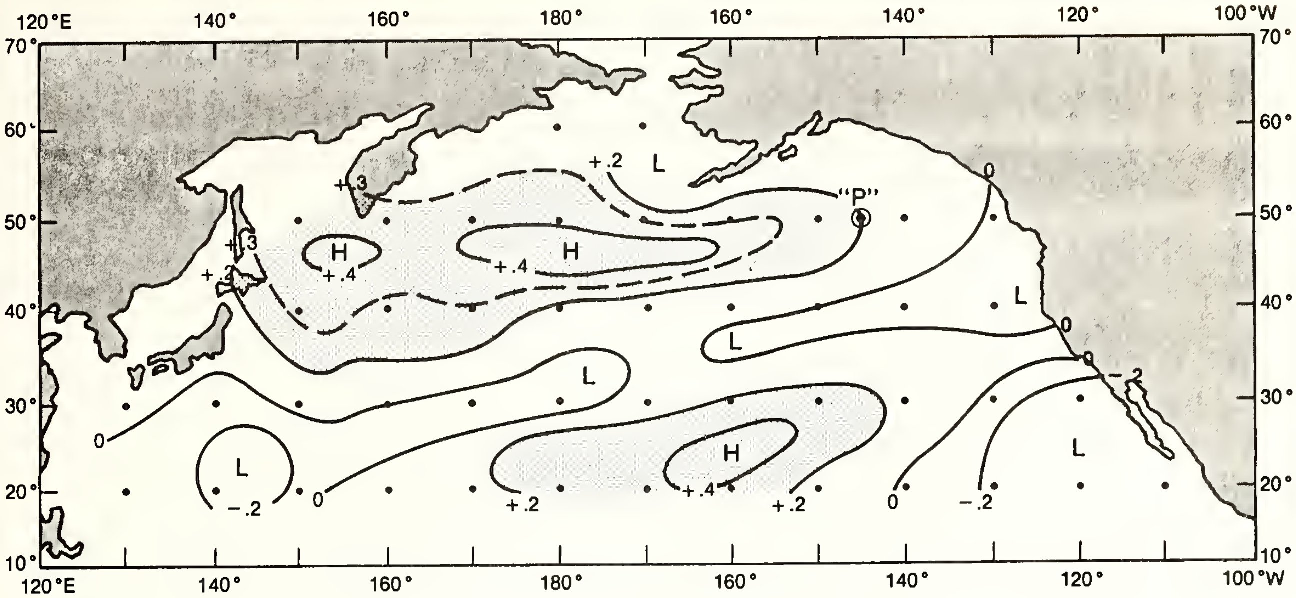

FIGURE 3

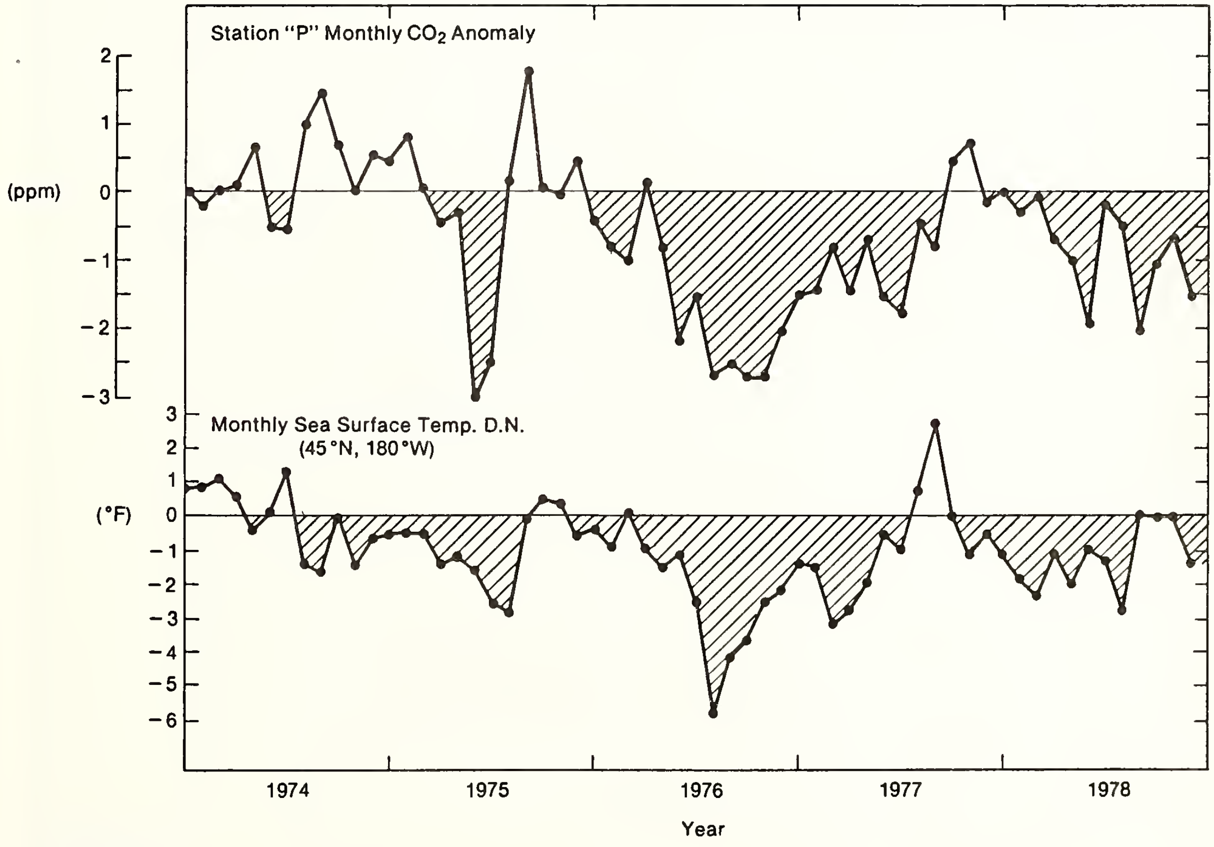
Station "P" Monthly CO_2 Anomaly

Monthly Sea Surface Temp. D.N. (45°N, 180°W)

FIGURE 4

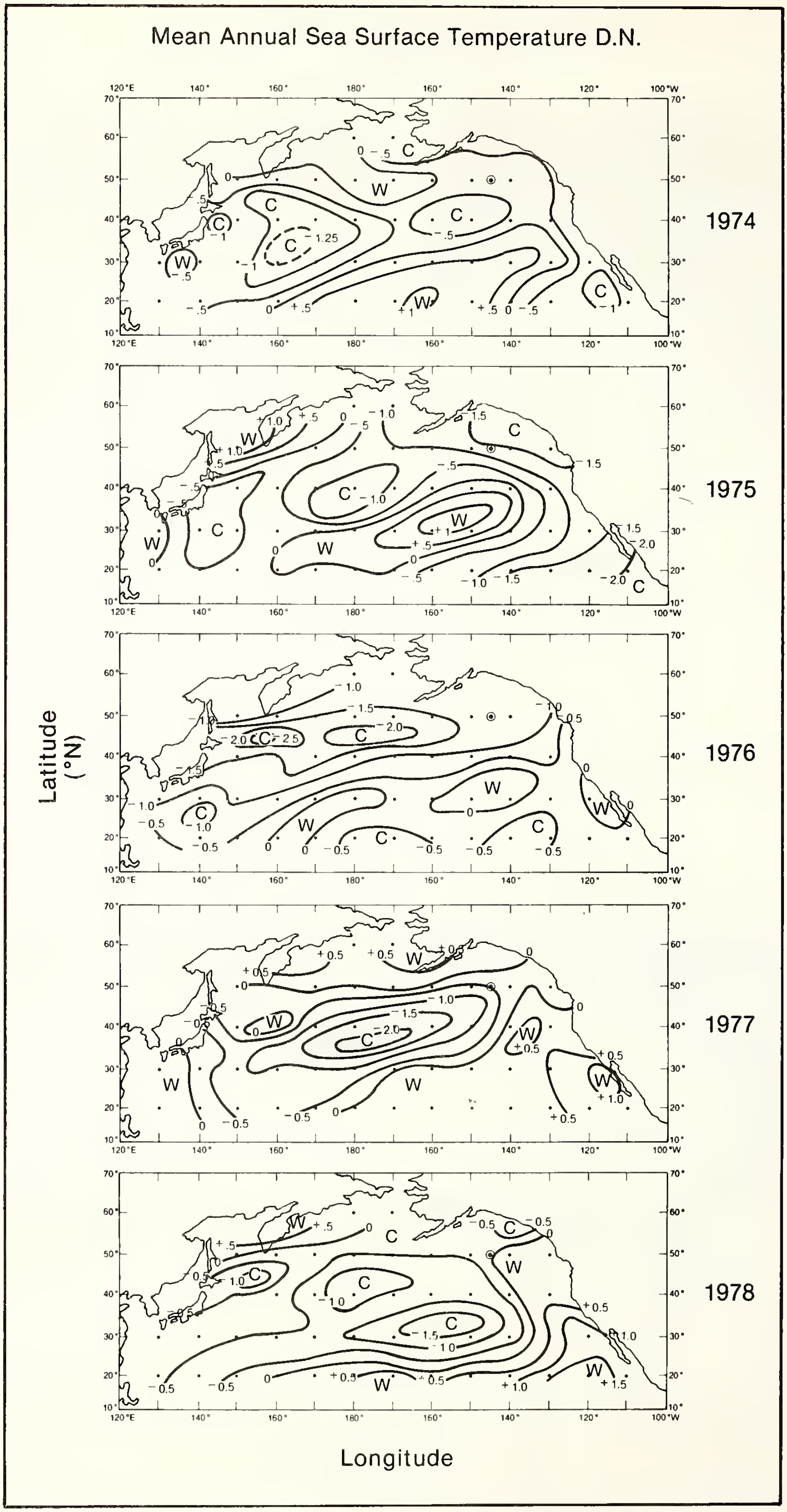
Mean Annual Sea Surface Temperature D.N.

FIGURE 5

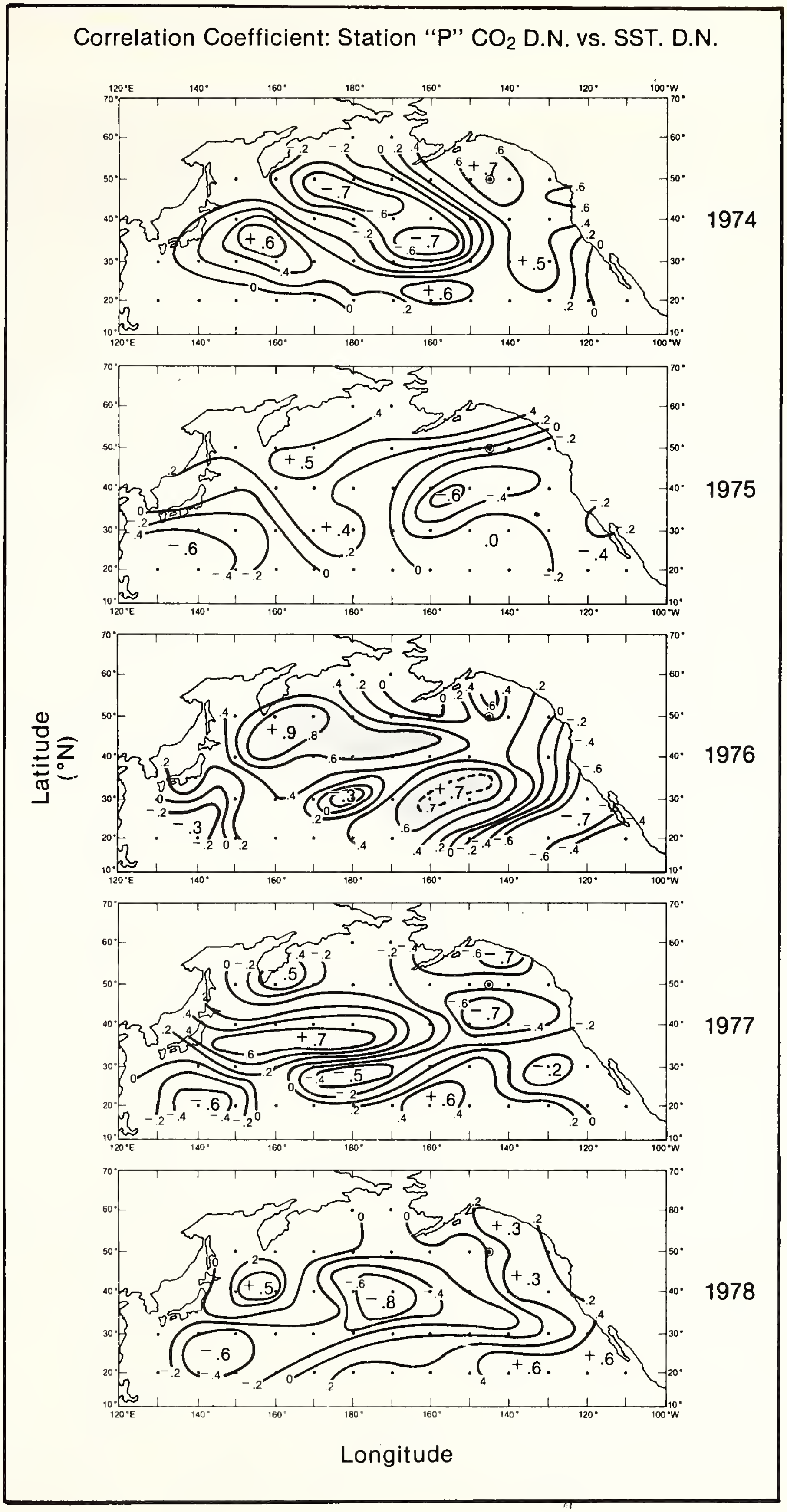

Correlation Coefficient: Station "P" CO_2 D.N. vs. SST. D.N.

FIGURE 6

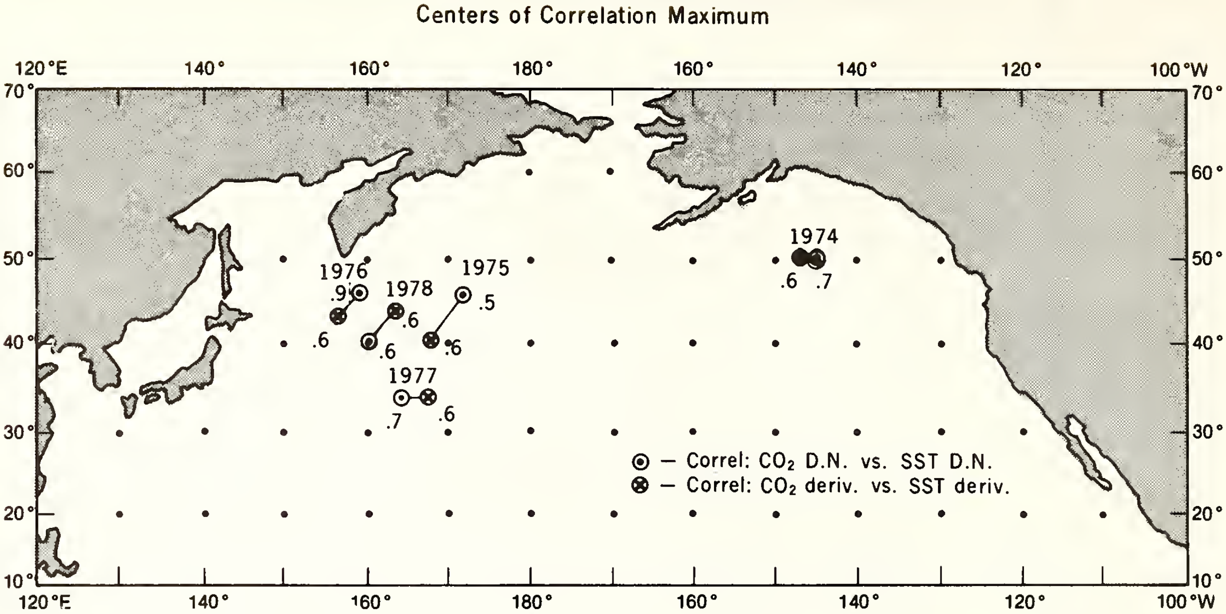
Centers of Correlation Maximum

FIGURE 7

TABLE 1

EOF analysis for the Pacific Ocean area from 25-55°N, and longitudes from Japan to the West Coast of North America.

Period of Data	Component	Percent of Variation (%)
1974-78	1	22.9
	2	15.4
	3	10.3
	4	6.4
	5	5.8
	6	3.8
	7-12	15.6
	(total)	80.2
1976-77	1	31.0
	2	19.3
	3	9.5
	4	6.5
	5	5.1
	6	4.5
	7-12	7.2
	(total)	82.6

Diagnostic equations in pressure coordinates including the effects of variable surface pressure

G.J. Boer
Numerical Studies Division
Canadian Climate Centre

There are two main results of this study. The first is a reformulation of the atmospheric equations of motion in pressure coordinates which makes use of the properties of the Heaviside unit and Dirac delta functions. This formalism is useful in obtaining derived equations such as the energy equations since boundary terms are automatically handled and use of Leibnitz rule is avoided. The second result stems from the use of this formalism in typical general circulation diagnostic calculations. Ambiguities in the treatment of diagnostic terms evaluated on pressure surfaces pierced by topography are removed. Moreover certain boundary related terms arise naturally in the derivation of the diagnostic equations which have apparently been neglected heretofore.

The simplicity of the equations of motion in pressure coordinates is not so obvious when the lower boundary condition is taken into account. For diagnostic calculations the fact that integration and averaging cannot be interchanged,

$$\overline{\int_0^{p_s} X\,dp} \neq \int_0^{p_s} \overline{X}\,dp$$

also leads to difficulties and ambiguities when calculating diagnostic terms. This may be avoided by rewriting the equations in the form

$$\frac{d\beta\mathbb{V}}{dt} + f\vec{k}\times\mathbb{V} + \beta\nabla\phi = \beta\mathbb{F}$$

$$C_p\frac{d\beta T}{dt} = \beta\omega\alpha + \beta Q$$

$$\frac{\partial\beta}{\partial t} + \nabla\cdot\beta\mathbb{V} + \frac{\partial}{\partial p}\beta\omega = 0$$

$$\frac{\partial}{\partial p}\beta(\phi-\phi_s) = -\beta\alpha$$

$$\frac{d\beta q}{dt} = \beta S$$

where $\beta(\lambda,\varphi,p,t) = \beta(p_s-p) = \begin{cases} 1, & p \leq p_s \\ 0, & p > p_s \end{cases}$ is the Heaviside unit function which, in these equations, carries the information as to whether the point in question is above the topography. The Dirac delta function is the derivative of the unit function and it follows that

$$\frac{\partial\beta}{\partial p} = -\delta(p_s-p)$$

$$\frac{\partial\beta}{\partial t} = \frac{d\beta}{d(p_s-p)}\,\frac{\partial(p_s-p)}{\partial t} = \delta\frac{\partial p_s}{\partial t}$$

and similarly for λ, φ.

The equations may be taken to apply to the domain $0 \le p \le p_s$ where p_0 is a constant always greater than p_s. The bottom boundary condition becomes

$$\beta = 0 \quad \text{at} \quad p = p_0$$

This form of the equations of motion is useful in obtaining various derived equations since boundary terms are handled automatically. The simplest example is the derivation of the surface pressure equation from the continuity equation. Using $\partial\beta/\partial t = \delta\, \partial p_s/\partial t$ and integrating gives directly that

$$\frac{\partial p_s}{\partial t} + \nabla \cdot \int_0^{p_0} \beta \mathbb{V}\, dp = 0$$

or

$$\frac{\partial p_s}{\partial t} + \nabla \cdot \int_0^{p_s} \mathbb{V}\, dp = 0$$

since $\int_0^{p_0} \beta X dp = \int_0^{p_s} X\, dp$ Other derived equations can be similarly obtained.

The formalism allows an unambigious development of the diagnostic equations and of the usual diagnostic statistics which accounts for the presence of topography through the β term. As an example, the basic statistics of the temperature field may be considered. Global data from the NMC analysis for January 1979 are used. This data is available on standard pressure surfaces with "estimated" values given below the topography. Mean and variance terms under time and zonal averaging, for example, are often obtained as

$$T = [\bar{T}] + \bar{T}^* + T'$$
$$[\overline{T^2}] = [\bar{T}]^2 + [\overline{T}^{*2}] + [\overline{T'^2}]$$

where the decomposition is into mean, standing eddy and transient eddy components. The zonal mean temperature $[\bar{T}]$ and the standing eddy term $[\bar{T}^{*2}]$ which are obtained in this way, taking the data as given, are shown in Figure 1. These statistics have, however, treated "subterrainian" values as if they were real. The mean and variance terms that arise from manipulation and averaging of the reformulated equations are of the form $[\overline{\beta T}]$ and $[\overline{\beta T^2}]$. The decomposition is somewhat different in this case,

$$T = [\bar{T}]_R + \bar{T}^* + T'$$
$$[\overline{\beta T^2}] = [\bar{\beta}][\bar{T}]_R^2 + [\bar{\beta}\bar{T}^{*2}] + [\overline{\beta T'^2}]$$

where

$$\bar{T}^R = \overline{\beta T}/\bar{\beta},\ \beta \neq 0 \qquad ,\ T' = T - \bar{T}^R$$
$$[\bar{T}]_R = [\overline{\beta T}]/[\bar{\beta}],\ [\bar{\beta}] \neq 0 \qquad ,\ T^* = \bar{T}^R - [\bar{T}]_R$$

$\bar{T}^R$ and $[\bar{T}]_R$ are the so called "representative" values, i.e. values based only on data above the topography.

The values of $[\bar{\beta}]$, $[\overline{\beta T}] = [\bar{\beta}][\bar{T}]_R$ and $[\bar{\beta}\bar{T}^{*2}]$ are displayed in Figure 2. $[\bar{\beta}]$ represents the percentage of points around the latitude circle which are above the topography. $[\overline{\beta T}]$ is the appropriate mean temperature for use in diagnostic calculations. If temperature is taken to represent the internal energy density of the fluid for instance then $[\overline{pT}]$ is the proper contribution to the net energy. It contains no contributions from subterrainian points. This field is quite different from that of $[\overline{\overline{T}}]$ which is obtained by taking the NMC data at face value and which includes a contribution from non-existent subterrainian air. The representative temperature $[\overline{\overline{T}}]_R$ (not shown) is similar to $[\overline{\overline{T}}]$ as it represents average (real) air temperatures where they exist around the latitude circle. At lower levels the effect of topography is to confine the air to regions over the relatively warm oceans (in January) so that $[\overline{\overline{T}}]_R$ is typically warmer than $[\overline{\overline{T}}]$. Similar kinds of remarks apply to the standing eddy variance terms $[\bar{p}\overline{\overline{T}}^{*2}]$ and $[\overline{\overline{T}}^{*2}]$

It is apparent that topography should not be neglected in the calculation of typical diagnostic quantities. There are two other aspects of the problem which cannot be discussed here. The first is the possibility of obtaining useful approximate formulae by making consistent approximations based on the exact formulae. The second arises in the derivation of diagnostic equations such as those for kinetic and available potential energy. As has been mentioned, the derivation of these formulae based on the formalism outlined above gives rise to boundary terms which are apparently not considered in the usual diagnostic formulae. These terms may be important both for physical understanding of the processes of the general circulation and for correct budget calculations.

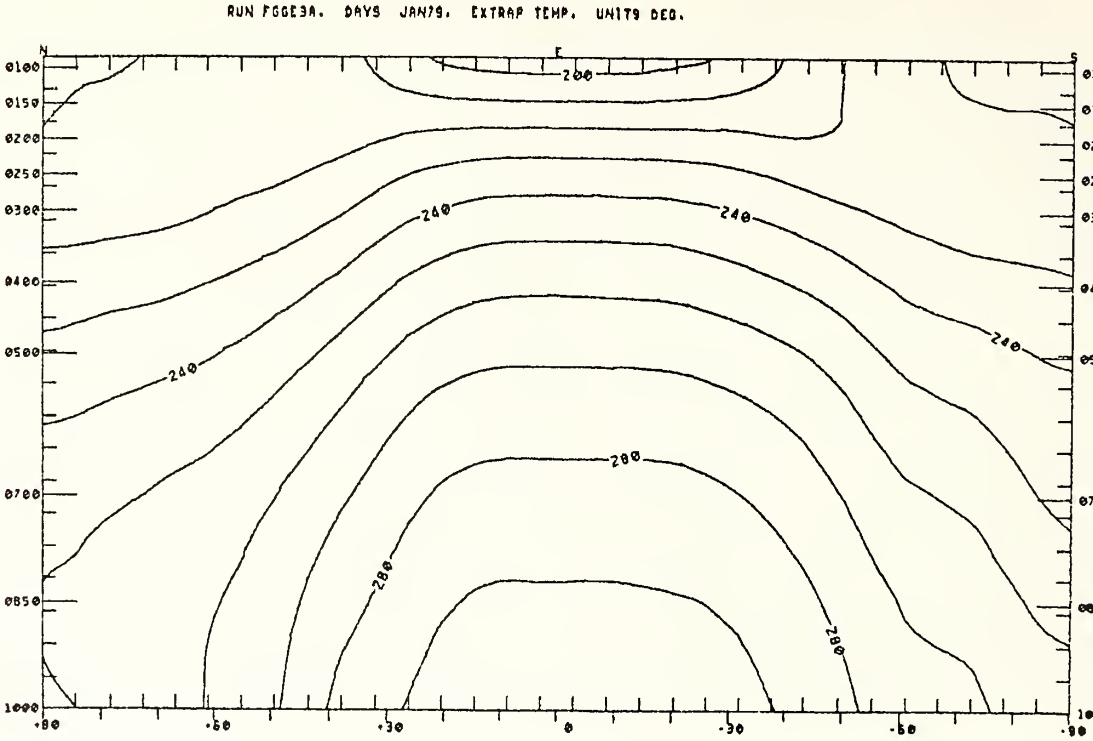

Fig. 1a. $[\overline{T}]$. Zonally and time averaged temperature using the data as given. Units: $^{\circ}$K.

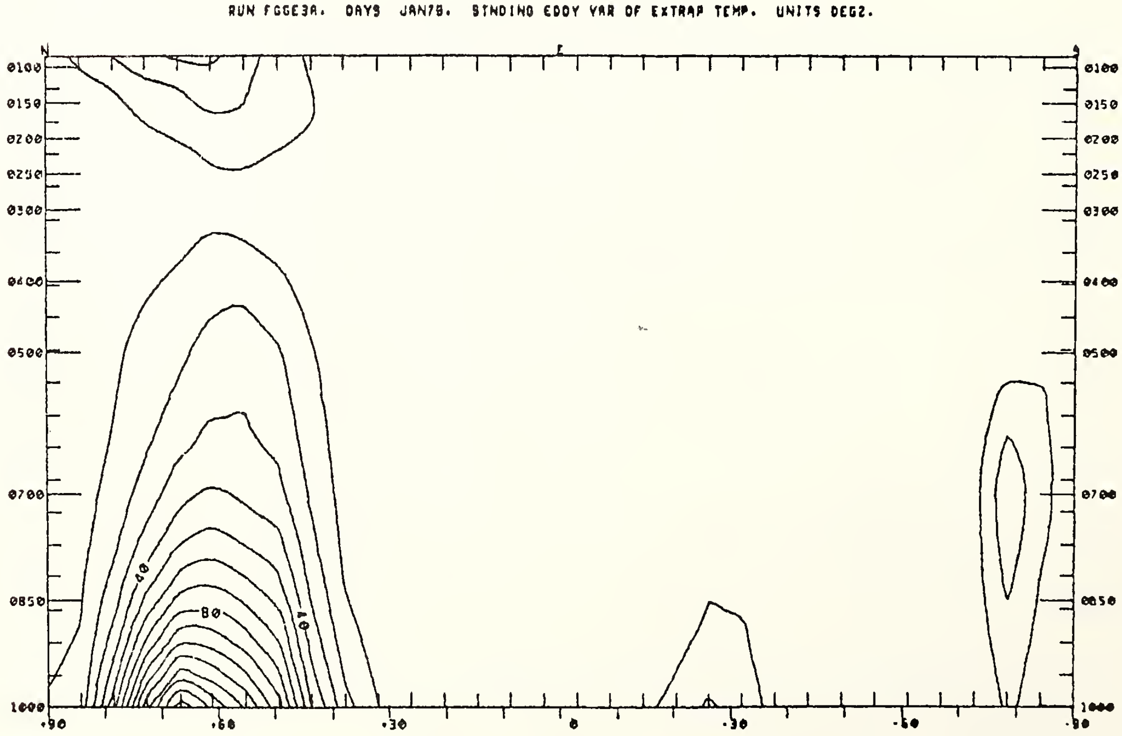

Fig. 1b. $[\overline{T}^{*2}]$. Standing eddy variance of temperature using the data as given. Units = $(^{\circ}C)^2$.

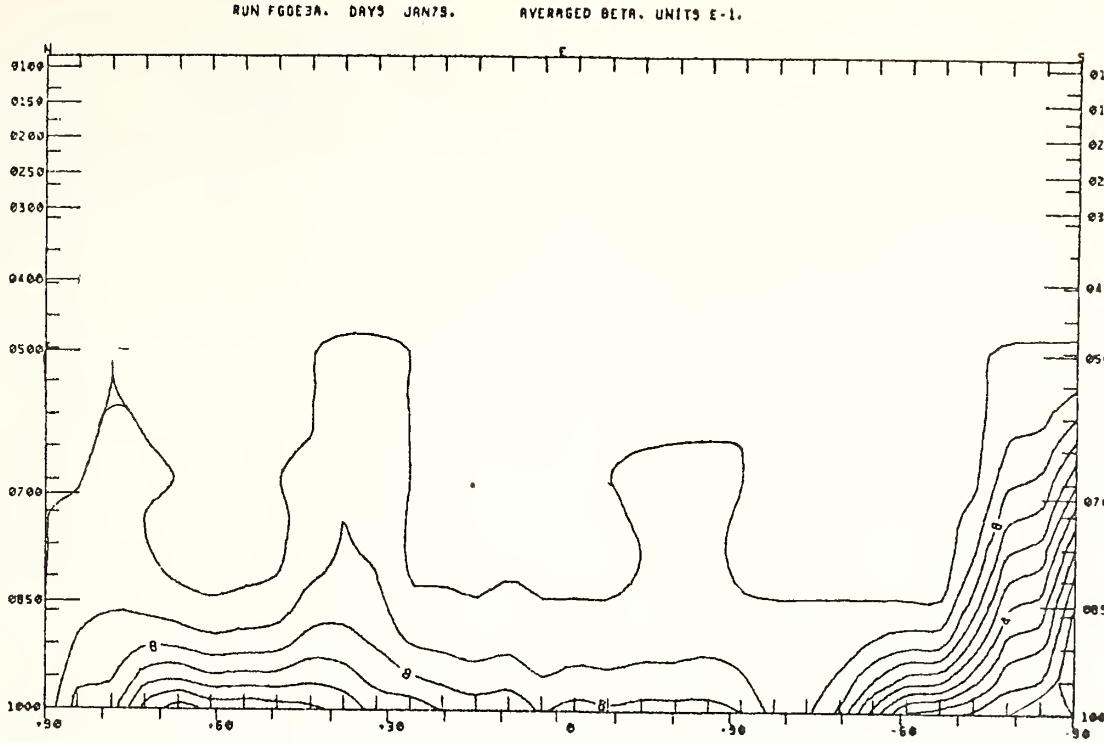

Fig. 2a. $[\overline{\beta}]$. A measure of the fraction of gridpoints above the topography under time and zonal averaging. Units: 10^{-1}.

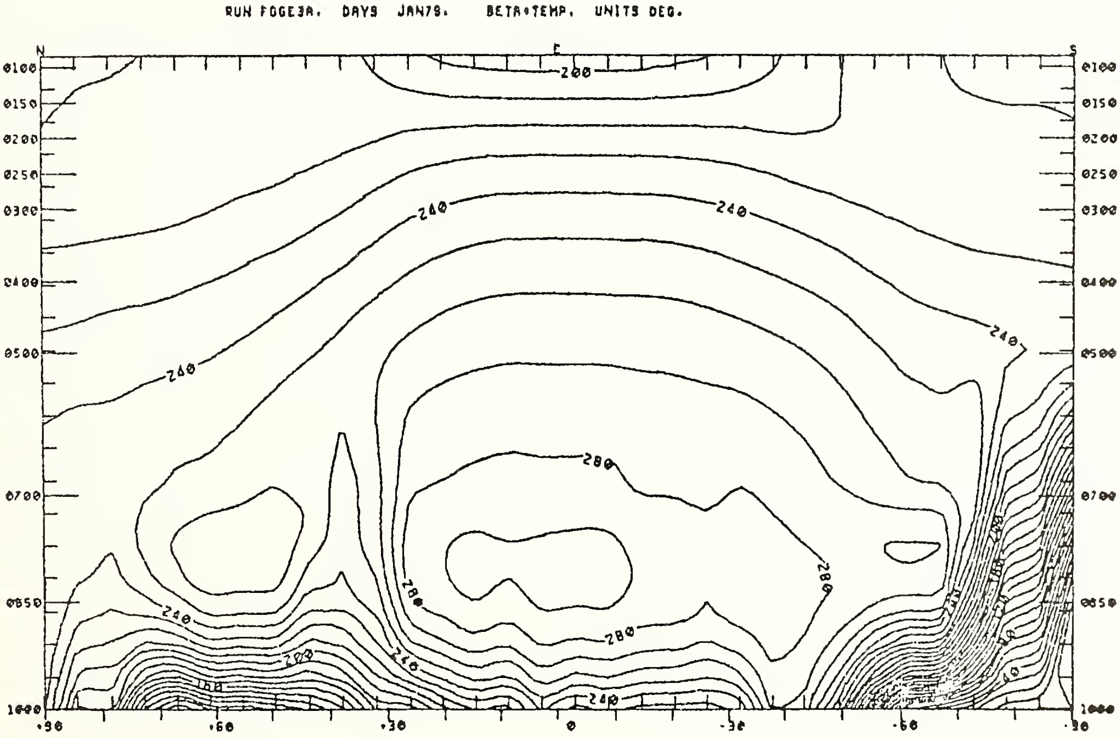

Fig. 2b. $[\overline{\beta T}]$. Zonally and time averaged temperature with subterrainian values set to zero. This is the proper contribution to an integral. Alternatively it may be interpreted as the averaged energy density of the fluid as measured by temperature. Units: °K.

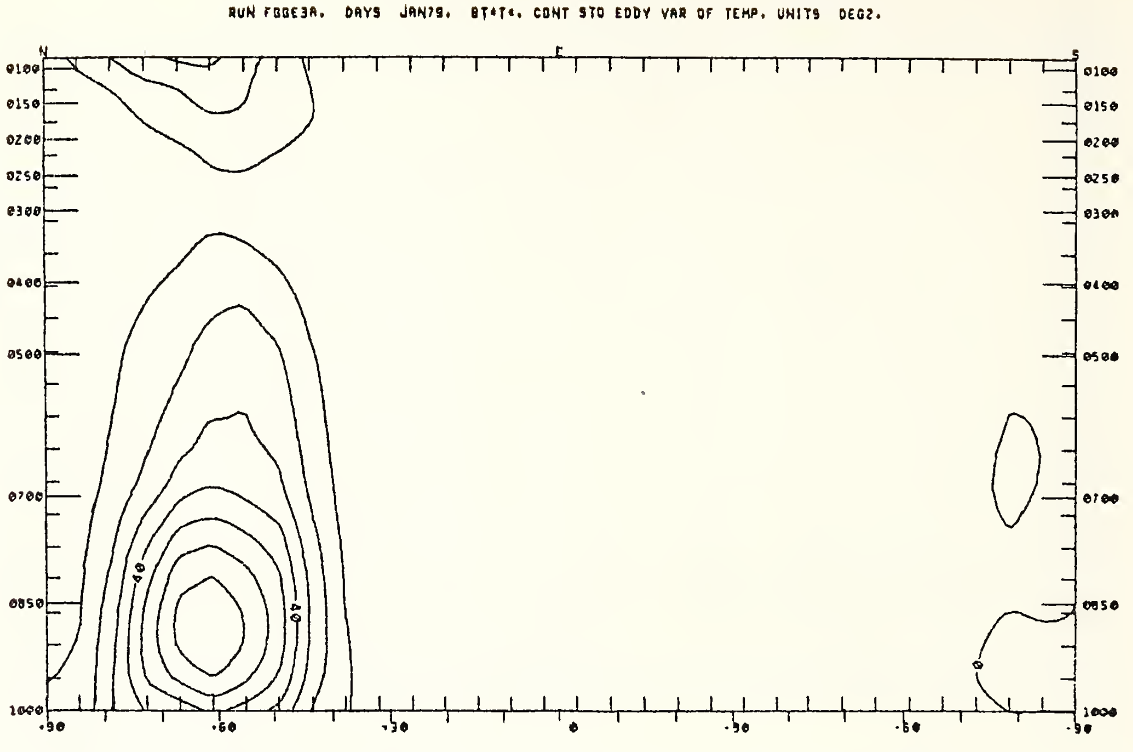

Fig. 2c. $[\overline{\beta}\overline{T}^{*2}]$. Standing eddy variance of temperature without contribution from subterrainian values. This is the proper contribution to an integral or the integrand of available potential energy. Units: $(^{\circ}C)^2$.

Seasonal simulation experiments with a low-order general circulation model

Bette L. Otto-Bliesner and David D. Houghton
Department of Meteorology
University of Wisconsin
Madison, Wisconsin 53706

The purpose of this study is to gain a better understanding of the dynamics of seasonal change through analysis of long-term integrations of a low-order general circulation model. The numerical model used is a global, spectral, primitive equation model with five equally spaced sigma levels in the vertical and triangular truncation at wavenumber 10 in the horizontal. Included in the model are: orography; simplified parameterizations of radiation, convection, condensation, diffusion, and surface transports; and, a surface heat budget over land areas.

The external seasonal forcing of the model is composed of smooth time-varying functions for the latitude of snowcover, solar radiation, and sea-surface temperatures. The snowline over land is determined from a sinusoidal function in time, which, in the Northern Hemisphere gives a maximum southern extent to 45°N on January 26 and a minimum extent to 75°N on July 26. The diurnal mean of incoming solar radiation is controlled by a seasonal sinusoidal variation in the declination angle which affects both the zenith angle and the length of daylight. The time-varying, but prescribed, sea-surface temperatures (SST) are calculated from monthly mean climatological data. The change of sea-surface temperatures from January to July is generally less than 5°C except over small areas in the northern oceans and near Antartica (Figure 1).

Model performance has been evaluated from a 5-year seasonal simulation. An example of the model's capability is the simulation of the zonal wind field (Figure 2). The basic features of the midlatitude jets are reproduced, but they are placed at the top model level. The observed easterlies at tropical latitudes are somewhat underestimated.

Two experiments are run to investigate the effect of the external forcing on the seasonal cycle. In the first, designated "Seasonal R_o", only the incoming solar radiation is allowed to vary seasonally. The latitude of snowcover is fixed at 60° in both hemispheres, and the sea-surface temperatures, sea ice, cloud amounts, and long-wave emissivities are set at their annual mean values. In the second, designated "Seasonal SST", only the sea-surface temperatures and sea-ice boundaries are varied seasonally. Both experiments are started from January 1 of the third year of the 5-year seasonal simulation and integrated for one year. Results from the third year of the original simulation are considered the control.

Seasonal variations of the computed surface temperatures over land are similar in the control and seasonal R_o experiments (Figure 3). Differences in the southern extent of the freezing isotherm are tied to the snowcover limit. The seasonal SST simulation has much less seasonal variability for surface temperatures over land. Note the reversal of the polarity of the land-sea contrast in both the control and seasonal R_o experiments which is absent in the seasonal SST experiment.

The transfer of sensible heat between the surface and the first model level (Figure 4) is also affected by variations in the radiative forcing. Without this seasonal cycle, the air above the winter continents is warmer, so that as it flows over the warm Gulf and Kuroshio currents, less sensible heat is imparted to it.

At upper levels, the effect of solar radiation variations is even more pronounced (Figure 5). The magnitudes of the midlatitude westerly jets show a distinct seasonal variation in the control and seasonal R_o integrations, especially in the Northern Hemisphere. The changes are somewhat less in the seasonal R_o experiment than in the control due to the snowcover being fixed at its annual mean in the former rather than retreating poleward in summer. In the seasonal SST simulation, the westerly jets have less annual variation, and during the northern summer, the tropical easterly jet is poorly developed.

Finally, time series of the vertically integrated eddy kinetic energy averaged from 23.21°N to 81.11°N (Figure 6) can be used to assess the relative influences of the external forcings on the seasonal cycles within the atmosphere. No annual variation is apparent in the eddy kinetic energy present in the seasonal SST experiment. Both the control and seasonal R_o simulations display seasonal cycles of eddy kinetic energy, but the variation is more sinusoidal in the latter. In the control run, the eddy kinetic energy decreases gradually through spring and summer, reaching a minimum in September, and then increases rapidly in October, as also observed. The results suggest that seasonal SST variations might explain this asymmetry.

In conclusion, these experiments show that variations in the direct heating of the atmosphere and land surfaces by incoming solar radiation are generally more important than variations in the specified sea-surface temperatures and sea-ice boundaries for determining the annual variations of atmospheric parameters in a general circulation model. In particular, solar radiative heating plays a large role in forcing the north-south as well as east-west (land-sea) temperature contrasts and their seasonal changes, which, in turn, affects the seasonal variations of the winds, surface transports, and energetics. These results have implications for the design of coupled ocean-atmosphere climate models.

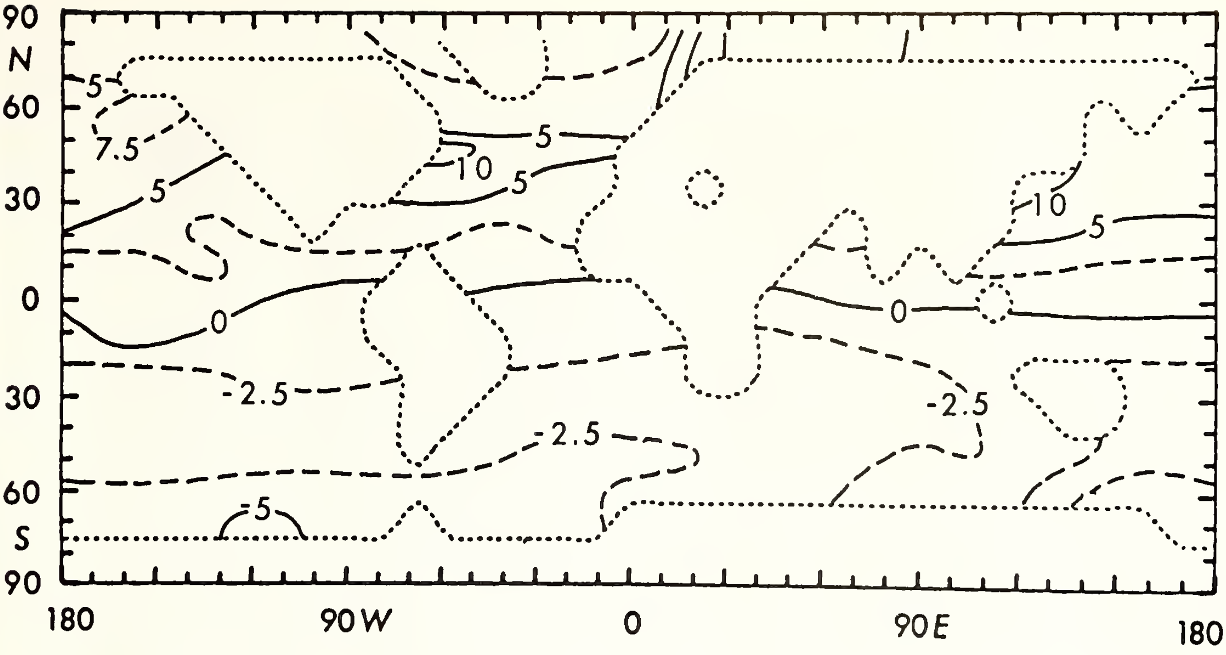

Figure 1: Distribution of July minus January prescribed sea-surface temperatures (°C).

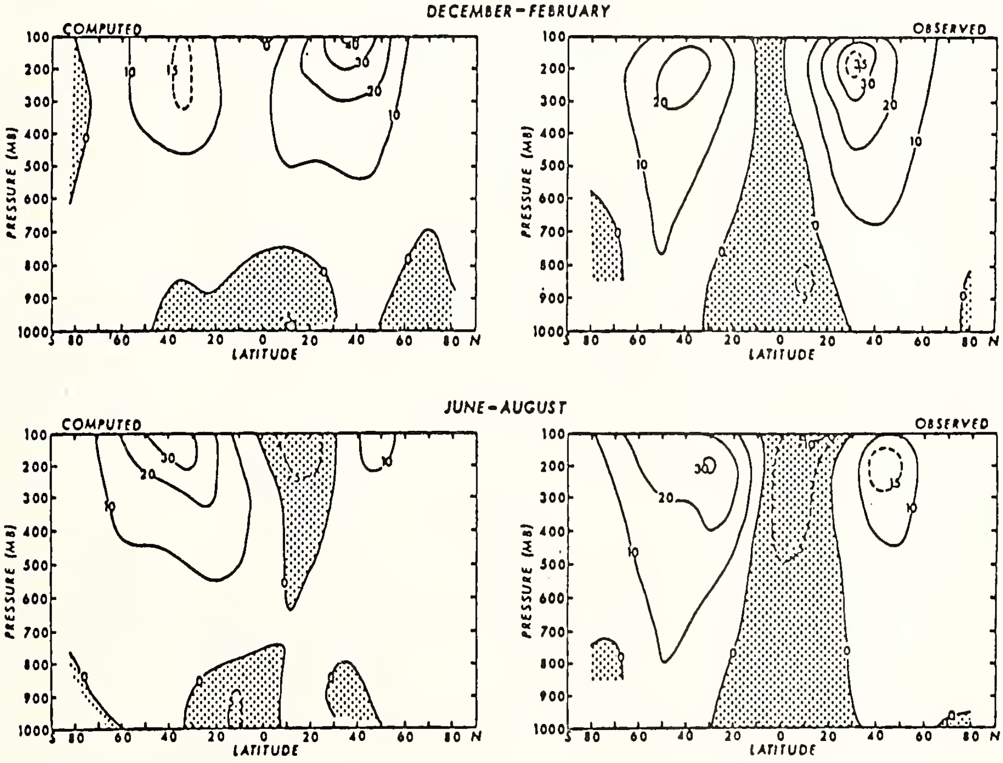

Figure 2: Computed and observed zonal distributions of zonal wind component (m/s).

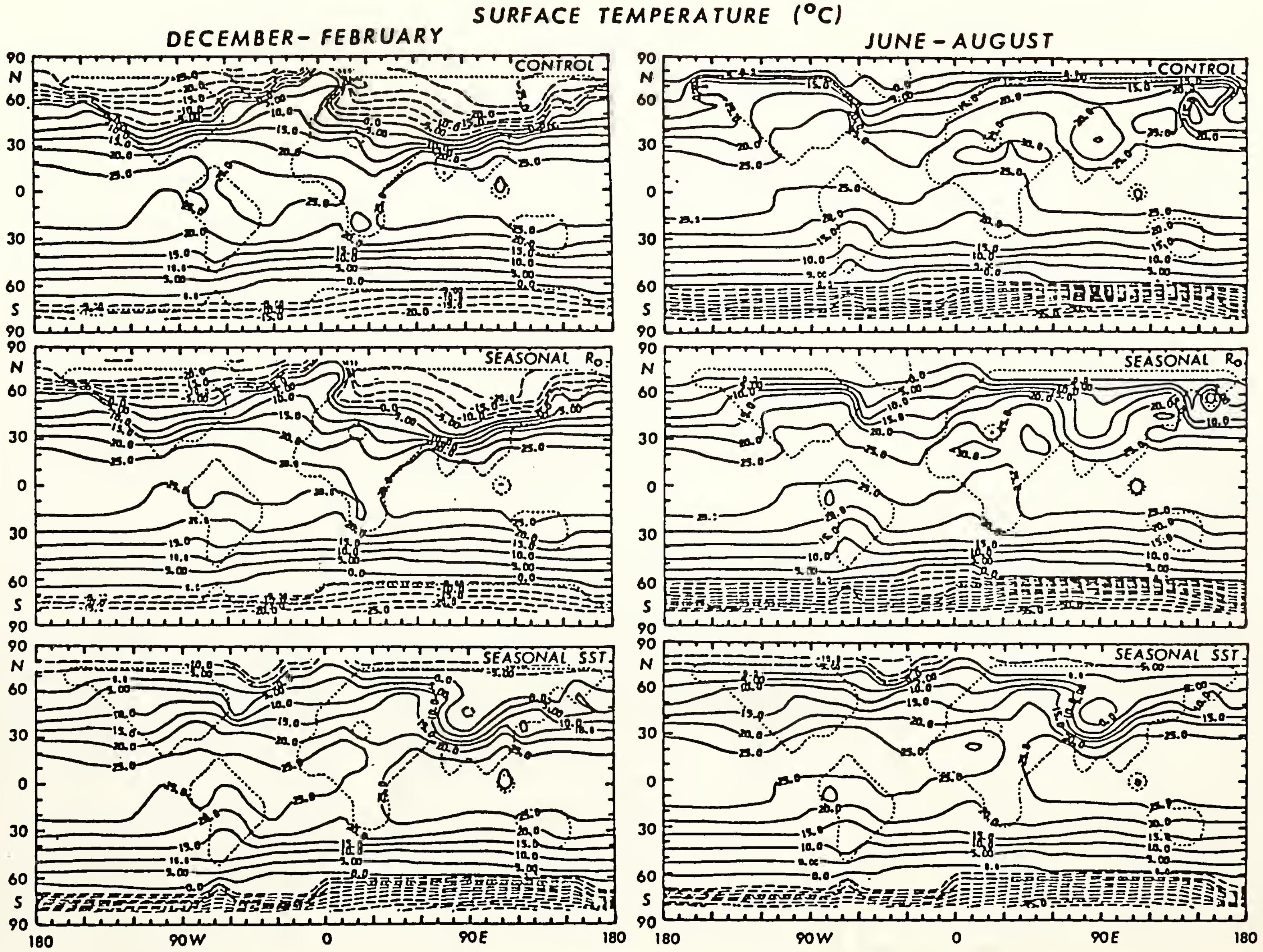

Figure 3: Distributions of surface temperatures in control, seasonal R_o, and seasonal SST simulations. Contour interval is 5°C. Negative contours are dashed.

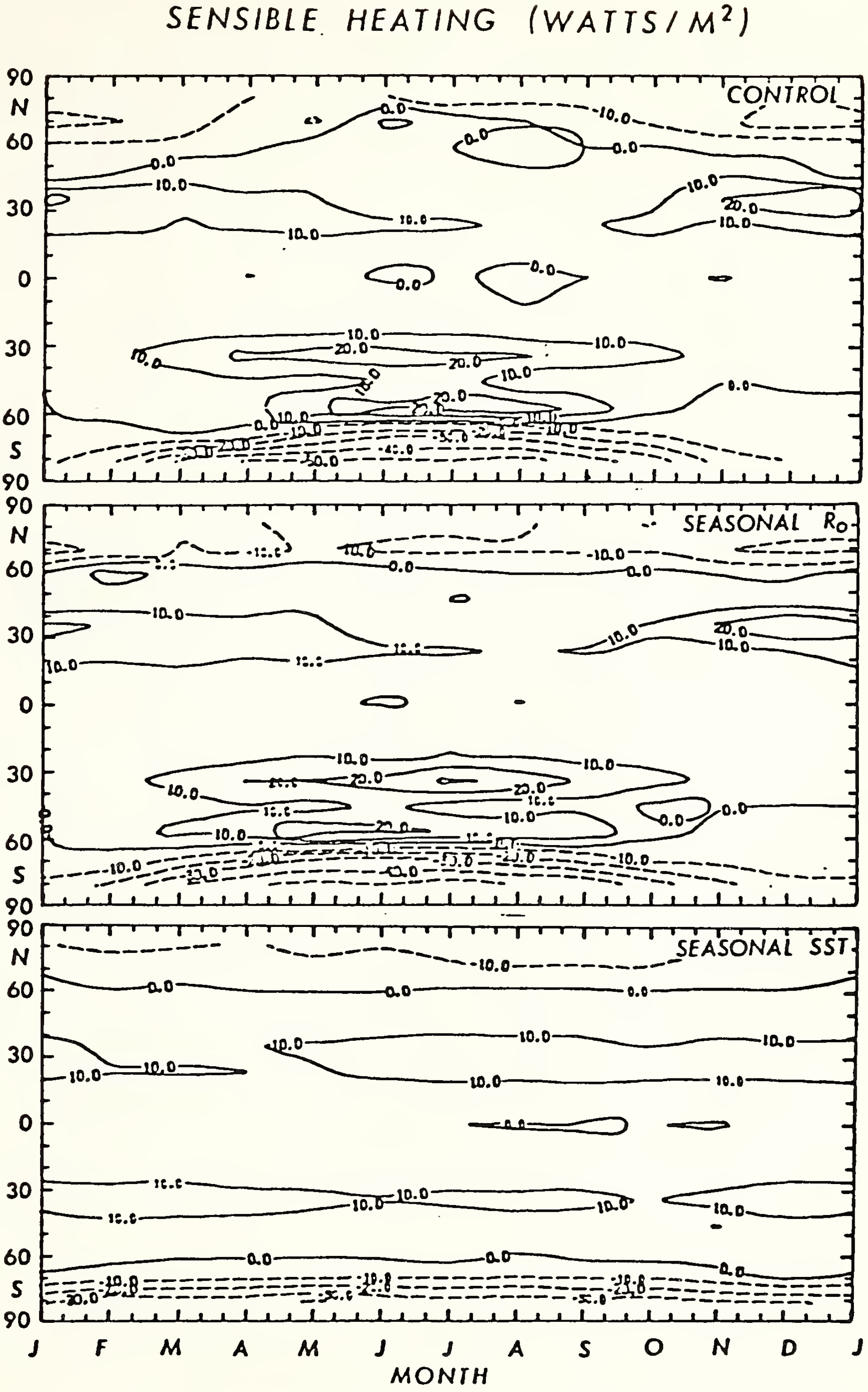

Figure 4: Latitude-time sections of computed sensible heat transfer between the earth's surface and the first model level in the control, seasonal R_o, and seasonal SST simulations. Solid contours represent upward flux.

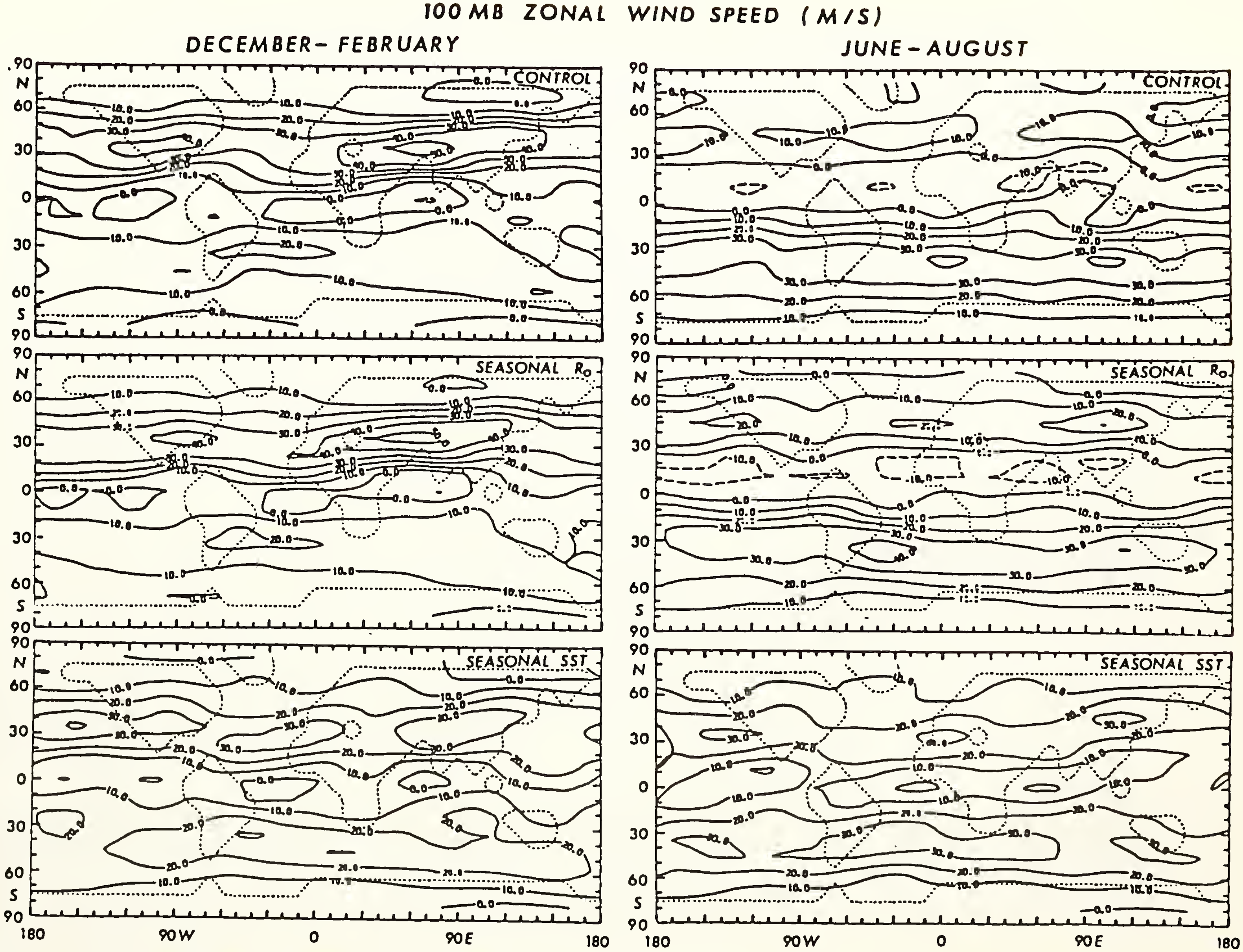

Figure 5: Distributions of zonal wind speed at 100 mb in control, seasonal R_o, and seasonal SST simulations. Contour interval is 10 m/s. Dashed contours represent easterly flow.

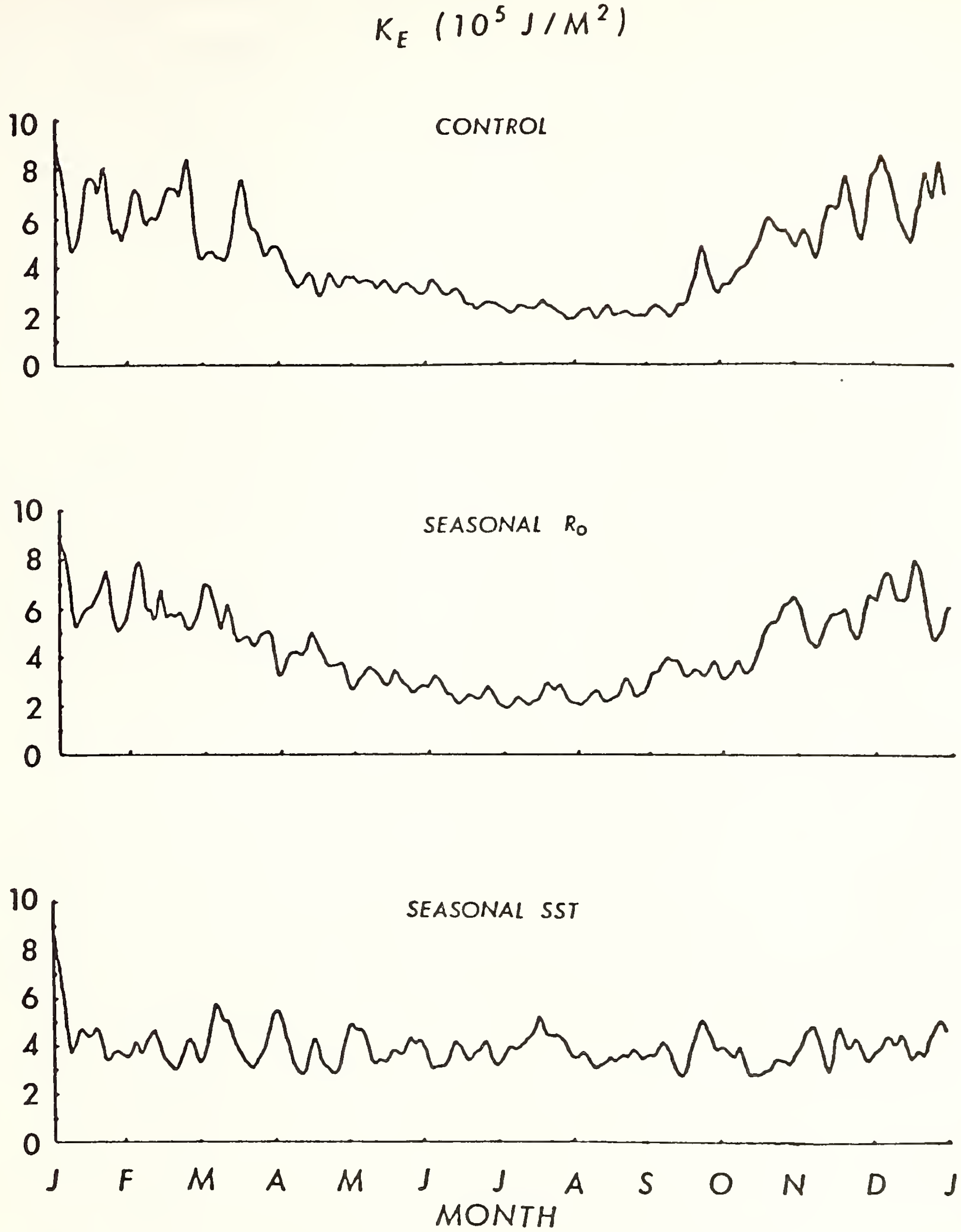

Figure 6: Daily time series of the eddy kinetic energy averaged from 23.21°N to 81.11°N and from the surface to 100 mb for the control, seasonal R_o, and seasonal SST simulations.

PRELIMINARY ANALYSIS OF THE ANGULAR MOMENTUM BALANCE IN THE OSU TWO-LEVEL ATMOSPHERIC GENERAL CIRCULATION MODEL

J.-W. Kim and W. Grady

Climatic Research Institute
and
Department of Atmospheric Sciences
Oregon State University
Corvallis, Oregon 97331

The atmospheric angular momentum balance is studied by analyzing the data during a simulated January of the OSU two-level atmospheric general circulation model. Monthly zonal means of the Coriolis torques, the vertical transfer of relative angular momentum by penetrating convection, midlevel convection, background viscosity, pressure force, and vertical motion, the meridional transfer of relative angular momentum by the standing mean motion, standing eddies and transient motion, and the surface exchange of relative angular momentum by oceanic and continental friction and mountain torque are computed.

The overall picture given by the model is realistic. The global atmosphere angular momentum is in general drained by the mountain torques and created by the surface friction. From Figs. 1 and 2 we can deduce that the global relative angular momentum in the upper layer is a balance between the downward transfer and the transformation of Ω-momentum into relative angular momentum, whereas the global relative angular momentum in the lower layer is a balance between the downward transfer from the upper-layer and the transformation of relative angular momentum into Ω-momentum. The subtropical jets are maintained by a balance between the Coriolis torques on the poleward branches of the Hadley circulations and the downward transfers and divergent poleward fluxes, whereas the upper westerlies in higher latitudes are maintained by a balance between the convergent poleward fluxes and the downward transfer and Coriolis torque on the equatorward branches of the Ferrel circulation.

Fig. 3 shows that the mountain torques are downward momentum transfers with a maximum at 30°N and another at 20°S except for minor upward transfers in the northern equatorial latitudes and north of 60°N, and the frictional torques are upward momentum transfers in the subtropics and downward transfers in the middle latitudes, and generally dominate the mountain torques except in the Northern Hemisphere middle latitudes.

It is found from Fig. 4 that midlevel convection is a negligible component in the momentum balance, and the midlevel pressure torque is a significant downward transfer only in the Northern Hemisphere middle latitudes where the major mountains of the model exist. The momentum transfers by penetrating convection and background viscosity are comparable and generally downward, except for the upward momentum transfer by the penetrating convection at the latitudes near the Equator. Finally, from Fig. 5 we see that the standing mean motion transports momentum downward in the subtropics and upward in higher latitudes, whereas the standing eddy and transient motions are negligible components of the momentum balance except for the significant upward transfers by the transient motion in the roaring forties of the Southern Hemisphere.

Hellerman, S., 1967: An updated estimate of the wind stress on the world ocean. *Mon. Wea. Rev.*, *95*, 607-626. Corrigendum on *Mon. Wea. Rev.*, *96*, 63-74.

Newton, C. W., 1971: Mountain torques in the global angular momentum balance. *J. Atmos. Sci.*, *28*, 623-628.

Oort, A. H., and E. M. Rasmusson, 1971: Atmospheric circulation statistics. NOAA Prof. Paper 5, U.S. Department of Commerce, Rockville, MD, 323 pp.

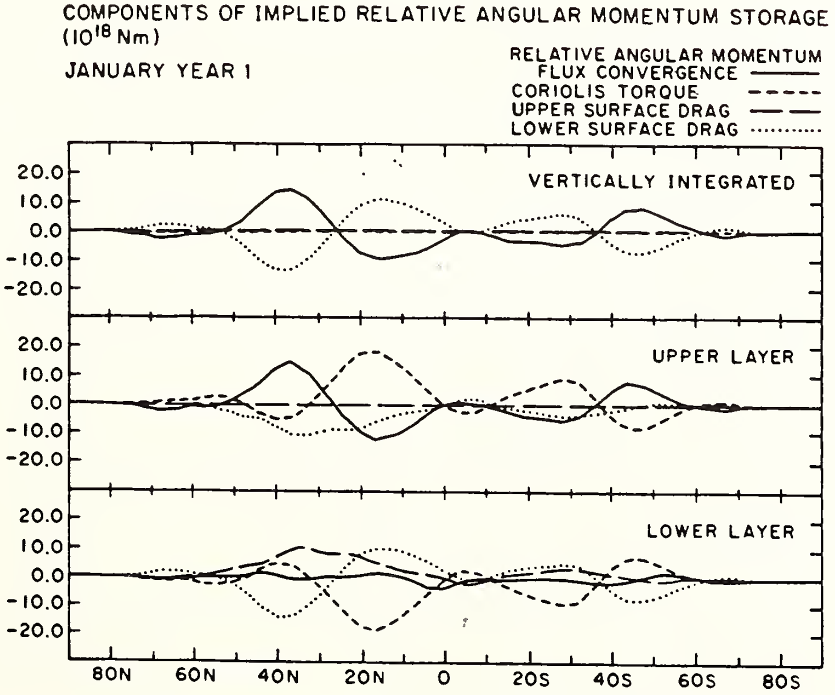

Fig. 1. Components of the implied storage of relative angular momentum for 4°-lat. zonal bands for January of Year 1 for the vertically-integrated case (upper panel), upper layer (middle panel) and lower layer (lower panel). Relative angular momentum flux convergence is shown by solid curves, the Coriolis torque by short-dashed curves, the vertical transfer at the top of each layer by long-dashed curves, and the vertical transfer at the bottom of each layer by dotted curves.

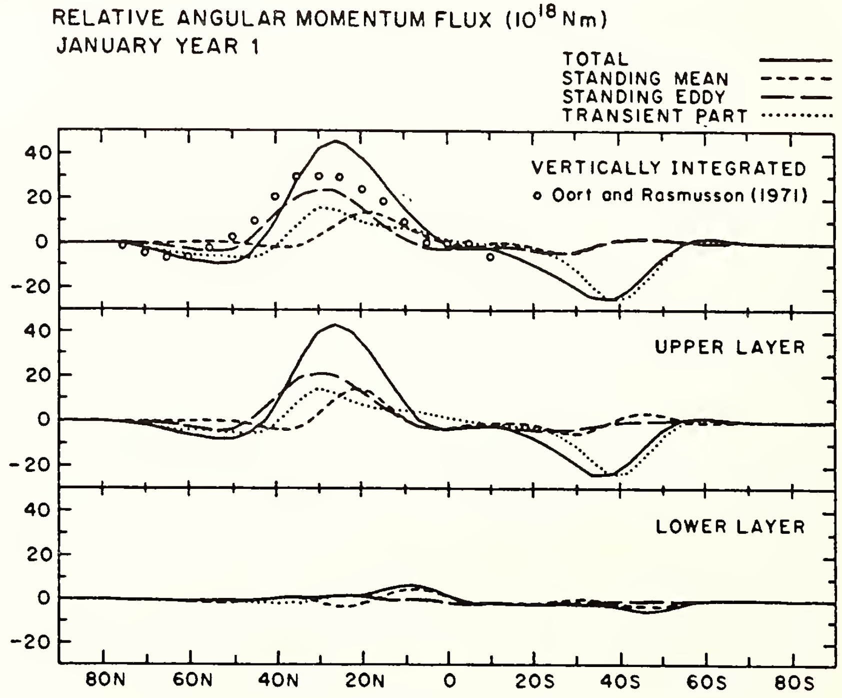

Fig. 2. Relative angular momentum flux for January of Year 1 for the vertically-integrated case (upper panel), the upper layer (middle panel) and the lower layer (lower panel). The total is shown by solid curves, standing mean motion by short-dashed curves, standing eddy motion by long-dashed curves, and transient motion by dotted curves. The observed tropospheric northward flux of relative angular momentum from Oort and Rasmusson (1971) is shown by the open circles.

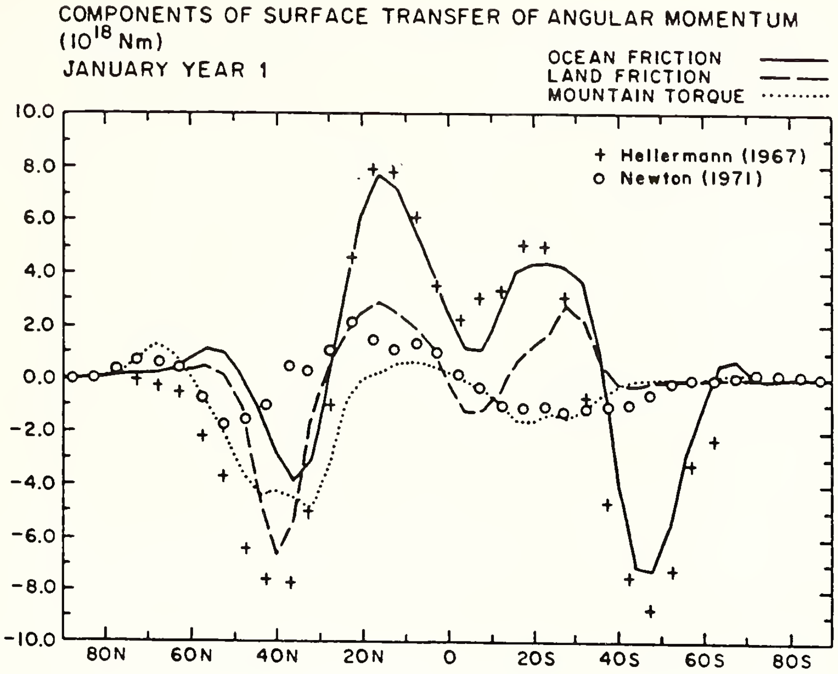

Fig. 3. Components of surface transfer of angular momentum for 4^{o}-lat. zonal bands for January of Year 1. Ocean friction is shown by solid curves, continental friction by dashed curves, and mountain torque by dotted curves. The observed angular momentum flux from Hellerman (1967) for Dec.-Feb. over the world ocean is shown by crosses, and the observed January mountain torque converted to 4^{o}-lat. bands from Newton (1971) is shown by open circles.

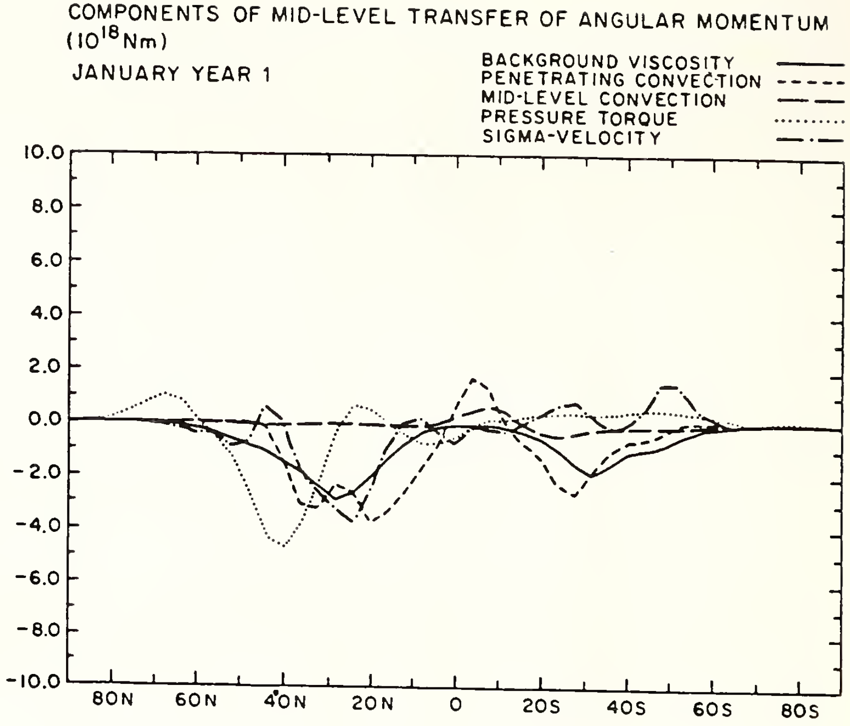

Fig. 4. Components of the mid-level transfer of angular momentum in 4^{o}-lat. zonal bands for January of Year 1. Background viscosity is shown by solid curves, penetrating convection by dashed curves, mid-level convection by long-dashed curves, pressure torque by dotted curves, and sigma-velocity by dashed-dotted curves.

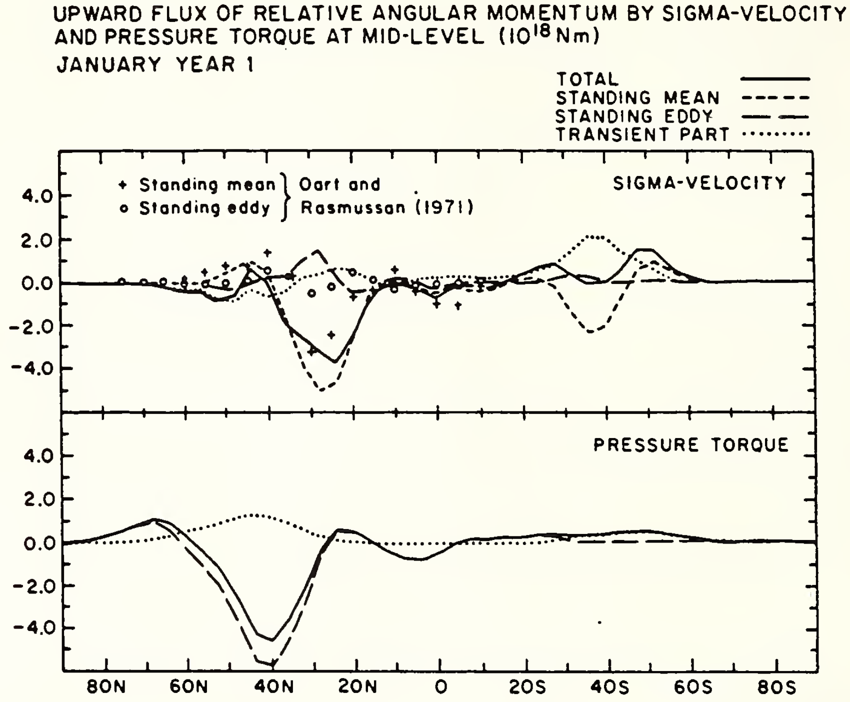

Fig. 5. Mid-level momentum transfer by sigma-velocity (upper panel) and pressure torque (lower panel) for January of Year 1. The total is shown by solid curves, standing mean motion by short-dashed curves, standing eddy motion by long-dashed curves, and transient motion by dotted curves. The observed vertical transfer at 600 mb from Oort and Rasmusson (1971) is shown by crosses for the mean meridional circulation and by open circles for the stationary eddies.

Comparison of the Earth-atmosphere Radiation Budget and Albedo Determined by a Climate Model and by Satellite Observations*

Julian Adem

Centro de Ciencias de la Atmosfera y Facultad de Ciencias,
UNAM, Mexico 20, D. F. and
Lamont-Doherty Geological Observatory of Columbia University
Palisades, N. Y. 10964
and

William L. Donn

Lamont-Doherty Geological Observatory of Columbia University,
Palisades, N. Y. 10964

Winston et al. (1979) have published global charts and zonally averaged values of the outgoing long-wave radiation, the absorbed solar radiation, net radiation, and the planetary albedo for the period June 1974 to February 1978. These data can be used to test how realistic is the radiation budget generated internally in a climate model. The comparison of the satellite observations with the model computations may allow an improvement in the parameterization of the radiation budget used in the models, but also it can possibly be used to improve the satellite values by suggesting an adjustment in their calibration.

The climate model used in these computations is the hemispheric low resolution grid model developed by one of the authors, and which is described in a recent paper (Adem, 1979). The model generated charts of forecasts of temperature and precipitation as well as of the heating functions involved for the 12 months of the year. However, we show here only the results for the months at the middle of the seasons.

Figures 1 to 8 show maps of the absorbed solar radiation, the outgoing long radiation, the net radiation, and the planetary albedo for January and July. Parts A and C are the satellite-derived values and parts B and D the corresponding values computed by the model. There is an overall good agreement. However, there exist discrepancies which vary with the geographic position and the time of the year.

In order to determine the average differences at each latitude a comparison of the zonally averaged values is also presented. Fig. 9 shows the zonally averaged values of outgoing longwave radiation and absorbed solar radiation for October, January, April, and July. The values estimated from the satellite data and from the model are shown for the outgoing radiation by the dashed and the dotted lines, respectively, and for the absorbed solar radiation by the solid and the dotted-dashed lines, respectively. This figure shows good agreement of the computed values with the satellite observations. However, in general the computed values are smaller than the satellite values.

---

* Lamont-Doherty Geological Observatory of Columbia University Contribution Number 3066

Figures 10 and 11 show the zonally averaged values of the net radiation and of the albedo, respectively. The solid lines correspond to the satellite observations and the dashed lines to the values computed by the model. According to Fig. 10 the net radiation computed by the model and determined from satellite observations, respectively, agree quite well.

Fig. 11 shows that the albedo values computed by the model are, in general, higher than those derived from satellite observations. The largest discrepancies occur in April.

Table 1 shows the differences: satellite values minus computed values of absorbed solar radiation (ABS), outgoing longwave radiation (OUT) and net radiation (NET) for October, January, April, and July.

Table 2 shows the annual averages of the differences of the satellite values minus the computed values of the radiation components. The satellite values for the absorbed and the outgoing radiations are for all latitudes larger than the model values. In lower and in middle latitudes the differences for the absorbed and the outgoing radiation are of the same order of magnitude and, therefore, yield very small differences for the net radiation. In higher latitudes the differences for the absorbed radiation are much smaller than those for the outgoing radiation and, therefore, the net radiation differences are of the same order of magnitude of those for the outgoing radiation.

Table 3 shows, in percent, the differences of the satellite values minus the computed values of the albedo, in the Northern Hemisphere, for October, January, April, and July, as well as for the annual average also.

References

Adem, J. 1979. Low resolution thermodynamic grid models. _Dyn. Atmos. Oceans_, 3, 433-451.

Winston, Jay S. _et al_. 1979. Earth-atmosphere radiation budget analyses derived from NOAA satellite data, June 1974-February 1978. Vols. I and II. _Meteorological Satellite Laboratory_, Washington, D. C.

Acknowledgements

This work was supported by NOAA Grant NA-79-AA-D-00066.

TABLE 1. Zonally averaged, Northern Hemisphere differences of satellite values minus model computed values of absorbed solar radiation (ABS) outgoing longwave radiation (OUT) and net radiation, in WM^{-2}.

LAT.	OCTOBER			JANUARY			APRIL			JULY		
	ABS	OUT	NET	ABS	OUT	NET	ABS	OUT	NET	ABS	OUT	NET
20	20	18	2	5	20	-15	35	22	13	20	15	5
30	15	25	-10	0	25	-25	25	20	5	20	15	5
40	15	22	-7	10	25	-15	25	25	0	30	20	10
50	20	30	-10	10	30	-20	40	30	10	28	25	3
60	10	30	-20	0	40	-40	-10	35	-45	15	25	-10
70	10	35	-25	-5	44	-49	0	50	-50	0	25	-25
80	10	40	-30	-5	60	-65	10	45	-35	10	35	-25

TABLE 2. Annual zonally averaged, Northern Hemisphere differences of satellite values minus model computed values of absorbed solar radiation (ABS), outgoing longwave radiation (OUT) and net radiation, in WM^{-2}.

LAT	ABS	OUT	NET
20	20	19	1
30	15	21	-6
40	20	23	-3
50	25	29	-4
60	4	32	-29
70	1	38	-37
80	6	45	-39

TABLE 3. Zonally averaged, Northern Hemisphere differences of satellite values minus model computed values of albedo, in percent.

LAT.	OCT.	JAN.	APRIL	JULY	ANNUAL
20	5	1	10	7	6
30	2	0	8	4	3
40	2	5	10	5	5
50	4	7	13	4	7
60	2	4	0	5	3
70	2	0	0	0	0
80	-	-	-5	-10	-8

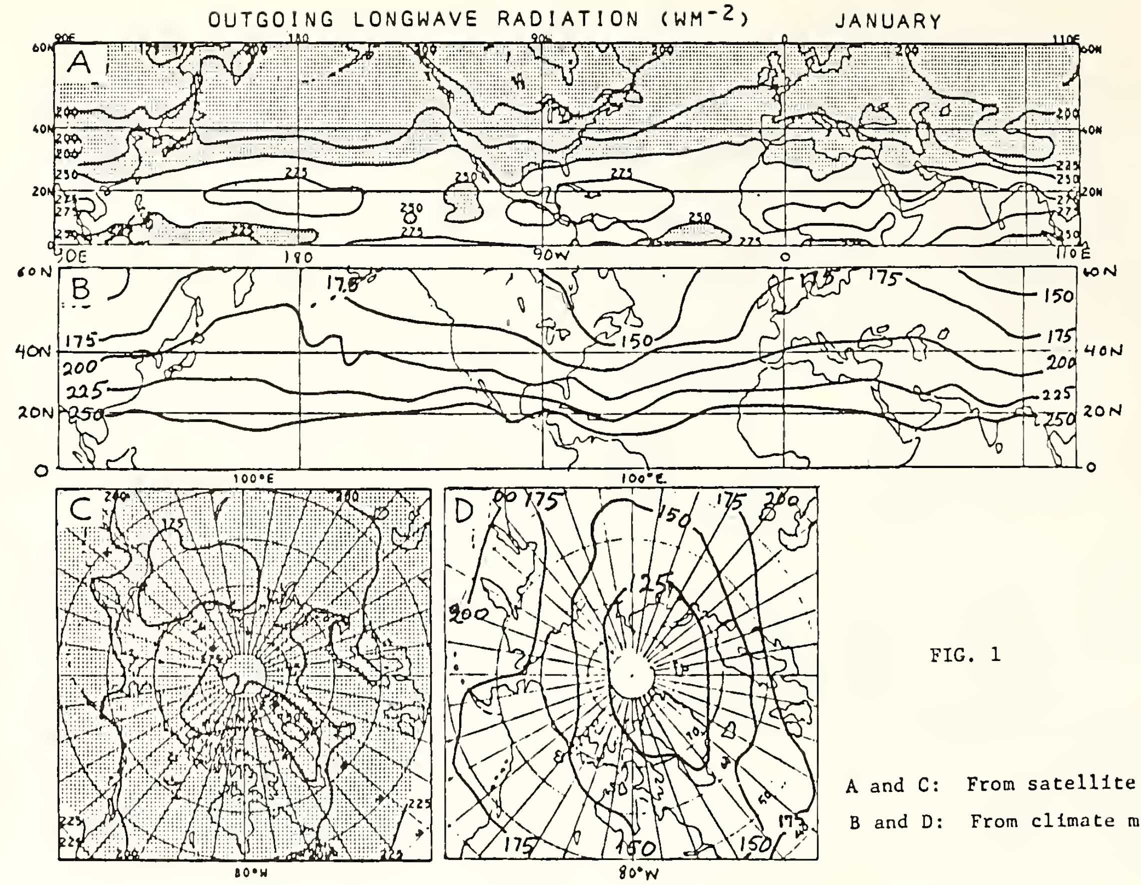

FIG. 1

A and C: From satellite data

B and D: From climate model

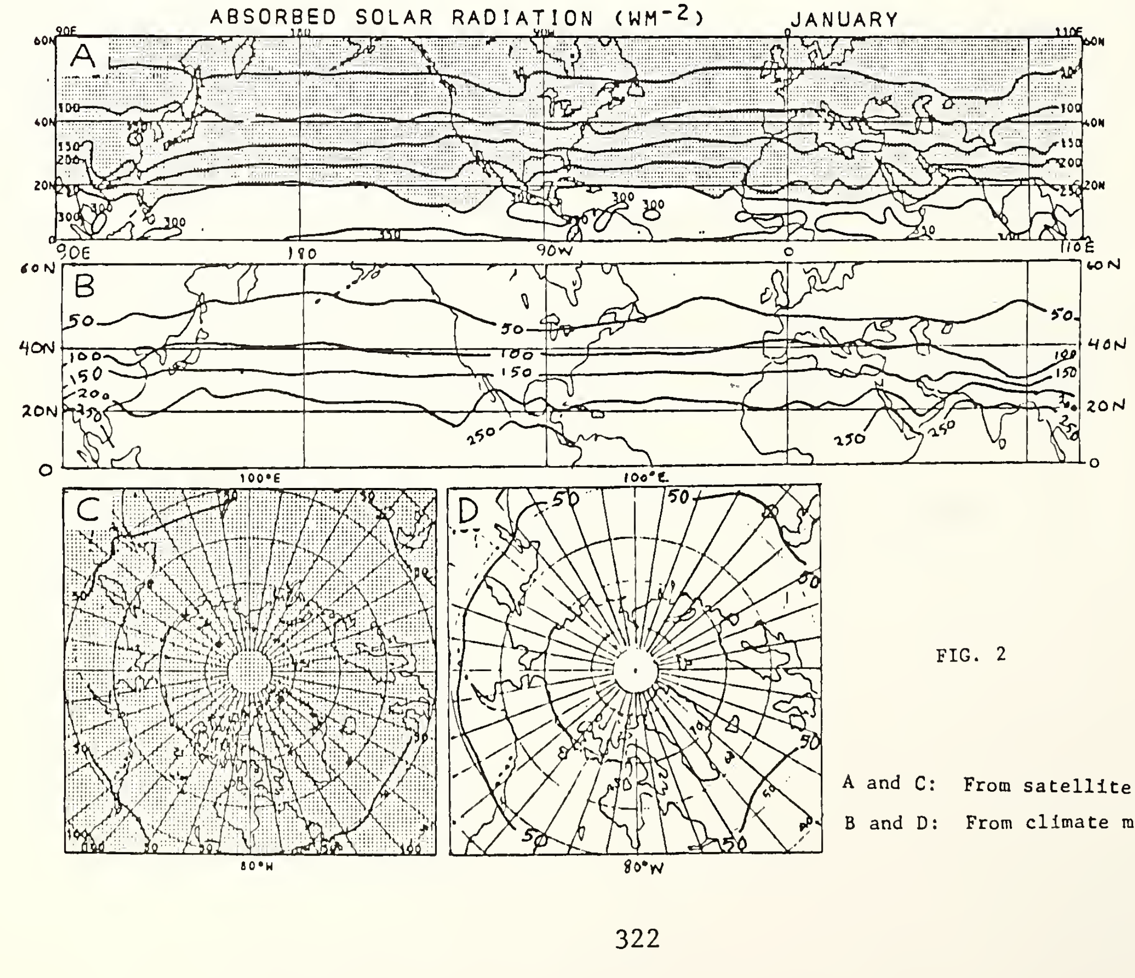

FIG. 2

A and C: From satellite data

B and D: From climate model

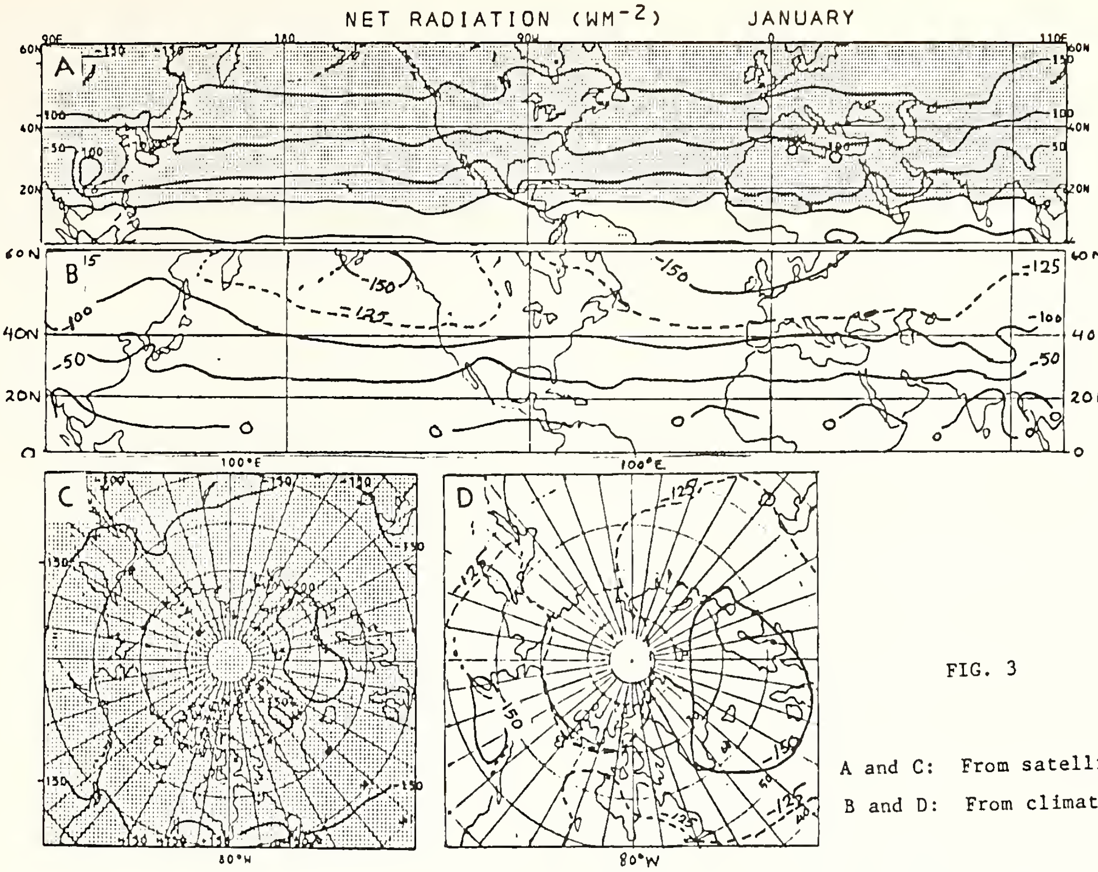

FIG. 3

A and C: From satellite data

B and D: From climate model

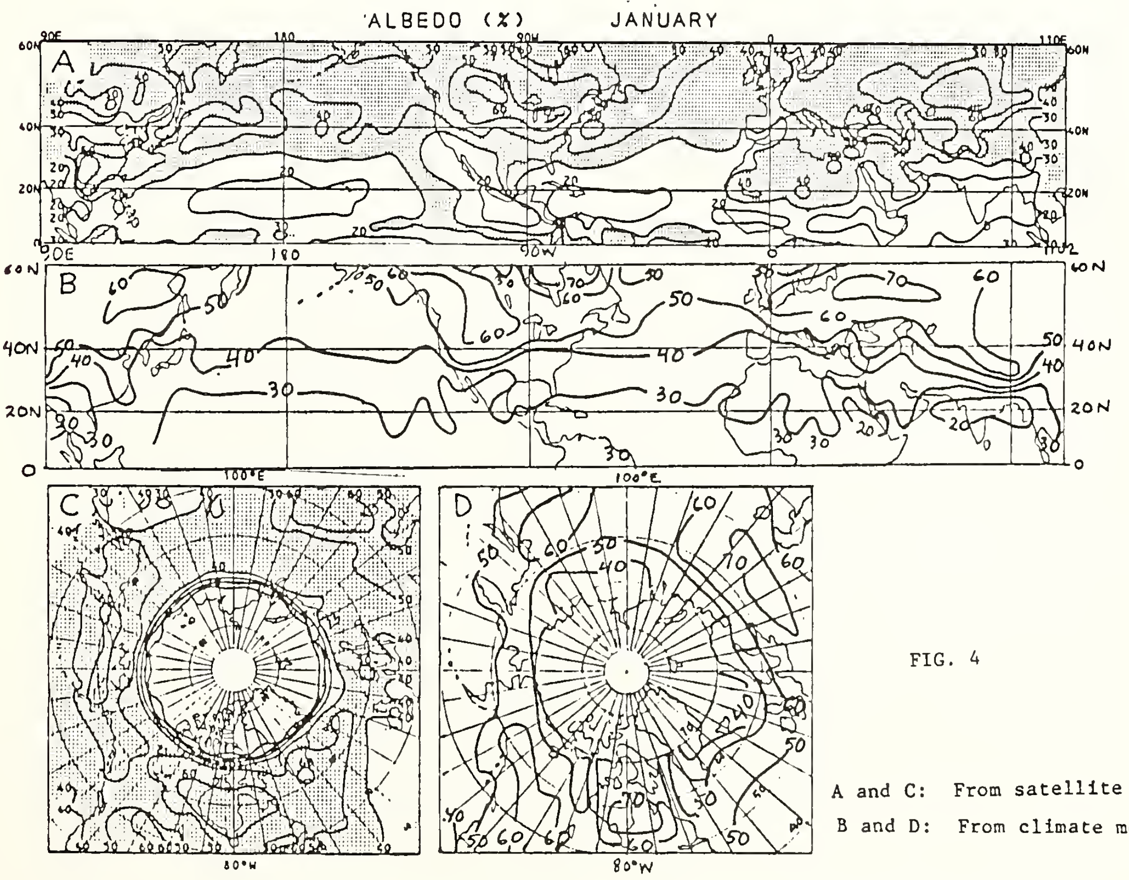

FIG. 4

A and C: From satellite data

B and D: From climate model

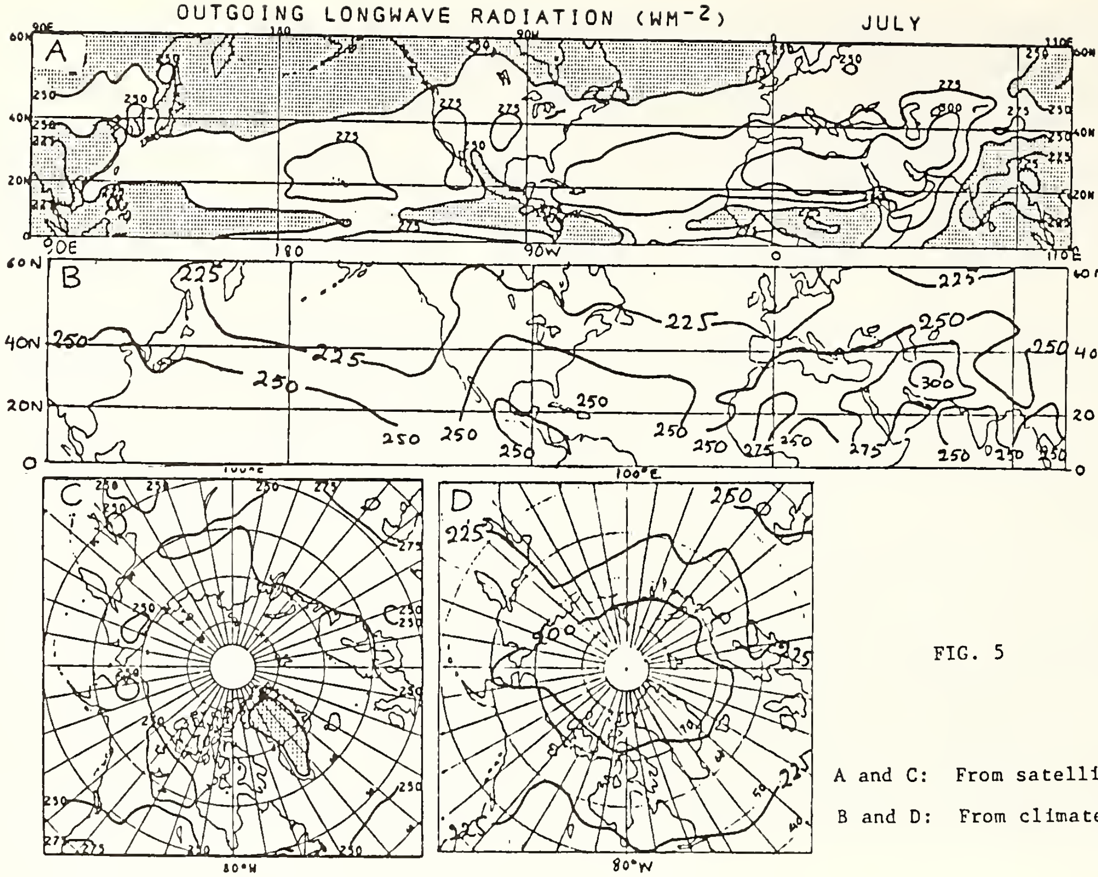
OUTGOING LONGWAVE RADIATION (WM^{-2}) JULY

FIG. 5

A and C: From satellite data

B and D: From climate model

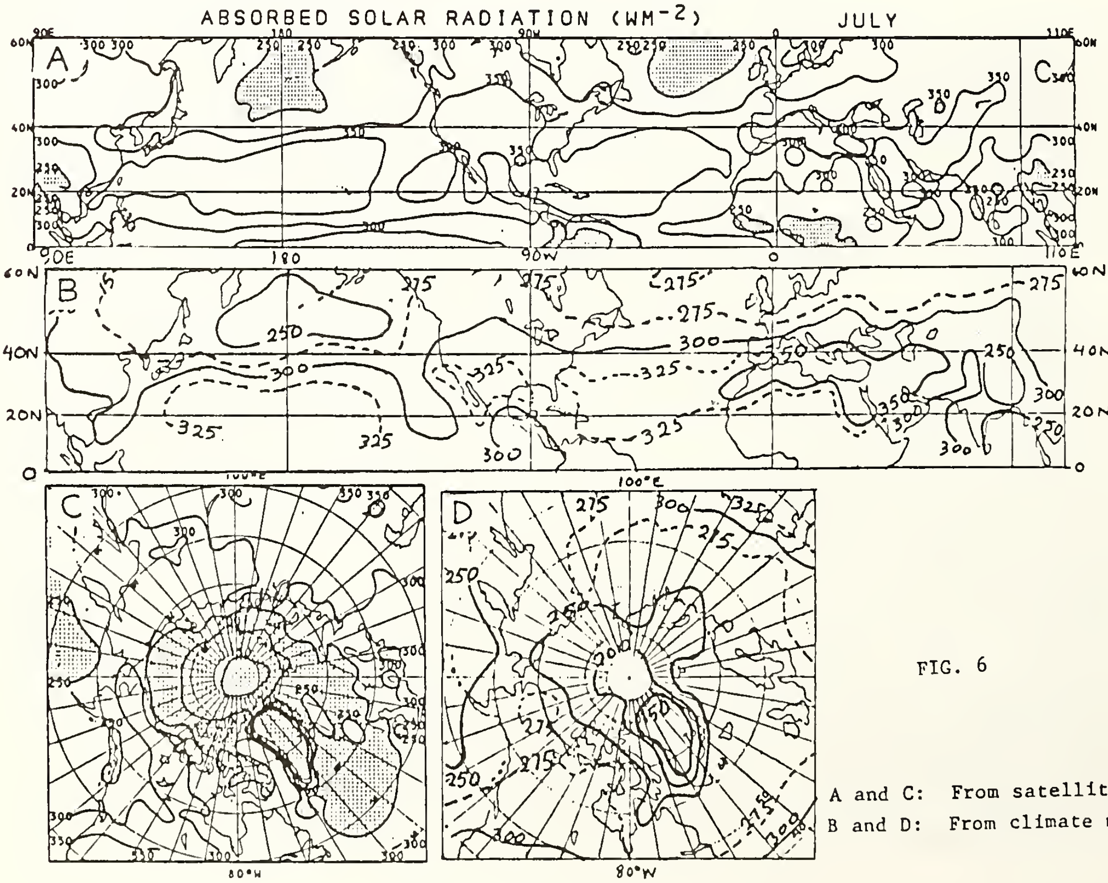
ABSORBED SOLAR RADIATION (WM^{-2}) JULY

FIG. 6

A and C: From satellite data

B and D: From climate model

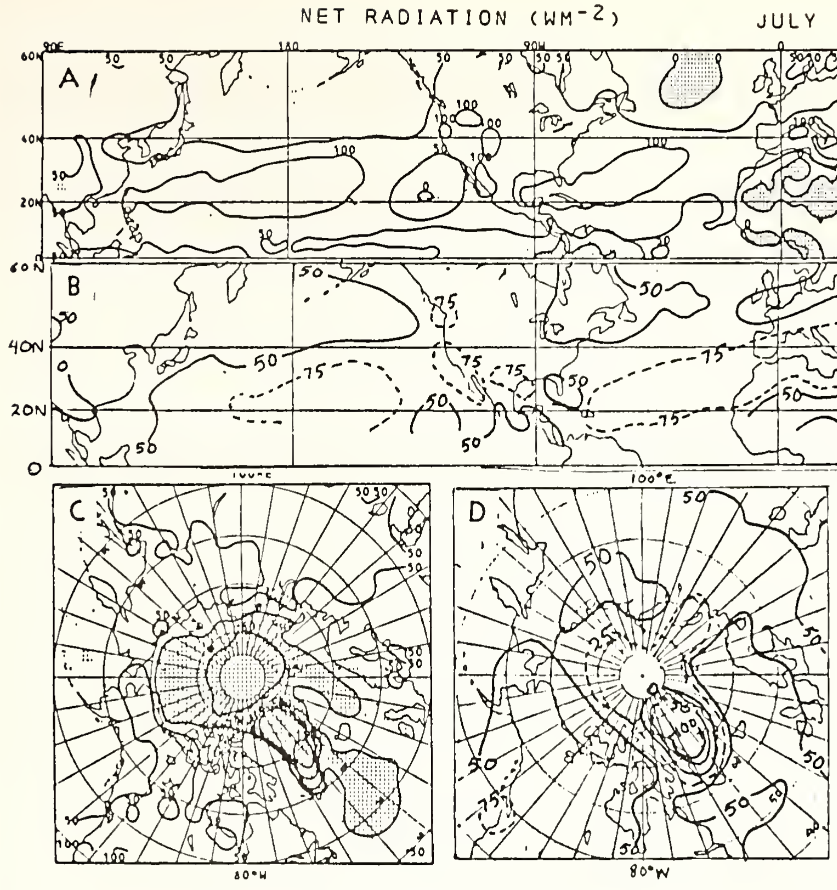

FIG. 7

A and C: From satellite data

B and D: From climate model

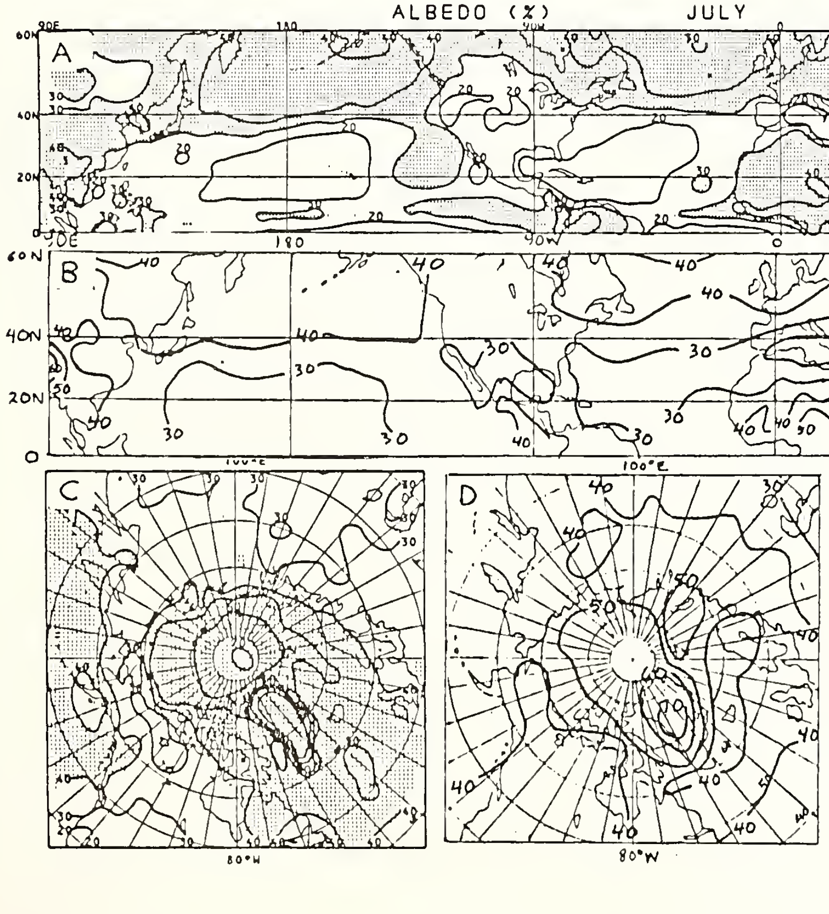

FIG. 8

A and C: From satellite data

B and D: From climate model

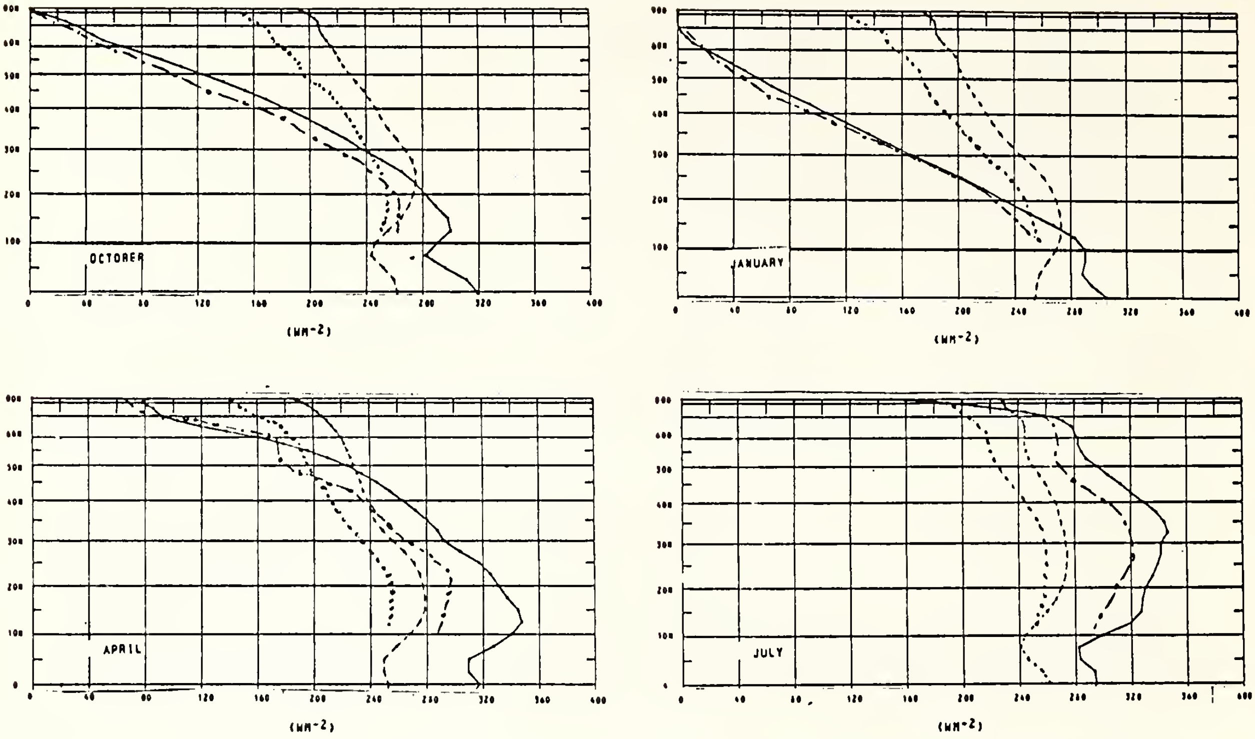

Fig. 9. Northern Hemisphere zonally averaged values of absorbed solar radiation derived from satellite data (solid line) and from model computations (dashed-dotted line); and of outgoing longwave radiation derived from satellite data (dashed line) and from model computations (dotted line).

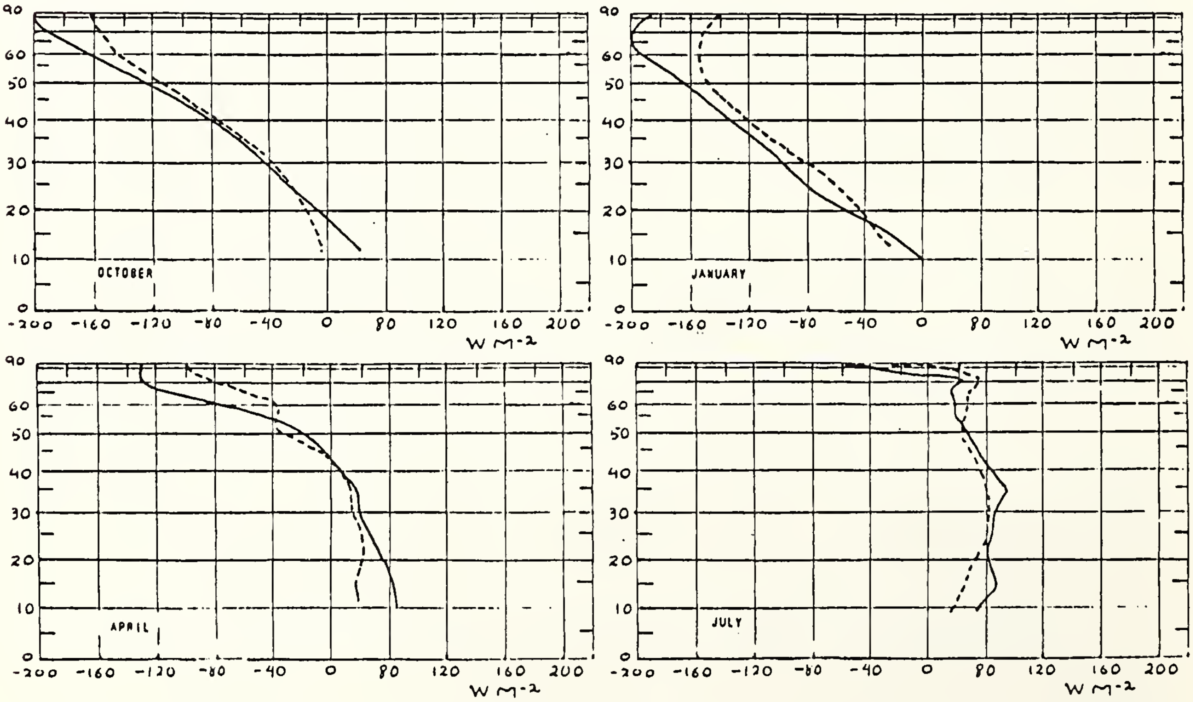

Fig. 10. Northern Hemisphere zonally averaged values of net radiation derived from satellite data (solid line) and from model computations (dashed line).

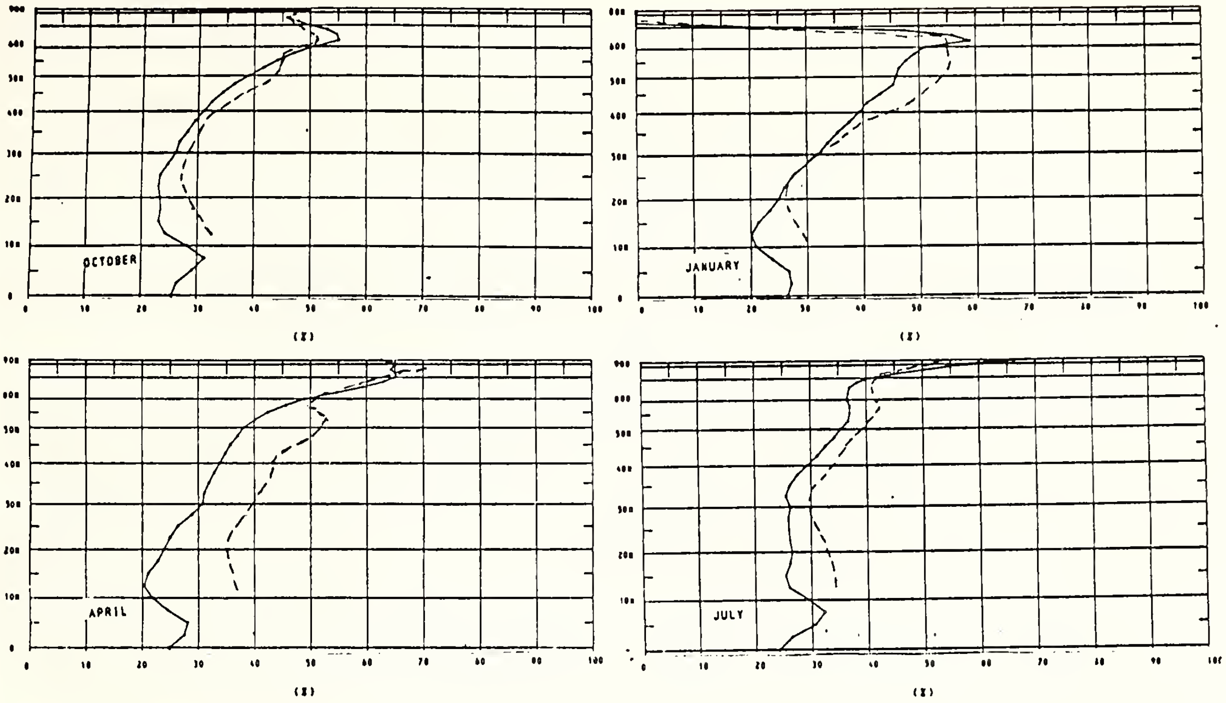

Fig. 11. Northern Hemisphere zonally averaged values of albedo derived from satellite data (solid line) and from model computations (dashed line).

STUDIES OF THE RADIATION BUDGET AND CLOUDINESS IN A CIRCULATION MODEL AND BY SATELLITE DATA

E. Raschke, A. Hense, H.-J.Preuß and E. Ruprecht:
Institut of Geophysics and Meteorology, University
5 Köln 41, Germany
F. Geleyn: European Center for Medium Range Weather Forecasts
Reading, Berkshire, England

For the period of 5-25 Febr. 1976 the radiation budgets computed with the numerical forecast model of the European Center for Medium Range Weather Forecasts in Reading, England, is compared with measurements made with the NOAA-scanning radiometers.

In the model the radiative transfer has been calculated with two different versions of a modified two-stream routine using only the model parameters as input data(Geleyn+ Hollysworth, 1979). Clouds have been generated based on the relative humidity and the vertical instability (Geleyn, 1980). We assumed a most probable overlap and also a random distribution of clouds present in all layers, the NOAA-data were received on tape from the archive. Since here a period of only 10 days has been considered we limited our interest to the time history of radiation budget components at the top of the atmosphere.

Several figures have been shown:

Comparison of zonal averages of the planetary albedo and heat exitance, and time histories of computed and measured radiation budget during the period.
The circulation model, starting on 15 February with an initialized field, suffers a considerable "radiation shock" during the first two days of integration, where the cloudiness and consequently the planetary albedo increases(Fig.1). The two cloud-paramatrization schemes lead to entirely different values of the global cloud-coverage.
While the radiant heat exitance to space, depending primarily on the surface temperatures and cloud-top heights, computed with both schemes, compares satisfactorily with the measurements(Fig.2), the planetary albedo differs considerably over subtropical and tropical regions.

The radiation routine of the University of Cologne used in the model still overestimates the reflected solar radiation, because this model overestimates the optical thickness of computed cloudfields(Thus both methods need a careful redesign). On the other side, the radiation budget data as derived from the operational NOAA-satellite scanning radiometers have various systematic errors: measurements in narrow spectral intervals, incomplete angular corrections, calibration problems. Therefore we intend to repeat these studies for the same time period and also for a period within October 1979, where also data of the Nimbus 7 ERB-radiometers are available.

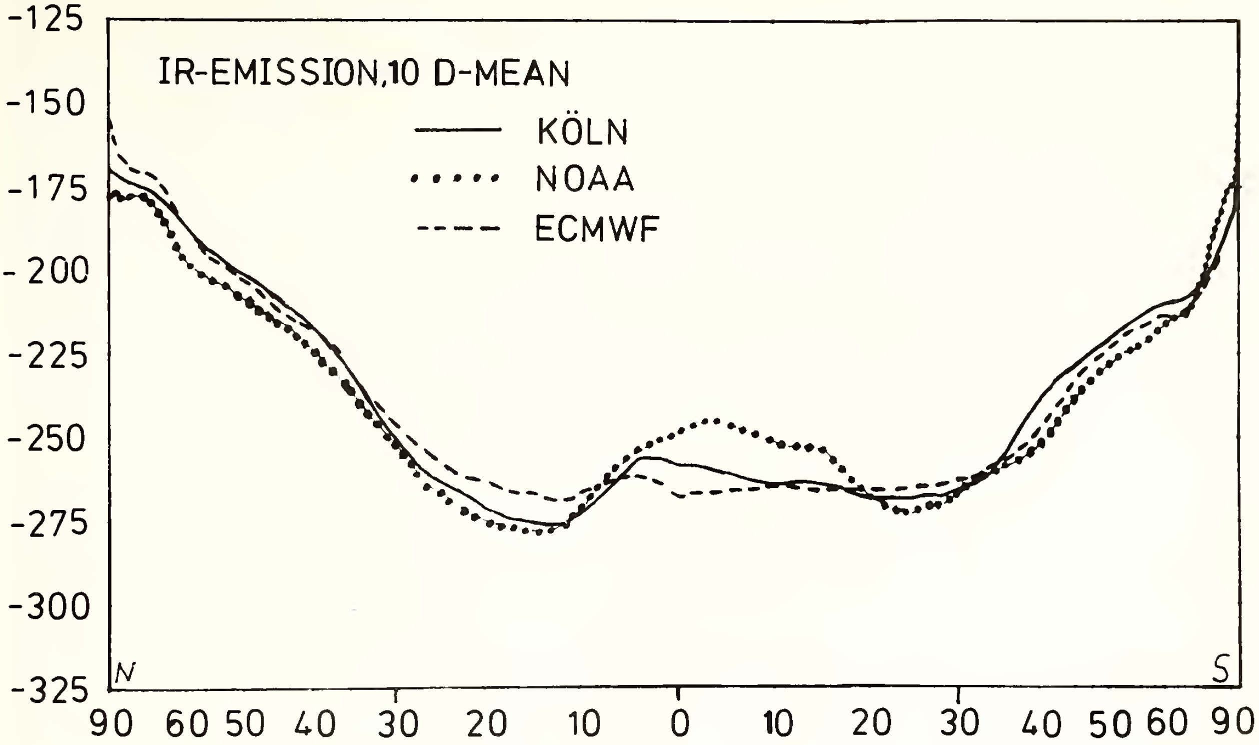
-125
-150
-175
-200
-225
-250
-275
-300
-325
IR-EMISSION,10 D-MEAN
KÖLN
NOAA
ECMWF
N
S
90 60 50 40 30 20 10 0 10 20 30 40 50 60 90

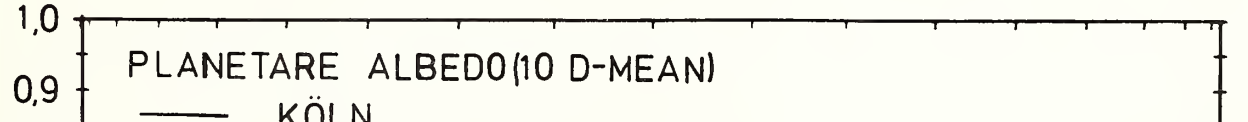
1,0
0,9
0,8
0,7
0,6
0,5
0,4
0,3
0,2
0,1
0,0
PLANETARE ALBEDO(10 D-MEAN)
KÖLN
NOAA
ECMWF
N
S
90 60 50 40 30 20 10 0 10 20 30 40 50 60 90

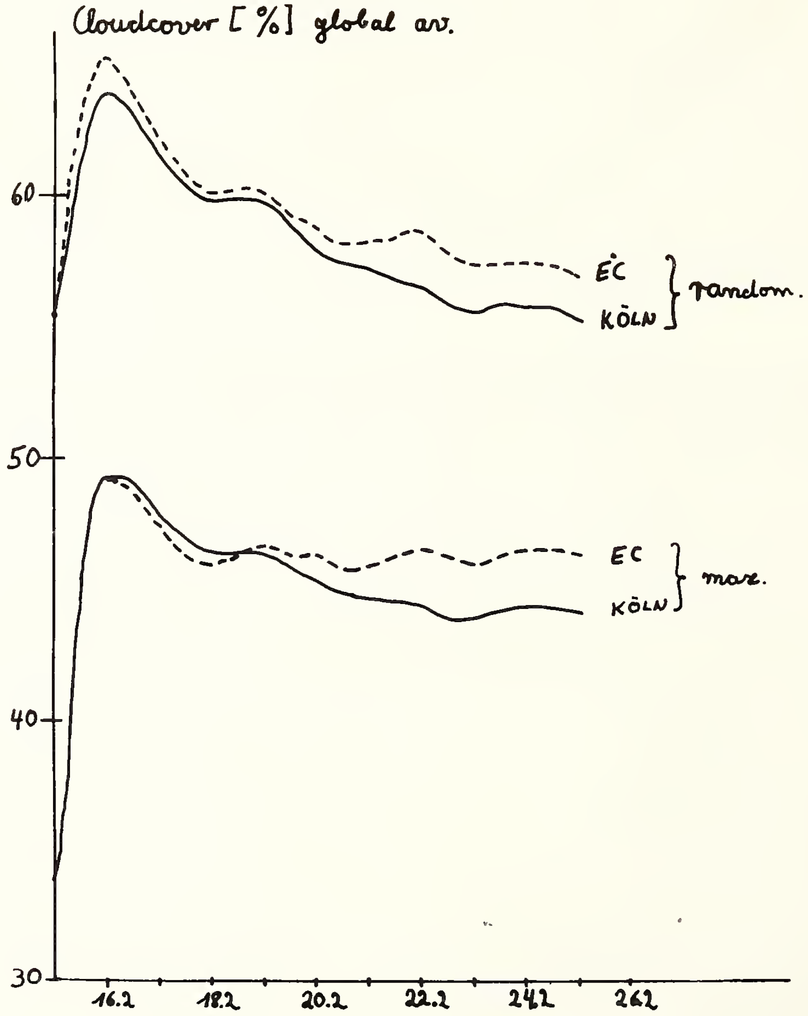
Cloudcover [%] global av.
60
50
40
30
16.2
18.2
20.2
22.2
24.2
26.2
EC
KÖLN
random.
EC
KÖLN
max.

SIMULATION OF A BLOCKING EVENT IN JANUARY 1977

K. Miyakoda, T. Gordon, R. Caverly, W. Stern, J. Sirutis, and W. Bourke

Geophysical Fluid Dynamics Laboratory/NOAA
Princeton University
Princeton, New Jersey 08540

Several numerical simulations of January 1977 were generated by GFDL's finite difference and spectral general circulation models in conjunction with the use of the so-called A2 and E4 vertical turbulent parameterization schemes. The purpose of these simulations is to assess, for the sake of model development, the impact that different numerical formulations and physics parameterization schemes have on a 30-day global numerical simulation. Particular attention is focussed on the rather anomalous blocking ridge that persisted over the west coast of North America throughout the month of January.

Apart from the numerics and a somewhat different horizontal resolution, the two GCM's were identical in that they integrated the same set of primitive equations in 9 sigma levels using the same climatological forcing. The A2 physics makes use of a constant neutral surface drag coefficient, Prandtl mixing in the Ekman layer, and no turbulent transport in the free atmosphere so that convective adjustment is necessary. The E4 physics is much more physically realistic than the simple A2 physics. Monin-Obukhov similarity theory is used to compute a stability dependent surface drag coefficient, and the Mellor-Yamada level 2.5 second-order turbulent closure scheme is used throughout the atmosphere. The latter scheme explicitly computes the transport of heat so that the model's atmosphere can mix towards a stable lapse rate, thus eliminating the need for dry convective adjustment.

The limit of deterministic prediction is about 10 days, because the predictability of the short waves fails after this period. We hypothesize that, if a numerical model realistically treats all the physical processes and is of sufficient resolution, the planetary waves can be well-predicted throughout a long range integration. To better appreciate the planetary wave forecast, the ill-predicted short wave noise can be filtered out by time averaging the daily deterministic forecasts. Our hypothesis can be illustrated by showing what happens to the skill of the time averaged forecasts as the averaging time increases. In Figure 1 the daily and the 5-, 10-, 20-, and 30-day running mean 500-mb geopotential height correlations between the E4 grid point model forecast and NMC's analysis are plotted as a function of time. Also plotted for reference is the 10-day mean persistence curve. It is clear from Figure 1 that as the averaging time is increased, the skill increases and becomes more stable with time. This happens only for models that do not bias in some way the forecast of the planetary waves.

The performance of the other January 1977 simulations, particularly those produced by the spectral models, fail to predict well the planetary waves. To show this, the 10-day running mean 500-mb geopotential height correlations of all the simulations are plotted in Figure 2 where it can be seen that the spectral model forecasts of the planetary waves progressively decay with time. It is also evident in Figure 2 that the more sophisticated physics greatly improves both the grid point and spectral model forecasts of the planetary waves.

In order to conveniently show the daily forecasts of selected simulations, Hovmöller diagrams were constructed using the 40° to 50° meridionally averaged 500-mb geopotential heights from NMC's analysis, the grid point A2 and E4 model forecasts, and the spectral A2 model forecast. These diagrams are compared to each other in Figures 3 and 4. The stationarity and amplitude of the Aleutian low, the blocking ridge, and the Eastern United States trough are simulated by the grid point E4 model even to the extent that some hint is evident of the deepening of the eastern United States trough in the last 5 days of January. Like the E4 physics, the A2 physics scheme in the grid point model gives a forecast similar in appearance but is not able to develop the amplitude of the blocking ridge to the same extent as the E4 physics. The A2 spectral model loses completely the amplitude and stationarity of the blocking ridge and adjacent U.S. trough by day 20. Though not shown, the E4 spectral model was able to maintain some amplitude of the blocking ridge but could not simulate its stationarity.

The day 10 and the 25- to 30-day mean 500-mb geopotential height fields forecasted by the A2 and the E4 grid point and spectral models are compared to each other in Figures 5 and 6, respectively. The difference between these forecasts is not so great by day 10, but the difference is quite substantial for the 25-30 day mean. These figures show that the two spectral model forecasts have more of a tendency towards zonality than the two grid point model forecasts. Similarily, the A2 physics has more of a tendency to inject zonality into its forecast than does the E4 physics. Why the GFDL spectral numerical formulation should more zonally bias the forecast than the finite difference formulation is not clear. As for the physics parameterization schemes, the land-sea and other surface contrasts are more retained by the Monin-Obukhov surface physics and are more realistically mixed aloft by the Mellor-Yamada turbulent closure scheme than does the A2 physics. With more retention of zonal structure, it seems reasonable to believe that the E4 physics should retain more of the meandering nature of the westerlies as observed in Figure 5. It appears that the less zonal bias a model gives to its forecast the better its chances of simulating a block in the westerlies. This, we believe, is the reason for the success of the grid point E4 model simulation of the January 1977 blocking event.

In Figure 7 the last 20-day mean 500-mb geopotential height field of the grid point E4 forecast and NMC's analysis are shown along with the January climatology. The associated observed and forecasted anomalous 500-mb height fields are compared to each other in Figure 8. One observes that the unusually high pressure polar vortex was not forecasted at all, the forecasted Aleutian negative anomaly is displaced over Eastern Asia, and the Eastern United States trough was extended out into the Atlantic by the model to cause a rather large unobserved negative anomaly there. In spite of these failures, the last two of which might be improved upon by using the anomalous sea surface temperatures, the blocking ridge and Eastern United States anomalies and the other anomalies over North America, Greenland, Western Europe, and North Africa are sufficently well-forecasted to lend additional optimism to the eventual success of monthly numerical prediction.

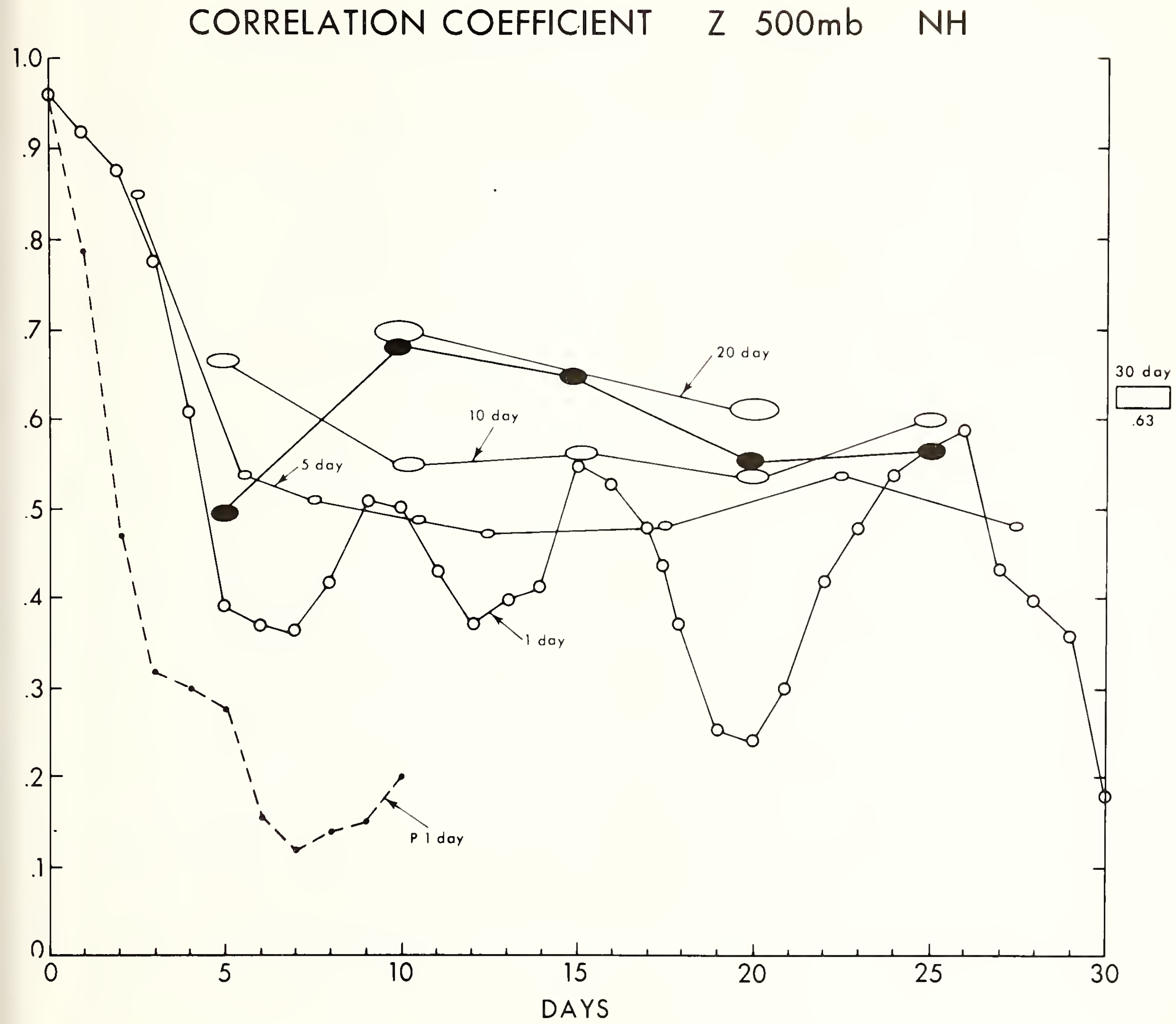

Figure 1. The daily (open circles) and the 5,10,20 (open ovals) and the 30-day (open rectangle) running mean 500-mb geopotential height correlations between the grid point E4 model forecasts and NMC analysis. For clarity the one day persistence (P 1 day; solid circles) is not continued byond day 10 as this curve oscillates within the other curves. The 10-day running mean persistence curve (solid ovals) is also shown and was computed using the Dec. 23, 1976, to Jan. 1, 1977, mean 500-mb geopotential heights.

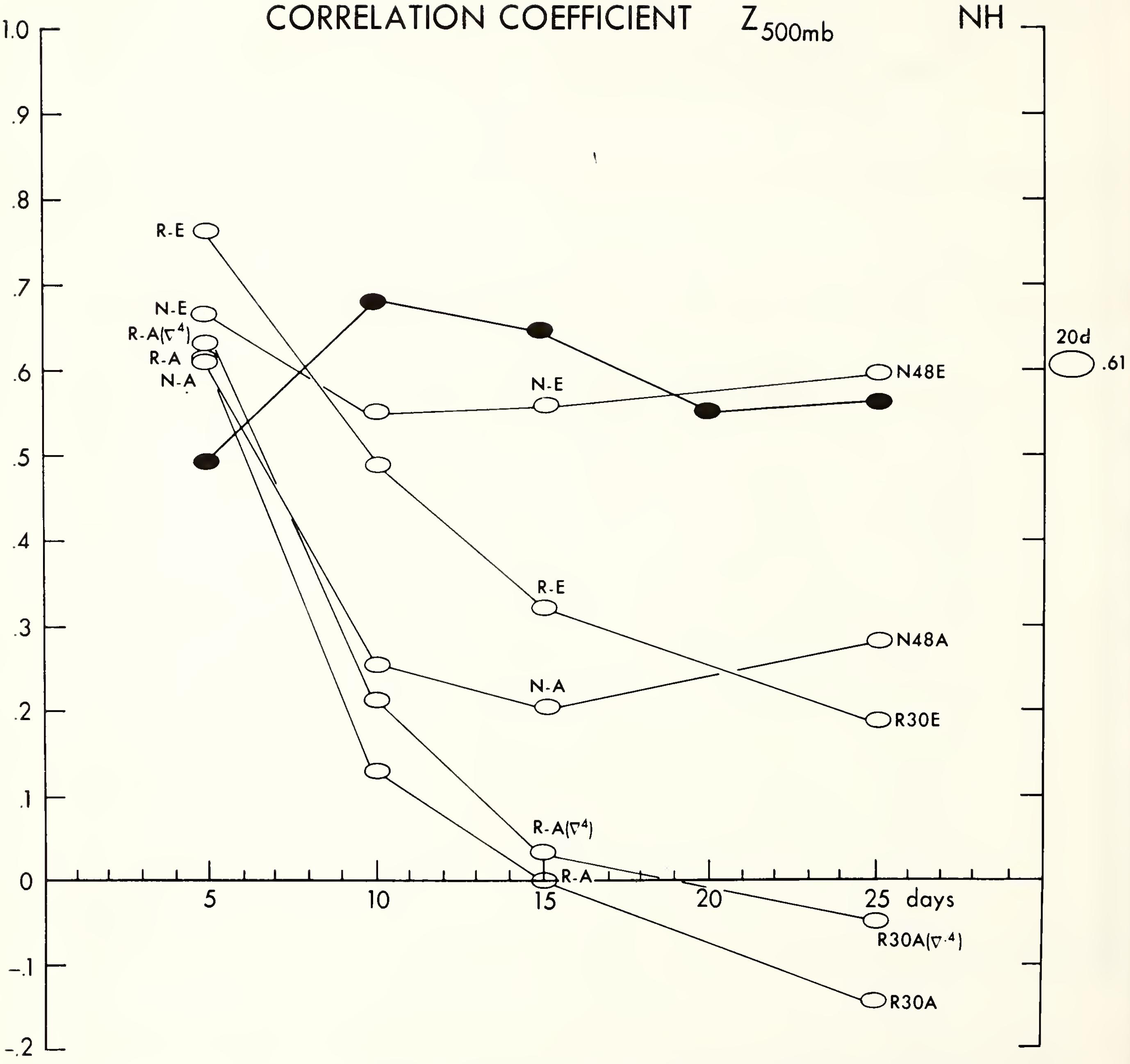

Figure 2. The 10-day running mean 500-mb geopotential height correlations between all the model forecasts and NMC analysis. The 10-day running mean persistence is shown as solid ovals and is the same persistence curve shown in Figure 1. N48 or N refers to the grid point model forecasts; R30 or R refers to the spectral model forecasts; the A and E refer to the A2 and E4 physics parameterizations, respectively; the del 4 refers to the uses of linear diffusion where all other forecasts not marked by del 4 used nonlinear diffusion.

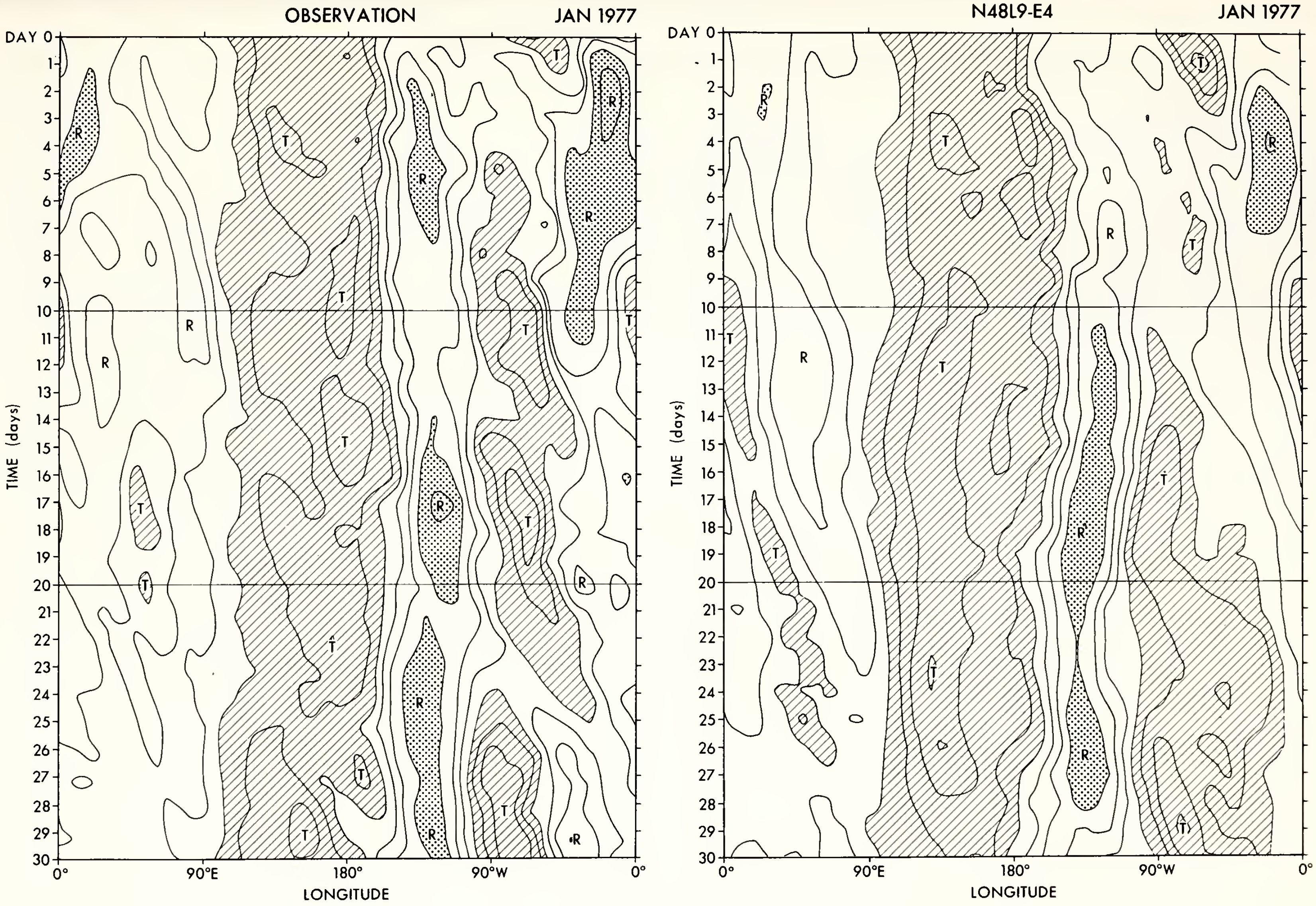

(a)

(b)

Figure 3. 40° to 50° meridionally averaged 500-mb geopotential heights vs. time for: (a) NMC January 1977 analysis (observations) (b) the grid point E4 model forecast (N48L0-E4; N48=48 grid rows between Equator and pole, L9=9 sigma levels, E4=Monin Obukhov and Mellor and Yamada turbulent transport formulations). Ridges and troughs are marked by R's and T's.

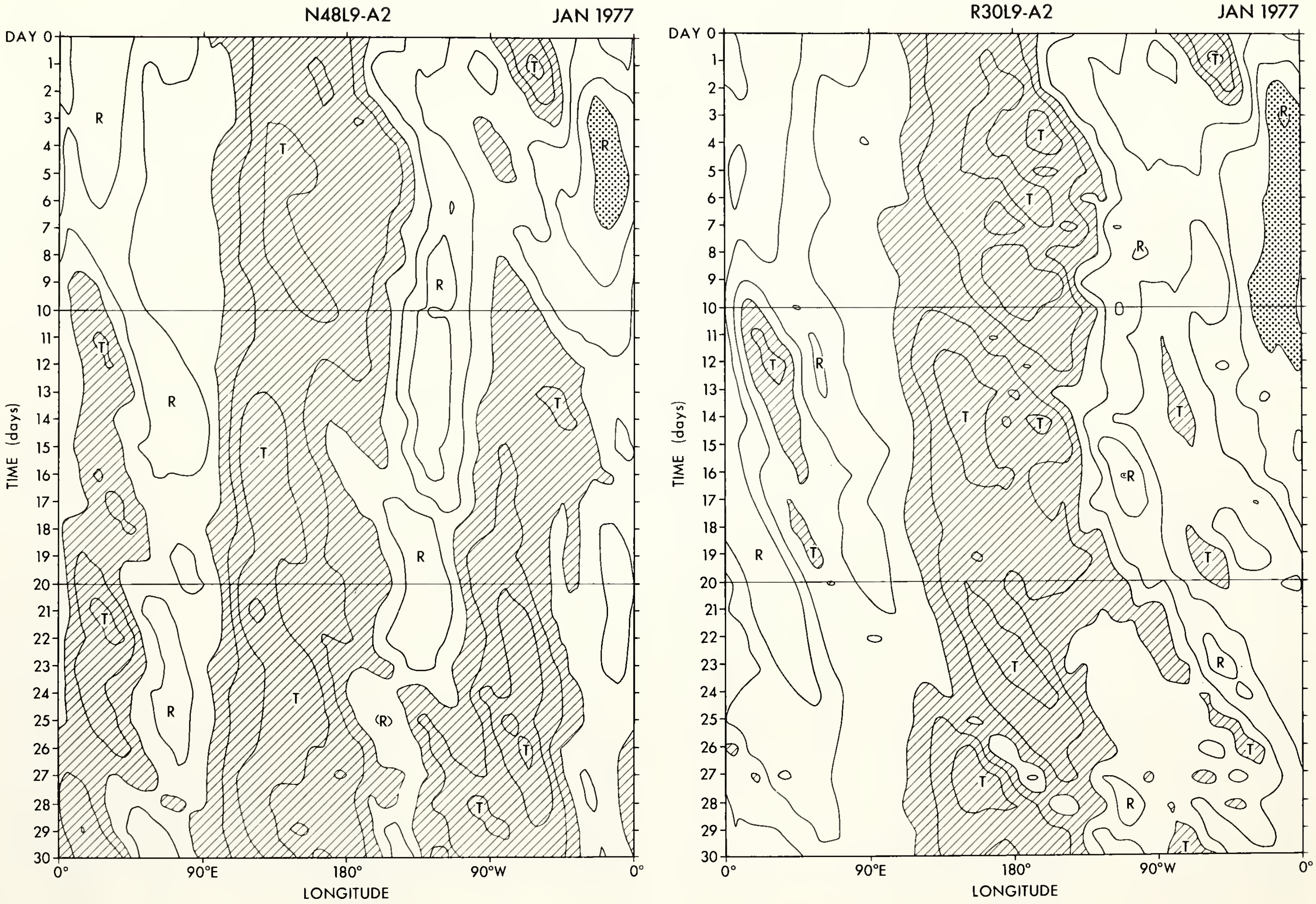

(a) (b)

Figure 4. Same as Figure 3 except for (a) the grid point A2 model forecast (N48L9-A2); (b) spectral A2 model forecast (R30L9-A2; R30 = rhomboidal 30 wave truncation).

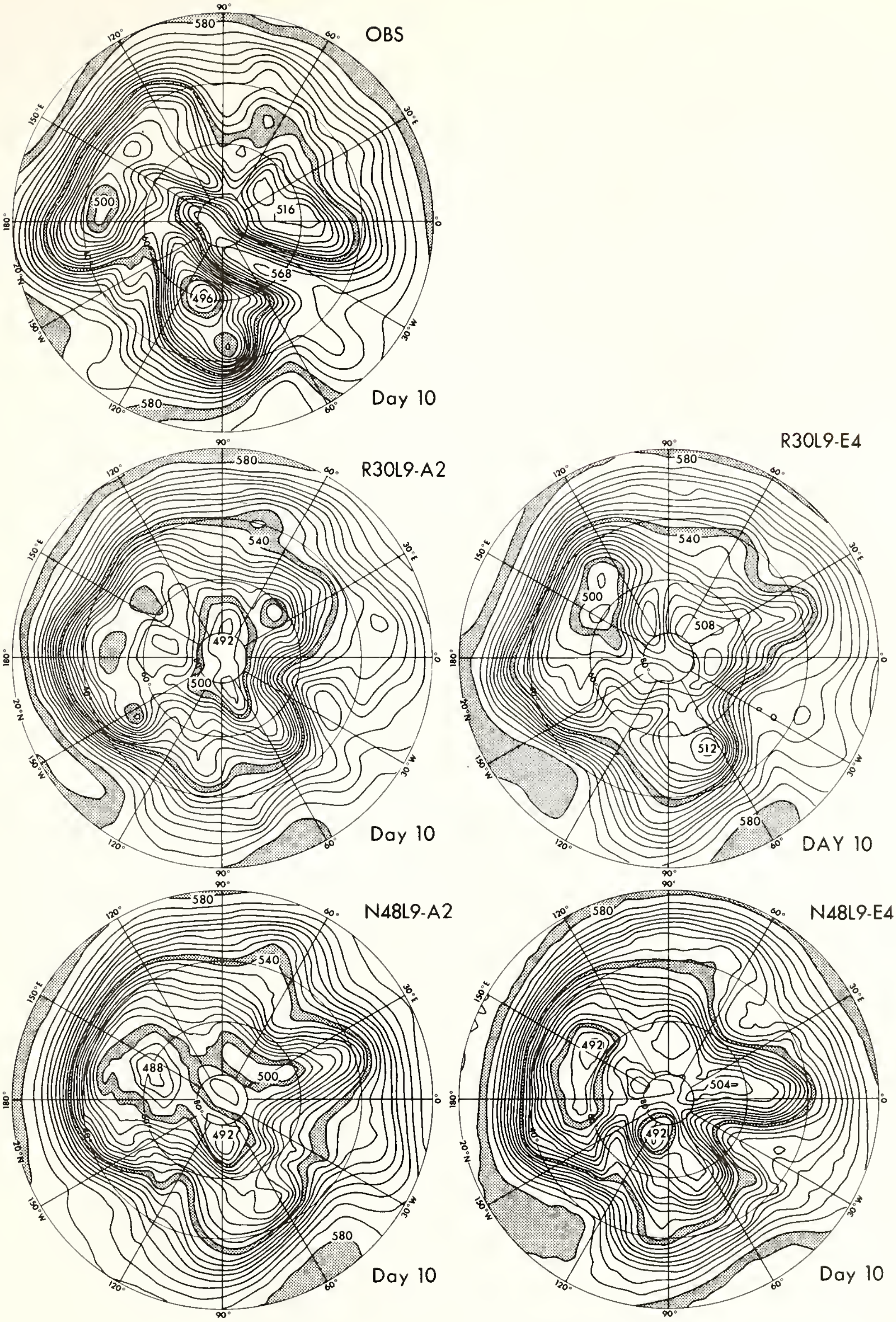

Figure 5. The day 10 500-mb geopotential height fields of the NMC analysis (obs), the spectral A2 and E4 forecasts (R30L0-A2; E4), and the grid point model forecasts (N48L9-A2; E4).

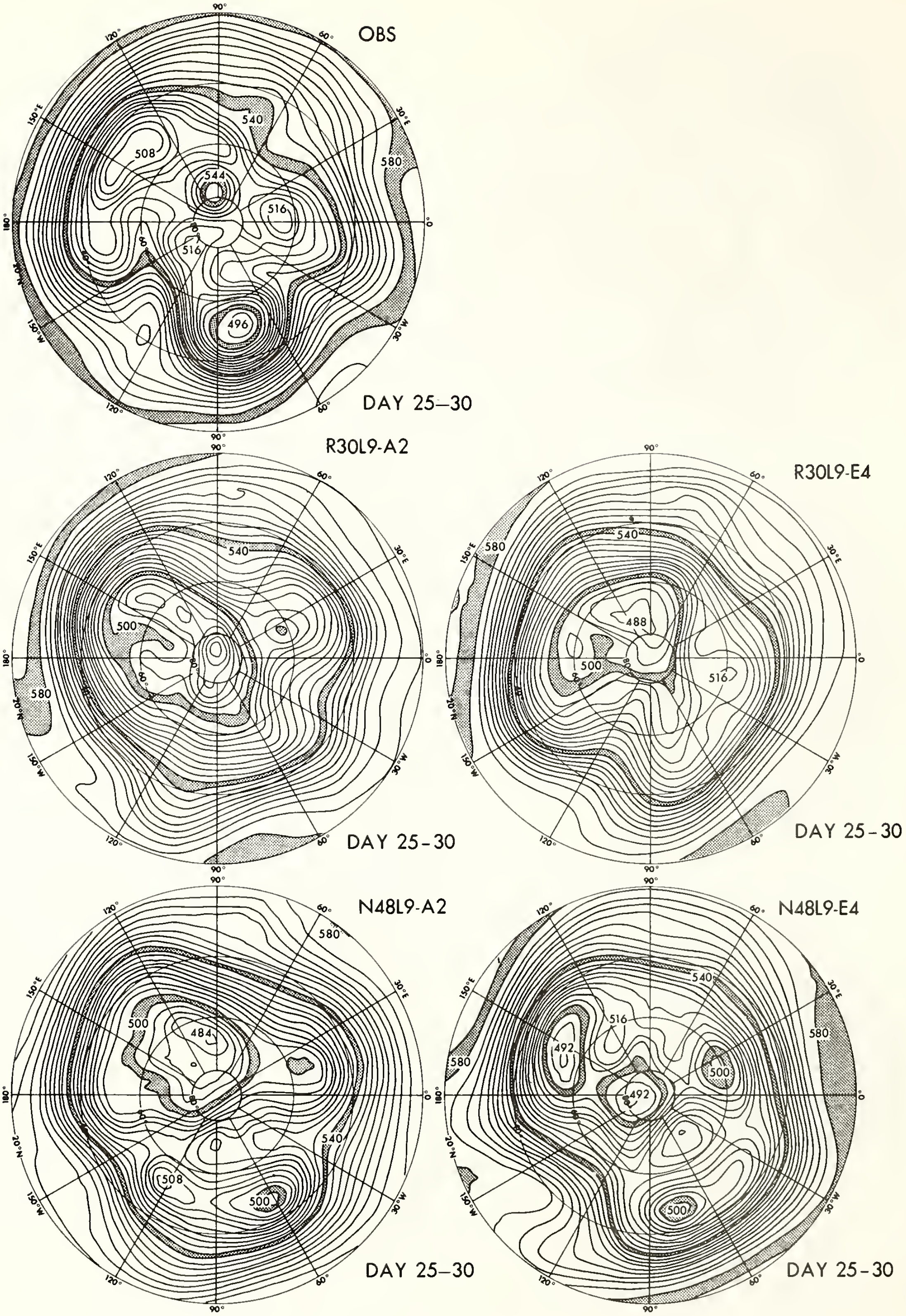

Figure 6. The 25- to 30-day mean 500-mb geopotential fields of the NMC analysis (obs), the spectral model A2 and E4 forecasts (R30L9-A2; E4), and the grid point A2 and E4 model forecasts (N48L9-A2; E4).

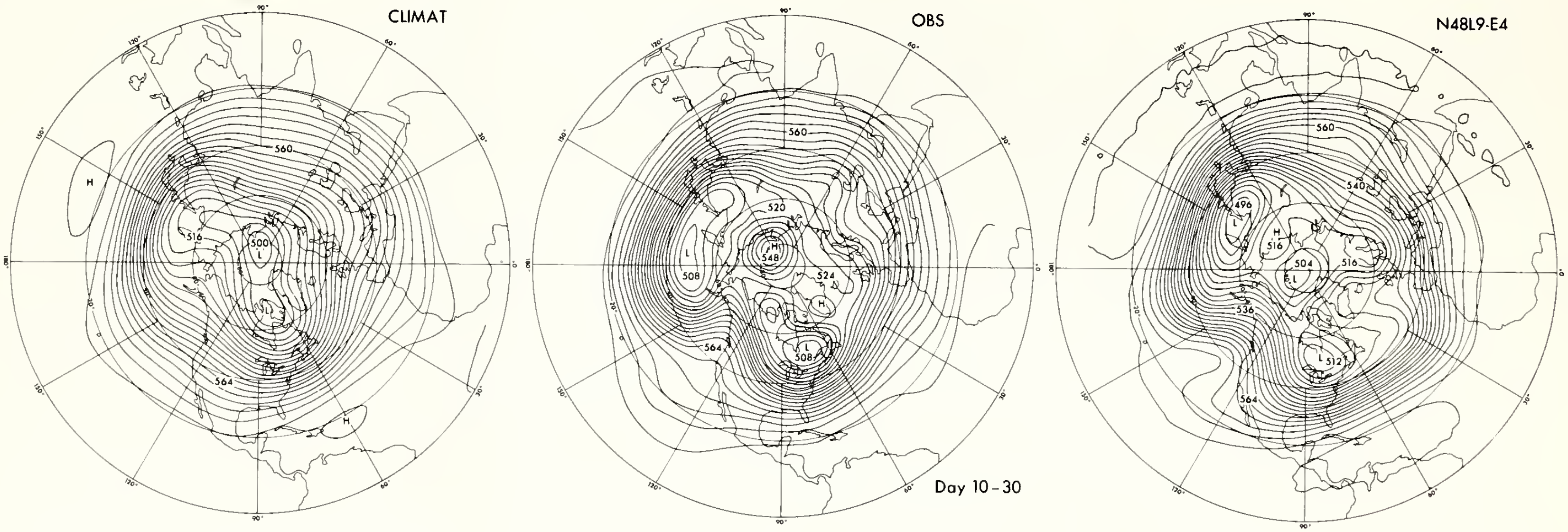

(a) (b) (c)

Figure 7. The Northern Hemisphere 500-mb geopotential heights for: (a) January climatology, (b) the 10-30 day mean January 1977 observations (NMC analysis), and (c) the 10-30 day mean grid point E4 model forecast.

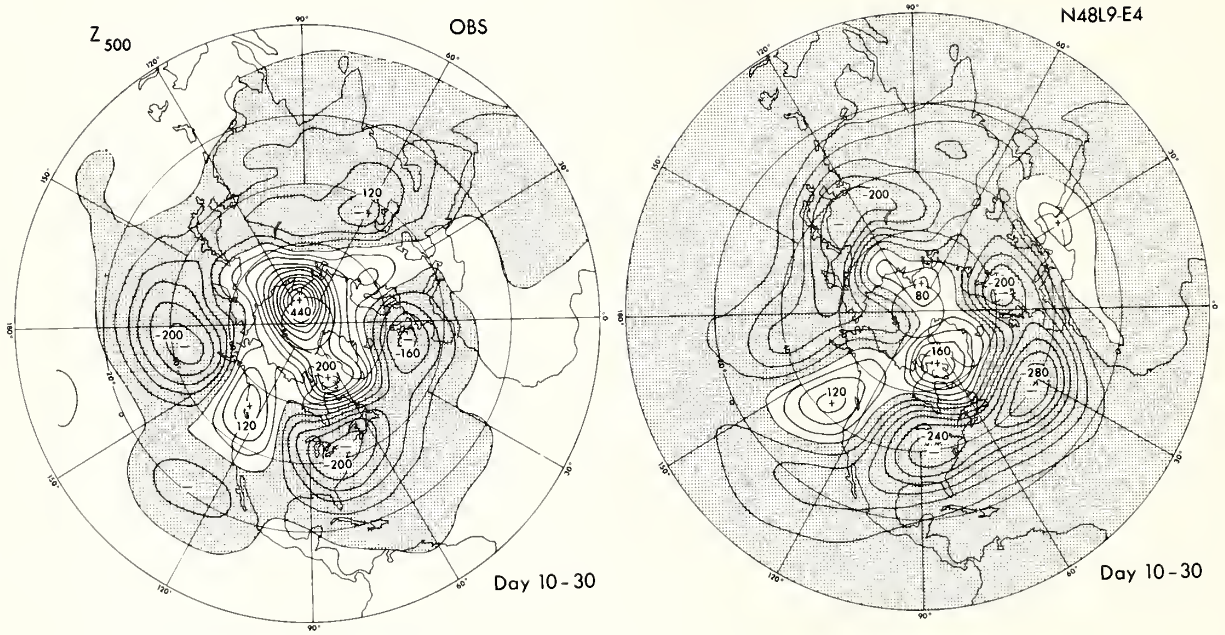

(a)

(b)

Figure 8. The 10-30 day mean 500-mb geopotential height anomaly (Figures 7b and 7c minus climatology) fields for (a) observations (NMC's analysis), and (b) grid point E4 model forecast.

SOME PRELIMINARY THOUGHTS ON COMPARING GENERAL CIRCULATION MODELS WITH OBSERVED DATA FIELDS

R. W. Preisendorfer and T. P. Barnett

Methods for rigorously comparing the full output from general circulation models (GCM) with observed data fields are generally not at hand. The limited methods that could be used for these purposes, where available, are generally not applied to evaluate the validity of the GCM. With this in mind we are striving to find simple, yet rigorous, means for determining the validity of first and second moments of the fields produced by the general circulation models.

One of the approaches we are investigating that appears promising is that of the minimal spanning tree. This technique essentially works with the relative separations and connections between, say, two clusters of data. Examples of typical clusters are shown in Figures 1 and 2. In both cases the clusters have been centered on zero mean so we are looking at a measure of the variability of the data fields. Suppose one were to ask, with regard to Figure 1, are the two data sets different? The answer, from looking at the diagram, would be clearly yes. Realizing that the diagram consists of January (X) and August (O) monthly temperatures for Charleston and Jacksonville, one would say that intuition has been correct. The second diagram, on the other hand shows the January (X) and February (O) temperatures again at these two southern stations. If one were now asked, is February significantly different from January at the two stations, the answer would not be so clear. The minimum spanning tree approach, however, is designed to quantitatively just make such destinctions.

So far results with this method have been encouraging. We are presently engaged in measuring the "power" of the technique with respect to various of its competitors. Figure 3 shows examples of these power tests.

The upper panel shows the results for what we call a scale test, i.e., is the scatter of the two data sets in Figures 1 and 2 the same or not? Given an idealized data set, we can make many simulations of the minimum spanning tree approach to arrive at an estimate of what percentage of the time the technique would be able to discern between two data sets that had similar, but different, standard deviations. The upper diagram shows that if one data set had variance equal σ and the other variance 0.8 σ and then with 90% confidence (power = 0.9) we would be able to say that the data sets were drawn from different populations.

The lower panel of Figure 3 shows what we call a location test, i.e., a test of the difference of the mean fields between two given data sets. It is also possible on this diagram to show the power of the Hotelling's T^2 test, the classical way of measuring the statistical similarity between two mean fields when each field has the same variance. The test shows that the minimum spanning tree approach is only slightly less powerful than the Hotelling T^2 test. However, the results show that if the variability of the two fields that are being compared is different, e.g., $\sigma_1 = 1, \sigma_2 = 0.2$, then the Hotelling approach has no power for relative offset of one unit between the fields, i.e., the testing procedure is inapplicable. The same restriction does not apply to the minimum of spanning tree method.

We are now actively developing a battery of tests that can be used to evaluate the similarity in space and time of any two fields, be they a comparison of model-data, a comparison of model-model, or finally an intercomparison of two supposedly similar data fields. We feel that these tests, when finished, will be of particular use in a wide range of geophysical problems.

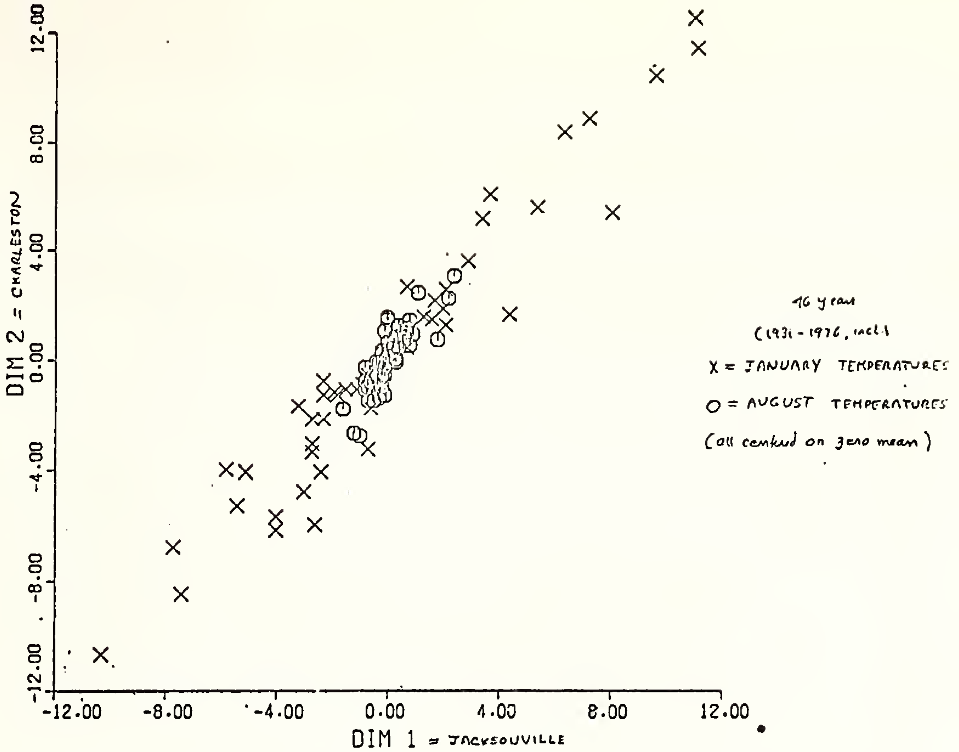

Fig. 1 Two dimensional projection of 32-dimensional swarm of 46 temperatures on two selected cities.

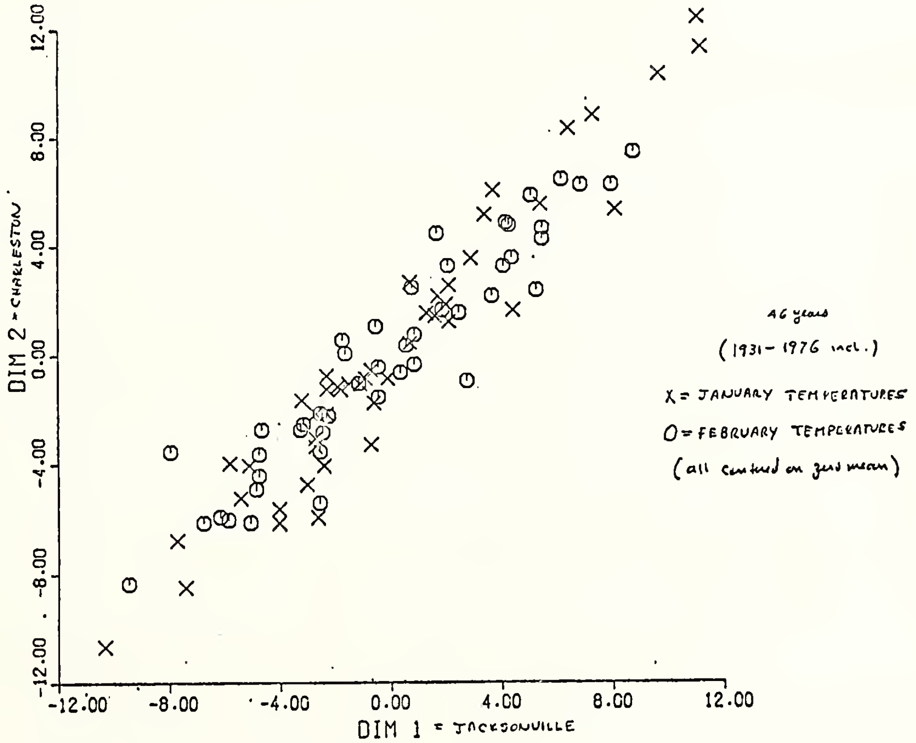

Fig. 2 Two dimensional projection of 32-dimensional swarm of 46 temperatures on two selected cities.

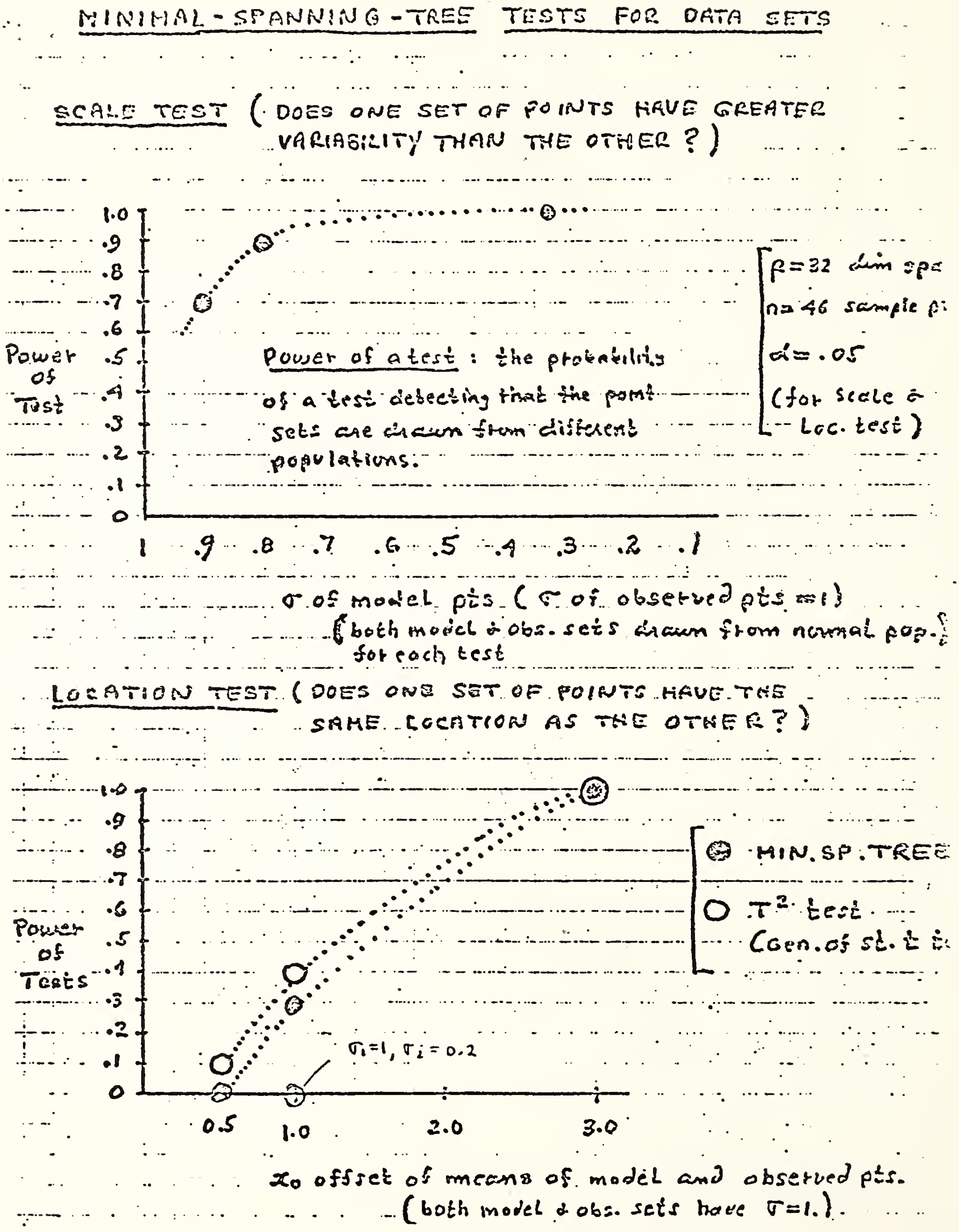
MINIMAL-SPANNING-TREE TESTS FOR DATA SETS
SCALE TEST (DOES ONE SET OF POINTS HAVE GREATER VARIABILITY THAN THE OTHER ?)
1.0
.9
.8
.7
.6
.5
.4
.3
.2
.1
0
Power of Test
Power of a test : the probability of a test detecting that the point sets are drawn from different populations.
p=32 dim sp
n=46 sample p
α=.05
(for Scale & Loc. test)
1
.9
.8
.7
.6
.5
.4
.3
.2
.1
σ of model pts (σ of observed pts =1)
{both model & obs. sets drawn from normal pop. for each test
LOCATION TEST (DOES ONE SET OF POINTS HAVE THE SAME LOCATION AS THE OTHER ?)
1.0
.9
.8
.7
.6
.5
.4
.3
.2
.1
0
Power of Tests
MIN. SP. TREE
T² test
(Gen. of st. t
σ₁=1, σ₂=0.2
0.5
1.0
2.0
3.0
x₀ offset of means of model and observed pts.
(both model & obs. sets have σ=1.)

Fig. 3

Atmospheric Response To Sea Surface Temperature Anomalies

Peter J. Webster
CSIRO Division of Atmospheric Physics, Aspendale, Victoria, Australia

A simple model is used to study the mechanisms which control the local and remote (teleconnection) response of the atmosphere to the thermal forcing resulting from sea surface temperature (SST) anomalies located at various latitudes. The model chosen is a linear baroclinic spherical primitive equation model containing a zonally symmetric basic state with horizontal and vertical shear which resembles the observed annual mean. A total quasi-non-linear diabatic heating format which reacts to the sea-surface temperature anomaly is developed.

Depending upon the latitudinal location the SST anomaly two major limits of atmospheric response may be identified. The first, the "diabatic limit", occurs with the SST anomaly embedded in weak low-latitude basic flow and results in a strong enhancement of the initial anomaly response through a vigorous positive dynamics-diabatic heating feedback. Strong teleconnections are evident between low and high latitudes. The second domain, the "advective limit", occurs when the SST anomaly is placed at higher latitudes in the vicinity of the westerly maximum. The local response is extremely small due to the creation of an indirect zonal circulation in the vicinity of the anomaly which is related to the strength of the local basic flow and the latitude of the forcing due to rotational limitations on the relative scale of the vertical velocity.

Fig. 1 shows the vertical velocity response of the model atmosphere relative to the influence of an SST anomaly centered at the solid circle. As the SST anomaly is moved from $\mu_o = 0.1$ (7°N) to $\mu_o = 0.6$ (37°N), the vertical velocity response decreases in amplitude and the rising motion tends towards quadrature with the heating, clearly indicating the diabatic and advecture limits of the response. Figs. 2 and 3 show the upper tropospheric model response (geopotential and velocity vector) for the $\mu_o = 0.1$ and 0.6 cases.

The model results are used to interpret the experiments of general circulation models (GCM) and provide a rationale for the existence of teleconnections found between low and high latitudes when SST anomalies were imposed in the equatorial oceans.

GCM experiments fall into two classes. Experiments in which the SST anomaly is placed near the Equator show a strong local response near the Equator and a significant response at high latitudes, whereas when the anomaly is at high latitude the response is minimal. As the GCM's used January or mean annual insolation distributions, their response is interpreted as approximating the "diabatic" limit with an equatorial anomaly and an "advective" limit when the anomaly is at high latitudes. Furthermore, the results suggest why "super-SST-anomalies" were required in mid-latitudes in some GCM experiments in order to produce a response which was measurable above the "noise level" of the model.

The model results are used to interpret the apparent paradox shown by the statistical observations of Namias and Davis. It is suggested that SST anomalies in the winter middle and higher latitudes possess little climatic influence because the response is in the advective limit. On the other hand, the influence of the SST anomalies in the summer middle and high latitudes will be greater as with the significantly smaller basic westerly winds, the response is closer to the "diabatic" limit than the "advective" limit.

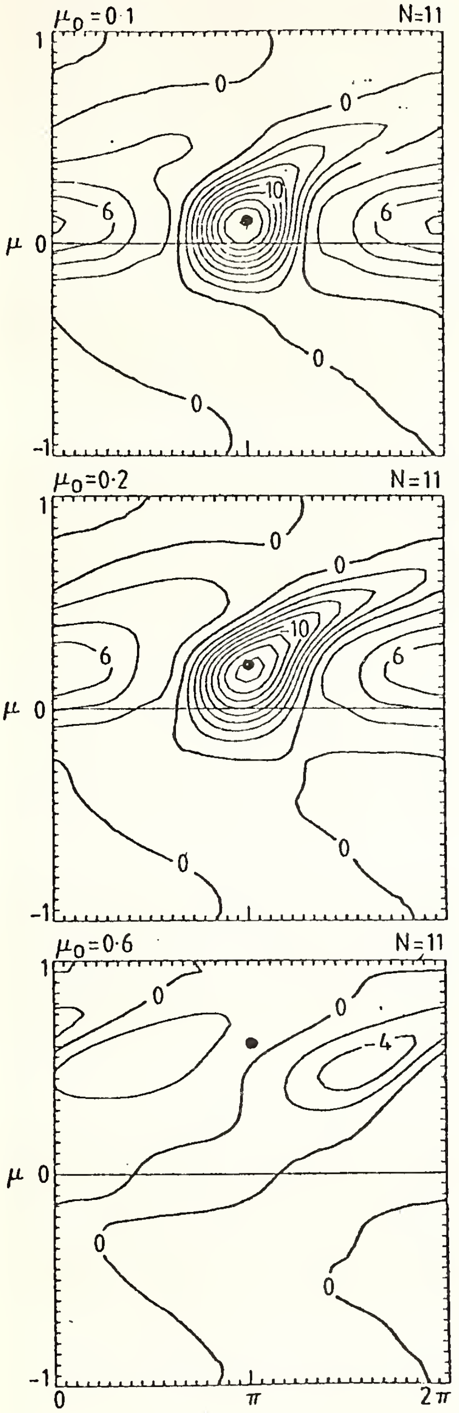

Fig.1: Converged vertical velocity fields (units 10^{-3}N m^{-2}s^{-1}) for SST anomaly locations 5.7°N, 11.5°N, and 36.9°N. Solid circle indicates the location of the heating maximum. Negative values indicate rising motion.

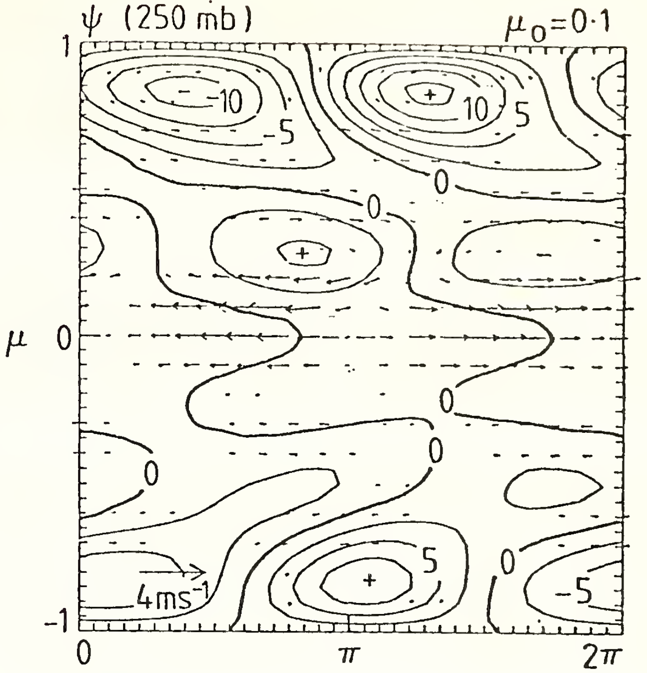

Figure 2. Associated fields of horizontal velocity and geopotential (units: m) at 250 mb for the SST anomaly located at μ_o = .1 (7°N). Velocity vector scale denoted in bottom left corner of panel. Vectors of magnitude less than .5 m s^{-1} are omitted.

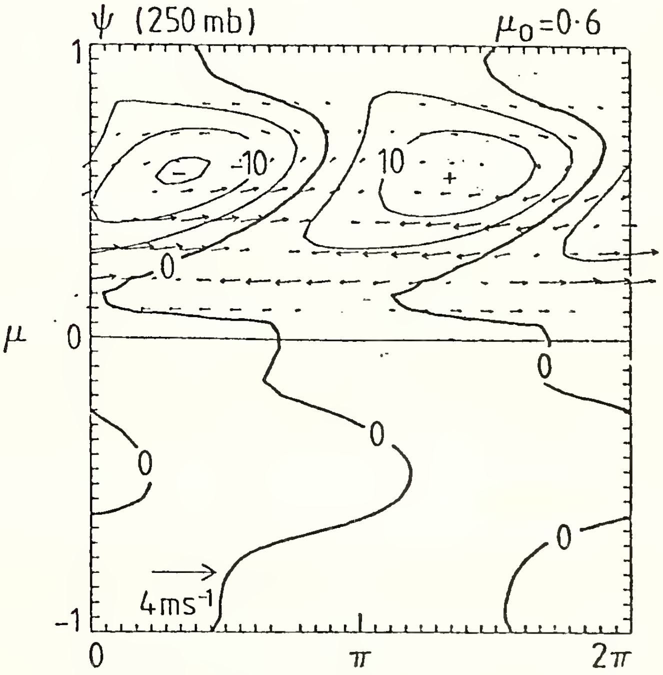

Figure 3: Same as Fig.2, but for the SST anomaly located at μ_o = .6 (36.0°N).

Measuring Skill In Climate Model Forecasts

Lt Col Gerald J. Dittberner
USAF Environmental Technical Applications Center
Scott AFB IL 62225

I. Introduction

How good is a set of climate forecasts? More fundamentally, at a time when current methods have notoriously limited skill, can it be shown that such a method has skill at all? Answers to these questions require an organized framework in which to exercise carefully conceived procedures.

We have developed a quantitative evaluation capability in an attempt to determine if models have skill. It uses the probability-based skill score developed by I. Gringorten (1965) of the Air Force Geophysics Laboratory (AFGL). Using P_F for the cumulative climatic probability, less than or equal to the predicted quantity (F), P_V for the cumulative climatic probability, less or equal to the observed (or verified) quantity (V), then the score (s_{FV}) assigned to a pair (F,V) is given by

$$s_{FV} = -\ell n \; \{ (1-P_F)P_V \} -1 \quad \text{when } P_V \geq P_F$$

$$= -\ell n \; \{ (1-P_V)P_F \} -1 \quad \text{when } P_V < P_F$$

For example, using the winter of 1976 in St Louis, we find that the mean winter temperature is 1.01C and the standard deviation is 1.75C. The observed temperature for 1976 was 2.0C, which gives a cumulative probability of 0.715. The forecast value was 1.8C, which yields a cumulative probability equal to 0.681. The equation above then yields a skill, in this case, of 0.478.

Other attributes of the scoring system are illustrated in the plot of P_F against s in Figure 1. The range of possible scores depends on the chosen forcast (P_F). the range is narrow for a median forecast, but can vary from -1.0 to very large scores when a rare event is successfully predicted. An unskilled forecast always has an expected, or average value, of zero. Hence, the strategy of selecting a certain forecast for perfect forecasting will vary from 0.37 to infinity, still averaging 1.0.

2. Procedure

The methodology for deciding how much confidence we have in saying a model is skillful is relatively straightforward. It is purposely designed for models which produce forecasts of parameter values, i.e., 10.1C, or 57mm.

Step 1. Write down the confindence level above which you are willing to say that skill exists. For the purpose of illustration, we choose the value 95%.

Step 2. Design a theoretical model of no skill. The no-skill model used here is composed of actual forecasts and random observations. Since we found that the distribution of skill scores depends, sometimes significantly, on the distribution of actual scores, this selection automatically accounts for the bias that would otherwise be introduced.

Step 3. Generate the test (no-skill) distribution of skill scores. This can be done in several ways. One is by selecting a large number (say 18,496) of random observations for each normalized forecast value to determine the skill score distribution for no-skill forecasts. Another is the calculate, for a given forecast value, the probability that chance has a score, s, exceeding some specified threshold value, and forming a histogram of scores by stepping through a series of threshold values. Further details can be found in Gringorten, et al. 1980. An example of this theoretical distribution can be seen as a solid curve in Figure 2.

Step 4. Calculate and plot the distribution of actual skill scores, based on actual forecasts and actual observations. This is represented in Figure 2 by the dashed line.

Step 5. Compare the two distributions. Use one of the many standard statistical tests to determine the level of confidence with which one can say that the two distributions are different. We compared the percent of actual scores, beyond the point at which there are 10% of the no-skill scores. In Figure 2, we found 12.1% beyond this 10% point. The probability of attaining 12.1% when only 10% are expected from 12,336 independent samples, is much much less than one in ten thousand, or, a confidence of greater than 99.99% that the two distributions are different. Since this is greater than the confidence level chosen in step 1, we conclude that the model in question has skill.

We must point out here, that the question of independence was not addressed in detail and remains unresolved. However, even if the number of independent scores is only one tenth of the total number of scores, the confidence level decreases only to about 99.5%. This can be seen by comparing the likelihoods expressed in Figures 5 (7550 samples) and Figure 6 (618 samples).

3. Results

Several climate models have been subject to the scrutiny of this evaluation capability. Some results are shown in Figures 2 - 6.

We have already alluded to seasonal temperature forecasts from the USAFETAC Sea Level Pressure (SLP) Analog Model (Schofield and Barnett, 1978) in Figure 2. Under our evaluation technique, this model is skillful.

Among other models we examined, a version of the University of Wisconsin model called "1980-MARK II" (details are presented elsewhere in this volume) is also deemed skillful. Figure 3 shows the evaluation of the best month (March) for year-ahead monthly temperature forecasts. Figure 4 shows "all months" (we did not have April and May). We conclude that these year-ahead forecasts of monthly mean temperature are skillful.

Figure 5 shows the evaluation of the best month (March) for year-ahead precipitation amount forecasts from the same model, and Figure 6 shows the "all months" (again only ten months) evaluation showing skill in year ahead precipitation forecasts.

4. Conclusions

In conclusion:

1. We have developed a rudimentary, quantative, climate model skill evaluation capability, which seems to successfully indicate the existence of skill.

2. Some details of the technique remain to be examined further, notably the question of independence.

3. Several models were examined, leading to the conclusions that:

a. USAFETAC SLP Analog forecasts of seasonal mean temperature are skillful.

b. University of Wisconsin 1980-II year-ahead forecasts of monthly mean temperature are skillful.

c. University of Wisconsin 1980-II year-ahead forecasts of monthly total precipatation are skillful.

4. The question of "how good forecasts are" is a different question than "can the existance of skill be demonstrated." Only the latter has been addressed here. The former remains as a continuing challenge to us all.

Reference

Gringorten, I. I., 1965: A measure of skill in forecasting a continuous variable. J. Appl. Meteor, 4, pp 47-53.

Gringorten, I. I., G. J. Dittberner, A. R. Boehm and J. G. Schofield, 1980: Evaluation of forecasts with scores based on climatic probabilities. Preprints, WMO Symposium on Probabilistic and Statistical Methods in Weather Forecasting, Nice, France, 8-12 Sep 80, pp 189-193.

Schofield, J. G., and T. P. Barnett, 1978: A sea level pressure analog model for predicting temperature over the Northern Hemisphere. Proceedings of the Third Annual Climate Diagnostics Workshop, Miami, Florida, 13 October - 2 November 1978, pp 34-1 to 34-6.

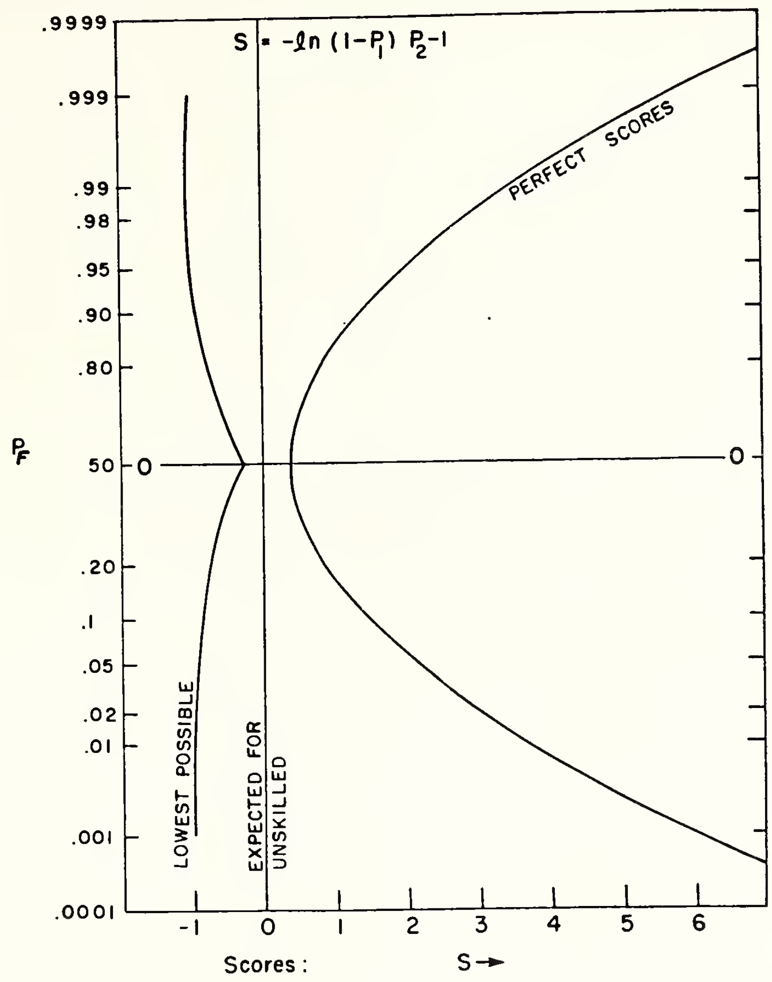

FIGURE 1

The distribution of scores as a function of P_F, from the lowest possible to the maximum, or perfect score.

Actual vs. Theoretical Distribution of 12336 Individual Gringorten Scores

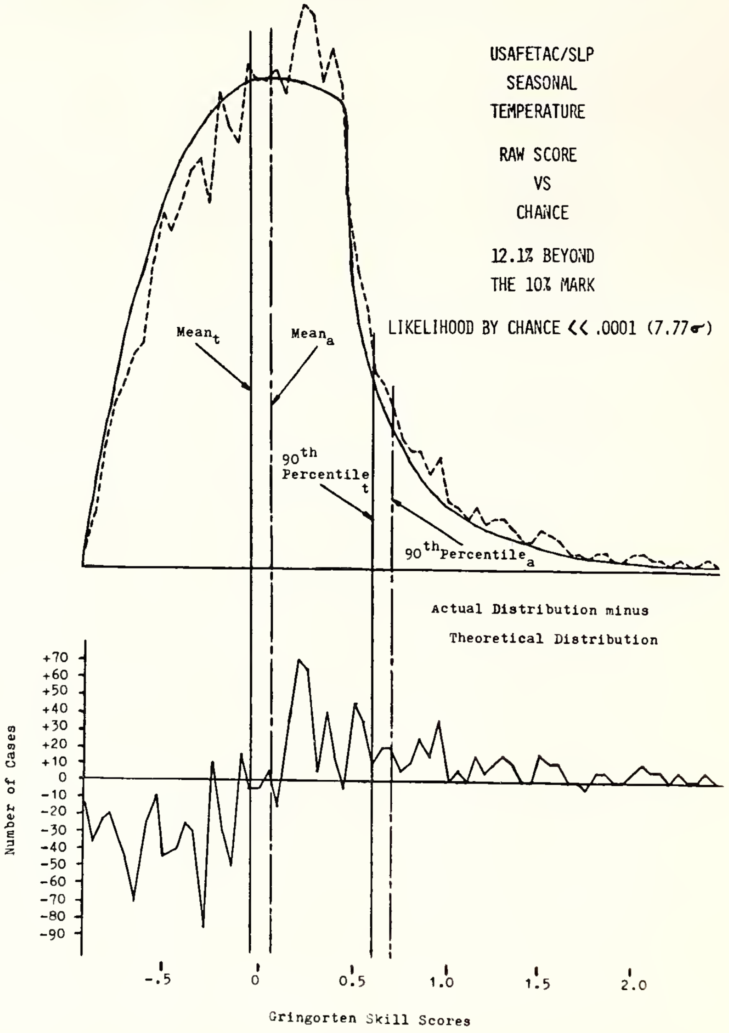

FIGURE 2

Actual vs. Theoretical Distribution of 759 Individual Gringorten Scores

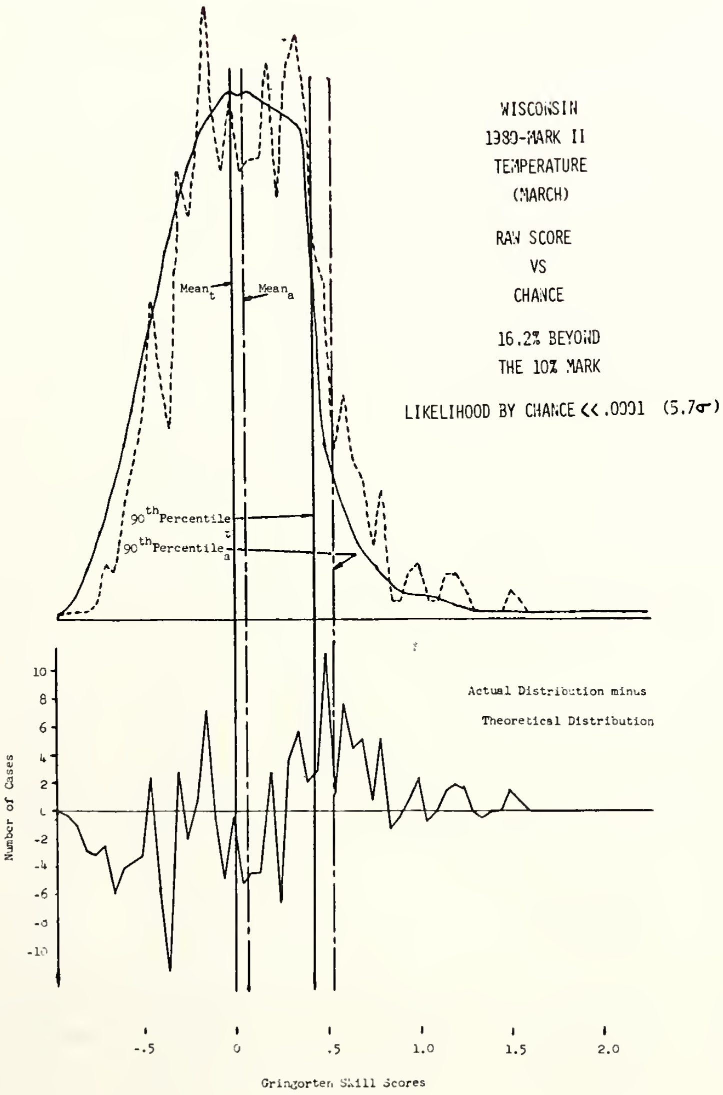

FIGURE 3

Actual vs. Theoretical Distribution of 7791 Individual Gringorten Scores

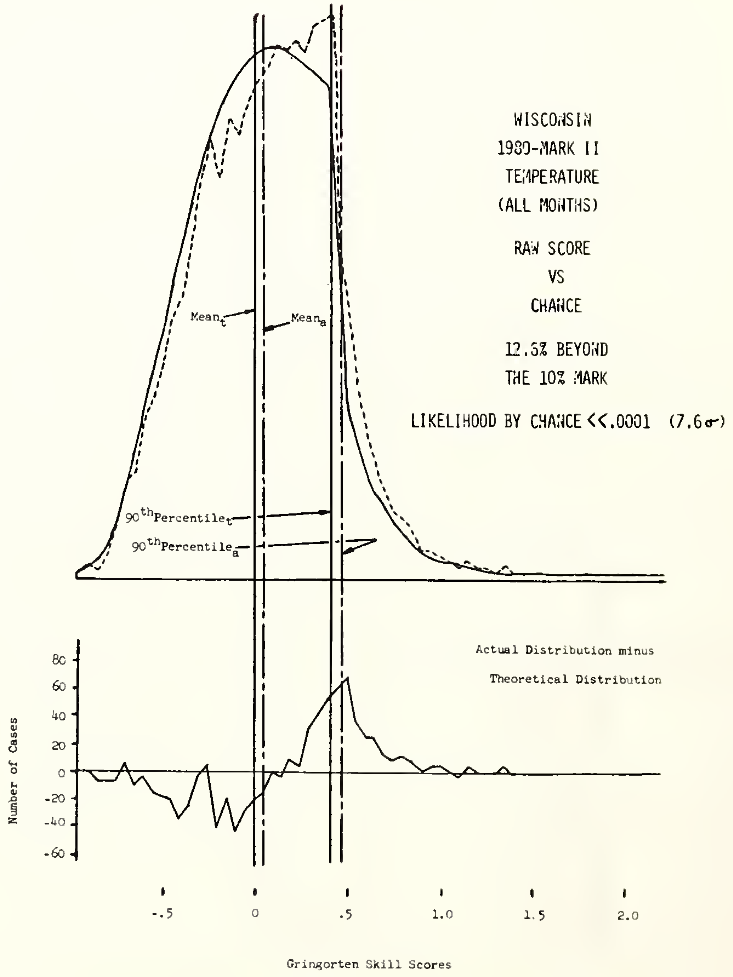

CONCLUSION: WISCONSIN 1980-MARK II TEMPERATURE FORECASTS ARE SKILLFUL.

FIGURE 4

Actual vs. Theoretical Distribution of 618 Individual Gringorten Scores

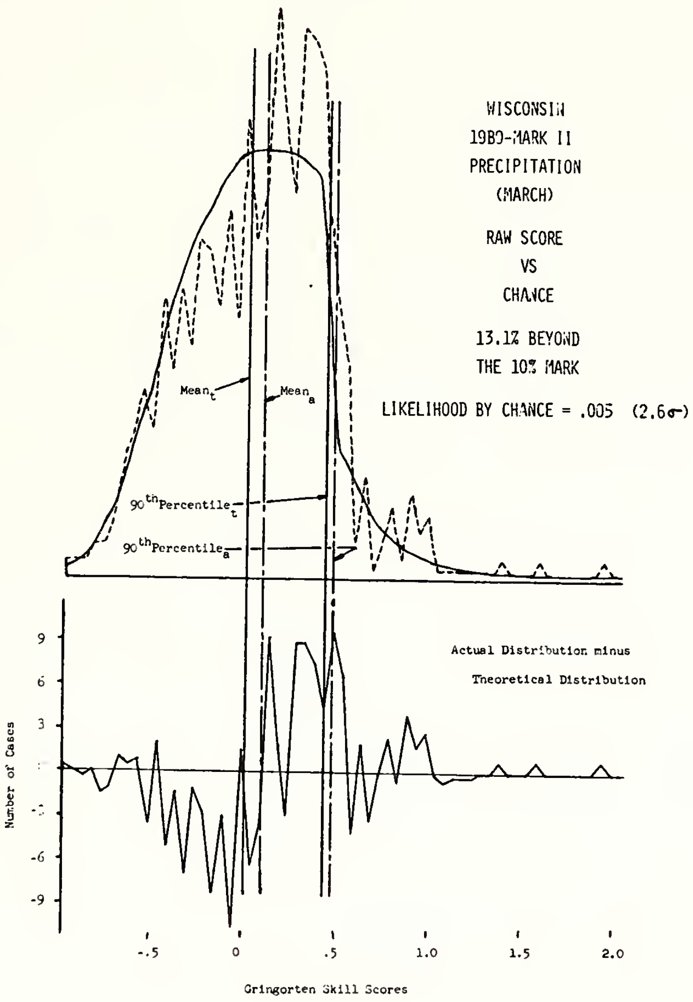

FIGURE 5

Actual vs. Theoretical Distribution of 7550 Individual Gringorten Scores

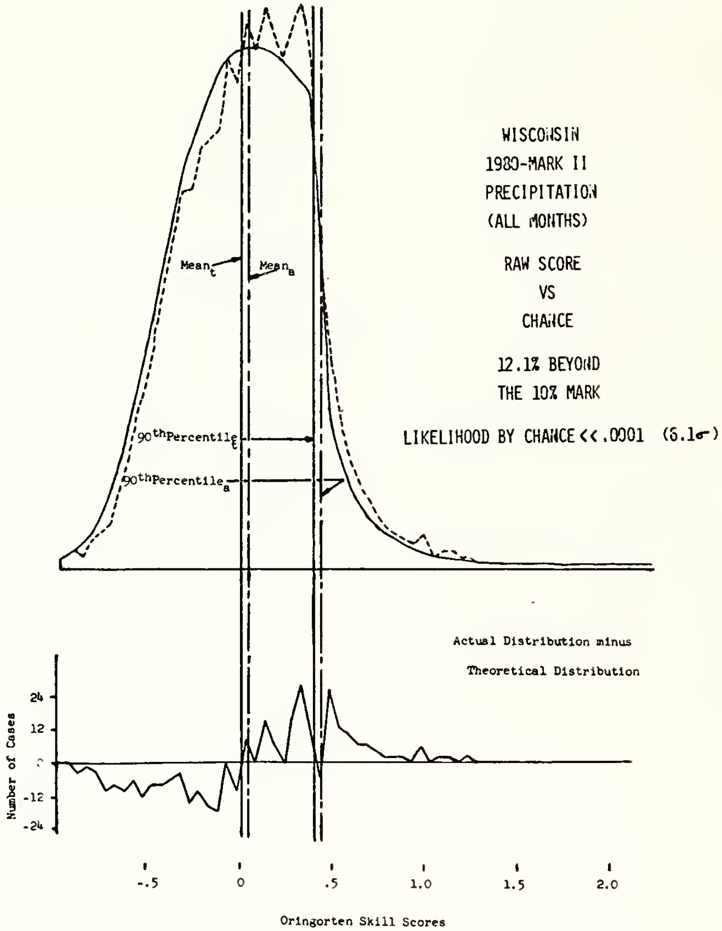

CONCLUSION: WISCONSIN 1980-MARK II PRECIPITATION FORECASTS ARE SKILLFUL.

FIGURE 6

On the Inherent Superiority of the Persister in Forecasting Markovian Weather Patterns

Rudolph W. Preisendorfer
Pacific Marine Environmental Laboratory/NOAA
3711 15th Avenue Northeast
Seattle, Washington 98105

1. Introduction

It is a fact that, on the average, the predictions of seasonal temperature and precipitation patterns over the mainland United States are best done by the method of persistence. In this method, one simply predicts the next season's temperature and precipitation pattern by using as the prediction the current season's temperature and precipitation pattern. Knowledgeable forecasters, poring over their charts and tables, drawing on their intuition to supplement hard data, and placing all these things into a hopper still cannot consistently beat the Persister, i.e., the forecaster, using the method of persistence. In this article we cannot give a full analysis of this interesting state of affairs in short-term climate predictability. However, we will perform a simple thought experiment in which three well-known types of 'mechanical' forecasters are given the problem of forecasting a Markovian weather pattern of the simplest type. The forecasters are: the Persister, Markover, and the Analoger. In this simple setting the Persister's superiority is again evident. Moreover, having put the Persister and his two competitors under glass, we will be able to see, at least in this one controlled setting, why the Persister is so good. Before defining these forecasters in the context of the present discussion, we will review briefly the notion of a Markovian weather pattern.

2. Markovian Weather Patterns

Picture a map of the United States (say). Fix in mind a point on the map. Simplify the temperature variations at that point so as to be describable using only A, N, and B classes (above, normal, below). As time goes on (season to season, say) the temperature will change from one of these three classes to another (possibly the same) class. Given the records one could make a table of transition probabilities for the probability of going from one state to another in successive seasons. If this transition probability from season n to n+1 depends only on the state in the present season, i.e., season n, then the weather pattern at that point is Markovian. (If the transition probability depended on the states in one or more seasons in the past, it would not be Markovian, but rather of a more general stochastic kind.) Therefore, a Markovian weather pattern can be characterized by a 3x3 matrix:

$$\underline{W} = \begin{bmatrix} w_{11} & w_{12} & w_{13} \\ w_{21} & w_{22} & w_{23} \\ w_{31} & w_{32} & w_{33} \end{bmatrix} \tag{2.1}$$

where w_{ij} gives the probability that the weather will be in state j in season n+1 if it is in state i in season n. Here, for notational simplicity, we set 1=B, 2=N, 3=A. The rows and columns of $\underline{W}$ are chosen to add up to 1, in order that it represent a regular Markovian weather pattern.

We will define here a simple instance of (2.1), namely a one-parameter Markovian transition matrix of the form

$$\underline{W} = \begin{bmatrix} w & 1/2(1-w) & 1/2(1-w) \\ 1/2(1-w) & w & 1/2(1-w) \\ 1/2(1-w) & 1/2(1-w) & w \end{bmatrix} \tag{2.2}$$

Here w is the weather persistence index, $o \leq w \leq 1$. If w is near 1, the weather is highly persistent. If w is near 0, the weather is highly variable, as may be checked by studying (2.2), and recalling the meaning of w_{ij}. If w=1/3, all entries of $\underline{W}$ are 1/3, indicating a uniformly random occurrence of the three states. The value w=1/3 is the dividing point between the variable and persistent regimes in the index range $o \leq w \leq 1$.

3. Markovian Weather Forecasters

One may anticipate a better performance than that of the Persister if the forecaster had some strategy based on knowledge of past weather patterns, say in the form of a table of forecast probabilities of the form

$$\underline{F} = \begin{bmatrix} f_{11} & f_{12} & f_{13} \\ f_{21} & f_{22} & f_{23} \\ f_{31} & f_{32} & f_{33} \end{bmatrix} \tag{3.1}$$

where f_{ij} is the probability of the prediction being in state j in season n+1 when weather is in state i in season n. Such a table can be made from the recorded performances of a given forecaster. The structure of $\underline{F}$ is analogous to that of $\underline{W}$. Hence the class of forecasters following the strategy summarized in (3.1) can be called Markovian forecasters.

The Persister is a Markovian forecaster whose $\underline{F}$ matrix is the identity matrix: $\underline{F} = \underline{I}$, i.e., $f_{ij}=0$ if $i \neq j$ and $f_{ii}=1$ for $i=1,2,3$.

Suppose a forecaster knew that the weather pattern's $\underline{W}$ matrix was of a specific form, say that in (2.2). It would seem that he could do better than the Persister if he chose his strategy matrix $\underline{F}$ equal to $\underline{W}$, rather than the identity $\underline{I}$. We will call such a forecaster a Markover.

4. Probability of a Correct Forecast in the Markovian Setting

To have a basis for judging whether a Markover can out-perform the Persister in predicting Markovian weather, we develop a formula for the probability a_o of a forecaster making a correct prediction.

Let w_i be the probability that the weather pattern at the fixed point at season n will be in state i. Next observe that products of the form $w_{ij}\ f_{ij}$ may be interpreted as: the probability that, the weather being in state i at season n, the forecaster will independently and correctly predict the weather to be in state j at season n+1. Summing over all such products and using the meaning of w_i, we find the requisite formula for a_o:

$$a_o = \sum_{i=1}^{3} w_i \sum_{j=1}^{3} w_{ij} f_{ij} \tag{4.1}$$

Example 1 For the Persister, we have $\underline{F}=\underline{I}$ and $\underline{W}$ is as given in (2.2). Hence (4.1) yields

$$a_o=w \tag{4.2}$$

Example 2 For the Markover, we have $\underline{F}=\underline{W}$ and $\underline{W}$ is as given in (2.2). Hence (4.1) yields

$$a_o=1/2[3w^2-2w+1] \tag{4.3}$$

5. The Markover vs. the Persister

A plot of (4.2) and (4.3) over the whole range of the persistence index, $o \le w \le 1$, is shown in the figure. It is clear that over the range $1/3<w<1$, we have a_o (Markover)$<a_o$(Persister), i.e., the Persister has the higher skill over the range of persistent weather. Below $w=1/3$, the weather is predominantly variable. The Markover understandably does better than the Persister in this range.

6. The Analoger vs. the Persister

The third curve of the figure shows the performance of the analog method of prediction tailored to the present simple context. It works as follows: given a present state i of the weather at season n one goes back in time over the weather record and looks for the earliest recurrence of the state i. This is the analog state. The state in the record subsequent to this analog state is then used for the prediction of the state at season n+1. Some reflection shows that this analog method must be better than that of the Markover: the latter uses probabilities to predict a state subsequent to state i (he has to spin a pointer, so to speak, to determine his move) while the analoger simply selects as his prediction the realized state of the weather immediately following the analog. It is this latter mode of selection, in turn, which prevents the Analoger from being as good as the Persister when w>1/3. For at this point, the Analoger allows chance (via the record) to decide his prediction. This is not as bad, however, as the Markover who, as we saw, lets chance act twice to decide his prediction--once to evolve the weather from season n to season n+1, and once to determine his choice of how the weather goes from season n to n+1. Numerical verification of these arguments have been made for the case of W as given in (2.2). However, the form of the above argument seems to be independent of W, and so our conclusion would appear to be generally valid, i.e, for Markovian weather patterns of arbitrary W as given in (2.1). This matter can certainly be investigated analytically; however, it will not be done here.

7. Conclusions

The surprising outcome of the simple thought experiment in this note is that, in the context of Markovian weather patterns, one cannot on the average out-predict the Persister if one uses the probability table (2.2) by which the weather is made (!) or even if one has the past weather record from which to choose analogs! As long as the Markovian type weather exhibits some persistence (w>1/3), the best prediction, on the average, would simply project the present state of the weather into the next season.

RELATIVE THEORETICAL PREDICTIVE SKILLS for MARKOVIAN CLIMATES

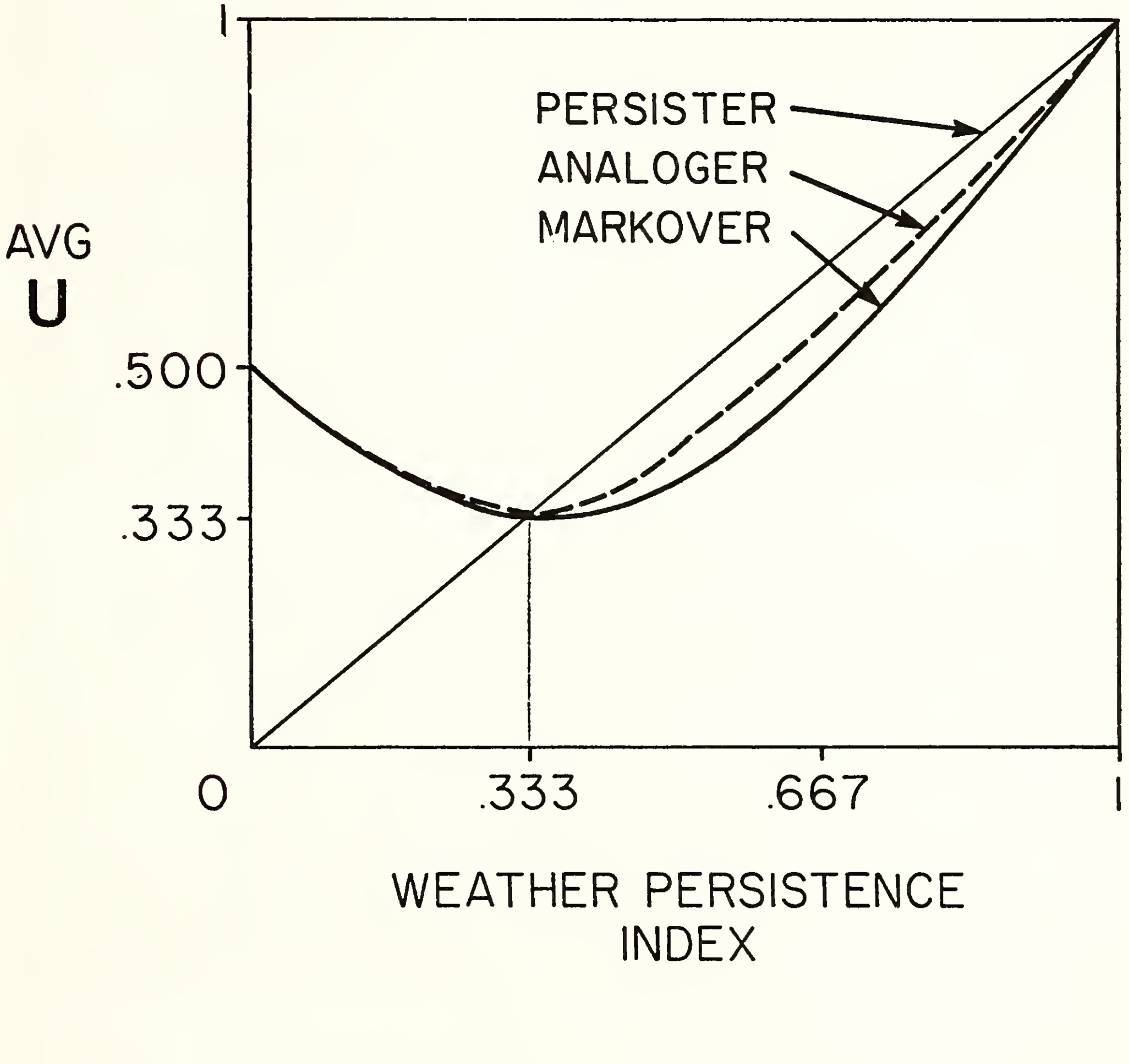

An Experimental Short-term Climate Forecasting Procedure for U. S. Winter Temperatures and its Verification

Alfredo R. .avato

Dept. of Meteorology and Physical Oceanography, Massachusetts Institute of Technology, Cambridge, Mass. 02139

A linear multivariate regression model for continental United States January surface air temperatures is presented. The predictors enter the regression equation at more than one lag if their effects on the predictand tend to be spread over several months rather than be completed in one month. We took the monthly mean surface temperatures for 12 cities to be representative of temperatures for the regions around them. The predictand series then consisted of annual January values for each representative city. We derived a separate regression equation for the annual departures from the long term means for January for each city. Our procedure, therefore, predicts the interannual variability for January. The regression equations for interannual variability were able to explain a much higher percentage of variance compared to the corresponding regression equations for monthly variability. We can apply the same procedure to obtain prediction equations for other months. The higher percentage is to be expected if we consider that there must be differences in the operation of temperature-controlling physical mechanisms which are dependent on the march of the seasons.

A chain of evidence now links equatorial Pacific SST's to the midlatitude tropospheric circulation and, thereby, to United States surface climatic parameters. Using general circulation numerical models, Rowntree (Quart. J. Roy. Met. Soc., 1976, 1979) showed that (in terms of a Fourier decomposition of 500-mb geopotential heights around latitude circles in midlatitudes) warm anomalies in the equatorial Pacific Ocean tend to induce increased amplitudes in the long wavelength planetary waves, specifically wave numbers 1 to 5. He noted that the midlatitude effects of tropical SST anomalies are much larger than those of extratropical anomalies. His model showed a strong 3-wave pattern at 300 mb at 50°N in response to tropical forcing which is given by the longitudinal pattern of SST, the major feature of which is the zonal gradient across the equatorial Pacific.

Then Austin (Q. J. R. Met. Soc., 1980) found that blocking episodes in the Northern Hemisphere midlatitudes are associated with interference or reinforcement between planetary waves which have increased amplitudes but normal phases. The ridge line for both wave numbers 2 and 3 at 500 mb is at about 140°W. Using the 700-mb geopotential height anomaly maps (for winters) compiled by Namias (1979), we find a correlation of 0.45 with the January Pacific SST eigenvector time series coefficients for the first mode. Thus, just over 20% of the variance can be explained by a physical process, sea-air interaction.

One of the most significant orderly patterns of SST and air temperature anomalies, which shows up in an eigenvector analysis of global SST's (Newell and Chiu, 1980) is the "Southern Oscillation" (Walker, 1923 - 1937). Zonal pressure gradients in the tropical Pacific change first, followed by SST's in the eastern equatorial Pacific, followed by zonal mean tropical air temperature, followed by zonal mean middle latitude air temperature. Employing modern analysis techniques and a broader data base, Kidson (1975) confirmed Walker's notion: the Southern Oscillation stands out as the major pattern of SLP variations. His first eigenvector of the global surface pressure field showed evidence of a three-wave pattern which corresponds in time to Southern Oscillation changes. Moreover, this pattern is global in extent. His results also suggested that when the Hadley (north-south) circulation is weak, the Walker (east-west) circulation is strong. This global connection establishes the role of an index of the strength of the Southern Oscillation (SOI) in forecasting midlatitude climatic parameters even though the interlocking processes are not well understood.

The experimental forecast method used was to determine a linear multiple regression equation for each of 12 representative cities by ordinary least-squares estimation. Step-wise regression was used to select the predictors and an arbitrary limit of three predictor terms was set for each equation. The collection of predictors consisted of annual series of June, July, August, September, and October values of Pacific Ocean SST zonal means representing the latitude band between the Equator and 5°S (and from 140°W eastward to the coast), and the SOI obtained by taking the difference of mean sea level pressure between two Pacific locations, Easter Island and Darwin. The regression equations for the mean January temperature anomalies for twelve representative cities are given below. DT denotes mean January temperature anomaly in units of standard deviation. PJun denotes Pacific Ocean zonal SST nonseasonal anomalies for the month of June. PJul denotes SST anomalies for July, and so forth. SJun denotes the SOI nonseasonal anomaly for June, SJul for July, and so on. SST anomalies are in degrees C, while SOI anomalies are in mb.

Region	Regression Equation	Explanation of Variance
Asheville	DT = -.465 PJun - .202 SAug + .149 SJun	46.4 %
Atlanta	DT = -.418 PJun - .187 SAug - .163 SJun	45.4 %
Boston	DT = .723 PJul - .537 PJun + .129 SJun	31.9 %
Buffalo	DT = .214 SJun + .207 PJul - .169 SAug	32.1 %
Chicago	DT = .371 PJul + .141 SJul + .0937 SOct	25.4 %
North Platte	DT = .484 PJun + .124 SOct + .0720 SJul	20.1 %
Portland, Ore.	DT = .585 PJun + .0836 SOct + .0785 SSep	23.1 %
Sacramento	DT = -.229 SSep - .221 PAug + .181 SAug	35.3 %
San Antonio	DT = -.530 PJun + .158 SOct - .113 SSep	30.1 %
San Diego	DT = .445 PJun + .126 SAug	20.1 %
Spokane	DT = .599 PJun + .112 SOct + .0864 SJul	27.7 %
Wichita	DT = .430 PSeP + .132 SJul + .111 SOct	25.8 %

We used three forecast categories, normal (N), below normal (B), and above normal (A). Above normal means a 2-to-1 chance that the mean January temperature will be above the long-term mean (from about 1940 to 1975, depending on the length of record available for a station) temperature for January. The below normal category has an analogous meaning. The normal category implies at least a 1-to-2 chance that the mean temperature will be within one-half standard deviation of the long-term mean. The forecasts for January, 1980, were as follows:

Asheville	A
Atlanta	A
Boston	N
Buffalo	A
Chicago	B
North Platte	B
Portland, Ore.	B
Sacramento	B
San Antonio	B
San Diego	N
Spokane	B
Wichita	B

A comparison of the forecast with actual observed mean January temperatures is shown in Figure 1. There was general agreement except notably in Sacramento, San Antonio, and Chicago. This forecast was submitted in November, 1979, to the Lawrence Livermore Laboratory as a contribution toward the formation of an experimental consensus forecast for the 1979-1980 winter for the Department of Energy.

The following contingency table summarizes the forecast and observed temperatures.

	Forecast Temperature			
Observed Temperature	Above	Normal	Below	Total
Above	1	1	1	3
Normal	2	1	2	5
Below	0	0	4	4
Total	3	2	7	12

$$\text{Skill score} = \frac{R - E}{T - E} = \frac{6 - 4}{12 - 4} = 0.25$$

where R is the number of correct forecasts, T is the total number of forecasts, and E is the number of forecasts expected to be correct by chance.

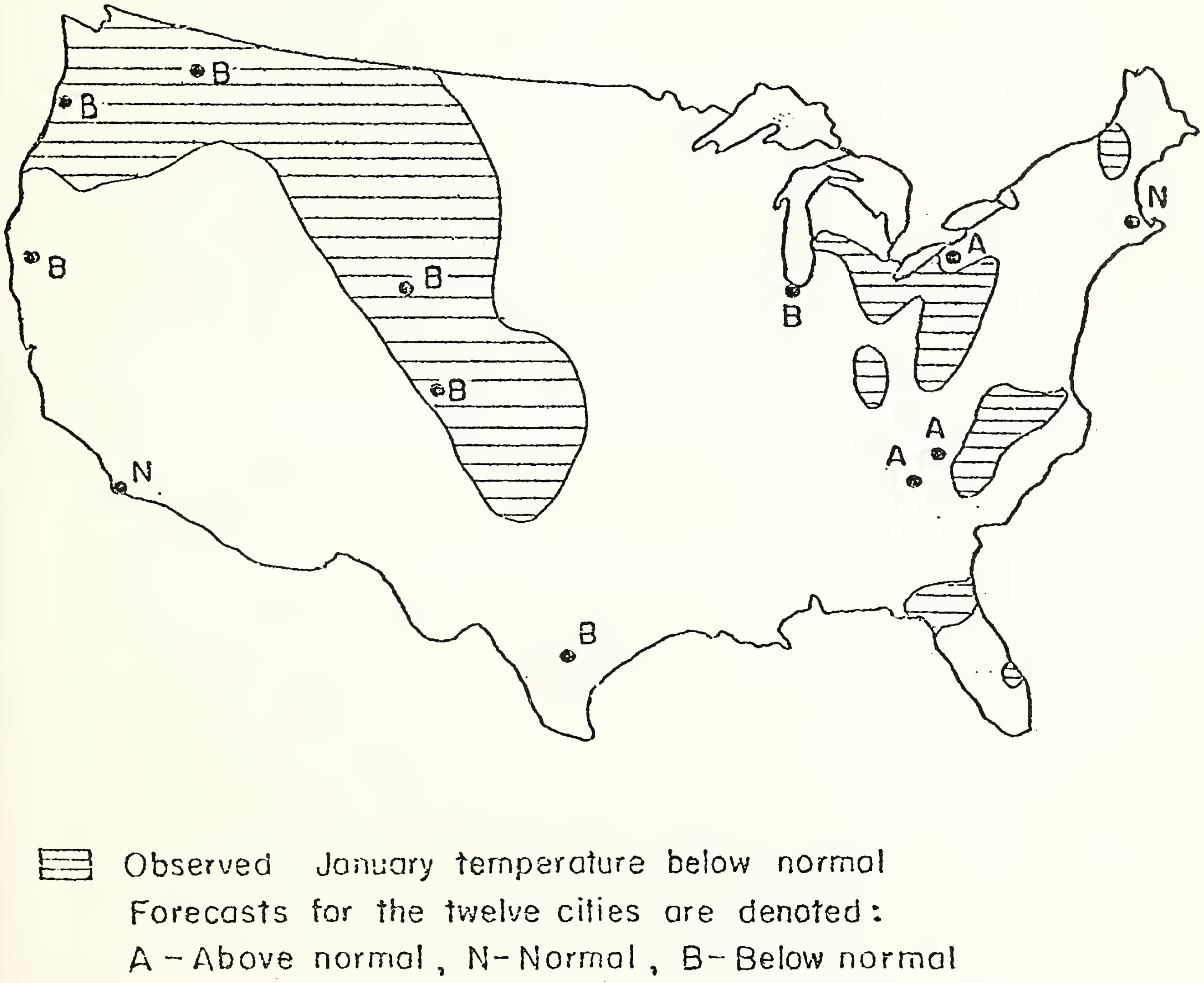
B
B
B
B
B
N
B
B
A
N
A
A
B
▤ Observed January temperature below normal
Forecasts for the twelve cities are denoted:
A - Above normal, N - Normal, B - Below normal

Figure 1. Comparison of forecast temperatures with observed temperatures as reported in the Weekly Weather and Crop Bulletin 67, no. 6, 1980, published by the National Weather Service

Multi-regression approach in the seasonal range forecasting with antecedent patterns of the large-scale circulation.

Ernest C. Kung
Department of Atmospheric Science
University of Missouri-Columbia
Columbia, Missouri 65211

One practical approach to the problem of the seasonal-range forecasting is the empirical methods which are consistent with the observed operational mode or behavior of the general circulation. The use of standard methods of linear prediction may be justified with a premise that the information of nonlinear processes of the atmosphere is implicitly contained in the near past data of the atmospheric circulations. Our statistical analyses indicate that at the seasonal range the predictors may be related linearly to predictands, and the data period seems to be at its optimum in the 15-20 years' range.

In the actual procedure, first a group of meteorological variables may be considered for various reasons of circulation patterns, teleconnections, possible dynamics and energetics associated with predictands, etc. An extensive correlation analysis is then applied to identify approximately 10 to 15 candidates among these variables as possible predictors. These parameters are finally reduced to four to six after statistical selection procedures, such as R^2 procedures and stepwise regression procedures, and the regression coefficients are determined. At this point an independent principal component analysis is performed to confirm that multicollinearity among the predictors is effectively eliminated.

The predictand may be any large-scale parameter which can reasonably represent an element of the seasonal weather pattern of an area. The predictors may be selected inside and outside the forecast region. The lead time between X and Y depends on the choice of X.

The choice of predictors X almost determines the ability of the model. In our earlier model of Indian monsoon onset forecasting, eight April upper air parameters were used as predictors at the forecast point through the process described above. In a subsequent modification of the model the number of predictors was reduced to five, which includes two upper air parameters (April upper air height and 700-mb kinetic energy over India), one April Indian ocean surface temperature, and two Australian upper air parameters (January 700-mb v wind and March 700-mb temperature). A rather dramatic improvement of the model is seen in Fig. 1 in the current model as the result of modification. In the earlier model we only described the instability of the Indian upper air in terms of April mean parameters over the forecast point. In the current model the number of predictors was reduced, but the land-sea temperature contrast and Southern hemispheric circulation were also considered in terms of Indian sea surface temperature and Australian upper air parameters.

The same type of forecasting model has also been developed for the summer rainfall in Central India with six predictors, including four April upper air parameters over India (100-mb u and v winds, 200-mb temperature and 700-mb u wind), one February sea surface temperature over the Indian Ocean, and one April upper air parameter over Australia (200-mb height). This model is shown to predict the summer rainfall (as defined by 15 reporting stations) with a 6% accuracy. The result is illustrated in Fig. 2.

Table 1 compares the regression forecasting of the monsoon onset date and rainfall by the method of the meteorological variables and by the principal components. The compatibility seems clear.

Because of the time variation of the patterns of the general circulation, the constant updating of the regression equation should be an integral part of this type of forecasting scheme.

TABLE 1

Maximum R^2 and MSE in regression fitting of the monsoon onset date (from 1 April) and monsoon rainfall (mm) using meteorological variables and principal components (after Kung and Sharif).

Monsoon Onset

Number of variables or components	Meteorological variables		Principal components	
	MSE	R^2	MSE	R^2
1	51.16	0.373	28.23	0.654
2	37.86	0.562	21.44	0.751
3	21.21	0.769	19.03	0.792
4	14.61	0.850	17.41	0.822
5	11.98	0.886	15.76	0.849
6	11.54	0.898	14.05	0.876
7	11.15	0.909	12.58	0.897
8	10.11	0.924	10.98	0.918
9	8.96	0.939	9.36	0.936
10	9.22	0.943	4.41	0.955

Monsoon Rainfall

Number of variables or components	Meteorological variables		Principal components	
	MSE	R^2	MSE	R^2
1	14847.73	0.432	15731.02	0.399
2	107744.00	0.612	11665.38	0.579
3	9013.20	0.694	9097.03	0.691
4	6972.54	0.778	6239.24	0.801
5	5903.68	0.824	3884.88	0.884
6	2195.15	0.939	3018.22	0.917
7	2074.34	0.947	2327.03	0.941
8	1962.28	0.954	1669.23	0.961
9	1575.41	0.967	941.94	0.980
10	1394.81	0.970	738.97	0.986

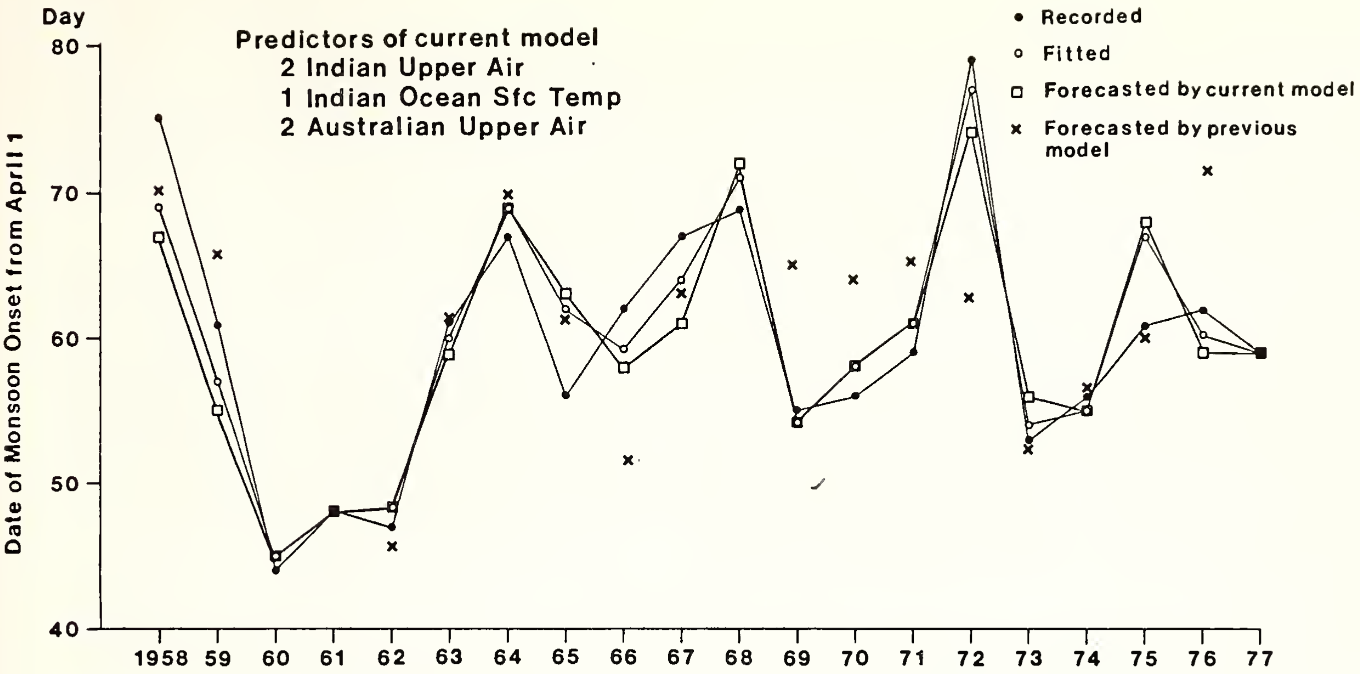

Fig. 1 The recorded, fitted, and forecasted monsoon onset dates from 1958 to 1977. Forecast is by regression equation without involving the data of the forecast year. The previous model had 8 upper-air predictors. (Kung and Sharif).

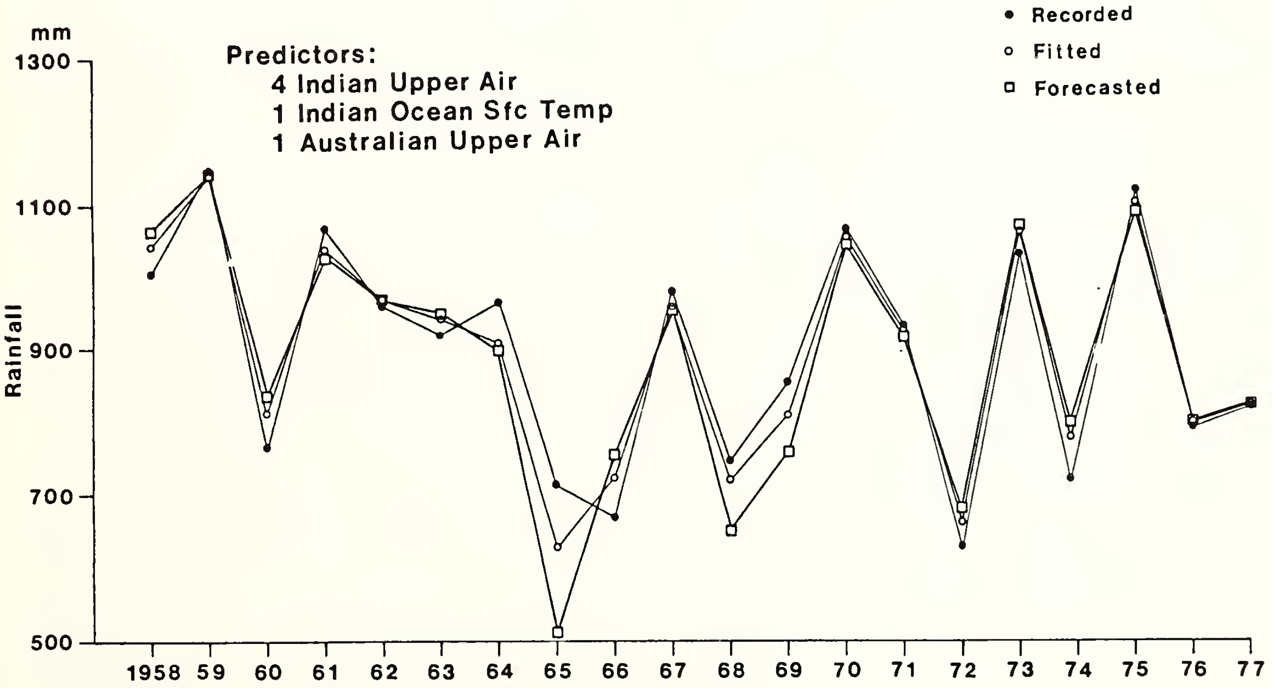

Fig.2 The recorded, fitted, and foredasted monsoon rainfall in Central India from 1958 to 1977.

APPLICATION OF SEASONALLY NONSTATIONARY LINEAR PREDICTION MODELS

T. P. Barnett

Climate Research Group
Scripps Institution of Oceanography
University of California, San Diego
La Jolla, California, 92093 U.S.A.

Abstract

Methods of constructing linear prediction models for the time series with seasonally nonstationary statistics are applied to several important prediction problems. These formalisms suggest it is possible to forecast El Niño events at least one year in advance. They also show regions over North America where surface air temperature is predictable at lead times of one season from prior knowledge of equatorial Pacific sea surface temperatures. Both of these examples demonstrated the superiority of the non stationary modeling methods over standard approaches.

1.0 Introduction

Most work on linear prediction theory assumes the statistics of the data fields to be time invariant. Recent summaries of this work, as it applies in geophysics and particularly climate prediction, may be found in Davis (1977) and Barnett and Hasselmann (1979, hereafter called BH). In a companion paper presented in this symposium, Hasselmann (H) modifies the latter work to include situations in which the statistics are periodic in time. This work is extended in Hasselmann and Barnett (1980, hereafter called HB). The result of these papers is a method of statistical modeling applicable to climatic phenomena which show strong relation to the phase of the annual cycle, e.g., the effect of air/sea heat flux on the atmospheric system. Numerous analyses of climatic data sets suggest such methods will be required in many parts of the world.

This paper describes the application of periodic statistical models to two problems: 1) Forecasting El Niño events and 2) forecasting surface air temperatures over North America. The results are contrasted with those obtained from current theoretical methods for developing prediction models. The notation and analytic details backing the discussion may be found in H.

2.0 Model Selection

At least three types of linear statistical models can be considered. In the case of "time invariant," or TI, models, the associated time series must be stationary and independent of seasonal phase. "Fixed phase" (FP) models, on the other hand, are constructed for a single month or season of the year, e.g., the prediction of winter air temperature from previous predictors. Since these models are phase specific, they can be applied in cases of seasonal nonstationarity. "Phase averaged" (PAV) models, by contrast, are dependent on an assumed functional form for seasonal nonstationarity, e.g., a Fourier expansion of the prediction coefficients (see HB and H). Thus one need not estimate a different model for every month/season as in the FP case, but rather estimate only one model over the entire data set. This generally increases the degrees of freedom and thereby provides a better opportunity to find a significant model.

The determination of which modeling formalism to choose, stationary or nonstationary, can be made based on the time-dependent correlation of the predictors and/or predictands... but *not* their cross correlation. For example, Figure 1 is the time-dependent correlation for the first empirical orthogonal function (EOF) or North Pacific sea surface temperature (SST) anomalies. The 95% significance level, which depends on season is roughly 0.4.

The EOF is clearly nonstationary with respect to seasonal phase. Thus models FP or PAV are required if this variable is to be properly employed in a modeling procedure.

The above method offers an objective *a priori* rationale for deciding which type of model one should use in developing prediction algorithms. The rest of this paper, however, will purposely employ all three modeling approaches to demonstrate the difficulties that can arise if an investigator blindly chooses the traditional analysis methods in the presence of significant nonstationarity.

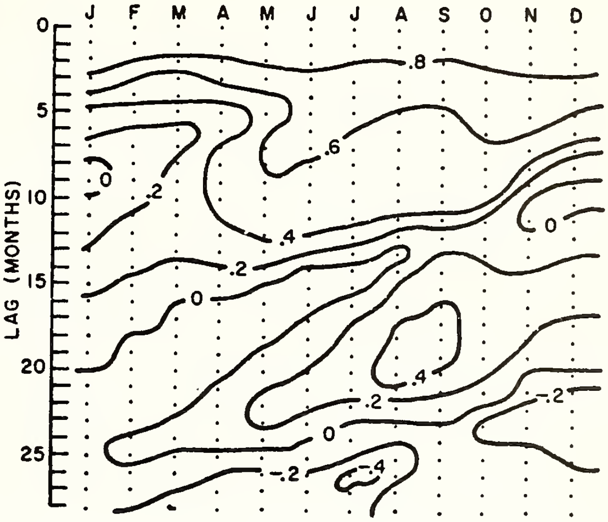

Figure 1

Time dependent correlation function for amplitude of first empirical function of anomalous SST in the North Pacific. Month of the year is indicated at the top of the diagram.

3.0 Notation

It is convenient to repeat here some of the notation of HB and H so the reader will not have to refer back and forth between this article and those references. The predictand (y) at lead time q is estimated ($\hat{y}$) by the predictors (x_α) via the linear relation.

$$\hat{y}(t+q) = \sum_{\alpha} x_\alpha(t)\ [E_{\alpha 1}+E_{\alpha 2}\cos\kappa t+E_{\alpha 3}\sin\kappa t] \qquad (1)$$

The prediction coefficients, $E_{\alpha\beta}$, are found in the usual manner. The subscript α contains information on both predictor type and time lag with respect to t, while κ represents the phase of the cycle, e.g., κ=1 in winter, =2 in spring, and so on.

The term in square brackets is termed the 'seasonally modulated Green's function'. The lag dependence (α) of the $E_{\alpha\beta}$ give an estiamte of the standard Green's function as used in BH. The β-dependence of the $E_{\alpha\beta}$ show the level of seasonality in the Green's function. For instance, if $|E_{\alpha 1}| >> |E_{\alpha 2} + E_{\alpha 3}|$ then the original series are essentially stationary to first order and TI models would have described y(t) adequately. If, on the other hand, the seasonal coefficients ($E_{\alpha 2}$, $E_{\alpha 3}$) are comparable with $E_{\alpha 1}$ then the associated time series are nonstationary and some measure of seasonal phase must be included in the analysis of their properties and differential equations that describe their evolution.

A measure of the seasonal symmetry within a nonstationary model is given by $\theta = \tan^{-1} |E_{\alpha 3}/E_{\alpha 2}|$. Values of θ near 0 or $\pi/2$ suggest prediction relations or physical interactions that are confined to opposite phases of the annual cycle, e.g., summer and winter only. If $E_{\alpha 1}$ is of the same order of magnitude as max ($E_{\alpha 2}$, $E_{\alpha 3}$) predictability will only exist on one season since the coefficients will reinforce each other in one season but cancel in the opposite season. Values of θ near 1, coupled with the approximate equality of the $E_{\alpha\beta}$ suggest interaction of predictors and predictand in consecutive seasons. Indeed the sign and magnitude of the $E_{\alpha\beta}$ and the value of θ can be used to determine the seasonal character of the predictive skill resulting from each of the lagged predictor series.

The skill (S_H) of the models is measured as percentage of variance accounted for in the modeling procedure, i.e.,

$$S_H = \frac{<(y-\hat{y})^2>}{<(y^2)>}$$

where the <···> indicate time averages and $<y> = <\hat{y}> = 0$.

4.0 Predicting El Niño

Time invariant formalisms of BH have been used to show El Niño events may be predicted marginally at lead times of one year from knowledge of the Trade Wind Field (TWF) alone (Barnett, 1980a). No effort was made to optimize that model. It is known from a variety of sources that EL Niños tend to occur at certain seasons of the year and that measures of El Niño are closely related to changes in sea level. These facts were used to construct a more refined El Niño prediction model.

The predictors were chosen to represent: 1) regions of the TWF found most important to predicting ocean/atmosphere variables in the tropical Pacific, 2) a measure of the east/west sea-level slope variability and 3) prior values of the predictand. This latter quantity is the SST anomaly at Talara, Peru. All data series extended over 20 years at monthly intervals. See Barnett (1980a) for more details on predictors/predictand definition and characteristics.

Three models were constructed to predict Talara SST. The first (A_{TI}) assumed that the Talara SST statistics were time invariant and so S_H was assumed independent of season. The second model (A_{FP}) was a fixed phase model and attempted to forecast Talara SST in July, a time when El Niños normally reach high intensity. Model A_{PAV} was a phase averaged model of the type described by equation 1. All models forecast for a lead time of one year and used the previous 12 month's data in the lagged predictor fields.

The significance measure of the models (ρ^2, see BH) is shown in Figure 2. Model A_{TI} (time invariant) is significant at the 95% level for model order $p = 4$, while Model A_{PAV} (phase averaged) is significant to at least $p = 10$. Model A_{FP}, the fixed phase model for July, is not significant for any order. In fact, the large number of predictors and relatively few years available for analysis make the modeling process indeterminate beyond $P = 3$.

The skill of each model is shown in Figure 3. The model A_{FP} had a high skill (76%) but was not significant at even the 90% level and must, therefore, be rejected. This again points up the fact that model skill and significance are not always synonymous. The skill of A_{TI} indicated by $<\overline{A}_{TI}>$ is 26% and presumably the same for all months. Actual evaluation of A_{TI} on a monthly basis, however, shows the skill* to vary widely over the course of the year. In October, November, and January the skill is negative. The model does well during the summer. It is clear that the average skill normally associated with such a time invariant model (26%) is somewhat misleading in a nonstationary environment. The nonstationary model (A_{PAV}) shows positive skill in *all* months and is particularly strong during the summer when El Niños generally reach their highest intensity.

The behavior of models A_{TI} and A_{PAV} can be understood through their Green's functions (Section 3). Figure 4 shows the functions as they relate the prior years' variation in one of the predictors (the zonal counterpart of the Southeast Trade Winds, USET) to the year in advance fluctuations in SST. For the time invariant model, only $E_{\alpha 1}$ exists and its lag dependence is shown by the curve marked A_{TI}. The seasonally modulated Green's functions from A_{PAV} are shown for January and July. The A_{TI} results suggest a strong relation exists between USET and SST in all seasons of the year. The A_{PAV} results, on the other hand, show this relation exists for summer (July) fluctuations in SST but not winter variations, i.e., $\theta \doteq 0$ and $E_{\alpha 1} \doteq E_{\alpha 2}$. Thus the predictive relationship is determined principally by the covariance contribution between summer SST and the predictor. This explains why the skill of A_{TI} is nearly as good for summer as the skill from A_{PAV}. It also explains the negative skill of A_{TI} during the winter for the estimated predictand/predictor relationship for this season does not hold; it is due solely to the strong summertime relationship.

---

* This skill is figured as a percentage of the individual monthly variance accounted for by A_{TI} and so directly comparable to S_H.

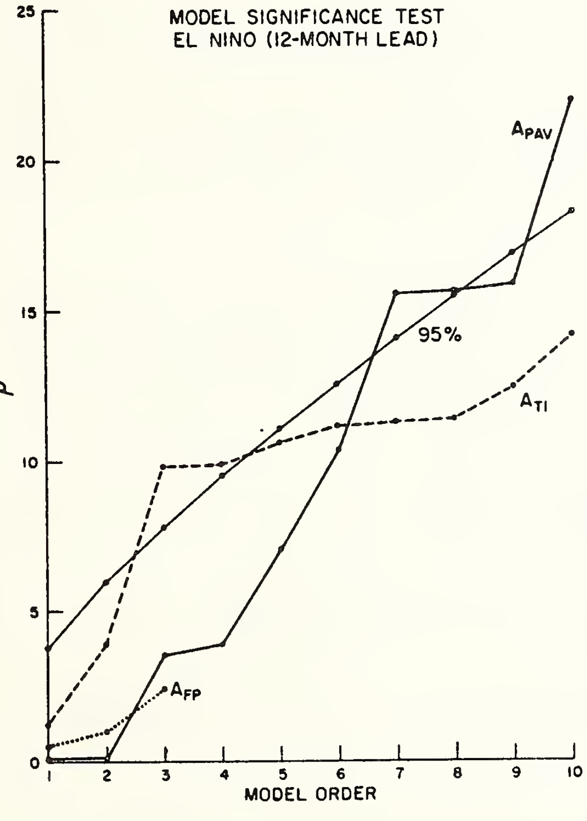

Figure 2

Model significance tests: El Niño prediction at 12-month lead. The significance parameter (ρ^2) is shown for the various models. The 95% confidence limit is also indicated.

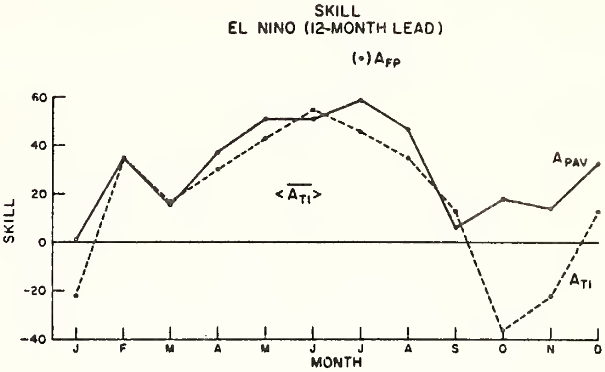

Figure 3

Skill, by month, for various one-year-in-advance El Niño prediction models. See text for description of the symbols.

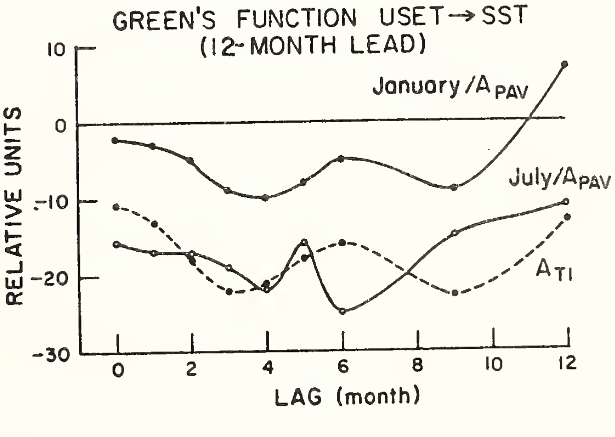

Figure 4

Green's functions relating SST and Trade Wind strength in El Niño prediction models at 12-month lead. See text for discussion of the symbols.

5.0 Predicting Seasonal Air Temperature Over North America

The relation between fluctuations in ocean/atmosphere parameters in the Pacific and subsequent air temperature anomalies over North America further illustrate the appropriateness of seasonally nonstationary models. A detailed analysis of the Pacific/North American interactions is given elsewhere (Barnett, 1980b). Here we excerpt from that study several of the results relating SST to subsequent air temperature variations.

Three prediction models were again constructed: 1) Model B_{TI} assumed the statistics of all data series were stationary; 2) Models B_{FP} were fixed phase, i.e., they were set up to predict only one season and 3) Model B_{PAV} was a phase average model of the form (1). In this case the difference between Models B_{FP} and B_{PAV} is rather small, because the number of free coefficients is only one less than in B_{FP}. All models forecast air temperature at a lead time of one season and used the previous four seasons data in the SST predictor field. The SST predictors come from equatorial and mid-latitude regions identified by Bjerknes (1969) and Namias (1975), respectively, as being potentially important to subsequent events over North America. Seasonal data for the period 1902-1972 were available for analysis.

The significance measure of the models is shown in Figure 5 for a typical station (Jacksonville). A model of the form B_{TI} could not be constructed at this station with 95% significance. Fixed phase models (B_{FP}) were found to be significant (>95%) for three seasons out of the year. The highest and lowest ρ^2 distribution for these models is shown. The other two seasons fall in between these extremes. The skill in the significant fixed phase models ranged from 6-22%. This range, plus the seasonal dependence, explains the negative performance of B_{TI}. The phase averaged model (B_{PAV}) was significant at a higher level than its competitors. This is due to its ability to handle seasonal variability in predictive skill while maximizing degrees of freedom in the analysis.

The skill of the different classes of model is illustrated in Figure 6 for 36 North American stations. The left-hand panels show the annual average skill for stationary (B_{TI}) and phase averaged (B_{PAV}) models. These averages are somewhat misleading, since they contain strong seasonal variability. The seasonal character of ocean/atmosphere interaction that gave the predictive skill (Barnett, 1980b) clearly makes B_{TI} inferior to B_{PAV}. Comparison of the ability of models B_{FP} and B_{PAV} to forecast winter air temperatures is shown in the right-hand panel of Figure 6. The fixed phase models have somewhat higher skill at many individual stations as expected, since the models were tuned for the particular station/season forecast. Note, however, that models of the form B_{FP} could not be constructed at many stations where B_{PAV} shows low, but significant skill. This is due to the additional degrees of freedom associated with the phase averaged models.

Significant models B_{PAV} occassionally produced negative skill scores at some stations/seasons. In most cases these resulted when the station was rather strongly predictable in only one season, e.g., $\theta \doteq 0$ and $E_{\alpha 2} > E_{\alpha 1}$. In this case the approximation to seasonal nonstationary, the Fourier expansion shown in (1), is poor and so is the corresponding model result. Models B_{TI} also generally gave negative skills for these stations/seasons. In these cases, models of the form B_{FP} could not be constructed at a reasonable level of significance.

Examples of the seasonally modulated Green's functions are shown in the upper panels of Figure 7 for two widely separated individual predictand stations and SST off Peru, the most important predictor variable. A generalization of these functions may be derived for the entire predictand field via principal predictors (cf., Davis, 1977; Barnett, 1980b). In this case the Green's functions relate SST off South America (predictor) and the numerically largest pattern of predictable air temperature fluctuations over all of North America. The seasonal character of this function is shown in the lower part of Figure 7. The seasonality of the interaction is obvious. Winter forecast skill is strongly dependent on the equatorial SST during the prior three seasons (fall through spring). The summer forecast, on the other hand, is only weakly dependent on equatorial SST, or any other predictor for that matter, since summer predictability is much lower than that obtained for winter. The stationary models B_{TI} suggests a strong coupling between the tropics and mid-latitudes in all seasons. This apparent result leads to negative skill scores for many stations/seasons (not shown) as in the example of Section 4.0

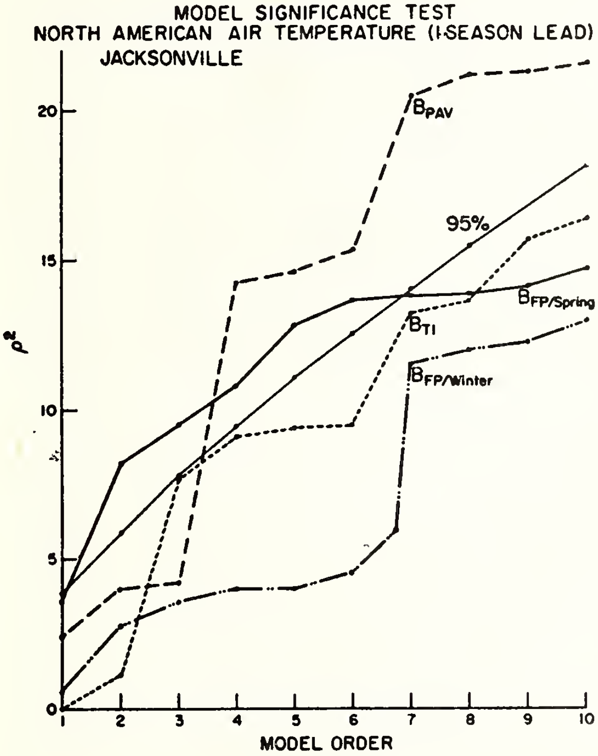

Figure 5

Model significance tests: North American surface air temperature at one-season lead.

6.0 Conclusion

Methods of predictively modeling seasonally nonstationary time series have been developed and shown to be superior to other commonly used methods in a variety of circumstances. The cautious investigator would be wise to test for the stationarity of this data (cf. Section 2) *prior* to deciding on an analysis method. Failure to do this is apt to give discouraging and/or misleading results.

Acknowledgment

This work was supported by the National Science Foundation under grant ATM-7918206.

References

Barnett, T. P., 1980a: Predictability of ocean/atmosphere fluctuations in the tropical Pacific (submitted to Journal of Physical Oceanography).

Barnett, T. P., 1980b: Predictability of North American air temperatures: Pacific predictors (submitted to Journal of Atmos. Sci.).

Barnett, T. P. and K. Hasselmann, 1979: Techniques of linear prediction with application to oceanic and atmospheric fields in the tropical Pacific. Reviews of Geophysics and Space Physics, 17(5), 949-968.

Bjerknes, J., 1969: Atmospheric teleconnections from the equatorial Pacific. Mon. Wea. Rev., 97(3), 163-172.

Davis, R. E., 1977: Techniques for statistical analysis and prediction of geophysical fluid systems. Geophysical and Astrophysical Fluid Dynamics, 8, 245-277.

Hasselmann, K., 1980: Theory of linear prediction models for a seasonally variance of statistics. Proc. WMO Symposium on Probabilistic and Statistical Methods in Weather Forecasting, Nice, France, 8-12 Sept. 1980.

Hasselmann, K. and T. P. Barnett, 1980: Techniques of linear prediction for systems with periodic statistics (in press).

Namias, J., 1975: Short Period Climatic Variations; Collected Works of J. Namias 1934 through 1974, 2 volumes, University of California, San Diego, 905 pp.

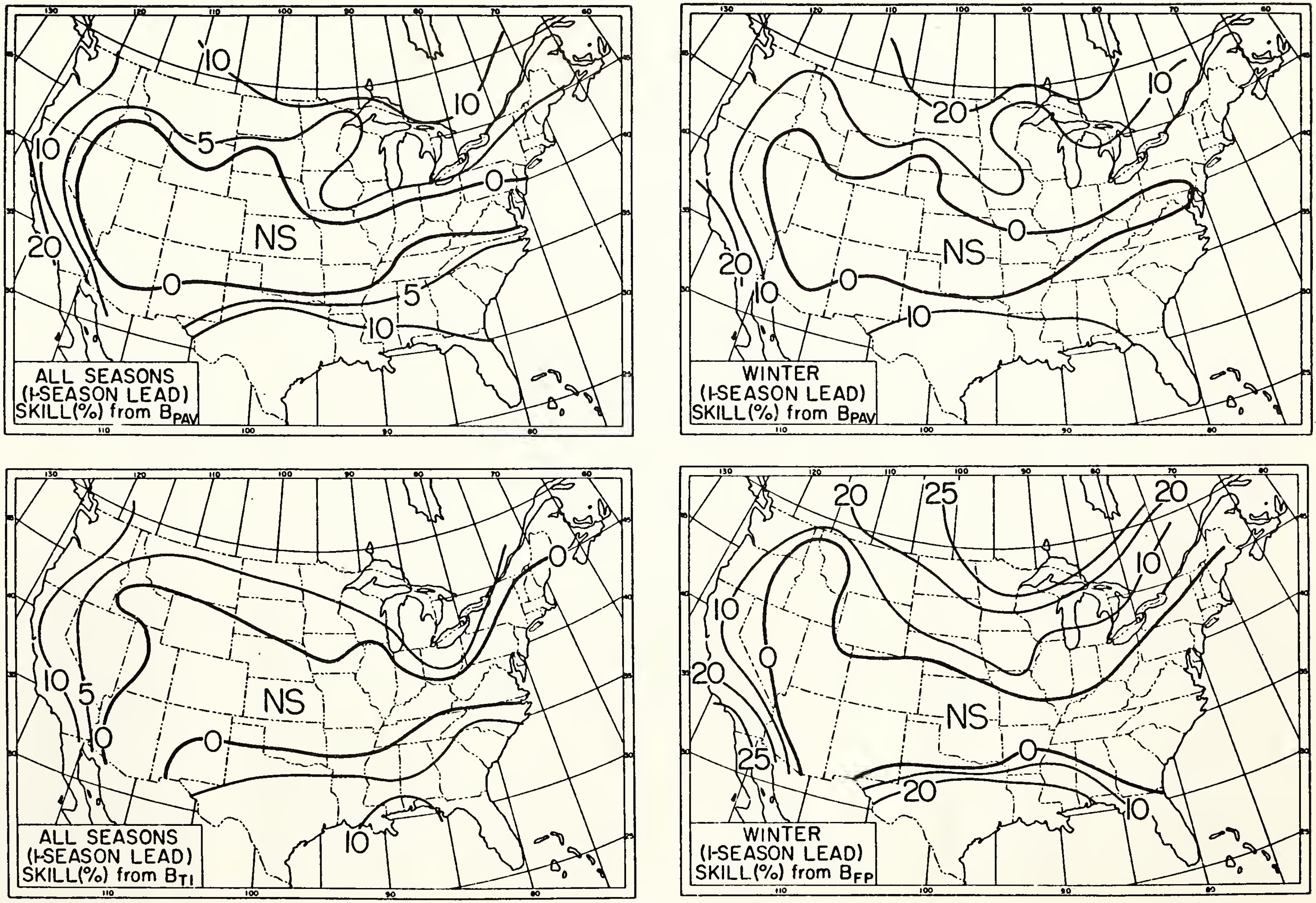

Figure 6

Skill: North American surface air temperature one season in advance. Left: Annual average skill for phase averaged (upper) and time invariant (lower) models. Right: Winter skill for phase average (upper) and fixed phase (lower) models.

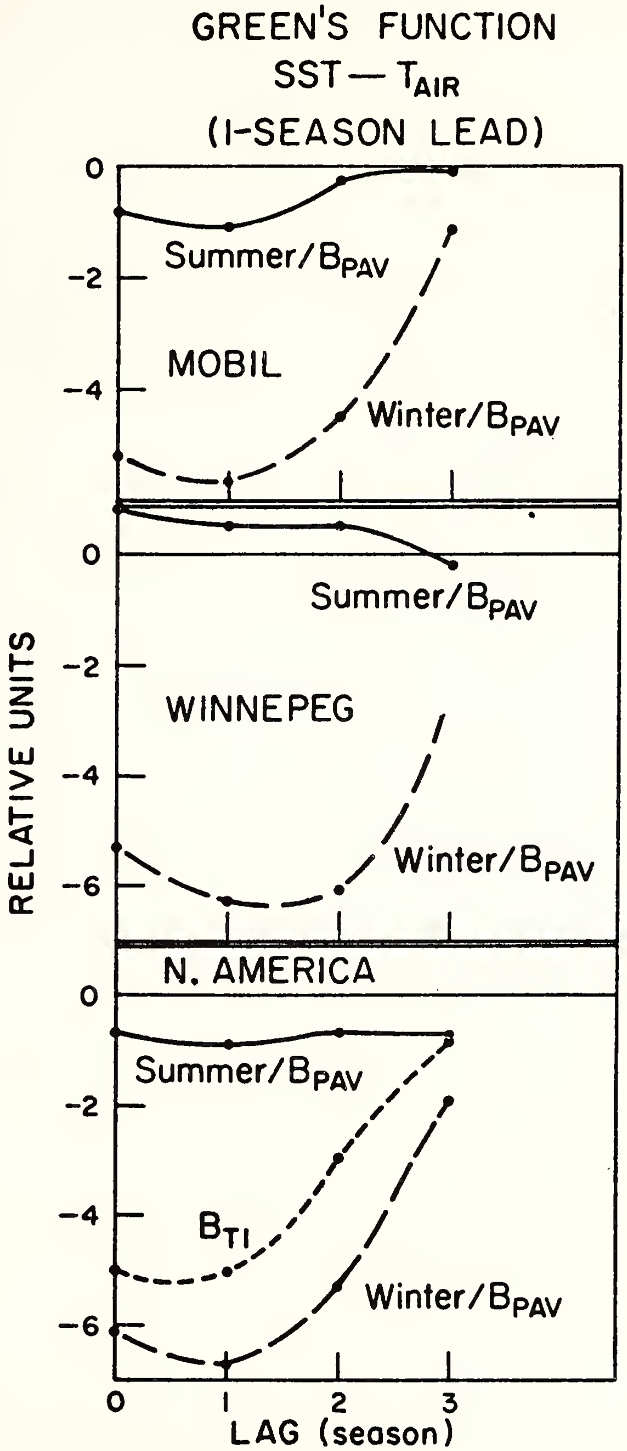

Figure 7

Seasonally modulated Green's functions relating equatorial sea-surface temperature and North American surface air temperature at one-season lead.

Some diagnostic results and experimental forecasts Using the ARIMA Procedure

Leonard Steinberg
Atmospheric Environment Service
Downsview, Ontario

A univariate ARIMA procedure was applied to about 30 years of 50-100 kPa thickness anomalies over most of the Northern Hemisphere. The adequacy of the model was judged using 1) the individual values of the auto correlation function, 2) the portmanteau test based on the sum of squares of the A.C.F. and 3) the reduction of residual variance.

The model chosen (based upon the above criteria) for the experimental forecast consisted of AR terms of lags 1 and 2, MA terms of lags 1 and 12 and applied to all points on the grid (5° lat - 10° long). The parameters were evaluated at each point and used to make one month ahead forecasts for each month of the last year.

Results

A) Diagnostic Study

Eighteen grid points which showed the lowest degree of fit to a simple model were chosen for detailed study.

The best model containing 1,2, and 12 lag factors was found to be an AR(1,12): MA(1, 2,12) model (Table 1). In five of the eighteen cases little difference was discerned among the models.

The residual variance (Table 2) shows reductions of the order of 5-15%. This may be taken as an estimate of signal to noise ratio.

A seven-year (1971-77) subset of the data was decomposed into symmetrical spherical harmonics and subjected to the ARIMA procedure. Almost all of the signal is found to reside in the largest scales (m=o, n=o, 2) (Table 3).

B) Forecast Study

ARIMA forecast with a AR(1,2), MA(1,12) model have been made with one-month lead time for the past year. The ARIMA, forecast, the US Climate Analysis Centre's surface temperature forecast, and the observed anomaly thickness field for April are presented in Fig. 1a, b, and c, respectively.

The April forecast for the 500-1000 mb thickness anomaly may be compared to the surface temperature prediction produced by the United States Climatic Center. Points in common are positive anomalies over most of Canada and the Pacific states; negative anomalies over the southern tier of the U.S., Gulf of Alaska, and Greenland.

The major disagreement was in the Atlantic and in this car the ARIMA forecast of negative anomaly proved correct. Both forecasts were correct over most of Canada, predicting positive anomaly. The negative anomaly in the Northern half of the United States is somewhat better indicated in the ARIMA forecast. The positive anomalies in the Gulf States and Caribbean and negative anomaly centered over Newfoundland are not captured in either forecast.

A series of three ARIMA forecasts with the verifying field are shown in Figures 2 and 3. The nature of the ARIMA forecast is such as to diminish the variance. Therefore, note should generally be taken of the sign and position of the predicted anomalies and not of their absolute values.

The strong influence of the previous month's values (persistence) on the forecast may be seen by comparing 2b with 3a or 2c with 3b.

Objective verification remains to be performed, and therefore the series of forecasts is presented here for the readers' subjective evaluation.

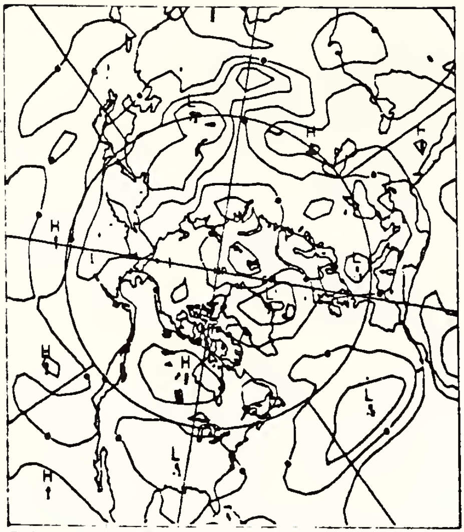

FIG. a EXPERIMENTAL ARIMA FORECAST OF 500-1000 MB THICKNESS FOR MAY 1980 ADDITIVE AR(1,12), MA (1,12)

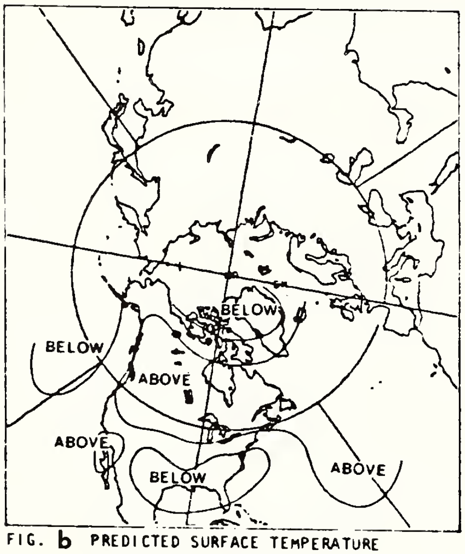

FIG. b PREDICTED SURFACE TEMPERATURE ANOMALIES FOR MAY 1980 U.S. CLIMATE CENTER.

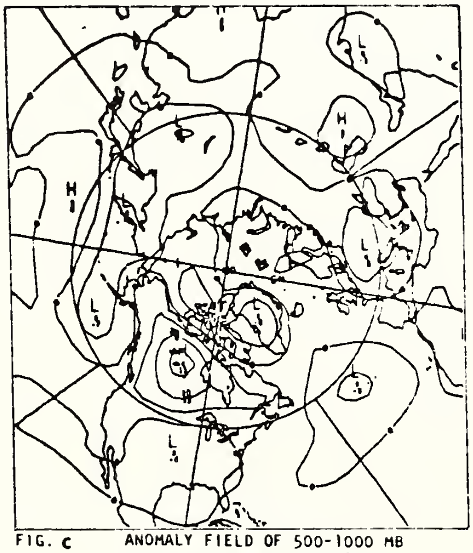

FIG. c ANOMALY FIELD OF 500-1000 MB THICKNESS FOR APRIL 1980.

model (p,d,q) orders OOF / grid point number	(0,0,0) 29		1 (2,0,2) (1,2) (1,2) 25		2 (2,0,3) (1,2,) (1,2,12) 24		3 (2,0,3) (1,12) (1,2,12) 24		Best model If adequate
	Q	L	Q	L	Q	L	Q	L	
4	68.7	1,12,26	41	12,3,10	33	3,10,5	35	3,5,16	none
8	34.2	1	33	1,18	20	18	21	18	2,3
26	31.6	1,4	12	-	10	-	11	-	all
33	22.8	2	16	-	15	-	17	-	all
45	52.6	1,2	28	26	28	26,14	33	-	1,2
52	24.1	1,2	21	1	22	1	17	-	3
66	50.9	1	28	11,15	28	11,15	28	11	all
79	42.2	2,1	20	-	19	26	15	-	3
115	48	1,2	19	-	18	-	15	-	3
152	62	1,25	29	25,14,5	27	25	27	-	all
197	48	1,3	28	19,15	29	19,15	28	19,15	all
249	50	1,3,13	27	13,24	26	13,24	25	13,24,7	all
267	36	23,2,15	27	23,2,17	26	2	17	17	3
284	239	1,2	34	13,23,8	34	13,23,8	32	13	none
296	45	1,5	41	19,24	31	19	36	3,9,19	none
299	50	1,25	30	9,12	25	9	29	25	2
337	43	1,25,14	27	25,12,7	34	1,25	30	25	1
353	179	1,12	30	3	28	3	17	-	3

TABLE 1 Values of Q and Lags (L) at which A.C.F.>2 St. ERR.

model (p,d,q) order DOF / grid point number	(0) (0,0,0) 29	(1) (2,0,2) (1,2) (1,2) 25	(2) (2,0,3) (1,2) (1,2,12) 24	(3) (2,0,3) (1,12)(1,2,12) 24	S/N%
4	4.5(20.3)	4.4(19.7)	4.4(19.4)	4.4(19.3)	5.2
8	4.1(17.0)	4.1(16.4)	4.1(16.7)	4.1(16.8)	3.5
26	4.2(17.4)	4.1(16.8)	4.1(16.7)	4.1(16.7)	4.0
33	4.0(16.2)	4.0(16.0)	4.0(16.0)	4.0(16.0)	1.25
45	3.9(15.2)	3.8(14.5)	3.8(14.5)	3.8(14.2)	7.0
52	4.6(21.4)	4.7(21.7)	4.7(21.9)	4.6(20.9)	2.4
66	4.7(22.3)	4.5(20.6)	4.5(20.6)	4.5(20.7)	8.25
79	4.7(22.4)	4.6(21.3)	4.6(21.3)	4.6(21.4)	5.5
115	3.8(14.7)	3.7(13.5)	3.7(13.5)	3.7(13.6)	8.9
152	4.0(15.8)	3.8(14.4)	3.8(14.4)	3.7(13.9)	13.7
197	3.8(14.1)	3.7(13.4)	3.7(13.4)	3.6(13.3)	6.0
249	3.3(11.0)	3.1(9.6)	3.1(9.7)	3.1(9.7)	14.6
267	2.4(5.9)	2.4(5.9)	2.4(5.9)	2.4(5.8)	1.7
284	3.3(10.8)	2.9(8.2)	2.9(8.2)	2.9(8.3)	31.7
296	2.6(6.7)	2.5(6.5)	2.5(6.3)	2.4(5.9)	13.6
299	3.0(9.0)	3.0(8.7)	2.9(8.6)	2.9(8.6)	4.6
337	2.1(4.4)	2.0(4.1)	2.0(4.2)	2.0(4.0)	10.0
353	2.4(5.9)	2.0(3.9)	2.0(3.9)	1.9(3.6)	63.9

TABLE 2 Residual Standard Deviation (dkm) (Residual mean variance)

model (p,d,q) order DOF / Component	(0,0,0) 35		(1,0,1) $(1)_{33}(1)$		
	Q	RMS	Q	RMS	S/N
1	327	1.04	35	.29	2.6
2	156	.74	22	.37	1.0
3	28	.58	19	.48	.21
4	43	.38	35	.33	.15
5	68	.31	20	.24	.29
6	32	.13	16	.12	.085
7	44	.07	24	.07	0

TABLE 3 Portmanteau Test and S/N ratio for Zonal Harmonics

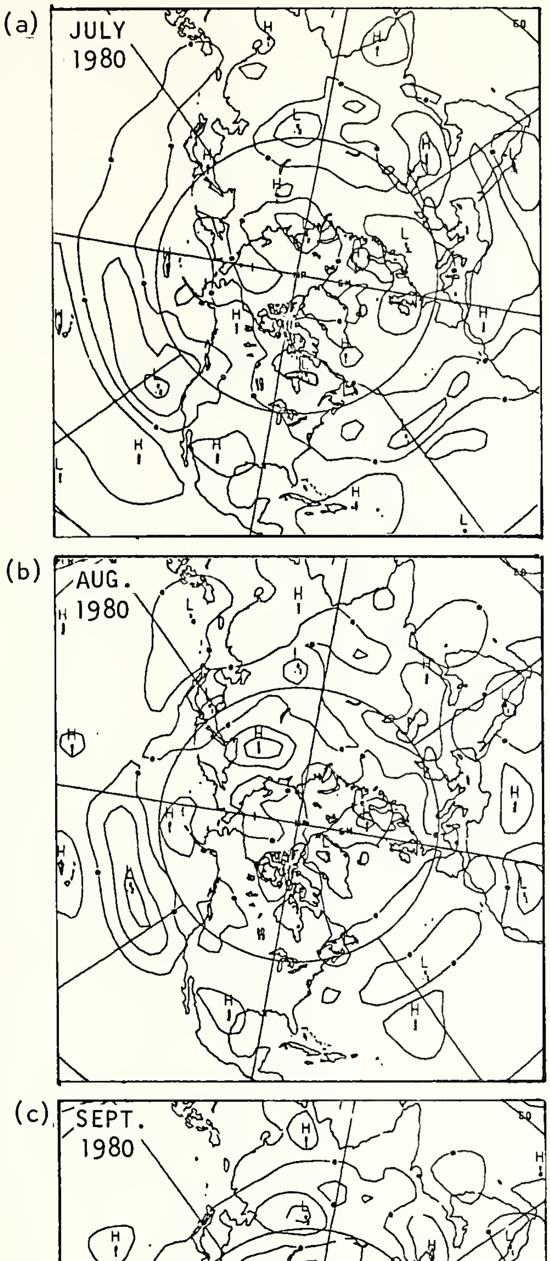

fig: 2(a)(b)(c)

ARIMA Forecasts of 50-100 kPa thickness anomalies (AR(1,2), MA(1,12))

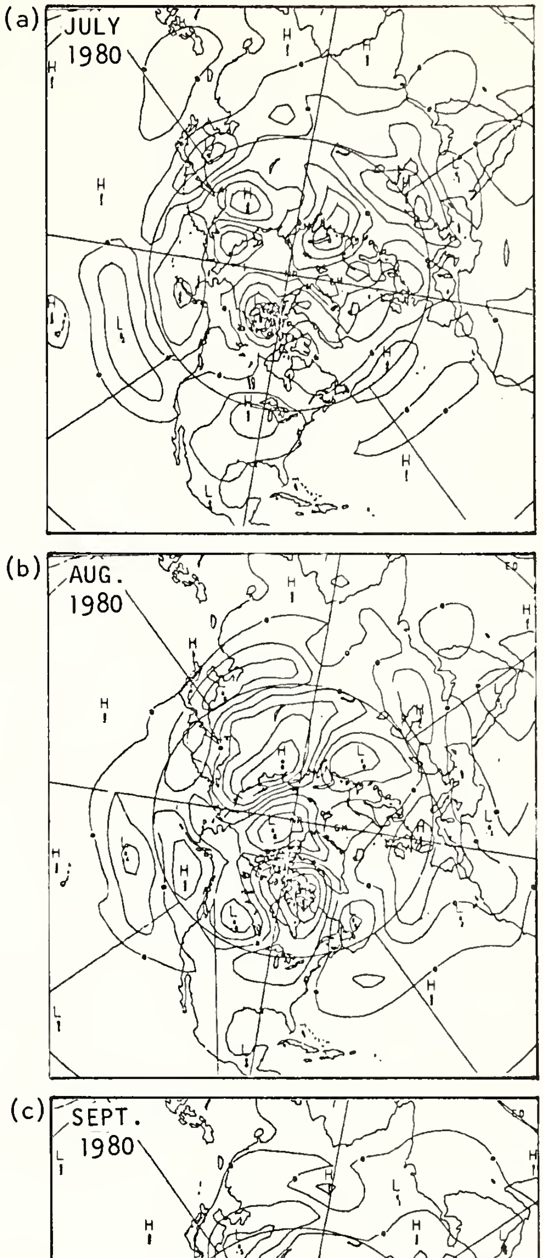

fig: 3(a)(b)(c)

Observed anomaly thickness fields

USAFETAC Sea Level Pressure Model
Seasonal Outlook for the Past Year

By

Capt James G. Schofield
U.S. Air Force Environmental Technical Applications Center
Scott AFB IL 62225

At the 1978 Climate Diagnostics Workshop, Dr Tim Barnett and James Schofield introduced a sea level pressure analog model for predicting seasonal temperature over North America. This model was adopted for use at the United States Air Force Environmental Technical Applications Center and has been used for the past 18 months to make experimental seasonal outlooks. This presentation addresses the seasonal outlooks for fall 1979 and winter, spring, summer 1980 and assesses the relative skill of the model over those four seasons.

The Sea Level Pressure Analog Model uses empirical orthogonal functions to represent the historical sea level pressure field for the area 150°E to 20°W, 20-60°N. The SLP data run from 1899 to the present. Climatic analogs are chosen based on the closest match between the EOF's of the SLP fields preceding the forecast season and an SLP field in the historical record. For example, the forecast for winter 1980 was obtained by searching for the closest match between the fall 1979 SLP field and a fall pattern in the historical record. Fall 1939 was selected as the best analog match. The temperature field for winter 1940 is then used as the forecast temperature field for winter 1980.

Figure 1 shows the network of 33 stations used in the forecast scheme. (This presentation is limited to continental United States stations only). Figure 2 depicts the forecast and observed temperature field for fall 1979. (Fall is defined as Sep, Oct, Nov.) Twenty-seven percent of the stations were forecast in the correct category. We would expect to hit 33% by chance, so this forecast was not very successful, Next we have the forecast and observed fields (figure 3) for winter 1980 (Dec 1979, Jan, Feb 80). Sixty-one percent of the forecasts were in the right category. This is considered to be an excellent forecast.

Figure 4 shows spring 1980 (Mar, Apr, May), where 45% of the forecasts were correct. This forecast can be characterized as successful. Finally, we have the forecast (figure 5) for summer, 1980 (Jun, Jul, Aug). As can be readily observed, this was a very poor forecast, with only 21% of the stations falling in the correct category.

When we lump all four seasons together, we find that the model was correct 38.5% of the time. A skill evaluation done during model development suggests that the skill of the model over the long run will average about 37% correct. The results for the four seasons fall 79 - summer 80 are consistent with this result.

In summary, the performance of the Sea Level Pressure Analog Model over the past year included one successful and one highly successful forecast and two very poor forecasts. The overall performance of the model is consistent with the expected skill level.

FIGURE 1

FORECAST NETWORK

(33 STATIONS)

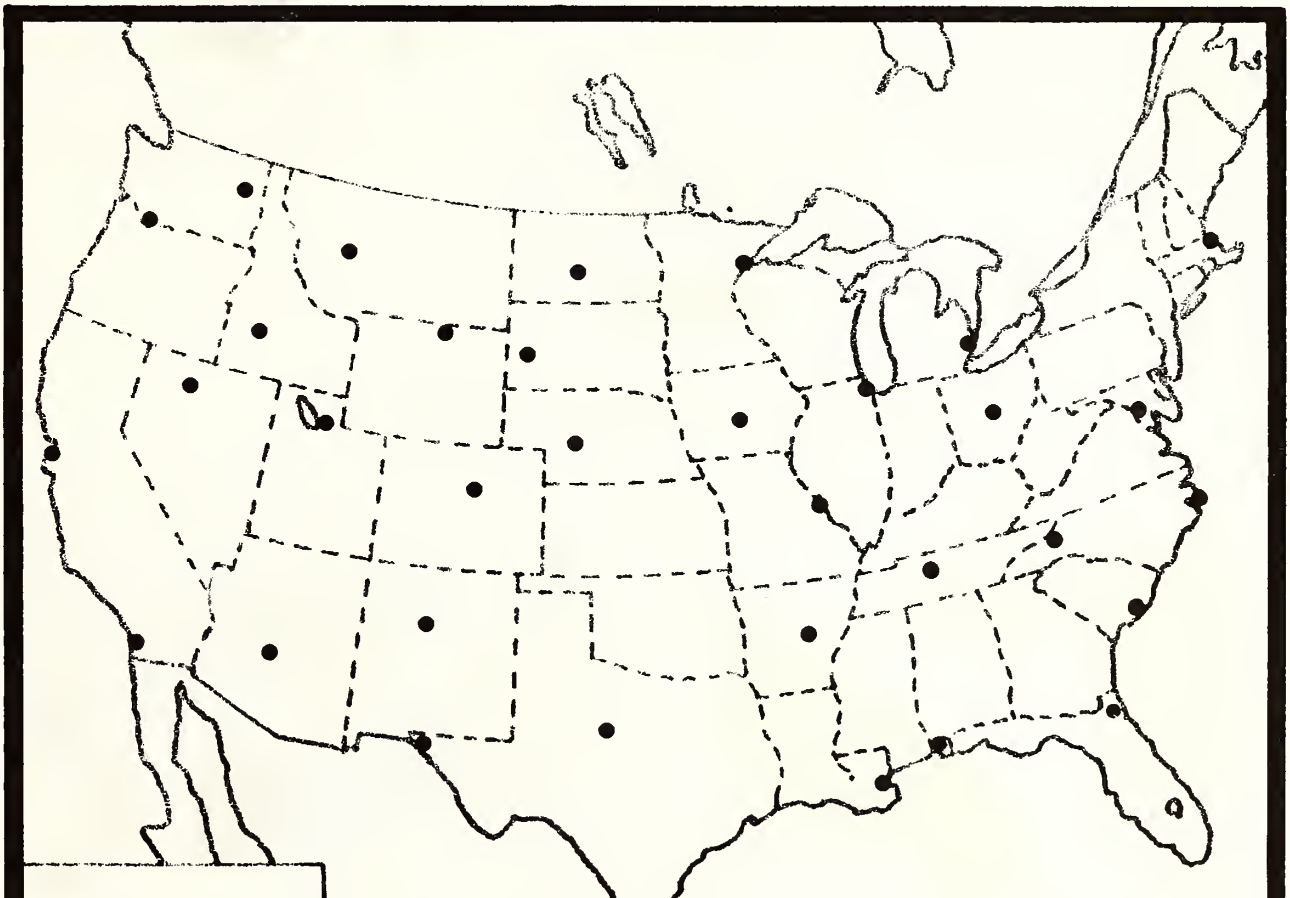

FIGURE 2

FALL 1979 - 27% CORRECT

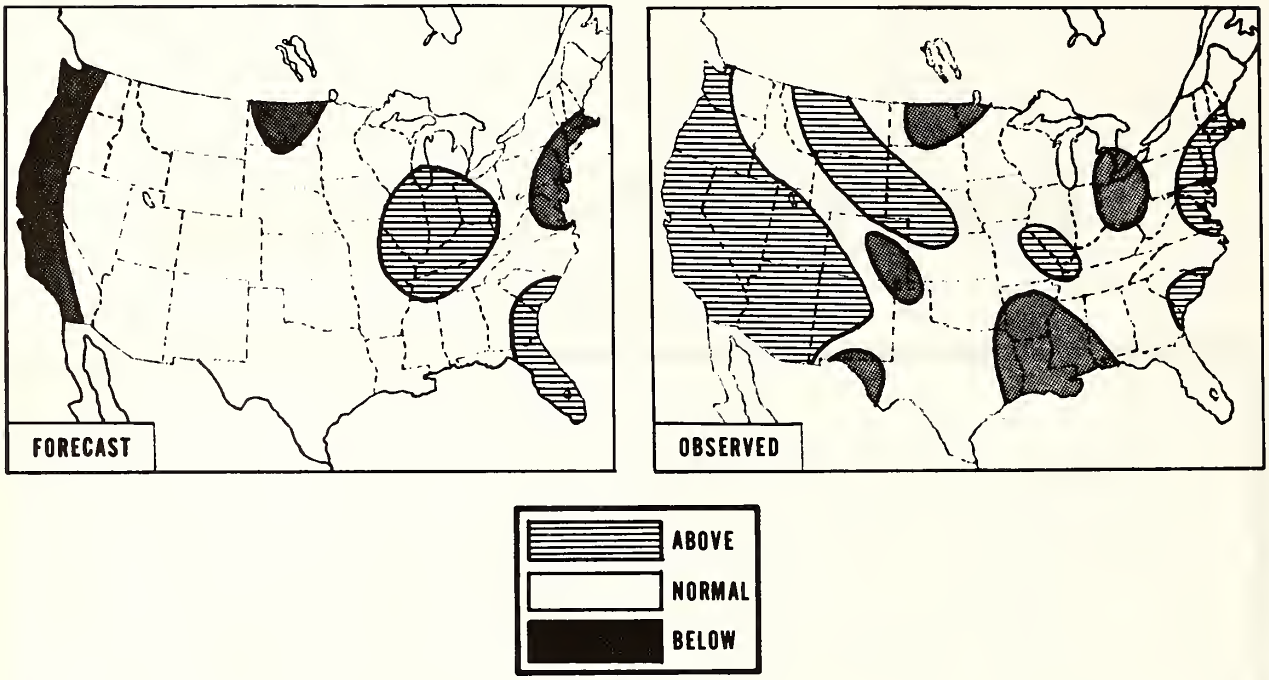

FIGURE 3

WINTER 1980 - 61% CORRECT

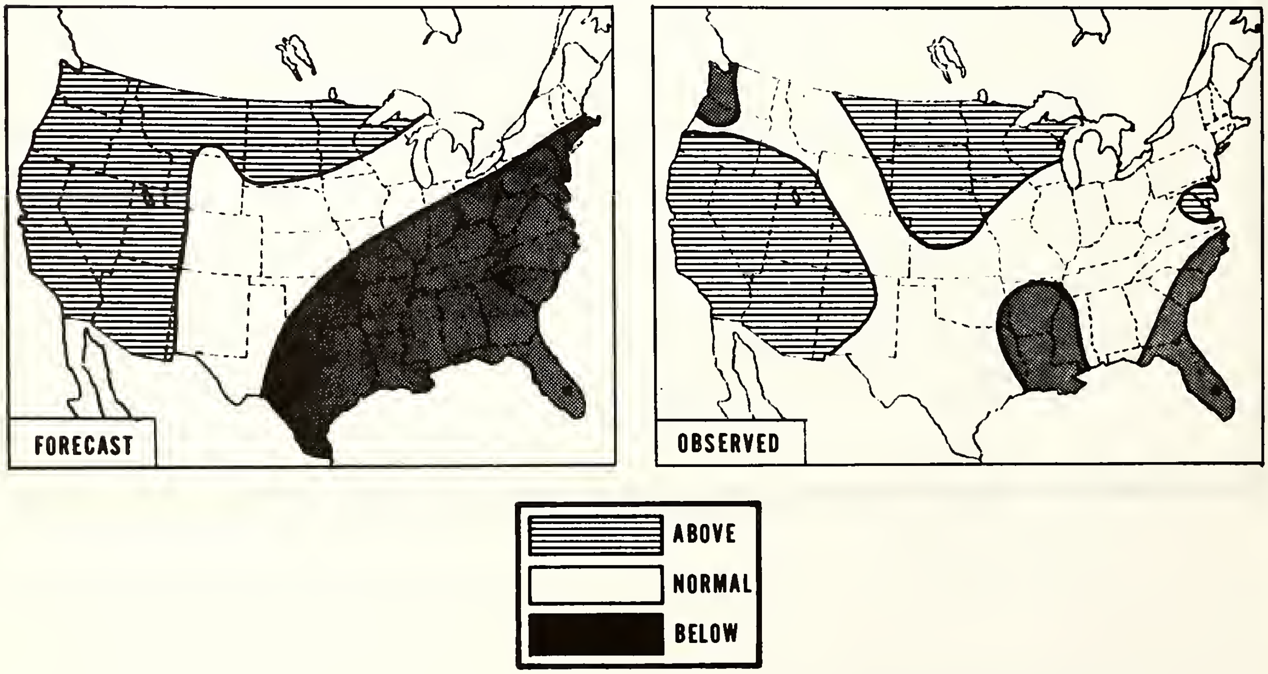

FIGURE 4
SPRING 1980 - 45% CORRECT

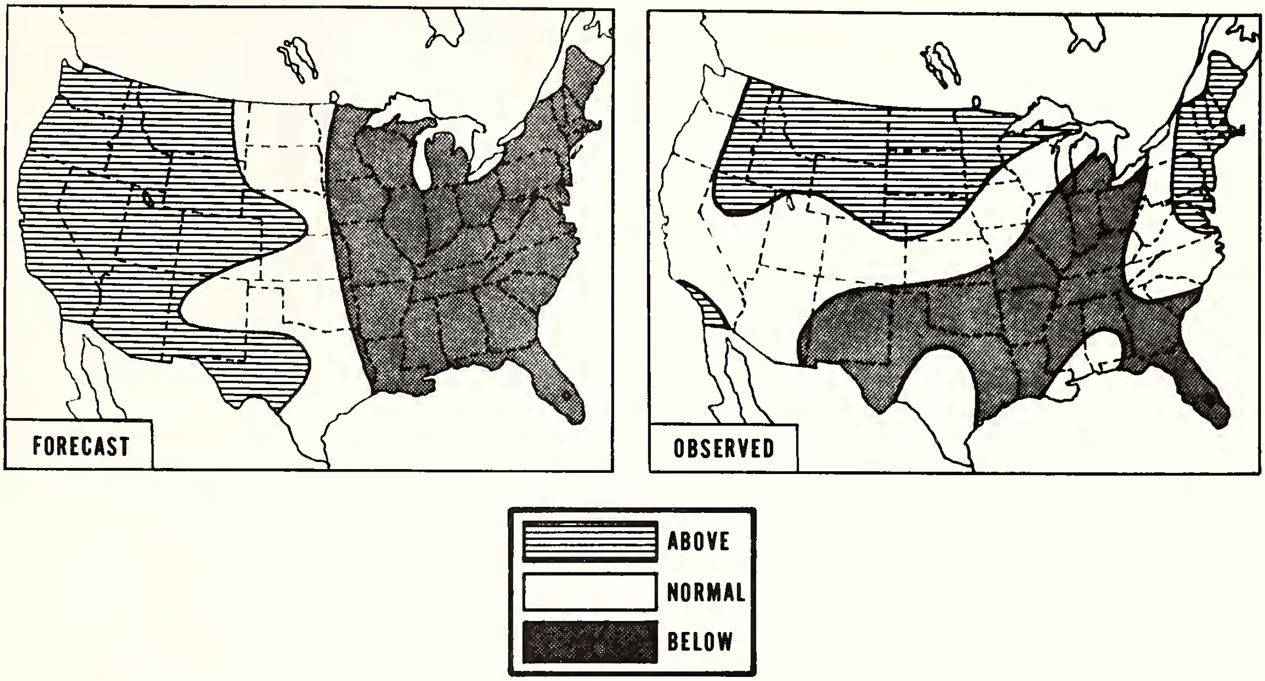

FIGURE 5
SUMMER 1980 - 21% CORRECT

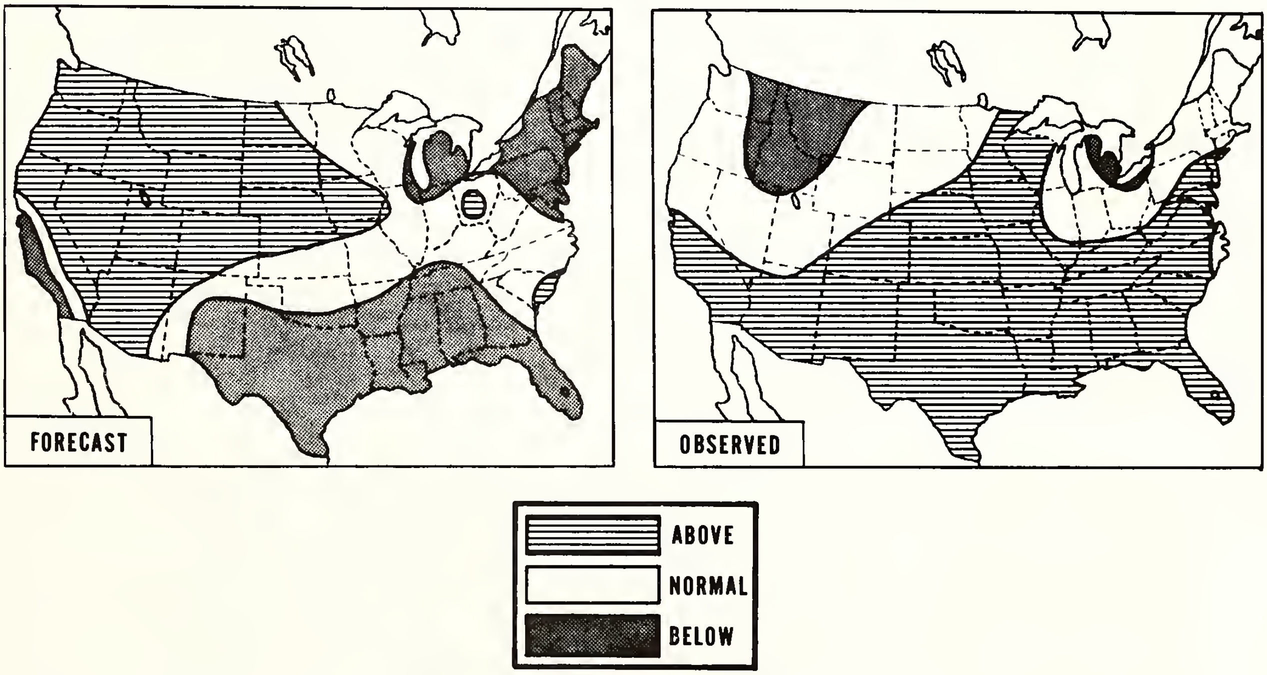

Long range precipitation forecasting with a new UW model

Jerome B. Blechman and Reid A. Bryson
Center for Climatic Research
University of Wisconsin
Madison, Wisconsin 53706

The University of Wisconsin long range forecast model has evolved since Dittberner's (1978) report on its effectiveness for multiyear prediction. The current version is denoted UW 80 MK II. In addition to the low frequency and high frequency submodels cited by Dittberner, a very high frequency input based on the quasi-biennial oscillation was used in the current model.

Another modification in method was the identification of "predictors" which, because of deficiencies in the linear regression technique, were inappropriate in certain geographical areas (also from Dittberner, 1978). These were not used in forecasting for such areas, thus allowing the more realistic predictors to dominate the forecasts. To ensure that forecast value was a result of physically realistic processes being modeled, all UW 80 MK II forecasts were subject to control criteria designed to maximize compatibility between the dependent and independent data.

For 1-year-ahead forecasts, UW 80 MK II compiled monthly 2x2 and 3x3 skill scores as shown in Table 1. These scores are based on equal partitioning of the data into two (2x2) and three (3x3) categories. Also shown, for comparison, are the scores achieved by a simple 1-year-persistence forecast scheme. Table 1 shows a complex yearly variation of skill, especially 2x2 skill, with highest scores in February, December, and September. The model outperformed persistence consistently.

8380 forecasts were analyzed (up to 19 consecutive independent years for each station) and aggregate yearly skill scores were .198 (2x2) and .050 (3x3). Based on a binomial distribution of forecast events, confidence that skill was not due to chance alone was greater than 99.9% for both of these scores.

Figs. 1-3 show UW 80 MK II forecasts for precipitation for June to August, 1980, along with corresponding verifications. Only predictions for which verifications were available at the time of this writing are shown. These were real-time 1-year forecasts made using data through 1979 and were not included in the scores in Table 1. 2x2 skills for these three maps were .267 for June, .231 for July, and .138 for August. Summer 1981 forecasts, shown in Figs. 4-6, indicate the possibility of another severe drought in the southern United States.

A feature missed by the model was the heavy precipitation in August, 1980, in the Great Lakes area (Fig. 3). This underscores the need for further improvement. Two possibilities are nonlinear, rather than linear regression, and areal, rather than station forecasts. Nonlinear regression would allow amplitudes of the prediction parameters to be modeled. This would help in prediction of extremes and should improve the 3x3 skill scores. Areal forecasts would allow a more complete geographical coverage, since difficult local effects (such as urban heat islands), which sometimes prevent meaningful station forecasts, could be circumvented.

REFERENCE

Dittberner, G.J., 1978: Application of the University of Wisconsin model to climate prediction. Proceedings of the Third Annual Climate Diagnostics Workshop. pp. 32-1 to 32-4.

Table 1

Summary of UW 80 MK II Precipitation Skill Scores

	Jan	Feb	Mar	Apr	May	June	July	Aug	Sept	Oct	Nov	Dec	Year
FCSTS	797	778	588	494	494	645	702	681	739	778	908	776	8380
STAS	42	41	31	26	26	34	37	36	39	41	48	41	442
2x2 (I)	.197	.242	.228	.057	.158	.169	.197	.219	.288	.165	.205	.250	.198
3x3 (I)	.031	.053	.084	.037	.071	.040	.056	.007	.050	.036	.060	.078	.050
2x2 (P)	-.022	-.015	.000	-.041	.000	.001	.088	-.089	-.029	.023	.038	.033	-.001
3x3 (P)	.021	-.035	.013	-.005	.038	.026	.056	-.038	-.032	.012	.060	.023	.012

KEY: I = Independent data skill scores; P = Persistence skill scores;

STAS = Number of stations; FCSTS = Number of forecasts (up to 19 for each station).

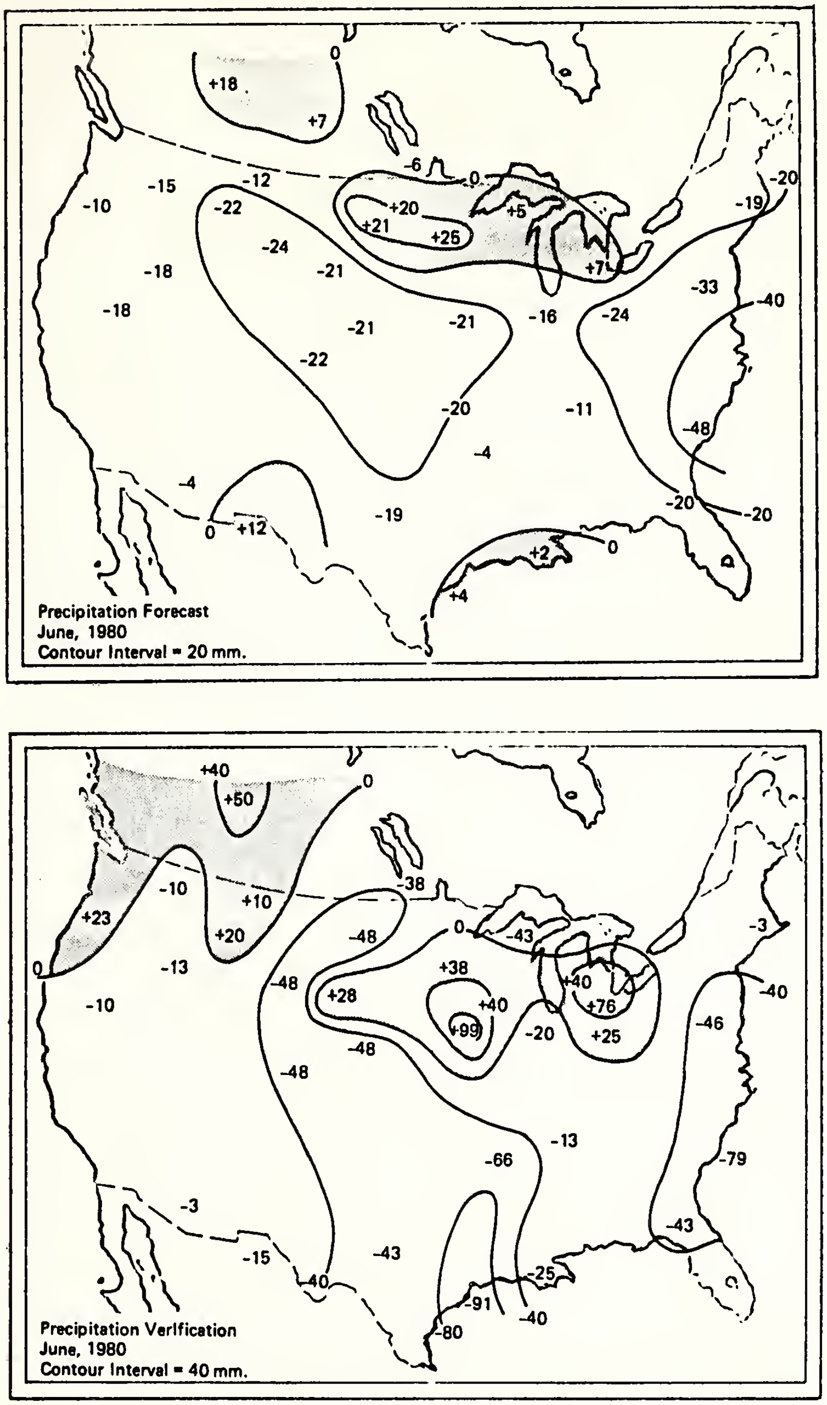

Fig. 1. UW 80 MK II forecast (top) and verification from teletype reports (bottom) for June, 1980. Departures from 1941-70 means in millimeters. Positive anomalies shaded. Map correlation = 0.204.

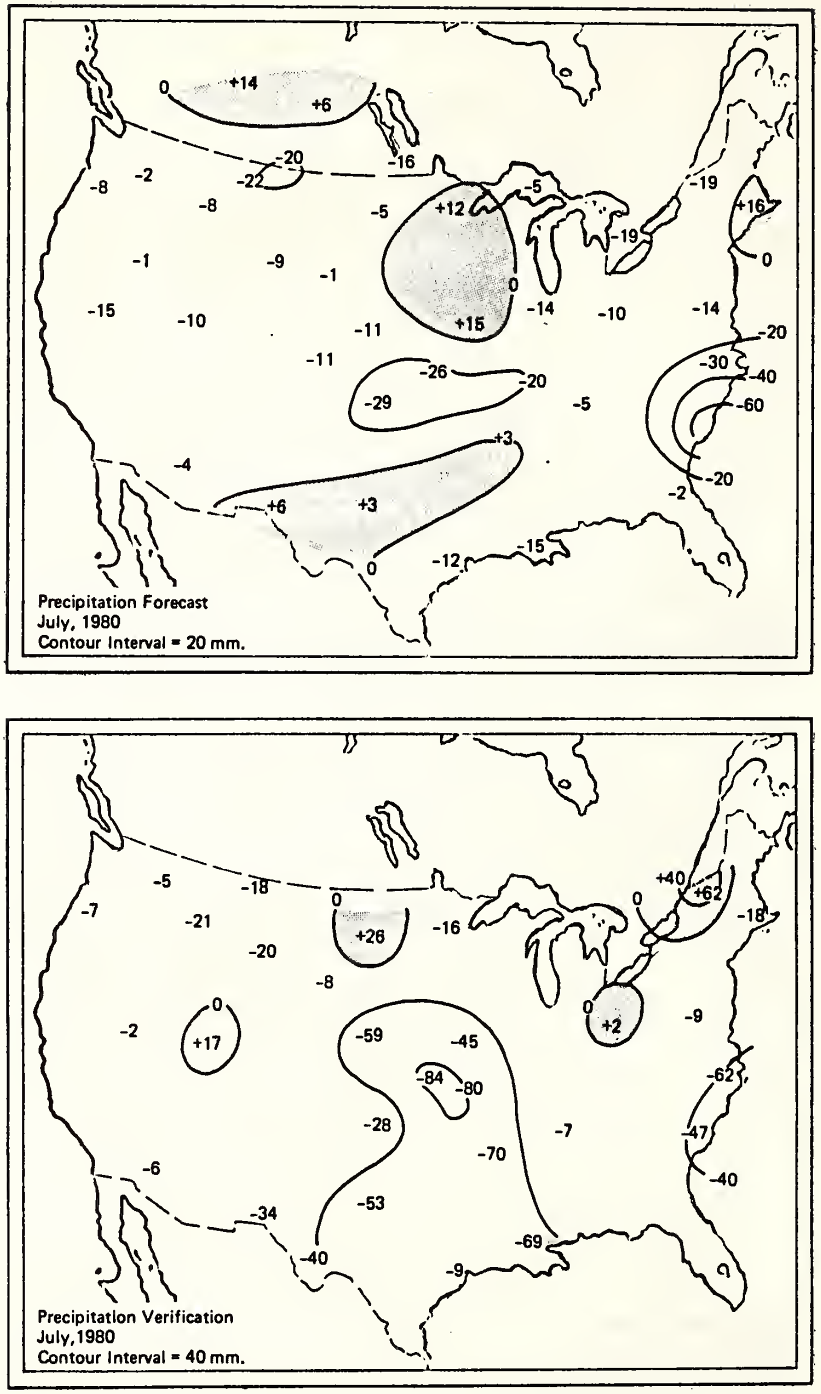

Fig. 2. As in Fig. 1, except for July, 1980.
Map correlation = 0.131.

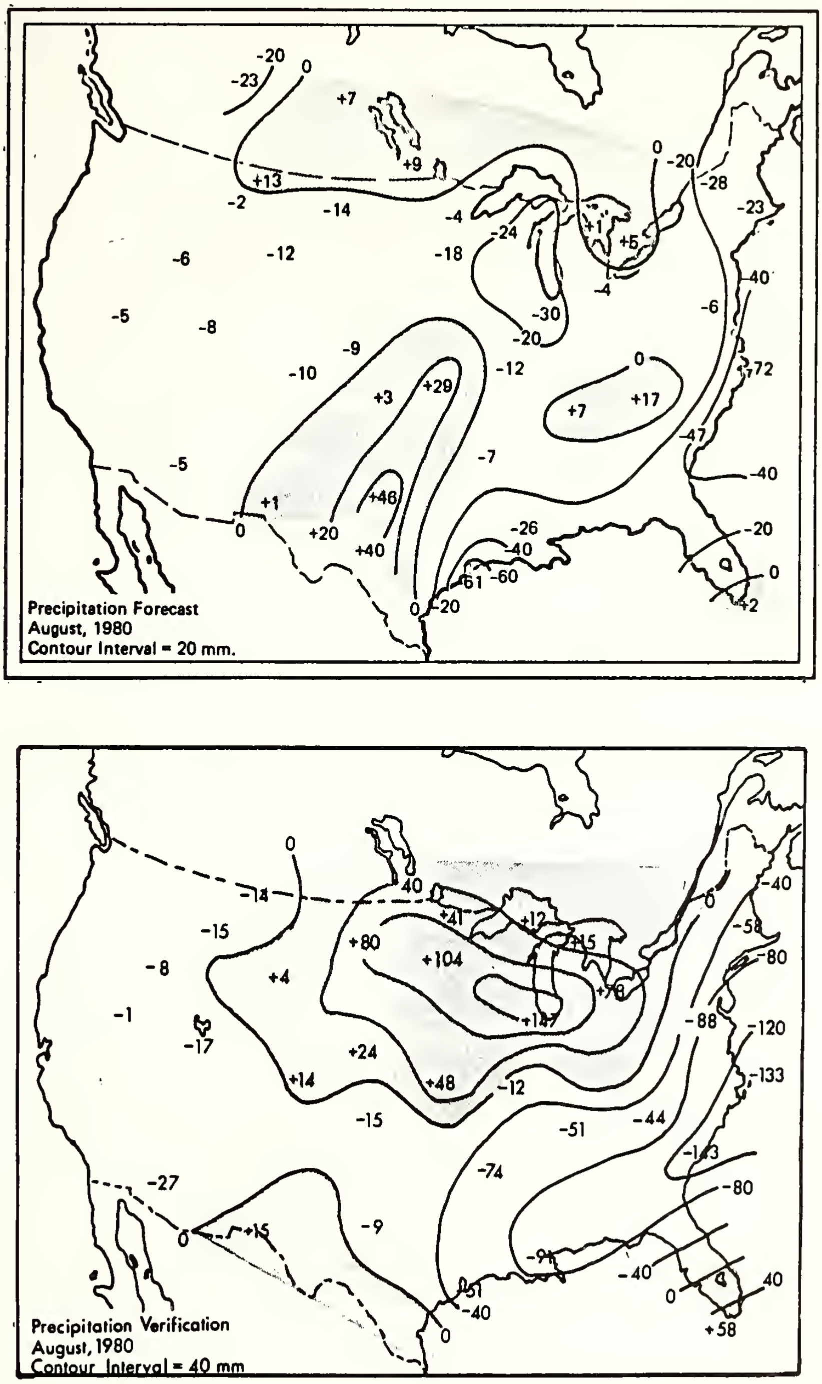

Fig. 3. As in Fig. 1, except for August, 1980.
Map correlation = 0.332.

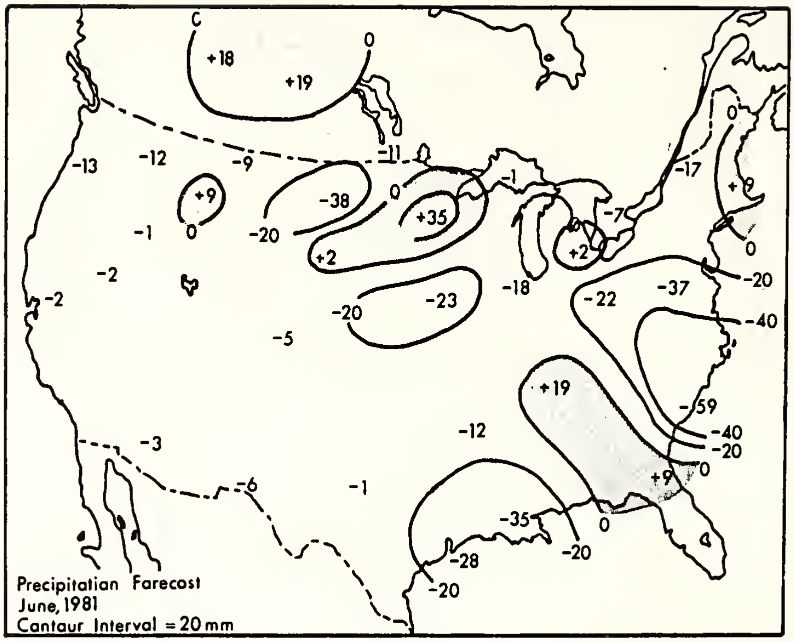

Fig. 4. UW 80 MK II forecast for June, 1981. Departures from 1941-70 means in millimeters. Positive anomalies shaded.

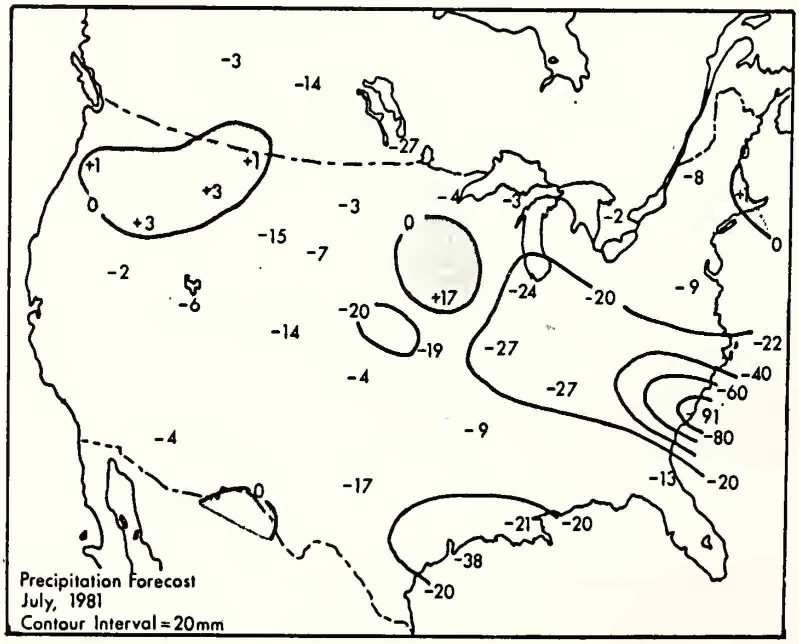

Fig. 5. As in Fig. 4, except for July, 1981.

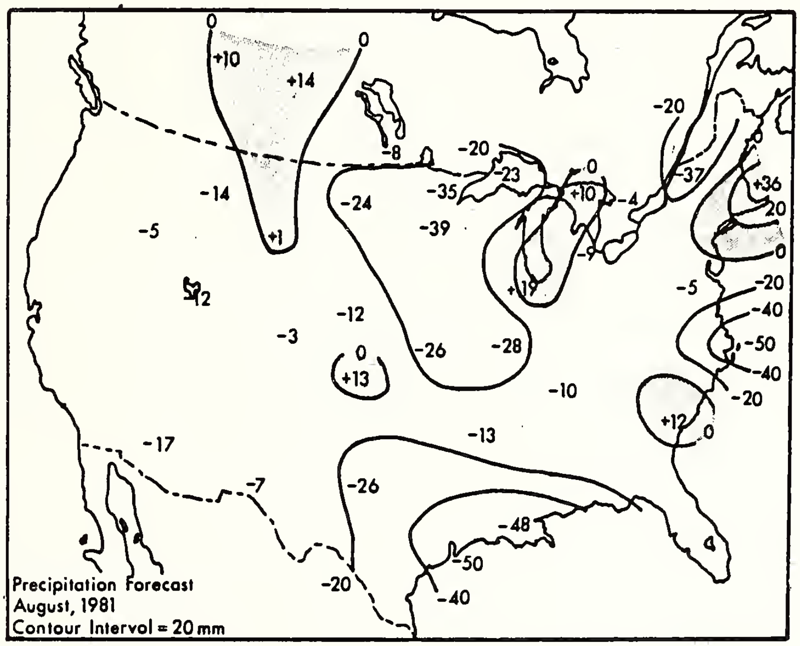

Fig. 6. As in Fig. 4, except for August, 1981.

☆U.S. GOVERNMENT PRINTING OFFICE: 1981-340-997/1609

A000014321153